JNM

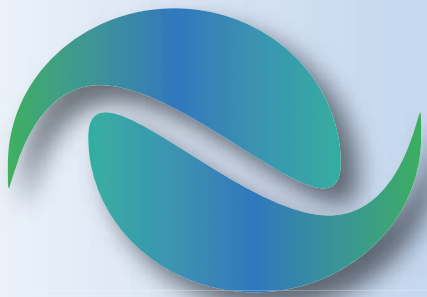## The Journal of Nuclear Medicine

FEATURED ARTICLE

CD8-Targeted PET Imaging of Tumor-Infiltrating T Cells in Patients with Cancer: A Phase I First-in-Humans Study of ^{89}Zr-Df-IAB22M2C, a Radiolabeled Anti-CD8 Minibody. Michael Farwell et al. See page 720.

^{18}F-FDG–avid melanoma metastases

Baseline: ^{18}F-FDG PET/CT

Lymph Nodes
Spleen
Bone Marrow

CD8+ melanoma metastases

1 Month After Immunotherapy: Whole-body CD8 PET/CT

Complete response

21 Months After Immunotherapy: CT

SNMMI | Value Initiative
SOCIETY OF NUCLEAR MEDICINE & MOLECULAR IMAGING
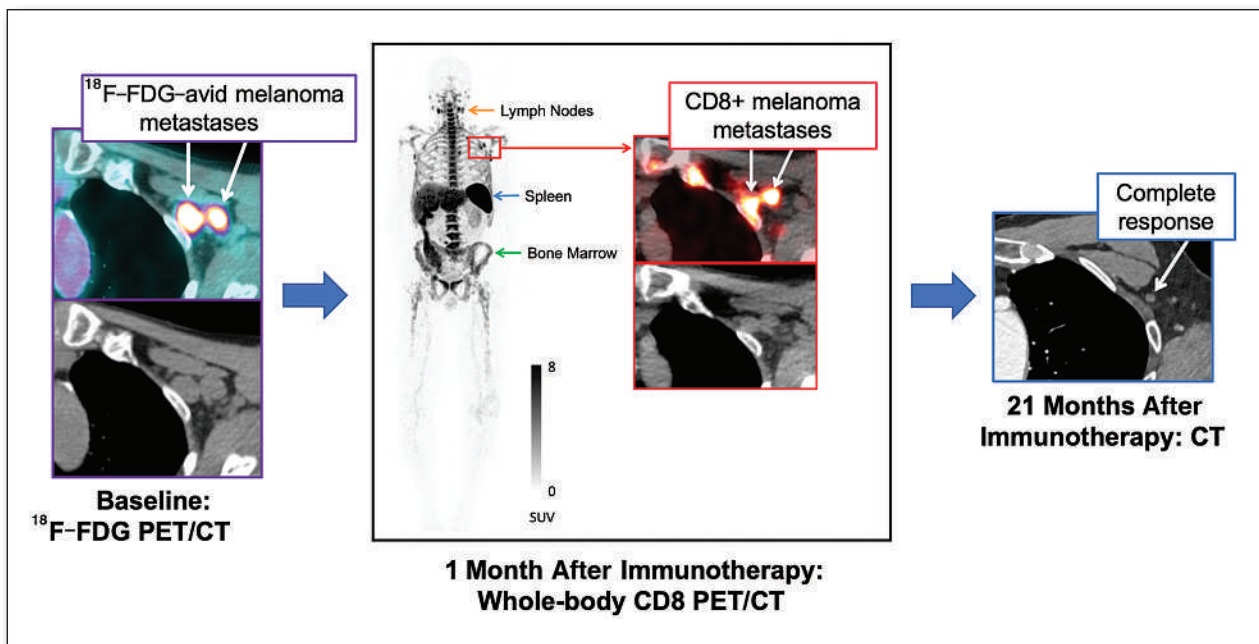
Accuracy counts!

Avoid patient administration errors!
THE FIRST EVER simulated
I-131 source using
NIST traceable Ba-133.

RADQUAL

Global Sources

♦ Ensure that your I-131measurements are accurate to within + or -5% utilizing RadQual's new Simulated I-131 Sources. Available in two different geometries.

♦ RadQual's Patent Pending source designs are intended to mimic a 5 cc syringe or a capsule contained in a 15ml vial.

♦ New Patent Pending Simulated I-131 Capsule design allows calibration of individual doses.

Simulated I-131 Source vs Ba-133 Source Measured Activity (uCi)

- Ba-133 Activity
- Simulated I-131 Activity
- Unattenuated Ba-133 response on I-131 Channel
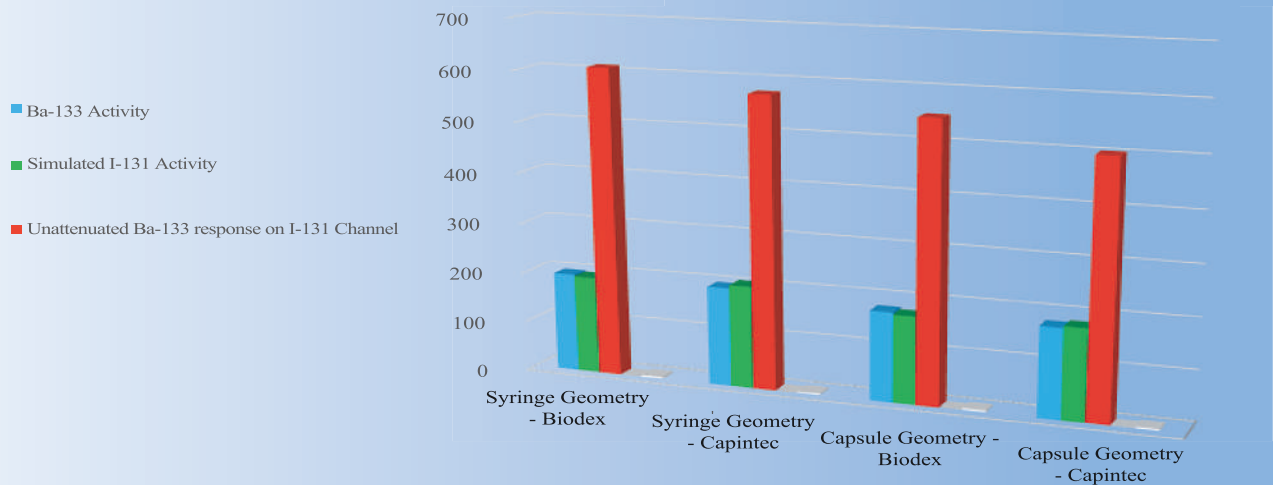
	Syringe Geometry - Biodex	Syringe Geometry - Capintec	Capsule Geometry - Biodex	Capsule Geometry - Capintec
Simulated I-131 Error	-1.57%	3.62%	-2.35%	2.02%
Ba-133 Overestimate on I-131 Channel	310%	293%	309%	282%

The design of RadQual's patent pending Simulated I-131 Source geometries better aligns the photon energy spectrum and yield, giving results within 5% of the NIST traceable Ba-133 activity, when measured on the I-131 dial setting of the dose calibrator.

www.radqual.com   (208) 524-5300   Email: info@radqual.com

JNM

ATTEND THE SNMMI 2022 ANNUAL MEETING

The **SNMMI 2022 Annual Meeting** provides you with access to 130+ scientific and CE sessions, more than 1,000 scientific posters, pre-meeting categorical seminars, industry-led satellite symposia, and great networking events. Plus, you can learn about leading products and innovations in the field from more than 150 exhibiting companies.

It's the can't miss opportunity for you to elevate your skills and be the expert in your clinic on the latest developments, research, and clinical applications advancing precision medicine and therapy. *View page 4 for the Schedule-at-a-Glance.*

June 11-14
2022
SNMMI ANNUAL MEETING
Vancouver, British Columbia Canada

Register Today

WWW.SNMMI.ORG/AM2022

SNM MI | 2022 Annual Meeting

Virtual registration options are also available.

SNMMI ANNUAL MEETING
Schedule-at-a-Glance

SATURDAY
JUNE 11, 2022

7:30 am–3:00 pm
Categorical Seminars

8:00 am–4:45 pm
Nuclear Medicine Review Course (NMRC) – Day 1

8:00 am–4:00 pm
SNMMI-TS CE Courses

9:00 am–4:45 pm
Educators Forum I & II

1:30–4:45 pm
SNMMI CE Courses

3:15–4:45 pm
Scientific Sessions

5:00-6:00 pm
Opening Ceremony

6:00–8:00 pm
Welcome Reception: Exhibit and Poster Hall Opening

8:00 pm–End
User Meetings

SUNDAY
JUNE 12, 2022

6:00–8:00 am
User Meetings

6:30–7:45am
Women in Nuclear Medicine (WINM) Breakfast

6:45–7:45 am
Satellite Symposia

8:00 am–5:30pm
Nuclear Medicine Review Course (NMRC) – Day 2

8:00–9:30 am
Opening Plenary Session: Henry N. Wagner Jr., MD, Lectureship

9:30 am–4:30 pm
Exhibit Hall Open

10:00 am–8:30 pm
Poster Hall Open

11:15 am–12:15 pm
Satellite Symposia

12:15–2:00 pm
Technologist Plenary Session & Awards Recognition

12:30-2:00 pm
Nuclear Medicine Knowledge Bowl

12:30–6:15 pm
SNMMI CE Courses & Scientific Abstract Presentations

2:45–4:45 pm
Educators Forum III

3:00–6:15 pm
SNMMI-TS CE Courses & Scientific Abstract Presentations

4:45–6:15 pm
Radiopharmaceutical Sciences Council (RPSC)/ CMIIT Basic Science Summary Session

4:30–6:00 pm
Emerging Technologies Session (CMIIT) #1 (Non-CE)

6:30–7:30 pm
Satellite Symposia

6:30–8:30 pm
Poster Mixer

6:30 pm–End
User Meetings

MONDAY
JUNE 13, 2022

6:00–8:00 am
User Meetings

6:45–7:45 am
Satellite Symposia

8:00–9:30 am
SNMMI Special Plenary/ Cassen Lectureship

9:00 am–6:00 pm
Poster Hall Open

9:30 am–4:30 pm
Exhibit Hall Open

10:00-11:30 am
Emerging Technologies Session (CMIIT) #2 (Non-CE)

10:00 am–4:45 pm
SNMMI-TS CE Courses

10:00 am–5:30 pm
SNMMI CE Courses & Scientific Abstract Presentations

11:45 am–12:45 pm
Satellite Symposia

2:45 - 3:34 pm
Early Career Professionals (ECP) Awards Ceremony

3:00–7:00 pm
Emerging Technologies Session (CMIIT) #3 (Non-CE)

4:00–5:30 pm
Instrumentation and Data Analysis Basic Science Summary Session

4:45–6:15 pm
SNMMI-TS Business Meeting

5:45–7:00 pm
Meet the Author/Poster Hall Reception

6:00 pm–End
User Meetings

TUESDAY
JUNE 14, 2022

6:00–8:00 am
User Meetings

6:45–7:45 am
Satellite Symposia

8:00 am–11:30 am
SNMMI-TS CE Courses

8:00 am–4:30 pm
SNMMI CE Courses & Scientific Abstract Presentations

9:00 am–5:00 pm
Poster Hall Open

9:30 am–3:00 pm
Exhibit Hall Open

11:45 am–12:45 pm
Satellite Symposia

3:00–4:30 pm
Poster Hall - POPs Session

4:45–6:30 pm
Henry N. Wagner, Jr., MD Highlights Symposium

6:30 pm
Closing Celebration

SNMMI

2022 Annual Meeting

Register Today
WWW.SNMMI.ORG/AM2022

Virtual registration options are also available.

JNM

The Journal of
NUCLEAR MEDICINE

The Official Publication of **SNMMI**

MISSION STATEMENT: *The Journal of Nuclear Medicine* advances the knowledge and practice of molecular imaging and therapy and nuclear medicine to improve patient care through publication of original basic science and clinical research.

DISCLOSURE OF COMMERCIAL INTEREST: Johannes Czernin, MD, editor-in-chief of *The Journal of Nuclear Medicine,* has indicated that he is a founder of Sofie Biosciences and holds equity in the company and in intellectual property invented by him, patented by the University of California, and licensed to Sofie Biosciences. He is also a founder and board member of Trethera Therapeutics and holds equity in the company and in intellectual property invented by him, patented by the University of California, and licensed to Triangle. He also serves on the medical advisory board of Actinium Pharmaceuticals and on the scientific advisory boards of POINT Biopharma, RayzeBio, and Jubilant Pharma and is a consultant for Amgen. No other potential conflicts of interest were reported. Manuscripts submitted to *JNM* with potential conflicts are handled by a guest editor.

EDITORIAL COMMUNICATIONS should be sent to: Editor-in-Chief, Johannes Czernin, MD, *JNM* Office, SNMMI, 1850 Samuel Morse Drive, Reston, VA 20190-5316. Phone: (703) 326-1185; Fax: (703) 708-9018. To submit a manuscript, go to https://submit-jnm.snmjournals.org.

BUSINESS COMMUNICATIONS concerning permission requests should be sent to the publisher, SNMMI, 1850 Samuel Morse Drive, Reston, VA 20190-5316; (703) 708-9000; home page address: jnm.snmjournals.org. Subscription requests and address changes should be sent to Membership Department, SNMMI at the address above. Notify the Society of change of address and telephone number at least 30 days before date of issue by sending both the old and new addresses. Claims for copies lost in the mail are allowed within 90 days of the date of issue. Claims are not allowed for issues lost as a result of insufficient notice of change of address. For information on advertising, contact Team SNMMI (Kevin Dunn, Rich Devanna, and Charlie Meitner; (201) 767-4170; fax: (201) 767-8065; TeamSNMMI@cunnasso.com). Advertisements are subject to editorial approval and are restricted to products or services pertinent to nuclear medicine. Closing date is the first of the month preceding the date of issue.

INDIVIDUAL SUBSCRIPTION RATES for the 2022 calendar year are $603 within the United States and Canada; $648 elsewhere. Make checks payable to the SNMMI. CPC IPM Sales Agreement No. 1415158. Sales of individual back copies from 1999 through the current issue are available for $60 at http://www.snmmi.org/subscribe (subscriptions@snmmi.org; fax: (703) 667-5134). Individual articles are available for sale online at http://jnm.snmjournals.org.

The ideas and opinions expressed in *JNM* do not necessarily reflect those of the SNMMI or the Editors of *JNM* unless so stated. Publication of an advertisement or other product mentioned in *JNM* should not be construed as an endorsement of the product or the manufacturer's claims. Readers are encouraged to contact the manufacturer with any questions about the features or limitations of the products mentioned. The SNMMI does not assume any responsibility for any injury or damage to persons or property arising from or related to any use of the material contained in this journal. The reader is advised to check the appropriate medical literature and the product information currently provided by the manufacturer of each drug to be administered to verify the dosage, the method and duration of administration, and contraindications.

Achieve the True Mark of

Excellence in Patient Care

for Your Facility with IAC

ACCREDITED FACILITY

IAC
INTERSOCIETAL
ACCREDITATION
COMMISSION

Earning IAC accreditation indicates that your facility is:

Dedicated to Quality and Patient Safety

IAC's seal of approval verifies the quality your patients deserve. By earning IAC accreditation, you are showing referring physicians, patients and insurers that **your facility has undergone a rigorous evaluation, has been found to be in compliance with industry standards and is committed to continuous quality improvement**.

Engaged in Continuous Improvement

The IAC accreditation process is more than an update every three years. Accredited facilities receive a detailed Application Review Findings document as a **tool for improving the overall quality of their facility**. Special topic webinars, a CE finder and the IAC Quality Improvement (QI) Self-Assessment Tool are offered complimentary. Facilities use the QI Tool to assess case studies and final reports and receive a quantitative report targeting opportunities for continuous process improvement.

Complying with Reimbursement and Regulatory Mandates

IAC notifies CMS and third-party payers of the status of accredited facilities to help ensure compliance with related mandates. Physicians may also utilize IAC accreditation to satisfy a component of the Centers for Medicare & Medicaid Services (CMS) MIPS Improvement Activity as part of the MACRA Quality Payment Program. The IAC QI Tool is an independent option that may also be utilized to satisfy the MIPS Improvement Activity and MOC.

Diagnostic Imaging Accreditation

Vascular Testing . Echocardiography
Nuclear/PET . MRI . CT / Dental CT

IAC

Vascular and Cardiac Intervention Accreditation

Carotid Stenting . Cardiac Electrophysiology
Vein Center . Cardiovascular Catheterization

Improving health care through accreditation® | **intersocietal.org** | 800.838.2110

Coming Soon! Deep Venous Intervention . Hemodialysis Access Intervention . Peripheral Arterial Intervention
Perioperative Transesophageal Echocardiography . Adult Congenital Transthoracic Echocardiography

RADIATION SAFETY+ Review and Essentials

Let the SNMMI-TS Help You Prepare for the NMTCB's Radiation Safety Exam

Get the tools you need to successfully prepare for the exam with the **Radiation Safety + Review and Essentials** program. This 5 module/7.75 VOICE credit course provides a comprehensive review of all aspects of radiation safety including:

- Radiation physics and instrumentation
- Dosimetry
- Mathematics
- Security and control
- Shipping and receiving

- Disposal
- Emergency procedures
- Regulations
- Radiation protection and ALARA
- Radionuclide therapy best practices

You'll review content on CT. X-ray, fluoroscopy, and MRI, as well as optimizing radiation exposure, including appropriateness criteria, Image Wisely/Image Gently, and special populations. Plus, test what you've learned with a 150 question "Mock Exam," to ensure you're fully prepared for the exam.

Member: $99 | Non-Member: $249

Get started today!
www.snmmi.org/RadiationPlus

SNMMI | **Technologist Section**

SOCIETY OF NUCLEAR MEDICINE & MOLECULAR IMAGING

Explore SNMMI's Online Career Center!

Explore the benefits of the SNMMI Career Center by logging in or creating a new account today.

careercenter.snmmi.org

SNMMI | Value Initiative
SOCIETY OF NUCLEAR MEDICINE & MOLECULAR IMAGING

FDA Approves Pluvicto/Locametz for Metastatic Castration-Resistant Prostate Cancer

On March 23, the U.S. Food and Drug Administration (FDA) announced the approval of Pluvicto (^{177}Lu-vipivotide tetraxetan, referred to previously and in the nuclear medicine literature as ^{177}Lu–prostate-specific membrane antigen–617 [^{177}Lu-PSMA-617]) for treatment of adult patients with PSMA-positive metastatic castration-resistant prostate cancer (mCRPC) who have been treated with androgen-receptor pathway inhibition and taxane-based chemotherapy. On the same day, the FDA approved Locametz (kit for preparation of ^{68}Ga-gozetotide injection), a PET agent for PSMA-positive lesions, including selection of patients with metastatic prostate cancer for whom ^{177}Lu-vipivotide tetraxetan PSMA-directed therapy is indicated. Locametz is the first radioactive diagnostic agent approved in the United States for patient selection in the use of a radioligand therapeutic agent. Pluvicto is the first FDA-approved targeted radioligand therapy for eligible patients with mCRPC that combines a targeting compound (ligand) with a therapeutic radioisotope. Novartis (Basel, Switzerland) announced on the same day that its radiopharmaceutical company, Advanced Accelerator Applications USA, Inc. (Millburn, NJ), expected to have both Pluvicto and Locametz available to physicians and patients within weeks of the approval.

The FDA granted Priority Review for ^{177}Lu-PSMA-617 in September 2021 based on positive data from the multicenter phase III VISION study (NCT 03511664), which provided the efficacy data on which the current approval was based. The study was a randomized (2:1), multicenter, open-label trial that evaluated ^{177}Lu-PSMA-617 plus best standard of care or best standard of care alone (control arm) in 831 men with progressive, PSMA-positive mCRPC. All patients received a gonadotropin-releasing hormone analog or had prior bilateral orchiectomy. Patients were required to have received at least 1 androgen-receptor pathway inhibitor, and 1 or 2 prior taxane-based chemotherapy regimens. Patients in the treatment arm ($n = 551$) received 7.4 GBq (200 mCi) Pluvicto every 6 weeks for a total of up to 6 doses plus best standard of care. The remaining 280 patients in the control arm received best standard of care alone. The trial demonstrated a statistically significant improvement in the primary endpoints of overall survival and radiographic progression-free survival. The hazard ratio for overall survival was 0.62 (95% CI: 0.52, 0.74) for comparison of the treatment arm versus the best-standard-of-care-alone arm. Median overall survival was 15.3 months in the treatment arm and 11.3 months in the control arm. Interpretation of the magnitude of the radiographic progression-free survival effect was limited because of the number of early dropouts in the control arm. About a third (30%) of patients with evaluable disease at baseline demonstrated an overall response (per RECIST 1.1) with Pluvicto plus standard of care, compared to only 2% in the control arm. The most common adverse events (all grades) reported in the Pluvicto arm of the study were fatigue (43%), dry mouth (39%), nausea (35%), anemia (32%), decreased appetite (21%), and constipation (20%).

The FDA advised that patients with previously treated mCRPC should be selected for treatment with Pluvicto using Locametz or another approved PSMA-11 imaging agent based on PSMA expression in tumors. PSMA-positive mCRPC was defined as having at least 1 tumor lesion with ^{68}Ga-gozetotide uptake greater than normal liver uptake.

"We are delighted by the FDA approval of this transformational, innovative therapy for men with advanced metastatic castrate-resistant prostate cancer," said SNMMI President Richard L. Wahl, MD, in an SNMMI press release praising the approval. "We are proud of the society members who contributed substantially to this new theranostic paradigm, as well as all of the authors who published articles on this therapy in *The Journal of Nuclear Medicine*."

This work builds on the success of prior radiopharmaceutical therapies such as ^{177}Lu-DOTATATE, which has provided significant clinical benefit to patients with neuroendocrine tumors. SNMMI indicated that it plans to provide guidance and support to physicians and patients as the newly approved agents become more widely available. The society has updated its appropriate use criteria for PSMA PET imaging to include an indication of "Evaluation of eligibility for patients being considered for PSMA-targeted radioligand therapy" (see story, this issue). In addition, resources will be developed to educate patients with mCRPC about the new therapy.

"The FDA approval of ^{177}Lu-PSMA-617 is a testament to what nuclear medicine innovators, working closely with clinical colleagues in the prostate cancer care domains, can accomplish with their unique combination of expertise in basic biology, radiochemistry, physics, and instrumentation," said Wahl. "The development of radiopharmaceutical therapies is advancing rapidly, and we fully expect there will be more to come as they can be so effective and beneficial for patients fighting cancer."

U.S. Food and Drug Administration
SNMMI

Updates to Appropriate Use Criteria for PSMA PET

Thomas A. Hope, MD, University of California, San Francisco, CA; and Hossein Jadvar, MD, PhD, MPH, MBA, University of Southern California, Los Angeles, CA

As an indication of how quickly the field of nuclear medicine is advancing, the Appropriate Use Criteria (AUC) for Prostate-Specific Membrane Antigen (PSMA) PET document has been updated (*1*). This is due to the recent U.S. Food and Drug Administration (FDA) approval of ^{177}Lu-PSMA-617 (Pluvicto, ^{177}Lu-vipivotide tetraxetan; Novartis [Basel, Switzerland]/Advanced Accelerator Applications USA, Inc. [Millburn, NJ]) radiopharmaceutical therapy (RPT). Previously the AUC had scored the indication for a posttreatment prostate-specific antigen (PSA) rise in the metastatic castration-resistant prostate cancer (mCRPC) setting as "may be appropriate." This was because no available PSMA-targeted therapies would benefit from imaging using PSMA PET. With the approval of PSMA RPT, the PSMA PET AUC Working Group has split this indication into 2 distinct indications (see supplemental materials, available at http://ow.ly/ABfv30sh3uO). The first is "Posttreatment PSA rise in the mCRPC setting in a patient not being considered for PSMA-targeted radiopharmaceutical therapy," which was again scored as "may be appropriate," because the clinical value of improved tumor localization in grossly metastatic disease is not clear in patients who are not being considered as candidates for PSMA RPT. The second indication is "Evaluation of eligibility for patients being considered for PSMA-targeted radiopharmaceutical therapy," which was scored as "appropriate" given the availability of a PSMA-targeted therapy.

An important point is that the AUC Working Group agreed that both ^{18}F-DCFPyL (Pylarify, ^{18}F-piflufolastat; Lantheus [Billerica, MA]) and ^{68}Ga-PSMA-11 (Illuccix and Locametz, ^{68}Ga-gozetotide; Telix Pharmaceuticals Ltd. [Melbourne, Australia], and Novartis/AAA, respectively) should be considered equivalent for selection of patients for treatment with ^{177}Lu-PSMA-617. In the prescribing information for ^{177}Lu-PSMA-617, the FDA recommended selection of "patients for treatment using Locametz or an approved PSMA-11 imaging agent based on PSMA expression in tumors." However, given the near equivalency of ^{68}Ga-PSMA-11 and ^{18}F-DCFPyL, either of these radiotracers can be used for patient selection.

Another consideration for patient selection is what cutoff should make a patient eligible. Two randomized trials have evaluated ^{177}Lu-PSMA-617 therapy: the VISION and TheraP trials. Optimal PSMA PET criteria for patient selection are not yet well established. In the VISION trial, eligibility required uptake in disease greater than that in the liver, and no measurable disease with uptake less than that in the liver (*2*). Eligibility in the TheraP study required an SUV ≥ 20 at 1 site of disease, an SUV ≥ 10 at measurable soft tissue sites, and no ^{18}F-FDG–positive PSMA-negative sites of disease (*3*). It should be noted that, in general, the higher the uptake on PSMA PET, the better patients respond to treatment (*4,5*). PSMA PET is not only a prognostic biomarker but was shown to be predictive in the TheraP trial, with patients who had an SUV$_{mean}$ ≥ 10 having a higher likelihood of PSA response compared to chemotherapy (cabazitaxel) (*6*). Although the decision in the VISION trial was binary, uptake may be used to help weigh various treatment options. The debate as to whether ^{18}F-FDG PET/CT should also be used to screen patients prior to PSMA RPT is outside of the scope of the PSMA PET AUC, although ^{18}F-FDG PET may provide additional value in identifying ^{18}F-FDG–positive/PSMA-negative sites of disease (*3*).

PSMA PET plays a significant role in the appropriate selection of patients for PSMA RPT. With the approval and availability of 2 PSMA PET agents, this imaging study should be widely available. Overall, these 2 imaging agents are considered equivalent for patient selection.

REFERENCES

1. Jadvar H, Calais J, Fanti S, et al. Appropriate use criteria for prostate-specific membrane antigen PET imaging. *J Nucl Med.* 2022;63:59–68.
2. Kuo PH, Benson T, Messmann R, Groaning M. Why we did what we did: PSMA-PET/CT selection criteria for the VISION trial. *J Nucl Med.* January 2022:jnumed.121.263638.
3. Hofman MS, Goh JC, Tan TH, et al. [177Lu]Lu-PSMA-617 versus cabazitaxel in patients with metastatic castration-resistant prostate cancer (TheraP): A randomised, open-label, phase 2 trial. *Lancet.* 2021;351:1502–1506.
4. Gafita A, Calais J, Grogan TR, et al. Nomograms to predict outcomes after ^{177}Lu-PSMA therapy in men with metastatic castration-resistant prostate cancer: An international, multicentre, retrospective study. *Lancet Oncol.* 2021;22:1115–1125.
5. Seifert R, Seitzer K, Herrmann K, et al. Analysis of PSMA expression and outcome in patients with advanced prostate cancer receiving ^{177}Lu-PSMA-617 radioligand therapy. *Theranostics.* 2020;10:7812–7820.
6. Buteau JP, Martin AJ, Emmett L, et al. PSMA PET and FDG PET as predictors of response and prognosis in a randomized phase 2 trial of ^{177}Lu-PSMA-617 (LuPSMA) versus cabazitaxel in metastatic, castration-resistant prostate cancer (mCRPC) progressing after docetaxel (TheraP ANZUP 1603) [abstract]. *J Clin Oncol.* 2022; 40(6; suppl):10-10.

ASNC/SNMMI Radionuclide Authorized User Training Course

The joint American Society of Nuclear Cardiology (ASNC) and SNMMI "80 Hour Radionuclide Authorized User Training Course" was launched on April 12 as a 1-of-a-kind online educational resource for a broad community of radionuclide users. The collaborative project is the result of significant investment of time and energy from subject-matter experts and staff from both professional societies. "This was a more than 2-year cooperative effort directly addressing a genuine need in both the nuclear medicine and nuclear cardiology communities," said Vasken Dilsizian, MD, who, as the 2019–2020 SNMMI president, initiated planning for the course and, with James A. Case, PhD, oversaw its development. "As someone who is closely involved with education of radiology, nuclear medicine, and nuclear cardiology trainees, I've long believed that we're missing a key element in preparing our workforce on some of the basics in radionuclide knowledge and technique," said Dr. Dilsizian. "A partnership between 2 of our leading professional societies, leveraging the expertise of their members and the organizational skills of their experienced staffs, has provided an extraordinarily productive environment for creation of this rich and rigorous new resource."

The course is targeted at nuclear medicine physicians and cardiologists who wish to complete the 80 hours of classroom training required by the U.S. Nuclear Regulatory Commission (NRC) to meet 10 CFR 35.290 training and Agreement State equivalents in basic radionuclide handling techniques for medical use of unsealed byproduct material for imaging and localization studies in order to become Authorized Users (U.S. NRC 10 CFR 35.200). Individuals who complete the course will still need hands-on training in simultaneous clinical work experience in their local nuclear laboratories in the required specified areas as attested to by their Authorized User preceptors. "I am particularly pleased that this course will be available to residents in nuclear medicine and fellows in nuclear cardiology," said Dr. Dilsizian. "As diagnostic, therapeutic, and theranostic applications of radionuclides grow in number and complexity and as the range of approved radiopharmaceuticals expands, we will need more Authorized Users with a solid understanding of the requisite knowledge and the adaptability to build on that knowledge along with changing technologies and novel discoveries." In the future, the course may also be useful for nuclear medicine technologists, especially those who intend to take the Nuclear Cardiology Technologist specialty examination. In addition, the course may be useful for other allied health care professionals, such as radiation safety officers and health physicist specialists.

The online course includes 93 modules of video and slide presentations in 5 sections (see Table 1 for content overview). Each module is divided into 2 or 3 chapters, with quiz questions to assess comprehension on chapter content. Participants may go back to review presentation content and reanswer incorrect questions to meet the required passing score. Those who successfully complete the 80 hours of classroom training will receive a certificate of completion from ASNC/SNMMI, which will be recognized by the NRC and Agreement States as part of their Authorized User training requirements.

TABLE 1
ASNC/SNMMI Radionuclide Authorized User Training Course: Content Overview

Section 1: Radiation Protection and Safe Radioisotope Handling
- Regulatory Requirements
- Forms of Radiation
- Radiation Units
- Radiation Protection

Section 2: Physics and Instrumentation
- SPECT and Planar Nuclear Imaging: Gamma Cameras
- SPECT and Planar Nuclear Imaging: Data Corrections
- SPECT and Planar Nuclear Imaging: Tomographic Imaging
- SPECT and Planar Nuclear Imaging: Quality Control
- PET Imaging: PET Cameras
- Dedicated PET and PET/CT Imaging: Tomographic Imaging
- PET Imaging: Quality Control
- Image Post Processing
- Tracer Kinetics
- Clinical Optimization of Radiopharmaceutical Dosing
- Application of Technology for Radiation Reduction
- Other Clinical Applications of Planar, SPECT and PET Imaging: Image Acquisition and Processing

Section 3: Radiochemistry and Radiopharmaceuticals
- Managing a Hot Lab
- Radionuclide Production and Radiopharmaceuticals
- Quality Control of Radiopharmaceutical Production Kits

Section 4: Radiation Biology
- Radiation Biology Overview
- Radiation Injury, Cell, and Organ Responses
- Risk Models, Exposure Limits, Deterministic and Stochastic Effects

Section 5: Nuclear Medicine Mathematics and Statistics
- Measuring Radioactive Decay
- Shielding Calculations
- Mathematics of Imaging
- Mathematics of Radioactivity

SNMMI's Role in the Nuclear Medicine Renaissance

Richard L. Wahl, MD, SNMMI President

Nuclear medicine is undergoing a renaissance, as evidenced by the steady introduction and approval of new radiopharmaceuticals, theranostics, and instrumentation. In the past year alone, we have celebrated the U.S. Food and Drug Administration (FDA) approval of new PSMA-targeted prostate imaging and therapy agents, breakthrough research for FAPI PET/CT, new generic SPECT agents, and great advances in artificial intelligence. SNMMI has been there every step of the way to support the field of nuclear medicine and molecular imaging, promoting quality of practice, research and discovery, outreach, and advocacy, all while helping ensure an adequate workforce pipeline for the future.

SNMMI strives to enhance the practice of nuclear medicine by providing professionals with the resources needed to deliver high-quality care. In light of recent advances in the field, SNMMI released appropriate use criteria for PSMA PET imaging and musculoskeletal infection imaging, as well as new procedure standards to assist in obtaining high-quality examinations while simultaneously controlling costs. In February, SNMMI launched its Radiopharmaceutical Therapy Center of Excellence program, which offers options for site designation, and later this year will begin its pilot program for the Radiopharmaceutical Therapy Registry (RaPTR), which supports ongoing data collection and quality improvement in theranostics. SNMMI's Therapeutics Conference, held in March, was well attended and provided education to practitioners wishing to expand their practices to include radiopharmaceutical therapies, such as ^{177}Lu-PSMA-617.

A key SNMMI focus over the past year has been to encourage research. A new initiative, the "Mars Shot" for molecular imaging, focuses on advancing the research and development of diagnostic and therapeutic nuclear medicine. A dosimetry supplement in *The Journal of Nuclear Medicine* addresses both the rapid progress and challenges in applying patient-specific radiation dosimetry to guide radiopharmaceutical therapies, providing a useful starting point for sites considering implementing dosimetry in their clinical practices or research operations. A therapy toolkit has been developed to assist new sites as they begin research projects. An Artificial Intelligence (AI) Summit was held in March to help drive development of AI tools for nuclear medicine. In addition, the society created and awarded 2 Radiopharmaceutical Therapy Research Fellowships to grow the number of trained investigators in our field.

The society has also been successful in advancing its issues and becoming a valued partner among public policy stakeholders. SNMMI is working hard to encourage legislators and regulators to support and pass the bipartisan Facilitating Innovative Nuclear Diagnostics (FIND) Act, a bill to ensure patient access to nuclear medicine scans (www.snmmi.org/FindAct). A summit was held in March to educate regulatory representatives about health disparities and barriers to patient access to nuclear medicine procedures. The society has also actively worked to maintain and increase reimbursement for the nuclear medicine community, successfully expanding Centers for Medicare & Medicaid Services coverage for nononcologic PET and ^{18}F-FDG PET for infection and inflammation.

Richard L. Wahl, MD

With so much work being done to advance the field, SNMMI realizes the importance of developing a robust pipeline of professionals qualified to practice in all areas of nuclear medicine and molecular imaging, both now and in the future. In the past year, 3 working groups (focused on physicians, scientists, and technologists) were formed to develop content and curricula on radiopharmaceutical therapies and diagnostic procedures for residents. A dedicated resident, medical student, and program director website was also created with tailored content for each group. The society introduced a new education initiative—the Quality Systems Personnel Training Program—to educate individuals with a pharmacy or chemistry background in the production and release of clinical radiopharmaceuticals. SNMMI also launched a new online Career Center which, as of January 2022, has posted more than 2,500 jobs.

Another component of SNMMI's work is outreach. The society reaches referring physicians through presentations at specialty events, such as the Pediatric Endocrine Society meeting and the San Antonio Breast Cancer Symposium. To connect with patients, SNMMI hosted its annual Patient Education Day, which was attended by 223 participants and has received more than 1,000 on-demand views to date. In-person patient roadshows are scheduled to return in 2022. Two new organizations joined SNMMI's Patient Advisory Board in 2021, bringing the total number of participants to 15. Internationally, SNMMI's Department of Energy Grant Taskforce continues to work closely with the Korle Bu Teaching Hospital in Accra, Ghana, to assist in building its nuclear medicine program.

As always, SNMMI supports nuclear medicine and molecular imaging through its meetings and journals. Held virtually last year, the 2021 Annual Meeting welcomed more than 6,000 participants from more than 60 countries, with an expanded scientific program including 80 continuing education and

scientific sessions, 189 scientific oral presentations, 14 satellite symposia, 1,000 scientific posters, and 115 exhibitors. *The Journal of Nuclear Medicine* continues to promote innovative research and dramatically increased its impact factor last year, now ranking third among all medical imaging journals.

In the fall of 2021 SNMMI kicked off a new consumer-focused public relations initiative to raise awareness about what nuclear medicine is and what it can accomplish. By focusing on consumer broadcast media—print and digital news publications, radio, and TV—SNMMI has been able to reach a broad audience, including patients, referring physicians, legislators, regulators, payers, and other media. After only 6 months, the program has provided content to a potential 1 billion consumers.

SNMMI is stable, financially secure, and ready to lead in a new era of nuclear medicine and molecular imaging. As the nuclear medicine renaissance continues, the society is committed to our members and the patients we serve.

"This would not have been possible without the generous volunteer efforts of the more than 40 course leads and section faculty who participated in multiple planning meetings and devoted substantial time in developing and preparing highly specialized material for this unique effort," said Dr. Dilsizian. "Kathleen Flood, ASNC CEO, and Virginia Pappas, CAE, SNMMI CEO, deserve special credit for their willingness to bring together their members and staffs to coordinate these efforts. Dawn Edgerton, MA, ASNC Director of Strategic Projects, was an exceptional organizational leader on the project from start to completion."

The leads for Section 1, Radiation Protection and Safe Radioisotope Handling, are R. Glenn Wells, PhD, and David Wolinsky, MD, with section faculty including Dr. Wells and Brian Abbott, MD; Adam Alessio, PhD; Mouaz Al-Mallah, MD, MSc; Jon Aro, BSc; Stephen A. Bloom, MD; Tyler Bradshaw, MD; James A. Case, PhD; Rami Doukky, MD, MSc, MBA; Dawn Edgerton, MA; Michael King, PhD; Ran Klein, PhD, Elec Eng; Yi-Hwa Liu, MD; April Mann, MBA, CNMT, NCT, RT(N); Frederic J. Mis, PhD, CHP; and William Van Decker, MD.

The second section, on Physics and Instrumentation, is led by Keisha McCall, PhD, and Krishna Patel, MD, MSc, with section faculty including Dr. McCall and Mouaz Al-Mallah, MD, MSc; Ian Armstrong, PhD; James A. Case, PhD; Frederic H. Fahey, DSc; James R. Galt, PhD; Ernest V. Garcia, PhD; Saurabh Malhotra, MD; A. Iain McGhie, MD; Zhihua Qi, PhD; Piotr Slomka, PhD; Brett Sperry, MD; and Stephanie Thorn, PhD.

The third section, on Radiochemistry and Radiopharmaceuticals, is led by Saurabh Malhotra, MD, and Sally Schwarz, RPh, MS, with faculty including Dr. Schwarz and William Crisp, PharmD; Reiko Oyama, RPh, MS; Stephen Moerlein, PharmD; Peggy Squires, BS, CNMT; and William Van Decker, MD.

Section 4, on Radiation Biology, is led by Frederic J. Mis, PhD, CHP, and Ronald G. Schwartz, MD, MS, who serve as section faculty along with Andrew Einstein, MD, PhD.

The fifth section, on Nuclear Medicine Mathematics and Statistics, is led by James A. Case, PhD, and Frederic J. Mis, PhD, CHP, who serve as section faculty along with Maria L. Mackin, CNMT, and Ronald G. Schwartz, MD, MS.

Special recognition is also due to Tina Buehner, PhD, CNMT, for her service on the task force and her contributions to the content of this course. The cost of the course for SNMMI and ASNC members is $400 for cardiology fellows and nuclear medicine residents and $550 for physicians. For nonmembers the cost is $700. To learn more about the course and to enroll, see: https://sites.snmmi.org/SNMMIMAIN/80_Hour_Course/80_Hour_Radionuclide_Authorize_User_Training_Course.aspx or https://www.ASNC.org/80Hour.

American Society of Nuclear Cardiology
SNMMI

Petten HFR Restarts Production

NRG (Petten and Arnhem, The Netherlands) announced on March 17 that its High Flux Reactor (HFR) in Petten had been restarted that morning and reached a power output of 45 MW. "Within 2 wk, the first medical isotopes for nuclear medicine will be delivered to hospitals," said Vinod Ramnandanlal, commercial director for NRG and its project partner PALLAS. "We are pleased that NRG can once again meet the global demand for medical isotopes."

The HFR did not start a scheduled production run on 20 January because of a leak in a test facility water system outside of the reactor core. NRG initiated inspections and preparations to restore the system. This required modifications to the facility and submission of an application for regulatory review and approval. This permit was granted on March 9. Directors and staff at reactors in Europe and the United States changed production schedules and methods during the Petten outage to meet radioisotope supply demands.

"This is extremely good news. Medical isotopes are of enormous importance for many patients," said Andor Glaudemans, MD, PhD, president of the Dutch Association for Nuclear Medicine.

The HFR was commissioned in 1961 to develop nuclear technology for energy generation. Beginning in the 1980s, the reactor was increasingly used for production of medical isotopes, particularly for diagnostic applications. Today >30,000 patients/d are treated with medical isotopes from the HFR.

NRG

FDA Guidances Target Cancer Clinical Trials

On March 1, the U.S. Food and Drug Administration (FDA) issued 3 final guidances for industry related to cancer clinical trials. In a press release, the FDA noted that these guidances "parallel the goals of President Biden's recently announced effort to renew and build upon his 2016 Cancer Moonshot initiative to facilitate continued advancement in cancer prevention, detection, research, and patient care." The goals for this renewed initiative are: to reduce death rates from cancer by at least 50% over the next 25 years, to improve the experience of people and their families living with and surviving cancer, and "to end cancer as we know it today."

"With today's actions the FDA is recommending important principles that involve addressing inequities, targeting the right treatments to the right patients, speeding progress against the most deadly and rare cancers, and learning from the experience of all patients," said Richard Pazdur, MD, director for the FDA's Oncology Center for Excellence. "All of these are tenets of Cancer Moonshot's mission."

The first new finalized guidance, "Inclusion of Older Adults in Cancer Clinical Trials," provides recommendations to sponsors and institutional review boards for including older patients (≥65 y) in clinical trials of drugs for cancer treatment. Enrollment of older adults in early-phase cancer clinical trials is recommended, as appropriate, to better inform later-phase studies. Also included are recommendations for trial design, recruitment strategies, information collection, and developing and reporting on more precisely defined older age groups to encourage trial enrollment of this historically excluded population. This guidance is available at: https://public-inspection.federalregister.gov/2022-04399.pdf.

The second new guidance for industry is "Expansion Cohorts: Use in First-in-Human Clinical Trials to Expedite Development of Oncology Drugs and Biologics." Advice is provided on designing and conducting trials with multiple expansion cohorts that allow for concurrent accrual of patients into different cohorts to assess safety, pharmacokinetics, and antitumor activity of first-in-human cancer drugs. Pharmaceutical companies and researchers can use trials with expansion cohort designs to assess different aspects of a drug in a single clinical trial to expedite efficient clinical development of the drug. This guidance is available at: https://public-inspection.federalregister.gov/2022-04397.pdf.

The new guidance on "Master Protocols: Efficient Clinical Trial Design Strategies to Expedite Development of Oncology Drugs and Biologics" addresses master protocol design, including information on what sponsors should submit to the FDA as part of these trial approaches. It also directs sponsors on interactions with the FDA to facilitate efficient review and mitigate risks to patients. These clinical trials can expedite clinical development of a drug by allowing more than 1 investigational drug or biologic, more than 1 disease type, or more than 1 patient population to be evaluated under a single clinical trial structure. This guidance is available at: https://public-inspection.federalregister.gov/2022-04398.pdf.

All FDA Oncology Center of Excellence documents are available through the portal at: https://www.fda.gov/about-fda/oncology-center-excellence/oncology-center-excellence-guidance-documents.

U.S. Food and Drug Administration

NCI and Molecular Characterization of Childhood Cancers

The National Cancer Institute (NCI) announced on March 21 the launch of the Molecular Characterization Initiative for pediatric tumors. The program, hosted by NCI's Childhood Cancer Data Initiative, offers tumor molecular characterization (biomarker testing) to children, adolescents, and young adults with newly diagnosed central nervous system tumors who are being treated at hospitals affiliated with the Children's Oncology Group (COG). This NCI-supported clinical trials group includes more than 200 hospitals and institutions treating children diagnosed with cancer in the United States.

Participants with central nervous system cancers will be eligible to receive molecular characterization of their tumors free of charge through this voluntary program. DNA and RNA from tumor and blood samples will be analyzed,

and, later in 2022, the program will be expanded to include soft tissue sarcomas and other rare tumors.

"The ultimate dream has really been for every child with cancer to have a state-of-the-art diagnosis and the safest and most effective therapy," said Brigitte C. Widemann, MD, special advisor to the NCI director for childhood cancer. "The Molecular Characterization Initiative is a transformative collaboration that will entail participation of the entire community."

Comprehensive tumor molecular characterization has previously been available to children enrolling in some clinical trials or being treated at larger institutions with internal resources that offer such state-of-the-art diagnostics. Data on tumor biomarkers have been stored exclusively at the hospital or institution at which a child was treated, with limited data sharing among institutions. The new program will make tumor molecular characterization broadly available, with data collected in a central location accessible to researchers.

"We can help make molecular characterization available throughout the country so that it will be a standard of care that every child can get," said Maryam Fouladi, MD, leader of the COG central nervous system tumor disease committee. "An accurate molecular diagnosis can inform optimal treatment for every child."

In addition to providing detailed information to use in making an accurate diagnosis, the data can also be used to determine whether a child is eligible for a clinical trial. Enrollment in the Molecular Characterization Initiative is initially offered through participation in Project Every Child (http://www.projecteverychild.org/), a childhood cancer registry maintained by COG. Initial participants will include newly diagnosed children, adolescents, and young adults ≤25 y old at the time of diagnoses. Young adults >25 y old who are being screened

for eligibility into a COG clinical trial may also be included. Additional information on the initiative is available at: https://www.cancer.gov/research/areas/childhood/childhood-cancer-data-initiative/molecular-characterization.

National Cancer Institute

NIH All of Us Research Program Releases 100,000 Whole-Genome Sequences

The National Institutes of Health (NIH) announced on March 17 the release of nearly 100,000 diverse whole-genome sequences through its All of Us Research Program. About 50% of the data is from individuals who identify with racial or ethnic groups that have historically been underrepresented in research. These data will enable researchers to address new questions about health, disease, and disparities.

"Until now, over 90% of participants from large genomics studies have been of European descent. The lack of diversity in research has hindered scientific discovery," said Josh Denny, MD, chief executive officer of the All of Us Research Program. "All of Us participants are leading the way toward more equitable representation in medical research through their involvement. And this is just the beginning. Over time, as we expand our data and add new tools, this dataset will become an indispensable resource for health research."

The genomic data are available via a cloud-based workbench platform (https://www.researchallofus.org/) and also include genotyping arrays from 165,000 participants. Whole-genome sequencing provides information about almost all of an individual's genetic makeup, whereas genotyping arrays, the more commonly used genetic testing approach, capture a specific subset of the genome.

In addition to the genomic data, the All of Us workbench contains information

from many of the participants' electronic health records, Fitbit devices, and survey responses. The platform also links to data from the Census Bureau's American Community Survey to provide more details about the communities in which participants live. This combination of data will allow researchers to better understand how genes can cause or influence diseases in the context of other health determinants. The ultimate goal is to enable more precise approaches to health care for all populations. To protect participants' privacy, the program has removed all direct identifiers from the data and upholds strict requirements for researchers seeking access.

In a press release, NIH noted that these data are made available for research through the contributions of All of Us participants, who have the opportunity to receive personal DNA results at no cost. The program has offered genetic ancestry and trait results to more than 100,000 participants so far, with plans underway to begin to share health-related DNA results on hereditary disease risk and medication–gene interactions later this year. All of Us works with a consortium of partners across the United States to engage participants and collect data and samples. The Researcher Workbench is managed by Vanderbilt University Medical Center, in collaboration with the Broad Institute of MIT and Harvard and Verily. The program's genome centers generate the genomic data and process about 5,000 participant samples each week. These centers include Baylor College of Medicine, Johns Hopkins University, the Broad Institute, the Northwest Genomics Center at the University of Washington, and partners. Color, a health technology company, works with the program to return personalized results to participants on genetic ancestry and traits and the forthcoming health-related genetic results.

National Institutes of Health

FROM THE LITERATURE

Each month the editor of Newsline selects articles on diagnostic, therapeutic, research, and practice issues from a range of international publications. Most selections come from outside the standard canon of nuclear medicine and radiology journals. These briefs are offered as a window on the broad arena of medical and scientific endeavor in which nuclear medicine now plays an essential role. The lines between diagnosis and therapy are sometimes blurred, as radiolabels are increasingly used as adjuncts to therapy and/or as active agents in therapeutic regimens, and these shifting lines are reflected in the briefs presented here. We have also added a small section on noteworthy reviews of the literature.

Radiation Dose to NM Techs from PET/MR and PET/CT

Soret et al. from the Hôpital Universitaire Pitié Salpêtrière (Paris, France) reported on March 16 ahead of print in the *Journal of Radiological Protection* on a study comparing nuclear medicine technologists' radiation doses when performing routine PET/MR and PET/CT acquisitions in the same department. Over 13 mo, daily radiation doses received by technologists were collected with electronic personal dosimeters. Factors included in the retrospective analyses were the total numbers of PET/MR and PET/CT acquisitions, type of study (brain or whole-body PET), ^{18}F-FDG injected activity per day and per patient, and time spent with patients after injection. The researchers found that technologists' whole-body exposure for PET/MR averaged 10.3 ± 3.5 nSv per MBq injected ^{18}F-labeled tracer, compared to only 4.7 ± 1.2 nSv per MBq injected for PET/CT. The additional exposure with PET/MR was attributed to additional time spent in patient positioning and MR coil placement, particularly in whole-body studies. They concluded that "for an equal injected activity, PET technologist radiation exposure for PET/MR was 2-fold that of PET/CT. To minimize radiation dose to staff, efforts should be made to optimize patient positioning, even in departments with extensive PET/CT experience."

Journal of Radiological Protection

Monoclonal Antibodies in Alzheimer Disease

In a study published on March 5 ahead of print in the *Journal of Alzheimer's Disease*, Lacorte et al. from the Italian National Institute of Health (Rome), Sapienza University (Rome), Fondazione IRCCS Ca' Granda Ospedale Maggiore Policlinico (Milan), and the Casa Cura Policlinico (Milan, all in Italy) provided a systematic review and metaanalysis of published and unpublished clinical trials on the safety and efficacy of monoclonal-based antibody therapies in Alzheimer disease (AD). After a systematized search of clinical trial and literature databases, 101 studies were identified, using a total of 27 monoclonal antibodies. Trial results were available on 50 of these investigations (18 with data from published and unpublished sources, 21 with data from published sources only, and 11 with only unpublished data) using a total of 12 monoclonal antibodies. Assessment of reported amyloid-related imaging abnormalities (ARIAs) in these studies showed overall risk ratios of 10.65 for ARIA-E (MR signal alterations thought to represent vasogenic edema and related extravasated fluid phenomena) and 1.75 for ARIA-H (MR signal alterations attributable to microhemorrhages and hemosiderosis). Metaanalyses of PET SUV ratios indicated an overall significant effect of monoclonal antibodies in reducing amyloid burden. Although data from administration of Clinical Dementia Rating Scale–Sorting Box evaluations showed statistically significant lower rates of worsening in treated patients, these were "clinically nonrelevant." The authors concluded that these results suggested that the risks/benefits of monoclonal antibodies remain unclear. They advised that "research should focus on clarifying the effect of amyloid on cognitive decline, providing data on treatment response rate, and accounting for minimal clinically important differences." In addition, research should investigate the possible long-term impact of ARIA events, including potential predictors of onset.

Journal of Alzheimer's Disease

CTA vs SPECT/CT V/Q in Pulmonary Embolism

Martins et al. from the University of Campinas (Brazil) reported on February 27 ahead of print in *Perfusion* on a direct comparison of multidetector CT angiography (CTA) and ventilation/perfusion (V/Q) SPECT/CT in detection of acute pulmonary emboli (PE) in routine practice. The study included 28 patients (15 men, 13 women; median age, 51.5 y) with suspected acute PE who underwent both imaging procedures. The median duration of symptoms from onset to imaging was 4 d (range, 1–14 d), with a median Wells score of 3.5 (range, 1.5–6). Final diagnoses were determined by clinician consensus (general radiologists and/or nuclear medicine physicians) and supporting clinical, laboratory, and follow-up data. The sensitivity, specificity, positive and negative predictive values, and accuracy for SPECT/CT V/Q in identifying PEs were 84.6%, 80.0%, 78.6%, 85.7%, and 82.1%, respectively. For CTA, the corresponding percentages were 46.1%, 100%, 100%, 68.2%, and 75.0%, with overall agreement between the methods at 57.1%. Ten of the 22 patients with negative CTA findings were positive on SPECT/CT V/Q, and 7 of these were determined to be true-positives. The authors concluded that these results suggested that SPECT/CT V/Q "is more sensitive and accurate than CTA when interpreted by general radiologists and nuclear medicine physicians."

Perfusion

Thyroidectomy Without ^{131}I in DTC

In an article published on March 10 in the *New England Journal of Medicine* (2022;386[10]:923–932) Leboulleux and

a consortium of nuclear medicine, endocrinology, and thyroid cancer experts from throughout France reported on a study using results from a prospective phase 3 trial to compare radioiodine therapy (1.1 GBq ^{131}I after injections of recombinant human thyrotropin) with no radioiodine therapy in patients with low-risk differentiated thyroid cancer after thyroidectomy. The primary objective was to determine whether, in the 2 randomly assigned groups of patients, no radioiodine therapy was "noninferior" to radioiodine therapy, taking into account functional, structural, and biologic abnormalities at 3 y. Noninferiority was defined as between-group differences of <5 percentage points in the presence of abnormal foci of ^{131}I uptake on whole-body imaging that required subsequent treatment (in the radioiodine group only), abnormal findings on neck ultrasound, or elevated levels of thyroglobulin or thyroglobulin antibodies. The researchers also looked at molecular characterization and prognostic factors. The trial included 730 patients (mean age, 52 y; 606 women, 124 men; 367 in the no-radioiodine group and 363 in the radioiodine group) with tumors ≤2 cm in diameter. At 3-y follow-up, the percentages of patients in the no-radioiodine group without an event was 95.6%. The corresponding percentage in the group that received radioiodine therapy was 95.9%. Documented events in both groups included structural or functional abnormalities in 8 patients and biologic abnormalities in 23 patients. Events were found to be more frequent in patients with postoperative serum thyroglobulin levels >1 ng/mL during thyroid hormone treatment. No differences in molecular alterations were noted in the 2 groups, and no treatment-related adverse events were reported. The authors concluded that "in patients with low-risk thyroid cancer undergoing thyroidectomy, a follow-up strategy that did not involve the use of radioiodine was noninferior to an ablation strategy with radioiodine regarding the occurrence of functional, structural, and biologic events at 3 years." The article received wide coverage in the public media and professional literature. In a commentary accompanying the article (*N Engl J Med.* 2022;386[10]:990–991), David S. Cooper, MD (Johns Hopkins University School of Medicine, Baltimore, MD) praised the study's focus and noted that other trial results may soon provide additional data on this subject, adding "it is noteworthy that although radioiodine therapy for differentiated thyroid cancer was introduced in the 1940s and 1950s, we will finally have definitive evidence to enable clinicians to maximize its benefits and minimize its risks."

New England Journal of Medicine

Dynamic SLN Biopsy Technique in Penile Cancer

O'Brien et al. from the Peter MacCallum Cancer Centre, the Royal Melbourne Hospital, the Young Urology Researchers Organisation, MURAC Health, and the EJ Whitten Prostate Cancer Research Centre at Epworth Healthcare (all in Melbourne, Australia) presented on March 11 ahead of print in *Urology* a narrated video of an operative standard for dynamic sentinel lymph node biopsy (DSLNB) in penile cancer and a retrospective clinical analysis and discussion of the accuracy of this approach. The study included 64 patients (127 groins) who underwent DSLNB for inguinal lymph node staging of histologically proven penile squamous cell carcinoma. Data analyzed included primary tumor histology, DSLNB pathology, progression to radical inguinal lymph node dissection (RILND), and recurrence patterns. Of the total 64 patients, 53 (82.8%) underwent penile-sparing surgery. Tumor histology in 56 (88%) patients showed pT1–pT2 disease. Of the total 127 groins explored with DSLNB, 19 were positive for malignancy and 108 were negative. Over a mean follow-up of 29 mo, 36 groins progressed to RILND. Only 2 previously negative DSLNB findings were positive on RILND (1 in the groin, 1 in the pelvis). DSLNB was found to have a false-negative rate of 1.9% and a sensitivity of 90.5%, allowing 71.7% of groins to proceed for surveillance instead of prophylactic RILND. The authors concluded that "DSLNB is a safe and accurate method for assessing inguinal lymphadenopathy in men with intermediate- to high-risk penile squamous cell carcinoma and impalpable groins." Their video study was intended to establish an operative standard in this setting consistent with international guidelines and expectations. They added that "standardized use of DSLNB by an experienced team will reduce morbidity while maintaining oncological safety for men with intermediate- to high-risk penile cancer and cN0 disease."

Urology

In-Transit Metastases in Distal Extremity Rhabdomyosarcoma

In an article published on March 12 ahead of print in the *European Journal of Surgical Oncology,* Terwisscha van Scheltinga et al. from the Princess Máxima Center for Pediatric Oncology (Utrecht, The Netherlands), the University Paris-Saclay/Hôpitaux de Paris (France), University Hospitals Bristol and Weston NHS Foundation Trust (UK), Royal Manchester Children's Hospital (UK), Hospital Universitari Infantil Vall d'Hebron (Barcelona, Spain), University of Bari (Italy), University Hospital of Padua (Italy), Great Ormond Street Hospital (London, UK), Amsterdam UMC/University Amsterdam (The Netherlands), the Royal Marsden Hospital (Sutton, UK), Institut Gustave Roussy (Villejuif, France), University Hospital of Wales (Cardiff, UK), and the University Medical Center Utrecht (The Netherlands) reported on a study evaluating the frequency, staging, and survival of pediatric patients with in-transit metastases in distal extremity rhabdomyosarcoma. In-transit metastases are defined as metastatic lymph nodes or deposits occurring between the primary tumor and proximal draining lymph node basin. The study included 109 patients (median age, 6.2 y; range, 0–21 y) with extremity rhabdomyosarcoma distal to the elbow or knee and enrolled in the European Paediatric Soft Tissue Sarcoma Group RMS 2005 trial between 2005 and 2016.

Thirty-seven patients (34%) had lymph node metastases at diagnosis, and 19 of these had in-transit metastases, most in the lower extremities. In 51 patients who underwent ^{18}F-FDG PET/CT, suspicious lymph nodes were detected in 24 (47%), with 14 of these having in-transit metastases (solitary or in combination with proximal nodes). In the 58 patients not undergoing PET/CT, suspicious lymph nodes were detected in 13 (22%), with in-transit metastases in 5. At a median follow-up of 6.3 y (range, 2–12.5 y), 60 (55%) patients were in first complete remission and 9 (8%) were in remission after relapse. One patient was alive with disease, and 37 (34%) had died (2 patients lost to follow-up). The 5-y event-free survival rates for patients with in-transit metastases, proximal lymph nodes, or combined proximal/in-transit metastases were 88.9%, 21.4%, and 20%, respectively. Corresponding 5-y overall survival rates were 100%, 25.2%, and 15%. The authors summarized their findings that in-transit metastases constituted more than 50% of all lymph node metastases in this group of patients with distal extremity rhabdomyosarcoma and that ^{18}F-FDG PET/CT improved nodal staging by detecting more regional and in-transit metastases. In addition, patients with proximal (axillary or inguinal) lymph node involvement appeared to have worse prognoses. The authors advised that "popliteal and epitrochlear nodes should be considered as true (distal) regional nodes, instead of in-transit metastases," recommending biopsy of these nodes especially in distal extremity rhabdomyosarcoma of the lower limb.

European Journal of Surgical Oncology

Assessing [131]I Capsule Activity and Reducing Staff Exposure

Zuhayra et al. from the University Hospital of Schleswig–Holstein (Germany) reported on March 17 in *Physica Medica* (2022;96:157–165) on a method for estimating ^{131}I capsule activity by measuring the dose rate at contact of the delivered lead-closed container carrying the capsules and thereby estimating radiation exposure. This method was compared to that of conventional ^{131}I capsule measurement using a dose calibrator. The dose rate on the surface of the closed lead container was measured at 2 locations and correlated linearly with ^{131}I capsule activity measured in a dose calibrator to create calibrating curves. The hand and whole-body (effective) doses were determined with official dose meters during validation of the proposed method in clinical practice. The determination coefficients of linear calibration curves were >0.9974. The total relative uncertainty for estimating ^{131}I capsule activity with the proposed method was less than ±7.5%. The reduction of the hand dose with the proposed method was 97% of the conventional measurements of the ^{131}I capsules by dose calibrators. The authors summarized their findings that "measuring dose rate on the surface of the closed lead containers enables the ^{131}I capsule activity to be estimated simply, reliably, and with sufficient accuracy" to result in significant reduction of radiation exposure for medical staff.

Physica Medica

^{68}Ga-PSMA-11 PET/CT and ADT Monitoring

In an article published on March 4 in *Cancers (Basel)* (2022;14[5]:1329), Tseng et al. from the New Taipei Municipal TuCheng Hospital, Chang Gung University School of Medicine (Taoyuan), and Linkou Chang Gung Memorial Hospital (Taoyuan, all in Taiwan) reported on a pilot study evaluating ^{68}Ga–prostate-specific membrane antigen–11 (^{68}Ga-PSMA-11) PET/CT findings in patients with advanced or metastatic hormone-naïve prostate cancer after 3 mo of androgen-deprivation therapy. The prospective study included 30 men with untreated stage III or IV disease scheduled to receive therapy for at least 6 mo. Participants underwent ^{68}Ga-PSMA-11 PET/CT imaging before the start of therapy and at 10–14 wk. Response was assessed using a number of factors, including the modified PET Response Criteria in Solid Tumors 1.0, with a subgroup analyzed by International Society of Urological Pathology (ISUP) grade. After 3 mo of treatment, all PET/CT variables indicated significant reductions in disease, showing partial response in 24 patients, complete response in 2, stable disease in 2, and disease progression in 2. In 16 patients with ISUP grade 5, SUV_{max} reduction was less marked, and none reached complete response. The authors concluded that these pilot results indicated that "[68]Ga-PSMA-11 PET/CT imaging holds promise to monitor treatment response after the first 3 mo of androgen-deprivation therapy."

Cancers (Basel)

PSMA-Guided Mets-Directed Therapy in Oligometastatic PCa

Mazzola et al. from the IRCCS Sacro Cuore Don Calabria Hospital (Verona), the Azienda Ospedaliera Universitaria Careggi (Firenzi), University of Florence, University and Spedali Civili Hospital (Brescia), University of Perugia, Humanitas University (Milan), IRCCS Humanitas Research Hospital (Milan), and the University of Brescia (all in Italy) reported on March 9 ahead of print in *Clinical and Experimental Metastasis* on a multiinstitutional study of prostate-specific membrane antigen (PSMA)–guided metastases-directed radiation therapy in patients with bone oligometastatic prostate cancer. The study included 40 men with 56 bone oligometastases detected by PSMA-based PET and with no concurrent androgen-deprivation therapy. Oligometastatic disease presented as a single lesion in 28 patients, 2 lesions in 9 patients, 3 lesions in 2, and 4 lesions in 1 patient (30.3% spine metastases, 69.7% non-spine metastases). All patients underwent stereotactic body radiation therapy (SBRT) with a median dose of 30 Gy (range, 24–40 Gy) in 3–5 fractions. Over a median follow-up of 22 mo (range, 2–48 mo), 1- and 2-y local control rates were 96.3% and 93.9%, respectively, with corresponding distant progression-free survival rates of 45.3% and 27%. Additional analyses showed that the lower prostate-specific

antigen values after radiation were significantly related to distant progression-free survival. Seven patients were directed to a second radiation course with concurrent androgen-deprivation therapy, and 11 patients with polymetastatic spread received androgen deprivation alone. A lower number of treated oligometastases was correlated with higher androgen-deprivation–free survival rates. The authors concluded that PSMA PET–guided SBRT "resulted in excellent results in terms of clinical outcomes, representing a helpful tool with the aim to delay the start of androgen-deprivation therapy."

Clinical and Experimental Metastasis

Bone Marrow Activation, Metabolic Syndrome, and Early Atherosclerosis

In an article published on March 11 ahead of print in the *European Heart Journal,* Devesa and a consortium of investigators from Madrid (Spain) and New York (NY) reported on a study of the associations between cardiovascular risk factors, bone marrow activation, and subclinical atherosclerosis. The study included 745 apparently healthy individuals (624 men, 121 women; median age, 50.5 y, range, 46.8–53.6 y) from the Progression of Early Subclinical Atherosclerosis study. Participants underwent whole-body vascular ^{18}F-FDG PET/MR imaging. Bone marrow activation (tracer uptake above the median SUV_{max}) was assessed in the lumbar vertebrae (L3–L4), and systemic inflammation was evaluated from circulating biomarkers. Early atherosclerosis was assessed by ^{18}F-FDG uptake in 5 vascular territories, and late atherosclerosis was assessed by fully formed plaques on MR imaging. Men were more likely than women to have bone marrow activation (87.6% and 80.0%, respectively) and to have metabolic syndrome (22.2% and 6.7%, respectively). Bone marrow activation was significantly associated with all metabolic syndrome characteristics, with increased hematopoiesis, and with markers of systemic inflammation, including high-sensitivity C-reactive protein, ferritin, fibrinogen, P-selectin, and vascular

cell adhesion molecule-1. In a subgroup of participants with no systemic inflammation, bone marrow activation remained correlated with metabolic syndrome and increased erythropoiesis. The coexistence of bone marrow activation and arterial ^{18}F-FDG uptake on PET was associated with more advanced plaque presence on MR imaging. The authors summarized their findings that in "apparently healthy individuals, bone marrow ^{18}F-FDG uptake is associated with metabolic syndrome and its components, even in the absence of systemic inflammation, and with elevated counts of circulating leucocytes." In addition, bone marrow activation was associated with early atherosclerosis, characterized by high arterial metabolic activity on PET, and appeared to be an early phenomenon in atherosclerosis development.

European Heart Journal

Pediatric Multisystem Inflammatory Syndrome After COVID-19

Astley et al. from the University of Sao Paulo/University of Sao Paulo School of Medicine (Brazil) reported in the March issue of *Physiological Reports* (2022;10[5]:e15201) on a case series of 5 pediatric survivors of multisystem inflammatory syndrome after COVID-19 infection (3 girls, 2 boys; median age, 9; range, 7–18 y). The researchers evaluated the children at a mean follow-up of 1.9 mo (range, 1.3–6.2 mo) with ^{13}N-ammonia PET/CT assessment of myocardial blood flow, standard echocardiography, brachial flow–mediated dilation using Doppler ultrasound, a maximal cardiopulmonary exercise test, and blood markers (C-reactive protein, D-dimer, fibrinogen, and troponin-T). At follow-up, 2 patients showed severe perfusion defects in the left ventricular cavity, suggesting extensive myocardial ischemia (myocardial blood flow <2.0), and 1 showed persistent mild pericardial effusion. Another 2 patients showed endothelial dysfunction. None of the patients had chronic conditions predating their COVID hospitalizations. All patients had findings that indicated

impairment in cardiorespiratory and oxidative metabolism during physical exercise with consistently lower than predicted values. The authors summarized their findings that this small-group study suggested that previously healthy pediatric patients had impaired myocardial blood flow, endothelial dysfunction, and lower cardiopulmonary capacity at follow-up after multisystem inflammatory syndrome associated with COVID-19. They added that additional exploration of their assessment techniques might aid in clinical decision making for these patients.

Physiological Reports

PET/CT and Sarcopenia in Elderly Mantle Cell Lymphoma

In an article in the February 23 issue of the *Journal of Clinical Medicine* (2022;11(5):1210), Albano et al. from the ASST Civil Brescia, the University of Brescia, and the ASST Valcamonica Esine (all in Italy) reported on a comparative study of the prognostic roles of ^{18}F-FDG PET/CT and CT-estimated sarcopenia in elderly individuals with mantle cell lymphoma. Fifty-three patients (39 men, 14 women; average age, 72.7 y) were included. All participants underwent PET/CT before and at the end of their institutions' standard chemotherapy regimens. Metabolic response was assessed at end-of-treatment PET/CT using Deauville scores. Sarcopenia was assessed as skeletal muscle index derived from low-dose PET/CT images at the L3 level, with specified cutoffs. Thirty-two (60%) patients were defined as sarcopenic. The 3- and 5-y progression-free survival rates were 29% and 23%, respectively. The corresponding overall survival rates were 43% and 33%. At a median follow-up of 50 mo, disease progression or relapse was documented in 37 patients (70%, average time of 17.2 mo; range, 2–62 mo); 26 of those patients had died. Metabolic response, total metabolic tumor volume, total lesion glycolysis, and sarcopenia were all found to be independent prognostic factors for progression-free survival, although no variable was correlated with overall survival. The authors

concluded that baseline evaluation of CT and PET may help to define sarcopenia in elderly patients with mantle cell lymphoma.

Journal of Clinical Medicine

Apatinib in ¹³¹I-Refractory DTC

In an article in the February 23 issue of *Frontiers in Endocrinology (Lausanne)*, Du et al. from Affiliated Cancer Hospital of Zhengzhou University/Henan Cancer Hospital (Zhengzhou, China) and People's Hospital of Changshou District (Chongqing, China) described their experience using apatinib in a group of patients with radioiodine-refractory differentiated thyroid carcinoma (DTC). The study included 47 patients (19 men, 28 women; mean age, 55.8 y; range, 48–68 y) who received 500 mg of apatinib daily for a 4-wk cycle. Participants underwent CT or MR imaging at 4 and 8 wk after initiation of treatment and every 8 wk thereafter. Although no patients achieved complete response, 36 (76.6%) achieved partial response and 8 (17.0%) saw stable disease, respectively. The objective response and disease control rates were 76.6% and 93.6%, respectively. The median progression-free and overall-survival rates were 18 and 59 mo, respectively. Of the 91 adverse events documented, 21 were grade 3 or higher. The authors concluded that apatinib has distinct efficacy in radioiodine-refractory DTC in terms of objective response rates and progression-free and overall survival, with a favorable safety profile.

Frontiers in Endocrinology (Lausanne)

Reviews

Review articles provide an important way to stay up to date on the latest topics and approaches through valuable summaries of pertinent literature. The Newsline editor recommends several general reviews accessioned into the PubMed database in February and March. Roussel et al. from University Hospitals Leuven (Belgium), the San Raffaele Scientific Institute (Milan, Italy), Fox Chase Cancer Center/Temple University Health System (Philadelphia, PA), Radboud University Medical Center (Nijmegen, The Netherlands), University of Texas Southwestern Medical Center (Dallas, TX), the Johns Hopkins University School of Medicine (Baltimore, MD), and the University of Pittsburgh School of Medicine (PA) published "Novel imaging methods for renal mass characterization: A collaborative review" on February 22 ahead of print in *European Urology*.

Karapanou et al. from the General Military Hospital of Athens, Evangelismos Athens General Hospital, and Alexandra Hospital Athens University School of Medicine (all in Greece) provided an overview of "Advanced RAI-refractory thyroid cancer: An update on treatment perspectives" on March 1 ahead of print in *Endocrine-Related Cancer*. In an article in the February 25 issue of *Frontiers in Endocrinology (Lausanne)*, Morris et al. from the National Institutes of Health Clinical Center (Bethesda, MD) reviewed "Parathyroid imaging: Past, present, and future." Alzghoof et al. from Amsterdam UMC/Vrije Universiteit (The Netherlands) and the University of Turku (Finland) summarized "α-Synuclein radiotracer development and in vivo imaging: Recent advancements and new perspectives" on March 15 ahead of print in *Movement Disorders*. Giovanella et al. from the Imaging Institute of Southern Switzerland/Ente Ospedaliero Cantonale (Bellinzona, Switzerland), the University of Turin (Italy), University Hospital of the European University (Limassol, Cyprus), the University of Messina (Italy), and the University Hospital Center Sestre Milosrdnice (Zagreb, Croatia) reported in the March 1 issue of *Cancers (Basel)* (2022;14[5]:1272) on "Molecular imaging and theragnostics of thyroid cancers."

Translational Cancer Research Priorities and the Role of Molecular Imaging

A Conversation Between Chi Van Dang, Elizabeth Jaffee, and David Mankoff

Chi Van Dang[1], Elizabeth Jaffee[2], and David Mankoff[3]

[1]Johns Hopkins, Baltimore, Maryland; [2]National Institutes of Health, Bethesda, Maryland; and [3]University of Pennsylvania, Philadelphia, Pennsylvania

David Mankoff, associate editor for *The Journal of Nuclear Medicine,* talked with Chi Van Dang and Elizabeth Jaffee about their leadership in guiding national priorities for translational cancer research and their perspectives on the role of molecular imaging and theranostics.

Dr. Dang is the scientific director of the Ludwig Institute for Cancer Research (New York, NY), where he oversees the execution of Ludwig's scientific strategy to advance the prevention, diagnosis, and treatment of cancer. He is also a professor of Molecular and Cellular Oncogenesis at the Wistar Institute Molecular and Cellular Oncogenesis Program (Philadelphia, PA). His work focuses on cancer cell metabolism, and his laboratory established the first mechanistic link between the MYC cancer gene and cellular energy metabolism. Dr. Dang is a national leader in cancer research, including roles as former director of the University of Pennsylvania's Abramson Cancer Center, former National Cancer Institute (NCI) Board of Scientific Advisors chair, and member of the Blue Ribbon Panel for the Biden Cancer Moonshot Initiative. He is the current editor-in-chief of *Cancer Research* and cochair of the NCI Clinical Trials and Translational Research Advisory Committee (CTAC) Translational Research Strategy Subcommittee.

Dr. Jaffee runs a National Institutes of Health–funded laboratory dedicated to developing novel therapies for pancreatic cancer and has more than 200 peer-reviewed publications. She serves as the deputy director of the Sidney Kimmel Comprehensive Cancer Center at Johns Hopkins (Baltimore, MD), where she is a professor of oncology. She is also the inaugural director of the new Johns Hopkins Cancer Convergence Institute, which aims to marry emerging technologies with computational biology and to cross-train scientists in biology and data science. She has served on numerous national committees, including as chair of the National Cancer Advisory Board, cochair of the Blue Ribbon Panel of the Cancer Moonshot Initiative, and as president of the American Association for Cancer Research (AACR). She was elected to the National Academy of Medicine and is a fellow of the American College of Physicians, the AACR, and the Society for Immunotherapy of Cancer Academy of Immuno-Oncology.

Dr. Mankoff: *What are the major accomplishments of the Cancer Moonshot Program thus far? What areas still have work to be done?*

Dr. Jaffee: There were 10 original recommendations for prioritizing research funds. These spanned basic discovery to implementation science and included new technology and data science platforms, with emphasis on health disparities throughout all priorities. In the relatively short time since this program was funded (5 y), there has been implementation of NCI-supported and -guided multicenter consortiums and programs in most areas, including discovery science in previously underfunded cancers such as glioblastoma, pancreatic cancer, and pediatric cancers; investment in translational and clinical studies; new and enhanced implementation studies (colorectal cancer as one example); and increased funding opportunities in health disparities through R01s, Specialized Programs of Research Excellence, etc. We are already seeing measurable outcomes, such as Human Tumor Atlas data uncovering new pathways in different tumor types, new multicenter clinical trials, etc.

Chi Van Dang, MD, PhD

Elizabeth Jaffee, MD

Dr. Dang: There are already some clearly tangible results from the Moonshot Program. I think one important result that the NCI has been able to accomplish is to create networks of investigators who can come together to work on specific issues. For example, the Moonshot has created immunology and immune oncology networks. These networks have worked to standardize immunooncology reagents and assays for translational and clinical research and will play a large role in translational research and advancements in immune oncology research and clinical practice. Another area that has advanced well is the Human Tumor Atlas via the network that was created. This network is now generating several very nice papers on mapping human tumors at the single-cell level, including single-cell imaging and sequencing. That's another tangible accomplishment of the Moonshot Program.

Dr. Mankoff: *I noted your February 2021 Cancer Moonshot 2.0 commentary in* Lancet Oncology *(2021;22:164–165), which called for a new Cancer Moonshot Commission to follow up the prior Commission report published in 2017. What are the priorities for that new commission? Are there specific areas of cancer science and technology you anticipate prioritizing?*
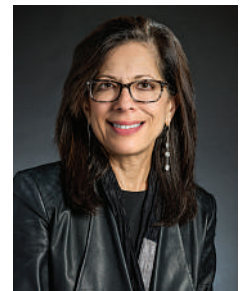
Dr. Jaffee: Data science—all aspects—require critical investments. Multiomic, single-cell, and imaging technologies are rapidly expanding and generating unprecedented quantities of data that will require new approaches for safe storage that can handle large quantities of data, processing, and analyzing. In addition, we emphasized development and implementation of new forms of health-care technologies to improve health-care access and real-time assessment in changes in disease states.

Dr. Dang: I agree. We have a ton of clinical data, and researchers and research organizations such as NCI should help support work to leverage these data. People are really starting to use machine learning and artificial intelligence to discern features in clinical data that will inform both cancer research and oncologic clinical practice. Imaging should be a priority here. Whether it's digital pathology or radiology, imaging is obviously a natural fit for data science methods.

Dr. Mankoff: *I was delighted that the 2017 Lancet Oncology Commission report included a section on nuclear medicine and molecular imaging. In that section, there are several priorities put forth on using imaging to guide therapy, combining in vitro and in vivo diagnostics, using big data and image analytics to inform cancer decision making, advancing theranostic treatments, creating clinical decision models to guide the use-effective and cost-effective imaging in cancer care, and streamlining regulatory, payment, and clinical integration for molecular imaging and theranostics. Which of these areas have seen progress, and which need more work?*

Dr. Jaffee: Imaging should continue to be a high priority. We need to do better with molecular imaging to help guide molecular-based diagnosis and treatment response and resistance. I am very

imaging playing a role in helping us identify and measure factors mediating tumor plasticity and related therapeutic resistance.

Dr. Mankoff: *Theranostics, a term used to describe radionuclide therapy and paired companion imaging diagnostics, has gotten considerable notice recently, with notable advances in neuroendocrine tumors and prostate cancer, for example. From your viewpoints, how does theranostics fit into the future of cancer research and cancer care?*

Dr. Dang: I would say that this is a great field. There are still a relatively small number of agents in the clinic, but it would be good to bring theranostics to greater public attention and say: "Look, these agents make a difference in the clinic." I think you may be doing this already through the SNNMI, but more public awareness of the success of radioisotope therapy across a range of venues will help. I would love to see more Food and Drug Administration–approved agents, but at the same time you need to increase the pipeline. This means you need more funding to work on this area for new targets and to provide proof of concept for these targets. There is some new cancer science that may help this process. For example, can you probe proteomics to identify targets with sufficient differences in surface proteomes between tumors and normal tissue, so that you can hit the target and deliver a therapeutic radioisotope payload? This is a process that can be informed by advances in proteomic methods along with advances in science and technology in pairing diagnostic and therapeutic radiopharmaceuticals. This type of approach could yield new targets and agents. I'd love to see more theranostics approved.

Dr. Mankoff: *Liz, another area of emphasis in molecular imaging has been in immune-specific imaging. As a cancer immunotherapy leader, what are the priorities for diagnostics in the field, and how can molecular imaging help?*

˝Imaging should continue to be a high priority. We need to do better with molecular imaging to help guide molecular-based diagnosis and treatment response and resistance.˝

---

excited to be working with my nuclear medicine colleagues on developing immune-targeted imaging approaches. Imaging can also help us understand cancer development and progression. Invasive biopsies are not easy to obtain, and serial analysis is difficult. Nuclear medicine can provide new ways to do "noninvasive" molecular analyses over time to study cancer development and evolution. Finally, moving to interception, we need new ways to uncover early premalignant changes to intervene early with surgery, immunotherapy, targeted therapies, etc.

Dr. Dang: We need to prioritize funding for people to do more research on image analysis and new imaging technology. For example, we have come to understand—more and more every day—the importance of the tumor microenvironment: how the immune system impacts tumor behavior and response to treatment. Can we image and quantify regional tumor microenvironmental properties? For example, tumor-associated macrophages are increasingly recognized as a factor in tumor initiation and progression, and it would be helpful to be able to not only identify them, as has been done in early studies, but to characterize their phenotypes and behavior in response to treatment. It would be lovely to develop more tools for imaging these phenomena in vivo and for guiding immune oncology practice. Another area of need is in the issue of tumor plasticity and the role of metabolism and epigenetics in mediating changes in tumor behavior, including things such as dormancy. These are still areas we don't completely understand. As we learn more, I can see

Dr. Jaffee: As per my answer on imaging priorities, I think the ability to identify immunotherapy targets and assess immune activation will be important components of the ongoing development and refinement of immune-directed cancer therapies and could play an important role in guiding cancer immunotherapy in the clinic.

Dr. Mankoff: *Chi, in addition to your role in the Cancer Moonshot, you've helped lead efforts on translational research on major NCI advisory panels, including serving as coleader on the CTAC Translational Research Strategy Subcommittee. From this viewpoint, what are some areas of translational research priority where nuclear medicine can play an important role?*

Dr. Dang: One priority to address is imaging across the scale from microscopic images to images that encompass the whole body. In the future, could we see coregistration of histologic section/tissue assay data with the type of macroscopic imaging data that come from medical imaging? Can advances in imaging technology, at all scales and together with machine learning and data science, help us here? For example, in the immune microenvironment, can we relate measures of immune cells, such as M1 and M2 macrophages and different classes of T cells, to features on a PET or CT scan at the site of tissue sampling and use that approach to enrich what can be learned from both microscopic and macroscopic imaging to help guide immune-targeted therapy?

Related to this question, is it possible to get more than one parameter at a time out of molecular and functional imaging?

Cancer tissue samples undergo increasing numbers of assays for a range of molecular processes relevant to diagnosis and treatment. Advancing technologies for tissue analysis are making multiplexed assays easier and more efficient. Can imaging do the same thing? I know, Dave, that you are working on multiple tracer injections to measure cancer metabolism as part of your Cancer Moonshot–funded effort, as are others in the field. I don't know what factors limit your ability to image multiple processes, but can you push molecular imaging to yield information on a greater number of molecular features at the same time?

Dr. Mankoff: You have both emphasized integration and collaboration in cancer research. How can nuclear medicine play a role in this effort? Through technology integration efforts? Through specific areas of collaboration with cancer biology, oncology, or radiation oncology research efforts?

Dr. Jaffee: Nuclear medicine is central to multiinvestigator translational science. A major limitation in understanding disease development, progression, and response to new therapies is the lack of noninvasive techniques that can be used safely and repeatedly to get data. Molecular targets for nuclear medicine need to be identified, as well as new ways to assess functional changes in tumors that are specific to pathway changes. These need to be prioritized.

Dr. Dang: I have also been impressed that nuclear medicine can be foundational in translational research. This is an area in which more formal inclusion of nuclear medicine in guiding cancer translational research would be helpful. You've done some of this, Dave, as a member of the NCI CTAC Translational Research Subcommittee that I colead, and I know others in nuclear medicine have had similar roles in other NCI research groups. I think nuclear medicine and cancer leaders should look for even more

changers. We are able to quickly uncover and assess changing cancer signals with the tumor microenvironment to understand cancer development and progression, cancer heterogeneity, and cancer sensitivity and resistance to different therapies. This is already allowing us to improve patient-specific treatments, develop more effective and less toxic drugs, and consider interventions at earlier cancer stages and even at the precursor stage.

Dr. Dang: I have a related answer. I suspect I'm going to be wrong about this, but I think that over the last several decades, the major hubs of cancer biology have been identified. We know what the hubs are; now we need to better understand how they connect. We know that epigenetic modifiers play a big role. But now what we are confronting is a complex network with major hubs that have modifiers tugging on them. What matters in the clinic is whether a system of cancer biology hubs is going to collapse under the weight of a specific therapeutic approach or is robust enough to resist treatment. We are starting to confront this complexity, in that we realize that we need to really understand the complexity of the tumor, its microenvironment, and the related systems biology of the host. But we need more tools for this task. I think this is the most important remaining challenge in cancer research: to be able to understand in vivo cancer biology across the scale from fundamental molecular processes to integration of biologic systems across the whole body. I think nuclear medicine can help here.

Dr. Mankoff: Do you have any other advice or suggestions for nuclear medicine scientists and physicians working in cancer research?

Dr. Dang: My big push right now is team science, especially in my role as scientific director of the Ludwig Institute. I realize that

---

˝We need to prioritize funding for people to do more research on image analysis and new imaging technology.˝

---

opportunities to bring nuclear medicine expertise to the organization that guide translational cancer research.

Dr. Mankoff: The Cancer Moonshot Blue Ribbon Panel and Lancet Oncology Commission reports both emphasized a need for improved training in cancer research. For highly specialized and technical fields such as ours, how might this be best accomplished? Any advice on how we can best train the next generation of imaging/nuclear cancer research leaders?

Dr. Jaffee: We need to cross-train the next generation on technologies, biology systems, and data science. Organizations such as AACR can be helpful in providing national education platforms. Collaborations between different national and international societies would be a great first step.

Dr. Dang: Imaging will be one area in which we want to train both basic and clinical scientists who really are interested in making a difference in the clinic. This should continue to be emphasized in both clinical and research training in nuclear medicine, across all relevant areas of expertise in the field.

Dr. Mankoff: What are the next game changers in cancer research? How can we best support advances in these areas?

Dr. Jaffee: Single-cell and spatial technologies and their associated analytic platforms including artificial intelligence are game

individual investigators have their own labs and are a force for innovative, completely new ideas. We want to continue to encourage this innovation. However, I think translating lab discoveries to the clinic for the benefit of patients requires team science. We need to create more incentive for people to collaborate. As an interesting example of a novel approach, one idea that I posed jokingly in a talk I gave was the idea of a "circular" author list for scientific papers—no beginning and no end to the author list. Kind of a crazy idea, but library science might be able to handle this.

As another example, I mentioned artificial intelligence and data science earlier, an area that most cancer biologists know very well. How can we bring together these 2 distinct areas of biology and technology? Nuclear medicine has always lived at the intersection of technology and clinical biology and can perhaps help lead this charge.

Dr. Mankoff: Liz and Chi, thanks so much for taking the time to have this conversation. I know that, as leaders in cancer research and major cancer research organizations, you are both extraordinarily busy. I and the readers of The Journal of Nuclear Medicine *greatly appreciate your thoughts about priorities for translational cancer research and the role of nuclear medicine and molecular imaging. Thank you both!*

A Guideline for Clinicians Performing Clinical Studies with Fluorescence Imaging

Wido Heeman*[1–3], Jasper Vonk*[4], Vasilis Ntziachristos[5,6], Brian W. Pogue[7], Rudi A.J.O. Dierckx[8], Schelto Kruijff[2,8], and Gooitzen M. van Dam[8,9]

[1]University of Groningen, Faculty Campus Fryslân, Leeuwarden, The Netherlands; [2]Department of Surgery, University Medical Center Groningen, University of Groningen, Groningen, The Netherlands; [3]LIMIS Development B.V., Leeuwarden, The Netherlands; [4]Department of Oral and Maxillofacial Surgery, University Medical Center Groningen, University of Groningen, Groningen, The Netherlands; [5]Chair of Biological Imaging, Center for Translational Cancer Research (TranslaTUM), Technical University of Munich, Munich, Germany; [6]Institute of Biological and Medical Imaging, Helmholtz Zentrum München, Neuherberg, Germany; [7]Thayer School of Engineering and Department of Surgery, Dartmouth College, Hanover, New Hampshire; [8]Department of Nuclear Medicine and Molecular Imaging, Medical Imaging Center, University Medical Center Groningen, University of Groningen, Groningen, The Netherlands; and [9]AxelaRx/TRACER B.V., Groningen, The Netherlands

Fluorescence imaging is an emerging imaging technique that has shown many benefits for clinical care. Currently, the field is in rapid clinical translation, and an unprecedented number of clinical trials are performed. Clinicians are inundated with numerous opportunities and combinations of different imaging modalities. To streamline this process, a multidisciplinary approach is needed with drug discovery, software and systems engineering, and translational medicine. Here, we discuss the main constituents of a uniform fluorescence imaging protocol to match the clinical need and ensure consistent study designs and reliable data collection in clinical trials. In an era in which the potential of fluorescence imaging has become evident, consistent conduct of studies, data analysis, and data interpretation is essential for implementation into the standard of care.

Key Words: optical; research methods; clinical translation; fluorescence imaging; molecular imaging; optical imaging

W ide-field fluorescence imaging (FI) is a rapidly evolving imaging technique. By probing optical contrast, FI visualizes biochemical, physiologic, or pathophysiologic processes that human vision cannot detect (*1*). In medicine, and specifically in surgery, the potential of FI has been shown for nontargeted indications such as assessment of tissue perfusion, retinal vasculature, and sentinel lymph node mapping (*2–5*). Efforts to improve the specificity of the signal have led to the development of targeted FI for the detection of malignant or premalignant lesions and locoregional metastases (e.g., lymph node or peritoneal metastases), delineation of tumor margins, evaluation or

prediction of treatment response, and, more recently, visualization of critical anatomic structures, such as nerves (*6–10*). Although the field has grown exponentially in FI camera system performance and fluorescent tracers, broad implementation into the standard of care has not yet been established (*11–13*).

Currently, the first phase II and III trials are being reported—overviews of currently ongoing clinical trials have been presented recently (*12,14*), and the first Food and Drug Administration breakthrough therapy designation has been assigned for use in breast cancer surgery (*15*). As such, the number of clinicians having access to FI camera systems (e.g., surgical robot–assisted systems with incorporated FI) is also rapidly increasing. Choosing the appropriate imaging approach for a clinical problem is based on the strengths and weaknesses of the available FI imaging systems and fluorescent tracers. This requires a basic understanding of the underlying physics of FI and the chemistry of the fluorescent tracers used.

Swift implementation of FI into the standard of care requires a multidisciplinary approach, which is especially important when conducting a clinical study with FI. We strongly advise clinicians to partner with FI experts (e.g., engineers, physicists, and chemists) in early phases of trial design. The fluorescent tracer and FI camera system must be chosen carefully. Perhaps most importantly, it requires the users to be cognizant of both the drug and device limitations for clinical use. The protocol should result from multiple constituents, such as clinical indication, applied FI camera system, target moiety, signaling compound, standardized imaging acquisition, data processing, and, finally, image interpretation. An inadequate imaging approach leads to a flawed clinical trial or individual imaging procedure but, more importantly, comes with unnecessary patient risk and societal burden. These risks include elongated anesthesia and operation time, unnecessary health-care costs, and exposure to novel compounds without a fully elucidated pharmacologic profile.

Clinical FI studies should be based on a scientifically substantiated imaging approach that relies on the cornerstones of science, standardization, and reproducibility. This paper aims to provide a guideline for clinicians who want to perform wide-field FI trials that lead to clinical implementation or for translational research and development.

DEFINING THE CLINICAL INDICATION AND IDENTIFYING THE APPROPRIATE TARGET

The driving motivator for a new trial is a clinician with a clinical challenge and the desire to test a new optical imaging approach, potentially leading to the birth of a new relevant application. In contrast to radiographic imaging techniques, FI can be seamlessly integrated into the standard of care. It relates directly to the surgeon's vision and uses portable and relatively low-cost instrumentation, nonionizing radiation, and real-time feedback (16). Yet, the clinician needs to think of the clinical value and practical issues. For example, an urgent surgical procedure requires fluorescent tracers that accumulate rapidly at the target site.

When such practical issues have been addressed, a more refined imaging approach can be developed (Fig. 1). FI imaging in the visible spectrum (e.g., fluorescein or methylene blue) is often not sufficient because of its low penetration depth resulting from strong photon absorption in this spectrum. Most clinical indications require assessment of subsurface structures (i.e., >1 mm), with the absorption and scattering of light being the main limiters of penetration depth. The user should be aware of the tissue of interest's optical properties (i.e., scattering and absorption) and its impact on light propagation (17). Tissue types exhibit specific optical properties; for example, more absorption occurs in a highly vascularized liver than in muscle tissue. Penetration depth can be improved by imaging in the near-infrared window (i.e., 750–1,700 nm). This spectral region benefits from reduced scattering and lowest absorption by tissue chromophores (e.g., hemoglobin and water). A critical note here is that the signal is heavily surface-weighted because of light attenuation in tissue (i.e., absorption and scattering) and that the spatial resolution decreases with depth because of scattering (Fig. 2) (18).

When the user is aware of the tissue of interest's optical properties, the biochemical phenomenon or the physiologic or pathophysiologic process should be concretized. All possible targets, including biomarkers and phenomena or processes, should be examined to determine which is most suitable for localization or evaluation of the target tissue. For example, one can image breast
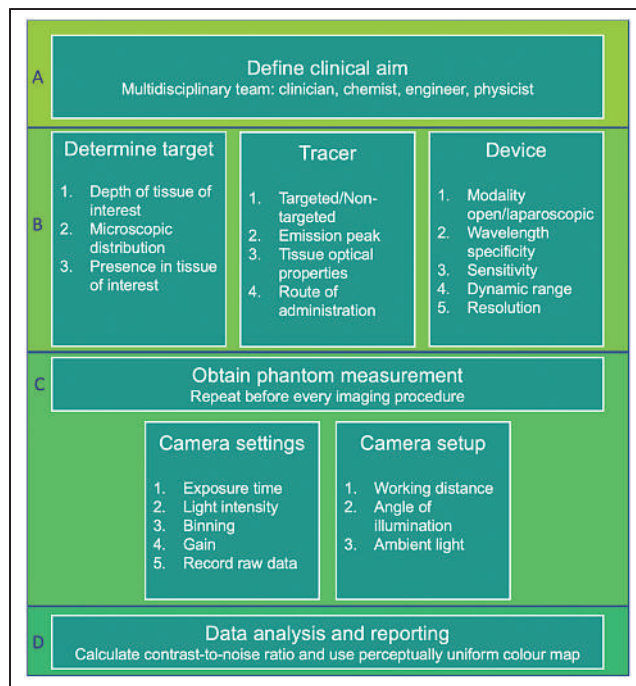
FIGURE 1. Checklist for performing in vivo FI studies. Step-by-step approach is used to ensure standardized and reproducible FI clinical trial, including trial design, imaging acquisition, data analysis, and reporting results. First, clinician involved should define clear and specific clinical aim in close cooperation with chemist, engineer, and physicist. Team then defines biologic target with microscopic distribution and required penetration depth in mind. Tracer must match target and should be selected on basis of targeted or nontargeted approach, tracer's emission peak, tissue optical properties, and administration route. Simultaneously, device emission and excitation filters must match tracer's wavelength. Also, form factor should be determined, along with desired resolution, sensitivity to light, and dynamic range. Before every imaging procedure, phantom measurements should be obtained to evaluate performance characteristics over time. User should set camera settings such as exposure time, binning, gain, and emission light intensity, and data should be recorded without any preprocessing. Moreover, camera setup should be identical in every procedure, with respect to working distance, angle of illumination, and ambient light levels, to compare results across patients. After data analysis, performance of fluorescent tracer and imaging device combination should be reviewed on basis of CNR ratio. Images should be processed using perceptually uniform color maps.

NOTEWORTHY

- An FI protocol results from multiple constituents, such as clinical indication; applied FI camera system; target moiety; signaling compound; and standardized image acquisition, data processing, and image interpretation.

- Benchmarking of camera systems is required for intercomparable data since results are greatly affected by characteristics such as camera detection sensitivity, depth sensitivity, field illumination homogeneity, exposure time, resolution, and dynamic range.

- Imaging procedures must be standardized regarding tracer administration, working distance, incident angle, and ambient light.

- Clinical acceptance of FI requires standardized and reproducible clinical data based on an imaging approach that relies on the cornerstones of science: standardization and reproducibility.

- The discriminatory power of a tracer for a certain indication should be reported using the CNR ratio, and images should be presented using perceptually uniform science-derived color maps.

cancer through visualizing nonspecific intratumoral phenomena (e.g., enhanced permeability and retention effect), a specific cell membrane–bound receptor, or a pathophysiologic phenomenon in the tumor microenvironment. Methods for target selection have been reported previously (19,20). Briefly, the potential target should prevail in the target tissue compared with directly adjacent tissue, benefiting high binding sensitivity and specificity as well as improving the contrast. Target expression is commonly determined by immunohistochemistry. However, it is increasingly questioned whether the target is representative of the complete tumor because of tumor heterogeneity and variations in target expression over time. Data-driven methods based on genomic alterations are studied to identify and prioritize relevant targets for clinical trials (21). In addition, many targets (e.g., cell membrane receptors) are present in a microscopically heterogeneous pattern. For solid tumors that require wide local excision, the latter does not per se impede guiding the surgeon in tumor resection since the margin is of primary interest (22–24). In contrast, in
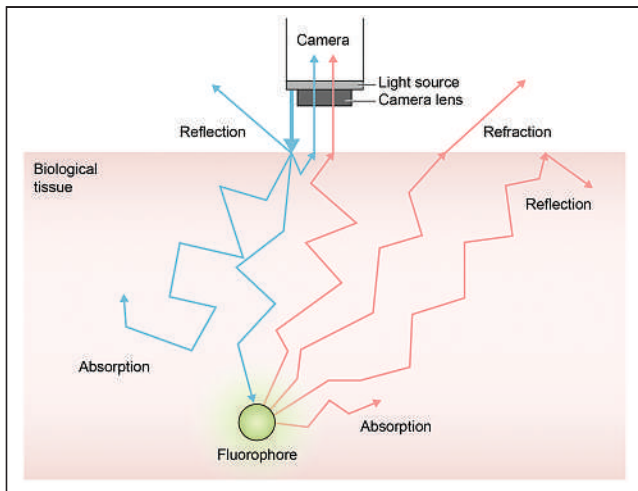
FIGURE 2. Basic principles of fluorescence and tissue optical properties. Fluorescent contrast generation starts with illuminating tissue at appropriate wavelength for excitation of fluorophore (i.e., endogenous or exogenous contrast). Fluorophore is excited from ground state to excited state by short-lived light absorption. Immediately after excitation, fluorophore relaxes to lower energy state and emits light of lower energy and longer wavelength than excitation light. Emitted light propagates out of tissue and is detected by fluorescence detector, which converts recorded light into image demonstrating number of photons detected. Light propagation and imaging depth are limited by tissue optical properties. Absorption causes light energy to be transferred to tissue, decreasing light intensity. Scattering is process of short-lived absorption of photon (typically) without energy loss but with change of initial direction. Also, scattering decreases ability to distinguish details. If there is no correction for tissue optical properties, signal registered is rather qualitative than quantitative.

debulking surgery procedures (e.g., glioblastoma surgery), homogeneous contrast is of clinical importance since microscopic residues should be identified in order to excise all tumor tissue (25,26).

SELECTION OF THE APPROPRIATE IMAGING MODALITY

When selecting FI camera systems for a clinical trial, the system's form factor must fit in the expected clinical setting. For instance, in oral cancer, tumors can be visualized using an open system, but perfusion assessment during minimally invasive surgery requires a laparoscopic system. Next, the user should be aware of the system's performance characteristics to obtain the desired imaging data, as these parameters greatly affect the results (11). There are numerous parameters to consider, but one should focus on those that directly influence imaging data, such as the camera detection sensitivity to the desired tracer, depth sensitivity, field illumination homogeneity, spatial and temporal resolution, and dynamic range. These minimum requirements for these parameters should be fine-tuned for a specific imaging study, preferably in cooperation with an engineer and a physicist.

The camera detection sensitivity describes the ability of an FI camera system to detect

a certain concentration of a specific contrast (i.e., fluorescent dye and corresponding emission wavelength). This determination should be made for every combination of an FI camera system and a fluorescent tracer since the system's foremost influential characteristic is the sensitivity to the fluorescent tracer's emission peak. Commercially available FI camera systems are equipped with specific narrow-band optical filters. A mismatch between the optical filters and the fluorescent tracer results in a low fluorescence intensity and could lead to an erroneous conclusion that a fluorescent tracer dose or microdose does not accumulate in the region of interest since the contrast-to-noise ratio (CNR) is low (Fig. 3B).

Depth sensitivity is the ability to measure fluorescent signal at a certain depth. This is largely dependent on the type of light (i.e., coherent or noncoherent) and the wavelength-specific penetration depth of the excitation light. Ideally, devices should evolve to account for this automatically, yet the user should be aware for each clinical application of interest (27). For margin assessment, the imaging depth may vary among different tumors, since the definition of an adequate margin is different. Head and neck cancer requires a tumor-free margin of at least 5 mm, whereas for breast cancer this is at least 1 mm. Although the penetration depth of light increases with longer wavelengths (i.e., near-infrared versus visible spectrum), this does automatically translate to increased measurement depth. When deeper tissues are imaged because of increased scattering, the discrimination between target and surrounding tissue is impaired because of a decreasing CNR with imaging depth (i.e., low depth sensitivity) (Fig. 2).

Field homogeneity describes how uniformly the region of interest is illuminated. Inhomogeneous field illumination can lead to over- or underestimation of the fluorescent signal throughout the field of view. Perfect field homogeneity is rarely achieved in practice, and only a few FI camera systems have implemented algorithms to improve field homogeneity. Most systems, especially endoscopic ones, have highly inhomogeneous light fields that lead to steep intensity fall-off toward the edge of the field. The user should validate the field homogeneity before every imaging procedure using
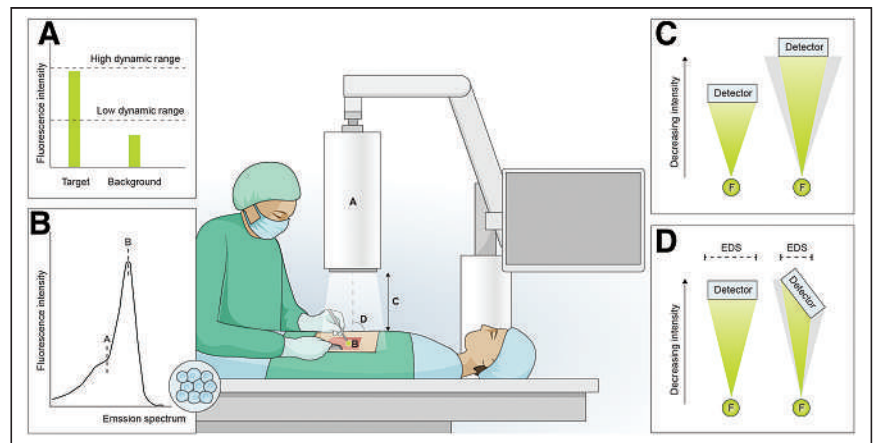
FIGURE 3. Potential pitfalls in FI studies. (A) CNR ratio is strongly dependent on dynamic range of FI camera system concerning fluorescent tracer. When imaging tissue using fluorescent tracer with high quantum yield, system with high dynamic range would result in higher CNR ratio than would system with low dynamic range. (B) Fluorescence intensity detected by FI camera system is dependent on match between system's optical filter and emission peak of fluorescent tracer used. Mismatch between emission peak and optical filter will result in suboptimal fluorescence intensity detected (wavelength A) compared with most optimal (wavelength B). (C) Fluorescence intensity exponentially decreases with increased working distance because of diverging nature of light. (D) When detector is not placed perpendicular to tissue of interest, effective detection surface that can detect emitted photons is smaller. As such, fluorescence intensity is falsely reduced, possibly leading to erroneous conclusions. EDS = effective detection surface.

a calibration phantom. An inhomogeneous field illumination is not an insurmountable problem, as long as the user is aware and knows how to interpret and correct for it (28).

The resolution of an FI camera system is characterized by spatial and temporal resolution. The spatial resolution dictates the modality's ability to differentiate between the smallest fluorescent sources. The spatial resolution should at least be half the size of the smallest feature that has to be detected, as described by the Nyquist theorem. The temporal resolution dictates the modality's ability to detect changes in signal over time. This ability is of importance when a dynamic phenomenon is of interest, such as organ perfusion (e.g., semiquantitative indocyanine green) (29).

The dynamic range greatly influences the ability to measure fluorescent signal. The dynamic range (i.e., the detector's quantum efficacy) is the measure for the highest and lowest amount of measurable light for a set exposure time. A camera system with a low dynamic range can measure either very high or very low signals, depending on exposure time. However, the camera cannot do so both at the same time. Hence, a camera with a high dynamic range can measure both very bright (i.e., high quantum yield) and very dim (i.e., low quantum yield) fluorescent signals (Fig. 3A).

BENCHMARKING OF FLUORESCENCE IMAGING CAMERA SYSTEMS

To compare different FI camera systems, universal standards are required for benchmarking their performance, as is common in the other medical imaging modalities (30). As such, solid-tissue–mimicking phantoms have been developed to characterize the different FI imaging systems quantitatively. Wells filled with different concentrations of nanoparticles (i.e., quantum dots) are used to measure camera detection sensitivity versus optical properties, depth sensitivity, dynamic range, field homogeneity, and spatial resolution (28). We advise that users acquire an FI camera system with high camera detection sensitivity in combination with a high dynamic range. Also, the camera wavelength specificity and emission light sources should match the excitation and emission spectra of the fluorescent tracer (Fig. 3B) (27,31,32).

Performing phantom measurements before each imaging procedure informs on system stability over time and provides users better insight into the performance capabilities. A standardized image of an FI phantom should be taken under strict imaging acquisition parameters (i.e., camera distance, incidence angle, and ambient light) and processed according to a strict protocol (28,31,32). Automated log files should be constructed according to a standardized format and recorded for review purposes, safeguarding a quality management system for FI in clinical use. Ideally, these log files are archived with the patient data and imaging results, allowing for calibration in later analysis of batch data, similar to the metadata archived in DICOM images taken with radiologic imaging systems. We propose a quality management system to enable comparative multicenter clinical trials and implementation in general practice, enabling uniformity.

Additionally, FI camera systems should have the option to export raw data without interference from undesired image postprocessing to obtain quantitative or semiquantitative data rather than qualitative images. However, some commercial intraoperative imaging devices often opt for an underlay for the surgeon's orientation purposes, which impedes the possibility of quantification (11).

FLUORESCENCE CONTRAST

Fluorescence contrast can be either endogenous (i.e., autofluorescence of intrinsic tissue compounds) or exogenous (i.e., administered fluorescent tracer) (33). Although the use of endogenous contrast has some advantages, such as inherent nontoxicity and absence of regulatory issues, we focus on the use of exogenous contrast as this has been shown to increase specificity and detection sensitivity (34). The main criteria for selecting a fluorescent tracer include efficient fluorescent light output (i.e., quantum yield), biodistribution and pharmacokinetic characteristics, signal enhancement strategies (i.e., "always-on" versus "activatable" or "smart"), and regulatory approval (12). Lastly, the clinician must be aware of regulatory issues that can result in tremendous costs when designing and using new fluorescent tracers, such as intellectual property, animal toxicology studies, availability of compounds in a good-manufacturing-practice facility. and regulatory approval (35,36).

Generally, exogenous fluorescent tracers can be divided into targeted and nontargeted tracers. Nontargeted tracers do not bind to biomarkers for disease specificity but accumulate passively into the tissue through metabolism or nonspecific uptake (e.g., enhanced permeability and retention effect in tumors). A well-known nontargeted fluorescent tracer is indocyanine green, which has Food and Drug Administration approval for tissue perfusion assessment, sentinel lymph node mapping, and biliary duct visualization. As fluorescent dyes themselves are not tumor-specific, efforts to improve specificity have led to the development of targeted fluorescent tracers that bind to receptors or biomarkers (37). Particularly in interventional oncology (e.g., surgery or gastroenterology), phase I studies have shown the potential of these tracers for margin assessment and characterization of lesions. Recently, breakthrough therapy designations have been assigned by the Food and Drug Administration (i.e., Pegloprastide [Avelas Biosciences], a ratiometric fluorescent probe for breast-conserving surgery) (15).

The clinical indication should be leading when one is deciding between a targeted and nontargeted approach. The targeted approach is generally more complex and thus not always preferred. A nontargeted tracer could suffice for sentinel lymph node mapping as such a tracer generates contrast between the lymph nodes and the adjacent tissue. Contrarily, tumor delineation requires a targeted tracer with higher tumor specificity. Even though targeted tracers are used, one should realize that the signal is not proportional to the concentration of the target but is confounded by nonspecific sources of contrast. This nonspecific accumulation of fluorescent tracer is intrinsically determined by its receptor affinity but is also affected by physiologic phenomena, such as vascularity, vascular permeability, interstitial pressure, and lymphatic drainage (38). Paired imaging methods are currently being studied to correct for the nonspecific tracer accumulation by coadministering an untargeted control agent with similar pharmacokinetics (39,40). A wide range of fluorescent tracers is currently being studied in clinical trials, including small molecules, peptides, proteins, and nanoparticles, as described elsewhere (37).

Current developments to improve fluorescent contrast include the use of activatable or smart fluorescent tracers that fluoresce only after interaction with or binding to the target (41,42). Rather than visualizing one fluorescent tracer in a single lesion, multispectral imaging (i.e., imaging fluorescent probes at different or multiple wavelengths) could simultaneously visualize multiple fluorescent tracers that report on different targets within the same patient. The advantages include the delivery of a more homogeneous signal, increased sensitivity, and the ability to obtain anatomic–molecular information (43). For example, one might strive to both perform molecular imaging of the tumor and identify critical structures (e.g., nerves), both contributing to an optimal surgical outcome and both requiring a specific tracer with different fluorescent excitation and emission wavelengths. Technical

challenges include accurately separating signals and correcting for differences in fluorescent dyes (i.e., efficiency of fluorescent signal generation and wavelength-dependent tissue optical properties), as described elsewhere (44). The clinical introduction, safety, and applicability of multispectral FI remain to be investigated in clinical trials.

IMAGE ACQUISITION: REPRODUCIBILITY AND STANDARDIZATION

Reproducibility and standardization should be central within the 2 primary components of an FI study protocol: tracer administration and image acquisition. Similarly to PET, the tracer administration must be dosed and timed consistently throughout the entire study population (45). The exact dose is commonly determined using dose-escalation schemes, with pharmacokinetics, biodistribution, and toxicology studies in animals, healthy volunteers, or subjects belonging to the target population. Whether timing between tracer administration and image acquisition is crucial depends on the biodistribution and pharmacokinetic profile of the tracer. When studying a dynamic perfusion assessment (i.e., semiquantitative use of indocyanine green), the timing comes down to seconds. In such a setting, the administration can be standardized by using a syringe pump with a preprogrammed infusion rate. On the other hand, many targeted fluorescent tracers need substantial time (i.e., days) to bind to the target moiety and ensure clearance of unbound tracer from the blood.

The detected fluorescence is dependent on different specifications of the FI camera system (e.g., exposure time and gain) in combination with the contrast, as well as variable imaging parameters of the experiment itself (e.g., working distance, incident angle, and ambient light). Imaging with varying working distances substantially impacts the data consistency since the intensity measured is distance-dependent (Fig. 3C). Consequently, higher fluorescence intensity is detected when the distance from the tissue of interest to the detector decreases, even when the fluorescent light emitted is the same. The camera should be perpendicular to the tissue to maximize the effective surface area of the detector (Fig. 3D). When all variable imaging parameters are standardized in every FI measurement, the imaging data allow for reproduction and represent the tracer distribution more realistically (27). Ideally, all imaging parameters should also be registered to allow for post hoc correction.

Although the impact of ambient light in FI has never been underestimated (46), it is rarely standardized or corrected for. The most common solution is to keep the ambient light to a constant minimum, as relatively few systems can deal with high ambient-light intensity. The choice of lighting in the operating room can be optimized, typically by minimizing near-infrared light. This is specifically emitted from commonly used tungsten bulbs, which could simply be replaced by light-emitting diodes. Needless to say, this solution reduces the problem only for near-infrared-based emission probes such as indocyanine green.

REPORTING ON FI DATA

Apart from a standardized imaging protocol, standardized data processing, representation, and reporting are necessary for the implementation of FI in the standard of care. Contrary to some other imaging techniques (e.g., CT), wide-field FI does not provide quantitative data. Even when imaging parameters are standardized, variations in tissue optical properties affect the fluorescent signal. Additionally, the signal is heavily surface-weighted, meaning that anything closer to the surface will generate more fluorescent signal. These factors need to be taken into account when analyzing FI

data. The most used semiquantitative unit is mean fluorescence intensity, defined as the average pixel intensity within a region of interest. Yet, reporting the mean fluorescence intensity as an absolute and quantitative measure without a thoroughly standardized protocol can lead to incorrect conclusions.

Since FI is a detection or discrimination method, relative measures (i.e., ratios) are more appropriate for FI as these demonstrate the ratio between the target and the background. Commonly used ratios in clinical FI include tumor-to-background ratio, signal-to-background ratio, and CNR (47). We advocate the use of CNR, defined as the target's mean fluorescence intensity subtracted by the background's mean fluorescence intensity, divided by the SD of the background. Using a CNR is favorable since this is more informative on the detectability of the contrast (i.e., target) of interest (48). A high CNR indicates good discrimination between the target and background tissue. Still, the CNR is influenced by the FI camera system's dynamic range and quantum efficiency. For example, using a fluorescent tracer with a relatively high quantum yield together with 2 different FI camera systems with a low and high dynamic range may result in 2 very different CNRs. In other words, an FI camera system with a low dynamic range may underestimate the CNR because the signal of the tumor is limited (Fig. 3A). Also, despite the seemingly straightforward definition, these quantities are prone to bias due to the strong dependency on the definition of the surrounding tissue. Ideally, the target and the background are based on the gold standard (i.e., histopathology). The appropriate background must be adjacent tissue, as it mimics the clinical scenario.

Clinical use of FI relies on the interpretation of data that are typically shown as an image or video, even though the ratios are most important in clinical trials. Fluorescence images should be uniformly reported across the field to avoid difference in image interpretation. This reporting includes the choice of color map, functions for the lookup table, and image compression. Perceptually uniform science-derived color maps represent actual data variations, reduce complexity, and are accessible for color-deficient people (49). Yet, even when data are uniformly reported, the interpretation of FI signal without correction for tissue optical properties may lead to inaccurate conclusions. Lack of correction may, for example, lead to erroneous tumor delineation (due to scattering) in margin assessment when interpreted by different clinicians, Lastly, the used FI camera system settings must be described in detail. Reporting these settings is essential for the reproducibility of study results, as the FI camera system settings severely influence the obtained FI data.

CONCLUSION

The rapidly increasing interest in FI has led to serious improvements in the FI camera systems and fluorescent tracers available. Although FI has shown enormous potential for a variety of indications, the field has not yet established clinical implementation. Here, we have provided a guideline for clinicians to perform FI clinical trials (Fig. 1). The same conceptual thinking applies to other optical imaging modalities, such as laser speckle contrast imaging or spectroscopy-based techniques. Similar to the classic medical imaging field, the FI field should focus on training clinicians and supportive staff in a multidisciplinary way to better understand the underlying physics and chemistry. Still, we advise clinicians to collaborate with researchers who have experience with FI camera systems and fluorescent tracers in order to correctly acquire, analyze, and interpret the imaging data in an accurate and reproducible manner. To establish the clinical implementation of FI, phase II and III trials need to

commence using a consistent study design, imaging protocol, and data analysis. By emphasizing standardization and reproducibility, we can realize the full potential of FI and prove its clinical value.

DISCLOSURE

Vasilis Ntziachristos is an equity owner and consultant of iThera Medical GmbH, an owner of Spear UG, and a member of the Scientific Advisory Board of SurgVision B.V./Bracco Sp.A. Gooitzen M. van Dam is the chief executive officer and a founder and shareholder of TRACER Europe B.V./AxelaRx. No other potential conflict of interest relevant to this article was reported.

REFERENCES

1. Weissleder R. A clearer vision for in vivo imaging. *Nat Biotechnol.* 2001;19:316–317.
2. Koch M, Ntziachristos V. Advancing surgical vision with fluorescence imaging. *Annu Rev Med.* 2016;67:153–164.
3. Dell'Oglio P, de Vries HM, Mazzone E, et al. Hybrid indocyanine green-⁹⁹ᵐTc-nanocolloid for single-photon emission computed tomography and combined radio- and fluorescence-guided sentinel node biopsy in penile cancer: results of 740 inguinal basins assessed at a single institution. *Eur Urol.* 2020;78:865–872.
4. Yamaguchi S, De Lorenzi F, Petit JY, et al. The "perfusion map" of the unipedicled TRAM flap to reduce postoperative partial necrosis. *Ann Plast Surg.* 2004;53:205–209.
5. Craandijk A, Van Beek CA. Indocyanine green fluorescence angiography of the choroid. *Br J Ophthalmol.* 1976;60:377–385.
6. Gao RW, Teraphongphom NT, van den Berg NS, et al. Determination of tumor margins with surgical specimen mapping using near-infrared fluorescence. *Cancer Res.* 2018;78:5144–5154.
7. Tjalma JJJ, Koller M, Linssen MD, et al. Quantitative fluorescence endoscopy: an innovative endoscopy approach to evaluate neoadjuvant treatment response in locally advanced rectal cancer. *Gut.* 2020;69:406–410.
8. Atreya R, Neumann H, Neufert C, et al. In vivo imaging using fluorescent antibodies to tumor necrosis factor predicts therapeutic response in Crohn's disease. *Nat Med.* 2014;20:313–318.
9. Gonzales J, Pirovano G, Chow CY, et al. Fluorescence labeling of a Na$_V$1.7-targeted peptide for near-infrared nerve visualization. *EJNMMI Res.* 2020;10:49.
10. Vonk J, de Wit JG, Voskuil FJ, et al. Epidermal growth factor receptor targeted fluorescence molecular imaging for postoperative lymph node assessment in patients with oral cancer. *J Nucl Med.* September 16, 2021 [Epub ahead of print].
11. DSouza AV, Lin H, Henderson ER, Samkoe KS, Pogue BW. Review of fluorescence guided surgery systems: identification of key performance capabilities beyond indocyanine green imaging. *J Biomed Opt.* 2016;21:80901.
12. Hernot S, van Manen L, Debie P, Mieog JSD, Vahrmeijer AL. Latest developments in molecular tracers for fluorescence image-guided cancer surgery. *Lancet Oncol.* 2019;20:e354–e367.
13. Azari F, Kennedy G, Bernstein E, et al. Intraoperative molecular imaging clinical trials: a review of 2020 conference proceedings. *J Biomed Opt.* 2021;26:050901.
14. Lauwerends LJ, van Driel PBAA, Baatenburg de Jong RJ, et al. Real-time fluorescence imaging in intraoperative decision making for cancer surgery. *Lancet Oncol.* 2021;22:e186–e195.
15. Avelas receives FDA breakthrough therapy designation for pegloprastide (AVB-620) for use during breast cancer surgery. News release. Avelas Biosciences; December 14, 2020.
16. Pogue BW, Rosenthal EL, Achilefu S, van Dam GM. Perspective review of what is needed for molecular-specific fluorescence-guided surgery. *J Biomed Opt.* 2018;23:1–9.
17. Jacques SL. Optical properties of biological tissues: a review. *Phys Med Biol.* 2013;58:R37–R61.
18. Ntziachristos V, Bremer C, Weissleder R. Fluorescence imaging with near-infrared light: new technological advances that enable in vivo molecular imaging. *Eur Radiol.* 2003;13:195–208.
19. van Oosten M, Crane LM, Bart J, van Leeuwen FW, van Dam GM. Selecting potential targetable biomarkers for imaging purposes in colorectal cancer using TArget Selection Criteria (TASC): a novel target identification tool. *Transl Oncol.* 2011;4:71–82.
20. Boonstra MC, de Geus SW, Prevoo HA, et al. Selecting targets for tumor imaging: an overview of cancer-associated membrane proteins. *Biomark Cancer.* 2016;8:119–133.
21. Koller M, Hartmans E, de Groot DJA, et al. Data-driven prioritization and review of targets for molecular-based theranostic approaches in pancreatic cancer. *J Nucl Med.* 2017;58:1899–1903.
22. de Jongh SJ, Tjalma JJJ, Koller M, et al. Back-table fluorescence-guided imaging for circumferential resection margin evaluation using bevacizumab-800CW in patients with locally advanced rectal cancer. *J Nucl Med.* 2020;61:655–661.
23. Steinkamp PJ, Pranger BK, Li MF, et al. Fluorescence-guided visualization of soft-tissue sarcomas by targeting vascular endothelial growth factor A: a phase 1 single-center clinical trial. *J Nucl Med.* 2021;62:342–347.
24. Voskuil FJ, de Jongh SJ, Hooghiemstra WTR, et al. Fluorescence-guided imaging for resection margin evaluation in head and neck cancer patients using cetuximab-800CW: a quantitative dose-escalation study. *Theranostics.* 2020;10:3994–4005.
25. Wei L, Roberts DW, Sanai N, Liu JTC. Visualization technologies for 5-ALA-based fluorescence-guided surgeries. *J Neurooncol.* 2019;141:495–505.
26. Vonk J, Voskuil FJ, de Wit JG, et al. Fluorescence grid analysis for the evaluation of piecemeal surgery in sinonasal inverted papilloma: a proof-of-concept study. *Eur J Nucl Med Mol Imaging.* November 5, 2021 [Epub ahead of print].
27. Koch M, Symvoulidis P, Ntziachristos V. Tackling standardization in fluorescence molecular imaging. *Nat Photonics.* 2018;12:505–515.
28. Anastasopoulou M, Koch M, Gorpas D, et al. Comprehensive phantom for interventional fluorescence molecular imaging. *J Biomed Opt.* 2016;21:091309.
29. Noltes ME, Metman MJH, Heeman W, et al. A novel and generic workflow of indocyanine green perfusion assessment integrating standardization and quantification toward clinical implementation. *Ann Surg.* 2021;274:e659–e663.
30. Busemann Sokole E, Płachcínska A, Britten A; EANM Physics Committee. Acceptance testing for nuclear medicine instrumentation. *Eur J Nucl Med Mol Imaging.* 2010;37:672–681.
31. Gorpas D, Koch M, Anastasopoulou M, Klemm U, Ntziachristos V. Benchmarking of fluorescence cameras through the use of a composite phantom. *J Biomed Opt.* 2017;22:16009.
32. Ruiz AJ, Wu M, LaRochelle EPM, et al. Indocyanine green matching phantom for fluorescence-guided surgery imaging system characterization and performance assessment. *J Biomed Opt.* 2020;25:1–15.
33. Rana M, Zapf A, Kuehle M, Gellrich NC, Eckardt AM. Clinical evaluation of an autofluorescence diagnostic device for oral cancer detection: a prospective randomized diagnostic study. *Eur J Cancer Prev.* 2012;21:460–466.
34. Kobayashi H, Choyke PL. Target-cancer-cell-specific activatable fluorescence imaging probes: rational design and in vivo applications. *Acc Chem Res.* 2011;44:83–90.
35. Tummers WS, Warram JM, Tipirneni KE, et al. Regulatory aspects of optical methods and exogenous targets for cancer detection. *Cancer Res.* 2017;77:2197–2206.
36. Pogue BW, Rosenthal EL. Review of successful pathways for regulatory approvals in open-field fluorescence-guided surgery. *J Biomed Opt.* 2021;26:030901.
37. Zhang RR, Schroeder AB, Grudzinski JJ, et al. Beyond the margins: real-time detection of cancer using targeted fluorophores. *Nat Rev Clin Oncol.* 2017;14:347–364.
38. Jain RK. Delivery of molecular and cellular medicine to solid tumors. *Adv Drug Deliv Rev.* 2001;46:149–168.
39. Tichauer KM, Samkoe KS, Gunn JR, et al. Microscopic lymph node tumor burden quantified by macroscopic dual-tracer molecular imaging. *Nat Med.* 2014;20:1348–1353.
40. Tichauer KM, Wang Y, Pogue BW, Liu JT. Quantitative in vivo cell-surface receptor imaging in oncology: kinetic modeling and paired-agent principles from nuclear medicine and optical imaging. *Phys Med Biol.* 2015;60:R239–R269.
41. Voskuil FJ, Steinkamp PJ, Zhao T, et al. Exploiting metabolic acidosis in solid cancers using a tumor-agnostic pH-activatable nanoprobe for fluorescence-guided surgery. *Nat Commun.* 2020;11:3257.
42. Yim JJ, Harmsen S, Flisikowski K, et al. A protease-activated, near-infrared fluorescent probe for early endoscopic detection of premalignant gastrointestinal lesions. *Proc Natl Acad Sci USA.* 2021;118:e2008072118.
43. Chen J, Jiang Y, Chang TS, et al. Multiplexed endoscopic imaging of Barrett's neoplasia using targeted fluorescent heptapeptides in a phase 1 proof-of-concept study. *Gut.* 2021;70:1010–1013.
44. van Beurden F, van Willigen DM, Vojnovic B, et al. Multi-wavelength fluorescence in image-guided surgery, clinical feasibility and future perspectives. *Mol Imaging.* 2020;19:1536012120962333.
45. Boellaard R, Delgado-Bolton R, Oyen WJ, et al. FDG PET/CT: EANM procedure guidelines for tumour imaging—version 2.0. *Eur J Nucl Med Mol Imaging.* 2015;42:328–354.
46. Zhu B, Rasmussen JC, Sevick-Muraca EM. Non-invasive fluorescence imaging under ambient light conditions using a modulated ICCD and laser diode. *Biomed Opt Express.* 2014;5:562–572.
47. Tummers WS, Warram JM, van den Berg NS, et al. Recommendations for reporting on emerging optical imaging agents to promote clinical approval. *Theranostics.* 2018;8:5336–5347.
48. Torres VC, Vuong VD, Wilson T, Wewel J, Byrne RW, Tichauer KM. Cranial nerve contrast using nerve-specific fluorophores improved by paired-agent imaging with indocyanine green as a control agent. *J Biomed Opt.* 2017;22:096012.
49. Crameri F, Shephard GE, Heron PJ. The misuse of colour in science communication. *Nat Commun.* 2020;11:5444.

Total-Body PET: Will It Change Science and Practice?

Austin R. Pantel, David A. Mankoff, and Joel S. Karp

Department of Radiology, University of Pennsylvania, Philadelphia, Pennsylvania

Total-body (TB) PET scanners with an axial field of view (AFOV) of at least 60 cm can image dynamic radiopharmaceutical distributions in the whole body. Although the benefits of the fine temporal sampling and dramatic increase in system sensitivity afforded by TB PET imaging have been postulated for some time, it was not until the last few years that such systems have become available in both clinical and research settings. This article summarizes what we have learned in this short time and explores the long-term impact of TB PET.

INSTRUMENTATION

Existing Devices

Two human TB PET scanners became operational in 2018: United Imaging's uEXPLORER scanner (AFOV, 194 cm), initially installed at Shenzhen Hospital in China and at the University of California Davis (1), and the PennPET Explorer scanner (AFOV, 64–142 cm), built and installed at the University of Pennsylvania (2). In 2020, Siemens introduced the Biograph Quadra scanner (AFOV, 106 cm), installed at Bern Hospital in Switzerland (3). Compared with PET scanners with a standard AFOV (16–30 cm), the total sensitivity grows significantly as the axial length increases, up to 50 times for a 2-m axial length, whereas the peak sensitivity gain for a point (or organ) reaches a maximum of about 2.5–3 times at 80–120 cm (depending on the patient's body mass index) (4); longer systems maintain this peak sensitivity over a wider axial range. Although the underlying technology for TB PET scanners was already available, there were many challenges to make these systems robust, to efficiently handle the very large datasets, and to optimize the data acquisition and processing of oblique coincidence pairs. As is evident from the many hundreds of TB PET studies performed to date, the data correction and image reconstruction methods result in high-quality, quantitative images with improved accuracy of kinetic parameter estimation (5). The imaging protocols have been adjusted to leverage the enhanced performance, with no major problems or significant failures discovered in these first-generation TB PET scanners.

Future Directions

The key challenge to wider dissemination of TB PET systems is cost, which is determined largely by the AFOV and the volume of the detectors. One can argue that the increased cost is justified, leading to benefits in research knowledge and clinical diagnostics, potentially with increased patient throughput. Or, we can consider ways to reduce the cost. Notably, the PennPET Explorer was designed to be scalable in axial length to allow for a choice in matching the benefits of TB PET for particular applications. In addition, given a preferred AFOV, the number of detectors used in the design of the system may be reduced, taking advantage of the huge redundancy of data used for 3-dimensional image reconstruction. This idea has been explored in several simulation studies (6,7) and has been demonstrated in practice with the PennPET Explorer, which has operated with inter-ring gaps that correspond to 30% of the detector's active length (2,7). Alternatively, the cost of the detector can be significantly reduced by using a less expensive material (8) than the lutetium-based scintillators used in all modern PET/CT scanners. Efforts are also under way to develop systems with improved performance through the use of monolithic detectors to provide improved spatial resolution throughout the imaging field of view (9).

CLINICAL IMAGING WITH TB PET

Clinical translation of TB PET has long been a goal in the development of these scanners. In only the short time since implementation, many of the proposed clinical applications have been borne out.

Improved Detection of Disease

The gain in sensitivity and resultant improved image quality with TB PET can be leveraged to improve the ability to stage or restage disease and increase diagnostic confidence. For example, the PennPET Explorer detected a paracardiac ^{18}F-FDG–avid lymph node that was seemingly occult on the standard-of-care PET (2). Because TB PET scanners provide significantly better image quality, the increased lesion contrast and detection may necessitate new interpretation paradigms to integrate into preexisting imaging criteria (e.g., the Deauville criteria) while not losing specificity (e.g., overcalling benign lymph nodes that can be more easily visualized).

Optimization of Scan Protocols

The increased sensitivity of TB PET can be leveraged to achieve images of diagnostic quality with less injected activity or shorter scans. Images obtained with 25 MBq (0.7 mCi) of ^{18}F-FDG were obtained on the uEXPLORER (1), and ^{18}F-FDG PET scans (clinical dose) with a 2-min duration proved satisfactory on

the prototype PennPET Explorer (2). Shorter scans can increase clinical throughput and minimize the effects of patient motion— both gross movement and internal organ motion. Using a low injected activity enables imaging of tracers that are difficult to produce (^{68}Ga-DOTATATE), serial imaging of patients with a low injected activity, or imaging of children. In human translation of novel tracers, TB PET imaging could inform the scanning protocol. These instruments may have particular use for tracers with relatively fast kinetics (e.g., simultaneous early imaging of the abdomen and pelvis to optimize lesion contrast with ^{18}F-fluciclovine before washout) or slow kinetics (e.g., delayed imaging to leverage increased trapping of ^{18}F-FDG in malignancy or improved lesion contrast with prostate-specific membrane antigen tracers in prostate cancer). Indeed, on the uEXPLORER at the University of California Davis, a 2-h uptake time is routinely used for ^{18}F-FDG PET.

Nononcologic Applications

For clinical applications that do not require full-body coverage, such as dedicated cardiac or brain imaging, the single-organ sensitivity gains of TB PET scanners without axial coverage of the entire body may prove particularly valuable while mitigating cost. Superb image quality has been demonstrated with all new systems, noting again that increasing the AFOV beyond approximately 80–100 cm does not benefit single-organ imaging, providing an opportunity to match the AFOV with the intended application. Moreover, for high-sensitivity imaging of relatively static processes, such as leukocyte imaging of infection at 24 h or later with a ^{89}Zr-labeled minibody, TB PET scanners without full-body coverage may still be used to image the total body at multiple bed positions.

RESEARCH INVESTIGATIONS WITH TB PET

The technical advantages afforded by TB PET enable unique research applications of PET that are difficult, if not impossible, with standard-AFOV systems. A range of applications is described here.

Better Definition of Radiopharmaceutical Kinetics and Biodistribution

TB PET provides a unique tool for characterizing the behavior of new imaging agents or understanding the nuances of existing agents (10). For first-in-humans studies of novel radiopharmaceuticals, TB PET may be leveraged to study pharmacokinetics in both diseased and normal tissues, to estimate radiation dosimetry, and to guide optimal acquisition protocols. The ability to image the biodistribution of the radiotracer late after injection can provide a powerful tool to estimate the delivered radiation dose for diagnostic–therapeutic theranostic pairs. TB PET may also provide unique insights into commonly used radiotracers. For example, kinetic analysis of dynamic ^{18}F-FDG images revealed nuanced differences in regional kinetics in both normal tissues and tumors. On the PennPET Explorer, markedly delayed imaging of ^{18}F-FDG out to 10 half-lives clearly demonstrated the late loss of tracer in the normal brain due

to dephosphorylation of FDG-6P (2). This ability could have clinical utility in distinguishing brain tumors (which often do not dephosphorylate FDG-6P) from normal brain tissue.

Novel Analysis of Dynamic PET Data

The acquisition of large volumes of 4-dimensional data (3-dimensional plus time) lends itself to, and even necessitates, innovative approaches to image analysis. The inclusion of both diseased and normal tissue, and differences in radiopharmaceutical transport and metabolism between different tissues, may require adjusting the kinetic model to different tissues (11) or considering dynamic PET data as a spatially varying mixture of characteristic kinetic curves. Model-free approaches to estimating key components such as tracer delivery and retention may offer computational efficiency and linear scaling, which can be especially helpful for large 4-dimensional datasets. Early efforts using artificial intelligence or data science on 4-dimensional data to predict survival by characterizing tissue heterogeneity have shown promise (12). Finally, image reconstruction algorithms that consider pixel time course as part of the image reconstruction process may offer improved image quality and quantitative accuracy (13).

Applications to Systems Biology

Perhaps most exciting is the ability of TB PET to characterize human systems biology and to look at multisystemic interactions. Such opportunities include studying the heart–brain axis, the role of liver metabolism in drug addiction, and the interaction between tumors and host tissues such as immune reactions. A preclinical study of the interaction of bone metabolism with other organ systems provides a specific example of a study possible with TB PET but not with standard scanners (14). The ability to combine multiple PET tracers in a single study can be improved by TB PET imaging and offers the possibility of studying time-varying processes that require closely timed PET imaging studies. Recent studies of alternative energy substrates—glucose and glutamine (Fig. 1)—for aggressive breast cancers provide an example of a research area that is translating to humans and is uniquely enabled by TB PET.

SUMMARY

The introduction of TB PET systems at several sites throughout the world has been remarkably impactful, with both research and

| 18 s (scan time, 2 s) | 30 s (scan time, 15 s) | 2:30 min (scan time, 30 s) | 30 min (scan time, 5 min) |

Time after injection
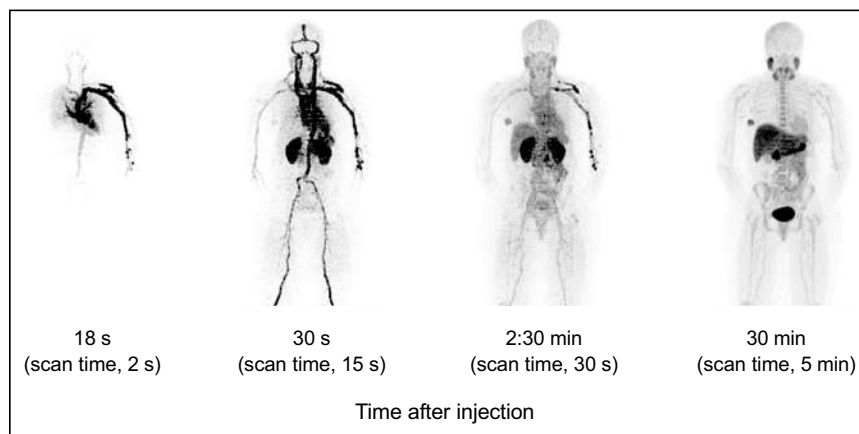
FIGURE 1. Illustration of TB PET imaging, showing dynamic sequence at representative postinjection times and scan times. Breast cancer patient was imaged with ^{18}F-fluoroglutamine on PennPET Explorer to quantify glutamine metabolism.

clinical successes. The benefits of TB PET with these first-generation systems became clear after the first human studies (*1,2*) and have become only more apparent with greater use. Ideally, we will find an optimal AFOV that provides maximum benefit for each application, although system cost and diagnostic yield may temper the widespread adoption of TB PET scanners that truly encompass the entire body. Yet, when appropriately matched to a clinical or research indication, these powerful scanners have the potential to transform patient care and PET research beyond the scope of current investigations to change both science and practice.

DISCLOSURE

REFERENCES

1. Badawi RD, Shi H, Hu P, et al. First human imaging studies with the EXPLORER total-body PET scanner. *J Nucl Med.* 2019;60:299–303.
2. Pantel AR, Viswanath V, Daube-Witherspoon ME, et al. PennPET Explorer: human imaging on a whole-body imager. *J Nucl Med.* 2020;61:144–151.
3. Alberts I, Hünermund JN, Prenosil G, et al. Clinical performance of long axial field of view PET/CT: a head-to-head intra-individual comparison of the Biograph Vision Quadra with the Biograph Vision PET/CT. *Eur J Nucl Med Mol Imaging.* 2021;48:2395–2404.
4. Surti S, Pantel AR, Karp JS. Total body PET: why, how, what for? *IEEE Trans Radiat Plasma Med Sci.* 2020;4:283–292.
5. Viswanath V, Pantel AR, Daube-Witherspoon ME, et al. Quantifying bias and precision of kinetic parameter estimation on the PennPET Explorer, a long axial field-of-view scanner. *IEEE Trans Radiat Plasma Med Sci.* 2020;4:735–749.
6. Zein SA, Karakatsanis NA, Issa M, Haj-Ali AA, Nehmeh SA. Physical performance of a long axial field-of-view PET scanner prototype with sparse rings configuration: a Monte Carlo simulation study. *Med Phys.* 2020;47:1949–1957.
7. Daube-Witherspoon ME, Viswanath V, Werner ME, Karp JS. Performance characteristics of long axial field-of-view PET scanners with axial gaps. *IEEE Trans Radiat Plasma Med Sci.* 2021;5:322–330.
8. Moskal P, Kowalski P, Shopa RY, et al. Simulating NEMA characteristics of the modular total-body J-PET scanner: an economic total-body PET from plastic scintillators. *Phys Med Biol.* 2021;66:175015.
9. Stockhoff M, Decuyper M, Van Holen R, Vandenberghe S. High-resolution monolithic LYSO detector with 6-layer depth-of-interaction for clinical PET. *Phys Med Biol.* 2021;66:155014.
10. Zhang X, Xie Z, Berg E, et al. Total-body dynamic reconstruction and parametric imaging on the uEXPLORER. *J Nucl Med.* 2020;61:285–291.
11. Wang G, Nardo L, Parikh M, et al. Total-body PET multiparametric imaging of cancer using a voxel-wise strategy of compartmental modeling. *J Nucl Med.* November 18, 2021 [Epub ahead of print].
12. Chitalia R, Viswanath V, Pantel AR, et al. Functional 4-D clustering for characterizing intratumor heterogeneity in dynamic imaging: evaluation in FDG PET as a prognostic biomarker for breast cancer. *Eur J Nucl Med Mol Imaging.* 2021;48:3990–4001.
13. Reader AJ, Verhaeghe J. 4D image reconstruction for emission tomography. *Phys Med Biol.* 2014;59:R371–R418.
14. Suchacki KJ, Alcaide-Corral CJ, Nimale S, et al. A systems-level analysis of total-body PET data reveals complex skeletal metabolism networks in vivo. *Front Med (Lausanne).* 2021;8:740615.

Radiotracers to Address Unmet Clinical Needs in Cardiovascular Imaging, Part 1: Technical Considerations and Perfusion and Neuronal Imaging

John C. Stendahl*[1], Jennifer M. Kwan*[1], Darko Pucar[2], and Mehran M. Sadeghi[1,3]

[1]Section of Cardiovascular Medicine, Yale University School of Medicine, New Haven, Connecticut; [2]Department of Radiology and Biomedical Imaging, Yale University School of Medicine, New Haven, Connecticut; and [3]Veterans Affairs Connecticut Healthcare System, West Haven, Connecticut

Learning Objectives: On successful completion of this activity, participants should be able to describe (1) key technical considerations pertaining to cardiovascular radiotracer development; (2) basic concepts in cardiac and peripheral perfusion imaging and associated radiotracers; and (3) basic concepts in cardiovascular neuronal imaging and associated radiotracers.

CME Credit: SNMMI is accredited by the Accreditation Council for Continuing Medical Education (ACCME) to sponsor continuing education for physicians. SNMMI designates each *JNM* continuing education article for a maximum of 2.0 AMA PRA Category 1 Credits. Physicians should claim only credit commensurate with the extent of their participation in the activity. For CE credit, SAM, and other credit types, participants can access this activity through the SNMMI website (http://www.snmmilearningcenter.org) through May 2025.

The development of new radiotracers for PET and SPECT is central to addressing unmet diagnostic needs related to systemwide trends toward molecular characterization and personalized therapies in cardiovascular medicine. In the following 2-part review, we discuss select emerging radiotracers that may help address important unmet diagnostic needs in central areas of cardiovascular medicine, such as heart failure, arrhythmias, valvular disease, atherosclerosis, and thrombosis. Part 1 examines key technical considerations pertaining to cardiovascular radiotracer development and reviews emerging radiotracers for perfusion and neuronal imaging. Highlights of this work include discussions on the development of ^{18}F-flurpiridaz, an emerging PET perfusion tracer, and the development of ^{18}F-based radiotracers for cardiovascular neuronal imaging, such as ^{18}F-fluorobenguane. Part 2 of this review covers emerging radiotracers for the imaging of inflammation, fibrosis, thrombosis, calcification, and cardiac amyloidosis.

Key Words: cardiology (basic/technical); cardiology (clinical); molecular imaging; inflammation; myocardial perfusion imaging

Despite considerable progress in patient care, cardiovascular disease remains a major cause of morbidity and mortality. Improved diagnostics, treatments, and risk factor management have altered the landscape of patient care and have likely contributed to the increasing prevalence of chronic cardiovascular disease. For example, the number of patients living with heart failure is expected to increase from 5.8 million in 2012 to 8.5 million in 2030 (*1*). This evolution of patient demographics and an improved understanding of cardiovascular pathophysiology underpin many current diagnostic and risk stratification gaps in cardiovascular medicine. Emerging molecular imaging techniques have the potential to address many of these unmet needs (Table 1).

Myocardial perfusion imaging, myocardial viability imaging, and equilibrium radionuclide angiocardiography have traditionally constituted most nuclear cardiology procedures. However, use patterns in nuclear cardiology laboratories have been changing because of advances in molecular imaging, the emergence of alternative diagnostic techniques, and evolving evidence questioning established approaches to diagnose and risk-stratify coronary artery disease. PET and SPECT have several advantages for physiologic and precision molecular applications in cardiovascular imaging, including their sensitivity, versatility, and quantitative nature. This is evident in the fact that PET- and SPECT-based molecular imaging techniques are now routinely performed clinically for the diagnosis of cardiac sarcoidosis and amyloidosis. Moreover, the feasibilities of neurohormonal and device infection imaging have been demonstrated, although their specific roles in patient management remain to be established. Many additional cardiovascular applications of PET and SPECT are in earlier stages of preclinical and clinical development, and their advancement to mainstream clinical use is critically dependent on the physical, chemical, and biologic properties of their radiotracers.

In the following 2-part review, we discuss select emerging radiotracers that may help address key unmet clinical diagnostic needs in cardiovascular medicine. For simplicity, these tracers are organized by general pathobiologic processes rather than specific diseases. Part 1 of

TABLE 1
Unmet Diagnostic Needs in Cardiovascular Medicine

Clinical field	Unmet need
Heart failure and cardiomyopathies	Heart failure with preserved ejection fraction: phenotypic characterization, therapeutic development
	Heart failure with reduced ejection fraction: prognostication, precision approaches to therapy
	Post–myocardial infarction remodeling: prognostication
	Immunotherapy/chemotherapy-related cardiotoxicity: prediction, early recognition, prognostication, and assessment of treatment response
	Cardiac amyloidosis: single-scan diagnosis and typing (light-chain amyloidosis vs. transthyretin amyloidosis)
	Cardiac sarcoidosis: reduce dependence on dietary preparation, differentiate from other types of myocarditis/nonspecific uptake
	Genetic cardiomyopathies: risk stratification in asymptomatic or phenotype-negative carriers and those carrying variants of unknown significance
	Cardiac fibrosis: reproducible quantification, distinguish between active and stable disease
	Left ventricular assist devices: prediction of left ventricular myocardial recovery
	New medical therapies (e.g., angiotensin receptor neprilysin inhibitors, sodium glucose cotransporter 2 inhibitors): determination of mechanism of action, track therapeutic response
Arrhythmias	Sudden cardiac death: risk stratification, prediction of implantable cardiac defibrillator benefit
	Genetic arrhythmia syndromes: risk stratification in asymptomatic or phenotype-negative carriers and those carrying variants of unknown significance
	Atrial fibrillation: patient selection for ablation/cardioversion/antiarrhythmic drugs
Valvular disease	Valvular regurgitation/stenosis: determination of risk for progression, prediction of optimal timing of interventions, selection for medical therapy, tracking of therapeutic response
	Endocarditis or device infections: detection
Vascular disease	Atheroma: risk stratification
	Aortic aneurysm: risk stratification, prediction of endoleak
	Thrombosis or embolization: whole-body detection, determination of chronicity
	Perfusion: high-spatial-resolution imaging with absolute blood flow quantification, hybrid perfusion/angiographic imaging
	Peripheral artery disease: risk stratification, prediction of interventional benefit

the review examines key technical considerations pertaining to cardiovascular radiotracer development and reviews the development of radiotracers for perfusion and neuronal imaging (Table 2). Part 2 covers emerging radiotracers for the imaging of inflammation, fibrosis, thrombosis, calcification, and cardiac amyloidosis.

TECHNICAL CONSIDERATIONS FOR OPTIMAL NUCLEAR CARDIOVASCULAR IMAGING

Multiple variables related to radiotracers, instrumentation, and image analysis contribute to the generation of useful nuclear imaging data. PET offers several distinct advantages over SPECT for cardiovascular imaging, including greater spatial resolution and more established quantification methods (2). However, SPECT is usually less expensive and more widely available in clinical nuclear cardiology laboratories. With recent improvements in SPECT technology such as cardiorespiratory gating and cadmium-zinc-telluride (CZT) detectors (3–5), differences between the 2 modalities may be less significant. One potential advantage of SPECT over PET in cardiovascular molecular imaging is its capability for simultaneous

multitracer imaging (Fig. 1) (4,6–8). CZT SPECT cameras facilitate multitracer imaging by providing greater spatial and energy resolution than traditional Anger cameras (5).

Cardiac imaging with PET and SPECT is facilitated by the large size of the organ, although motion remains a challenge. Vascular imaging presents additional challenges, including the small size of vessels. This may be addressed by hybrid imaging with CT or MRI, which provides anatomic definition and helps to correct partial-volume effects. Cardiovascular molecular imaging applications would benefit from improved quantitation tools, as the semiquantitative techniques developed for perfusion imaging to assess relative radiotracer uptake are not suitable for hot-spot imaging, which is common in molecular imaging applications.

Radiotracer kinetics govern acquisition protocols and greatly influence data quality. Fast blood pool clearance is desirable for most non–blood pool cardiovascular applications because it improves target-to-background ratios. For perfusion imaging, it is desirable to have high levels of target tissue extraction and retention, with lesser uptake or greater washout in surrounding organs. For molecular imaging,

TABLE 2
Select Perfusion and Neuronal Signaling Radiotracers in Cardiovascular Medicine

Application	Radiotracer	Mechanism/target	Status	Reference
Perfusion	^{18}F-flurpiridaz	Mitochondrial complex 1	Phase 3 clinical	(10,13–16)
	^{18}F-rhodamine 6G	Mitochondrial membrane voltage sensor	Initial clinical evaluations	(20)
	^{18}F-fluorophenyltriphenylphosphonium	Mitochondrial membrane voltage sensor	Initial clinical evaluations	(21)
	^{123}I-CMICE-013	Mitochondrial complex 1	Initial clinical evaluations	(22)
	^{123}I-ZIROT	Mitochondrial complex 1	Preclinical	(23)
Neuronal signaling				
Presynaptic				
	^{123}I-MIBG	Norepinephrine transporter	FDA-approved for prognostication in heart failure	(35,38,39,45,61)
	^{11}C-HED	Norepinephrine transporter	Clinical evaluations	(34,36,37,48,49)
	^{11}C-epinephrine	Norepinephrine transporter	Initial clinical evaluations	(48)
	^{11}C-phenylephrine	Norepinephrine transporter	Initial clinical evaluations	(48)
	^{18}F-FBBG	Norepinephrine transporter	Initial clinical evaluations	(54,55)
	^{18}F-4F-MHPG, ^{18}F-3F-PHPG	Norepinephrine transporter	Initial clinical evaluations	(58)
	^{18}F-MFBG	Norepinephrine transporter	Initial clinical evaluations	(56,57)
Postsynaptic				
	^{11}C-CGP-12177, ^{11}C-CGP-12388	β-receptor antagonists	Initial clinical evaluations	(37,49,59–61)
	^{11}C-GB67	α$_1$-receptor antagonist (prazosin analog)	Initial clinical evaluations	(63,64)
Parasympathetic				
	^{11}C-donepezil	Acetylcholinesterase antagonist	Initial clinical evaluations	(65)
	^{11}C-methylquinuclidinyl benzilate	Muscarinic receptor antagonist	Initial clinical evaluations	(40)
	2-deoxy-2-^{18}F-fluoro-ᴅ-glucose-A85380	Selective α$_4$β$_2$ nicotinic receptor agonist	Initial clinical evaluations	(67)
	^{18}F-fluoroethoxybenzovesamicol	Vesicular acetylcholine transporter	Initial clinical evaluations	(69)

^{18}F-4F-MHPG = 4-^{18}F-fluoro-meta-hydroxyphenethylguanidine; ^{18}F-3F-PHPG = 3-^{18}F-fluoro-para-hydroxyphenethylguanidine; FDA = Food and Drug Administration.
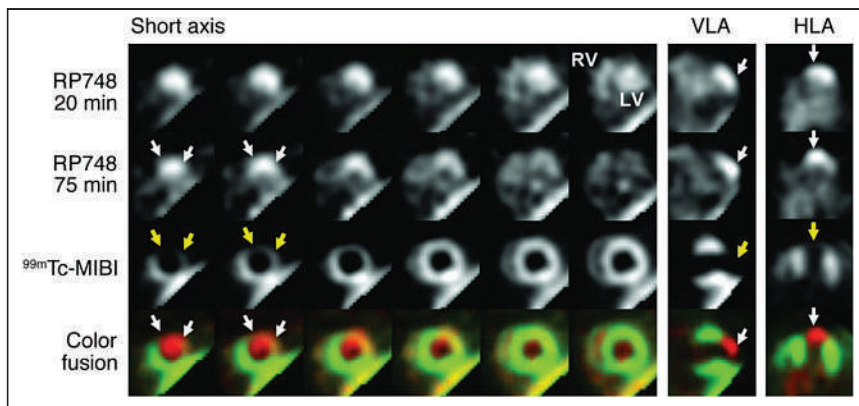
FIGURE 1. Dual-tracer SPECT imaging of postmyocardial infarction angiogenesis in a canine model using ^{111}I-RP748, an $\alpha_v\beta_3$ integrin–targeted agent. Shown are in vivo ^{111}In-RP748 SPECT images acquired at 20 and 45min after tracer administration (top 2 rows), ^{99m}Tc-sestamibi images (third row), and fused ^{99m}Tc-sestamibi (green) and 45-min ^{11}In-RP748 (red) images (bottom row) in a dog 3 wk after left anterior descending coronary artery occlusion. ^{99m}Tc-sestamibi perfusion images demonstrate anterior perfusion deficit (yellow arrows). ^{111}In-RP748 images demonstrate corresponding increased uptake in hypoperfused region (white arrows). Authors demonstrate that 4-fold increase in ^{111}In-RP748 uptake in infarct region corresponds to increased $\alpha_v\beta_3$ expression and histologic evidence of angiogenesis. LV = left ventricle; MIBI = sestamibi; RV = right ventricle; VLA = vertical long axis; HLA = horizontal long axis. (Reprinted with permission of (8).)

high levels of specific target binding relative to the background are critical for achieving useful data. In this regard, radiotracer uptake depends on delivery of the tracer as well as target expression and binding affinity, thus raising challenges for comparing uptake values, such as in areas of myocardium with differing levels of perfusion. The incorporation of regional perfusion data from kinetic modeling could potentially improve the accuracy of molecular imaging techniques.

The chemical and physical properties of radionuclides also influence synthesis and acquisition protocols and affect data quality (Table 3). Radionuclide chemical properties impact their incorporation into organic tracer molecules or, in the case of inorganic radiotracers (e.g., ^{82}Rb), their biologic uptake (9). Radionuclides with shorter half-lives are ideally suited for applications with faster pharmacokinetics and favorable count statistics. Shorter half-lives reduce radiation exposure to both patients and staff and typically permit greater imaging throughput. This advantage is especially useful in perfusion imaging to minimize delays between stress and rest scans. However, radionuclides with shorter half-lives are not always practical. For example, radiolabeled antibodies have slower pharmacokinetics than small molecules, and their binding to target molecules with low levels of expression can require hours to produce high-quality signals. As such, molecular imaging with antibodies often necessitates the use of radionuclides with a longer half-life, such as ^{64}Cu (half-life, 12.7 h) or ^{89}Zr (half-life, 78.4 h). Radionuclides with longer half-lives can also provide considerable procedural flexibility. For example, radionuclides with a longer half-life facilitate unit dose delivery in place of on-site generators and cyclotrons, which may not be cost-effective in lower-volume centers (10). Longer–half-life radionuclides also expand options for chemical modifications to radiotracers before administration. For myocardial perfusion imaging, longer–half-life radionuclides permit exercise stress (10) and may be favorable for nontraditional applications such as image-guided interventions (11). However, greater radiation exposure associated with these longer–half-life radionuclides and practical workflow considerations remain major limiting factors for cardiovascular applications, where risk–benefit

considerations may be different from, for example, imaging in patients with malignancies. In PET imaging, radionuclide positron energy influences image resolution. Lower-energy β-emitters such as ^{18}F and ^{64}Cu have shorter positron ranges in tissue and thus tend to produce images with spatial resolution superior to that of higher-energy positron emitters such as ^{82}Rb and ^{68}Ga (12). The benefits of high-resolution imaging are the greatest in small targets that are more susceptible to partial-volume effects, such as vessel walls. With anticipated improvements in resolution related to PET camera technology and motion correction, the effects of radionuclide positron range will likely become increasingly significant.

The mode of decay of radionuclides also affects their imaging properties. PET radionuclides such as ^{11}C, ^{13}N, ^{15}O, and ^{18}F are pure β^+-emitters and do not directly produce γ- or β^--emissions (9,12). Prompt γ-emissions from nonpure PET radionuclides such as ^{68}Ga, ^{82}Rb, and ^{124}I have traditionally been considered unfavorable because they increase radiation exposure and create spurious coincidences that degrade image quality (12). However, the presence of smaller levels of prompt γ-emissions in radionuclides with other favorable properties is not considered prohibitive, and image quality can potentially be improved by instituting corrections (12). Moreover, it has been proposed that radionuclides emitting prompt γ-emissions provide distinct emission signatures that could be harnessed for multitracer PET imaging (12).

RADIOTRACERS FOR PERFUSION IMAGING

There has been longstanding interest in the development of ^{18}F-based perfusion tracers given the intrinsic advantages of PET imaging and the limitations of current clinical perfusion tracers such as ^{99m}Tc sestamibi, ^{99m}Tc tetrofosmin, ^{82}Rb, and ^{13}N-NH$_3$ (13). ^{18}F is advantageous because it has a shorter mean positron range (0.6 mm, in water) than ^{82}Rb (7.1 mm) and ^{13}N (1.8 mm) and thus provides superior spatial resolution (12). In addition, ^{18}F has a longer half-life (109 min) than ^{82}Rb (76 s) and ^{13}N (10 min). Although this characteristic can be unfavorable from a dosimetric standpoint and may necessitate greater delays between rest and stress acquisitions, it also provides several distinct advantages. Most importantly, the longer half-life of ^{18}F permits unit dose delivery. In addition, the longer half-life of ^{18}F permits both exercise and pharmacologic stress protocols and makes repeat image acquisition possible in cases of motion or extracardiac radiotracer uptake.

^{18}F-flurpiridaz is a perfusion tracer that binds to mitochondrial complex 1 and is currently undergoing evaluation in clinical trials (10,13–17). In addition to the features listed above, ^{18}F-flurpiridaz has greater myocardial extraction at higher blood flow rates than traditional PET and SPECT perfusion radiotracers; thus, its uptake demonstrates a smaller deviation from linearity over the physiologic range of blood flow (Fig. 2) (18). This property potentially improves its sensitivity for detection of ischemia and is advantageous for quantification of absolute blood flow. In a recent phase 3 clinical evaluation, ^{18}F-flurpiridaz PET demonstrated increased sensitivity for the detection of obstructive coronary artery disease

TABLE 3
Properties of SPECT and PET Radionuclides with Existing or Potential Applications in Cardiovascular Imaging (9,12,70)

Radionuclide	Production	Half-life	Decay (%)	$E_{\beta+ \ max}$ (MeV)	$R_{\beta+ \ mean}$ (mm)	E_γ (MeV)
γ-emitters (SPECT)						
[99m]Tc	Generator ([99]Mo)	6.0 h	IT (88), IC	—	—	0.141
[201]Tl	Cyclotron	73.1 h	EC	—	—	0.068–0.083*
[123]I	Cyclotron	13.2 h	EC (87), IC	—	—	0.159†
Pure positron emitters (PET)						
[15]O	Cyclotron	2 min	β⁺ (99.9)	1.732	3.0	—
[13]N	Cyclotron	10.0 min	β⁺ (99.8)	1.199	1.8	—
[11]C	Cyclotron	20.4 min	β⁺ (99.8)	0.960	1.2	—
[18]F	Cyclotron	110 min	β⁺ (96.9)	0.634	0.6	—
Mixed emitters (PET)						
[64]Cu	Cyclotron	12.7 h	β⁺ (17.5)/EC	0.653	0.7	—
			β⁻ (38.5)	—	—	—
[89]Zr	Cyclotron	78.4 h	β⁺ (22.7)/EC	0.902	1.3	0.909‡
[82]Rb	Generator ([82]Sr)	1.3 min	β_1^+ (81.8)	3.378	7.1	—
			β_2^+ (13.1)/EC	2.601	5.0	0.777
[68]Ga	Generator ([68]Ge)	68 min	β_1^+ (87.7)	1.899	3.5	—
			β_2^+ (1.2)/EC	0.821	1.1	1.077
[124]I	Cyclotron	100.2 h	β_1^+ (11.7)/EC	1.535	2.8	0.602
			β_2^+ (10.7)	2.138	4.4	—
			β_3^+ (0.3)/EC	0.812	1.1	0.723
			EC	—	—	1.691

_____

$E_{\beta+ \ max}$ = maximum energy of positrons; $R_{\beta+ \ mean}$ = mean range of positrons in water; E_γ = γ emission energy; IT = isomeric transition; IC = internal conversion; EC = electron capture.

*Nongaussian photopeak.

†Emits small proportions of high-energy γ-photons (>0.400 MeV) in addition to its primary emission at 0.159 MeV.

‡Does not behave as prompt γ because of long half-life of metastable intermediate.

(as defined by >50% coronary stenosis by invasive angiography) in comparison to ^{99m}Tc-SPECT (71.9% vs. 53.7%, $P < 0.001$) but did not meet the predetermined noninferiority criterion pertaining to specificity (76.2% vs 86.6%, P = not significant) (10). Overall, on the basis of area under the receiver-operating-characteristic curve, ^{18}F-flurpiridaz PET demonstrated superior discrimination of obstructive coronary disease in comparison to ^{99m}Tc-SPECT myocardial perfusion imaging (0.78 vs. 0.72, $P < 0.001$). ^{18}F-flurpiridaz also exhibited better image quality than ^{99m}Tc-SPECT at lower radiation doses (6.1 ± 0.4 vs. 13.4 ± 3.2 mSv; $P < 0.001$) (10). Of note, this comparison was based solely on retention scans and did not incorporate ^{18}F-flurpiridaz myocardial blood flow quantification (19). It is also worth noting that this study did not compare ^{18}F-flurpiridaz with other PET perfusion tracers and that at least some of the differences likely represent intrinsic differences between SPECT and PET techniques, including a lack of attenuation correction for SPECT images. The effects of spatial resolution in ^{18}F-flurpiridaz PET were further illustrated in a subsequent analysis of the trial data that compared diagnostic performance in large and small ventricles. The diagnostic performance of ^{18}F-flurpiridaz PET for the detection of ischemia was similar in large and small left ventricles (area under the curve, 0.79 vs. 0.77, $P = 0.49$), but ^{99m}Tc-SPECT performance was reduced in smaller left ventricles (area under the curve, 0.75 vs. 0.67, $P = 0.03$),

likely because of its lower spatial resolution (Fig. 3) (17). Other ^{18}F-based PET perfusion tracers that are undergoing initial characterization and evaluation in humans include ^{18}F-rhodamine 6G (NCT04528758) (20) and ^{18}F-fluorophenyltriphenylphosphonium (NCT02252783) (21).

Several new SPECT perfusion agents are also in development, including the ^{123}I-labeled rotenone derivatives ^{123}I-CMICE-013 (22) and ^{123}I-ZIROT (23). These agents target mitochondrial complex 1 in a similar fashion to ^{18}F-flurpiridaz and are intended to address the shortcomings of existing SPECT perfusion agents by potentially combining the benefits of greater myocardial extraction across the physiologic range of blood flow, with favorable imaging characteristics and dosimetry. Moreover, as these agents are labeled with ^{123}I rather than ^{99m}Tc, they could also address ongoing concerns about the stability of the ^{99m}Tc supply. In initial preclinical studies on pigs, ^{123}I-CMICE-013 demonstrated greater myocardial uptake than the conventional SPECT tracers ^{201}Tl, ^{99m}Tc-tetrofosmin, and ^{99m}Tc-sestamibi at blood flows exceeding 1.5 mL/min/g ($P < 0.05$) (Fig. 4) (22). Similarly, ^{123}I-ZIROT demonstrated greater myocardial uptake than ^{201}Tl and ^{99m}Tc-sestamibi at blood flows greater than 1.5 mL/min/g, with linear uptake extending to greater flow values (23). ^{123}I-CMICE-013 recently completed a phase 1 clinical evaluation (NCT01558362). One potential technical issue with ^{123}I-based perfusion agents is that ^{123}I emits small proportions of high-energy photons (>400 keV) in addition to its primary emission at 159 keV. These
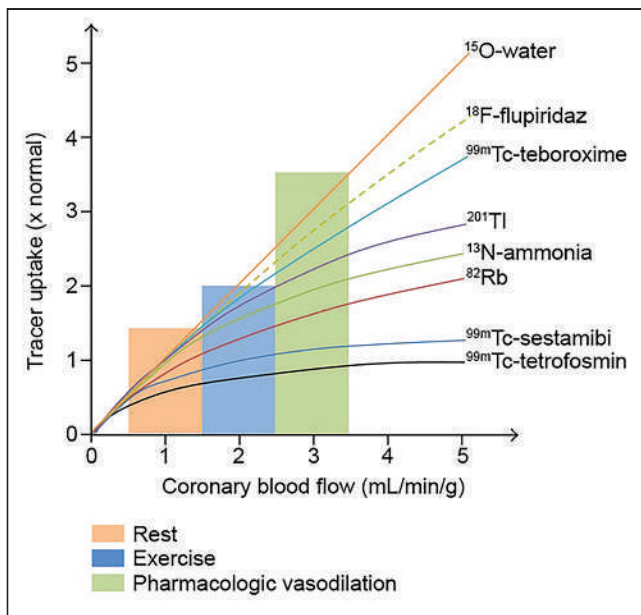
FIGURE 2. Schematic representation of myocardial uptake of various PET and SPECT perfusion radiotracers in relation to coronary blood flow. Background colors in figure show typical ranges of myocardial blood flow during rest (peach), exercise stress (blue), and pharmacologic vasodilator stress (green). ^{15}O-H$_2$O displays nearly linear uptake over physiologic range of blood flow but has limited clinical utility because of suboptimal imaging characteristics. ^{18}F-flurpiridaz maintains high levels of myocardial extraction at stress-level blood flows, and its uptake-flow curve thus demonstrates only minimal deviation from linearity. By contrast, ^{99m}Tc-sestamibi and ^{99m}Tc-tetrofosmin have more significant reductions in myocardial extraction at moderate and high blood flow rates, and their uptake-flow curves demonstrate significant deviations from linearity. ^{201}Tl, ^{13}N-NH$_3$, and ^{82}Rb have intermediate uptake-flow properties. (Reprinted from (18).)

high-energy photons can degrade image quality and impair quantitative analyses by penetrating septa on standard low-energy, high-resolution collimators. Collimators with thicker septa may be used in ^{123}I SPECT imaging to decrease septal photon penetration, although thicker septa tend to decrease spatial resolution (24).

Despite the trend toward greater use of PET for perfusion imaging, improved SPECT radiotracers may still have a significant clinical impact, as SPECT myocardial perfusion imaging is expected to continue being the most common perfusion modality for years to come because of advantages in cost and availability. Moreover, with technologic advances such as attenuation correction (25) and CZT detectors (5), modern SPECT imaging systems provide substantially better image quality at a more favorable dosimetry than prior-generation instruments. The combination of advances in instrumentation and the development of perfusion tracers with better myocardial extraction characteristics also raises the possibility of applying SPECT-based quantitative blood flow assessments in clinical settings (26).

A potentially significant area for growth and possible application for these new perfusion agents is skeletal muscle perfusion imaging. Peripheral artery disease affects more than 200 million people worldwide (27) and presents significant challenges for clinical assessment and treatment. SPECT and PET perfusion imaging with traditional radiotracers has been applied to help diagnose peripheral artery disease, stratify risk, and evaluate responses to treatment (28–31). Although not currently part of mainstream clinical peripheral artery disease management, radiotracer imaging techniques may provide supplemental information to better assess risk for acute limb ischemia and potential for wound healing, as well as to direct optimal approaches for revascularization. The high spatial resolution, quantitative potential, and ability to accommodate exercise stress protocols are features of the new ^{18}F-based tracers that make them attractive for peripheral perfusion applications.

RADIOTRACERS FOR CARDIOVASCULAR NEURONAL IMAGING

Neuronal signaling in the myocardium plays a critical role in maintaining cardiac function and homeostasis by modulating electromechanical behavior, vasoreactivity, metabolism, and remodeling (32). Neuronal signals are transmitted to the heart via the sympathetic and parasympathetic branches of the autonomic nervous system. Sympathetic activation of the heart has mainly stimulatory effects, including increased inotropy and chronotropy (32). Preganglionic sympathetic neurons originate in the spinal cord and transmit signals to postganglionic fibers that innervate the atria, ventricles, and coronary arteries. On stimulation, the termini of these postganglionic neurons release stored norepinephrine into the synaptic cleft. Sympathetic effects are mediated by binding of
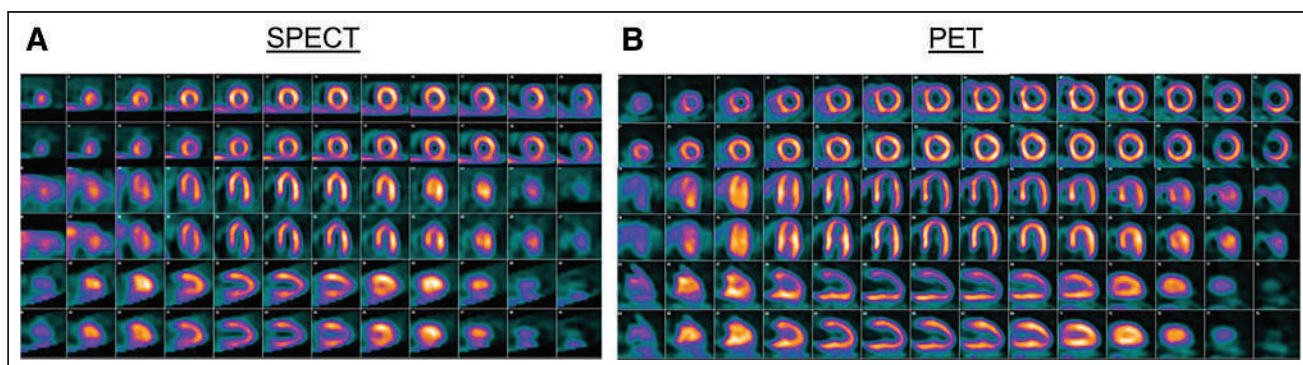
FIGURE 3. Representative rest–stress ^{99m}Tc-SPECT and ^{18}F-flurpiridaz PET images in patient with small heart. Images were acquired in 66-y-old woman with left ventricular end diastolic volume of 82 mL. Reversible anterior perfusion defect is more evident in ^{18}F-flurpiridaz PET images (B) than ^{99m}Tc-SPECT images (A) and is consistent with 82% stenosis of left anterior descending coronary artery that was found on invasive coronary angiography. Greater sensitivity of ^{18}F-flurpiridaz PET for detection of myocardial ischemia partially relates to its greater spatial resolution and more linear uptake over physiologic range of blood flow. (Reprinted from (17).)
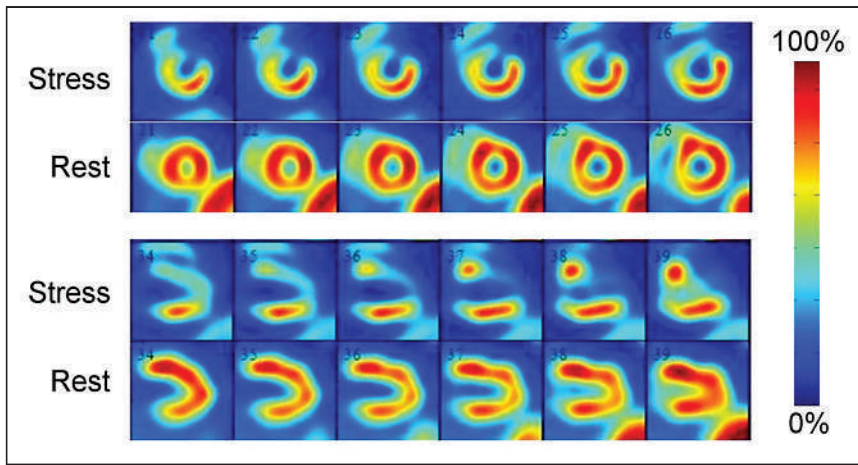
FIGURE 4. Representative ^{123}I-CMICE-013 SPECT perfusion images in a porcine model with left anterior descending coronary artery occlusion during dipyridamole stress. Images were acquired 15 min after injection and provide clear definition of occluded region. (Reprinted from (*22*).)

norepinephrine to postsynaptic α- and β-adrenergic receptors in the cardiac tissue. In contrast, parasympathetic activation tends to be inhibitory, with negative chronotropic and, to a lesser extent, negative inotropic effects (*32*). Parasympathetic signals are transmitted from the medulla oblongata to the heart by way of the vagus nerve. The termini of postganglionic vagal efferents are concentrated in the atria and conduction nodes and release acetylcholine when stimulated. Signal transmission is completed by binding of acetylcholine to muscarinic and nicotinic receptors. Muscarinic acetylcholine receptors are present in cardiomyocytes and intracardiac ganglia, and their stimulation decreases both inotropy and chronotropy (*33*). Nicotinic acetylcholine receptors are present in the myocardium and vasculature, although their roles are less well defined (*33*). In addition to efferent sympathetic and parasympathetic innervation of the heart, there are numerous afferent sympathetic and vagal nerve fibers that travel from the heart for sensory purposes and to mediate cardiac reflexes.

Alterations to cardiac neuronal activity play important roles in the pathophysiology of arrythmias, myocardial infarction, and heart failure related to various types of cardiomyopathy (*34–42*). In the case of heart failure, it is postulated that chronically elevated sympathetic activity drives desensitization or downregulation of both presynaptic norepinephrine reuptake transporters and postsynaptic β-adrenergic receptors, which leads to progressive dysfunction and remodeling and creates substrates for arrhythmias (*43*). The development of radiotracers for targeted noninvasive imaging of various aspects of cardiac innervation has improved our understanding of complex cardiovascular diseases and has helped to guide treatments. Recent efforts in the field have focused on developing new tracers and improving image acquisition and analysis techniques to expand diagnostic capabilities and provide more accurate and reproduceable assessments (*44*).

Presynaptic Sympathetic Imaging

[123]I-metaiodobenzylguanidine (^{123}I-MIBG) targets the norepinephrine transporter and was the first neuronal radiotracer to be extensively studied in hearts and Food and Drug Administration–approved for cardiac applications. Myocardial ^{123}I-MIBG uptake can be imaged by both planar scintigraphy and SPECT/CT, although quantification has traditionally been performed with heart-to-mediastinum ratios in planar images. Reduced myocardial uptake of ^{123}I-MIBG has been associated with various cardiac diseases and has demonstrated clinical predictive

value. In the ADMIRE-HF trial (AdreView Myocardial Imaging for Risk Evaluation in Heart Failure) of patients with heart failure with reduced ejection fraction, a ^{123}I-MIBG heart-to-mediastinum ratio of at least 1.6 was predictive of decreased adverse outcomes such as heart failure progression (hazard ratio, 0.49; $P = 0.002$), serious arrhythmic events (hazard ratio, 0.37; $P = 0.020$), and cardiac death (hazard ratio, 0.14; $P = 0.006$) as compared with a heart-to-mediastinum ratio of less than 1.6 (*35*). Although ^{123}I-MIBG has been criticized because assessments are often global and semiquantitative (*45*), improved SPECT technology such as cardiorespiratory gating and CZT detectors have renewed interest by improving spatial resolution and sensitivity. Recent examples of new applications generated by these technical improvements include the localization of left atrial ganglionic plexi, which could aid in the development of more effective catheter ablation procedures for treating atrial fibrillation (*39*), and detailed assessments of innervation–perfusion mismatch in patients with ischemic heart disease, which could provide valuable insight into patient risk for developing potentially lethal ventricular arrhythmias (*38*).

Despite the proven utility of ^{123}I-MIBG SPECT imaging, PET neuronal imaging has gained popularity because of greater tracer variety, superior sensitivity and spatiotemporal resolution, and more developed means of quantification (*46,47*). PET offers several radiotracers that target predominantly the norepinephrine transporter to image presynaptic sympathetic activity. The earliest norepinephrine transporter–targeted PET radiotracers were ^{11}C-labeled agents, including ^{11}C-hydroxyephedrine (^{11}C-HED), ^{11}C-epinephrine, and ^{11}C-phenylephrine (*48*). Alterations in the presynaptic uptake of these radiotracers have been demonstrated in numerous cardiac diseases, including heart failure, ischemic heart disease, and arrhythmias (*37,48–50*).

[11]C-HED, a nonmetabolized analog of norepinephrine, is the most extensively studied radiotracer among the group of ^{11}C-labeled norepinephrine transporter–targeted radiotracers. Reduced retention of ^{11}C-HED corresponding to myocardial denervation has been demonstrated in the settings of acute myocardial infarction (*42*), ischemic (*34,37,49,51*) and nonischemic cardiomyopathies (*51,52*), hypertrophic cardiomyopathy (*36*), and heart failure with preserved ejection fraction (*53*). In the PAREPET trial (Prediction of Arrhythmic Events with PET) of individuals with ischemic cardiomyopathy, patients who experienced sudden cardiac arrest had greater volumes of denervated myocardium by ^{11}C-HED PET than did those without cardiac arrest (33% ± 10% vs. 26% ± 11% of the left ventricle; $P = 0.001$) (*34*). Interestingly, patients with sudden cardiac arrest did not have statistically greater infarct volumes (22% ± 7% vs. 19% ± 9% of the left ventricle; $P = 0.18$) or lower left ventricular ejection fractions (24% ± 8% vs. 28% ± 9% of the left ventricle; $P = 0.053$). In addition, work with ^{11}C-HED PET in patients with heart failure with a preserved ejection fraction demonstrated that a lower global retention index of ^{11}C-HED was independently associated with the presence of advanced diastolic dysfunction (grades 2 and 3) in a multivariate logistic regression analysis (odds ratio, 0.66 per 0.01 min^{-1}, $P = 0.044$) (*53*). Despite the established clinical relevance of ^{11}C-based radiotracers, their popularity has been limited
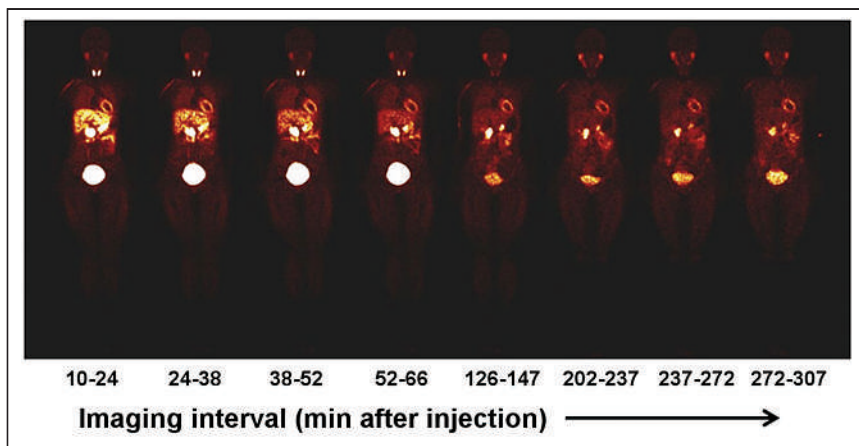
FIGURE 5. Presynaptic sympathetic imaging with ^{18}F-FBBG PET. Figure shows representative sequence of whole-body ^{18}F-FBBG coronal PET images in healthy volunteer. Myocardial signal persists after clearance from liver and surrounding organs. (Reprinted from (55).)

by a relatively short half-life (20 min) that necessitates on-site cyclotron production.

As a result of the intrinsic limitations of ^{11}C-based radiotracers, ^{18}F-based radiotracers targeting the norepinephrine transporter have generated significant interest. ^{18}F-flurobenguane (^{18}F-FBBG, also known as ^{18}F-LMI1195) is a benzylguanidine that is similar in structure to ^{123}I-MIBG (54,55). First-in-humans studies of ^{18}F-FBBG demonstrated favorable characteristics for imaging, including rapid blood pool clearance, moderate rates of liver and lung clearance, and stable myocardial uptake, with a myocardium-to-liver ratio of more than 2 at 4 h (Fig. 5) (55). Preliminary results of subsequent clinical evaluations demonstrated that ^{18}F-FBBG yields estimates of myocardial sympathetic innervation similar to those of ^{11}C-HED but has more favorable kinetics (54). Given the advantages of ^{18}F-FBBG for quantifying regional myocardial innervation, it was selected for evaluation in the PAREPET II trial to determine the risk of sudden cardiac death in patients with ischemic cardiomyopathy (NCT03493516). In addition to ^{18}F-FBBG, there are several other ^{18}F-labeled norepinephrine transporter–targeted radiotracers that are currently in development. ^{18}F-meta-fluorobenzylguanidine (^{18}F-MFBG) is another benzylguanidine with potential for use in cardiac applications; it has demonstrated rapid and sustained myocardial uptake with fast blood pool clearance in initial clinical evaluations (56,57) (NCT02348749). 4-^{18}F-fluoro-meta-hydroxyphenethylguanidine and its

structural isomer 3-^{18}F-fluoro-para-hydroxyphenethylguanidine are phenethylguanidines that were designed for slow neuronal uptake and irreversible presynaptic retention, features thought to be favorable for accurate detection and quantification of cardiac sympathetic denervation (58). First-in-humans studies with these radiotracers demonstrated high-quality images with reproducible measurements of regional cardiac sympathetic nerve density (NCT02669563) (58).

Postsynaptic Sympathetic Imaging

^{11}C-CGP-12177 (4-(3-tert-butylamino-2-hydroxypropoxy)-2H-benzimidazol-2-^{11}C-one) (37,49) and ^{11}C-CGP-12388 ((S)-4-(3-(2′-^{11}C-isopropylamino)-2-hydroxypropoxy)-2H-benzimidazol-2-one) (59,60) are nonselective β-receptor antagonists that have been used for postsynaptic adrenergic imaging. ^{11}C-CGP-12177 has been paired with presynaptic sympathetic tracers such as ^{123}I-MIBG (61) and ^{11}C-HED (36,37,49) to help elucidate the complex relationships between pre- and postsynaptic sympathetic function (Fig. 6). The studies show significant alterations in both pre- and postsynaptic sympathetic function in patients with various types of cardiomyopathies. Chronically increased sympathetic tone in the setting of heart failure is reflected in the decreased uptake or increased washout of presynaptic catecholamines and leads to the observed downregulation of postsynaptic β-adrenergic receptors (61). Although α-adrenergic signaling is less intensively investigated, it also plays a fundamental role in cardiovascular physiology (62) and is an intriguing target for therapeutics and molecular imaging. ^{11}C-labeled N-[6-[(4-amino-6,7-dimethoxyquinazolin-2-yl)-methylamino]hexyl]-N-methylfuran-2-carboxamide;hydrochloride (^{11}C-GB67) is a prazosin analog and α$_1$-adrenergic antagonist that has demonstrated myocardial uptake in preclinical and initial human studies, although its clinical role has yet to be established (63,64).

Parasympathetic Imaging

Techniques for radioligand imaging of cardiac parasympathetic activity remain far less developed than those for sympathetic imaging despite the central role that parasympathetic innervation plays in cardiovascular physiology. ^{11}C-donepezil is a reversible, noncompetitive antagonist of acetylcholinesterase that has been investigated in humans as a potential surrogate marker of cardiac parasympathetic innervation (65), although its utility is hindered by donepezil's significant affinity for σ$_1$-receptors, which are also plentiful in the heart (66). ^{11}C-methylquinuclidinyl benzilate is a specific hydrophobic antagonist of muscarinic acetylcholine receptors that has demonstrated significantly greater uptake in patients with dilated cardiomyopathy than in healthy controls (34.5 ± 8.9 vs. 25.0 ± 7.7 pmol/mL, $P < 0.005$) (40). In addition, 2-deoxy-2-^{18}F-fluoro-D-glucose-A85380 is a selective agonist of the α$_4$β$_2$ nicotinic receptor that was developed for central nervous system imaging and has demonstrated feasibility in humans for imaging
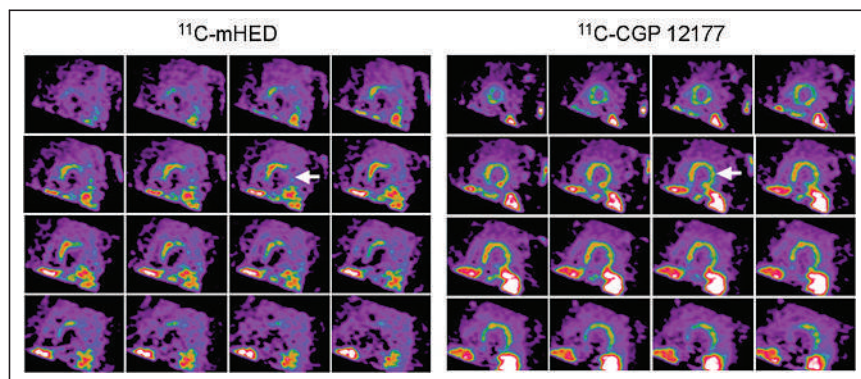
FIGURE 6. Pre- and postsynaptic sympathetic imaging with ^{11}C-HED and ^{11}C-CGP 12177 PET. Short axis ^{11}C-HED and ^{11}C-CGP 12177 PET images of patient with congestive heart failure. Significant pre- and postsynaptic mismatch are noted by arrows. (Reprinted from (49).)

nicotinic receptors in the heart (*67*) and vasculature (*68*). More recently, the vesicular acetylcholine transporter has been investigated as a potential target for radioligand imaging of cardiovascular cholinergic activity. ^{18}F-fluoroethoxybenzovesamicol is a noncompetitive inhibitor of the vesicular acetylcholine transporter that, in contrast to ^{11}C-donepezil, has low affinity for σ_1-receptors (*69*). ^{18}F-fluoroethoxybenzovesamicol has been extensively studied in the central nervous system and recently demonstrated favorable properties for quantitative cardiac imaging (*69*).

Overall, neuronal radiotracers have thus far not gained widespread use in cardiovascular medicine despite some intriguing preclinical and clinical findings. Multiple technical, clinical, and economic factors likely contribute to the slow advancement of neuronal imaging techniques, including incomplete definitions of their clinical roles and potential added value over established imaging techniques. Given the advantages of PET over SPECT, the field of cardiovascular neuronal imaging will likely continue to shift toward quantitative PET techniques, likely with ^{18}F-labeled tracers. This will require further development of ^{18}F-based radiotracers and related quantitative analysis techniques.

CONCLUSION

Cardiovascular imaging is evolving in response to systemwide trends toward molecular characterization and personalized therapies. The development of new radiotracers for PET and SPECT imaging is central to addressing the numerous unmet diagnostic needs that relate to these changes. Overall, there is a trend toward greater use of PET in cardiovascular medicine given its beneficial imaging properties and established methods for quantification, although SPECT remains highly used because of its favorable cost and availability and the numerous benefits of recent technical improvements. The development of radiotracers for improved characterization of cardiovascular neuronal activity as well as perfusion in both the myocardium and periphery has been discussed in part 1 of this review. Part 2 will present a detailed overview of emerging radiotracers for the imaging of cardiovascular inflammation, fibrosis, thrombosis, calcification, and cardiac amyloidosis.

REFERENCES

1. Heidenreich PA, Albert NM, Allen LA, et al. Forecasting the impact of heart failure in the United States: a policy statement from the American Heart Association. *Circ Heart Fail.* 2013;6:606–619.
2. Dobrucki LW, Sinusas AJ. PET and SPECT in cardiovascular molecular imaging. *Nat Rev Cardiol.* 2010;7:38–47.
3. Chan C, Harris M, Le M, et al. End-expiration respiratory gating for a high-resolution stationary cardiac SPECT system. *Phys Med Biol.* 2014;59:6267–6287.
4. Fan P, Hutton BF, Holstensson M, et al. Scatter and crosstalk corrections for ^{99m}Tc/^{123}I dual-radionuclide imaging using a CZT SPECT system with pinhole collimators. *Med Phys.* 2015;42:6895–6911.
5. Agostini D, Marie P-Y, Ben-Haim S, et al. Performance of cardiac cadmium-zinc-telluride gamma camera imaging in coronary artery disease: a review from the cardiovascular committee of the European Association of Nuclear Medicine (EANM). *Eur J Nucl Med Mol Imaging.* 2016;43:2423–2432.
6. Thorn SL, Barlow SC, Feher A, et al. Application of hybrid matrix metalloproteinase-targeted and dynamic ^{201}Tl single-photon emission computed tomography/computed tomography imaging for evaluation of early post-myocardial infarction remodeling. *Circ Cardiovasc Imaging.* 2019;12:e009055.
7. Caobelli F, Wollenweber T, Bavendiek U, et al. Simultaneous dual-isotope solid-state detector SPECT for improved tracking of white blood cells in suspected endocarditis. *Eur Heart J.* 2017;38:436–443.
8. Meoli DF, Sadeghi MM, Krassilnikova S, et al. Noninvasive imaging of myocardial angiogenesis following experimental myocardial infarction. *J Clin Invest.* 2004;113:1684–1691.
9. Holland JP, Williamson MJ, Lewis JS. Unconventional nuclides for radiopharmaceuticals. *Mol Imaging.* 2010;9:1–20.
10. Maddahi J, Lazewatsky J, Udelson JE, et al. Phase-III clinical trial of fluorine-18 flurpiridaz positron emission tomography for evaluation of coronary artery disease. *J Am Coll Cardiol.* 2020;76:391–401.
11. Stendahl JC, Liu Z, Boutagy NE, Nataneli E, Daghighian F, Sinusas AJ. Prototype device for endoventricular beta-emitting radiotracer detection and molecularly-guided intervention. *J Nucl Cardiol.* August 20, 2020 [Epub ahead of print].
12. Conti M, Eriksson L. Physics of pure and non-pure positron emitters for PET: a review and a discussion. *EJNMMI Phys.* 2016;3:8.
13. Calnon DA. Will ^{18}F flurpiridaz replace ^{82}rubidium as the most commonly used perfusion tracer for PET myocardial perfusion imaging? *J Nucl Cardiol.* 2019;26:2031–2033.
14. Maddahi J, Bengel F, Czernin J, et al. Dosimetry, biodistribution, and safety of flurpiridaz F 18 in healthy subjects undergoing rest and exercise or pharmacological stress PET myocardial perfusion imaging. *J Nucl Cardiol.* 2019;26:2018–2030.
15. Berman DS, Maddahi J, Tamarappoo BK, et al. Phase II safety and clinical comparison with single-photon emission computed tomography myocardial perfusion imaging for detection of coronary artery disease: flurpiridaz F 18 positron emission tomography. *J Am Coll Cardiol.* 2013;61:469–477.
16. Bourque JM, Hanson CA, Agostini D, et al. Assessing myocardial perfusion in suspected coronary artery disease: rationale and design of the second phase 3, open-label multi-center study of flurpiridaz (F-18) injection for positron emission tomography (PET) imaging. *J Nucl Cardiol.* 2021;28:1105–1116.
17. Packard RRS, Lazewatsky JL, Orlandi C, Maddahi J. Diagnostic performance of PET versus SPECT myocardial perfusion imaging in patients with smaller left ventricles: a substudy of the ^{18}F-flurpiridaz phase III clinical trial. *J Nucl Med.* 2021;62:849–854.
18. Sogbein OO, Pelletier-Galarneau M, Schindler TH, Wei L, Wells RG, Ruddy TD. New SPECT and PET radiopharmaceuticals for imaging cardiovascular disease. *BioMed Res Int.* 2014;2014:942960.
19. Gewirtz H, Narula J. A closer look at ^{18}flurpiridaz data in IHD: hiding in plain sight. *J Am Coll Cardiol.* 2020;76:402–404.
20. Bartholomä MD, Zhang S, Akurathi V, et al. ^{18}F-labeled rhodamines as potential myocardial perfusion agents: comparison of pharmacokinetic properties of several rhodamines. *Nucl Med Biol.* 2015;42:796–803.
21. Shoup TM, Elmaleh DR, Brownell AL, Zhu A, Guerrero JL, Fischman AJ. Evaluation of (4-[^{18}F]fluorophenyl)triphenylphosphonium ion. a potential myocardial blood flow agent for PET. *Mol Imaging Biol.* 2011;13:511–517.
22. Wells RG, Wei L, Petryk J, et al. Flow-dependent uptake of ^{123}I-CMICE-013, a novel SPECT perfusion agent, compared with standard tracers. *J Nucl Med.* 2015;56:764–770.
23. Broisat A, Ruiz M, Goodman NC, et al. Myocardial uptake of 7′-(Z)-[^{123}I]iodorotenone during vasodilator stress in dogs with critical coronary stenoses. *Circ Cardiovasc Imaging.* 2011;4:685–692.
24. Inoue Y, Shirouzu I, Machida T, et al. Collimator choice in cardiac SPECT with I-123-labeled tracers. *J Nucl Cardiol.* 2004;11:433–439.
25. Thompson RC, Heller GV, Johnson LL, et al. Value of attenuation correction on ECG-gated SPECT myocardial perfusion imaging related to body mass index. *J Nucl Cardiol.* 2005;12:195–202.
26. Wells RG, Marvin B, Poirier M, Renaud J, deKemp RA, Ruddy TD. Optimization of SPECT measurement of myocardial blood flow with corrections for attenuation, motion, and blood binding compared with PET. *J Nucl Med.* 2017;58:2013–2019.
27. Criqui MH, Aboyans V. Epidemiology of peripheral artery disease. *Circ Res.* 2015;116:1509–1526.
28. Alvelo JL, Papademetris X, Mena-Hurtado C, et al. Radiotracer imaging allows for noninvasive detection and quantification of abnormalities in angiosome foot perfusion in diabetic patients with critical limb ischemia and nonhealing wounds. *Circ Cardiovasc Imaging.* 2018;11:e006932.
29. Scholtens AM, Tio RA, Willemsen A, et al. Myocardial perfusion reserve compared with peripheral perfusion reserve: a [^{13}N]ammonia PET study. *J Nucl Cardiol.* 2011;18:238–246.
30. Scremin OU, Figoni SF, Norman K, et al. Preamputation evaluation of lower-limb skeletal muscle perfusion with H$_2$ ^{15}O positron emission tomography. *Am J Phys Med Rehabil.* 2010;89:473–486.
31. Chou TH, Alvelo JL, Janse S, et al. Prognostic value of radiotracer-based perfusion imaging in critical limb ischemia patients undergoing lower extremity revascularization. *JACC Cardiovasc Imaging.* 2021;14:1614–1624.
32. Battipaglia I, Lanza GA. Autonomic innervation of the heart. In: Slart RHJA, Tio RA, Elsinga PH, Schwaiger M, eds. *The Autonomic Nervous System of the Heart.* Springer; 2015:1–12.
33. Le Guludec D, Delforge J, Dolle F. Imaging the parasympathetic cardiac innervation with PET. In: Slart RHJA, Tio RA, Elsinga PH, Schwaiger M, eds. *The Autonomic Nervous System of the Heart.* Springer; 2015:111–135.

34. Fallavollita JA, Heavey BM, Luisi AJ Jr, et al. Regional myocardial sympathetic denervation predicts the risk of sudden cardiac arrest in ischemic cardiomyopathy. *J Am Coll Cardiol.* 2014;63:141–149.

35. Jacobson AF, Senior R, Cerqueira MD, et al. Myocardial iodine-123 meta-iodobenzylguanidine imaging and cardiac events in heart failure: results of the prospective ADMIRE-HF (AdreView Myocardial Imaging for Risk Evaluation in Heart Failure) study. *J Am Coll Cardiol.* 2010;55:2212–2221.

36. Schäfers M, Dutka D, Rhodes CG, et al. Myocardial presynaptic and postsynaptic autonomic dysfunction in hypertrophic cardiomyopathy. *Circ Res.* 1998;82:57–62.

37. John AS, Mongillo M, Depre C, et al. Pre- and post-synaptic sympathetic function in human hibernating myocardium. *Eur J Nucl Med Mol Imaging.* 2007;34:1973–1980.

38. Avendaño R, Hashemi-Zonouz T, Sandoval V, et al. Anger recall mental stress decreases ^{123}I-metaiodobenzylguanidine (^{123}I-MIBG) uptake and increases heterogeneity of cardiac sympathetic activity in the myocardium in patients with ischemic cardiomyopathy. *J Nucl Cardiol.* October 8, 2020 [Epub ahead of print].

39. Stirrup J, Gregg S, Baavour R, et al. Hybrid solid-state SPECT/CT left atrial innervation imaging for identification of left atrial ganglionated plexi: technique and validation in patients with atrial fibrillation. *J Nucl Cardiol.* 2020; 27:1939–1950.

40. Le Guludec D, Cohen-Solal A, Delforge J, Delahaye N, Syrota A, Merlet P. Increased myocardial muscarinic receptor density in idiopathic dilated cardiomyopathy. *Circulation.* 1997;96:3416–3422.

41. Todica A, Siebermair J, Schiller J, et al. Assessment of right ventricular sympathetic dysfunction in patients with arrhythmogenic right ventricular cardiomyopathy: an ^{123}I-metaiodobenzylguanidine SPECT/CT study. *J Nucl Cardiol.* 2020;27:2402–2409.

42. Allman KC, Wieland DM, Muzik O, Degrado TR, Wolfe ER Jr, Schwaiger M. Carbon-11 hydroxyephedrine with positron emission tomography for serial assessment of cardiac adrenergic neuronal function after acute myocardial infarction in humans. *J Am Coll Cardiol.* 1993;22:368–375.

43. Haider N, Baliga RR, Chandrashekhar Y, Narula J. Adrenergic excess, hNET1 down-regulation, and compromised mIBG uptake in heart failure poverty in the presence of plenty. *JACC Cardiovasc Imaging.* 2010;3:71–75.

44. Boutagy NE, Sinusas AJ. Recent advances and clinical applications of PET cardiac autonomic nervous system imaging. *Curr Cardiol Rep.* 2017;19:33.

45. Matsunari I, Aoki H, Nomura Y, et al. Iodine-123 metaiodobenzylguanidine imaging and carbon-11 hydroxyephedrine positron emission tomography compared in patients with left ventricular dysfunction. *Circ Cardiovasc Imaging.* 2010;3:595–603.

46. Bengel FM, Thackeray JT. Altered cardiac innervation predisposes to ventricular arrhythmia: targeted positron emission tomography identifies risk in ischemic cardiomyopathy. *J Am Coll Cardiol.* 2014;63:150–152.

47. Werner RA, Rischpler C, Onthank D, et al. Retention kinetics of the ^{18}F-labeled sympathetic nerve PET tracer LMI1195: comparison with ^{11}C-hydroxyephedrine and ^{123}I-MIBG. *J Nucl Med.* 2015;56:1429–1433.

48. Lautamaki R, Sasano T, Higuchi T, et al. Multiparametric molecular imaging provides mechanistic insights into sympathetic innervation impairment in the viable infarct border zone. *J Nucl Med.* 2015;56:457–463.

49. Caldwell JH, Link JM, Levy WC, Poole JE, Stratton JR. Evidence for pre- to postsynaptic mismatch of the cardiac sympathetic nervous system in ischemic congestive heart failure. *J Nucl Med.* 2008;49:234–241.

50. Sasano T, Abraham MR, Chang KC, et al. Abnormal sympathetic innervation of viable myocardium and the substrate of ventricular tachycardia after myocardial infarction. *J Am Coll Cardiol.* 2008;51:2266–2275.

51. Rijnierse MT, Allaart CP, de Haan S, et al. Sympathetic denervation is associated with microvascular dysfunction in non-infarcted myocardium in patients with cardiomyopathy. *Eur Heart J Cardiovasc Imaging.* 2015;16:788–798.

52. Bengel FM, Permanetter B, Ungerer M, Nekolla SG, Schwaiger M. Relationship between altered sympathetic innervation, oxidative metabolism and contractile function in the cardiomyopathic human heart; a non-invasive study using positron emission tomography. *Eur Heart J.* 2001;22:1594–1600.

53. Aikawa T, Naya M, Obara M, et al. Impaired myocardial sympathetic innervation is associated with diastolic dysfunction in heart failure with preserved ejection fraction: ^{11}C-hydroxyephedrine PET study. *J Nucl Med.* 2017;58:784–790.

54. Zelt JG, Britt D, Mair BA, et al. Regional distribution of fluorine-18-flubrobenguane and carbon-11-hydroxyephedrine for cardiac PET imaging of sympathetic innervation. *JACC Cardiovasc Imaging.* 2021;14:1425–1436.

55. Sinusas AJ, Lazewatsky J, Brunetti J, et al. Biodistribution and radiation dosimetry of LMI1195: first-in-human study of a novel ^{18}F-labeled tracer for imaging myocardial innervation. *J Nucl Med.* 2014;55:1445–1451.

56. Grkovski M, Zanzonico PB, Modak S, Humm JL, Narula J, Pandit-Taskar N. F-18 meta-fluorobenzylguanidine PET imaging of myocardial sympathetic innervation. *J Nucl Cardiol.* January 6, 2022 [Epub ahead of print].

57. Pandit-Taskar N, Zanzonico P, Staton KD, et al. Biodistribution and dosimetry of ^{18}F-meta-fluorobenzylguanidine: a first-in-human PET/CT imaging study of patients with neuroendocrine malignancies. *J Nucl Med.* 2018;59:147–153.

58. Raffel DM, Jung YW, Koeppe RA, et al. First-in-human studies of [^{18}F]fluorohydroxyphenethylguanidines. *Circ Cardiovasc Imaging.* 2018;11:e007965.

59. de Jong RM, Willemsen AT, Slart RH, et al. Myocardial β-adrenoceptor downregulation in idiopathic dilated cardiomyopathy measured in vivo with PET using the new radioligand (S)-[^{11}C]CGP12388. *Eur J Nucl Med Mol Imaging.* 2005;32:443–447.

60. Momose M, Reder S, Raffel DM, et al. Evaluation of cardiac β-adrenoceptors in the isolated perfused rat heart using (S)-^{11}C-CGP12388. *J Nucl Med.* 2004;45:471–477.

61. Tsukamoto T, Morita K, Naya M, et al. Decreased myocardial β-adrenergic receptor density in relation to increased sympathetic tone in patients with nonischemic cardiomyopathy. *J Nucl Med.* 2007;48:1777–1782.

62. Zhang J, Simpson PC, Jensen BC. Cardiac alpha1A-adrenergic receptors: emerging protective roles in cardiovascular diseases. *Am J Physiol Heart Circ Physiol.* 2021; 320:H725–H733.

63. Law MP, Osman S, Pike VW, et al. Evaluation of [^{11}C]GB67, a novel radioligand for imaging myocardial α1-adrenoceptors with positron emission tomography. *Eur J Nucl Med.* 2000;27:7–17.

64. Park-Holohan SJ, Asselin MC, Turton DR, et al. Quantification of [^{11}C]GB67 binding to cardiac α1-adrenoceptors with positron emission tomography: validation in pigs. *Eur J Nucl Med Mol Imaging.* 2008;35:1624–1635.

65. Gjerløff T, Jakobsen S, Nahimi A, et al. In vivo imaging of human acetylcholinesterase density in peripheral organs using ^{11}C-donepezil: dosimetry, biodistribution, and kinetic analyses. *J Nucl Med.* 2014;55:1818–1824.

66. Horsager J, Fedorova TD, Berge NVD, et al. Cardiac ^{11}C-donepezil binding increases with age in healthy humans: potentially signifying sigma-1 receptor upregulation. *J Cardiovasc Pharmacol Ther.* 2019;24:365–370.

67. Bucerius J, Joe AY, Schmaljohann J, et al. Feasibility of 2-deoxy-2-[^{18}F]fluoro-D-glucose-A85380-PET for imaging of human cardiac nicotinic acetylcholine receptors in vivo. *Clin Res Cardiol.* 2006;95:105–109.

68. Bucerius J, Manka C, Schmaljohann J, et al. Feasibility of [^{18}F]-2-fluoro-A85380-PET imaging of human vascular nicotinic acetylcholine receptors in vivo. *JACC Cardiovasc Imaging.* 2012;5:528–536.

69. Saint-Georges Z, Zayed VK, Dinelle K, et al. First-in-human imaging and kinetic analysis of vesicular acetylcholine transporter density in the heart using [^{18}F]FEOBV PET. *J Nucl Cardiol.* 2021;28:50–54.

70. NuDat 3.0. National Nuclear Data Center website. www.nndc.bnl.gov/nudat2. Accessed March 9, 2022.

Signaling Pathways That Drive ^{18}F-FDG Accumulation in Cancer

Jessica R. Salas and Peter M. Clark

Department of Molecular and Medical Pharmacology, UCLA, Los Angeles, California

^{18}F-FDG measures glucose consumption and is an integral part of cancer management. Most cancer types upregulate their glucose consumption, yielding elevated ^{18}F-FDG PET accumulation in those cancer cells. The biochemical pathway through which ^{18}F-FDG accumulates in cancer cells is well established. However, beyond well-known regulators such as c-Myc, PI3K/PKB, and HIF1α, the proteins and signaling pathways that cancer cells modulate to activate the facilitated glucose transporters and hexokinase enzymes that drive elevated ^{18}F-FDG accumulation are less well understood. Understanding these signaling pathways could yield additional biologic insights from ^{18}F-FDG PET scans and could suggest new uses of ^{18}F-FDG PET in the management of cancer. Work over the past 5 years, building on studies from years prior, has identified new proteins and signaling pathways that drive glucose consumption in cancer. Here, we review these recent studies and discuss current limitations to our understanding of glucose consumption in cancer.

Key Words: molecular imaging; oncology; ^{18}F-FDG PET; cancer; glucose consumption; signaling pathways

The glucose analog PET radiotracer ^{18}F-FDG measures glucose consumption and is an important tool for the diagnosis and management of cancer (*1,2*). ^{18}F-FDG PET imaging has demonstrated value in, for example, the initial staging and the identification of recurrences in lung, colorectal, and esophageal cancers (*1*). Additionally, preclinical and clinical studies suggest that changes in ^{18}F-FDG accumulation in tumors after certain therapies can be strongly predictive and can function as an early biomarker of therapeutic efficacy (*3,4*).

However, despite the proven clinical value of ^{18}F-FDG PET in cancer management and a clear understanding of the biochemical pathway that ^{18}F-FDG measures—glucose consumption—a comprehensive understanding of the signaling pathways that regulate glucose consumption and ^{18}F-FDG accumulation in cancer is lacking. Understanding these signaling pathways could provide a better context in which to understand ^{18}F-FDG PET scans in patients, might help to connect mechanistically the level of ^{18}F-FDG accumulation to specific and potentially targetable alterations in a given cancer type, and might aid in identifying additional therapies for which ^{18}F-FDG PET could be leveraged as an early predictor of therapeutic efficacy.

This review describes and categorizes new signaling pathways that regulate glucose consumption in cancer and that have been reported within the last 5 years. Most of these newly described pathways connect to well-established and previously identified regulators of cancer cell glucose consumption such as PI3K, HIF1α, and TXNIP. Work describing these and other previously identified regulators of glucose consumption can be found in prior reviews (*5–8*). Mechanisms through which therapies block ^{18}F-FDG accumulation and glucose consumption in cancer are important although beyond the scope of this review. Additionally, mechanisms that drive ^{18}F-FDG accumulation in immune cells in the tumor microenvironment and how that information could be used to monitor therapeutic responses to immune checkpoint inhibitors are an important additional topic but also outside the scope of this review and at least partially covered by a recent review (*9*).

THE BIOCHEMISTRY OF ^{18}F-FDG ACCUMULATION

^{18}F-FDG is transported across the cell membrane by facilitated glucose transporters (GLUTs) and is phosphorylated by hexokinase enzymes to ^{18}F-FDG-6-phosphate (*2*). The GLUTs are a large family of transporters containing 14 isoforms that transport glucose and related compounds (*10*). GLUT1 and GLUT3 both transport glucose and ^{18}F-FDG, are highly expressed in a variety of cancers, and are considered the key transporters of ^{18}F-FDG in most cancer cells (*10,11*). ^{18}F-FDG is not a substrate for sodium-dependent glucose transporters (*12*), although the exact contribution of these transporters to glucose flux in cancer remains to be determined. Cells express one or more of 4 different hexokinases (*13*). Hexokinase 1 (HK1) and hexokinase 2 (HK2), alone or in combination, are expressed in most cancer cells and are considered the key enzymes for phosphorylating ^{18}F-FDG to ^{18}F-FDG-6-phosphate in cancer cells (*13*). ^{18}F-FDG-6-phosphate can be dephosphorylated by glucose-6-phosphatase and transported out of the cell by the GLUTs (*14*).

Which of these biochemical steps is the major driver of ^{18}F-FDG accumulation is likely context-dependent, and low levels of the GLUTs or hexokinase enzymes or high levels of glucose-6-phosphatase are often found in cancers that accumulate low levels of ^{18}F-FDG. For example, in non–small cell lung cancer, GLUT1 and GLUT3 levels correlate better than HK1 and HK2 levels with ^{18}F-FDG accumulation (*15*). In pheochromocytomas and paragangliomas, HK2 levels correlate better than GLUT1 or GLUT3 levels with ^{18}F-FDG accumulation (*16*). ^{18}F-FDG accumulation can be variable in gastric and breast cancers, and in both cases, ^{18}F-FDG accumulation correlates with GLUT1 levels (*17,18*). Low ^{18}F-FDG accumulation in low-grade hepatocellular carcinoma tumors is associated with low hexokinase activity and high glucose-6-phosphatase activity (*19*).

Additional enzymes, including phosphoglucose isomerase and phosphoglucomutase, can further metabolize ^{18}F-FDG-6-phosphate (20), but how (if at all) changes in the activity of these enzymes affects ^{18}F-FDG accumulation at the time point usually used for imaging with ^{18}F-FDG remains unclear.

THE SIGNALING PATHWAYS THAT AFFECT GLUCOSE CONSUMPTION AND ^{18}F-FDG ACCUMULATION IN CANCER CELLS

Many well-validated methods exist for quantifying glucose consumption, including measuring 2-DG-6-phosphate levels in cells treated with 2-DG, measuring accumulated radioactivity in cells treated with a radiolabeled glucose analog, or measuring changes in glucose concentrations in cell culture media (21). An often-used but poor measure of glucose consumption is accumulated fluorescence in cells treated with a fluorescent glucose analog such as 2-[N-(7-nitrobenz-2-oxa-1,3-diazol-4-yl)amino]-2-deoxyglucose or 6-[N-(7-nitrobenz-2-oxa-1,3-diazol-4-yl)amino]-2-deoxyglucose. Various studies have identified multiple systems in which the accumulation of these fluorescent glucose analogs does not measure glucose consumption (22,23). As such, we will focus only on those studies that measure glucose consumption with well-validated methods.

Over the last 5 years, most studies have identified signaling pathways that regulate glucose consumption and ^{18}F-FDG accumulation by regulating the GLUT proteins and hexokinase enzymes at the transcriptional and posttranslational level.

TRANSCRIPTION (FIG. 1A)

Newly identified regulators of GLUT1 and GLUT3 transcription are varied and defy easy categorization. In squamous cell carcinoma cell lines, the transcription factors p63 and SOX2 drive glucose consumption by binding to an enhancer region of the GLUT1 gene and driving GLUT1 messenger RNA (mRNA) and protein expression (24). Our laboratory recently identified over 100 small molecules that block glucose consumption in 1 of 3 different non–small cell lung cancer cell lines using a high-throughput assay. We studied the small molecule milciclib and used it to determine that the cyclin-dependent kinase CDK7 activates GLUT1 transcription, glucose consumption, and ^{18}F-FDG accumulation downstream from mutant PIK3CA (25). In melanoma cells, lysine methyl transferase KMT2D loss-of-function mutants increase glucose consumption by repressing the expression of IGFBP5, a negative regulator of insulin signaling, and increase mRNA expression of GLUT1 and HK1 (26). In pre–B-cell acute lymphoblastic leukemia, B-lymphoid transcription factors Pax5 and IKZF1 function as tumor suppressors and downregulate mRNA levels of GLUT1 and HK2 (27). In breast and colorectal cancer cells, during cell detachment, the protein kinase SGK1 induces the expression of GLUT1 mRNA, leading to increased GLUT1 protein levels and glucose consumption (28). In pancreatic cancer, the transmembrane mucin glycoprotein MUC13 increases glucose consumption by activating nuclear factor κB, leading to increased mRNA expression of GLUT1 (29). Finally, in cervical cancer cells, long noncoding RNA NICI enhances glucose consumption during hypoxia by promoting the recruitment of RNA polymerase 2 to the GLUT3 promoter and increasing GLUT3 mRNA levels (30).

The transcription factor c-Myc continues to be an important regulator of glucose consumption, with attention in the last 5 years focusing on its role in regulating HK2 mRNA levels. In colon cancer cells, interleukin 22 enhances glucose consumption by activating STAT3, which induces c-Myc mRNA and protein levels, leading to increased mRNA and protein expression of HK2 (31). Alternatively, in pancreatic cancer cells, serotonin activates glucose consumption in cells by binding its receptor HTR2B, increasing protein levels of HIF1α and c-Myc, and increasing mRNA expression of HK2 (32). Inhibition of mTOR and c-Myc in lymphoma cell lines decreases glucose consumption, decreases mRNA levels of GLUT1, and increases mRNA levels of glucose-6-phosphatase (33).

Additional regulators of HK2 transcription include the transcription factor BACH1, the cytokine Gremlin-1, and the micro RNA miR-34c-3p. In lung cancer cells, BACH1, which is stabilized in the presence of antioxidants, binds to the HK2 promoter and induces HK2 mRNA levels, leading to increased glucose consumption (34). In breast cancer cells, Gremlin-1 induces glucose consumption by activating the reactive oxygen species–PKB (Akt)–STAT3 pathway, which leads to increased HK2 mRNA (35). Finally, in hepatocellular carcinoma cell lines, miR-34c-3p drives glucose consumption by downregulating guanylate kinase MAGI3. MAGI3 inhibits β-catenin transcriptional activity, and decreased MAGI3 levels leads to increased HK2 mRNA levels and glucose consumption (36).

PROTEIN EXPRESSION (FIG. 1B)

A few studies only looked at protein levels of GLUT1 and HK2. In osteosarcoma cells, the long noncoding RNA MALAT1 sponges up miR-485-3p, leading to higher levels of c-MET and Akt3, whose mRNA miR-485-3p targets. Higher c-MET and Akt3 protein levels increase mTOR signaling, GLUT1 and HK2 protein levels, and glucose consumption (37). In cervical cancer cells, programmed-death ligand 1 activates glucose consumption through the induction of SNAI1, which represses SIRT3 expression, leading to higher protein levels of HK2 and GLUT1 (38).

POSTTRANSLATIONAL REGULATION AND LOCALIZATION (FIG. 1C)

Recent work has focused on the posttranslational modifications of HK2 (39,40). SUMOylation and ubiquitination represent the conjugation of specific polypeptides to lysine residues on proteins. HK2 SUMOylation at lysine 315 and lysine 492 is added by the conjugating enzyme UBC2 and removed by the protease SENP1. In prostate cancer cells, HK2 SUMOylation weakens the interaction between HK2 and the anion channel VDAC on the outer mitochondrial membrane, leading to lower glucose consumption (39). In hepatocellular carcinoma, the COP9 signalosome subunit CSN5 is overexpressed and deubiquitinates HK2. HK2 ubiquitination is associated with its degradation, so CSN5 overexpression leads to increased HK2 protein levels and glucose consumption (40).

The α-arrestin family member TXNIP is a well-studied protein whose levels are induced by glucose, which binds to GLUT1, leading to GLUT1 internalization, and which decreases GLUT1 mRNA levels (41). In this capacity, TXNIP is a key effector of a negative-feedback loop that limits excess glucose consumption and a key node that is dysregulated in cancer cells to enhance glucose consumption (41). In recent work, the role of TXNIP in regulating glucose consumption continued to be affirmed, with studies identifying additional regulators of TXNIP levels (42–45).

Lower TXNIP levels lead to increased GLUT1 at the plasma membrane and increased glucose consumption (42). PI3K/Akt signaling in non–small cell lung cancer cell lines decreases TXNIP expression and increases glucose consumption. In a hepatocellular carcinoma cell line, growth factors induce rapid glucose uptake by activating

PI3K/Akt signaling, leading to the phosphorylation of TXNIP and yielding a weaker interaction between TXNIP and GLUT1 (*43,44*). Across a variety of cancer cell lines, reducing hyaluronan levels activates receptor tyrosine kinase signaling, leading to induction of the zinc finger protein ZNF36, which degrades TXNIP mRNA (*42*). ZNF36 also binds to and contributes to the degradation of HK2 mRNA (*46*), suggesting that ZNF36 may regulate glucose consumption through multiple mechanisms. In metastatic pancreatic cancer cells, elevated activity of the metabolic enzyme phosphogluconate dehydrogenase increases glucose consumption by depleting levels of its substrate, 6-phosphogluconate, leading to retention of the transcription factor MondoA in the cytoplasm and diminished expression

of the Mondo target gene TXNIP. Lower TXNIP levels lead to increased GLUT1 surface expression (*45*). In pancreatic cancer cells, the cell-surface glycoprotein MUC13 also directly interacts with and stabilizes GLUT1 at the cell surface, potentially synergizing with decreased levels of TXNIP (*29*).

The GTPase KRAS is highly mutated and activated in many different types of cancer and is well known to activate glucose consumption (*47*). However, mechanisms for how KRAS activates glucose consumption are not fully understood. KRAS is expressed as 2 splice variants, KRAS4A and KRAS4B. Recent work has shown that in multiple cancer cell lines, KRAS4A directly interacts with HK1 at the outer mitochondrial membrane, where it relieves
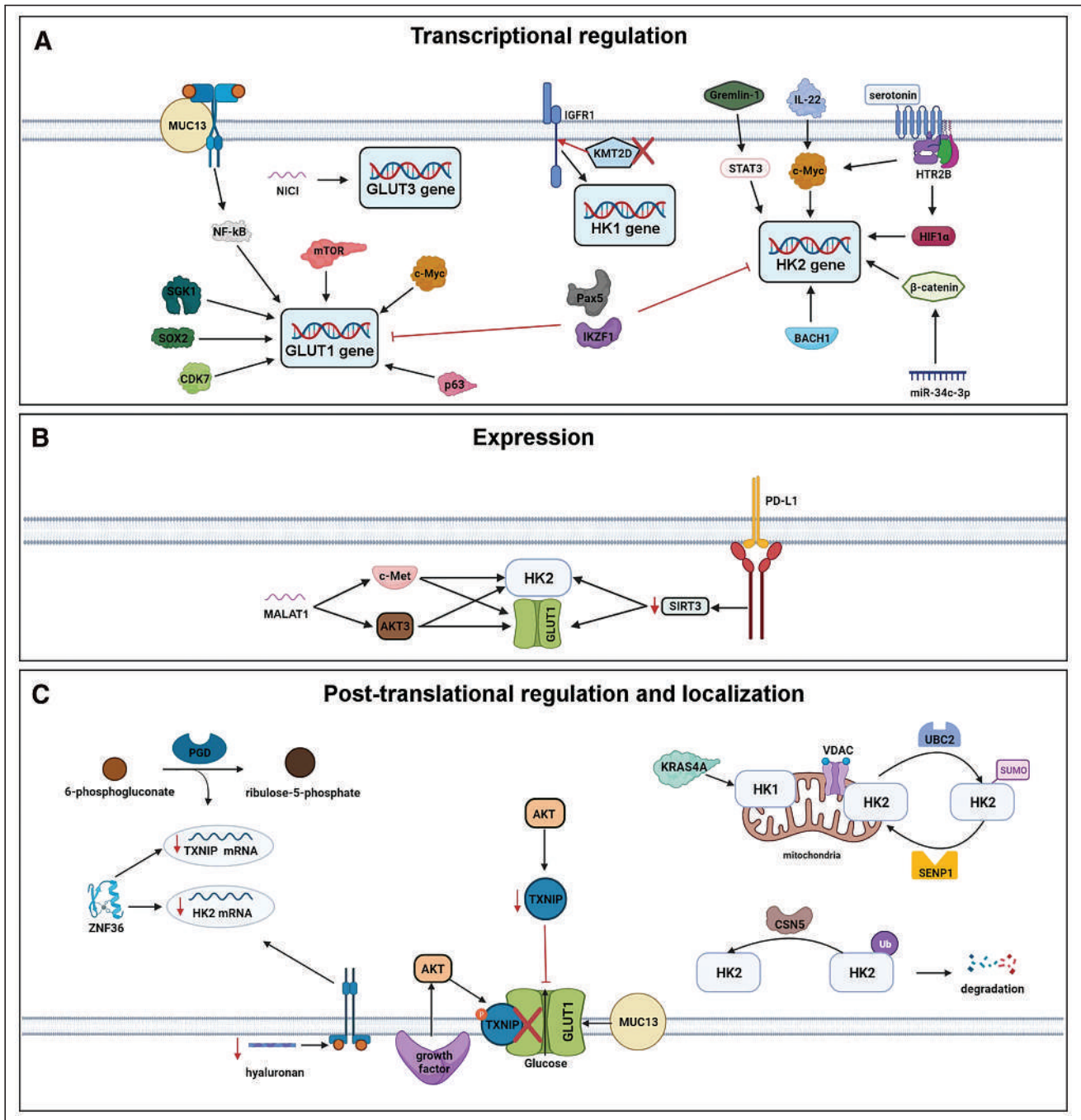
FIGURE 1. Recently described regulators of GLUT and hexokinase transcription (A), expression (B), and posttranslational regulation and localization (C).

glucose-6-phosphate–dependent product inhibition of HK1, leading to increased glucose consumption (48).

LIMITATIONS TO OUR CURRENT UNDERSTANDING OF GLUCOSE CONSUMPTION IN CANCER CELLS

Most proteins identified to regulate cancer cell glucose consumption have been shown to do so only in established cancer cell lines and in cell cultures despite the fact that metabolism can be very different between cell cultures and in vivo. Small-animal ^{18}F-FDG PET is an ideal and well-established assay for conducting such studies but is rarely used. Additional studies to evaluate regulators of glucose consumption in vivo are necessary. Ideally, these studies would be done using patient-derived xenografts implanted in orthotopic locations or genetically engineered mouse models.

Most proteins that have been shown to alter glucose consumption have been studied in one or a limited number of cell lines from the same cancer type. The activity of these proteins is often not linked to any known genetic alteration. Studies evaluating which signaling pathways are cancer-type–specific or are shared across different cancer types will be important for identifying the scope of any pathway identified. Studies determining the genetic or epigenetic alteration that activates a certain pathway to drive glucose consumption will serve the same purpose.

The data so far suggest that glucose consumption is regulated at multiple levels by various mechanisms. Largely understudied is the relative importance of each regulator in affecting glucose consumption. Proteins or pathways that drive a large proportion of the glucose consumption would likely have greater relevance for human ^{18}F-FDG PET.

An emerging but understudied theme is that blocking glucose consumption by affecting the identified pathways limits cell growth. For example, we have shown that the cyclin-dependent kinase inhibitor milciclib blocks cell growth by inhibiting glucose consumption (25). If this proves to be true across many different therapies and cancer types, it would provide a causal basis for correlative clinical studies showing that early changes in tumor ^{18}F-FDG accumulation in response to therapy can be predictive of therapeutic efficacy.

To identify additional drugs for which ^{18}F-FDG could function as a pharmacodynamic biomarker, it will be important to understand the kinetic time course over which glucose consumption is affected after a drug treatment. For example, because EGFR inhibitors block glucose consumption in glioblastoma cells within 4 h and through 24 h (4), a patient could be imaged with ^{18}F-FDG PET shortly after or up through a day after administration of an EGFR inhibitor. Milciclib affects glucose consumption only after 24 h (25); a patient would therefore need to be imaged with ^{18}F-FDG PET 24 h after milciclib treatment. Earlier imaging of a patient treated with milciclib could lead to the false impression that milciclib was not working in the tumor.

Tumors contain a complex mixture of cells, including cancer cells, immune cells, and stromal cells. The amount of glucose consumption in these various cell types and how that relates to the overall accumulation of ^{18}F-FDG in the tumor across different cancer types and locations remains to be fully determined. However, a recent study suggested that at least in certain tumor models, myeloid cells and T cells consume glucose at a higher rate than tumor cells (49). Further studies will be necessary to understand how much ^{18}F-FDG accumulation in tumors represents ^{18}F-FDG accumulation in cancer cells versus other cell types.

CONCLUSION

^{18}F-FDG PET is an established imaging approach for the management of many different types of cancer, but the full repertoire of signaling pathways that drive ^{18}F-FDG consumption in cancer are not well understood. A better understanding of these signaling pathways could yield new insights into ^{18}F-FDG PET imaging and will be important for developing additional uses of ^{18}F-FDG PET in cancer.

Critical and important work has been accomplished over the last 5 years to further elucidate the detailed mechanisms that cancer cells use to elevate their glucose consumption and that lead to increased ^{18}F-FDG accumulation in cancer cells. These studies continue to support the role of well-studied primary regulators of glucose consumption, including PI3K/Akt, mTOR, and HIF1α, while detailing the different ways in which these primary regulators control glucose consumption at the transcriptional and posttranslational level. Studies in the next 5 years should focus on how and whether the regulators of glucose consumption often identified in limited cell lines and in cell cultures translate in vivo to mice and potentially humans and across various types and subtypes of cancer.

DISCLOSURE

REFERENCES

1. Kostakoglu L, Agress H, Goldsmith SJ. Clinical role of FDG PET in evaluation of cancer patients. *Radiographics.* 2003;23:315–340.
2. Phelps ME. Positron emission tomography provides molecular imaging of biological processes. *Proc Natl Acad Sci USA.* 2000;97:9226–9233.
3. de Geus-Oei L-F, Vriens D, van Laarhoven HWM, van der Graaf WTA, Oyen WJG. Monitoring and predicting response to therapy with ^{18}F-FDG PET in colorectal cancer: a systematic review. *J Nucl Med.* 2009;50(suppl 1):43S–54S.
4. Mai WX, Gosa L, Daniels VW, et al. Cytoplasmic p53 couples oncogene-driven glucose metabolism to apoptosis and is a therapeutic target in glioblastoma. *Nat Med.* 2017;23:1342–1351.
5. Kato Y, Maeda T, Suzuki A, Baba Y. Cancer metabolism: new insights into classic characteristics. *Jpn Dent Sci Rev.* 2018;54:8–21.
6. DeBerardinis RJ, Lum JJ, Hatzivassiliou G, Thompson CB. The biology of cancer: metabolic reprogramming fuels cell growth and proliferation. *Cell Metab.* 2008;7: 11–20.
7. Hay N. Reprogramming glucose metabolism in cancer: can it be exploited for cancer therapy? *Nat Rev Cancer.* 2016;16:635–649.
8. Zhao M, Zhang Z. Glucose transporter regulation in cancer: a profile and the loops. *Crit Rev Eukaryot Gene Expr.* 2016;26:223–238.
9. Iravani A, Hicks RJ. Imaging the cancer immune environment and its response to pharmacologic intervention, part 1: the role of ^{18}F-FDG PET/CT. *J Nucl Med.* 2020;61:943–950.
10. Adekola K, Rosen ST, Shanmugam M. Glucose transporters in cancer metabolism. *Curr Opin Oncol.* 2012;24:650–654.
11. Jadvar H, Alavi A, Gambhir SS. ^{18}F-FDG uptake in lung, breast, and colon cancers: molecular biology correlates and disease characterization. *J Nucl Med.* 2009; 50:1820–1827.
12. Wright EM, Loo DDF, Hirayama BA. Biology of human sodium glucose transporters. *Physiol Rev.* 2011;91:733–794.
13. Xu S, Herschman HR. A tumor agnostic therapeutic strategy for hexokinase 1-null/hexokinase 2-positive cancers. *Cancer Res.* 2019;79:5907–5914.
14. Phelps ME, Huang SC, Hoffman EJ, Selin C, Sokoloff L, Kuhl DE. Tomographic measurement of local cerebral glucose metabolic rate in humans with (F-18)2-fluoro-2-deoxy-D-glucose: validation of method. *Ann Neurol.* 1979;6: 371–388.
15. de Geus-Oei L-F, van Krieken JHJM, Aliredjo RP, et al. Biological correlates of FDG uptake in non-small cell lung cancer. *Lung Cancer.* 2007;55: 79–87.

16. van Berkel A, Rao JU, Kusters B, et al. Correlation between in vivo ^{18}F-FDG PET and immunohistochemical markers of glucose uptake and metabolism in pheochromocytoma and paraganglioma. *J Nucl Med.* 2014;55:1253–1259.

17. Alakus H, Batur M, Schmidt M, et al. Variable ^{18}F-fluorodeoxyglucose uptake in gastric cancer is associated with different levels of GLUT-1 expression. *Nucl Med Commun.* 2010;31:532–538.

18. Bos R, van Der Hoeven JJM, van Der Wall E, et al. Biologic correlates of [18]fluorodeoxyglucose uptake in human breast cancer measured by positron emission tomography. *J Clin Oncol.* 2002;20:379–387.

19. Torizuka T, Tamaki N, Inokuma T, et al. In vivo assessment of glucose metabolism in hepatocellular carcinoma with FDG-PET. *J Nucl Med.* 1995;36:1811–1817.

20. Southworth R, Parry CR, Parkes HG, Medina RA, Garlick PB. Tissue-specific differences in 2-fluoro-2-deoxyglucose metabolism beyond FDG-6-P: a ^{19}F NMR spectroscopy study in the rat. *NMR Biomed.* 2003;16:494–502.

21. TeSlaa T, Teitell MA. Techniques to monitor glycolysis. *Methods Enzymol.* 2014; 542:91–114.

22. Sinclair LV, Barthelemy C, Cantrell DA. Single cell glucose uptake assays: a cautionary tale. *Immunometabolism.* 2020;2:e200029.

23. Hamilton KE, Bouwer MF, Louters LL, Looyenga BD. Cellular binding and uptake of fluorescent glucose analogs 2-NBDG and 6-NBDG occurs independent of membrane glucose transporters. *Biochimie.* 2021;190:1–11.

24. Hsieh M-H, Choe JH, Gadhvi J, et al. p63 and SOX2 dictate glucose reliance and metabolic vulnerabilities in squamous cell carcinomas. *Cell Rep.* 2019; 28:1860–1878.e9.

25. Ghezzi C, Wong A, Chen BY, Ribalet B, Damoiseaux R, Clark PM. A high-throughput screen identifies that CDK7 activates glucose consumption in lung cancer cells. *Nat Commun.* 2019;10:5444.

26. Maitituoheti M, Keung EZ, Tang M, et al. Enhancer reprogramming confers dependence on glycolysis and IGF signaling in KMT2D mutant melanoma. *Cell Rep.* 2020;33:108293.

27. Chan LN, Chen Z, Braas D, et al. Metabolic gatekeeper function of B-lymphoid transcription factors. *Nature.* 2017;542:479–483.

28. Mason JA, Cockfield JA, Pape DJ, et al. SGK1 signaling promotes glucose metabolism and survival in extracellular matrix detached cells. *Cell Rep.* 2021;34:108821.

29. Kumari S, Khan S, Gupta SC, et al. MUC13 contributes to rewiring of glucose metabolism in pancreatic cancer. *Oncogenesis.* 2018;7:19.

30. Lauer V, Grampp S, Platt J, et al. Hypoxia drives glucose transporter 3 expression through hypoxia-inducible transcription factor (HIF)-mediated induction of the long noncoding RNA NICI. *J Biol Chem.* 2020;295:4065–4078.

31. Liu Y, Xiang F, Huang Y, et al. Interleukin-22 promotes aerobic glycolysis associated with tumor progression via targeting hexokinase-2 in human colon cancer cells. *Oncotarget.* 2017;8:25372–25383.

32. Jiang S-H, Li J, Dong F-Y, et al. Increased serotonin signaling contributes to the Warburg effect in pancreatic tumor cells under metabolic stress and promotes growth of pancreatic tumors in mice. *Gastroenterology.* 2017;153:277–291.e19.

33. Broecker-Preuss M, Becher-Boveleth N, Bockisch A, Dührsen U, Müller S. Regulation of glucose uptake in lymphoma cell lines by c-MYC- and PI3K-dependent signaling pathways and impact of glycolytic pathways on cell viability. *J Transl Med.* 2017;15:158.

34. Wiel C, Le Gal K, Ibrahim MX, et al. BACH1 stabilization by antioxidants stimulates lung cancer metastasis. *Cell.* 2019;178:330–345.e22.

35. Kim NH, Sung NJ, Youn H-S, Park S-A. Gremlin-1 activates Akt/STAT3 signaling, which increases the glycolysis rate in breast cancer cells. *Biochem Biophys Res Commun.* 2020;533:1378–1384.

36. Weng Q, Chen M, Yang W, et al. Integrated analyses identify miR-34c-3p/MAGI3 axis for the Warburg metabolism in hepatocellular carcinoma. *FASEB J.* 2020;34: 5420–5434.

37. Wang Q, Liu M-J, Bu J, et al. miR-485-3p regulated by MALAT1 inhibits osteosarcoma glycolysis and metastasis by directly suppressing c-MET and AKT3/mTOR signalling. *Life Sci.* 2021;268:118925.

38. Wang S, Li J, Xie J, et al. Programmed death ligand 1 promotes lymph node metastasis and glucose metabolism in cervical cancer by activating integrin β4/SNAI1/SIRT3 signaling pathway. *Oncogene.* 2018;37:4164–4180.

39. Shangguan X, He J, Ma Z, et al. SUMOylation controls the binding of hexokinase 2 to mitochondria and protects against prostate cancer tumorigenesis. *Nat Commun.* 2021;12:1812.

40. Huang M, Xiong H, Luo D, Xu B, Liu H. CSN5 upregulates glycolysis to promote hepatocellular carcinoma metastasis via stabilizing the HK2 protein. *Exp Cell Res.* 2020;388:111876.

41. Wu N, Zheng B, Shaywitz A, et al. AMPK-dependent degradation of TXNIP upon energy stress leads to enhanced glucose uptake via GLUT1. *Mol Cell.* 2013;49: 1167–1175.

42. Sullivan WJ, Mullen PJ, Schmid EW, et al. Extracellular matrix remodeling regulates glucose metabolism through TXNIP destabilization. *Cell.* 2018; 175:117–132.e21.

43. Hong SY, Yu F-X, Luo Y, Hagen T. Oncogenic activation of the PI3K/Akt pathway promotes cellular glucose uptake by downregulating the expression of thioredoxin-interacting protein. *Cell Signal.* 2016;28:377–383.

44. Waldhart AN, Dykstra H, Peck AS, et al. Phosphorylation of TXNIP by AKT mediates acute influx of glucose in response to insulin. *Cell Rep.* 2017;19: 2005–2013.

45. Bechard ME, Smalling R, Hayashi A, et al. Pancreatic cancers suppress negative feedback of glucose transport to reprogram chromatin for metastasis. *Nat Commun.* 2020;11:4055.

46. Kim DJ, Vo M-T, Choi SH, et al. Tristetraprolin-mediated hexokinase 2 expression regulation contributes to glycolysis in cancer cells. *Mol Biol Cell.* 2019;30:542–553.

47. Ying H, Kimmelman AC, Lyssiotis CA, et al. Oncogenic Kras maintains pancreatic tumors through regulation of anabolic glucose metabolism. *Cell.* 2012;149: 656–670.

48. Amendola CR, Mahaffey JP, Parker SJ, et al. KRAS4A directly regulates hexokinase 1. *Nature.* 2019;576:482–486.

49. Reinfeld BI, Madden MZ, Wolf MM, et al. Cell-programmed nutrient partitioning in the tumour microenvironment. *Nature.* 2021;593:282–288.

[11]C-Methionine PET for Identification of Pediatric High-Grade Glioma Recurrence

Asim K. Bag[1], Melissa N. Wing[1], Noah D. Sabin[1], Scott N. Hwang[1], Gregory T. Armstrong[2], Yuanyuan Han[3], Yimei Li[3], Scott E. Snyder[1], Giles W. Robinson[4], Ibrahim Qaddoumi[4,5], Alberto Broniscer[4], John T. Lucas[6], and Barry L. Shulkin[1]

[1]Department of Diagnostic Imaging, St. Jude Children's Research Hospital, Memphis, Tennessee; [2]Department of Epidemiology and Cancer Control, St. Jude Children's Research Hospital, Memphis, Tennessee; [3]Department of Biostatistics, St. Jude Children's Research Hospital, Memphis, Tennessee; [4]Department of Oncology, St. Jude Children's Research Hospital, Memphis, Tennessee; [5]Department of Global Pediatric Medicine, St. Jude Children's Research Hospital, Memphis, Tennessee; and [6]Department of Radiation Oncology, St. Jude Children's Research Hospital, Memphis, Tennessee

Differentiating tumor recurrence or progression from pseudoprogression during surveillance of pediatric high-grade gliomas (PHGGs) using MRI, the primary imaging modality for evaluation of brain tumors, can be challenging. The aim of this study was to evaluate whether ^{11}C-methionine PET, a molecular imaging technique that detects functionally active tumors, is useful for further evaluating MRI changes concerning for tumor recurrence during routine surveillance. **Methods:** Using ^{11}C-methionine PET during follow-up visits, we evaluated 27 lesions in 26 patients with new or worsening MRI abnormalities for whom tumor recurrence was of concern. We performed quantitative and qualitative assessments of both ^{11}C-methionine PET and MRI data to predict the presence of tumor recurrence. Further, to assess for an association with overall survival (OS), we plotted the time from development of the imaging changes against survival. **Results:** Qualitative evaluation of ^{11}C-methionine PET achieved 100% sensitivity, 60% specificity, and 93% accuracy to correctly predict the presence of tumors in 27 new or worsening MRI abnormalities. Qualitative MRI evaluation achieved sensitivity ranging from 86% to 95%, specificity ranging from 40% to 60%, and accuracy ranging from 85% to 89%. The interobserver agreement for ^{11}C-methionine PET assessment was 100%, whereas the interobserver agreement was only 50% for MRI ($P < 0.01$). Quantitative MRI and ^{11}C-methionine PET evaluation using receiver-operating characteristics demonstrated higher specificity (80%) than did qualitative evaluations (40%–60%). Postcontrast enhancement volume, metabolic tumor volume, tumor-to-brain ratio, and presence of tumor as determined by consensus MRI assessment were inversely associated with OS. **Conclusion:** ^{11}C-methionine PET has slightly higher sensitivity and accuracy for correctly predicting tumor recurrence, with excellent interobserver agreement, than does MRI. Quantitative ^{11}C-methionine PET can also predict OS. These findings suggest that ^{11}C-methionine PET can be useful for further evaluation of MRI changes during surveillance of previously treated PHGGs.

Key Words: MRI; ^{11}C-MET PET; ^{11}C-methionine PET; pediatric high-grade glioma; pseudoprogression; recurrence

It has only recently been discovered that pediatric high-grade gliomas (PHGGs) are biologically distinct from adult high-grade gliomas (1). However, this new knowledge has not yet changed diagnoses, classifications, World Health Organization grading, or treatment of PHGGs (2). PHGGs in children older than 3 y are treated with a combination of maximal safe surgical resection, radiation therapy with or without adjuvant chemotherapy, and subsequent continued chemotherapy, similar to the treatment regimen for adult high-grade gliomas (3–5). Despite this aggressive therapy, outcomes in young children are dismal, with a local 1-y failure-free survival rate of 60% (6), suggesting that recurrence is common. Accurate diagnosis of tumor recurrence is important because the median overall survival (OS) of recurrent PHGGs is 4–7 mo (7) and because treatment of pseudoprogression is different from that of tumor recurrence. However, the diagnosis of recurrence is not always straightforward with MRI, which is the clinical standard-of-care test for assessing response to treatment. Indeed, treatment-related effects, including pseudoprogression, frequently mimic tumor recurrence, thereby leading to misdiagnosis and incorrect management (8,9).

Pseudoprogression is characterized by temporary enlargement and increased enhancement of clinical target volumes with MRI (10) and occurs in up to 20% of patients treated with radiation therapy and adjuvant chemotherapy (11). The incidence of pseudoprogression after initial therapy of PHGGs is similar to the incidence in adults after treatment of high-grade gliomas (12). Tumor recurrence is also characterized by enlargement of tumor volume, with increased enhancement making the distinction challenging (13–15). Many advanced MRI techniques have been extensively studied to differentiate treatment-related effects from true tumor progression, with variable benefits (16–19). PET with various radiotracers has been studied to distinguish true tumor progression from pseudoprogression (17,20–24). Of the many PET radiotracers used to evaluate tumor recurrence, study results using amino acid PET tracers (i.e., ^{11}C-methionine, O-(2-^{18}F-fluoroethyl)-L-tyrosine [^{18}F-FET], and ^{18}F-dihydroxyphenylalanine) in adults suggest that a reduction in amino acid uptake or a decrease in the metabolically active tumor volume is a sign of treatment response associated with long-term outcome (25). The Response Assessment in Neuro-Oncology working group and the European Association for Neuro-Oncology now suggest that ^{18}F-FET may facilitate the diagnosis of pseudoprogression in glioblastoma patients within the first 12 wk after completion of chemoradiotherapy (25). ^{11}C-methionine, a true amino acid PET tracer with properties similar to ^{18}F-FET PET, has recently been shown to differentiate true tumor progression from treatment-related

effects better than other PET tracers can in adults, with a sensitivity and specificity of 91.2% and 87.5%, respectively (26). Although the utility of ^{11}C-methionine PET for evaluating nonenhancing PHGGs has been investigated (27), its use to evaluate tumor recurrence in PHGGs has not been systematically investigated.

Here, we evaluated whether ^{11}C-methionine PET can be useful for the identification of tumor recurrence in previously treated PHGGs. Specifically, we compared the accuracy of ^{11}C-methionine PET with that of MRI for predicting the presence of tumors when recurrence is suspected. We also compared the interobserver agreement of ^{11}C-methionine PET and MRI to determine whether ^{11}C-methionine PET imaging adds value to conventional MRI and whether ^{11}C-methionine PET or MRI can predict OS.

MATERIALS AND METHODS

Study Subjects

We retrospectively included all subjects with PHGGs who were enrolled in the ongoing "Methionine PET/CT Studies in Patients with Cancer" clinical trial (NCT00840047) at St. Jude Children's Research Hospital since 2009. This study was approved by the St. Jude Institutional Review Board, and each subject or a parent or legal guardian gave written informed consent to participate. The inclusion criteria for this study were as follows: previously treated World Health Organization grade III or IV PHGGs that demonstrated worsening or new imaging abnormalities on fluid-attenuated inversion recovery (FLAIR) sequences, on postcontrast T1-weighted sequences, or on both sequences during routine surveillance MRIs, in comparison with the MRI findings from the baseline or from the best response; ^{11}C-methionine PET scans obtained within 3 wk of the surveillance MRI scans; and establishment of a definitive diagnosis of tumor recurrence within 8 wk of either the MRI surveillance scan or the ^{11}C-methionine PET scan.

Imaging Acquisition

[11]C-Methionine PET. ^{11}C-methionine was prepared as previously described (28). ^{11}C-methionine PET imaging followed at least 4 h of fasting. Each subject received intravenous injections of 740 MBq (20 mCi) of ^{11}C-methionine per 1.7 m^2 of body surface area (maximum prescribed dose, 740 MBq). Transmission CT images (for attenuation correction and lesion localization) and PET images were acquired approximately 5–15 min (mean $\pm$ SD, 8.7 $\pm$ 3.3 min) after ^{11}C-methionine injection with a Discovery 690 PET/CT scanner or a Discovery LS PET/CT scanner (GE Healthcare) using these parameters: field of view, 30 cm; matrix, 192 $\times$ 192; reconstruction method, VUE point HD; quantification method, SharpIR; filter cutoff, 5.0 mm; subsets, 34; iterations, 4; and z-axis filter, standard. The Q.Clear 350 SharpIR quantification method was used in only 1 subject. The CT acquisition parameters were as follows: 0.5-cm slice thickness, 0.8-s tube rotation, 1.5 cm/rotation table speed, 1.5:1 pitch, 120 kV, and 90 mA with dose modulation. PET images were acquired in 3-dimensional mode for 15 min. Data were reconstructed into multiplanar cross-sectional images with standard vendor-supplied software and displayed on a nuclear medicine workstation (Hermes Medical Systems, Inc.) for analysis.

MRI. The following sequences were acquired with a 1.5-T Avanto magnet or a 3-T TrioTim, Skyra, or Prisma magnet (Siemens Medical Solutions) with a 0.1 mmol/kg dose of intravenous gadobutrol (Gadavist; Bayer Healthcare): 3-dimensional magnetization-prepared rapid gradient-echo (1 mm^3 isotropic acquisition, 1,590-ms repetition time, 2.7-ms echo time, 900-ms inversion time, and 15° flip angle); 2-dimensional (2D) transverse T1-weighted fast low-angle shot (4-mm slice thickness, no gap, 259-ms repetition time, 2.46-ms echo time, and 70° flip angle); 2D transverse diffusion-weighted sequence and postcontrast 2D transverse T1-weighted fast low-angle shot (parameters identical to those of

precontrast axial 2D T1-weighted); 2D transverse T2-weighted turbo spin-echo (4-mm slice thickness, no gap, 4,810-ms repetition time, 87-ms echo time, and 180° flip angle); 2D transverse T2-weighted FLAIR (4-mm slice thickness, no gap, 10,000-ms repetition time, 106-ms echo time, 2,600-ms inversion time, and 130° flip angle); and 3-dimensional sagittal T1-weighted (parameters identical to those of precontrast sagittal 3-dimensional T1-weighted). Apparent diffusion coefficient maps were calculated from the diffusion images with the vendor-provided software (Syngo; Siemens Healthcare).

Qualitative Image Analysis

MRI. Each surveillance MRI was evaluated 4 times. The first evaluation was performed during generation of the clinical report by one of the neuroradiologists assigned to the clinical service. The second evaluation was performed by a single neuroradiologist (observer 1) with 12 y of experience evaluating response assessments in pediatric brain tumors. The third evaluation was performed by a single neuroradiologist (observer 2) with 8 y of experience evaluating response assessments in pediatric brain tumors. Both observers were masked to the ^{11}C-methionine PET findings and did not have access to any clinical information or any imaging studies obtained after the index surveillance MRI. The fourth evaluation consisted of a consensus evaluation by observers 1 and 2. New or worsening MRI abnormalities were subjectively categorized as definitely tumor (score of 1), definitely not tumor (score of 2), or indeterminate (score of 3). The consensus readings were also scored with the same 1–3 scale. If a discrepancy in opinion occurred between 2 observers, the reading was scored as 3. The first rating from neuroradiologists on clinical duties was scored with the same scale on the basis of the clinical reports. Diffusion and apparent diffusion coefficient maps were used together for subjective evaluation only.

[11]C-Methionine PET. ^{11}C-methionine PET images were independently reviewed by 2 observers, one with 15 y of experience and the other with 2 y of experience in molecular imaging for assessment of treatment response in pediatric brain tumors. The observers were provided the location of the MRI abnormality and had access to the MR images. The ^{11}C-methionine PET images were rated qualitatively on a 4-point scale relative to frontal white matter (in all included subjects, at least some component of the frontal lobe white matter was free of tumor): 0, no detectable uptake; 1, mild uptake but less than in the contralateral frontal lobe white matter; 2, mild uptake similar to that in the contralateral frontal lobe white matter; or 3, uptake greater than in the contralateral frontal lobe white matter. Finally, the results of visual assessment were consolidated into just 2 groups. The first group was "no uptake or uptake the same as or lower than in the reference region" (grades 0, 1, and 2), and the second group was "uptake higher than in the reference region" (grade 3).

Quantitative Imaging Analysis

Worsening or new imaging abnormalities on postcontrast T2-weighted FLAIR and T1-weighted sequences were manually segmented using Vitrea Advanced Visualization (Vital Images) software. Three patients had subtle enhancement on T1-weighted sequences, and their T1-weighted regions of interest were drawn on the Δ-T1 images (precontrast T1-weighted images were subtracted on a voxel-by-voxel basis from the postcontrast T1-weighted images).

SUVs for the ^{11}C-methionine PET images were calculated using Hermes software. After coregistration of the PET dataset with FLAIR or postcontrast T1-weighted MRI sequences, regions of interest were manually drawn either around the areas of abnormal ^{11}C-methionine uptake or around the MRI abnormality. In addition, quantitative tumor metrices (metabolic tumor volume and tumor-to-brain ratio [TBR]) were calculated as suggested by Law et al. (29). However, instead of using a crescentic region of interest, we used a 1.0-cm^3 sphere to calculate the SUV$_{mean}$ of the contralateral normal prefrontal lobe cortex and juxtacortical white matter as suggested by Hotta et al. (22) for consistency. Briefly,

SUV_{mean} of the contralateral normal frontal lobe cortex and juxtacortical white matter was calculated using a 1.0 cm^3 sphere. The 3-dimensional metabolic tumor volume with an SUV more than 1.3 times that of the normal brain cortex (obtained in the prior step) was automatically contoured using Hermes software, which automatically calculated the SUV_{max} and SUV_{mean} of the tumor. TBR and TBR_{max} were then manually calculated by dividing the tumor SUV_{max} by the SUV_{mean} of the contralateral normal frontal lobe cortex. TBR_{mean} was manually calculated by dividing the tumor SUV_{mean} by the SUV_{mean} of the contralateral normal frontal lobe cortex. In lesions with an SUV less than 1.3 times that of the contralateral frontal lobe, a volume of interest was manually drawn on the FLAIR-abnormal areas and agreed on by both nuclear medicine physicians, and then the volumes of interest were copied to the PET images. The SUV_{max} of the volumes of interest were automatically calculated by the software. The TBR was then calculated as described above.

Final Outcomes

The final outcomes of the lesions evaluated with MRI and ^{11}C-methionine PET were determined with the following methods: Response Assessment in Neuro-Oncology criteria applied to imaging and clinical findings (30); biopsies; or follow-up imaging and clinical course. Tumor was defined as present in the evaluated lesions if the lesions were treated as progressive disease (defined by Response Assessment in Neuro-Oncology criteria), if a predominant tumor was evident via biopsy, if progressive worsening was evident by follow-up MRI within 8 wk of the surveillance MRI or ^{11}C-methionine PET scan, or if the subject died of tumor progression without any other identifiable cause. Because all evaluated lesions were included at recurrence, OS was calculated from the date of diagnosis of recurrent tumor or pseudoprogression.

Statistical Analysis

MRI and ^{11}C-methionine PET readings were defined as true positive when tumor scores correctly identified the final outcome and as false positives when tumors scores differed from the final outcome. Ratings were defined as true negatives when tumor scores did not correctly identify the final outcome and as false negatives when tumor scores did not differ from the final outcome. Sensitivity and specificity were calculated by standard statistical definitions. Accuracy was defined as the proportion of true positives and true negatives in all scans. Interobserver agreement between different MRI and ^{11}C-methionine PET observers was calculated with Cohen κ-values, which were interpreted as previously indicated (31). Log-rank tests were used to assess the association of subjective ^{11}C-methionine PET and MRI findings with OS. By using optimal cutoffs, we generated Kaplan–Meier curves for MRI parameters (T1-enhancing volumes, FLAIR volumes), and a PET parameter (SUV_{max}) to test whether these measurements from quantitative imaging analysis were associated with OS.

The sensitivity and specificity of metabolic tumor volume, TBR, T1-enhancing volume, FLAIR volume, and SUV_{max} using optimal cutoffs for predicting final outcomes were evaluated. We used the optimized cutoffs to categorize these imaging features, and log-rank tests were performed to test whether each of these features was associated with OS values, which were calculated from the time of the MRI and ^{11}C-methionine PET scans to the death of the subjects or—for subjects still alive—to the date of the last follow-up. The 95% CIs for all diagnostic accuracy measures were calculated using bias-corrected bootstrap methods with resampling. All statistical analyses were done using R Statistical Software.

RESULTS

We used May 2020 as the cutoff for our analysis and found 27 patients who matched our inclusion criteria. We excluded 1 patient with L-2-hydroxyglutaric aciduria because differentiating tumor tissue from healthy brain was challenging because of diffuse brain signal abnormalities in the entire brain due to this condition. Of the remaining 26 patients, 27 tumors (1 patient had a left frontal lobe recurrence that was treated and evaluated similarly to the original tumor in the cerebellum) were included in the analysis. Details of patient demographics and tumors are shown in Table 1 and Supplemental Table 1 (supplemental materials are available at http://jnm.snmjournals.org). The details of the previous treatment, tumor location, and genetic alterations are included in Supplemental Table 2.

Qualitative MRI and ^{11}C-Methionine PET Interpretations for Predicting Final Outcomes

The final outcome in 5 of the 27 lesions evaluated were no tumor present (i.e., pseudoprogression), and in the remaining 22 lesions it was presence of tumor (i.e., tumor progression). The final outcomes were confirmed by follow-up MRI in 16 cases, by biopsy in 4, and by Response Assessment in Neuro-Oncology criteria in 7.

The sensitivity, specificity, and accuracy of correctly predicting the presence of tumors from MRI were 86% (95% CI, 64%–96%), 80% (95% CI, 0%–100%), and 85% (95% CI, 63%–93%), respectively, for observer 1 and 95% (95% CI, 73%–100%), 40% (95% CI, 0%–100%), and 85% (95% CI, 63%–93%), respectively, for observer 2. The interobserver agreement was fair (Cohen κ = 0.49; $P < 0.001$). The sensitivity, specificity, and accuracy for correctly predicting the presence of tumors by consensus readings were 95% (95% CI, 71%–100%), 60% (95% CI, 0%–100%), and 89% (95% CI, 67%–93%), respectively. The details are summarized in Table 2.

The sensitivity, specificity, and accuracy for correctly predicting the presence of tumors with ^{11}C-methionine PET scans were 100% (95% CI, not applicable), 60% (95% CI, 0%–100%), and 93% (95% CI, 70%–96%), respectively, and the interobserver

TABLE 1
Demographics of Patients Included in Study ($n = 27$)

Characteristic	Patients (n)
Diagnosis	
Glioblastoma	17
World Health Organization grade III astrocytoma	5
High-grade neuroepithelial tumor	2
High-grade glioma	2
Anaplastic pleomorphic xanthoastrocytoma	1
Age at time of PET imaging (y)	
0–5	4
6–10	2
11–15	8
16–20	8
20–25	4
Sex	
Male	16
Female	10
Patient status	
Deceased	22
Alive	4

TABLE 2
Diagnostic Accuracy for Tumor Detection

Index	Qualitative MRI reading	Qualitative PET reading	T1-enhancing volume	FLAIR volume	SUV_{max}	MTV	TBR_{max}	TBR_{mean}
Sensitivity	0.95 [0.71–1]	1 [NA]	0.73 [0.50–0.88]	0.86 [0.64–0.96]	0.60 [0.36–0.78]	0.90 [0.69–1]	0.77 [0.55–0.91]	0.72 [0.50–0.88]
Specificity	0.60 [0–1]	0.60 [0–1]	0.80 [0–1]	0.80 [0–1]	1 [NA]	0.80 [0–1]	1 [NA]	0.40 [0–1]
Accuracy	0.89 [0.67–0.93]	0.93 [0.7–0.96]	0.74 [0.52–0.85]	0.85 [0.63–0.93]	0.67 [0.44–0.81]	0.89 [0.64–0.96]	0.81 [0.59–0.89]	0.67 [0.44–0.78]

PET = ^{11}C-methionine PET; MTV = metabolic tumor volume; NA = not applicable.
Data in brackets are 95% CIs.

agreement was 100% (Cohen κ = 1). Positive ^{11}C-methionine PET readings had higher sensitivity, specificity, and accuracy for correctly predicting the presence of tumors than did individual MRI readings. ^{11}C-methionine PET also had higher sensitivity and accuracy for correctly predicting the presence of tumors than did the consensus MRI readings. The consensus MRI and ^{11}C-methionine PET readings were concordant in 88.9% of cases and discordant in 11.1%. In 1 subject, there was significant discrepancy between the MRI abnormality and the PET abnormality; in this subject, there were considerable surgery-related MRI abnormalities because the scans were obtained 21 d after surgery (Fig. 1).

We tested the accuracy between MRI observer 1, MRI observer 2, MRI consensus reads, and ^{11}C-methionine PET reads in pairs with McNemar tests. There were no significant differences for any pair in the comparisons. In 5 of the 27 lesions, a discrepancy occurred between MRI observer 1, MRI observer 2, or the consensus MRI read for correctly predicting the final outcome, but ^{11}C-methionine PET correctly predicted the final outcomes in all these cases. The final outcome of 3 of these 5 lesions was presence of tumor, and the final outcome of 2 of these lesions was pseudoprogression. Only 1 case was indecisive for changes related to tumor treatment versus changes not related to tumor treatment in the consensus MRI interpretation but was correctly predicted by the ^{11}C-methionine PET evaluation (Fig. 2).

Quantitative Imaging Parameters from Both ^{11}C-Methionine PET and MRI for Predicting Final Outcomes

The receiver-operating-characteristic curves for SUV_{max}, metabolic tumor volume, TBR_{max}, TBR_{mean}, T1-enhancing tumor volume, and abnormal tumor volume by FLAIR were assessed for their ability to predict the final outcomes (32). The optimal SUV_{max} cutoff to differentiate between the presence and absence of tumors was 3.3, with sensitivity, specificity, and accuracy of 60% (95% CI, 36%–78%), 100% (95% CI, not applicable), and 67% (95% CI, 44%–81%), respectively. The optimal metabolic tumor volume cutoff was 0.98 cm^3, with sensitivity, specificity, and accuracy of 90% (95% CI, 69%–100%), 80% (95% CI, 0%–100%), and 89% (95% CI, 64%–96%), respectively. The optimal TBR_{max} cutoff was 1.82, with sensitivity, specificity, and accuracy of 77% (95% CI, 55%–91%), 100% (95% CI, not applicable), and 81% (95% CI, 59%–89%), respectively. The optimal TBR_{mean} cutoff was 1.4, with sensitivity, specificity, and accuracy of 72% (95% CI, 50%–88%), 40% (95% CI, 0%–100%), and 67% (95% CI, 44%–78%), respectively. The optimal T1-enhancing volume cutoff was 2.4 cm^3 or greater, with sensitivity, specificity, and accuracy of 73% (95% CI, 50%–88%), 80% (95% CI, 0%–100%), and 74% (95% CI, 52%, 85%), respectively. The optimal abnormal FLAIR volume cutoff was 13.76 cm^3, with sensitivity, specificity, and accuracy of 86% (95% CI, 64%–96%), 80% (95% CI, 0%–100%), and 85% (95% CI, 63%–93%), respectively. The details are summarized in Table 2.
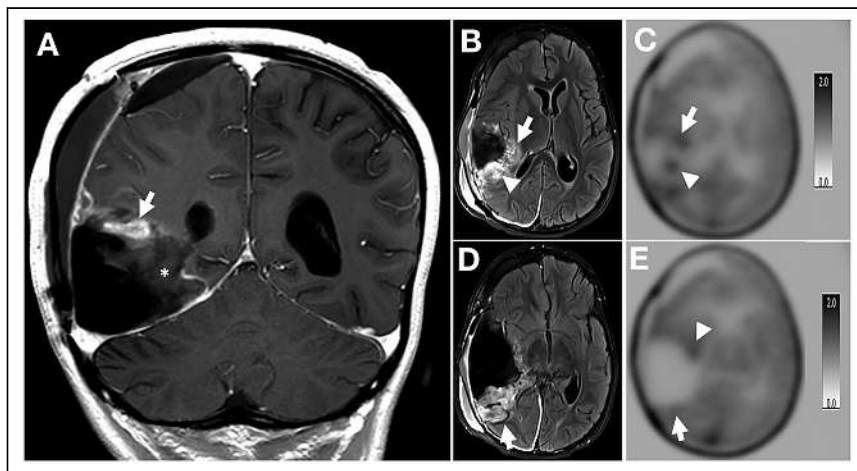
FIGURE 1. (A) Postcontrast coronal T1-weighted image demonstrates nodular enhancement (arrow) at superior surgical margin. (B) Axial T2-weighted FLAIR image obtained through level of nodular enhancement seen in A demonstrates areas of heterogeneously hyperintense tissue at medial (arrow) and posterior (arrowhead) surgical margin. (C) Axial reconstruction of ^{11}C-methionine PET images through this level shows 2 foci of tracer uptake at medial (arrowhead) and posterior (arrow) surgical margin. (D) Axial T2-weighted FLAIR image obtained through plane (demarcated by asterisk in A) inferior to plane of images B and C demonstrates relatively large areas of heterogeneously hyperintense tissue at posterior surgical margin (arrow). (E) Axial reconstruction of ^{11}C-methionine PET images through this level shows no ^{11}C-methionine uptake at posterior surgical margin (arrow). There is minimum uptake at anteromedial surgical margin (arrowhead). This area was not included in metabolic tumor volume because of low SUV (lower than 1.3 times that of contralateral frontal lobe cortex).
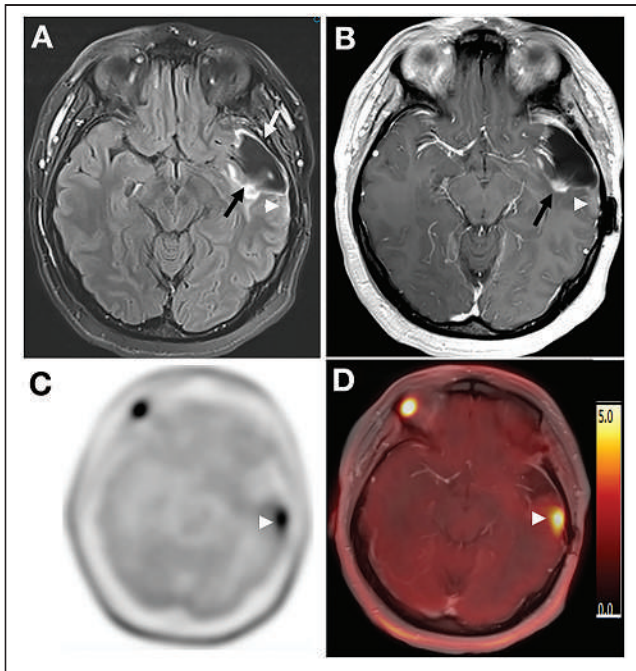
FIGURE 2. (A) Axial T2-weighted FLAIR image through level of midbrain shows large cystic resection cavity in left temporal lobe (white arrow). There is ill-defined T2 abnormality at medial aspect of resection cavity (black arrow). No obvious abnormality is noted posterior and lateral to resection cavity (arrowhead). (B) Axial postcontrast T1-weighted image through same level better shows focal area of contrast enhancement (arrow). This enhancing focus has been followed up since prior treatment. Subtle contrast enhancement, new finding compared with previous MRIs, is noted posterior and lateral to resection cavity (arrowhead). (C) Axial reconstruction of ^{11}C-methionine PET images through same level shows intense ^{11}C-methionine uptake posterior and lateral to resection cavity (arrowhead) corresponding to new subtle T1 enhancement. (D) Postcontrast T1-weighted ^{11}C-methionine PET/MRI image also shows that ^{11}C-methionine abnormality corresponds to new subtle enhancement at posterior and lateral aspect of resection cavity (arrowhead).

Quantitative MRI and ^{11}C-Methionine PET Interpretations Associated with OS

We used the optimized cutoffs to categorize imaging features, including the T1-enhancing volume, FLAIR volume, SUV_{max},

metabolic tumor volume, and TBR. T1-enhancing tumor volume, metabolic tumor volume, and TBR were significant by themselves for predicting the final outcome. However, the association of final outcome with quantitative imaging parameters was not significant when tested with multivariable analysis. Log-rank tests were performed to test whether these imaging features are associated with OS. Using the cutoffs determined by receiver-operating-characteristic curves, we found that OS was significantly associated with metabolic tumor volume ($P = 0.0074$), TBR_{max} ($P = 0.027$), and T1-enhancing volume ($P = 0.016$) (Figs. 3 and 4). However, SUV_{max}, TBR_{mean}, and FLAIR volume did not show a significant association with OS.

DISCUSSION

Differentiating true tumor progression from treatment-related effects can be challenging because of overlapping features (*11,19,25*). Many advanced MRI techniques and molecular imaging techniques have been studied to address this challenge (*19,25*). Recent evidence suggests that amino acid PET tracers (i.e., ^{18}F-dihydroxyphenylalanine PET and ^{18}F-FET PET) can assist conventional MRI at correctly identifying surgical margins and distinguishing between tumoral and nontumoral changes (*15,33–36*). ^{11}C-methionine PET, in particular, has shown substantial promise (*37–40*), but these studies were performed only on adults, and many included metastatic nonprimary CNS tumors. Therefore, we explored the role of ^{11}C-methionine PET in evaluating only recurrent PHGGs.

The ^{11}C-methionine uptake is directly related to L-type amino acid transporter 1 expression (*41*); high ^{11}C-methionine uptake characteristically occurs in tumors with a high degree of neoangiogenesis and cellular proliferation (*8,41*). Previous studies have found ^{11}C-methionine PET to have high sensitivity and specificity for diagnosing high-grade tumors (*8,42*). In our study, we found that the sensitivity and accuracy of ^{11}C-methionine PET for correctly differentiating true tumor progression from treatment-related effects were 100% and 93%, respectively, compared with the reported 70%–80% sensitivity and 75% accuracy in previous studies (*37,38,40*). This difference may be due to the heterogeneous samples in the previous studies, which included both metastases and gliomas that were treated with different radiation doses and chemotherapy regimens. However, the sensitivity and specificity of the ^{11}C-methionine PET for differentiating tumor progression from treatment-related effects in our study were similar to the
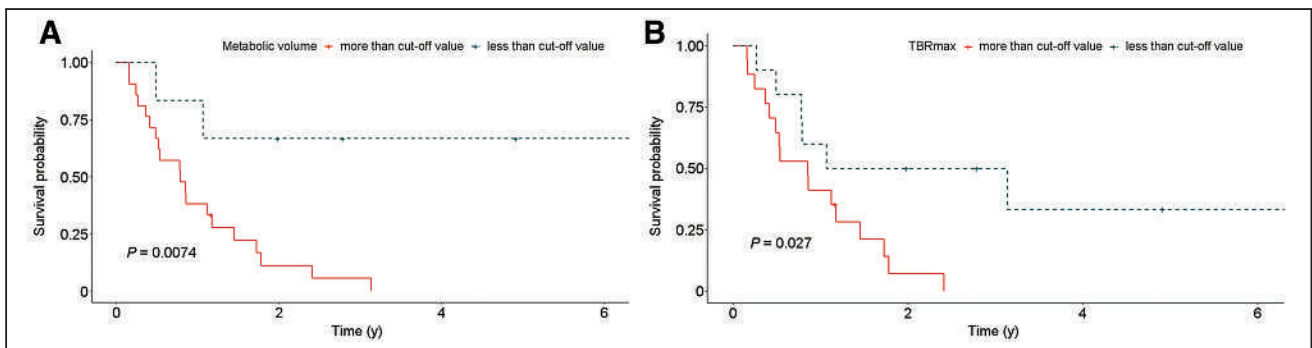
FIGURE 3. Kaplan–Meier curves demonstrating OS probability of subjects according to ^{11}C-methionine PET quantitative metrics. *P* values of log-rank tests of Kaplan–Meier curves are given for metabolic tumor volume (A) and TBR_{max} (B).
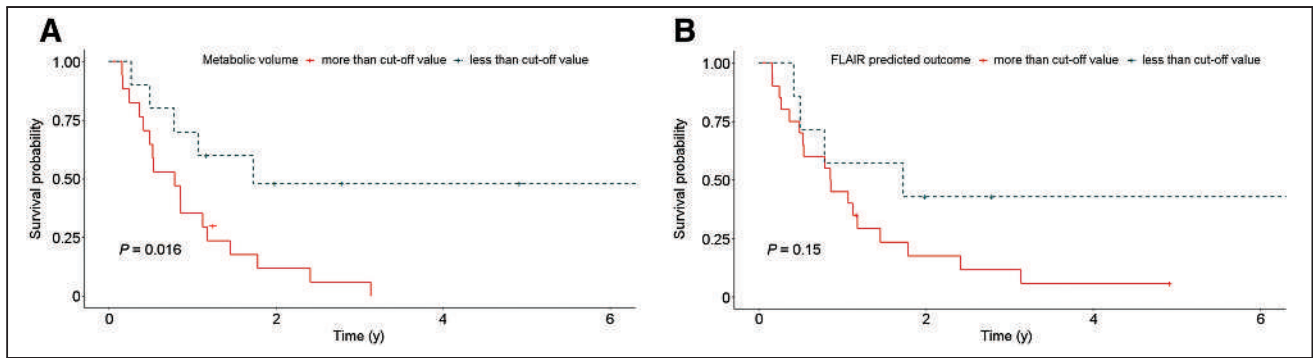
FIGURE 4. Kaplan–Meier curves demonstrating OS probability of subjects according to quantitative MRI metrics. *P* values of log-rank tests of Kaplan–Meier curves are given for postcontrast T1-enhancing volume (A) and FLAIR volume (B).

results of a study by Dunkl et al. (*43*). Our study also found the quantitative PET evaluation to have higher specificity than qualitative evaluation. This is in contrast to a study by Minamimoto et al. (*37*), which found no significant difference between qualitative and quantitative ^{11}C-methionine PET evaluations for assessment of tumor progression. More recently, a study by Marner et al. also found ^{18}F-FET PET to have high specificity and accuracy for differentiating tumor from nontumor lesions (*44*).

Qualitative interpretation of MRI findings is the standard of care for follow-up of high-grade gliomas after treatment (*19*). Unlike qualitative ^{11}C-methionine PET assessments, qualitative interpretation of MRI findings involves careful evaluation of many different MRI sequences that exploit the different magnetic properties of tissues and changes in these magnetic properties with MRI contrast compounds. This multifactorial evaluation process inherently leads to interpretation bias, as we observed in our study. The sensitivity, specificity, and accuracy of the 2 MRI observers in our study significantly differed, although both observers had expertise in evaluating pediatric brain tumors for 10 y or more. Such interpretation bias influences the diagnostic performance of MRI; indeed, we found that the consensus MRI interpretation performed significantly better, similar to that of ^{11}C-methionine PET, than did the individual MRI readings. Because consensus MRI interpretations by multiple neuroradiologists are not practical in routine clinical practice, the addition of ^{11}C-methionine PET imaging for suggestive MRI findings adds value to the overall care of patients with PHGGs.

Our study demonstrated a significant association of metabolic tumor volume and TBR$_{max}$ with OS, as previously described (*45,46*). Additionally, postcontrast T1-enhancing volume was also significantly associated with OS, similar to multiple prior studies (*47,48*).

Our study included limitations. The sample size was small but relatively large, considering the rarity of this tumor. As this study was initiated in 2009, the acquisition time of our PET scan was set to 15 min instead of the currently recommended 20 min. In addition, the criteria for performing ^{11}C-methionine PET on the included patients were based on a high clinical suspicion for recurrence or a high likelihood of tumor recurrence on MRI findings. Consequently, there was a high pretest probability that the MRI abnormalities would represent tumor recurrence, thereby introducing selection bias. A larger prospective multiinstitutional

study with regularly scheduled ^{11}C-methionine PET scans might alleviate such selection bias. These studies should be sufficiently powered to examine whether ^{11}C-methionine PET SUV$_{max}$ cutoffs and qualitative interpretations can quantitatively predict final outcomes. However, because of the short half-life of [11]C ($\sim$20 min), ^{11}C-methionine is currently available only at institutions with access to a cyclotron; such a study would need to be restricted to centers with ^{11}C-methionine–synthesizing capability or institutions able to refer patients with suggestive findings on MRI to a center with ^{11}C-methionine–synthesizing capability. To mitigate this problem, ^{18}F-FET PET with a longer half-life is increasingly used in assessments of gliomas in many countries (*49–52*).

CONCLUSION

Our study showed that ^{11}C-methionine PET has slightly higher sensitivity, specificity, and accuracy for correctly predicting the presence of tumor recurrence than does MRI when new or worsening imaging abnormalities are detected during surveillance of previously treated PHGG. The interobserver agreement on interpretation for ^{11}C-methionine PET findings was excellent and better than that of MRI. Our study also showed that quantitative ^{11}C-methionine PET and MRI can also predict OS. These findings indicate that ^{11}C-methionine PET imaging may add value for predicting PHGG recurrence. However, the results from this small cohort should be validated in larger prospective, preferably multiinstitutional studies.

DISCLOSURE

ACKNOWLEDGMENTS

KEY POINTS

QUESTION: How does the diagnostic performance of ^{11}C-methionine PET compare with that of MRI for predicting tumors in lesions suggestive of recurrence during follow-up of PHGGs?

PERTINENT FINDINGS: ^{11}C-methionine PET had 100% sensitivity, 60% specificity, and 93% accuracy for correctly predicting the presence of tumors in new or worsening MRI abnormalities suggestive of tumors, in contrast to 95%, 60%, and 89%, respectively, for qualitative MRI interpretation. The interobserver agreement for ^{11}C-methionine PET was higher than that for MRI.

IMPLICATIONS FOR PATIENT CARE: ^{11}C-methionine PET is a modality complementary to MRI for evaluating lesions suggestive of recurrence in previously treated PHGG.

REFERENCES

1. Gajjar A, Bowers DC, Karajannis MA, Leary S, Witt H, Gottardo NG. Pediatric brain tumors: innovative genomic information is transforming the diagnostic and clinical landscape. *J Clin Oncol.* 2015;33:2986–2998.

2. Varlet P, Le Teuff G, Le Deley MC, et al. WHO grade has no prognostic value in the pediatric high-grade glioma included in the HERBY trial. *Neuro-oncol.* 2020; 22:116–127.

3. Reifenberger G, Wirsching HG, Knobbe-Thomsen CB, Weller M. Advances in the molecular genetics of gliomas: implications for classification and therapy. *Nat Rev Clin Oncol.* 2017;14:434–452.

4. Fangusaro J. Pediatric high grade glioma: a review and update on tumor clinical characteristics and biology. *Front Oncol.* 2012;2:105.

5. Wolff JE, Driever PH, Erdlenbruch B, et al. Intensive chemotherapy improves survival in pediatric high-grade glioma after gross total resection: results of the HIT-GBM-C protocol. *Cancer.* 2010;116:705–712.

6. Vern-Gross TZ, Schreiber JE, Broniscer A, Wu S, Xiong X, Merchant TE. Prospective evaluation of local control and late effects of conformal radiation therapy in children, adolescents, and young adults with high-grade glioma. *Neuro Oncol.* 2014;16:1652–1660.

7. Kline C, Felton E, Allen IE, Tahir P, Mueller S. Survival outcomes in pediatric recurrent high-grade glioma: results of a 20-year systematic review and meta-analysis. *J Neurooncol.* 2018;137:103–110.

8. Garcia JR, Cozar M, Baquero M, et al. The value of ^{11}C-methionine PET in the early differentiation between tumour recurrence and radionecrosis in patients treated for a high-grade glioma and indeterminate MRI. *Rev Esp Med Nucl Imagen Mol.* 2017;36:85–90.

9. Winter SF, Loebel F, Loeffler J, et al. Treatment-induced brain tissue necrosis: a clinical challenge in neuro-oncology. *Neuro Oncol.* 2019;21:1118–1130.

10. Reardon DA, Weller M. Pseudoprogression: fact or wishful thinking in neuro-oncology? *Lancet Oncol.* 2018;19:1561–1563.

11. Brandsma D, Stalpers L, Taal W, Sminia P, van den Bent MJ. Clinical features, mechanisms, and management of pseudoprogression in malignant gliomas. *Lancet Oncol.* 2008;9:453–461.

12. Carceller F, Fowkes LA, Khabra K, et al. Pseudoprogression in children, adolescents and young adults with non-brainstem high grade glioma and diffuse intrinsic pontine glioma. *J Neurooncol.* 2016;129:109–121.

13. Langen KJ, Galldiks N, Hattingen E, Shah NJ. Advances in neuro-oncology imaging. *Nat Rev Neurol.* 2017;13:279–289.

14. Dhermain FG, Hau P, Lanfermann H, Jacobs AH, van den Bent MJ. Advanced MRI and PET imaging for assessment of treatment response in patients with gliomas. *Lancet Neurol.* 2010;9:906–920.

15. Galldiks N, Dunkl V, Stoffels G, et al. Diagnosis of pseudoprogression in patients with glioblastoma using O-(2-[18F]fluoroethyl)-L-tyrosine PET. *Eur J Nucl Med Mol Imaging.* 2015;42:685–695.

16. Chu HH, Choi SH, Ryoo I, et al. Differentiation of true progression from pseudoprogression in glioblastoma treated with radiation therapy and concomitant temozolomide: comparison study of standard and high-b-value diffusion-weighted imaging. *Radiology.* 2013;269:831–840.

17. Hu LS, Eschbacher JM, Heiserman JE, et al. Reevaluating the imaging definition of tumor progression: perfusion MRI quantifies recurrent glioblastoma tumor fraction, pseudoprogression, and radiation necrosis to predict survival. *Neuro Oncol.* 2012;14:919–930.

18. Elshafeey N, Kotrotsou A, Hassan A, et al. Multicenter study demonstrates radiomic features derived from magnetic resonance perfusion images identify pseudoprogression in glioblastoma. *Nat Commun.* 2019;10:3170.

19. Ellingson BM, Chung C, Pope WB, Boxerman JL, Kaufmann TJ. Pseudoprogression, radionecrosis, inflammation or true tumor progression? Challenges associated with glioblastoma response assessment in an evolving therapeutic landscape. *J Neurooncol.* 2017;134:495–504.

20. Dankbaar JW, Snijders TJ, Robe PA, et al. The use of ^{18}F-FDG PET to differentiate progressive disease from treatment induced necrosis in high grade glioma. *J Neurooncol.* 2015;125:167–175.

21. Maurer GD, Brucker DP, Stoffels G, et al. ^{18}F-FET PET imaging in differentiating glioma progression from treatment-related changes: a single-center experience. *J Nucl Med.* 2020;61:505–511.

22. Hotta M, Minamimoto R, Miwa K. ^{11}C-methionine-PET for differentiating recurrent brain tumor from radiation necrosis: radiomics approach with random forest classifier. *Sci Rep.* 2019;9:15666.

23. Tan H, Chen L, Guan Y, Lin X. Comparison of MRI, F-18 FDG, and ^{11}C-choline PET/CT for their potentials in differentiating brain tumor recurrence from brain tumor necrosis following radiotherapy. *Clin Nucl Med.* 2011;36:978–981.

24. Kim YH, Oh SW, Lim YJ, et al. Differentiating radiation necrosis from tumor recurrence in high-grade gliomas: assessing the efficacy of ^{18}F-FDG PET, ^{11}C-methionine PET and perfusion MRI. *Clin Neurol Neurosurg.* 2010; 112:758–765.

25. Albert NL, Weller M, Suchorska B, et al. Response Assessment in Neuro-Oncology working group and European Association for Neuro-Oncology recommendations for the clinical use of PET imaging in gliomas. *Neuro Oncol.* 2016;18:1199–1208.

26. Takenaka S, Asano Y, Shinoda J, et al. Comparison of ^{11}C-methionine, ^{11}C-choline, and ^{18}F-fluorodeoxyglucose-PET for distinguishing glioma recurrence from radiation necrosis. *Neurol Med Chir (Tokyo).* 2014;54:280–289.

27. Lucas JT Jr, Serrano N, Kim H, et al. ^{11}C-methionine positron emission tomography delineates non-contrast enhancing tumor regions at high risk for recurrence in pediatric high-grade glioma. *J Neurooncol.* 2017;132:163–170.

28. Vavere A, Snyder SE. Synthesis of L-[methyl-^{11}C] methionine (^{11}C-MET). In: Scott PJ, Hockley B, eds. *Radiochemical Syntheses.* Wiley; 2012:199–212.

29. Law I, Albert NL, Arbizu J, et al. Joint EANM/EANO/RANO practice guidelines/ SNMMI procedure standards for imaging of gliomas using PET with radiolabelled amino acids and [^{18}F]FDG: version 1.0. *Eur J Nucl Med Mol Imaging.* 2019;46: 540–557.

30. Wen PY, Macdonald DR, Reardon DA, et al. Updated response assessment criteria for high-grade gliomas: Response Assessment in Neuro-Oncology working group. *J Clin Oncol.* 2010;28:1963–1972.

31. Landis JR, Koch GG. The measurement of observer agreement for categorical data. *Biometrics.* 1977;33:159–174.

32. Vermont J, Bosson JL, Francois P, Robert C, Rueff A, Demongeot J. Strategies for graphical threshold determination. *Comput Methods Programs Biomed.* 1991;35: 141–150.

33. Galldiks N, Stoffels G, Filss C, et al. The use of dynamic O-(2-^{18}F-fluoroethyl)-L-tyrosine PET in the diagnosis of patients with progressive and recurrent glioma. *Neuro Oncol.* 2015;17:1293–1300.

34. Herrmann K, Czernin J, Cloughesy T, et al. Comparison of visual and semiquantitative analysis of ^{18}F-FDOPA-PET/CT for recurrence detection in glioblastoma patients. *Neuro Oncol.* 2014;16:603–609.

35. Kebir S, Fimmers R, Galldiks N, et al. Late pseudoprogression in glioblastoma: diagnostic value of dynamic O-(2-[^{18}F]fluoroethyl)-L-Tyrosine PET. *Clin Cancer Res.* 2016;22:2190–2196.

36. Pirotte BJ, Lubansu A, Massager N, et al. Clinical impact of integrating positron emission tomography during surgery in 85 children with brain tumors. *J Neurosurg Pediatr.* 2010;5:486–499.

37. Minamimoto R, Saginoya T, Kondo C, et al. Differentiation of brain tumor recurrence from post-radiotherapy necrosis with ^{11}C-methionine PET: visual assessment versus quantitative assessment. *PLoS One.* 2015;10:e0132515.

38. Nihashi T, Dahabreh IJ, Terasawa T. Diagnostic accuracy of PET for recurrent glioma diagnosis: a meta-analysis. *AJNR.* 2013;34:944–950.

39. Felip-Falg s e E, Teruel I, Domenech S, et al. C-methionine PET (Met-PET) for a diagnosis algorithm for pseudoprogression (PsP), radiations necrosis (RN) and progression (P) after an indeterminate magnetic resonance imaging (MRI) in glioblastoma (GBM) [abstract]. *J Clin Oncol.* 2018; 36(suppl):e14039.

40. Terakawa Y, Tsuyuguchi N, Iwai Y, et al. Diagnostic accuracy of ^{11}C-methionine PET for differentiation of recurrent brain tumors from radiation necrosis after radiotherapy. *J Nucl Med.* 2008;49:694–699.

41. Okubo S, Zhen HN, Kawai N, Nishiyama Y, Haba R, Tamiya T. Correlation of L-methyl-^{11}C-methionine (MET) uptake with L-type amino acid transporter 1 in human gliomas. *J Neurooncol.* 2010;99:217–225.

42. Grosu AL, Astner ST, Riedel E, et al. An interindividual comparison of O-(2-[18F]fluoroethyl)-L-tyrosine (FET)- and L-[methyl-11C]methionine (MET)-PET in patients with brain gliomas and metastases. *Int J Radiat Oncol Biol Phys.* 2011;81:1049–1058.

43. Dunkl V, Cleff C, Stoffels G, et al. The usefulness of dynamic O-(2-18F-fluoroethyl)-L-tyrosine PET in the clinical evaluation of brain tumors in children and adolescents. *J Nucl Med.* 2015;56:88–92.

44. Marner L, Lundemann M, Sehested A, et al. Diagnostic accuracy and clinical impact of [18F]FET PET in childhood CNS tumors. *Neuro Oncol.* 2021;23:2107–2116.

45. Van Dijken B, Ankrah A, Stormezand G, van Laar PJ, Dierckx R, van der Hoorn A. Prognostic value of 11C-methionine PET in patients with IDH wild-type glioma [abstract]. *J Nucl Med.* 2019;60(suppl 1):1501.

46. Vigil C, Prieto E, Ribelles M, et al. Prediction of recurrence and survival analysis after radiotherapy of glioblastoma using 11C-methionine PET/CT and MR [abstract]. *J Nucl Med.* 2014;55(suppl 1):12.

47. Huang RY, Rahman R, Hamdan A, et al. Recurrent glioblastoma: volumetric assessment and stratification of patient survival with early posttreatment magnetic resonance imaging in patients treated with bevacizumab. *Cancer.* 2013;119:3479–3488.

48. Ellingson BM, Kim HJ, Woodworth DC, et al. Recurrent glioblastoma treated with bevacizumab: contrast-enhanced T1-weighted subtraction maps improve tumor delineation and aid prediction of survival in a multicenter clinical trial. *Radiology.* 2014;271:200–210.

49. Chan DL, Hsiao E, Schembri G, et al. FET PET in the evaluation of indeterminate brain lesions on MRI: differentiating glioma from other non-neoplastic causes—a pilot study. *J Clin Neurosci.* 2018;58:130–135.

50. Jena A, Taneja S, Gambhir A, et al. Glioma recurrence versus radiation necrosis: single-session multiparametric approach using simultaneous O-(2-18F-fluoroethyl)-L-tyrosine PET/MRI. *Clin Nucl Med.* 2016;41:e228–e236.

51. Jeong SY, Lim SM. Comparison of 3′-deoxy-3′-[18F]fluorothymidine PET and O-(2-[18F]fluoroethyl)-L-tyrosine PET in patients with newly diagnosed glioma. *Nucl Med Biol.* 2012;39:977–981.

52. Song S, Cheng Y, Ma J, et al. Simultaneous FET-PET and contrast-enhanced MRI based on hybrid PET/MR improves delineation of tumor spatial biodistribution in gliomas: a biopsy validation study. *Eur J Nucl Med Mol Imaging.* 2020;47:1458–1467.

Epidermal Growth Factor Receptor–Targeted Fluorescence Molecular Imaging for Postoperative Lymph Node Assessment in Patients with Oral Cancer

Jasper Vonk*[1], Jaron G. de Wit*[1], Floris J. Voskuil[1,2], Yang Hang Tang[1], Wouter T.R. Hooghiemstra[3], Matthijs D. Linssen[3], Evert van den Broek[2], Jan J. Doff[2], Sebastiaan A.H.J. de Visscher[1], Kees-Pieter Schepman[1], Bert van der Vegt[2], Gooitzen M. van Dam[4,5], and Max J.H. Witjes[1]

[1]Department of Oral and Maxillofacial Surgery, University Medical Center Groningen, University of Groningen, Groningen, The Netherlands; [2]Department of Pathology and Medical Biology, University Medical Center Groningen, University of Groningen, Groningen, The Netherlands; [3]Department of Clinical Pharmacy and Pharmacology, University Medical Center Groningen, Groningen, The Netherlands; [4]Department of Nuclear Medicine and Molecular Imaging and Medical Imaging Center, University Medical Center Groningen, University of Groningen, Groningen, The Netherlands; and [5]TRACER BV, Groningen, The Netherlands

In most oral cancer patients, surgical treatment includes resection of the primary tumor combined with excision of lymph nodes (LNs), either for staging or for treatment. All LNs harvested during surgery require tissue processing and subsequent microscopic histopathologic assessment to determine the nodal stage. In this study, we investigated the use of the fluorescent tracer cetuximab-800CW to discriminate between tumor-positive and tumor-negative LNs before histopathologic examination. Here, we report a retrospective ad hoc analysis of a clinical trial designed to evaluate the resection margin in patients with oral squamous cell carcinoma (NCT02415881). **Methods:** Two days before surgery, patients were intravenously administered 75 mg of cetuximab followed by 15 mg of cetuximab-800CW, an epidermal growth factor receptor–targeting fluorescent tracer. Fluorescence images of excised, formalin-fixed LNs were obtained and correlated with histopathologic assessment. **Results:** Fluorescence molecular imaging of 514 LNs (61 pathologically positive nodes) could detect tumor-positive LNs ex vivo with 100% sensitivity and 86.8% specificity (area under the curve, 0.98). In this cohort, the number of LNs that required microscopic assessment was decreased by 77.4%, without missing any metastases. Additionally, in 7.5% of the LNs false-positive on fluorescence imaging, we identified metastases missed by standard histopathologic analysis. **Conclusion:** Our findings suggest that epidermal growth factor receptor–targeted fluorescence molecular imaging can aid in the detection of LN metastases in the ex vivo setting in oral cancer patients. This image-guided concept can improve the efficacy of postoperative LN examination and identify additional metastases, thus safeguarding appropriate postoperative therapy and potentially improving prognosis.

Key Words: fluorescence molecular imaging; lymph node metastasis; cetuximab-800CW; epidermal growth factor receptor; head and neck cancer

In oral squamous cell carcinoma (OSCC), the presence of lymph node (LN) metastasis has a major impact on prognosis and is associated with a significantly reduced survival (*1,2*). Consequently, assessment of LN status is important for determining the postoperative treatment strategy for the neck and consists of clinical assessment and preoperative radiographic imaging (i.e., MRI, CT, or ultrasound). If clinically suggestive LNs (cN+) are identified, a therapeutic neck dissection is indicated. However, even for a clinically node-negative neck (cN0), an elective neck dissection or sentinel node dissection is widely performed for staging because up to 30% of these patients have occult LN metastases or micrometastases (*3,4*). Postoperatively, the neck dissection specimen is macroscopically analyzed by the pathologist for the presence of LNs (*5*), and all LNs are sectioned and stained with hematoxylin and eosin or cytokeratin for microscopic evaluation. Other techniques for identifying LN metastasis are not clinically available yet. It is therefore interesting to explore other methods of identifying metastasis in LNs, especially when the tissue is intact, before routine processing.

Fluorescence molecular imaging (FMI), especially in the near-infrared window, is a rapidly evolving imaging technique in surgical oncology (*6*). FMI can provide real-time information on subsurface tissue by visualizing tumor-specific contrast agents (*7*), particularly when a controlled imaging environment is ensured (*8*). An interesting target for FMI is the epidermal growth factor receptor (EGFR), which is overexpressed in up to 90% of OSCC (*9*). Several phase I studies have shown the potential of EGFR-targeted FMI for intraoperative ex vivo tumor margin assessment in OSCC (*10–13*). However, little is known about EGFR-targeted imaging and identification of OSCC metastasis in LNs. FMI may allow for simultaneous ex vivo assessment of LN status when a neck dissection is performed together with removal of the primary tumor.

In this study, we explored the potential of FMI using cetuximab-800CW for discrimination between pathologically positive and negative LNs before histopathologic examination. The

LNs were harvested as part of a clinical trial for resection margin assessment in OSCC patients (NCT03134846) (*10*).

MATERIALS AND METHODS

Clinical Trial Design

This prospective, cross-sectional, single-center diagnostic study was performed at the University Medical Center Groningen. The study was a retrospective ad hoc analysis of a clinical trial for resection margin evaluation (NCT02415881) (*10*). The clinical trial was approved by the Institutional Review Board of the University Medical Center Groningen (METc 2016/395) and was performed following the Dutch Act on Medical Research involving Medical Subjects and the Declaration of Helsinki (adapted version 2013). Written informed consent was obtained from all patients before any study-related procedures took place.

Study Population

Patients with biopsy-confirmed OSCC who were scheduled for surgical removal of the tumor with concurrent neck dissection were eligible for inclusion in this study. Patients were excluded if they had a life expectancy of less than 12 wk, a Karnofsky performance status of less than 70%, a history of infusion reactions to monoclonal antibody therapies, QT prolongation on a screening electrocardiogram, uncontrolled medical conditions or episodes within 6 mo before enrollment (including uncontrolled hypertension, a cerebrovascular accident, or significant cardiopulmonary or liver disease), pregnancy, an abnormal electrolyte status, use of a class IA or III antiarrhythmic drug, or administration of an investigational drug within 30 d before the infusion of cetuximab-800CW.

Synthesis of Cetuximab-800CW

Cetuximab-800CW was produced in the good-manufacturing-practice facility of the University Medical Center Groningen, as previously described (*14*). In short, cetuximab (Erbitux; ImClone LLC) was conjugated to IRDye800CW (LI-COR Biosciences Inc.) and purified using PD-10 desalting columns (Cytiva Life Sciences) under controlled conditions. Cetuximab-800CW was formulated in a sodium-phosphate buffer at a concentration of 1.0 mg/mL.

Study Procedures

The complete study workflow is summarized in Figure 1. Patients enrolled in the study received an unlabeled dose of 75 mg of cetuximab by slow infusion, followed by a bolus injection of 15 mg of cetuximab-800CW 2 d before surgery to ensure optimal visualization of the primary tumor (*10*). All patients underwent tumor surgery with concurrent neck dissection according to the standard of care. After surgery, neck dissection specimens were transferred to the Department of Pathology and formalin-fixed for at least 24 h. LNs were identified by visual and tactile inspection of the neck dissection specimen, were bisected when large enough, and subsequently were collected in cassettes. Single LNs were imaged in a closed-field fluorescence imaging system (Pearl Trilogy; LI-COR BioSciences) at the 800-nm channel, with the center cutting plane (i.e., inner side of the LN) faced toward the camera. Regions of interest were drawn around the entire tissue specimen included in the cassette, before microscopic assessment.

According to the standard of care, tissue was embedded in paraffin, and 4-μm tissue sections were cut from all formalin-fixed paraffin-embedded tissue blocks and then stained with hematoxylin and eosin. After routine tissue processing, we performed fluorescence flatbed scanning of these tissue blocks (Odyssey CLx; LI-COR Biosciences). EGFR immunohistochemistry was performed of LNs from patients harboring metastases to correlate fluorescence localization with histology. A head and neck pathologist, unaware of the results of FMI, analyzed all tissue sections for the presence of tumor cells and immunohistochemistry results.

Statistical Analysis

Statistical analyses and graph designs were performed using Prism (version 9.0; GraphPad Software Inc.). Descriptive statistics were performed on patient demographics. The mean fluorescence intensities (FI_{mean}) and maximal fluorescence intensities (FI_{max}) of all LNs were calculated in ImageJ (Fiji, version 2.0.0) from the images obtained with the Pearl Trilogy. FI_{mean} was defined as total counts per region-of-interest pixel area (signal per pixel). FI_{max} was defined as the highest count measured within a region-of-interest pixel area. To improve the readability of this article, fluorescence intensities have been multiplied by 10^2. Data were tested for a gaussian distribution using Shapiro–Wilk and Anderson–Darling tests; none of the data were normally distributed. We used the Mann–Whitney U test for statistical analysis of data; all data were unpaired. Correlations were measured using the Spearman rank correlation coefficient. Cutoffs were based on the Youden index. Data were presented as median with range or interquartile range (IQR). Statistical significance was determined as a P value of less than 0.05.

RESULTS

Between January 2019 and February 2020, 22 patients were enrolled in this study. In total, 21 patients received the study drugs, consisting of an unlabeled dose of 75 mg of cetuximab followed by 15 mg of cetuximab-800CW, 2 d before surgery. One patient developed an adverse reaction during the unlabeled-cetuximab administration and was therefore excluded from the study. All remaining 21 patients completed the imaging protocol. The study procedures are summarized in Figure 1. Preoperative radiographic imaging (CT or MRI) was performed on all patients according to the standard of care. Thirteen (61.9%) of 21 patients were staged as cN0, 2 (9.5%) as cN1, 4 (19.0%) as cN2, and 2 (9.5%) as cN3. Five patients presented with extranodal extension. Fourteen elective neck dissections and 12 therapeutic neck dissections were performed, with 5 patients undergoing bilateral neck dissection. In total, 733 specimens considered to involve a LN were submitted for processing and subsequent microscopic analysis. Of these, 145 specimens were excluded because inking of the neck dissection specimen interfered with fluorescence imaging, resulting in a total of 588 specimens suitable for analysis. Of these, 514 included LNs based on final histopathology.
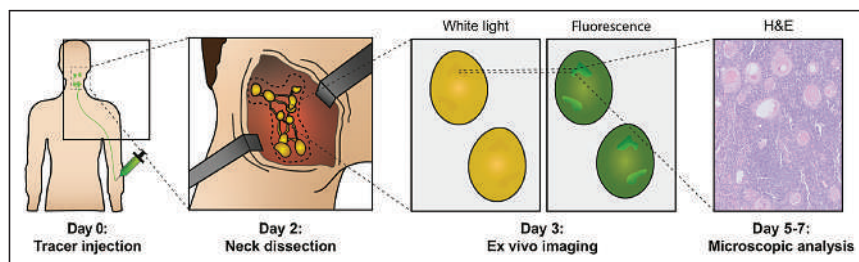
FIGURE 1. Summary of study workflow. All patients were administered fluorescent tracer cetuximab-800CW intravenously 2 d before surgery. After primary tumor surgery and neck dissection, nodal specimens were submitted to Department of Pathology and subsequently fixated in formalin for at least 24 h. All formalin-fixed tissue that could involve LNs was imaged in closed-field imaging system and underwent standard-of-care microscopic evaluation to correlate fluorescence signal with hematoxylin and eosin histopathology. H&E = hematoxylin and eosin.

The remaining 74 specimens contained no LNs. The number of LNs imaged after bisection was 239, whereas the number imaged intact was 275. Specimen and patient characteristics are shown in Table 1.

Differentiation Between Pathologically Positive and Negative LNs

All specimens that were clinically considered as LNs ($n = 588$) were imaged after formalin fixation and before histopathologic examination. Six of 21 patients were diagnosed with LN metastasis on final histopathology, with a total of 61 pathologically positive LNs. Two parameters were measured during fluorescence imaging, FI_{mean} and FI_{max}. At least a 3-fold increase in both FI_{max} and FI_{mean} was found in pathologically positive LNs ($n = 61$), compared with negative LNs ($n = 453$) or non-LN adipose or connective tissue

(non-LNs) ($n = 74$) (Figs. 2A and 2B). The FI_{max} of pathologically positive LNs was 2.19 arbitrary units (a.u.) (IQR, 1.68–2.71 a.u.), compared with 0.57 a.u. (IQR, 0.39–0.80 a.u.) in negative LNs ($P < 0.0001$) and 0.51 a.u. (IQR, 0.36–0.65 a.u.) in non-LNs ($P < 0.0001$) (Fig. 2C). FI_{mean} was 0.92 a.u. (IQR, 0.73–1.20 a.u.) in pathologically positive LNs versus 0.22 a.u. (IQR, 0.14–0.33 a.u.) in negative LNs ($P < 0.0001$) and 0.21 a.u. (IQR, 0.13–0.32 a.u.) in non-LNs ($P < 0.0001$) (Supplemental Fig. 1A; supplemental materials are available at http://jnm.snmjournals.org).

The Impact of LN Bisection on Fluorescence Intensity

During pathology processing, LNs were bisected if large enough and imaged with the center cutting plane (i.e., inner side of the LN) faced toward the camera. Bisected LNs showed a higher

TABLE 1
Patient Demographics and Tumor Characteristics of All Patients

Characteristic	pN+ ($n = 7$)	pN− ($n = 14$)	All patients ($n = 21$)
Age (y)	67 (65–82)	64 (29–78)	66 (29–82)
Female	6 (85.8)	8 (57.1)	14 (67.7)
Weight (kg)	73 (52–105)	84 (53–140)	80 (52–140)
BSA (m^2)	1.87 (1.52–2.17)	1.99 (1.58–2.67)	1.96 (1.52–2.67)
LNs	261	358	619
Level I	49 (18.8)	72 (20.1)	121 (19.5)
Level II	50 (19.2)	102 (28.5)	152 (24.6)
Level III	74 (28.4)	121 (33.8)	195 (31.5)
Level IV	58 (22.2)	47 (13.1)	105 (17.0)
Level V	30 (11.5)	16 (4.5)	46 (7.4)
Positive LNs[†]	64	NA	64
Level I	5 (7.8)		5 (7.8)
Level II	11 (17.2)		11 (17.2)
Level III	19 (29.7)		19 (29.7)
Level IV	19 (29.7)		19 (29.7)
Level V	10 (15.6)		10 (15.6)
Patients with ENE	5 (62.5)	NA	5 (23.8)
pN-stage*			
N0	0 (0)	14 (100)	14 (66.7)
N1	2 (28.6)	0	2 (9.5)
N2	4 (81.6)	0	4 (19.0)
N3	1 (20.4)	0	1 (4.8)
pT-stage			
T1	1 (14.3)	5 (35.7)	6 (28.6)
T2	2 (28.6)	3 (21.4)	5 (23.8)
T3	1 (4.8)	0	1 (4.8)
T4	3 (42.9)	6 (42.9)	9 (42.9)
Neck dissection[†]			
Elective	11 (64.7)	3 (33.3)	14 (53.8)
Therapeutic	6 (35.3)	6 (66.7)	12 (46.2)

*Initially, 6 patients were diagnosed with pathologically positive neck. Since 3 additional metastases were found on basis of FMI, total of 64 tumor-positive LNs was found, and 1 patient was upstaged from pN0 to pN1.

[†]Five patients received bilateral neck dissection, and total number of neck dissections therefore equals 26.

BSA = body surface area; ENE = extranodal extension.

Qualitative data are number and percentage; continuous data are median and range.
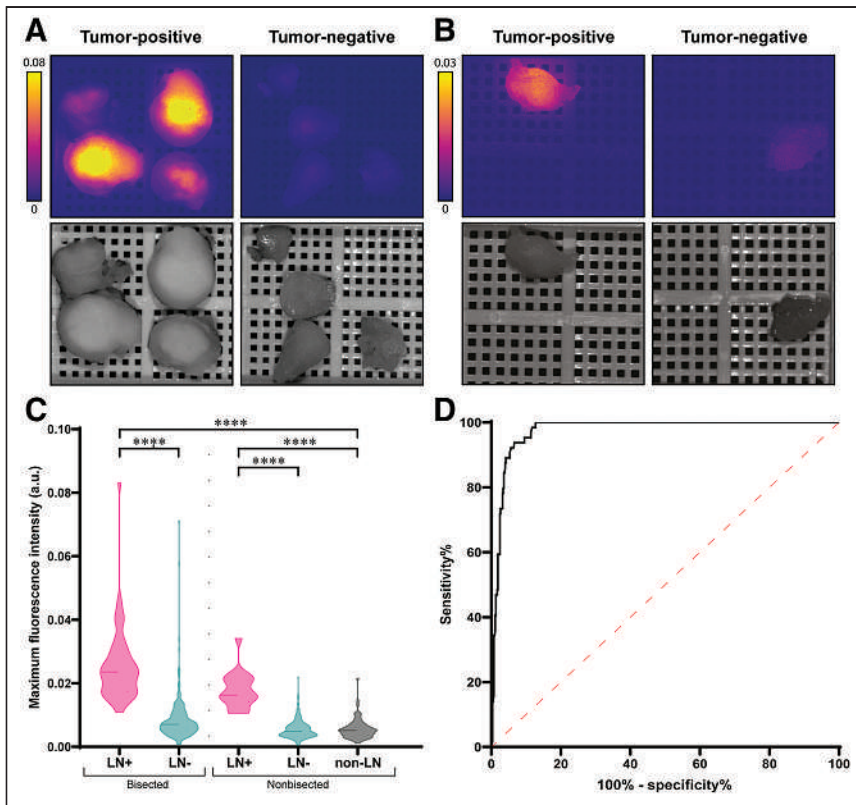
FIGURE 2. FMI with cetuximab-800CW enables discrimination between positive and negative LNs. (A and B) Representative images of bisected (A) and nonbisected (B) pathologically positive and negative formalin-fixed LNs from subject who was diagnosed with metastases on final histopathology. Increased fluorescence intensity was observed in both bisected and nonbisected pathologically positive LNs, compared with pathologically negative LNs. (C) FI_{max} is significantly increased in pathologically positive LNs, compared with negative LNs and non-LNs, both in bisected and in nonbisected LNs. (D) Receiver-operating-characteristic curve–based FI_{max} shows high area under curve of 0.98. ****$P < 0.0001$.

0.48 a.u. (IQR, 0.36–0.68 a.u.) and an FI_{mean} of 0.19 a.u. (IQR, 0.12–0.29 a.u.) in nonbisected LNs ($n = 258$) (both $P < 0.0001$). In addition, body surface area showed a low correlation with FI_{max} ($R = -0.44$, $P = 0.048$) but not with FI_{mean} ($R = -0.37$, $P = 0.103$) in bisected pathologically negative LNs. The correlation between body surface area and FI_{max} ($R = -0.64$, $P = 0.002$) and FI_{mean} ($R = -0.57$, $P = 0.011$) was moderate in nonbisected pathologically negative LNs.

The Impact of LN Size and Tumor Volume on Fluorescence Intensity

Topographic studies show that a metastatic tumor does not always involve the largest node within a neck dissection specimen (*15*), emphasizing the need to develop a tool that can also detect small metastases. First, to study the impact of LN size on fluorescence intensity, we correlated the diameter of pathologically negative LNs with both FI_{max} and FI_{mean}. In all LNs ($n = 514$), a weak correlation was found between LN diameter and FI_{max} ($R = 0.239$, $P < 0.0001$) and FI_{mean} ($R = 0.334$, $P < 0.0001$). Subsequently, in pathologically positive LNs, we studied the impact of total tumor surface area and viable tumor surface area (i.e., total tumor surface area minus necrotic surface area) on fluorescence intensity. A moderate correlation was found between total tumor surface area and FI_{max} ($R = 0.65$, $P < 0.0001$) and FI_{mean} ($R = 0.52$, $P < 0.0001$). Viable tumor surface area also showed a moderate correlation with FI_{max} ($R = 0.64$, $P < 0.0001$) and FI_{mean} ($R = 0.53$, $P < 0.0001$).

fluorescence intensity than did intact LNs (Figs. 2A and 2B; Supplemental Fig. 1A). Within pathologically positive LNs, bisected LNs ($n = 44$) showed an FI_{max} of 2.39 a.u. (IQR, 1.81–3.01 a.u.) and an FI_{mean} of 1.02 a.u. (IQR, 0.77–1.29 a.u.), compared with an FI_{max} of 1.63 a.u. (IQR, 1.42–2.12 a.u.) and an FI_{mean} of 0.78 a.u. (IQR, 0.62–0.93 a.u.) in nonbisected LNs ($n = 17$) ($P = 0.0013$ and 0.031, respectively). In pathologically negative LNs, bisected LNs ($n = 195$) showed an FI_{max} of 0.71 a.u. (IQR, 0.51–1.04 a.u.) and an FI_{mean} of 0.26 a.u. (IQR, 0.18–0.41 a.u.), compared with an FI_{max} of

The Impact of FMI on Efficacy of LN Evaluation and Identification of Additional Metastases

Next, we evaluated whether FMI could discriminate between benign LNs and LNs containing metastasis. To mimic the clinical situation, we included all tissue fragments submitted to the pathologist (i.e., including non-LNs) in the analysis. On the basis of the Youden index, the cutoff rendered for FI_{max} was 1.048 a.u., resulting in 100% sensitivity, 86.8% specificity, a 48.9% positive predictive value, a 100% negative predictive value, and 88.2%

TABLE 2
Performance of Fluorescence Imaging Using Cetuximab-800CW at Optimal Cutoff for Selection of At-Risk LNs

Cutoff	Sensitivity (%)	Specificity (%)	PPV (%)	NPV (%)	Accuracy (%)	Preselected LNs (%)
$FI_{max} \geq 1.048$	100.0%	86.8%	48.9%	100.0%	88.2%	22.6%
$FI_{mean} \geq 0.508$	91.8%	91.9%	59.6%	99.0%	91.9%	17.2%

PPV = positive predictive value; NPV = negative predictive value.

Based on receiver-operating-characteristic curves, optimal fluorescence intensity cutoffs were determined to discriminate between positive LNs and negative LNs. Here, 100% sensitivity and NPV were applied as main criteria for use of FMI as selection tool for pathologist. Missing LN metastases should be avoided since appropriate postoperative therapy is essential to optimize prognosis.

accuracy, with an area under the curve of 0.98 (Table 2; Fig. 2D). As such, the FI_{max} cutoff allowed for a 77.4% decrease in LNs requiring microscopic examination without missing LN metastasis. For FI_{mean}, the cutoff rendered was 0.508 a.u., resulting in 91.8% sensitivity, 91.9% specificity, a 59.6% positive predictive value, a 99.0% negative predictive value, and 91.9% accuracy, with an area under the curve of 0.98 (Table 2; Supplemental Fig. 1B). Receiver-operating-characteristic curves for both bisected and nonbisected LNs are provided in Supplemental Figure 2.

Since FI_{max} resulted in a negative predictive value of 100%, a random sample of 40 false-positives based on FI_{max} (i.e., FI_{max} above the cutoff, pathologically tumor-negative) were additionally examined by serial sectioning according to the sentinel LN protocol to trace any missed metastases or micrometastases by the standard of care, as previously described (4). This random sample showed a median FI_{max} of 1.38 a.u. (IQR, 1.27–1.62 a.u.), compared with 1.34 a.u. (IQR, 1.17–1.65 a.u.) in the complete false-positive cohort ($P = 0.35$) and thus was considered a representative sample. Three additional positive LNs (7.5%) were identified in 2 patients. In both patients, the additional positive LNs resulted in upstaging of the neck from pN1 to pN2b. In 1 patient, this would have resulted in an intensified postoperative therapy, which, on the basis of standard-of-care histopathology, had not been performed.

Microscopic Analysis of LNs

To study the distribution of cetuximab-800CW at the microscopic level, EGFR immunohistochemistry was performed on a selection of pathologically positive and negative LNs. No EGFR expression was found in the negative LNs. In positive LNs, variable expression of EGFR was observed. Although EGFR expression colocalized with fluorescence signal, tumor regions without EGFR expression also showed high fluorescence, suggesting that a tumor-specific fluorescence signal is not mediated only by EGFR expression (Fig. 3).

To explain this observed fluorescence signal distribution, hematoxylin- and eosin-stained sections of pathologically positive LNs were further analyzed. Heterogeneous fluorescence intensities were observed between different tumor deposits. Within tumor deposits, we observed a higher fluorescence signal in the periphery of tumor deposits than in the center, as agrees with previous studies (16). Generally, we observed an increased fluorescence signal in regions with high tumor cell density and poor differentiation. Regions with abundant desmoplastic stroma or keratinization, associated with low cellularity, showed very low fluorescence intensities. Lastly, in necrotic areas, no fluorescence signal was observed.

Fluorescence false-positive LNs were examined microscopically. As mentioned before, 3 (7.5%) additional metastases were detected. In other fluorescence false positives, we consistently found high vascularization compared with true-negative LNs, specifically colocalizing with areas showing a high fluorescence intensity at fluorescence flatbed scanning.
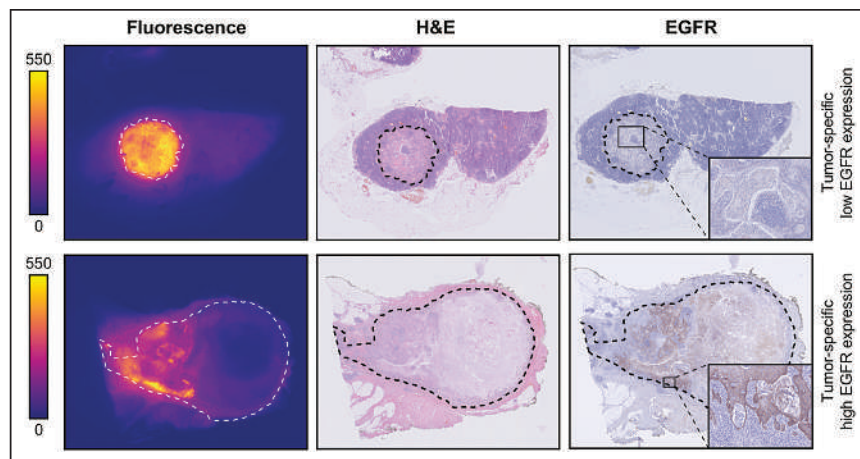
FIGURE 3. Microscopic analysis. Representative images of formalin-fixed LN metastases that were diagnosed on final histopathology. On both fluorescence images and hematoxylin- and eosin-stained slides, tumor region is delineated with dashed line. Fluorescence flatbed scanning shows increased fluorescence intensity in tumor deposits, compared with adjacent lymphoid and connective tissue. Although EGFR expression is variable within patients, fluorescence signal is tumor-specific, suggesting that other mechanisms play a role in cetuximab-800CW accumulation. H&E = hematoxylin and eosin.

DISCUSSION

This study demonstrated that EGFR-targeted FMI based on intravenously administered cetuximab-800CW can be used to discriminate pathologically positive LNs from negative LNs. A cutoff of 1.048 a.u. for FI_{max} resulted in the detection of positive LNs with 100% sensitivity and a 100% negative predictive value. Therefore, FMI can safely reduce the number of LNs requiring histopathologic examination by 77.4% and improve the efficiency of pathology processing without missing any metastases. Importantly, FMI detected pathologically positive LNs in 7.5% of the LNs initially false-positive on fluorescence imaging, which were missed by standard-of-care histopathology. Because the pathologic stage of the neck often drives recommendations for the postoperative therapy strategy, these missed positive LNs could have a major impact on the adequacy of postoperative treatment and, therefore, prognosis.

The use of EGFR-targeted FMI for the detection of LN metastasis in OSCC patients before formalin fixation has previously been evaluated (17–19). In dose-escalation studies with cetuximab-800CW and panitumumab-800CW, tumor-positive LNs were identified with high sensitivity, although a dose-dependent increase in falsely fluorescence-positive LNs was observed (18,19). One study showed that signal-to-noise ratio and FI_{mean} could guide the ex vivo assessment of nodal specimens and identify tumor-positive LNs with high sensitivity and specificity (18). Yet, because the use of signal-to-background ratio requires knowledge of the presence and dimensions of a possible tumor, this strategy cannot be applied to select at-risk LNs before histopathologic evaluation. More recently, Krishnan et al. reported the administration of 50 mg of panitumumab-800CW 1–5 d before surgery for LN assessment. When analyzing the top 5 LNs, the authors found that use of a fluorescence nodal ranking method achieved accurate nodal staging in all patients (17). Because this method is based on relative fluorescence intensities, microscopic examination of LNs is required in all patients, even when low absolute fluorescence intensities are observed. Since most patients (55.6% in their cohort) have a pathologically negative neck, we believe that using
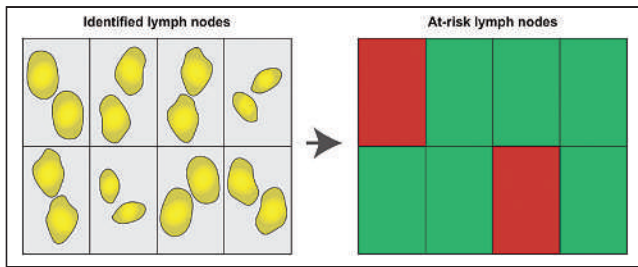
FIGURE 4. Grid selection of LNs for microscopic evaluation. Using grid, fluorescence imaging of identified LNs can automatically identify LNs that display FI_{max} above cutoff. In contrast to FI_{mean}, this approach does not require drawing region of interest around LNs. As such, at-risk LNs can be selected rapidly without interfering with standard of care.

an FI_{max} cutoff is favorable in that it rules out the need to examine LNs microscopically in all patients.

The uniqueness of our data, compared with the previous studies described, lies in the consistent administration of a single dose of cetuximab-800CW 2 d before surgery, allowing us to propagate a reliable cutoff for subsequent studies. We advocate the use of FI_{max} over FI_{mean} for swift clinical implementation since it does not require additional steps between imaging and selection, such as the drawing of regions of interest. Here, we propose using a grid to automatically identify LNs on the basis of the FI_{max} measured in each square of the grid (Fig. 4). This method enables user-friendly evaluation of all harvested LNs within minutes while reducing the LNs requiring microscopic assessment by 78.0%.

Although these results are promising for clinical use, our study had some limitations. Despite the use of a low dose of cetuximab-800CW, which empirically would decrease the number of false-positives (*18,19*), our dosing strategy was optimized for assessing the margin of the primary tumor rather than for evaluating LNs. Second, although we observed a high fluorescence intensity in all regions showing EGFR expression, high fluorescence intensities were also found in regions without EGFR expression. This varying colocalization was also described earlier by Nishio et al. (*18*) and coincides with studies finding that EGFR expression did not correlate with cetuximab uptake in PET imaging (*20,21*) and could not predict the response to cetuximab therapy (*22–24*). The significance of EGFR staining is questionable, as it has been shown that EGFR expression as determined by immunohistochemistry is not the sole reflection of tumor biology (*25*).

As such, we hypothesize that additional mechanisms within the tumor microenvironment influence the accumulation of cetuximab-800CW and that the presence of EGFR may not be the only determinant, as has also been observed in EGFR-targeted photodynamic therapy (*26,27*). Multiple studies on FMI and other imaging modalities have pointed out the role of vascularization and interstitial pressure in the accumulation of targeted contrast agents (*16,20,24*). This possible role does also fit the observation that the fluorescence false-positives in the current study showed aberrant vascularization, possibly leading to the accumulation of cetuximab-800CW through the effect of enhanced permeability and retention.

In future, studies could evaluate new dosing strategies dedicated to the assessment of LNs, such as adding a second, untargeted, tracer with different spectral properties. This strategy would enable correction for nonspecific tracer accumulation and increase the contrast between tumor tissue and nontumor tissue within LNs (*28*). This enhanced contrast may further increase the accuracy of

FMI for postoperative LN assessment. Second, we hypothesize that these FMI results can be translated to the assessment of freshly excised LN specimens, albeit fresh LNs may show slightly different fluorescence intensities as no formalin fixation is performed before imaging. This difference may impact the signal because of washout of nonspecific fluorescent tracer or alteration of tissue optical properties (*29,30*). Here, the intraoperative use of FMI depends on the surgical procedure performed on the neck. Intraoperative LN biopsies allow for immediate intraoperative imaging since single LNs are excised. However, FMI could also be used for the analysis of an elective neck dissection specimen, although this use is logistically more challenging since it requires intraoperative fluorescence analysis of LNs by a second clinician (e.g., a pathologist or a lab technician). Intraoperative identification of a tumor-positive LN enables direct extension to a therapeutic neck dissection if possible (*13*), which may prevent a second surgery and eventually will decrease both patient burden and health-care costs by reducing operation time.

CONCLUSION

Our findings suggest that FMI with the intravenously administered EGFR-targeting fluorescent tracer cetuximab-800CW can aid in the detection of LN metastases in the ex vivo setting in OSCC patients. We demonstrated that this method could improve the efficiency of postoperative LN assessment without missing LN metastases. Importantly, FMI may identify additional LN metastases, leading to more accurate staging of the neck and appropriate postoperative treatment, which may eventually improve prognosis.

DISCLOSURE

ACKNOWLEDGMENTS

KEY POINTS

QUESTION: Can EGFR-targeted FMI differentiate between tumor-positive and tumor-negative LNs?

PERTINENT FINDINGS: In this retrospective ad hoc analysis, we showed that preoperative intravenously administered cetuximab-800CW could detect tumor-positive LNs ex vivo with 100% sensitivity and 86.8% specificity (area under the curve, 0.98). Additionally, in 7.5% of the 38 LNs false-positive on fluorescence imaging, we identified additional metastases missed by the standard of care.

IMPLICATIONS FOR PATIENT CARE: This image-guided concept may improve the efficacy of LN processing while detecting additional metastases, thus safeguarding appropriate postoperative therapy and potentially improving the prognosis.

REFERENCES

1. Ho AS, Kim S, Tighiouart M, et al. Metastatic lymph node burden and survival in oral cavity cancer. *J Clin Oncol.* 2017;35:3601–3609.

2. Divi V, Chen MM, Nussenbaum B, et al. Lymph node count from neck dissection predicts mortality in head and neck cancer. *J Clin Oncol.* 2016;34:3892–3897.

3. Weiss MH, Harrison LB, Isaacs RS. Use of decision analysis in planning a management strategy for the stage N0 neck. *Arch Otolaryngol Head Neck Surg.* 1994;120:699–702.

4. Boeve K, Schepman KP, Schuuring E, et al. High sensitivity and negative predictive value of sentinel lymph node biopsy in a retrospective early stage oral cavity cancer cohort in the northern Netherlands. *Clin Otolaryngol.* 2018;43:1080–1087.

5. Woolgar JA, Triantafyllou A. Lymph node metastases in head and neck malignancies: assessment in practice and prognostic importance. *Diagn Histopathol.* 2010;16:265–275.

6. Weissleder R. A clearer vision for in vivo imaging. *Nat Biotechnol.* 2001;19:316–317.

7. Koch M, Ntziachristos V. Advancing surgical vision with fluorescence imaging. *Annu Rev Med.* 2016;67:153–164.

8. Koch M, Symvoulidis P, Ntziachristos V. Tackling standardization in fluorescence molecular imaging. *Nat Photonics.* 2018;12:505–515.

9. Grandis JR, Tweardy DJ. TGF-alpha and EGFR in head and neck cancer. *J Cell Biochem Suppl.* 1993;17F:188–191.

10. Voskuil FJ, de Jongh SJ, Hooghiemstra WTR, et al. Fluorescence-guided imaging for resection margin evaluation in head and neck cancer patients using cetuximab-800CW: a quantitative dose-escalation study. *Theranostics.* 2020;10:3994–4005.

11. Gao RW, Teraphongphom NT, van den Berg NS, et al. Determination of tumor margins with surgical specimen mapping using near-infrared fluorescence. *Cancer Res.* 2018;78:5144–5154.

12. Vonk J, de Wit JG, Voskuil FJ, Witjes MJH. Improving oral cavity cancer diagnosis and treatment with fluorescence molecular imaging. *Oral Dis.* 2021;27:21–26.

13. Voskuil FJ, Vonk J, van der Vegt B, et al. Intraoperative imaging in pathology-assisted surgery. *Nat Biomed Eng.* November 8, 2021 [Epub ahead of print].

14. Linssen MD, Ter Weele EJ, Allersma DP, et al. Roadmap for the development and clinical translation of optical tracers cetuximab-800CW and trastuzumab-800CW. *J Nucl Med.* 2019;60:418–423.

15. Woolgar JA. Detailed topography of cervical lymph-node metastases from oral squamous cell carcinoma. *Int J Oral Maxillofac Surg.* 1997;26:3–9.

16. Lu G, Fakurnejad S, Martin BA, et al. Predicting therapeutic antibody delivery into human head and neck cancers. *Clin Cancer Res.* 2020;26:2582–2594.

17. Krishnan G, van den Berg NS, Nishio N, et al. Metastatic and sentinel lymph node mapping using intravenously delivered panitumumab-IRDye800CW. *Theranostics.* 2021;11:7188–7198.

18. Nishio N, van den Berg NS, van Keulen S, et al. Optical molecular imaging can differentiate metastatic from benign lymph nodes in head and neck cancer. *Nat Commun.* 2019;10:5044.

19. Rosenthal EL, Moore LS, Tipirneni K, et al. Sensitivity and specificity of cetuximab-IRDye800CW to identify regional metastatic disease in head and neck cancer. *Clin Cancer Res.* 2017;23:4744–4752.

20. Aerts HJ, Dubois L, Perk L, et al. Disparity between in vivo EGFR expression and ^{89}Zr-labeled cetuximab uptake assessed with PET. *J Nucl Med.* 2009;50:123–131.

21. van Helden EJ, Elias S, Gerritse S, et al. [^{89}Zr] Zr-cetuximab PET/CT as biomarker for cetuximab monotherapy in patients with RAS wild-type advanced colorectal cancer. *Eur J Nucl Med Mol Imaging.* 2020;47:849–859.

22. Driehuis E, Kolders S, Spelier S, et al. Oral mucosal organoids as a potential platform for personalized cancer therapy. *Cancer Discov.* 2019;9:852–871.

23. Bossi P, Resteghini C, Paielli N, Licitra L, Pilotti S, Perrone F. Prognostic and predictive value of EGFR in head and neck squamous cell carcinoma. *Oncotarget.* 2016;7:74362–74379.

24. Even AJ, Hamming-Vrieze O, van Elmpt W, et al. Quantitative assessment of zirconium-89 labeled cetuximab using PET/CT imaging in patients with advanced head and neck cancer: a theragnostic approach. *Oncotarget.* 2017;8:3870–3880.

25. Chung KY, Shia J, Kemeny NE, et al. Cetuximab shows activity in colorectal cancer patients with tumors that do not express the epidermal growth factor receptor by immunohistochemistry. *J Clin Oncol.* 2005;23:1803–1810.

26. van Driel PBAA, Boonstra MC, Slooter MD, et al. EGFR targeted nanobody-photosensitizer conjugates for photodynamic therapy in a pre-clinical model of head and neck cancer. *J Control Release.* 2016;229:93–105.

27. Peng W, de Bruijn HS, Farrell E, et al. Epidermal growth factor receptor (EGFR) density may not be the only determinant for the efficacy of EGFR-targeted photo-immunotherapy in human head and neck cancer cell lines. *Lasers Surg Med.* 2018;50:513–522.

28. Tichauer KM, Samkoe KS, Gunn JR, et al. Microscopic lymph node tumor burden quantified by macroscopic dual-tracer molecular imaging. *Nat Med.* 2014;20:1348–1353.

29. Samkoe KS, Sardar HS, Bates BD, et al. Preclinical imaging of epidermal growth factor receptor with ABY-029 in soft-tissue sarcoma for fluorescence-guided surgery and tumor detection. *J Surg Oncol.* 2019;119:1077–1086.

30. Kapoor S, Lu G, van den Berg NS, et al. Effect of formalin fixation for near-infrared fluorescence imaging with an antibody-dye conjugate in head and neck cancer patients. *Mol Imaging Biol.* 2021;23:270–276.

^{90}Y Radioembolization in the Treatment of Neuroendocrine Neoplasms: Results of an International Multicenter Retrospective Study

Benedikt M. Schaarschmidt[1], Moritz Wildgruber[2,3], Roman Kloeckner[4], James Nie[5], Verena Steinle[6], Arthur J.A.T. Braat[7], Fabian Lohoefer[8], Hyun S. Kim[5], Harald Lahner[9], Manuel Weber[10], and Jens Theysohn[1]

[1]Department of Diagnostic and Interventional Radiology and Neuroradiology, University Hospital Essen, Essen, Germany; [2]Institute of Clinical Radiology, University Hospital of Muenster, Muenster, Germany; [3]Department of Radiology, University Hospital Ludwig Maximilians Universität, Campus Großhadern, Munich, Germany; [4]Department of Diagnostic and Interventional Radiology, University Medical Center of the Johannes Gutenberg University Mainz, Mainz, Germany; [5]Section of Interventional Radiology, Department of Radiology and Biomedical Imaging, Yale School of Medicine, New Haven, Connecticut; [6]Department of Diagnostic and Interventional Radiology, University Hospital of Heidelberg, Heidelberg, Germany; [7]Department of Radiology and Nuclear Medicine, University Medical Center Utrecht, Utrecht, The Netherlands; [8]Department of Radiology, Klinikum Rechts der Isar, Technical University of Munich, Munich, Germany; [9]Department of Endocrinology, Diabetes and Metabolism and Division of Laboratory Research, University Hospital Essen, Essen, Germany; and [10]Clinic of Nuclear Medicine, University Hospital Essen, Essen, Germany

In neuroendocrine neoplasms (NENs), the presence of distant metastases has a severe impact on survival leading to a relevant decrease in the 5-y survival rate. Here, ^{90}Y radioembolization (^{90}Y RE) might be an important treatment option; however, data to support clinical benefits for ^{90}Y RE are scarce. Therefore, the purpose of this study was to analyze the use of ^{90}Y RE in NEN patients with hepatic metastases in an international, multicenter retrospective analysis and assess the potential role of ^{90}Y RE in a multimodal treatment concept. **Methods:** In total, 297 angiographic evaluations in NEN patients before ^{90}Y RE were analyzed. Baseline characteristics and parameters derived from imaging evaluation and ^{90}Y RE were analyzed. Tumor response was assessed using RECIST 1.1, and survival data were collected. Mean overall survival (OS) between different groups was compared using Kaplan–Meier curves and the log rank test. A P value of less than 0.05 indicated statistical significance. **Results:** After ^{90}Y RE, the disease control rate according to RECIST 1.1 was 83.5% after 3 mo and 50.9% after 12 mo. OS in the entire population was 38.9 ± 33.0 mo. High tumor grade ($P < 0.006$) and high tumor burden ($P = 0.001$) were both associated with a significant decrease in OS. The presence of extrahepatic metastases ($P = 0.335$) and the type of metastatic vascularization pattern ($P = 0.460$) had no influence on OS. Patients who received ^{90}Y RE as second-line therapy had a slightly longer but not statistically significant OS than patients who had ^{90}Y RE in a salvage setting (44.8 vs. 30.6 mo, $P = 0.078$). Hepatic and global progression-free survival after ^{90}Y RE was significantly decreased in heavily pretreated patients, compared with patients with second-line therapy ($P = 0.011$ and $P = 0.010$, respectively). **Conclusion:** ^{90}Y RE could be an important alternative to peptide receptor radionuclide therapy as second-line treatment in patients with progressive liver-dominant disease pretreated with somatostatin analogs.

Key Words: radionuclide therapy; neuroendocrine neoplasm; radioembolization; SIRT; neuroendocrine carcinoma; neuroendocrine tumor

Neuroendocrine neoplasms (NENs) are rare, mostly slow-growing malignancies with an age-adjusted incidence rate of 6.98 per 100,000 in the United States (*1*). Because of the slow growth of well-differentiated tumors, overall outcomes are favorable, with a 5-y survival rate of up to 82%, depending on the tumor's primary location, grade according to World Health Organization criteria, and Ki-67 (*1–4*). As symptoms frequently occur in the later stages of the disease, distant metastases are present in up to 29% of all patients at the time of diagnosis (*4*). The presence of distant metastases has a severe impact on survival leading to a decrease in the 5-y survival rate from 82% to 35% in well- and moderately differentiated neuroendocrine tumors (NETs) (*4*). Distant metastases are located predominantly in the liver (*2*), and complete metastatic resection is possible in approximately only 20% of patients (*5*). In most cases, somatostatin analog treatment is considered the first-line treatment because of the favorable safety profile and the available evidence (*6–8*). If hepatic metastases progress during treatment, different therapies including tumor ablation, angiographic procedures such as bland transarterial embolization (TAE) or transarterial chemoembolization (TACE), liver transplantation, and systemic treatments such as chemotherapy or peptide receptor radionuclide therapy (PRRT) are proposed in the guidelines to address different clinical scenarios (*9–11*).

As hepatic metastases are frequently hypervascularized, injection of an embolic agent into a hepatic artery leads to intrametastatic accumulation of the injected material and consequent necrosis. ^{90}Y radioembolization (^{90}Y RE) might be an important adjunct to these procedures. In contrast to TAE or TACE, all patients have to undergo pretherapeutic angiographic evaluation, including local injection of ^{99m}Tc-labeled macroaggregated albumin (^{99m}Tc-MAA), subsequent planar scintigraphy, and SPECT or SPECT/CT to exclude relevant extrahepatic shunting. In a second session, intraarterial injection of a calculated dose of ^{90}Y glass microspheres (TheraSphere; Boston Scientific) or resin

microspheres (SIR-Spheres; Sirtex Medical) is performed on eligible patients for whole-liver, lobar, or segmental treatment. As hepatic metastases of NETs are usually hypervascularized, these microspheres emit a high local radiation dose to each metastasis. In combination with the short range of the β^--radiation emitted by ^{90}Y, effective local tumor control can be ensured with low systemic toxicity (12,13). Moreover, repeated therapies, as in the case of TAE or TACE, are not necessary. However, data to support clinical benefits for ^{90}Y RE are scarce, as previously published, retrospective analyses suffer from the low number of participants (14–17) or a lack of essential baseline characteristics due to a more technical focus (17,18).

Therefore, our study aimed to provide a retrospective analysis on the current use of ^{90}Y RE in different clinical scenarios and to assess why ^{90}Y RE was not performed on eligible patients to provide data missing from current publications.

MATERIALS AND METHODS

Data Collection

A retrospective data collection of patients with NETs who had undergone angiographic evaluations, including local ^{99m}Tc-MAA injection for ^{90}Y RE of hepatic metastases between May 2007 and August 2019, was performed in 6 tertiary-care centers in Europe (Germany and The Netherlands) and 1 in America.

All data were collected using a unified data collection form consisting of these subsections: baseline characteristics; imaging evaluation, including ^{99m}Tc-MAA injection; ^{90}Y RE; follow-up examinations after 3 and 12 mo, including tumor response (complete response, partial response, stable disease, and progressive disease) assessed at the contributing center based on RECIST 1.1 (19); and overall survival (OS). Additionally, hepatic and global progression-free survival (PFS) was assessed according to RECIST 1.1 (Supplement 1; supplemental materials are available at http://jnm.snmjournals.org).

Statistical Analysis

For all patients after undergoing the first ^{90}Y RE, survival characteristics were investigated using Kaplan–Meier curves and the log rank test for tumor grade, hepatic tumor burden, tumor vascularization, the presence of extrahepatic metastases, and the type of microspheres used for ^{90}Y RE. In addition, Kaplan–Meier curves and the log rank test were used to analyze differences in OS, as well as hepatic and global PFS, between patients who had undergone only surgery for the primary tumor or metastases and somatostatin analog treatment before ^{90}Y RE (second-line ^{90}Y RE) and patients with extensive systemic pretreatment (therapy additional to surgery for the primary tumor or metastases and somatostatin analog treatment before ^{90}Y RE [salvage ^{90}Y RE]).

A P value of less than 0.05 was considered statistically significant. SPSS Statistics 27 (IBM) was used for statistical analysis. Because of the exploratory nature of this study, no correction for α-error accumulation was performed (Supplement 2).

RESULTS

Baseline Characteristics

In total, 297 angiographic evaluations including local ^{99m}Tc-MAA injection were performed on 210 patients (91 women and 119 men; mean age $\pm$ SD, 59.1 $\pm$ 37.3 y) between May 2007 and August 2019 (Fig. 1). Multiple evaluations were performed on 72 patients (2 evaluations in 57 patients, 3 in 7 patients, and 4 in 4 patients). NETs were present in 90.9% (270/297), and neuroendocrine carcinomas in 9.1% (27/297), of all angiographic evaluations. In NET, a tumor grade of 1 was found in 25.6% (76/297), of 2 in 50.5% (150/297), and of 3 in 5.7% (17/297); the grade was unknown in 9.1% (27/297). Hypersecretion symptoms were observed in 32.7%
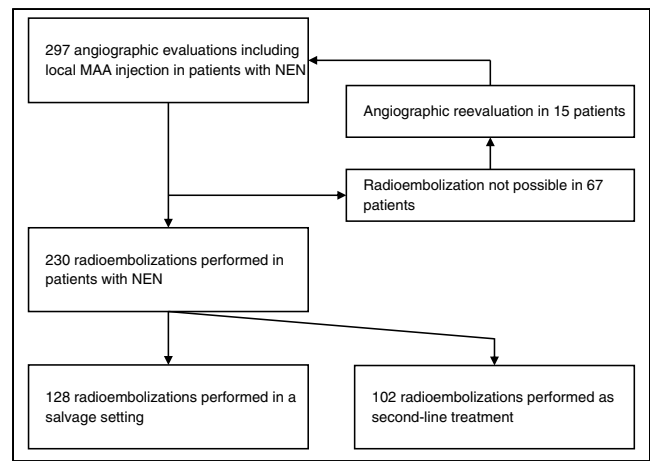
FIGURE 1. Flowchart of analyzed patient cohort.

(97/297), and extrahepatic metastases were observed in 41.4% (122/297) (Table 1; Supplemental Table 1). Before angiographic evaluation including ^{99m}Tc-MAA injection, different treatments were used in 91.6% (272/297), including external-beam radiotherapy in 1.7% (5/297), primary-tumor surgery in 64.3% (191/297), treatment of hepatic metastases by surgery in 18.2% (54/297), local ablation (e.g., radiofrequency ablation or microwave ablation) in 4.0% (12/297), and TACE or TAE in 8.8% (26/297). PRRT was used in 20.2% (60/297), antibody-based therapy in 2.4% (7/297), somatostatin analog therapy in 57.2% (170/297), prior ^{90}Y RE in 9.8% (29/297), liver transplantation in 0.3% (1/297), chemotherapy in 29.3% (87/297), and targeted therapy in 7.7% (23/297).

Imaging Evaluation Including ^{99m}Tc-MAA Injection

Before the angiographic evaluation, a CT scan was performed on 84.2% of patients (250/297) and an MRI scan on 24.2% (72/297). A hepatic tumor burden of 25% or less was present in 50.2% (149/297), 25%–50% in 31.0% (92/297), and 50% or more in 16.2% (48/297); the hepatic tumor burden was unknown in 2.7% (6/297). Metastases were hypervascularized in 63.6% (188/297), hypovascularized in 18.2% (54/297), and of a mixed or atypical appearance in 15.5% (46/297). The vascularization type was unknown in 3.0% (9/287).

Before ^{99m}Tc-MAA injection, vessel occlusion was necessary in 39.1% (116/297). Preexistent vessel occlusion due to prior coiling was found in 6.1% (18/297) (Table 2; Supplemental Table 2).

A central ^{99m}Tc-MAA injection was performed on 17.8% (53/297), a lobar ^{99m}Tc-MAA injection on 71% (211/297), and a segmental ^{99m}Tc-MAA injection on 2.7% (8/297). Other types of ^{99m}Tc-MAA injection were performed on 8.4% (25/297).

Complications occurred in 19 (6.4%) of the 297 patients, with 4 (1.4%) having vascular occlusion, 2 (0.7%) having dissection, and 1 each (0.3%) having the following complications: vasospasm, hypertension, a combination of pain/hypertension and tachycardia, complications associated with contrast medium, and coil dislocation. Complications in 8 additional patients were not specified (2.8%).

A mean lung shunt fraction of 5.7% $\pm$ 5.6% was observed in ^{99m}Tc-MAA scintigraphy (261 with a lung shunt fraction of $\leq$10%, 29 with >10%, and 7 with an unknown fraction).

^{90}Y RE

^{90}Y RE was performed after 77.4% of angiographic evaluations including local ^{99m}Tc-MAA injection (230/297; glass microspheres, 46.8% [139/297]; resin microspheres, 30.6% [91/297]) across a

TABLE 1
Baseline Characteristics of All Performed Imaging Evaluations

Parameter	%	n
Localization of primary tumor		
NET	90.9	270
Lung	3.0	9
Esophagus	0.7	2
Stomach	4.4	13
Pancreas	24.9	75
Small bowel or pancreas	0.7	2
Small bowel	31.1	92
Appendix	1.1	3
Colon	4.4	13
Rectum	5.1	15
Unknown primary	7.4	22
Not specified	8.1	24
Neuroendocrine carcinoma	9.1	27
Grading		
NET		
Grade 1	25.6	76
Grade 2	50.5	150
Grade 3	5.7	17
Unknown	9.1	27
Neuroendocrine carcinoma	9.1	27
Extrahepatic metastases		
Yes	41.1	122
No	58.9	175
Endocrine symptoms		
Yes	28.7	85
Carcinoid syndrome	5.7	17
Diabetes	6.4	19
Flush	9.7	29
Hedinger syndrome	1	3
Hypertonia	0.7	2
Hypoglycemia	1.3	4
Zollinger–Ellison syndrome	0.7	2
Unspecified	2.7	8
No	67.3	200
Unknown	4.0	12
Therapy before ^{90}Y RE		
Yes	91.6	272
No	8.4	25

TABLE 2
Imaging Evaluation Including ^{99m}Tc-MAA Injection

Parameter	%	n
Hepatic tumor burden		
<25%	50.2	149
25%–50%	31	92
>50%	16.2	48
Unknown	2.7	8
Vascularization pattern		
Hypervascularization	63.3	188
Hypovascularization	18.2	54
Mixed/atypical	15.5	46
Unknown	3.0	9
Vessel coiling present	39.1	116
Lateral left hepatic artery	2	0.7
Medial left hepatic artery	2.7	8
Gastroduodenal artery	25.3	75
Left gastric artery	0.7	2
Right gastric artery	14.8	44
Falciforme artery	0.3	1
Accessory vessel	11.0	33
Prior coiling		
Present	6.1	18
Absent	54.8	163
Preexisting portal vein thrombosis		
Partial	2.0	6
Complete	0.0	0
None	96.0	285
Unknown	2.0	6
Complications		
Present	6.4	19
Vasospasm	0.3	1
Dissection	0.7	2
Vascular occlusion	1.4	4
Hypertonia	0.3	1
Pain, hypertonia, or tachycardia	0.3	1
Complication associated with contrast medium	0.3	1
Coil dislocation	0.3	1
Not specified	2.8	8
Absent	92.2	274
Unknown	1.4	4
Lung shunt fraction		
≤10%	87.9	261
10%	9.8	29
Unknown	2.4	7

total of 176 patients (1 treatment, 71.6% [126/176]; 2 treatments, 26.7% [47/176]; 3 treatments, 0.7% [2/176]; 4 treatments, 0.3% [1/176]). For glass microspheres, dosimetry planning was performed using the single-compartment model with a perfused target volume dose of 80–150 Gy. For resin microspheres, the body-surface-area model was used. For resin microspheres, a mean activity of 1.26 ± 0.59 GBq was used for ^{90}Y RE, and for glass microspheres, the mean activity was 3.78 ± 2.24 GBq.

In 44.3% (102/230) of all cases, patients had been treated only by surgery or somatostatin analog therapy before ^{90}Y RE (second-line treatment, Fig. 2). In most other cases (55.7% [128/230]), ^{90}Y RE was performed in a salvage setting after extensive prior therapy.
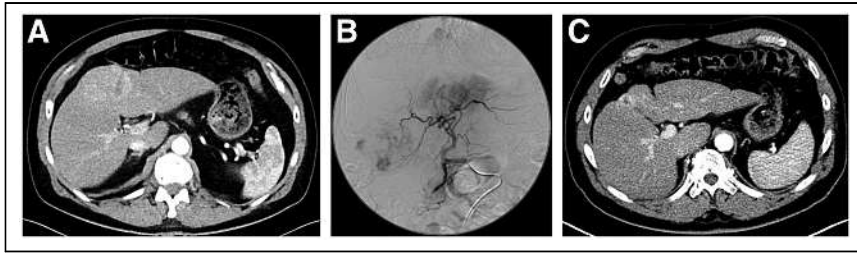
FIGURE 2. A 67-y-old man with grade 2 gastric NET and hepatic metastases. Hepatic tumor progression was observed with somatostatin analog treatment. (A) At time of ^{90}Y RE, hepatic tumor burden was less than 25%. (B) In angiographic evaluation, hypervascularized metastases were detected in both liver lobes; thus, same-session sequential therapy of whole liver with ^{90}Y glass microspheres was performed. (C) At follow-up, partial response was observed, with residual metastases in liver segment 4.

^{90}Y RE of the whole liver was used in 44.9% (108/230), and sequential whole-liver therapies was used in separate sessions in 33.1% (76/230). ^{90}Y RE was performed for a single lobe in 19.6% (45/230) and for a selected liver part in 0.4% (1/230).

Second-line ^{90}Y RE after a minimum of prior therapy (including surgery of the primary tumor or hepatic metastasis and somatostatin analog therapy) was used in 44.3% (102/230), whereas extensive prior therapy was used in 55.7% (128/230).

Procedural complications were observed in 4.8% of all cases (11/230, including 3 with vasospasm; 2 each with liver organ necrosis, pain, or stasis of blood flow; and 1 each with sepsis/pain and hemodynamic instability). No complications were observed in 73.7% (219/230). ^{90}Y RE was not performed on 22.6% (67/297) (Table 3; Supplement 3).

Survival Analysis

Entire Population. At the time of data collection, 59.7% of all patients (105/176) were deceased, 27.3% (48/176) were still alive,

TABLE 3
Reasons for Canceling ^{90}Y RE

Parameter	%	n
^{90}Y RE performed	77.4	230
^{90}Y RE not performed	22.6	67
Reasons for canceling ^{90}Y RE		
Extrahepatic shunting	8.1	24
Lack of ^{99m}Tc-MAA accumulation	3.4	10
Worsening of patient's general condition	2.0	6
Extrahepatic tumor progression	1.3	4
Different therapy	1.1	3
Hepatic tumor burden too high	1.1	3
Unfavorable vessel anatomy	1.1	3
Worsening of hepatic laboratory parameters	0.7	2
Residual primary tumor	0.3	1
Hepatic vessel occlusion	0.3	1
Inhomogeneous ^{99m}Tc-MAA distribution	0.3	1
Technical problems with vial	0.3	1
Contrast agent–associated problem	0.3	1
Patient did not appear	0.3	1
Unknown	2.0	6

0.4% were lost to follow-up, and in 12.5% (22/176) the last follow-up visit was used for survival analysis. Mean OS after ^{90}Y RE was 38.9 ± 33.0 mo.

After ^{90}Y RE, OS was longer in NET patients (40.8 mo; 95% CI, 27.0–54.7 mo) than in NEC patients (19.3 mo; 95% CI, 8.1–35.1 mo) (Fig. 3A). Differences between the 2 groups were found by the log rank test ($\chi^2_{(2)} = 6.88$, $P < 0.009$). In NET patients, patients with a grade 1 tumor had a more prolonged median OS (79.3 mo; 95% CI, 42.6–116.0 mo) than patients with a grade 2 tumor (30.6 mo; 95% CI, 25.2–36.0 mo) or grade 3 tumor (21.4 mo; 95% CI, 10.7–32.1 mo) (Fig. 3B). According to the log rank test, the survival distributions for the 3 different tumor grades were statistically significant ($\chi^2_{(2)} = 10.21$, $P < 0.006$).

An increase in hepatic tumor burden was associated with a reduction in median OS (burden < 25%: 63.2 mo, 95% CI of 36.0–90.4 mo; burden of 25%–50%: 30.3 mo, 95% CI of 25.8–34.8 mo; burden > 50%: 22.5 mo, 95% CI of 16.6–28.4 mo). Significant differences among these 3 survival groups were detected by the log rank test ($\chi^2_{(2)} = 14.10$, $P = 0.001$) (Fig. 3C).

Only slight differences were observed in OS after ^{90}Y RE in patients with different vascularization patterns of hepatic metastases (hypervascularization: 40.5 mo, 95% CI of 17.4–63.6 mo; hypovascularization: 30.3 mo, 95% CI of 20.1–40.5 mo; and mixed appearance: 17.7 mo, 95% CI of 26.5–95.9). The log rank test found no significant differences among the survival distributions for these 3 hepatic vascularization patterns ($\chi^2_{(2)} = 1.6$, $P = 0.460$) (Fig. 3D).

Median OS was similar in patients with extrahepatic metastases (30.6 mo; 95% CI, 19.4–41.8) and without (44.8 mo; 95% CI, 29.8–59.8). No significant differences between the 2 survival groups were observed in the log rank test ($\chi^2_{(2)} = 0.931$, $P = 0.335$) (Fig. 3E; Supplements 4 and 5; Supplemental Fig. 1).

Second-Line Therapy Versus Salvage Setting. Patients who received ^{90}Y RE as second-line therapy had a slightly longer OS (44.8 mo; 95% CI, 24.2–65.4 mo) than patients who had ^{90}Y RE in a salvage setting (30.6 mo; 95% CI, 18.5–42.7) (Fig. 4A). However, the log rank test did not yield a statistically significant result ($\chi^2_{(2)} = 3.109$, $P = 0.078$).

Median hepatic PFS (15.9 mo; 95% CI, 10.6–21.2 mo) and global PFS (14.7 mo; 95% CI, 10.5–18.9 mo) were worse in patients undergoing ^{90}Y RE in a salvage setting than in patients with ^{90}Y RE as second-line therapy (hepatic PFS: 18.6 mo, 95% CI of 14.0–23.2 mo; global PFS: 18.8 mo, 95% CI of 8.3–29.3 mo). The log rank test detected significant differences between the 2 survival groups for hepatic PFS ($\chi^2_{(2)} = 6.44$, $P = 0.011$) and global PFS ($\chi^2_{(2)} = 6.63$, $P = 0.010$) (Figs. 4B and 4C; Supplement 6; Supplemental Fig. 2).

In patients receiving ^{90}Y RE as salvage therapy, OS in patients with prior PRRT (30.3 mo; 95% CI, 26.2–34.3 mo) was comparable to that in patients who did not receive prior PRRT (36.2 mo; 95% CI, 19.8–52.5 mo). No significant differences between the 2 groups were found in the log rank test ($\chi^2_{(2)} = 0.16$, $P = 0.692$) (Fig. 5).

DISCUSSION

^{90}Y RE is a possible alternative to a surgical approach to achieve local tumor control in metastatic liver disease. However, alternatives to ^{90}Y RE are manifold, and systemic approaches such as PRRT or
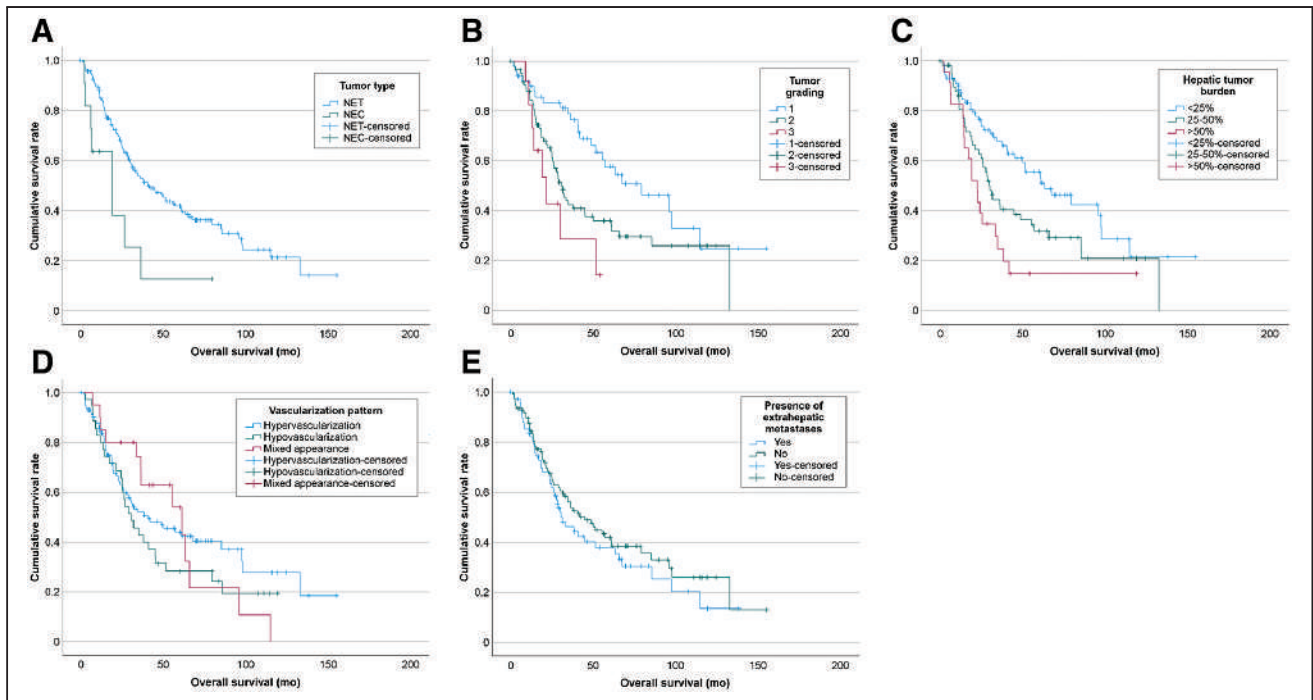
FIGURE 3. Kaplan–Meier survival curves investigating influence of 6 different parameters on survival in entire population: tumor type (A), NET tumor grading (B), hepatic tumor burden (C), metastatic vascularization (D), and extrahepatic metastases (E).

new chemotherapies challenge the concept of local liver ^{90}Y RE in general. Therefore, further data are necessary to balance the advantages and disadvantages of all available therapies in NEN patients with hepatic metastases. In this context, the results of this retrospective international multicenter study hold 3 key messages. First, second-line ^{90}Y RE is associated with increased OS and a significant increase in hepatic and global PFS, with OS slightly superior to that seen in published PRRT data. Second, the vascularization type of hepatic metastases does not significantly affect survival after ^{90}Y RE. Third, the presence of extrahepatic metastases in patients with liver-dominant disease does not significantly affect OS in patients undergoing ^{90}Y RE—neither in the entire population nor in patients receiving ^{90}Y RE as second-line therapy.

Successful surgical removal of hepatic metastases is associated with 5-y survival rates of 64%–100% (5,20), but only a minority of patients is eligible for this procedure (5). In patients with increased somatostatin expression who cannot undergo surgery,

systemic treatment using somatostatin analogs is considered the treatment of choice in the latest guidelines (9–11). In patients with progressive hepatic metastases, angiographic procedures such as TAE, TACE, or ^{90}Y RE or PRRT are possible treatment options. Although comparative studies among these options are not available, PRRT is recommended as the second-line therapy of choice in the most recent guidelines (9–11). Because of the lack of data, the treatment of sole hepatic metastases or liver-dominant disease remains a controversial topic. In a recent recommendation by Frilling et al., TAE, TACE, or ^{90}Y RE is proposed as a possible alternative in these 2 scenarios (21).

Our study results support these recommendations and further raise the question of whether ^{90}Y RE should be primarily performed in specific scenarios as second-line treatment before PRRT.

We found that patients who had undergone ^{90}Y RE as second-line treatment did show a relevant increase in OS and a significant increase in hepatic and global PFS, compared with patients with a
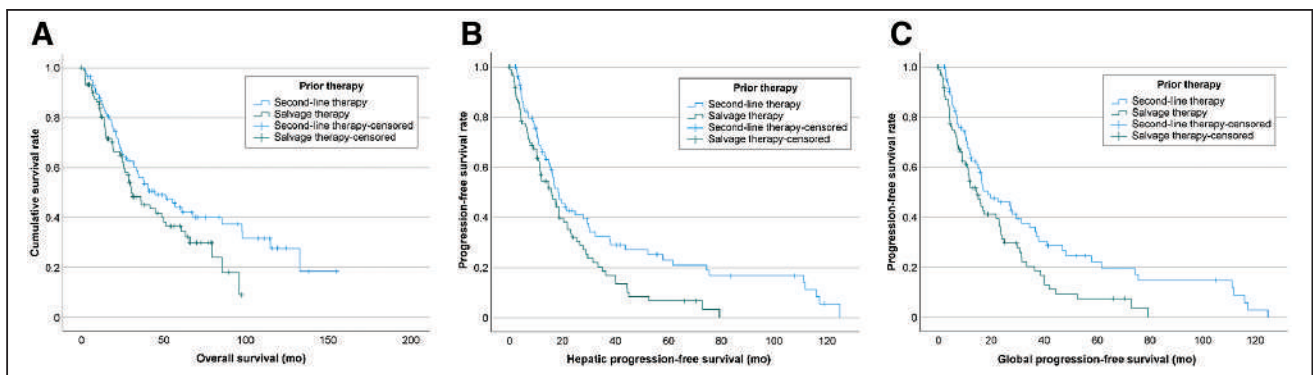
FIGURE 4. Kaplan–Meier survival curves investigating influence of extent of prior therapy (second-line therapy: prior surgery for primary tumor or metastases and somatostatin analog treatment before ^{90}Y RE vs. salvage therapy) on OS (A), hepatic PFS (B), and global PFS (C).
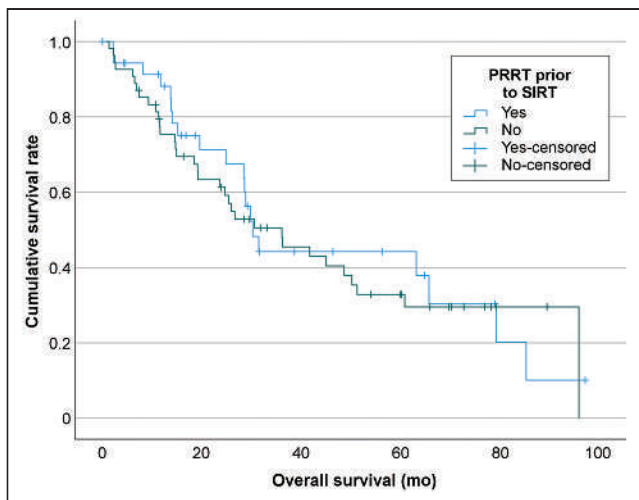
FIGURE 5. Kaplan–Meier survival curve investigating influence of prior PRRT on survival in patients receiving ^{90}Y RE as salvage therapy.

more extensive pretreatment. OS in patients with ^{90}Y RE as second-line treatment was only slightly worse than the results of PRRT in the Rotterdam cohort, with overlapping 95% CIs (44.8 mo, 95% CI of 24.2–65.4 mo, vs. 63 mo, 95% CI of 55–72 mo) (22). Furthermore, the presence of extrahepatic metastases does not influence OS after ^{90}Y RE as second-line therapy. In contrast to ^{90}Y RE in a salvage setting, hepatic tumor burden has no significant impact on OS if ^{90}Y RE is performed as a second-line therapy. Additionally, our data indicate that in 22.6% of all cases, ^{90}Y RE could not be performed because of contraindications associated with advanced hepatic disease such as shunting, a high tumor burden, or liver function deterioration. These findings further suggest that early ^{90}Y RE before PRRT could be beneficial in patients with the liver-dominant disease. In this clinical pathway, a successful local, liver-directed therapy using ^{90}Y RE could be ensured independently of hepatic tumor burden, and the risk of contraindications for ^{90}Y RE caused by advanced oncologic disease such as shunting could be avoided.

In certain scenarios, ^{90}Y RE might yield even further benefits. Although PRRT is limited to patients with increased somatostatin receptor expression compared with the background hepatic uptake (23), this requirement does not hinder ^{90}Y RE. Even hypovascularization of hepatic metastases in contrast-enhanced cross-sectional imaging does not influence OS after ^{90}Y RE. Additional benefits of ^{90}Y RE as second-line therapy in comparison to PRRT are the possibility of continuing somatostatin analog therapy during ^{90}Y RE, the absence of hematologic and renal toxicity, and the possibility of performing ^{90}Y RE as a 1-stop-shop treatment in contrast to the prolonged treatment duration of PRRT (12,22).

Furthermore, the benefits to this therapeutic approach do not seem to be limited to patients without extrahepatic metastases. The presence of extrahepatic metastases in liver-dominant disease did not have a significant impact on OS in our analysis and was not associated with a significant hazard ratio, in contrast to previous studies (12,24).

Hence, our findings stress the need for a prospective study comparing PRRT and ^{90}Y RE as second-line treatment in patients with progressive liver-dominant disease treated with somatostatin analogs.

Our study had some limitations. Because of its retrospective nature and the combined analysis of ^{90}Y RE performed with resin and glass microspheres, differences in the procedural technique could be possible. These limitations could be circumvented only by a prospective study. We did not perform a comparison between ^{90}Y RE and TAE or TACE. Because PRRT is recommended as the therapy of choice, TAE and TACE are considered by some authors as advantageous over ^{90}Y RE to avoid radiation-induced liver failure when PRRT and ^{90}Y RE are combined (25). However, recent findings by Braat et al., as well as our own findings on ^{90}Y RE as salvage therapy in patients with and without prior PRRT, indicate that ^{90}Y RE can be performed safely after PRRT without an increased risk of radiation-induced liver failure (26,27). Furthermore, there are several distinct disadvantages of TAE or TACE compared with ^{90}Y RE, most notably the higher proportion ($\leq$61%) of patients with pain, nausea, or treatment-associated fever (25,28,29) and the need to perform multiple therapies (30). Especially in the current raging coronavirus disease 2019 pandemic, ^{90}Y RE might be advantageous because of the reduced number of procedures necessary to achieve a favorable result and lower therapy-associated complications. However, a randomized trial between TAE or TACE and ^{90}Y RE might improve the acceptance of interventional procedures in general in NET patients with liver-dominant disease.

CONCLUSION

Our results show that ^{90}Y RE has potential as second-line therapy in patients with NENs with liver-dominant disease and thus could be an important alternative to PRRT in certain scenarios. However, a prospective study is necessary to support these promising data.

DISCLOSURE

KEY POINTS

QUESTION: Is ^{90}Y RE a potential a treatment option in patients with NENs?

PERTINENT FINDINGS: In this retrospective multicenter study, second-line ^{90}Y RE was associated with a significant increase in PFS, with satisfactory OS rates. The presence of extrahepatic metastases in patients with liver-dominant disease undergoing ^{90}Y RE did not affect OS.

IMPLICATIONS FOR PATIENT CARE: This study showed the potential of ^{90}Y RE as a treatment option in patients with NENs with liver-dominant disease and thus could be an important alternative to PRRT.

REFERENCES

1. Dasari A, Shen C, Halperin D, et al. Trends in the incidence, prevalence, and survival outcomes in patients with neuroendocrine tumors in the United States. *JAMA Oncol.* 2017;3:1335–1342.

2. Pape U-F, Berndt U, Müller-Nordhorn J, et al. Prognostic factors of long-term outcome in gastroenteropancreatic neuroendocrine tumours. *Endocr Relat Cancer.* 2008;15:1083–1097.

3. Modlin IM, Lye KD, Kidd M. A 5-decade analysis of 13,715 carcinoid tumors. *Cancer.* 2003;97:934–959.

4. Yao JC, Hassan M, Phan A, et al. One hundred years after "carcinoid": epidemiology of and prognostic factors for neuroendocrine tumors in 35,825 cases in the United States. *J Clin Oncol.* 2008;26:3063–3072.

5. Frilling A, Li J, Malamutmann E, Schmid K-W, Bockisch A, Broelsch CE. Treatment of liver metastases from neuroendocrine tumours in relation to the extent of hepatic disease. *Br J Surg.* 2009;96:175–184.

6. Rinke A, Müller H-H, Schade-Brittinger C, et al. Placebo-controlled, double-blind, prospective, randomized study on the effect of octreotide LAR in the control of tumor growth in patients with metastatic neuroendocrine midgut tumors: a report from the PROMID study group. *J Clin Oncol.* 2009;27:4656–4663.

7. Caplin ME, Pavel M, Ćwikła JB, et al. Lanreotide in metastatic enteropancreatic neuroendocrine tumors. *N Engl J Med.* 2014;371:224–233.

8. Caplin ME, Pavel M, Phan AT, et al. Lanreotide autogel/depot in advanced enteropancreatic neuroendocrine tumours: final results of the CLARINET open-label extension study. *Endocrine.* 2021;71:502–513.

9. Pavel M, Baudin E, Couvelard A, et al. ENETS consensus guidelines for the management of patients with liver and other distant metastases from neuroendocrine neoplasms of foregut, midgut, hindgut, and unknown primary. *Neuroendocrinology.* 2012;95:157–176.

10. Rinke A, Wiedenmann B, Auernhammer C, et al. Practice guideline neuroendocrine tumors - AWMF-Reg. 021-27 [in German]. *Z Gastroenterol.* 2018;56:583–681.

11. Pavel M, Öberg K, Falconi M, et al. Gastroenteropancreatic neuroendocrine neoplasms: ESMO clinical practice guidelines for diagnosis, treatment and follow-up. *Ann Oncol.* 2020;31:844–860.

12. Braat AJAT, Kappadath SC, Ahmadzadehfar H, et al. Radioembolization with ^{90}Y resin microspheres of neuroendocrine liver metastases: international multicenter study on efficacy and toxicity. *Cardiovasc Intervent Radiol.* 2019;42:413–425.

13. D'Souza D, Golzarian J, Young S. Interventional liver-directed therapy for neuroendocrine metastases: current status and future directions. *Curr Treat Options Oncol.* 2020;21:52.

14. Tsang ES, Loree JM, Davies JM, et al. Efficacy and prognostic factors for Y-90 radioembolization (Y-90) in metastatic neuroendocrine tumors with liver metastases. *Can J Gastroenterol Hepatol.* 2020;2020:5104082.

15. Rhee TK, Lewandowski RJ, Liu DM, et al. [90]Y radioembolization for metastatic neuroendocrine liver tumors: preliminary results from a multi-institutional experience. *Ann Surg.* 2008;247:1029–1035.

16. Cao CQ, Yan TD, Bester L, Liauw W, Morris DL. Radioembolization with yttrium microspheres for neuroendocrine tumour liver metastases. *Br J Surg.* 2010;97:537–543.

17. Paprottka PM, Hoffmann R-T, Haug A, et al. Radioembolization of symptomatic, unresectable neuroendocrine hepatic metastases using yttrium-90 microspheres. *Cardiovasc Intervent Radiol.* 2012;35:334–342.

18. Kennedy AS, Dezarn WA, McNeillie P, et al. Radioembolization for unresectable neuroendocrine hepatic metastases using resin ^{90}Y-microspheres: early results in 148 patients. *Am J Clin Oncol.* 2008;31:271–279.

19. Eisenhauer EA, Therasse P, Bogaerts J, et al. New response evaluation criteria in solid tumours: revised RECIST guideline (version 1.1). *Eur J Cancer.* 2009;45:228–247.

20. Schurr PG, Strate T, Rese K, et al. Aggressive surgery improves long-term survival in neuroendocrine pancreatic tumors: an institutional experience. *Ann Surg.* 2007;245:273–281.

21. Frilling A, Clift AK. Therapeutic strategies for neuroendocrine liver metastases. *Cancer.* 2015;121:1172–1186.

22. Brabander T, van der Zwan WA, Teunissen JJM, et al. Long-term efficacy, survival, and safety of [^{177}Lu-DOTA^0,Tyr^3]octreotate in patients with gastroenteropancreatic and bronchial neuroendocrine tumors. *Clin Cancer Res.* 2017;23:4617–4624.

23. Hope TA, Abbott A, Colucci K, et al. NANETS/SNMMI procedure standard for somatostatin receptor–based peptide receptor radionuclide therapy with ^{177}Lu-DOTATATE. *J Nucl Med.* 2019;60:937–943.

24. Do Minh D, Chapiro J, Gorodetski B, et al. Intra-arterial therapy of neuroendocrine tumour liver metastases: comparing conventional TACE, drug-eluting beads TACE and [90]yttrium radioembolization as treatment options using a propensity score analysis model. *Eur Radiol.* 2017;27:4995–5005.

25. Lehrman ED, Fidelman N. Liver-directed therapy for neuroendocrine tumor liver metastases in the era of peptide receptor radionuclide therapy. *Semin Intervent Radiol.* 2020;37:499–507.

26. Braat AJAT, Bruijnen RCG, van Rooij R, et al. Additional holmium-166 radioembolisation after lutetium-177-dotatate in patients with neuroendocrine tumour liver metastases (HEPAR PLuS): a single-centre, single-arm, open-label, phase 2 study. *Lancet Oncol.* 2020;21:561–570.

27. Braat AJAT, Ahmadzadehfar H, Kappadath SC, et al. Radioembolization with ^{90}Y resin microspheres of neuroendocrine liver metastases after initial peptide receptor radionuclide therapy. *Cardiovasc Intervent Radiol.* 2020;43:246–253.

28. Fiore F, Del Prete M, Franco R, et al. Transarterial embolization (TAE) is equally effective and slightly safer than transarterial chemoembolization (TACE) to manage liver metastases in neuroendocrine tumors. *Endocrine.* 2014;47:177–182.

29. Pericleous M, Caplin ME, Tsochatzis E, Yu D, Morgan-Rowe L, Toumpanakis C. Hepatic artery embolization in advanced neuroendocrine tumors: efficacy and long-term outcomes. *Asia Pac J Clin Oncol.* 2016;12:61–69.

30. Grozinsky-Glasberg S, Kaltsas G, Kaltsatou M, et al. Hepatic intra-arterial therapies in metastatic neuroendocrine tumors: lessons from clinical practice. *Endocrine.* 2018;60:499–509.

PD-L1 PET/CT Imaging with Radiolabeled Durvalumab in Patients with Advanced-Stage Non–Small Cell Lung Cancer

Jasper Smit*[1,2], Frank J. Borm*[1,2], Anna-Larissa N. Niemeijer[3], Marc C. Huisman[4], Otto S. Hoekstra[4], Ronald Boellaard[4], Daniela E. Oprea-Lager[4], Danielle J. Vugts[4], Guus A.M.S. van Dongen[4], Berlinda J. de Wit-van der Veen[5], Erik Thunnissen[6], Egbert F. Smit[1], and Adrianus J. de Langen[1]

[1]Department of Thoracic Oncology, NKI-AvL, Amsterdam, The Netherlands; [2]Department of Pulmonary Diseases, Leiden University Medical Centre, Leiden, The Netherlands; [3]Department of Pulmonary Diseases, Cancer Center Amsterdam, Amsterdam University Medical Centers (VU University Medical Center), Amsterdam, The Netherlands; [4]Department of Radiology and Nuclear Medicine, Cancer Center Amsterdam, Amsterdam University Medical Centers (VU University Medical Center), Amsterdam, The Netherlands; [5]Department of Nuclear Medicine, NKI-AvL, Amsterdam, The Netherlands; and [6]Department of Pathology, Cancer Center Amsterdam, Amsterdam University Medical Centers (VU University Medical Center), Amsterdam, The Netherlands

Better biomarkers are needed to predict treatment outcome in non–small cell lung cancer (NSCLC) patients treated with anti–programmed death-1/programmed death-ligand 1 (PD-1/PD-L1) checkpoint inhibitors. PD-L1 immunohistochemistry has limited predictive value, possibly because of tumor heterogeneity of PD-L1 expression. Noninvasive PD-L1 imaging using ^{89}Zr-durvalumab might better reflect tumor PD-L1 expression. **Methods:** NSCLC patients eligible for second-line immunotherapy were enrolled. Patients received 2 injections of ^{89}Zr-durvalumab: one without a preceding dose of unlabeled durvalumab (tracer dose only) and one with a preceding dose of 750 mg of durvalumab, directly before tracer injection. Up to 4 PET/CT scans were obtained after tracer injection. After imaging acquisition, patients were treated with 750 mg of durvalumab every 2 wk. Tracer biodistribution and tumor uptake were visually assessed and quantified as SUV, and both imaging acquisitions were compared. Tumor tracer uptake was correlated with PD-L1 expression and clinical outcome, defined as response to durvalumab treatment. **Results:** Thirteen patients were included, and 10 completed all scheduled PET scans. No tracer-related adverse events were observed, and all patients started durvalumab treatment. Biodistribution analysis showed ^{89}Zr-durvalumab accumulation in the blood pool, liver, and spleen. Serial imaging showed that image acquisition 120 h after injection delivered the best tumor–to–blood pool ratio. Most tumor lesions were visualized with the tracer dose only versus the coinjection imaging acquisition (25% vs. 13.5% of all lesions). Uptake heterogeneity was observed within (SUV_{peak} range, 0.2–15.1) and between patients. Tumor uptake was higher in patients with treatment response or stable disease than in patients with disease progression according to RECIST 1.1. However, this difference was not statistically significant (median SUV_{peak}, 4.9 vs. 2.4; $P = 0.06$). SUV_{peak} correlated better with the combined tumor and immune cell PD-L1 score than with PD-L1 expression on tumor cells, although neither was statistically significant ($P = 0.06$ and $P = 0.93$, respectively). **Conclusion:** ^{89}Zr-durvalumab was safe, without any tracer-related adverse events, and more tumor lesions were visualized using the tracer dose–only imaging acquisition. ^{89}Zr-durvalumab tumor uptake was higher in patients with a response to durvalumab treatment but did not correlate with tumor PD-L1 immunohistochemistry.

Key Words: PET imaging; PD-L1 inhibitor; non–small cell lung cancer; immunotherapy

W ith the introduction of immunotherapy, the treatment of non–small cell lung cancer (NSCLC) changed dramatically. Multiple trials with programmed death ligand 1 (PD-L1) checkpoint inhibitors in patients with (locally) advanced NSCLC have shown improved survival outcomes as compared with standard-of-care cytotoxic chemotherapy (*1–5*). Unfortunately, not all patients with NSCLC benefit equally, and the search for biomarkers that can predict treatment outcome is ongoing. Although PD-L1 immunohistochemistry and tumor mutational burden are associated with clinical benefit from checkpoint inhibitor therapy, they are far from perfect (*6–9*).

PD-L1 expression is a biopsy-based biomarker, with the disadvantage that a small biopsy specimen does not capture the full extent of tumor heterogeneity of PD-L1 expression and is associated with a higher chance of a false-negative test result (*6–8,10*). In addition, substantial heterogeneity of PD-L1 expression can be observed within and between tumor lesions of the same patient (*11*). As a consequence of this lack of a good predictive biomarker, most patients with advanced-stage NSCLC are treated with a PD-L1 checkpoint inhibitor, with or without chemotherapy (*2,5*). Inherently, a large patient group is treated with a potentially toxic treatment without clinical benefit.

Noninvasive biomarkers that can overcome the problem of intra- and intertumor heterogeneity are needed. Visualization and quantification of PD-L1 expression on all tumor cells could potentially be such a biomarker, and recent clinical studies have shown that with PD-L1–directed tracers such as ^{89}Zr-labeled atezolizumab and nivolumab, ^{18}F-BMS-986192, and ^{99m}Tc-NM-01, tumor lesions could be visualized and tracer uptake could be correlated with PD-L1 expression on tumor cells (*12–14*).

After the results of the PACIFIC trial, adjuvant durvalumab was registered for stage III NSCLC patients treated with concurrent platinum-based chemotherapy and radiation therapy (*15*). Adjuvant durvalumab prolonged progression-free survival (PFS) significantly, and this also resulted in an overall survival (OS) benefit (*16*). However, there is still a large group of patients with disease

relapse despite adjuvant durvalumab treatment. In the advanced-disease setting, the phase III MYSTIC trial evaluated durvalumab with or without tremelimumab and compared these treatments with standard chemotherapy as the first-line treatment for patients with stage IV NSCLC (*17*). Unfortunately, the primary endpoint of an improved OS was not met. This result supports the need for a better biomarker that can select patients who can benefit from durvalumab or durvalumab–tremelimumab combination treatment.

In this paper, we report the results of the first (to our knowledge) clinical PET imaging study conducted with [89]Zr-labeled durvalumab, an anti–PD-L1 monoclonal antibody, in patients with advanced-stage NSCLC. Imaging series were obtained after injection of a single tracer dose and after a combined injection with a full dose of unlabeled durvalumab and the tracer dose. The aim of this study was to investigate the safety and feasibility of [89]Zr-durvalumab PET/CT and to explore the relation of the imaging results to PD-L1 immunohistochemistry and treatment response. Because of the heterogeneity of PD-L1 expression in primary and metastatic lesions of individual patients, we hypothesize that [89]Zr-durvalumab PET/CT will show substantial differences in tracer uptake between lesions and allow exploration of the relation of the imaging results to clinical parameters such as PD-L1 immunohistochemistry and treatment response. This study was not powered to evaluate the predictive value of [89]Zr-durvalumab PET/CT for PD-L1 immunohistochemistry or treatment outcome. To study the safety and feasibility, 10 patients were required. The protocol allowed enrollment of additional patients in case a patient did not complete the PET scan acquisition.

MATERIALS AND METHODS

Patients

Patients with stage IV NSCLC who had progressed after at least 1 line of platinum-based doublet chemotherapy were asked to participate in this study. Earlier treatment with PD-L1 checkpoint inhibitors was not allowed. The study was conducted in accordance with the Declaration of Helsinki and was approved by the Institutional Review Board of the Amsterdam University Medical Centers for the Vrije Universiteit location. Before inclusion, each patient gave written informed consent after receiving a verbal and written explanation. The trial was registered at www.clinicaltrialsregister.eu (identifier 2019-000670-37).

Key eligibility criteria were pathologically proven EGFR-negative (wild-type) and ALK fusion–negative NSCLC, measurable disease according to RECIST 1.1 (*18*), an Eastern Cooperative Oncology Group performance status of 0–1, and the willingness to undergo a histologic biopsy immediately before the start of the study. The main exclusion criteria were symptomatic central nervous system metastases, use of corticosteroids with an equivalent of more than 10 mg of prednisone per day, or active autoimmune disease.

Tumor Biopsies

Histologic tumor biopsies were obtained before the first [89]Zr-durvalumab injection and after the last line of systemic therapy. Biopsies were obtained from 1 lesion (metastasis or primary tumor, depending on the size and location of the individual lesions) per patient. An experienced thoracic pathologist, unaware of the clinical information, evaluated the histology slides. Tumor PD-L1 expression was scored for tumor cells, the tumor proportion score (TPS), and—for both tumor and immune cells—the combined positive score (CPS) (*19,20*). Details on histochemical stains are found in Supplemental Table 1 (supplemental materials are available at http://jnm.snmjournals.org).

Durvalumab Radiolabeling

[89]Zr was purchased from Perkin-Elmer and coupled to durvalumab (human IgG1 κ-monoclonal antibody; primary route of elimination, protein catabolism; half-life, 18 d) (*21*) via the bifunctional chelator *N*-succinyl-desferal-tetrafluorophenyl ester (*22*). [89]Zr-durvalumab is produced in compliance with current good manufacturing practices at Amsterdam University Medical Centers for the Vrije Universiteit location. The procedures for radiolabeling of durvalumab with [89]Zr have been validated with respect to the final quality of the prepared conjugate and the production process. Details can be found in the supplemental materials.

Study Design

Two imaging series were scheduled for all included patients (Fig. 1). Whole-body (vertex to mid thigh) PET/CT with [89]Zr-durvalumab as the radiotracer was performed after injection of a single dose of the tracer (37 MBq, 2 mg of [89]Zr-durvalumab) on day 1. Twelve days later, a therapeutic nonradiolabeled dose of 750 mg of durvalumab was administered, followed within 2 h by a tracer dose injection (37 MBq, 2 mg of [89]Zr-durvalumab). This interval of 2 h resulted in a situation comparable to a simultaneous coadministration, because of the slow tissue uptake of large mAbs from the blood pool (*23*). The second imaging series was intended to overcome a possible sink effect: a small amount of radiotracer might be rapidly cleared from the circulation and accumulate in the liver, spleen, or other organs or compartments. This effect might be overcome by predosing with nonradiolabeled durvalumab, resulting in availability of sufficient amounts of radiotracer in the circulation for binding to PD-L1 receptors in tumor tissue. The first 3 enrolled patients were scanned 1, 72, 120, and 168 h after injection (for biodistribution purposes), both after the tracer only and after the combined radiolabeled and nonradiolabeled durvalumab injection. Subsequent patients underwent 2 PET scans after each tracer injection (72 and 120 h). The interval between the first [89]Zr-durvalumab injection and the second injection of combined tracer and nonradiolabeled durvalumab was 12 d, allowing for decay of radioactivity.

An ^{18}F-FDG PET scan, a diagnostic CT scan of the thorax and upper abdomen, and brain MRI were obtained before the initiation of treatment. After the image acquisition, durvalumab (750-mg flat dose) was administered every 2 wk until disease progression, unacceptable toxicity, or withdrawal of consent. Response was assessed with a diagnostic contrast-enhanced CT scan of the thorax and upper abdomen every 6 wk during treatment and interpreted according to RECIST 1.1 (*18*).

PET/CT Scan Analysis

Tumor lesions were identified and segmented on the [89]Zr-PET images using in-house–developed software (*24*), while also using the low-dose CT scan. The baseline ^{18}F-FDG PET/CT and diagnostic CT scans were used to differentiate between benign and malignant lesions. Volumes of interest (VOIs) were manually delineated over the entire tumor lesions when they could be distinguished from background on the attenuation-corrected images of the PET scan. In the case of tumor lesions without evident visual [89]Zr uptake, a spheric VOI of 1 cm^3 was drawn at the anatomic location of the tumor lesion, based on the low-dose CT, ^{18}F-FDG PET, and diagnostic CT data. To quantify radiotracer uptake in normal tissue, a fixed VOI with a diameter of 2 cm (4.2 cm^3) was used. Tracer uptake in all delineated VOIs was semiquantitatively assessed as SUV. From each VOI, the mean and peak activity concentrations (Bq/mL) were derived, normalized for body weight. SUV$_{mean}$ was reported for normal-tissue tracer uptake, and SUV$_{peak}$ was reported for tumor lesions. SUV$_{peak}$ was used to minimize the noise effect of [89]Zr, as SUV$_{max}$ is based on only 1

TABLE 1
Baseline Characteristics of Patients Included in Study

Patient no.	Age (y)	Sex	Histology	PD-L1 TPS (%)	PD-L1 CPS (%)	Treatment cycles (n)	BOR	Reason for treatment discontinuation	PFS (d)	OS (d)
1	59	F	Adenocarcinoma	0	12.5	7	SD	PD	86	823
2	53	M	Adenocarcinoma	0	0	1	PD	PD	19	19
3	75	F	Adenocarcinoma	0	7,5	1	PD	PD	<15	63
4	79	M	Adenocarcinoma	100	100	2	PD	PD	34	40
5	77	M	Adenocarcinoma	0	5	2	PD	PD	22	147
6	57	F	Squamous cell carcinoma	1	5	10	SD	PD	154	182
7	54	M	Adenocarcinoma	100	90	14	PR	PD	183	NR
8	70	M	Squamous cell carcinoma	NE	NE	9	PR	Toxicity	684	NR
9	70	M	Adenocarcinoma	0*	NE	1	PD	PD	9	15
10	64	M	Adenocarcinoma	0	0	1	PD	PD	2	2
11	72	M	Adenocarcinoma	1	25	22	NE	COVID-19 pandemic	NR	NR
12	72	F	Not otherwise specified	100	90	12	PR	Toxicity	NR	NR
13	69	M	Squamous cell carcinoma	0	0	3	PD	PD	41	78

*PD-L1 TPS derived from cytology.

BOR = best observed response; SD = stable disease; PD = progressive disease; NR = not reached; NE = not evaluable; PR = partial response.

voxel (25). To avoid partial-volume effects, only tumor lesions exceeding 20 mm in long-axis diameter were included in the analysis.

Blood Samples

For the first 3 patients, venous blood samples (7 mL each) were collected to determine ^{89}Zr-durvalumab activity at 5, 30, 60, and 120 min after injection and on days 3, 5, and 7 after injection. For the other patients, the samples were collected at 5 and 30 min after injection and on days 3 and 5 after injection.

Adverse Events

Tracer-related adverse events were recorded from the time of injection of the first tracer dose to the second full dose of durvalumab, which was 2 wk after the second imaging series. Before the first and second doses of durvalumab, patients visited the outpatient clinic for a review of adverse events. This consisted of a full physical examination and a laboratory assessment, including complete blood count, comprehensive serum chemistry, and thyroid-stimulating hormone level. The

National Cancer Institute Common Terminology Criteria for Adverse Events, version 4.0, were used to score adverse events (26).

Statistical Analysis

A Mann–Whitney U test was used to compare the SUV_{peak} of all lesions (long axis diameter $\geq$ 20 mm) in the different groups with and without progressive disease. Progressive disease was defined according to RECIST 1.1. The Kruskal–Wallis test was used to compare the SUV_{peak} in all response categories according to RECIST 1.1 (progressive disease, stable disease, partial response, and complete response). Further, the relation between the lesion-based ^{89}Zr-durvalumab accumulation and PD-L1 expression as assessed with immunohistochemistry (PD-L1 expression: 0%, 1%–49%, $\geq$50%) was also explored with the Kruskal–Wallis test.

The median SUV_{peak} of all delineated lesions (long axis diameter $\geq$ 20 mm) in the entire cohort was calculated and used to divide the patients into groups with high and low uptake. PFS and OS were summarized using Kaplan–Meier plots.

P values of less than 0.05 were considered to be statistically significant. All statistical analyses were performed using SPSS Statistics, version 25.0 (IBM), for Microsoft Windows.

RESULTS

Patients

Thirteen patients were enrolled between April 2018 and June 2019 (Table 1). All patients had pathologically confirmed NSCLC and confirmed progressive disease on prior chemotherapy. All patients received their first tracer dose injection. Eleven of 13 patients also received the second tracer injection according to the study protocol. One patient died as a result of
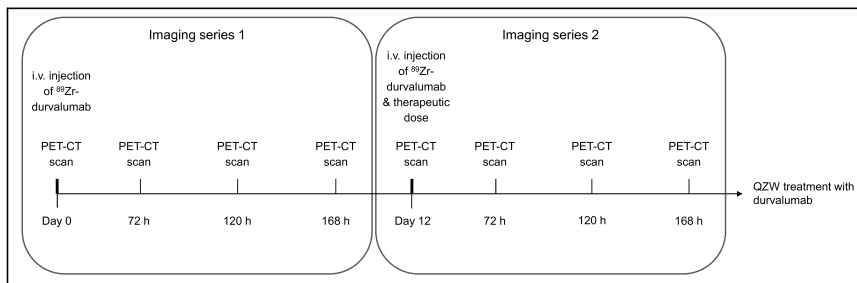
FIGURE 1. First 3 included patients received 4 PET/CT scans after each tracer injection (1, 72, 120, and 168 h after injection). Subsequent patients were scanned at 72 and 120 h after injection. i.v. = intravenous; QZW = once every two weeks.

TABLE 2
Adverse Events

Adverse event	Any grade	Grade 3 or 4
Anemia	8 (62%)	1 (8%)
Thrombocytopenia	5 (38%)	
Alkaline phosphatase increased	6 (46%)	
γ-glutamyl transferase increased	3 (23%)	
Aspartate aminotransferase increased	1 (8%)	
Hypercalcemia	1 (8%)	
Hypomagnesemia	2 (15%)	
Cough	3 (23%)	
Dyspnea	3 (23%)	1 (8%)
Pneumonia	1 (8%)	1 (8%)
Pain	7 (54%)	1 (8%)
Anorexia	4 (31%)	1 (8%)
Constipation	1 (8%)	
Epistaxis	1 (8%)	
Acute kidney injury	1 (8%)	
Vena cava superior syndrome	1 (8%)	1 (8%)

Data include all adverse events recorded from time of injection of first tracer dose to second full dose of durvalumab in 13 patients.

FIGURE 2. (A) Biodistribution at 1, 72, 120, and 168 h after injection of tracer dose (2 mg) only. (B) Biodistribution at 1, 72, 120, and 168 h after injection of tracer dose (2 mg) with unlabeled predose (750 mg) of durvalumab. (C) Average SUV$_{mean}$ of first 3 patients per organ without unlabeled predose of durvalumab. (D) Average SUV$_{mean}$ of patients 2 and 3 per organ with unlabeled predose of durvalumab. BM = bone marrow; p.i. = after injection.

rapidly progressive disease between scans, and 2 patients withdrew consent before the second imaging series. For the first 3 patients, the more extensive imaging protocol was followed (Supplemental Table 2).

Patients started durvalumab treatment on the day of the second tracer administration and received an average of 7 cycles of durvalumab (range, 1–21; median, 3). A response evaluation after 6 wk was performed on 7 of 13 patients; the other patients progressed earlier or died. The best observed response was a partial response in 3 patients, stable disease in 2 patients, and progressive disease in 1 patient. One patient was not evaluable according to RECIST 1.1.

The reasons for treatment discontinuation were death or progressive disease in 10 patients, durvalumab-related pneumonitis in 1 patient, the coronavirus disease 2019 pandemic in 1 patient, and the request of 1 patient because of sicca symptoms, grade II, probably related to durvalumab treatment. The median PFS was 1.3 mo (95% CI, 0.0–3.8), and median OS was 4.8 mo (95% CI, 0.2–9.4).

Biodistribution of [89]Zr-Durvalumab

PET imaging 1 h after injection (without a predose of unlabeled durvalumab) showed that [89]Zr-durvalumab uptake was present mainly in the blood pool (average SUV$_{mean}$, 7.2), liver (average SUV$_{mean}$, 6.7), and spleen (SUV$_{mean}$, 15.1). The [89]Zr-durvalumab activity in the blood pool decreased over time (average SUV$_{mean}$, 1.6 at 120 h) and was stable in the liver and bone marrow. The spleen showed the highest uptake, with a peak at 72 h after injection (average SUV$_{mean}$, 20.0). Low uptake was seen in the kidneys, non–tumor-bearing lung tissue, and brain (Figs. 2A and 2C; Supplemental Fig. 1).

When [89]Zr-durvalumab was administered after a nonradiolabeled therapeutic dose of durvalumab, a different pattern was observed. The extent of [89]Zr-durvalumab in the blood pool at 1 h

after injection was comparable to that in the first imaging series but remained 2-fold higher in the following scans than in the first series. This large difference was confirmed by the venous plasma samples (Fig. 3).

Further, [89]Zr-durvalumab uptake in the second scan series was less pronounced in the organs such as spleen, bone marrow and liver (Figs. 2B and 2D).

Safety

The most frequently reported adverse events from the time of injection of the first tracer dose to the second full dose of durvalumab were anemia and pain (Table 2), which were most likely related to previously administered chemotherapy or disease progression. No tracer-related adverse events were recorded.

Tumor Uptake

Visual Analyses. In total, 102 lesions from 13 patients were detected on the baseline ^{18}F-FDG PET/CT scans; 33 of these lesions had a long-axis diameter of at least 20 mm.

Of the 102 lesions, 26 (25%) were visualized on the [89]Zr-durvalumab PET/CT scans using the tracer-only imaging acquisition. Of the 33 lesions with a long-axis diameter of at least 20 mm, 10 (30%) were visible.
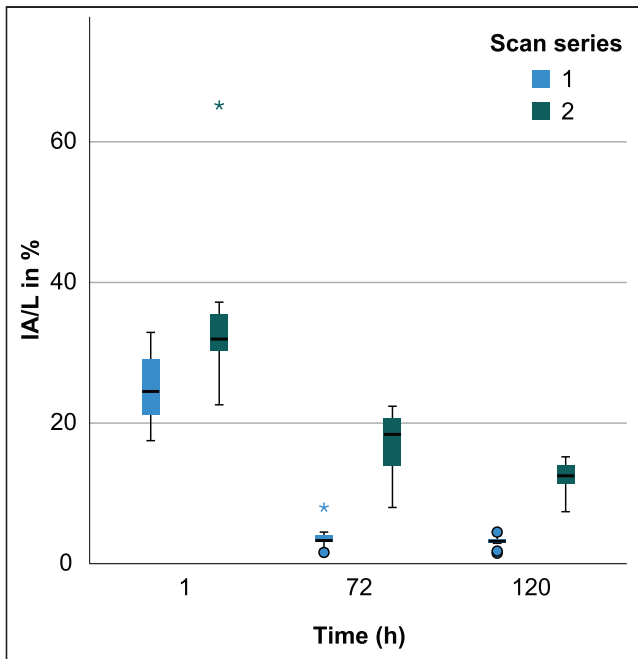
FIGURE 3. Venous plasma samples at 1, 72, and 120 h after injection of ^{89}Zr-durvalumab in average radioactivity in percentage injected activity per liter. Scan series 1 is without predose of unlabeled durvalumab. Scan series 2 is with 750 mg predose of unlabeled durvalumab. IA = injected activity.

In the imaging series of the first 3 patients, the tumor-to-background ratio was highest in the PET/CT scan obtained 120 h after injection, and tumor uptake was heterogeneous within and between patients, as shown in Figure 4.

The ^{89}Zr-durvalumab PET/CT scans that were obtained after the unlabeled therapeutic dose of durvalumab revealed a total of 14 (14%) lesions. Only 3 lesions that appeared on the second imaging series were not visible on the first imaging series. Two of these were small (<20 mm) lesions, whereas 1 was a large lung tumor (62 mm).

In total, 50 lesions with ^{89}Zr-durvalumab uptake (malignant and nonmalignant) were seen at 120 h after injection of the tracer dose–only scan series, whereas 15 ^{89}Zr-durvalumab–positive lesions (malignant and nonmalignant) were seen at 120 h after injection in the second scan series (tracer dose after unlabeled therapeutic dose of durvalumab). Of the 50 ^{89}Zr-durvalumab–positive lesions, 52% were also ^{18}F-FDG–positive and thus regarded as malignant. The
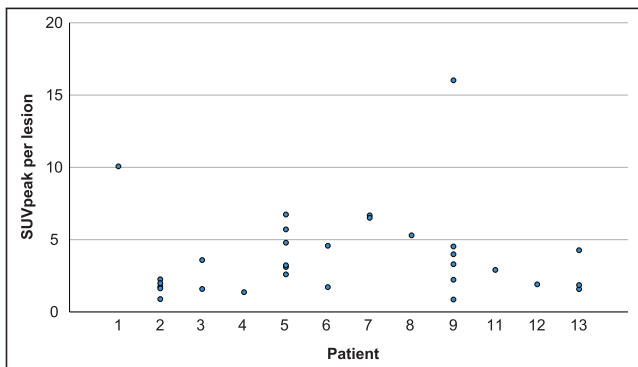
FIGURE 4. Tracer uptake for all patients per delineated tumor measuring at least 20 mm without predose of durvalumab at 120 h after tracer injection (scan of patient 12 is at 72 h, as 120-h scan was not available).
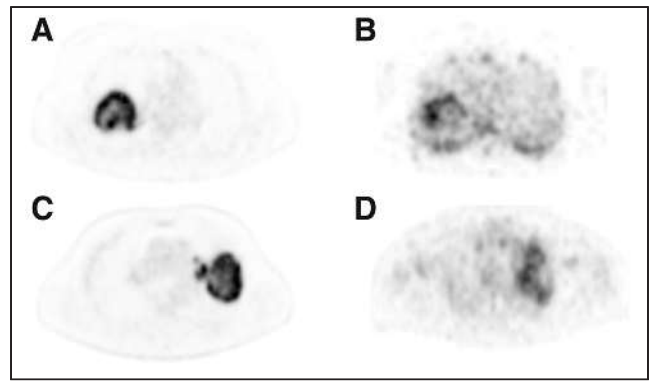
FIGURE 5. (A) ^{18}F-FDG PET of large, malignant lesion in right lung. (B) Same patient as in A, with heterogeneous uptake of ^{89}Zr-durvalumab in large malignant lesion in right lung. (C) ^{18}F-FDG PET uptake in large malignant lesion in left upper lobe. (D) Same patient as in C, with heterogeneous uptake of ^{89}Zr-durvalumab in large malignant lesion in left upper lobe.

^{89}Zr-durvalumab–positive and ^{18}F-FDG–negative (nonmalignant) lesions were mostly mediastinal lymph nodes, but axillary, abdominal, and supraclavicular lymph nodes were also seen. Interestingly, most of these did not show stable uptake. At 72 h after injection, 23 ^{89}Zr-durvalumab–positive, ^{18}F-FDG– negative (nontumor) lesions were seen. At 120 h, this number was 24. Only 12 of these lesions were seen both on the 72-h and on the 120-h scans.

Quantitative Analyses. The average SUV$_{peak}$ for all delineated tumor lesions, divided by the average SUV$_{peak}$ for the aorta, at 72 and 120 h was $4.1/2.2 = 1.8$ and $3.9/1.9 = 2.1$, respectively.

For subsequent quantitative analyses of tumor uptake, only ^{18}F-FDG–positive lesions at least 20 mm in size from the tracer dose–only acquisition were included and delineated on the PET scan at 120 h after the first tracer injection. The range of tracer uptake within patients with more than 1 lesion varied from an SUV$_{peak}$ of 0.2 (patient 3, with 2 lesions) to an SUV$_{peak}$ of 15.2 (patient 9, with 6 lesions). This large range was caused by the presence of a high-uptake lesion that was close to the spleen, with spill-in of splenic tracer activity in the tumor VOI. Without this outlier, the range varied between 0.2 and 4.1, with an average of 2.4. In large tumors, heterogeneous uptake was observed, most often with the highest tracer uptake in the periphery of the tumor. This observation might be due to impaired vascularization in the core of the tumor (due to necrosis), as this impairment was also observed on the ^{18}F-FDG PET. However, the periphery of the tumor showed an uptake pattern on ^{89}Zr-durvalumab PET different from that on ^{18}F-FDG PET (Fig. 5).

Response

There were 3 patients who had a partial response and 2 with stable disease lasting 3 and 5 months, respectively. The median SUV$_{peak}$ of tumor lesions in patients without progressive disease at 6 wk was 4.9, compared with 2.4 in patients with progressive disease at 6 wk. The difference was not statistically significant ($P = 0.06$). The median SUV$_{peak}$ in patients with progressive disease, stable disease, and partial response was 2.4, 4.6, and 5.9, respectively. These differences, however, were not statistically significant ($P = 0.12$) either (Fig. 6). Patients with an average SUV$_{peak}$ higher than the median (SUV$_{peak}$, 3.0) had a PFS of 7.3 mo. Those with an SUV$_{peak}$ lower than the median had a PFS of 5.5 mo ($P = 0.46$). Patients with an SUV$_{peak}$ higher than the median had a mean OS of 18.4 mo. Patients with an SUV$_{peak}$ lower than the
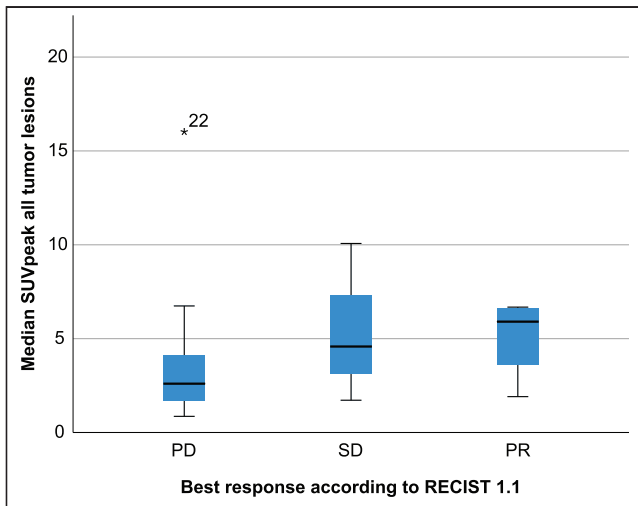
FIGURE 6. Median [89]Zr-durvalumab uptake at 120 h after injection for all tumor lesions (≥20 mm) per best RECIST response category. *22 represents one tumor lesion close to the spleen.

median had a mean OS of 5.9 mo. This difference was not statistically significant ($P = 0.13$). The above-mentioned outlier near the spleen in patient 9 was excluded from all response calculations.

Immunohistochemistry

Eleven of 13 patients were evaluable for programmed death 1 and PD-L1 expression on immune and tumor cells. Our cohort contained only biopsies with a PD-L1 TPS of 0%, 1%, and 100% (Supplemental Fig. 2). There was no correlation between PD-L1 TPS and the median [89]Zr-durvalumab uptake of all tumor lesions (≥20 mm) per patient ($P = 0.93$). Although not statistically significant, median [89]Zr-durvalumab uptake increased with higher PD-L1 CPS ($P = 0.06$). Again, in this calculation the outlier near the spleen was excluded (Fig. 7). No significant difference was observed in average [89]Zr-durvalumab uptake and programmed death 1 immunohistochemistry ($P = 0.10$).
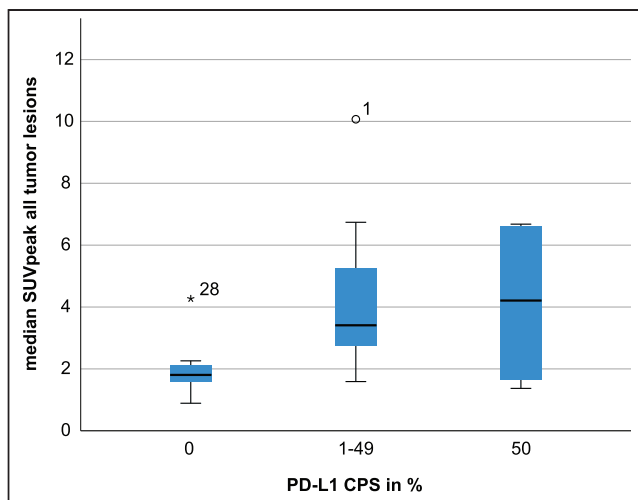
FIGURE 7. Correlation between median [89]Zr-durvalumab uptake at 120 h after injection for all tumor lesions (≥20 mm) and PD-L1 CPS. *28 represents one tumor lesion close to the spleen. °1 represents one tumor lesion in the right middle lobe with very high tracer uptake.

DISCUSSION

In this study, we showed that [89]Zr-durvalumab is safe and well tolerated, without any reported tracer-related adverse events. The biodistribution of [89]Zr-durvalumab was comparable to results observed in previous studies using [89]Zr-labeled immune checkpoint inhibitors (*12,13*). High uptake was seen in the liver (likely due to tracer catabolism) and spleen, where [89]Zr-durvalumab binds to PD-L1 receptors on lymphocytes and dendritic cells. As there are PD-L1–positive lymphocytes in the bone marrow, uptake there was slightly higher than in the blood pool. Low uptake was observed in the kidneys, lungs, and brain.

We showed the difference between 2 imaging acquisitions: one without a predose and one with a therapeutic predose of unlabeled durvalumab. The imaging series after the coinjection with unlabeled durvalumab showed a much lower uptake in target tissues (tumor, spleen, and bone marrow) than did the imaging series without a predose, as was likely due to saturation of the available PD-L1 receptors by a therapeutic dose much higher than the tracer dose (750 mg vs. 2 mg). Further, likely because of saturation of the catabolic capacity of the monoclonal antibody durvalumab, the liver also showed lower uptake in the second imaging series. Consequently, fewer tumor lesions were delineable on the PET scans that were made after the coinjection with unlabeled durvalumab.

The use of this unlabeled durvalumab was intended to overcome the so-called sink effect, wherein a substantial amount of the [89]Zr-labeled tracer accumulates in nontumor tissues with high specific (e.g., spleen) or nonspecific (e.g., liver) uptake. As a result, insufficient amounts of radiotracer are left in the circulation, available to bind to PD-L1 receptors on tumor cells. We demonstrated, however, that the imaging series without the unlabeled predose identified more tumor lesions than the imaging series with the predose. As a result of coinjection of the tracer with a full dose of unlabeled durvalumab, the latter occupies most PD-L1 receptors in normal tissue and tumor lesions and a larger fraction of the tracer remains present in the blood pool (Fig. 5B). This effect might also explain why a large tumor in the lung was not visualized on the first imaging series but showed higher uptake than the background in the second series. On the basis of contrast-enhanced CT evaluation, this was a well-vascularized tumor, and the tumor PD-L1 immunohistochemistry in this specific patient (patient 6) was 1%. The tumor was visualized in the second series due to the higher amount of tracer in the blood pool compared with the first series. Selection of the optimal tracer strategy for imaging of tumor lesions remains challenging. In this study, we showed adequate uptake in tumor lesions and target tissues using the tracer-only strategy. However, we studied only either a tracer-only dose or a coinjection with a full dose of unlabeled durvalumab, and the optimal imaging strategy might be coinjection of the tracer with a lower unlabeled dose. Further research is needed to explore whether such a strategy is better.

Although tumor lesions could be visualized and quantified, not every patient showed tracer uptake in tumor lesions. Absence of tracer uptake, however, did not rule out a treatment response. For example, the only tumor lesion of patient 12 did not show higher uptake than background, and the availability of tracer was sufficient (Fig. 3) and a partial response was achieved. Tumor uptake within and between patients was heterogeneous. There are numerous causes for this observation, such as a heterogeneous presence of PD-L1–positive malignant cells or a heterogeneous density of these cells in the tumor stroma. Also, immune cells can be more prevalent in one part of the tumor whereas the other part can be an immune

desert. PD-L1 expression on these immune cells can also be heterogeneous (6–8). In our data, especially in larger tumor lesions, uptake was more pronounced at the periphery of the tumor. This increased peripheral uptake can be caused by the binding site barrier effect, by which less penetration into the tumor mass occurs as a result of binding of the relatively large monoclonal antibody to receptors in the periphery of tumor lesions. Further, a higher perfusion rate at the edge of the tumor than at the center, or the higher prevalence of immune cells at the periphery of immune-infiltrate–excluded tumor lesions, could explain this observation (27).

Using the ^{18}F-FDG PET/CT obtained at baseline as a reference, we were able to differentiate between malignant and benign lesions that were visualized on the ^{89}Zr-durvalumab PET. To interpret ^{89}Zr-durvalumab PET results in future studies, we would advise use of an ^{18}F-FDG PET scan as a reference. An interesting difference in ^{89}Zr-durvalumab uptake by nonmalignant lesions, mostly lymph nodes, was observed between the scans obtained at 72 and 120 h after injection. Some of these lesions showed higher uptake at 72 h after injection, whereas others showed higher uptake at 120 h after injection. Since these lesions are lymphoid tissue, the change in uptake over time might be related to the immune cells' assembling in lymph nodes at one point in time and leaving them at the next point in time. Dendritic cells are known to travel from tissue to lymph nodes, and T cells are known to travel the opposite way (28).

Three patients developed an adverse event attributed to durvalumab treatment; predictive signs were not visible on ^{89}Zr-durvalumab PET/CT. Two patients were diagnosed with pneumonitis, and 1 patient experienced sicca symptoms. A higher ^{89}Zr-durvalumab uptake was not observed in the lung tissue of patients who developed pneumonitis during durvalumab treatment than in patients who did not develop pneumonitis. Further, the patient with sicca symptoms did not show uptake in the parotid glands on ^{89}Zr-durvalumab PET/CT.

Previous studies showed a correlation between PFS and a high tumor uptake on immuno-PET. In a clinical study with anti-PD-L1 ^{18}F-BMS-986192, uptake expressed as SUV_{peak} in tumors correlated with PD-L1 expression significantly (12). In the same study, patients were scanned with ^{89}Zr-nivolumab, and tumor uptake was significantly higher in patients whose tumor biopsies showed aggregates of programmed death 1–positive tumor-infiltrating immune cells. Further, uptake of ^{89}Zr-nivolumab and ^{18}F-BMS-986192 was higher in responding lesions than in lesions that were stable or grew. A study of another ^{89}Zr-labeled drug was conducted with the PD-L1 checkpoint inhibitor atezolizumab (13). Comparable results to those with the ^{89}Zr-nivolumab tracer were found: no correlation with PD-L1 expression on tumor cells, but significantly higher ^{89}Zr-atezolizumab uptake in responding patients. In our study, we found no difference in median SUV_{peak} between the PD-L1 TPS groups (0%, 1%–49%, and ≥50%). However, for PD-L1 CPS (both tumor and immune cell PD-L1 expression), a trend between the PD-L1 CPS groups and SUV_{peak} was found. Because of the spatial resolution of PET, the SUV_{peak} comprises tracer binding to PD-L1–positive tumor and immune cells. Therefore, PD-L1 CPS might be a better tissue correlative for PET than is PD-L1 TPS.

In our results, there was no significant correlation between response and SUV_{peak}, although a trend was seen. Since this study was not powered for treatment outcome, as the sample size was too small, future studies need to evaluate the predictive value of ^{89}Zr-durvalumab for durvalumab treatment outcome. Also, a relatively large number of patients deteriorated quickly. The clinical situation in patients with progressive NSCLC after a first line of chemotherapy often declines rapidly. The study design might also

have affected the clinical outcome. Because of the extensive imaging protocol, there was a study-related delay in the start of treatment.

Immuno-PET is a promising step forward in predicting response to checkpoint inhibitors. Identifying the best treatment strategy is of great importance to prevent unnecessary toxicity and costs (29–31). The group of patients who receive PD-L1 checkpoint inhibitors is growing. Recently, adjuvant durvalumab at stage III has been approved (15,16) and neoadjuvant immunotherapy for early-stage NSCLC might soon follow (32–34). However, in a substantial number of these patients, the disease will relapse. A one-size-fits-all strategy feels like a step backward. Immuno-PET tracers such as ^{89}Zr-durvalumab could potentially guide patient selection in the clinical setting and assist in the development of new treatment strategies.

CONCLUSION

This study showed that ^{89}Zr-durvalumab PET/CT imaging is safe and feasible. Tumor lesions could be visualized and quantified, and more tumor lesions could be delineated with only the tracer dose of durvalumab than with the use of an unlabeled therapeutic predose of durvalumab. ^{89}Zr-durvalumab uptake did not correlate with PD-L1 TPS. Nonsignificant correlations were found between clinical outcome during durvalumab treatment and tracer uptake and between PD-L1 CPS and tracer uptake. Further research is needed to investigate the potential role and optimal dose of ^{89}Zr-durvalumab as a biomarker in cancer patients treated with durvalumab.

DISCLOSURE

KEY POINTS

QUESTION: Is ^{89}Zr-durvalumab PET/CT a safe and feasible tool to visualize and quantify PD-L1–positive malignant lesions in NSCLC?

PERTINENT FINDINGS: In this single-arm, open-label exploratory pilot study, 13 patients underwent one or more ^{89}Zr-durvalumab PET/CT scans. There were no serious adverse events, and uptake was visualized and quantified in malignant lesions. Uptake showed heterogeneity within and between lesions and better correlated with PD-L1 CPS than with PD-L1 TPS immunohistochemistry, although neither was statistically significant.

IMPLICATIONS FOR PATIENT CARE: Further research is needed to investigate the potential role of ^{89}Zr-durvalumab as a biomarker in cancer patients treated with durvalumab.

REFERENCES

1. Reck M, Rodriguez-Abreu D, Robinson AG, et al. Pembrolizumab versus chemotherapy for PD-L1-positive non-small-cell lung cancer. *N Engl J Med.* 2016;375: 1823–1833.
2. Gandhi L, Rodriguez-Abreu D, Gadgeel S, et al. Pembrolizumab plus chemotherapy in metastatic non-small-cell lung cancer. *N Engl J Med.* 2018;378:2078–2092.
3. Borghaei H, Paz-Ares L, Horn L, et al. Nivolumab versus docetaxel in advanced nonsquamous non-small-cell lung cancer. *N Engl J Med.* 2015;373:1627–1639.
4. Brahmer J, Reckamp KL, Baas P, et al. Nivolumab versus docetaxel in advanced squamous-cell non-small-cell lung cancer. *N Engl J Med.* 2015;373:123–135.

5. Paz-Ares L, Luft A, Vicente D, et al. Pembrolizumab plus chemotherapy for squamous non-small-cell lung cancer. *N Engl J Med.* 2018;379:2040–2051.

6. Haragan A, Field JK, Davies MPA, Escriu C, Gruver A, Gosney JR. Heterogeneity of PD-L1 expression in non-small cell lung cancer: implications for specimen sampling in predicting treatment response. *Lung Cancer.* 2019;134:79–84.

7. McLaughlin J, Han G, Schalper KA, et al. Quantitative assessment of the heterogeneity of PD-L1 expression in non-small-cell lung cancer. *JAMA Oncol.* 2016;2:46–54.

8. Ilie M, Long-Mira E, Bence C, et al. Comparative study of the PD-L1 status between surgically resected specimens and matched biopsies of NSCLC patients reveal major discordances: a potential issue for anti-PD-L1 therapeutic strategies. *Ann Oncol.* 2016;27:147–153.

9. Hellmann MD, Ciuleanu TE, Pluzanski A, et al. Nivolumab plus ipilimumab in lung cancer with a high tumor mutational burden. *N Engl J Med.* 2018;378:2093–2104.

10. Bigras G, Mairs S, Swanson PE, Morel D, Lai R, Izevbaye I. Small biopsies misclassify up to 35% of PD-L1 assessments in advanced lung non-small cell lung carcinomas. *Appl Immunohistochem Mol Morphol.* 2018;26:701–708.

11. Moutafi MK, Tao W, Huang R, et al. Comparison of programmed death-ligand 1 protein expression between primary and metastatic lesions in patients with lung cancer. *J Immunother Cancer.* 2021;9:e002230.

12. Niemeijer AN, Leung D, Huisman MC, et al. Whole body PD-1 and PD-L1 positron emission tomography in patients with non-small-cell lung cancer. *Nat Commun.* 2018;9:4664.

13. Bensch F, van der Veen EL, Lub-de Hooge MN, et al. [89]Zr-atezolizumab imaging as a non-invasive approach to assess clinical response to PD-L1 blockade in cancer. *Nat Med.* 2018;24:1852–1858.

14. Xing Y, Chand G, Liu C, et al. Early phase I study of a ^{99m}Tc-labeled anti-programmed death ligand-1 (PD-L1) single-domain antibody in SPECT/CT assessment of PD-L1 expression in non-small cell lung cancer. *J Nucl Med.* 2019;60:1213–1220.

15. Antonia SJ, Villegas A, Daniel D, et al. Durvalumab after chemoradiotherapy in stage III non-small-cell lung cancer. *N Engl J Med.* 2017;377:1919–1929.

16. Antonia SJ, Villegas A, Daniel D, et al. Overall survival with durvalumab after chemoradiotherapy in stage III NSCLC. *N Engl J Med.* 2018;379:2342–2350.

17. Rizvi NA, Cho BC, Reinmuth N, et al. Durvalumab with or without tremelimumab vs standard chemotherapy in first-line treatment of metastatic non-small cell lung cancer: the MYSTIC phase 3 randomized clinical trial. *JAMA Oncol.* 2020;6:661–674.

18. Eisenhauer EA, Therasse P, Bogaerts J, et al. New response evaluation criteria in solid tumours: revised RECIST guideline (version 1.1). *Eur J Cancer.* 2009;45:228–247.

19. Tsao MS, Kerr KM, Kockx M, et al. PD-L1 immunohistochemistry comparability study in real-life clinical samples: results of blueprint phase 2 project. *J Thorac Oncol.* 2018;13:1302–1311.

20. Thunnissen E, Kerr KM, Dafni U, et al. Programmed death-ligand 1 expression influenced by tissue sample size. Scoring based on tissue microarrays' and cross-validation with resections, in patients with, stage I-III, non-small cell lung carcinoma of the European Thoracic Oncology Platform Lungscape cohort. *Mod Pathol.* 2020;33:792–801.

21. Imfinzi: EPAR—product information (annex I: summary of product characteristics). European Medicines Agency website. https://www.ema.europa.eu/en/documents/product-information/imfinzi-epar-product-information_en.pdf. Published October 30, 2018. Updated October 9, 2021. Accessed January 12, 2022.

22. Verel I, Visser GW, Boellaard R, et al. Quantitative [89]Zr immuno-PET for in vivo scouting of ^{90}Y-labeled monoclonal antibodies in xenograft-bearing nude mice. *J Nucl Med.* 2003;44:1663–1670.

23. Deng R, Bumbaca D, Pastuskovas CV, et al. Preclinical pharmacokinetics, pharmacodynamics, tissue distribution, and tumor penetration of anti-PD-L1 monoclonal antibody, an immune checkpoint inhibitor. *MAbs.* 2016;8:593–603.

24. Boellaard R, Oyen WJG, Lammertsma AA. Software tools for standardized analysis of FDG whole body studies in multi-center trials [abstract]. *J Nucl Med.* 2008;49(suppl 1):59P.

25. Jauw YWS, Heijtel DF, Zijlstra JM, et al. Noise-induced variability of immuno-PET with zirconium-89-labeled antibodies: an analysis based on count-reduced clinical images. *Mol Imaging Biol.* 2018;20:1025–1034.

26. *Common Terminology Criteria for Adverse Events (CTCAE) Version 4.03.* U.S. Department of Health and Human Services; 2010.

27. Binnewies M, Roberts EW, Kersten K, et al. Understanding the tumor immune microenvironment (TIME) for effective therapy. *Nat Med.* 2018;24:541–550.

28. Hamrah P, Dana R. Antigen-presenting cells in the eye and ocular surface. In: Dartt DA, ed. *Encyclopedia of the Eye.* Academic Press; 2010:120–127.

29. Ghosh S, Sharma G, Travers J, et al. TSR-033, a novel therapeutic antibody targeting LAG-3, enhances T-cell function and the activity of PD-1 blockade in vitro and in vivo. *Mol Cancer Ther.* 2019;18:632–641.

30. Johnston RJ, Comps-Agrar L, Hackney J, et al. The immunoreceptor TIGIT regulates antitumor and antiviral CD8(+) T cell effector function. *Cancer Cell.* 2014;26:923–937.

31. Hellmann MD, Bivi N, Calderon B, et al. Safety and immunogenicity of LY3415244, a bispecific antibody against TIM-3 and PD-L1, in patients with advanced solid tumors. *Clin Cancer Res.* 2021;27:2773–2781.

32. Lee JY, Kim JW, Lim MC, et al. A phase II study of neoadjuvant chemotherapy plus durvalumab and tremelimumab in advanced-stage ovarian cancer: a Korean Gynecologic Oncology Group study (KGOG 3046), TRU-D. *J Gynecol Oncol.* 2019;30:e112.

33. Mignard X, Antoine M, Moro-Sibilot D, et al. IoNESCO trial: immune neoadjuvant therapy in early stage non-small cell lung cancer [in French]. *Rev Mal Respir.* 2018;35:983–988.

34. Loibl S, Untch M, Burchardi N, et al. A randomised phase II study investigating durvalumab in addition to an anthracycline taxane-based neoadjuvant therapy in early triple-negative breast cancer: clinical results and biomarker analysis of Gepar-Nuevo study. *Ann Oncol.* 2019;30:1279–1288.

Biodistribution of ^{18}F-FES in Patients with Metastatic ER+ Breast Cancer Undergoing Treatment with Rintodestrant (G1T48), a Novel Selective ER Degrader

Ramsha Iqbal[1], Maqsood Yaqub[2], Daniela E. Oprea-Lager[2], Yeukman Liu[1], Anne Marije Luik[1], Andy P. Beelen[3], Robert C. Schuit[2], Albert D. Windhorst[2], Ronald Boellaard[2], and Catharina W. Menke-van der Houven van Oordt[1]

[1]Amsterdam UMC, Vrije Universiteit Amsterdam, Medical Oncology, Cancer Center Amsterdam, Amsterdam, Netherlands;
[2]Amsterdam UMC, Vrije Universiteit Amsterdam, Radiology and Nuclear Medicine, Cancer Center Amsterdam, Amsterdam, Netherlands; and [3]G1 Therapeutics Inc., Research Triangle Park, North Carolina

16α-^{18}F-fluoro-17β-estradiol (^{18}F-FES) is a PET tracer characterizing the expression of the estrogen receptor (ER). Because therapy can interfere with the kinetics and biodistribution of ^{18}F-FES, the aim of this study was to describe the biodistribution of ^{18}F-FES in patients with metastatic ER-positive (ER+) breast cancer undergoing treatment with rintodestrant (G1T48), a novel selective ER degrader. **Methods:** Eight patients underwent ^{18}F-FES PET/CT imaging at baseline, 4–6 wk during treatment with rintodestrant (interim), and after treatment. After intravenous administration of 200 MBq ($\pm$10%) of ^{18}F-FES, a 50-min dynamic PET/CT scan of the thorax was obtained, followed by a whole-body PET/CT scan 60 min after injection. Blood samples were drawn for measuring whole blood and plasma activity concentration and the parent fraction of ^{18}F-FES. Volumes of interest were placed in the aorta ascendens and in healthy tissues on both dynamic and whole-body PET scans. SUVs and target-to-blood ratios (TBRs) were calculated. Areas under the curve (AUCs) of input functions and time–activity curves were calculated as a measure of uptake in different regions. **Results:** ^{18}F-FES concentration in whole blood (and plasma) significantly ($P < 0.05$) increased at interim with median AUCs of 96.6, 116.6, and 110.3 at baseline, interim, and after treatment, respectively. In ER-expressing tissues, that is, the uterus and the pituitary gland, both SUV and TBR showed high ^{18}F-FES uptake at baseline, followed by a decrease in uptake at interim (uterus: SUV −50.6% and TBR −58.5%; pituitary gland: SUV −39.0% and TBR −48.3%), which tended to return to baseline values after treatment (uterus: SUV −21.5% and TBR −37.9%; pituitary gland: SUV −14.2% and TBR −26.0%, compared with baseline). In other healthy tissues, tracer uptake remained stable over the 3 time points. **Conclusion:** The biodistribution of ^{18}F-FES is altered in blood and in ER-expressing healthy tissues during therapy with rintodestrant. This indicates that rintodestrant alters the kinetics of the tracer, possibly affecting interpretation and quantification of ^{18}F-FES uptake. Of note, 6 d or more after treatment with rintodestrant ended, the biodistribution returned to baseline values, consistent with recovery of ER availability after washout of the drug.

Key Words: ^{18}F-FES; PET; estrogen receptor; breast cancer; biodistribution

Estrogen receptor–positive (ER+) breast cancer is the most common diagnosed breast cancer type among women worldwide (*1,2*). Patients with ER+ tumors can be treated with ER-targeted therapy, also known as endocrine therapy. Endocrine therapies include selective ER modifiers (SERMs) and degraders (SERDs) (*3*). These therapies decrease ER availability by binding to the ER to interfere with estrogen binding or degrading the ER, thus effectively eliminating ER expression.

The most frequently prescribed SERD in clinical practice is fulvestrant. However, its use is compromised by its poor bioavailability coupled with its intramuscular route of administration. Therefore, novel oral SERDs are being developed, including rintodestrant (G1T48), which can be administered at (relatively) higher doses with less patient discomfort (*4*).

For effective treatment of patients it is important to accurately describe and evaluate the mode of action of these novel ER-targeted therapies. PET/CT using ER-targeting tracers, such as 16α-^{18}F–fluoro-17β-estradiol (^{18}F-FES), is a promising approach to investigate this (*5,6*). ^{18}F-FES uptake, as measured 60 min after tracer administration using SUVs, correlates strongly with ERα expression (as compared with ER expression in tumor biopsies), with an overall sensitivity and specificity of 84% (95% CI, 73%–91%) and 98% (95% CI, 90%–100%), respectively (*7*). In addition to clinical studies to identify patients likely to respond to endocrine therapy, ^{18}F-FES PET appears to be an interesting tool for response prediction and dose finding for SERMs or SERDs (*3,5,8–12*). For patients receiving SERMs or SERDs, such as tamoxifen or fulvestrant, respectively, it is known that a decrease in ^{18}F-FES uptake after start of therapy correlates with response to these drugs (*10,12*). In addition, this during-therapy ^{18}F-FES PET imaging strategy can also help in dose-finding studies with novel ER-targeting drugs to establish the optimal dose to achieve maximum ER blockade (*7*).

However, to reliably assess changes in ER availability during endocrine therapy, it is essential to investigate the biodistribution of the tracer, that is, its uptake in blood pool and healthy tissues (with and without target expression) under various conditions (with and without therapy). In the case uptake changes during treatment, one can conclude that the given therapy interferes with the kinetics of the tracer. Therefore, the aim of this prospective substudy was to describe the biodistribution of the ^{18}F-FES tracer in patients with metastatic ER+ breast cancer undergoing treatment with rintodestrant.

MATERIALS AND METHODS

Postmenopausal female patients with histologically proven metastatic ER+/human epidermal growth factor receptor 2 (HER2)− breast cancer were prospectively included in this study (substudy of a phase I trial, NCT03455270) at the Amsterdam University Medical Centers – location VUmc. Patients had progressive disease after having received a maximum of 3 lines of cytotoxic chemotherapy and 3 lines of endocrine therapy in the metastatic setting. Patients were excluded when they received treatment with ER modulators (i.e., tamoxifen or fulvestrant) no more than 5 wk before inclusion as these drugs interfere with the availability of ER. All patients provided written informed consent in accordance with the regulations of the Medical Ethics Review Committee (METc no. 2018/085) of the Universitair Medisch Centrum Groningen.

Treatment

Eligible patients received rintodestrant orally once a day. A 3 + 3 dose escalation design was used to determine the recommended phase 2 dose (based on the pharmacokinetic, antitumor activity, and toxicity profile of the drug) (4). The starting dose in the first cohort was 200 mg, which could be escalated each time with 200 mg in the following cohorts, that is, cohort 2, 400 mg; cohort 3, 600 mg; and the like. The dose could be maximally escalated up to 2,000 mg/d. Patients would receive rintodestrant until clinically or radiographically progressive disease had been determined or there was unacceptable toxicity.

PET Imaging

PET scans were obtained on an Ingenuity TF PET/CT scanner (Philips). Patients underwent dynamic and whole-body ^{18}F-FES PET/CT imaging at 3 different time points: at baseline, 4 wk during treatment with rintodestrant (interim), and after treatment (scans were acquired within 10 d of the last dose of rintodestrant). All patients were instructed to fast for 4 h before the start of the scan to avoid high tracer uptake in the hepatobiliary and gastrointestinal tracts as these are the metabolization and elimination routes of the tracer. For each scan, patients received 2 venous cannulae, 1 for tracer injection and 1 for blood sampling. First, a low-dose CT scan of the thorax was obtained for attenuation correction. Next, a 50-min dynamic ^{18}F-FES PET scan of the thorax (18.4 cm axial field of view) was obtained, starting directly after intravenous administration of 200 (±10%) MBq of ^{18}F-FES. Subsequently, a whole-body low-dose CT scan was acquired for attenuation correction, followed by a whole-body ^{18}F-FES PET scan at 60 min after injection (skull vertex to mid-thigh), with 2–3 min per bed position depending on patient weight (2 min for 61–90 kg and 3 min for >90 kg).

PET data were normalized and corrected for dead time, randoms, scatter, and decay. In combination with CT-based attenuation correction, both scans provided images with a final voxel size of 4 × 4 × 4 mm and a spatial resolution of 5–7 mm in full width at half maximum. Dynamic PET scans were reconstructed using a 3-dimensional row action maximum-likelihood reconstruction algorithm (13) into 27 frames (1 × 10, 4 × 5, 3 × 10, 3 × 20, 2 × 30, 7 × 60, 2 × 150, 3 × 300, and 2 × 600 s). The whole-body scans were reconstructed using the BLOB-OS-TF reconstruction algorithm (14).

Blood Sampling

Before tracer administration, a venous blood sample was taken to determine estradiol and sex-hormone binding globulin (SHBG) levels, as these could potentially affect ^{18}F-FES uptake (15). After tracer administration, venous blood samples were collected at 5, 10, 20, 30, 40, 55, and ±90 min after injection. Before each sample, 2–5 mL of blood were drawn, followed by drawing a 7-mL sample and flushing of the cannula with 2.5 mL of saline afterward.

Blood was collected in a heparin tube and centrifuged for 5 min at 4,000 revolutions per minute (Hettich universal 16, Depex B.V.). Plasma was separated from blood cells, and 1 mL was diluted with

2 mL of 0.15 M HCl and loaded onto an activated tC2 Sep-Pak cartridge (Waters). The solid-phase extraction was washed with 5 mL of water. These combined fractions were defined as the polar radiolabeled metabolite. Thereafter, the tC18 Sep-Pak cartridge was eluted with 1.5 mL of methanol followed by 1.5 mL of water. This eluate was defined as the nonpolar fraction and was analyzed using high-performance liquid chromatography. The stationary phase was a Phenomenex Gemini C18, 10 × 250 mm, 5 μm, and the mobile phase was acetonitril/0.1% ammonium acetate in a mixture of 55/45 at a flow of 3 mL/min.

Whole-blood and plasma activity concentration and the parent fraction of ^{18}F-FES were measured. These data were used to correct the image-derived (whole-blood) input function to acquire a metabolite-corrected plasma input function.

Data Analysis: Dynamic and Whole-Body ^{18}F-FES PET Data

Volumes of interests (VOIs) were defined on PET and CT images using software developed in house (Accurate tool, Ronald Boellaard) (16). For the whole-body scans, fixed-size spheric VOIs with a diameter of 1, 2, or 4 cm (depending on the size of the organ) were placed in various healthy organs, that is, white matter in the brain, pituitary gland, lung, breast, bone, muscle, liver, spleen, subcutaneous fat, kidney, and uterus. Furthermore, if applicable up to 5 metastatic bone lesions were defined using a 40% isocontour of the max voxel value (17). PET activity concentration from these VOIs, both averaged SUVs and target-to-blood ratios (TBRs), were calculated according to Equations 1 and 2, respectively.

$$SUV = \frac{\text{activity concentration VOI (kBq/mL)}}{\text{administered dose (MBq)/patient weight (kg)}} \quad \text{Eq. 1}$$

$$TBR = \frac{\text{activity concentration target (kBq/mL)}}{\text{activity concentration blood (kBq/mL)}} \quad \text{Eq. 2}$$

Fixed-size VOIs were also defined in healthy organs that were visible on the dynamic ^{18}F-FES scans, that is, lung, breast, bone, muscle, and liver. For these VOIs, time–activity curves were generated, which were corrected for administered dose and body weight to generate SUV curves.

Image-derived input functions (IDIFs) were generated from dynamic ^{18}F-FES scans, using the early frames (0–2.5 min) in which the first pass of the bolus was best visualized. A fixed-size VOI of 1.5 cm was placed in 5 consecutive axial planes within the lumen of the ascending aorta on the PET scan. The low-dose CT scan was used as a reference for anatomic localization. These VOIs were then projected onto all image frames to generate a whole-blood IDIF. All IDIFs were calibrated using the radioactivity concentrations in the venous blood samples. In addition, IDIFs were corrected for both plasma-to-blood ratios and metabolites to obtain metabolite-corrected plasma input functions. Furthermore, SUV input curves were generated by normalizing the IDIFs for administered dose and body weight. The area under the input curves (AUCs) was calculated to more precisely describe the uptake over the duration of the dynamic scan.

Statistical Analysis

Statistical analyses were performed using SPSS Statistics 26 (IBM Corp.). For blood sampling data, tracer uptake in the blood pool and healthy organs and median and interquartile ranges (IQRs) were reported. For assessing changes in clinical parameters and tracer uptake in blood pool and healthy organs between the various scanning time points, the Wilcoxon signed-rank test was used (paired testing). Differences were considered significant for a P value of less than 0.05 for observing trends in data.

RESULTS

Patients

Eight female patients with metastatic ER+ breast cancer with an average (±SD) age of 63 (±7.35) y (Supplemental Table 1; supplemental materials are available at http://jnm.snmjournals.org)

were included. Patients received various doses of rintodestrant depending on the cohort in which they were included, ranging from 400 to 1,000 mg per day (Supplementals Table 1 and 2). A total of 20 dynamic and whole-body ^{18}F-FES PET/CT scans were obtained and evaluable: 8 scans were obtained at baseline, 7 scans at interim, and 5 scans after treatment. All patients scanned after treatment had discontinued treatment due to progressive disease with an average ($\pm$SD) treatment duration of 4.5 ($\pm$2.6) mo (Supplemental Table 1). After treatment, 3 scans were acquired at $\leq$2 d and 2 scans were acquired at $\geq$6 d after end of treatment (EoT). For 2 patients, the interim scans were obtained at 6 wk (instead of 4 wk) due to logistical issues.

The median injected ^{18}F-FES doses were 187 (IQR, 181–196), 187 (IQR, 180–195), and 183.2 (IQR, 177.4–188.2) MBq (Wilcoxon test, $P > 0.23$) at baseline, interim, and after treatment, respectively. Median body weight at baseline, interim, and after treatment was 77 (IQR, 65–105), 81 (IQR, 66–114), and 81 (IQR, 64–108), respectively (Supplemental Table 2). Body weight decreased significantly (maximum decrease in weight: 7.4%) between baseline and after treatment ($P = 0.04$). This decrease was accompanied by a significant increase in total body fat between baseline and after treatment ($P = 0.04$), with total body fat volumes of 28.1 (IQR, 19.2–43.6), 32.1 (IQR, 19.5–50.0), and 32.2 L (IQR, 18.8–52.1) at baseline, interim, and after treatment, respectively. However, the percentage injected dose of ^{18}F-FES in total body fat did not vary over the various time points ($P > 0.05$), with values of 24.2% (IQR, 19.7–28.4), 26.2% (IQR, 20.9–31.4), and 24.2% (IQR, 18.9–31.6) at baseline, interim, and after treatment, respectively.

Blood Sampling

Blood sampling data demonstrated that median estradiol levels in blood showed no difference over the various time points ($P > 0.18$), whereas SHBG levels changed after start of therapy: 66.5 (IQR, 26.0–121.5), 95.0 (IQR, 45.0–232.0), and 97.0 (IQR, 53.0–210.0) nmol/L at baseline, interim, and after treatment, respectively. SHBG levels showed a significant increase in values between baseline and interim ($P < 0.02$) and baseline and after treatment ($P < 0.04$; Supplemental Fig. 1).

Blood sampling data (Fig. 1) showed that median whole-blood activity concentrations, corrected for administered dose and patient weight, varied between SUVs of 1.4–1.5, 1.5–2.0, and 1.5–1.8 at baseline, interim, and after treatment, respectively (Fig. 1A). SUV increased at interim and tended to normalize to baseline values after treatment. The plasma–to–whole-blood ratios remained constant over the 3 different time points, ranging between 1.3 and 1.7 (Fig. 1B). The parent fraction of ^{18}F-FES in plasma showed a similar pattern over the 3 different time points: a rapid decrease to $\approx$20% in the first 20 min after injection (Fig. 1C) was observed.
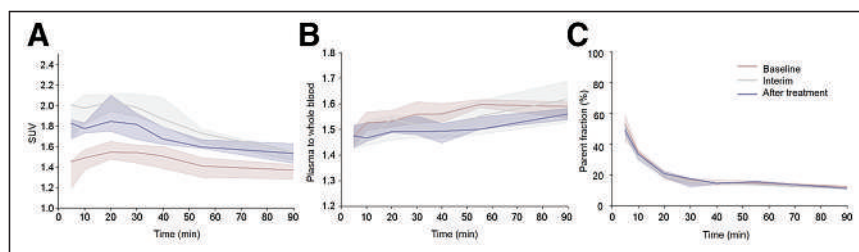
After the first 20 min, the parent fraction of ^{18}F-FES decreased quite slowly over time from 16% to 10%.

Tracer Uptake in Blood Pool

Median areas under the curve (AUCs) of the whole blood IDIFs (corrected for administered dose and body weight) at baseline, interim, and after treatment were 96.6 (IQR, 86.3–123.3), 116.6 (IQR, 112.5–144.9), and 110.3 (IQR, 97.9–132.1), respectively (Fig. 2A, Supplemental Table 3), showing increased levels of the tracer in blood at interim (Wilcoxon test, $P < 0.05$). These findings were in accordance with the AUCs of the whole-plasma IDIFs (Fig. 2B, $P < 0.05$). Median AUCs of the metabolite-corrected plasma input functions also showed an increase at interim: 54.6 (IQR, 52.7–75.0), 63.6 (IQR, 57.6–77.8), and 63.6 (IQR, 53.4–90.9) at baseline, interim, and after treatment (Fig. 2C). However, these differences at interim were not significant. For the whole-blood, plasma, and metabolite-corrected plasma input curves, no differences in AUCs could be seen in patients scanned $\leq$2 d versus $\geq$6 d after EoT (Supplemental Table 3).

Visual Assessment of ^{18}F-FES Uptake

Using the whole-body PET scans, ^{18}F-FES uptake in most healthy organs (except ER-expressing tissues such as the uterus and pituitary gland) was visually similar at all the imaging time points, with high tracer uptake in the liver, gallbladder, intestines, kidneys, and bladder (Fig. 3). At baseline, high ^{18}F-FES uptake could be seen in the uterus and pituitary gland, which decreased at interim. However, ^{18}F-FES uptake could be seen again in patients scanned several days after EoT. Patients scanned $\leq$2 d after EoT showed uptake similar to that seen at interim. In breast tissue, ^{18}F-FES uptake remained visually similar at all time points.

Visual assessment of metastatic lesions showed ^{18}F-FES uptake at baseline in 6 of 8 patients. At interim, no lesions could be visualized in 7 of 7 patients (Fig. 3). However, after treatment, lesions could be visualized again but only in patients scanned $\geq$6 d after EoT (2/5 patients).

Quantification of ^{18}F-FES Uptake

Using the dynamic scans, we generated SUV time–activity curves for healthy breast, lung, liver, muscle, and bone as these were located in the field of view of the dynamic scan (Fig. 4, Supplemental Table 4). For all these tissues, no changes in AUCs could be observed over the 3 different time points (Wilcoxon test, $P > 0.05$).

Using whole-body scans, we assessed tracer uptake in healthy tissues using SUV and TBR (Supplemental Figs. 2 and 3). For SUV and TBR, in most healthy tissues including the bone, breast, kidney, liver, lung, muscle, subcutaneous fat, and spleen, ^{18}F-FES uptake remained similar over the 3 different scanning time points. Quantification of tracer uptake in the uterus and pituitary gland confirmed the qualitative findings: for both SUV and TBR, ^{18}F-FES uptake decreased at interim (uterus: SUV -50.6% and TBR -58.5%; pituitary gland: SUV -39.0% and TBR -48.3%; compared with baseline). No correlation could be found between the various doses of rintodestrant that patients received and changes in tracer uptake in these tissues (Spearman ρ correlation, $P > 0.6$), possibly suggesting that even at the lowest dose, the blockade of these tissues was near 100% or at least sufficiently high to reduce ^{18}F-FES uptake below the level of detection. Interestingly after treatment, ^{18}F-FES uptake increased to baseline

FIGURE 1. Venous blood sampling data of all patients obtained at the 3 different time points. (A) SUV whole blood data. (B) Plasma-to-whole blood ratios. (C) Parent fraction of ^{18}F-FES in plasma. Data represent median of all values, with their corresponding IQRs.
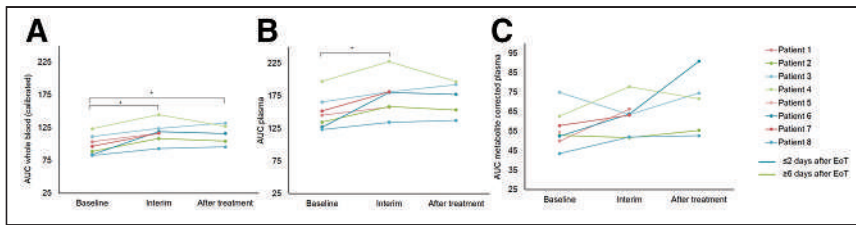
FIGURE 2. Tracer uptake in blood pool of each patient at 3 different time points. Whole blood calibrated with venous samples (A), plasma (B), and metabolite-corrected plasma (C) input curves. All curves have been corrected for administered dose and weight. At time of progression, patients were scanned ≤2 d (blue curves) or ≥6 d (green curves) after EoT. * $P < 0.05$

values in patients scanned several days after EoT (uterus: SUV −2.4% and TBR −21.7%; pituitary gland: SUV −9.6% and TBR −12.0%; compared with baseline) whereas it remained reduced in patients scanned shortly after EoT (uterus: SUV −34.3% and TBR −48.7%; pituitary gland: SUV −30.0% and TBR −47.2%; compared with baseline).

At baseline, metastatic bone lesions showed significantly higher tracer uptake than did healthy bone: median SUVs of 1.6 (IQR, 1.4–2.1) and 0.7 (IQR, 0.5–0.8) and TBR values of 1.2 (IQR, 1.1–1.6) and 0.5 (IQR, 0.4–0.5) for lesions and healthy bone, respectively (Supplemental Fig. 4; $P < 0.003$). However, at interim, lesions could not be detected whereas tracer uptake in healthy bone could be quantified. After treatment, lesions could be visualized again but only in patients scanned ≥6 d after EoT. Similar to baseline, these lesions showed high tracer uptake compared with healthy bone: SUVs of 1.9 (IQR, 1.4–2.0) and 0.7 (IQR, 0.7–0.8) and TBR values of 1.1 (IQR, 0.8–1.2) and 0.5 (IQR, 0.4–0.5) for lesions and healthy bone, respectively ($P < 0.003$).

DISCUSSION

In this study, dynamic and whole-body ^{18}F-FES PET/CT imaging was performed at baseline, interim and after treatment to determine the effect of rintodestrant on the biodistribution of the ^{18}F-FES tracer.

Blood Sampling and Input Data

Blood sampling and input data showed that whole-blood and plasma activity concentrations of the tracer increased at interim

and tended to return to baseline values after treatment. The increase in tracer activity concentrations is most likely the result of rintodestrant, which interferes with ER availability for binding ^{18}F-FES (4). Therefore, more free tracer will be available in the circulation, resulting in higher whole-blood and plasma activity concentrations. However, other effects caused by the therapy could also potentially lead to these increased tracer concentrations in blood. We also found increased levels of SHBG. SHBG is a plasma glycoprotein that plays an important role in the transport and bioavailability of steroid hormones, including estradiol (18). It is known that therapies that increase the estradiol levels in circulation lead to an increase in SHBG levels (19,20). We did not observe a change in estradiol levels during therapy; however, it might be possible that the SHBG levels increased as a response to therapy with rintodestrant. Peterson et al. (15). showed that SHBG levels are inversely associated with ^{18}F-FES uptake and subsequent higher levels of circulating ^{18}F-FES in blood, as also observed in our study.

The tracer metabolism was similar for all time points. The parent fraction of ^{18}F-FES rapidly decreased in the first 20 min after injection, indicating rapid metabolization of the tracer, in accordance with previous studies (5,21). After these 20 min, blood levels of radioactivity decreased quite slowly or remained fairly constant. Plasma–to–whole-blood ratios were constantly high over time, for all 3 time points. It is known that 35%–45% of the ^{18}F-FES tracer is plasma protein–bound and that red cell binding is low, which might explain these constant high ratios over time (21).

Visual Assessment and Quantification of ^{18}F-FES Uptake in Healthy Tissues

As seen in previous publications, our study confirmed physiologic high tracer uptake in the hepatobiliary, gastrointestinal, and urinary tract (5,22). This pattern was consistent over all time points. Additionally, in metastatic lesions and in ER-expressing healthy tissues (i.e., uterus and pituitary gland) high ^{18}F-FES uptake could be seen at baseline, which is in accordance with previous studies (22,23). Tracer uptake decreased at interim, most likely due to the down-regulatory effect of rintodestrant or the ER-blocking effect of the drug. Interestingly, after treatment ^{18}F-FES uptake returned to near baselines levels, specifically in patients scanned ≥6 d after EoT. In these cases, it is reasonable to assume that most of the administered drug is eliminated (half-life of rintodestrant: ≈16 h) (4) and that the ERs in lesions and in the uterus and pituitary gland are accessible for the tracer again. Indeed, in patients who were scanned shortly after EoT the uptake was still reduced, supporting that ER availability is still compromised due to the presence of the drug. These changes in ^{18}F-FES uptake could not be observed in breast tissue, which is also known to have ER expression. Breast tissue constantly showed low ^{18}F-FES uptake over the different time points. Compared with other ER-expressing tissues, for instance the uterus, the ER density

FIGURE 3. Visual assessment of ^{18}F-FES uptake in various healthy tissues in 1 patient at baseline (A), interim (B), and after treatment (C). This patient underwent interim scanning 10 d after EoT. Uterus, an ER-expressing organ, is not visible in these images as it is located behind bladder. Images are maximal-intensity projections.
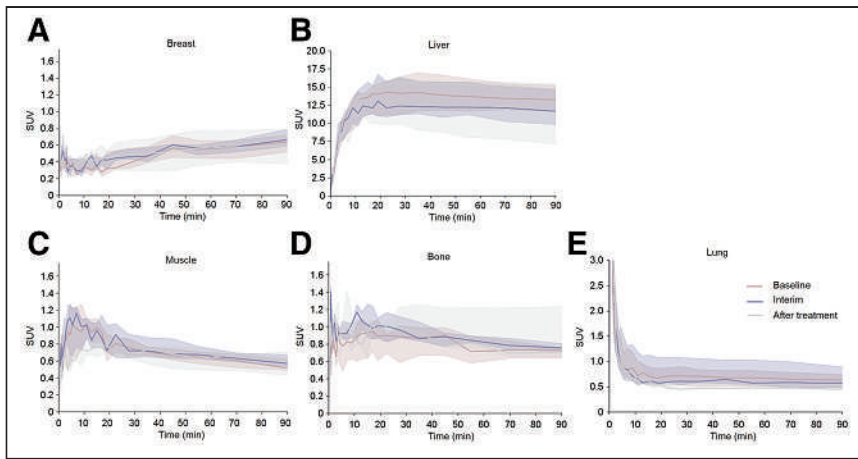
FIGURE 4. SUV time–activity curves (derived from dynamic scans) for various healthy tissue regions ([A] breast, [B] liver, [C] muscle, [D] bone. and [E] lung) of all patients at 3 different time points. Curves represent median of all values, with their corresponding IQRs.

in breast is significantly lower (*24*). Therefore, it can be expected that changes in uptake, potentially caused by therapy, are less prominent. In other healthy tissues, hardly any changes in tracer uptake could be detected, probably because in these tissues ER receptor expression is minimal or absent and thus the ^{18}F-FES uptake is aspecific (*24,25*).

For quantification of tracer uptake in healthy tissues at the various imaging time points, AUCs of the SUV input functions (derived from the dynamic scans) and TBR and SUV (derived from the whole-body scans) were used. In general, in all healthy tissues (except the uterus and pituitary gland), AUCs, TBR, and SUV showed that tracer uptake remained similar over the different time points. TBR seems to be slightly more sensitive than SUV for assessing changes in biodistribution, probably as it also takes into account changes in tracer concentration in the blood pool (which do occur during therapy as can be seen in the sampling data and input functions).

Visualization of lesions was only possible at baseline and after treatment, the latter only in patients scanned ≥6 d after EoT, most likely related to recovery of the ER availability after washout of the drug as mentioned earlier. Overall, bone lesions showed higher ^{18}F-FES uptake than healthy bone. These lesions are expected to have high ER expression causing more targeted uptake of the tracer, which is also more affected by ER degradation during treatment with rintodestrant. In healthy tissue the uptake is lower, consistent with aspecific uptake.

Limitations

Although the sample size may seem small, the strength of this study is that we collected dynamic and whole-body scans at 3 time points per patient, allowing a direct comparison of changes in biodistribution in a repeated measure design within 1 patient. As we investigated tracer uptake in healthy tissues, we expect that there will be limited variation between patients, which has been shown in similar previous PET biodistribution studies with comparable small sample sizes and which is also found in our study. Moreover, most quantitative PET study sample sizes are small, especially in the case in which an intensive scanning protocol is required, as was the case in this study.

Future Directions

^{18}F-FES imaging performed before the start of therapy can identify ER+ disease to select patients for ER-targeted therapy. Complete

blockage or degradation of the ER during treatment can be demonstrated by the absence of visual uptake in lesions. However, for quantification of more subtle changes in ^{18}F-FES uptake as a measure for ER availability and predictor of response to therapy with SERMs/SERDs, caution should be taken because our data show that during therapy the kinetics and biodistribution of the tracer are altered, possibly affecting interpretation.

CONCLUSION

The biodistribution of the ^{18}F-FES tracer is altered in blood and healthy tissues with high ER expression during therapy with rintodestrant. This indicates that rintodestrant alters the kinetics of the tracer, which could affect interpretation and quantification of ^{18}F-FES uptake. Of note, ≥6 d after ending treatment with rintodestrant, the biodistribution returned to baseline values, consistent with recovery of ER availability after washout of the drug.

KEY POINTS

QUESTION: How is the biodistribution of the ^{18}F-FES tracer and is it altered in patients with metastatic ER+ breast cancer undergoing treatment with rintodestrant?

PERTINENT FINDINGS: The biodistribution of the ^{18}F-FES tracer is altered in blood and in healthy tissues with high ER expression during therapy with rintodestrant. This indicates that rintodestrant affects the kinetics of the tracer, possibly affecting interpretation and quantification of ^{18}F-FES uptake.

IMPLICATIONS FOR PATIENT CARE: Changes in ER availability due to therapy that result in partial blockage or degradation of ER can potentially be quantified with ^{18}F-FES uptake. However, caution should be taken when doing so, because our data show that during therapy the kinetics and biodistribution of the tracer are altered, potentially affecting the interpretation.

REFERENCES

1. Bray F, Ferlay J, Soerjomataram I, Siegel RL, Torre LA, Jemal A. Global cancer statistics 2018: GLOBOCAN estimates of incidence and mortality worldwide for 36 cancers in 185 countries. *CA Cancer J Clin.* 2018;68:394–424.
2. Weigelt B, Geyer FC, Reis-Filho JS. Histological types of breast cancer: how special are they? *Mol Oncol.* 2010;4:192–208.

3. Liao GJ, Clark AS, Schubert EK, Mankoff DA. ^{18}F-fluoroestradiol PET: current status and potential future clinical applications. *J Nucl Med.* 2016;57:1269–1275.

4. Dees EC, Aftimos PG, Menke-van der Houven van Oordt, et al. Dose-escalation study of G1T48, an oral selective estrogen receptor degrader (SERD), in postmenopausal women with ER+/HER2- locally advanced or metastatic breast cancer (ABC). *Ann Oncol.* 2019;30:v104–v142.

5. Venema CM, Appollonio G, Hospers GA, et al. Recommendations and technical aspects of 16alpha-[18F]fluoro-17beta-estradiol PET to image the estrogen receptor in vivo: the Groningen experience. *Clin Nucl Med.* 2016;41:844–851.

6. Sundararajan L, Linden HM, Link JM, Krohn KA, Mankoff DA. ^{18}F-fluoroestradiol. *Semin Nucl Med.* 2007;37:470–476.

7. Fowler AM, Clark AS, Katzenellenbogen JA, Linden HM, Desdashti F. Imaging diagnostic and therapeutic targets: steroid receptors in breast cancer. *J Nucl Med.* 2016;57:75S–80S.

8. Peterson LM, Kurland BF, Schubert EK, et al. A phase 2 study of 16α-[18 F]-fluoro-17β-estradiol positron emission tomography (FES-PET) as a marker of hormone sensitivity in metastatic breast cancer (MBC). *Mol Imaging Biol.* 2014;16:431–440.

9. van Kruchten M, De Vries EG, Glaudemans AW, et al. Measuring residual estrogen receptor availability during fulvestrant therapy in patients with metastatic breast cancer. *Cancer Discov.* 2015;5:72–81.

10. Dehdashti F, Flanagan FL, Mortimer JE, Katzenellenbogen JA, Welch MJ, Siegel BA. Positron emission tomographic assessment of "metabolic flare" to predict response of metastatic breast cancer to antiestrogen therapy. *Eur J Nucl Med.* 1999;26:51–56.

11. Linden HM, Stekhova SA, Link JM, et al. Quantitative fluoroestradiol positron emission tomography imaging predicts response to endocrine treatment in breast cancer. *J Clin Oncol.* 2006;24:2793–2799.

12. Linden HM, Kurland BF, Peterson LM, et al. Fluoroestradiol (FES) positron emission tomography (PET) reveals differences in pharmacodynamics of aromatase inhibitors, tamoxifen, and fulvestrant in patients with metastatic breast cancer. *Clin Cancer Res.* 2011;17:4799–4805.

13. Matej S, Browne JA. *Three Dimensional Image Reconstruction in Radiology and Nuclear Medicine: Performance of a Fast Maximum Likelihood Algorithm for fully-3D PET Reconstruction.* Kluwer Academic Publishers; 1996:297–316.

14. Surti S, Kuhn A, Werner ME, Perkins AE, Kolthammer J, Karp JS. Performance of Philips Gemini TF PET/CT scanner with special consideration for its time-of-flight imaging capabilities. *J Nucl Med.* 2007;48:471–480.

15. Peterson LM, Kurland BF, Link JM, et al. Factors influencing the uptake of ^{18}F-fluoroestradiol in patients with estrogen receptor positive breast cancer. *Nucl Med Biol.* 2011;38:969–978.

16. Boellaard R. Quantitative oncology molecular analysis suite: ACCURATE. *J Nucl Med.* 2018;59(suppl 1):1753.

17. Krak NC, Boellaard R, Hoekstra OS, Twisk JW, Hoekstra CJ, Lammertsma AA. Effects of ROI definition and reconstruction method on quantitative outcome and applicability in a response monitoring trial. *Eur J Nucl Med Mol Imaging.* 2005;32:294–301.

18. Hryb DJ, Khan MS, Romas AN, Rosner W. The control of the interaction of sex-hormone-binding globulin with its receptor by steroid hormones. *J Biol Chem.* 1990;265:6048–6054.

19. Stomati M, Hartmann B, Spinetti A, et al. Effects of hormonal replacement therapy on plasma sex hormone-binding globulin, androgen and insulin-like growth factor-1 levels in postmenopausal women. *J Endocrinol Invest.* 1996;19:535–541.

20. Lønning PE, Johannessen DC, Lien EA, Ekse D, Fotsis T, Adlercreutz H. Influence of tamoxifen on sex hormones, gonadotrophins and sex hormone binding globulin in postmenopausal breast cancer patients. *J Steroid Biochem Mol Biol.* 1995;52:491–496.

21. Mankoff DA, Tewson TJ, Eary JF. Analysis of blood clearance and labeled metabolites for the estrogen receptor tracer [F-18]-16α-Fluorestradiol (FES). *Nucl Med Biol.* 1997;24:341–348.

22. Mankoff DA, Peterson LM, Tewson TJ, et al. [18F]fluoroestradiol radiation dosimetry in human PET studies. *J Nucl Med.* 2001;42:679–684.

23. Iqbal R. Menke-van der Houven van Oordt CW, Oprea-Lager DE, Booij J. [18F]FES uptake in the pituitary gland and white matter of the brain. *Eur J Nucl Med Mol Imaging.* 2021;48:3009–3010.

24. Human Protein Atlas. Protein Atlas website. http://www.proteinatlas.org. Accessed February 22, 2022.

25. Hua H, Zhang H, Kong Q, Jiang Y. Mechanisms for estrogen receptor expression in human cancer. *Exp Hematol Oncol.* 2018;7:24.

ER Imaging for Estrogen-Related Tumors Is Bothersome but Useful

Hidehiko Okazawa

Biomedical Imaging Research Center, University of Fukui, Eiheiji-cho, Japan

See the associated article on page 702.

Recent developments in molecular imaging methods have greatly contributed to the field of clinical nuclear medicine in terms of personalized cancer therapy as well as appropriate diagnosis of various diseases. Theranostics, the combination of therapy and diagnosis, is now not just a concept but a fusion of biologic diagnosis and its therapeutic application aiming at the goal of molecular imaging in oncology. The basics of theranostics are to elucidate specific biologic events or phenomena using molecular probes developed by molecular imaging technology. Conventional methods of assessing glucose metabolism and perfusion can be used to delineate the features of alteration in energy metabolism and blood flow; however, these are the results of pathophysiologic alterations caused by various diseases. Because the targets of molecular imaging are disease-specific biomarkers and phenotypic changes, the images delineate pathologic features of the disease. Imaging of amyloid and tau for diagnosis of Alzheimer disease is a good example of molecular imaging for pathogenic substances. Prostate-specific membrane antigen imaging and nuclear medicine therapy, a representative example of radiotheranostics, is now available in many hospitals and cancer centers for treatment of prostate cancer.

Estrogen receptor (ER) imaging, used for breast cancer and uterine tumors, is also a good example of molecular imaging that can well delineate features of cancers. In breast cancer studies, ER expression in cancer is important information not only for diagnosis but also for determining the suitability of hormone therapy (*1*). Conventional CT and MRI diagnosis can detect the size of lymph nodes, and ^{18}F-FDG PET can delineate the glucose avidity of tumors and metastatic lesions; however, these images cannot differentiate lymph node metastases from reactive lymphadenopathy. 16α-^{18}F-fluoro-17β-estradiol (^{18}F-FES) is a representative PET ligand for ER imaging and has been applied for decades in the diagnosis of breast cancers (*2*). Many studies have shown the usefulness of ^{18}F-FES PET, and its accumulation correlated well with ER expression in tumor tissue (*2–4*). ^{18}F-FES accumulation in enlarged lymph nodes indicates the presence of ER, that is, metastatic lesions from an ER-positive breast cancer, which improves the diagnostic ability in terms of staging of breast cancer. ^{18}F-FES has a 6.3-fold absolute affinity preference for ERα over ERβ (*5*), which is important information to estimate the prognosis of ER-related malignancies.

^{18}F-FES PET is also useful in diagnosis of uterine tumors such as endometrial cancer and leiomyosarcomas (*4,6*). Previous studies have shown its beneficial application for differential diagnosis and for prediction of prognosis (*3,4,6*). Since ^{18}F-FES accumulation correlates well with ER expression in endometrial cancer and sarcoma (*3,4*), SUVs can detect ER density in tumors. However, ER expression tends to be decreased in malignant tumors (*4,6*), and accumulation of ^{18}F-FES alone cannot improve the ability to diagnose malignancy because negative accumulation cannot distinguish between normal tissue and high-grade malignancy. Since this tendency is the same as for metastatic lesions, the diagnostic ability of ^{18}F-FES PET for metastasis is not so sufficient. Furthermore, in the endometrial tissue of a normal uterus, substantial ^{18}F-FES accumulation is observed in premenopausal women, and the intensity of accumulation varies according to menstrual cycle (*7*). Therefore, ^{18}F-FES PET scans in premenopausal patients should be performed during the secretory phase of the menstrual cycle to minimize the effect of normal endometrial uptake (*8*). Another problem with ^{18}F-FES PET in abdominal-to-pelvic scanning is excretion of the tracer to the intestine. The tracer shows high accumulation in the liver, where ^{18}F-FES is metabolized and excreted into the bile ducts. PET scans are usually performed about 60 min after the tracer injection, as is the case with ^{18}F-FDG PET scans. During this waiting time, ^{18}F-FES is metabolized and excreted into the intestine. Patients often show a strong intestinal accumulation of ^{18}F-FES due to excretion of metabolites, which may sometimes prevent observation of abdominal and pelvic lesions. This ^{18}F-FES accumulation in the abdomen and pelvic cavity has made it difficult to apply the useful tracer to gynecologic tumors. However, in previous ^{18}F-FES PET studies for these tumors, scans were performed after a substantial fasting time, and clear images were obtained in the pelvic regions (*3,4,6,8*). The combination of ^{18}F-FDG and ^{18}F-FES PET can provide useful information for evaluation of prognosis (*8,9*). In clinical practice, additional MR scanning is essential to delineate features of the primary tumor (*10*), because it is difficult to make a correct radiologic diagnosis of gynecologic tumors on the basis of PET/CT findings alone.

To improve image quality and contrast for assessment of ER expression, a new PET ligand, 4-fluoro-11β-methoxy-16α-^{18}F-fluoroestradiol (^{18}F-4FMFES), has been developed as a homolog of ^{18}F-FES and applied to diagnosis of breast cancer (*11*). Paquette

et al. compared ^{18}F-FES and [18]F-4FMFES PET images directly in a phase II clinical trial study for breast cancer and found that SUV_{max} was similar and image quality was better with [18]F-4FMFES PET than with ^{18}F-FES PET. Because of the improved tumor-to-background ratio with the new tracer, the image contrast has been improved, compared with the conventional one. Therefore, the new tracer seemed to be promising for diagnosis of ER expression of breast cancer. They also applied [18]F-4FMFES PET to endometrial cancer of the uterus and compared its diagnostic ability with that of ^{18}F-FDG PET (12). After tumor biopsy, patients with ERα-positive endometrial cancer were enrolled in the study and underwent ^{18}F-FDG and [18]F-4FMFES PET within an interval of less than 2 wk. They compared the diagnostic performance between [18]F-4FMFES and ^{18}F-FDG PET. Since high-grade endometrial cancers tend to reduce or lose ERα expression (3,6), the diagnostic performance of ^{18}F-FES or [18]F-4FMFES PET alone is not expected to be superior to that of ^{18}F-FDG PET. However, SUVs and diagnostic performance were preserved or surpassed in this study because only the ERα-positive cancers after tumor biopsy were enrolled. If PET scans are performed without tumor biopsy, the ^{18}F-FDG/[18]F-4FMFES ratio would be the most sensitive parameter to determine the grade and prognostic value of the tumor (6,8,9,12). The investigators added an evaluation of the effects of loperamide or butylbromide administration before tracer administration to reduce tracer excretion to the intestine. In the study of gynecologic tumors, the intense abdominal uptake may affect the diagnosis of uterine tumors, including metastatic lesions. Allowing for a substantial fasting period before scanning may be a more effective and less invasive method for improving image quality than is administration of antimotility medicine. The timing of the scan should also be chosen appropriately according to the patient's menstrual cycle so as to minimize normal endometrial uptake, which may impair discrimination between normal tissue and cancer. Since breast cancer and gynecologic tumors have different features, the study protocol should be determined in accordance with the tumor characteristics. [18]F-4FMFES PET has shown good image quality in breast cancer studies and would be promising for uterine cancer or sarcoma studies with proper preparation and scanning protocols using PET/CT

plus MRI or PET/MRI. Information on ERα expression is essential for application of hormonal therapy aimed at theranostics.

DISCLOSURE

No potential conflict of interest relevant to this article was reported.

REFERENCES

1. Allison KH, Hammond MEH, Dowsett M, et al. Estrogen and progesterone receptor testing in breast cancer: ASCO/CAP guideline update. *J Clin Oncol.* 2020;38: 1346–1366.
2. Mintun MA, Welch MJ, Siegel BA, et al. Breast cancer: PET imaging of estrogen receptors. *Radiology.* 1988;169:45–48.
3. Tsujikawa T, Yoshida Y, Kiyono Y, et al. Functional estrogen receptor α imaging in endometrial carcinoma using 16α-[18F]fluoro-17β-estradiol PET. *Eur J Nucl Med Mol Imaging.* 2011;38:37–45.
4. Zhao Z, Yoshida Y, Kurokawa T, Kiyono Y, Mori T, Okazawa H. FES- and FDG-PET for differential diagnosis and quantitative evaluation of mesenchymal uterine tumors: correlation with immunohistochemical analysis. *J Nucl Med.* 2013;54:499–506.
5. Yoo J, Dence CS, Sharp TL, Katzenellenbogen JA, Welch MJ. Synthesis of an estrogen receptor β-selective radioligand: 5-[18F]fluoro-(2R*,3S*)-2,3-bis(4-hydroxyphehyl) pentanenitrile and comparison of in vivo distribution with 16α-[18F]fluoro-17β-estradiol. *J Med Chem.* 2005;48:6366–6378.
6. Tsujikawa T, Yoshida Y, Kudo T, et al. Functional images reflect aggressiveness of endometrial carcinoma: estrogen receptor expression combined with FDG-PET. *J Nucl Med.* 2009;50:1598–1604.
7. Tsuchida T, Okazawa H, Mori T, et al. In vivo imaging of estrogen receptor concentration in the endometrium and myometrium using FES PET: influence of menstrual cycle and endogenous estrogen level. *Nucl Med Biol.* 2007;34:205–210.
8. Yamada S, Tsuyoshi H, Yamamoto M, et al. Prognostic value of 16α-[18F]-fluoro-17β-estradiol positron emission tomography as a predictor of disease outcome in endometrial cancer: a prospective study. *J Nucl Med.* 2021;62:636–642.
9. Yamamoto M, Tsujikawa T, Chino Y, et al. ^{18}F-FDG/^{18}F-FES standardized uptake value ratio determined using PET predicts prognosis in uterine sarcoma. *Oncotarget.* 2017;8:22581–22589.
10. Xiao M, Yan B, Li Y, Lu J, Qiang J. Diagnostic performance of MR imaging in evaluating prognostic factors in patients with cervical cancer: a meta-analysis. *Eur Radiol.* 2020;30:1405–1418.
11. Paquette M, Lavallée É, Phoenix S, et al. Improved estrogen receptor assessment by PET using the novel radiotracer [18]F-4FMFES in estrogen receptor–positive breast cancer patients: an ongoing phase II clinical trial. *J Nucl Med.* 2018;59:197–203.
12. Paquette M, Espinosa-Bentancourt E, Lavallée É, et al. [18]F-4FMFES and ^{18}F-FDG PET/CT in ER+ endometrial carcinomas: preliminary report. *J Nucl Med.* August 19, 2021 [Epub ahead of print].

^{18}F-4FMFES and ^{18}F-FDG PET/CT in Estrogen Receptor–Positive Endometrial Carcinomas: Preliminary Report

Michel Paquette[1], Esteban Espinosa-Bentancourt[1], Éric Lavallée[1], Serge Phoenix[1], Korine Lapointe-Milot[2], Paul Bessette[2], Brigitte Guérin[1], and Éric E. Turcotte[1]

[1]Department of Nuclear Medicine and Radiobiology, Université de Sherbrooke, Sherbrooke, Québec, Canada; and [2]Department of Obstetrics and Gynecology, Université de Sherbrooke, Sherbrooke, Québec, Canada

This article reports the preliminary results of a phase II clinical trial investigating the use of the estrogen receptor (ER)–targeting PET tracer 4-fluoro-11β-methoxy-16α-^{18}F-fluoroestradiol (^{18}F-4FMFES) and ^{18}F-FDG PET in endometrial cancers. In parallel, noninvasive interventions were attempted to slow progression of ^{18}F-4FMFES metabolites in the intestines to reduce abdominal background uptake. **Methods:** In an ongoing study, 25 patients who received prior pathologic confirmation of an ER-positive endometrial cancer or endometrial intraepithelial neoplasia agreed to participate in the ongoing clinical trial. Patients were scheduled for ^{18}F-FDG and ^{18}F-4FMFES PET/CT imaging in random order and within 2 wk. Patients were administered either 4 mg of loperamide orally before ^{18}F-4FMFES tracer injection or repeated intravenous injection of 20 mg of hyoscine N-butylbromide during ^{18}F-4FMFES PET/CT. Regions of interest covering the whole abdomen and excluding the liver, bladder, and uterus were drawn for the ^{18}F-4FMFES PET images, and an SUV threshold of more than 4 was applied. The volume of the resulting region was compared between the different interventions to estimate the extent of the intestinal background uptake. **Results:** Repeated injection of hyoscine N-butylbromide substantially reduced the intestinal background volume, whereas loperamide had a significant but moderate effect. ^{18}F-4FMFES tumor SUV$_{max}$ ranged from 3.0 to 14.4 (9.4 ± 3.2), whereas ^{18}F-FDG SUV$_{max}$ ranged from 0 to 22.0 (7.5 ± 5.1). Tumor-to-background ratio was significantly higher for ^{18}F-4FMFES (16.4 ± 5.4) than for ^{18}F-FDG (7.4 ± 4.6). Significant differences were observed between grade 1 and higher-grade tumors concerning ^{18}F-4FMFES uptake and contrast, ^{18}F-FDG uptake, and the ^{18}F-FDG/^{18}F-4FMFES uptake ratio. **Conclusion:** It is possible to improve ^{18}F-4FMFES abdominal background using hyoscine N-butylbromide. Both ^{18}F-FDG and ^{18}F-4FMFES PET are suitable for detection of ER-positive endometrial cancers, although ^{18}F-4FMFES yielded a better tumor contrast than did ^{18}F-FDG.

Key Words: endometrial carcinoma; ^{18}F-4FMFES; abdominal background

Endometrial cancers affected 382,069 women worldwide in 2018, and 89,929 died from the disease (1). About two thirds of endometrial cancers are diagnosed at an early, localized stage, for which prognosis is very favorable. The estrogen receptor (ER) is expressed in nearly 80% of uterine tumors (2), a patient subset that has an improved 5-y disease-free survival compared with ER-negative disease (3,4). Moreover, the success rate of adjuvant hormone therapies was shown to be dependent on ER status for endometrial cancers (5,6). As such, knowledge of ER status is increasingly evidenced to be crucial for this disease, both for prognosis and for therapy management.

Current diagnostic tools for endometrial cancers include transvaginal echography, CT, and MRI (7). More recently, the use of ^{18}F-FDG PET imaging has been spreading and has contributed to the detection and staging of those cancers (8,9). However, ^{18}F-FDG indicates only the relative avidity of tissues and tumors for glucose and as such is prone to false-negatives (hypometabolic tumors) and false-positives such as inflammation and physiologic uptake (10,11). As such, even if it supplements anatomic imaging such as CT and MRI, ^{18}F-FDG PET has a sensitivity and specificity ranging from poor to moderate for endometrial cancers (8).

To improve imaging of endometrial cancers and at the same time allow noninvasive assessment of ER status, a few groups have explored the use of the estrogenlike ^{18}F-16α-fluoroestradiol (^{18}F-FES) PET tracer in the clinical setting. ^{18}F-FES tumor uptake was shown to correlate well with the biopsy-determined ER status in endometrial cancers (12,13). The successive use of ^{18}F-FDG PET and ^{18}F-FES PET enabled discrimination between low- and high-grade endometrial carcinomas (14). The ^{18}F-FDG/^{18}F-FES tumor uptake ratio also correlated well with progression-free and overall survival in uterine sarcomas (15,16).

More recently, ^{18}F-FES PET was shown in a prospective study to be better than ^{18}F-FDG PET in evaluating endometrial cancer patient outcome, further displaying the potential of ER imaging for this disease (17). Despite those successes, ^{18}F-FES PET has some shortcomings, including slow blood clearance and rapid metabolization (18,19), both of which are factors increasing nonspecific signal and hence reducing tumor detectability.

To palliate the main weaknesses of ^{18}F-FES, our group developed an alternative ER-targeting molecule, 4-fluoro-11β-methoxy-16α-^{18}F-fluoroestradiol (^{18}F-4FMFES) (20,21), that was shown to resist hepatic metabolism in humans. Its very low binding to plasma globulins resulted in a 5-fold reduction of tracer in the blood pool in the clinical setting

(22,23). Combined, those 2 factors substantially reduced [18]F-4FMFES accumulation in nonspecific organs, compared with ^{18}F-FES, resulting in a much lower background signal (23). Consequently, [18]F-4FMFES generated a significantly better tumor contrast than did ^{18}F-FES in a phase II clinical study on a breast cancer cohort, allowing detection of more ER-positive (ER+) tumors than was previously possible (23). Preliminary reports indicated that [18]F-4FMFES complements standard ^{18}F-FDG PET imaging in breast cancer patients (24).

The recent success of [18]F-4FMFES PET in ER+ breast cancers in the clinical setting foretells its usability for ER+ endometrial cancers as well. Given the high prevalence of ER (2) and the importance of ER status (3,4) in endometrial cancers, this novel ER-targeting PET imaging modality might improve the diagnostic determination and the noninvasive ER status determination of those cancers. ^{18}F-FDG tumor uptake was shown to follow an inverse relationship with ER expression in breast cancers (25,26), and combined ^{18}F-FDG and ^{18}F-FES PET was shown superior to each tracer alone in breast cancers (27) and endometrial cancers (14,15). As such, the [18]F-4FMFES PET procedure was paired and compared with ^{18}F-FDG PET within a 2-wk interval to evaluate their complementarity for this new indication.

Hence, this report shows the preliminary trends and observations of a phase II clinical trial evaluating [18]F-4FMFES and ^{18}F-FDG PET in an endometrial cancer cohort. In parallel, we investigated the impact of using drugs to slow intestinal transit in combination with diuretics, as the hepatobiliary and urinary metabolites of [18]F-4FMFES generate an intense lower-abdomen background signal that could impair endometrial cancer assessment.

MATERIALS AND METHODS

The study was approved by the Sherbrooke University Hospital clinical research ethics committee and institutional board, performed under the authority of Health Canada and registered on ClinicalTrials.gov with the identifier NCT04823065. All patients signed an informed consent form, and the procedure was explained in lay terms by the investigators. Eligible patients were recruited after biopsy and as recommended by the gynecologic oncologists. Eligibility criteria included patients with newly diagnosed endometrial cancer, with a positive ERα status histologically confirmed. Exclusion criteria included pregnancy and concomitant endocrine therapy. In this ongoing study aiming to recruit 72 patients with ovarian and uterine cancers of various origins, the first 25 endometrial cancer patients recruited were examined using both ^{18}F-FDG and [18]F-4FMFES PET, as planned. Among them, 23 patients had ER+ endometrial carcinoma (including 16 who had the endometroid endometrial adenocarcinoma subtype), and 2 were diagnosed with endometrial intraepithelial neoplasia. Four of those patients were premenopausal, and 21 patients were postmenopausal. The gynecologic oncology team staged the patients according to the postsurgery pathology report. Table 1 summarizes the patient characteristics in more detail.

Radiochemistry

[18]F was prepared by the [18]O(p,n)[18]F reaction on ^{18}O-enriched water as target material using the TR-19 or TR-24 cyclotron (Advanced Cyclotron Systems, Inc.) of the Sherbrooke Molecular Imaging Center. [18]F-4FMFES precursor synthesis (20); its labeling (21) using an optimized automated procedure (28); and its preparation, formulation, and quality control procedures (23) were as described previously. Apparent molar activity for [18]F-4FMFES ranged from 20 to 123 GBq/µmol and was similar to what has been reported in the literature (23,24).

Pharmacologic Interventions to Slow Intestinal Transit

Patients were not allowed to drink from the time the [18]F-4FMFES was injected until the end of the imaging procedure. In addition, for [18]F-4FMFES examinations, patients received either 4 mg of loperamide orally 15 min before injection ($n = 12$) or 20 mg of the anticholinergic drug hyoscine N-butylbromide intravenously at 0, 20, and 40 min after tracer administration ($n = 11$). Two patients received no additional intervention and were pooled with the [18]F-4FMFES PET scans previously performed on breast cancer patients ($n = 31$) for the intestinal transit assessment analysis (23).

PET Imaging

A catheter was placed in the arm, and patients were injected intravenously with 210.6 ± 20.5 MBq of [18]F-4FMFES in a total volume of 10 mL of physiologic saline (0.9% NaCl). Thereafter, the line was flushed with 20 mL of saline. Within less than 2 wk, the same patients were injected with 320.3 ± 102.7 MBq of ^{18}F-FDG. The scans occurred in random order. For both imaging procedures, patients were injected with 40 mg of the diuretic furosemide shortly after tracer injection to clear the tracer via the urine.

All acquisitions were performed using a Discovery MI PET scanner (GE Healthcare) from mid thigh to vertex, including the upper limbs. One hour after injection, a low-dose CT acquisition was initiated, followed immediately by a PET acquisition (3–5 overlapping bed positions, 2 min each). All PET images were reconstructed using a 3-dimensional time-of-flight weighted line-of-response row-action maximum-likelihood algorithm, with attenuation correction derived from the CT attenuation map. The accuracy of the absolute count calibration of the scanner was validated against a uniform phantom containing ^{18}F at a known concentration. The measured activity was expressed as SUV for each voxel.

Image Analysis

Images were visualized and analyzed using MIM software, version 6.0 (MIM Software Inc.). Images were qualitatively evaluated with a focus on the apparent extent of the lower-abdomen background uptake emanating from the intestinal radioactive content by a nuclear medicine specialist. A region of interest (ROI) covering the whole abdomen and excluding the liver, bladder, and uterus was drawn. An arbitrary SUV threshold of more than 4, corresponding to a background value for which 80% of primary tumors observed during this study would be undetected or equivocal with 4FMFES PET, was applied to the ROI, and the volume of the resulting contour was extracted.

A volumetric ROI was drawn on each detectable tumor focus, and ROIs were also drawn in the area surrounding tumors (tumor background). The maximum-intensity voxel (SUV_{max}) was taken for tumor and uterine ROI quantification, whereas the averaged value of the voxels included in the ROIs (SUV_{mean}) was used for background regions. Tumor contrast was evaluated by the ratio of tumor uptake to its proximal background (T/B). Tumors with a T/B of less than 3.0 were considered equivocal.

Statistical Analysis

Data were reported as mean $\pm$ SD for patient numbers of 3 or more or as mean only for patient numbers of less than 3. Statistical analyses were performed using Prism software, version 7.0.4 (GraphPad Software Inc.). One-way ANOVA using the Tukey method for multiple comparisons was applied to compare [18]F-4FMFES and ^{18}F-FDG uptake, ^{18}F-FDG/[18]F-4FMFES uptake ratio, and T/Bs in tumors. The threshold for significance was set a priori to a P value of less than 0.05 for each compared group.

RESULTS

Drug-Induced Intestinal [18]F-4FMFES Slowdown

As was observed in the past with breast cancer patients (23,24), the natural elimination pathway of [18]F-4FMFES generated extensive abdominal contamination without any additional intervention (Fig. 1A). Both the use of 4 mg of loperamide 5 min before [18]F-4FMFES injection and the use of repeated injection of 20 mg of hyoscine

TABLE 1
Patient Characteristics

Parameter	Data
Patients (n)	25
Mean age ± SD (y)	63.4 ± 10.5 (median, 66; range, 41–79)
Premenopausal (n)	4
Postmenopausal (n)	21
Histology (n)	
Endometrial carcinoma	23
Endometrial intraepithelial neoplasia	2
Grade (n)	
1	5
2	12
3	8
Treatment (n)	
Loperamide (4 mg)	12
Hyoscine N-butylbromide (3 × 20 mg)	11
None	2 (plus 31 breast cancer patients (23))

N-butylbromide at 0, 20, and 40 min after ^{18}F-4FMFES injection appeared to be successful to slow progression of the radioactive intestinal bolus. The use of the diuretic furosemide along with ^{18}F-4FMFES injection reduced the bladder volume and uptake in most patients. Together, the combination of furosemide and hyoscine N-butylbromide improved the diagnostic quality of ^{18}F-4FMFES PET for endometrial cancers (Fig. 1A).

Application of an SUV threshold of more than 4 on an abdominal ROI allowed standardized estimation of the intestinal volume containing significant contamination with ^{18}F-4FMFES radiometabolites (Fig. 1B). In the absence of intervention, the measured volume reached 1,117.8 ± 413.4 mL, which was significantly reduced by the administration of either loperamide (677.9 ± 471.2 mL; $P < 0.01$) or hyoscine N-butylbromide (495.7 ± 341.9 mL; $P < 0.001$). However, the background ^{18}F-4FMFES uptake in the immediate vicinity of the primary endometrial tumor was not significantly different between the control (SUV$_{mean}$, 0.66 ± 0.12), loperamide (SUV$_{mean}$, 0.58 ± 0.13), and hyoscine N-butylbromide (SUV$_{mean}$, 0.63 ± 0.15) groups.

PET Image Qualitative Assessment

Both ^{18}F-FDG and ^{18}F-4FMFES PET were able to produce high-contrast visualization of endometrial carcinoma (Fig. 2). Two patients had sentinel node involvement, with sizes ranging from 2 to 5 mm in diameter according to pathology and lymphoscintigraphy. Those tumors could not be detected by PET imaging with either tracer and were considered within the reference range by CT. One patient had an endometroid endometrial adenocarcinoma that was detectable only using ^{18}F-4FMFES PET; the ^{18}F-FDG PET examination had negative results (Fig. 3). Pathologic examination of the surgical specimen confirmed the presence of a 2-cm grade 1 endometroid tumor. Two patients yielded a ubiquitous ^{18}F-FDG uptake (T/B, 1.9 and 2.2, respectively) that was clearly detected using ^{18}F-4FMFES PET (SUV$_{max}$, 11.1 and 8.5, respectively; T/B, 19.9 and 18.9, respectively). Two other patients harbored subcentimeter endometrial intraepithelial neoplasia tumors, both of which were better visualized using ^{18}F-4FMFES (average SUV$_{max}$, 5.7; T/B, 11.7) than ^{18}F-FDG (average SUV$_{max}$, 3,1; T/B, 4.8).

In 1 patient, ^{18}F-FDG PET spotted an inguinal node focus (SUV$_{max}$, 5.2; T/B, 7.2) that was ^{18}F-4FMFES–negative, but control ^{18}F-FDG PET/CT at a later time showed reduced uptake and a stable size reminiscent of a benign node (Fig. 4). ^{18}F-FDG PET was thus considered false-positive for this node assessment. Another patient had an ^{18}F-4FMFES–positive (SUV$_{max}$, 3.0; T/B, 5.0), ^{18}F-FDG–negative right iliac sentinel node (Fig. 5). Ten nodes were dissected at surgery (including the suspected one); all were negative on pathologic examination, and a control ^{18}F-FDG PET examination at 9 mo after the initial assessment showed no abnormal uptake at this site, indicating a false-positive result for ^{18}F-4FMFES for this patient.

Semiquantitative Assessment

Average endometrial tumor uptake on ^{18}F-4FMFES PET (SUV$_{max}$, 9.4 ± 3.2; range, 3.0–14.4) was slightly higher than on ^{18}F-FDG PET (SUV$_{max}$, 7.5 ± 5.1; range, 0–22.0), but the difference was not significant. Uptake did not significantly differ between endometroid tumors and endometrial carcinomas with either tracer (Fig. 6A). ^{18}F-FDG uptake followed a continuous increase according to grade, with a significant difference between grade 1 tumors (SUV$_{max}$, 4.0 ± 2.0) and grade 2 tumors (SUV$_{max}$, 8.0 ± 4.9; $P < 0.05$) and between grade 1 tumors and grade 3 tumors (SUV$_{max}$, 9.7 ± 3.0; $P < 0.01$). ^{18}F-4FMFES uptake peaked in grade 2 tumors at an SUV$_{max}$ of 11.4 ± 2.3, which was significantly higher than in grade 1 tumors (SUV$_{max}$, 6.9 ± 2.6; $P < 0.05$) but was not significantly different from grade 3 tumors (SUV$_{max}$, 9.2 ± 3.1; $P = 0.53$) (Fig. 6A).

Contrast values, as defined by T/Bs, were 2.3-fold higher ($P < 0.0001$) for ^{18}F-4FMFES than for ^{18}F-FDG (16.9 ± 6.3 and 7.4 ± 4.6,

FIGURE 1. (A) Qualitative maximum-intensity-projection whole-body assessment of effect of pharmacologic interventions to slow progression of radioactive intestinal bolus. Without use of any intervention (left panel), ^{18}F-4FMFES PET typically produces intense abdominal uptake caused by progression of radiometabolites excreted by gallbladder in intestines. Ingestion of 4 mg of loperamide 15 min before injection of radiotracer yielded mitigated results (center panel). Repeated intravenous injection of 20 mg of hyoscine N-butylbromide at 0, 20, and 40 min after ^{18}F-4FMFES injection apparently reduced lower-abdomen background and slowed transit of radioactive intestinal bolus (right panel). (B) Measured volume extracted from application of SUV threshold of >4 on abdominal ROI. Both use of loperamide and use of hyoscine N-butylbromide significantly reduced intestinal background volume. **$P < 0.01$. ****$P < 0.001$.

FIGURE 2. Representative case of endometrial carcinoma (arrows) imaged with ^{18}F-FDG PET/CT (top row) and ^{18}F-4FMFES PET/CT (bottom row), displayed in frontal maximum-intensity projection (MIP) and in sagittal views.

respectively). T/Bs significantly differed between grade 1 tumors (10.5 $\pm$ 3.8) and grade 2 tumors (18.0 $\pm$ 4.4; $P < 0.01$) and grade 3 tumors (17.5 $\pm$ 5.6; $P < 0.05$) using ^{18}F-4FMFES PET (Fig. 6B). Such T/B relationships according to grade were not found for ^{18}F-FDG PET (Fig. 6B), as the slight differences observed were not significantly different.

The ^{18}F-FDG/^{18}F-4FMFES uptake ratio was also measured according to grade (Fig. 6C), similarly to previous publications (13–15,17). Although the ^{18}F-FDG/^{18}F-4FMFES ratio was similar between grade 1 and 2 tumors (0.65 $\pm$ 0.35 and 0.77 $\pm$ 0.40, respectively), a significant increase ($P < 0.05$) over grade 1 was observed for grade 3 tumors, with a value of 1.25 $\pm$ 0.64.
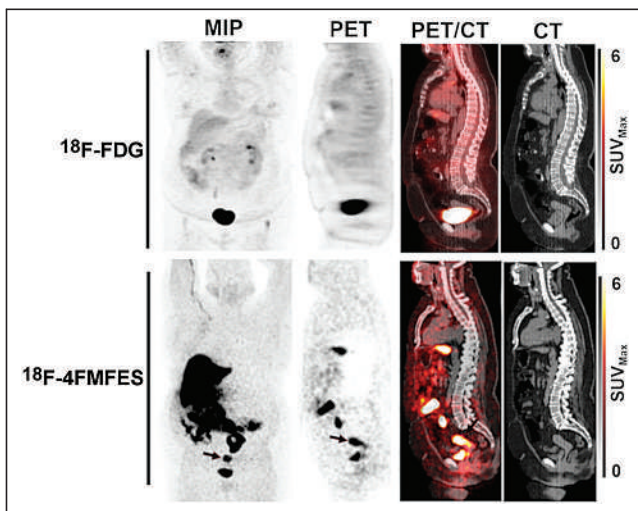
FIGURE 3. A 69-y-old endometroid adenocarcinoma patient with ^{18}F-FDG–negative, ^{18}F-4FMFES–positive primary tumor. ^{18}F-FDG PET did not yield any abnormal uptake in uterus, whereas ^{18}F-4FMFES PET revealed intense signal (SUV$_{max}$, 9.6; arrows) over 44 $\times$ 32 $\times$ 25 mm region. Postsurgery pathology report measured size of tumor to be 20 mm in its long axis, meaning ^{18}F-4FMFES overestimated size of tumor in this case.

DISCUSSION

In this preliminary assessment, the use of combined ^{18}F-FDG and ^{18}F-4FMFES PET imaging was investigated in recently diagnosed ER+ endometrial cancer patients. At first, the application of interventions aiming to slow progression of the radioactive intestinal bolus after ^{18}F-4FMFES injection to improve image quality in the abdomen produced variable results. Baseline ^{18}F-4FMFES image quality in the abdominal region was relatively poor because of the abundant presence of radioactive intestinal content. Predosing with loperamide, a peripheral opioid used mainly for control of diarrhea, moderately reduced the distribution of the abdominal contamination. Increasing the dosage of loperamide might yield better results, at the cost of the associated discomfort of prolonged constipation for the patient. In contrast, repeated injection of hyoscine *N*-butylbromide during tracer administration, a routine procedure for radiologic assessment of the intestines, substantially slowed transit of the intestinal content and improved overall abdominal ^{18}F-4FMFES image quality in assessed patients. Even if the PET/CT assessment of anatomic planes usually allows distinction between the uterus and the intestines, and even if the pharmacologic interventions do not impact the uterine region background, such an intervention might be useful for nonambiguous diagnosis of locoregional metastases using ^{18}F-4FMFES PET in advanced-stage patients.

Although both tracers yielded similar uptake overall in endometrial tumors, detectability was noticeably improved using ^{18}F-4FMFES over
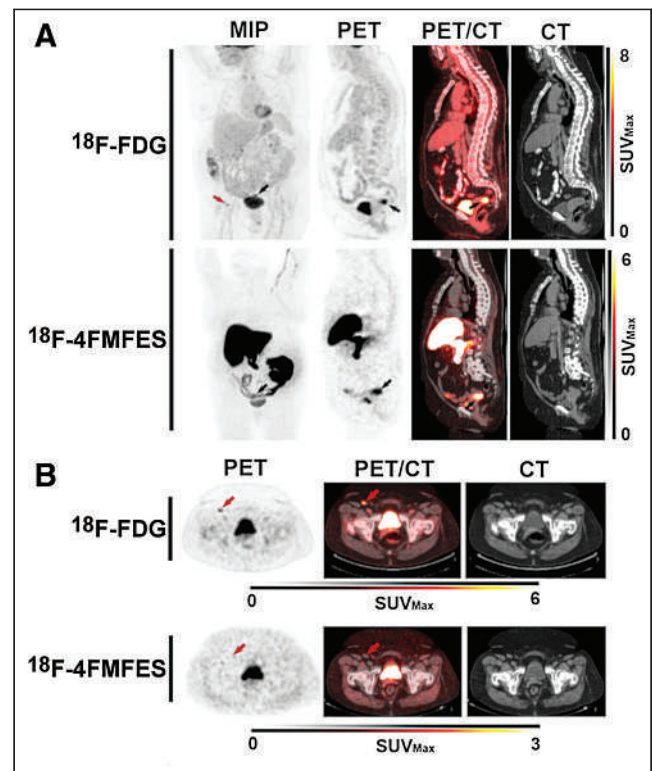
FIGURE 4. A 75-y-old endometroid adenocarcinoma patient with ^{18}F-FDG false-positive inguinal node. (A) Endometroid adenocarcinoma primary tumor, with SUV$_{max}$ uptake of 12.3 for ^{18}F-FDG and 8.9 for ^{18}F-4FMFES (black arrows). The ^{18}F-FDG PET also revealed a suspected right inguinal node metastasis (red arrow), which yielded SUV$_{max}$ of 5.2 (T/B, 7.2). (B) Transaxial slices of the suspected inguinal node metastasis (red arrows). The ^{18}F-FDG–positive node was ^{18}F-4FMFES–negative and of normal appearance in CT image. Pathology examination considered inguinal node as normal, meaning ^{18}F-FDG signal was false-positive.
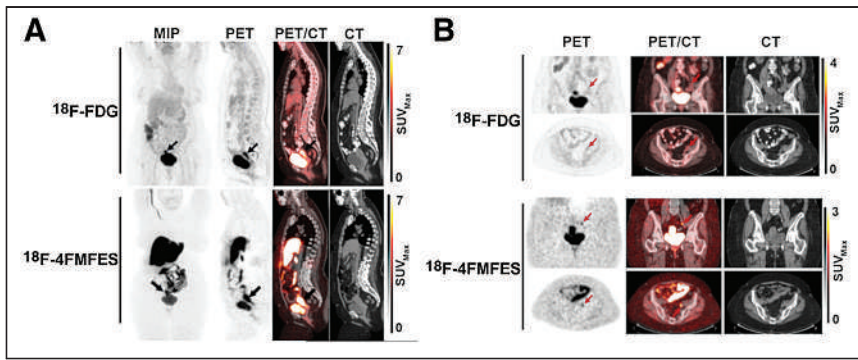
FIGURE 5. A 67-y-old endometrial carcinoma patient with ^{18}F-4FMFES false-positive iliac node. (A) Endometrial carcinoma primary tumor, with SUV$_{max}$ uptake of 12.9 for ^{18}F-FDG and 12.7 for ^{18}F-4FMFES (arrows). (B) Coronal (top) and transaxial (bottom) views centered on suspected left iliac sentinel node metastasis with ^{18}F-4FMFES (arrows), which was of normal aspect in CT images. Pathology examination after surgery considered iliac node normal, confirming false-positive result for ^{18}F-4FMFES.

^{18}F-FDG, as measured by the increased T/B obtained. As a result, all primary tumors assessed were clearly visualized using ^{18}F-4FMFES PET, whereas 2 patients obtained a ubiquitous signal (T/B < 3) at the tumor site using ^{18}F-FDG PET. Moreover, 1 patient was ^{18}F-FDG–negative

FIGURE 6. Semiquantitative ^{18}F-FDG and ^{18}F-4FMFES uptake and T/Bs. (A) ^{18}F-FDG and ^{18}F-4FMFES uptake (SUV$_{max}$) for whole sample (left) and according to grade (right) (B) ^{18}F-FDG and ^{18}F-4FMFES T/Bs for whole studied sample (left) and according to grade (right). (C) ^{18}F-FDG and ^{18}F-4FMFES T/Bs according to grade. $*P < 0.05$. $**P < 0.01$. $****P < 0.001$.

and ^{18}F-4FMFES+, with CT and surgical-sample examination instead showing the presence of a 20-mm tumor and confirming a false-negative result for ^{18}F-FDG. One patient presented with suspected sentinel node uptake on ^{18}F-FDG PET that was negative on ^{18}F-4FMFES PET, but its subsequent biopsy invalidated the presence of cancer in the assessed tissue, meaning a false-positive result for ^{18}F-FDG. Only 1 confirmed false-positive case was found for ^{18}F-4FMFES PET, in which a node with substantial ^{18}F-4FMFES uptake (and ^{18}F-FDG–negative) was exempt from cancer cells in the pathologic examination. Although anecdotal, those few examples in our relatively modest sample size might suggest a better overall sensitivity and specificity for ^{18}F-4FMFES over ^{18}F-FDG in ER+ endometrial cancers, as well as a good complementarity between the 2 tracers.

The 2 cases of endometrial interepithelial neoplasia observed so far in our study showed a slightly higher uptake for ^{18}F-4FMFES than for ^{18}F-FDG, along with a 2.4-fold higher T/B, and as such it could be interesting to investigate further the use of ^{18}F-4FMFES PET for this hard-to-detect small-sized subclass of endometrial tumor. Of equal interest would be other less frequent uterine cancers that were previously investigated with ^{18}F-FES PET, including ER+ mesenchymal (*13*) and sarcoma (*15*) tumors, and our group will actively seek to recruit patients harboring those subtypes during the ongoing trial.

A significantly higher tumor uptake of ^{18}F-4FMFES was observed for grade 1 tumors than for grade 2 tumors, whereas ^{18}F-FDG PET uptake was significantly different between grade 1 and grade 2 and 3 tumors. This trend contradicts a previously published result showing that grade 1 cancers yielded significantly higher ^{18}F-FES uptake than higher-grade tumors (*12*)—a result that will need to be further investigated. T/Bs for ^{18}F-FDG were unable to discern between grades. In contrast, ^{18}F-4FMFES T/Bs were able to properly differentiate low-grade tumors from grade 2 and 3 tumors. As such, both ^{18}F-4FMFES uptake and T/Bs can be useful to distinguish between low- and high-grade endometrial tumors.

The ^{18}F-FDG/^{18}F-4FMFES uptake ratio was also measured. A significantly higher ^{18}F-FDG/^{18}F-4FMFES ratio was measured for grade 3 than for grade 1 tumors, similar to what was previously observed for the ^{18}F-FDG/^{18}F-FES ratio in endometrial cancers (*12,14,15,17*). A higher ^{18}F-FDG/^{18}F-FES ratio also correlated with worse progression-free and overall survival (*17*). As such, the ^{18}F-FDG/^{18}F-4FMFES ratio could equal the usefulness of the previously evaluated ^{18}F-FDG/^{18}F-FES ratio in differentiating tumors of different grades or patient outcomes.

So far, all recruited patients have been newly diagnosed and at an early stage, thus disabling any comparison of ^{18}F-FDG and ^{18}F-4FMFES according to stage. In view of a previous study (*12*) in which a nonsignificant trend toward lower ^{18}F-FES uptake and higher ^{18}F-FDG uptake was observed for advanced endometrial cancers, the same tendency is expected using the similar ^{18}F-4FMFES tracer. A related drawback of this low-stage patient sample is the lack of metastatic disease in this study. Although the assessment of primary tumors with ^{18}F-4FMFES PET was an essential first step in evaluating the endometrial tumor–targeting properties of the tracer, PET imaging procedures are expected to reach their full usefulness on patients with

disseminated diseases that are more challenging to adequately assess using standard procedures. Further studies will be needed to evaluate [18]F-4FMFES PET in advanced endometrial cancer.

CONCLUSION

It is possible to lessen [18]F-4FMFES abdominal background uptake using hyoscine *N*-butylbromide. Both ^{18}F-FDG and [18]F-4FMFES PET are suitable for detection of ER+ endometrial cancers, although tumor contrast is better with [18]F-4FMFES than with ^{18}F-FDG.

DISCLOSURE

ACKNOWLEDGMENTS

KEY POINTS

QUESTION: Will [18]F-4FMFES PET, along with pharmaceutic interventions to reduce abdominal background uptake, improve the detection of ER+ endometrial cancers and allow grade segmentation in combination with ^{18}F-FDG PET?

PERTINENT FINDINGS: The use of hyoscine *N*-butylbromide in repeated intravenous injection significantly reduced the extent of the abdominal background uptake resulting from the natural elimination of [18]F-4FMFES. [18]F-4FMFES PET yielded better tumor contrast than did ^{18}F-FDG PET in ER+ endometrial cancers. Both tracers succeeded in distinguishing between low- and high-grade cancers.

IMPLICATIONS FOR PATIENT CARE: Because of the high tumor contrast it displays, [18]F-4FMFES PET in combination with repeated injection of hyoscine *N*-butylbromide may improve the locoregional and whole-body assessment of advanced ER+ endometrial cancers, compared with ^{18}F-FDG PET.

REFERENCES

1. Bray F, Ferlay J, Soerjomataram I, Siegel RL, Torre LA, Jemal A. Global cancer statistics 2018: GLOBOCAN estimates of incidence and mortality worldwide for 36 cancers in 185 countries. *CA Cancer J Clin.* 2018;68:394–424.
2. Köbel M, Atenafu EG, Rambau PF, et al. Progesterone receptor expression is associated with longer overall survival within high-grade histotypes of endometrial carcinoma: a Canadian high-risk endometrial cancer consortium (CHREC) study. *Gynecol Oncol.* 2016;141:559–563.
3. Vahrenkamp JM, Yang CH, Rodriguez AC, et al. Clinical and genomic crosstalk between glucocorticoid receptor and estrogen receptor α in endometrial cancer. *Cell Rep.* 2018;22:2995–3005.
4. Tomica D, Rami S, Danoli D, Šušnjar L, Peri-Balja M, Puljiz M. Impact of oestrogen and progesterone receptor expression in the cancer cells and myometrium on survival of patients with endometrial cancer. *J Obstet Gynaecol.* 2018;38:96–102.
5. Zhang Y, Zhao D, Gong C, et al. Prognostic role of hormone receptors in endometrial cancer: a systematic review and meta-analysis. *World J Surg Oncol.* 2015;13:208.
6. Thigpen T, Brady MF, Homesley HD, Soper JT, Bell J. Tamoxifen in the treatment of advanced or recurrent endometrial carcinoma: a Gynecologic Oncology Group study. *J Clin Oncol.* 2001;19:364–367.
7. Rieber A, Nussle K, Stohr I, et al. Preoperative diagnosis of ovarian tumors with MR imaging: comparison with transvaginal sonography, positron emission tomography, and histologic findings. *AJR.* 2001;177:123–129.
8. Kakhki VR, Shahriari S, Treglia G, et al. Diagnostic performance of fluorine-18 fluorodeoxyglucose positron emission tomography imaging for detection of primary lesion and staging of endometrial cancer patients: systematic review and metaanalysis of the literature. *Int J Gynecol Cancer.* 2013;23:1536–1543.
9. Narayanan P, Sahdev A. The role of ^{18}F-FDG PET CT in common gynaecological malignancies. *Br J Radiol.* 2017;90:20170283.
10. Yu JQ, Doss M, Alpaugh RK. Normal variants and pitfalls encountered in PET assessment of gynecologic malignancies. *PET Clin.* 2018;13:249–268.
11. Lakhani A, Khan SR, Bharwani N, et al. FDG PET/CT pitfalls in gynecologic and genitourinary oncologic imaging. *Radiographics.* 2017;37:577–594.
12. Tsujikawa T, Yoshida Y, Kiyono Y, et al. Functional oestrogen receptor α imaging in endometrial carcinoma using 16α-[^{18}F]fluoro-17β-oestradiol PET. *Eur J Nucl Med Mol Imaging.* 2011;38:37–45.
13. Zhao Z, Yoshida Y, Kurokawa T, Kiyono Y, Mori T, Okazawa H. ^{18}F-FES and ^{18}F-FDG PET for differential diagnosis and quantitative evaluation of mesenchymal uterine tumors: correlation with immunohistochemical analysis. *J Nucl Med.* 2013;54:499–506.
14. Tsujikawa T, Yoshida Y, Mori T, et al. Uterine tumors: pathophysiologic imaging with 16α-[^{18}F]fluoro-17β-estradiol and ^{18}F fluorodeoxyglucose PET: initial experience. *Radiology.* 2008;248:599–605.
15. Yamamoto M, Tsujikawa T, Yamada S, et al. ^{18}F-FDG/^{18}F-FES standardized uptake value ratio determined using PET predicts prognosis in uterine sarcoma. *Oncotarget.* 2017;8:22581–22589.
16. van Kruchten M, Hospers GA, Glaudemans AW, Hollema H, Arts HJ, Reyners AK. Positron emission tomography imaging of oestrogen receptor-expression in endometrial stromal sarcoma supports oestrogen receptor-targeted therapy: case report and review of the literature. *Eur J Cancer.* 2013;49:3850–3855.
17. Yamada S, Tsuyoshi H, Yamamoto M, et al. Prognostic value of 16α-^{18}F-fluoro-17β-estradiol PET as a predictor of disease outcome in endometrial cancer: a prospective study. *J Nucl Med.* 2021;62:636–642.
18. Mankoff DA, Tewson TJ, Eary JF. Analysis of blood clearance and labeled metabolites for the estrogen receptor tracer [F-18]-15α-fluorestradiol (FES). *Nucl Med Biol.* 1997;24:341–348.
19. Tewson TJ, Mankoff DA, Peterson LM, Woo I, Petra P. Interactions of 16α-[^{18}F]-fluoroestradiol (FES) with sex steroid binding protein (SBP). *Nucl Med Biol.* 1999;26:905–913.
20. Seimbille Y, Ali H, van Lier JE. Synthesis of 2,16α- and 4,16α-difluoroestradiols and their 11β-methoxy derivatives as potential estrogen receptor-binding radiopharmaceuticals. *J Chem Soc Perkin Trans.* 2002;1:657–663.
21. Seimbille Y, Rousseau J, Bénard F, et al. ^{18}F-labeled difluoroestradiols: preparation and preclinical evaluation as estrogen receptor-binding radiopharmaceuticals. *Steroids.* 2002;67:765–775.
22. Beauregard JM, Croteau E, Ahmed N, van Lier JE, Bénard F. Assessment of human biodistribution and dosimetry of 4-fluoro-11β-methoxy-16α-^{18}F-fluoroestradiol using serial whole-body PET/CT. *J Nucl Med.* 2009;50:100–107.
23. Paquette M, Lavallée É, Phoenix S, et al. Improved estrogen receptor assessment by PET using the novel radiotracer 4FMFES in ER+ breast cancer patients: an ongoing phase II clinical trial. *J Nucl Med.* 2018;59:197–203.
24. Paquette M, Lavallée É, Phoenix S, et al. Combined FDG and 4FMFES PET imaging in ER+ breast cancer patients for improved diagnostic and prognostic value [abstract]. *Eur J Nucl Med Mol Imaging.* 2017;44(suppl 2):OP-302.
25. Groheux D, Giacchetti S, Moretti JL, et al. Correlation of high ^{18}F-FDG uptake to clinical, pathological and biological prognostic factors in breast cancer. *Eur J Nucl Med Mol Imaging.* 2011;38:426–435.
26. Koo HR, Park JS, Kang KW, et al. ^{18}F-FDG uptake in breast cancer correlates with immunohistochemically defined subtypes. *Eur Radiol.* 2014;24:610–618.
27. Kurland BF, Peterson LM, Lee JH, et al. Estrogen receptor binding (FES PET) and glycolytic activity (FDG PET) predict progression-free survival on endocrine therapy in patients with ER+ breast cancer. *Clin Cancer Res.* 2017;23:407–415.
28. Ahmed N, Langlois R, Rodrigue S, Benard F, van Lier JE. Automated synthesis of 11β-methoxy-4,16α-[16α-^{18}F]difluoroestradiol (4F-M[^{18}F]FES) for estrogen receptor imaging by positron emission tomography. *Nucl Med Biol.* 2007;34:459–464.

^{18}F-FLT PET/CT as a Prognostic Imaging Biomarker of Disease-Specific Survival in Patients with Primary Soft-Tissue Sarcoma

Joseph G. Crompton*[1], Wesley R. Armstrong*[2], Mark A. Eckardt[3], Ameen Seyedroudbari[2], William D. Tap[4], Sarah M. Dry[5], Evan R. Abt[2], Jeremie Calais[2], Ken Herrmann[6], Johannes Czernin[2], Fritz C. Eilber[1], and Matthias R. Benz[2,6]

[1]Division of Surgical-Oncology, Department of Surgery, UCLA, Los Angeles, California; [2]Ahmanson Translational Theranostics Division, Department of Molecular and Medical Pharmacology, UCLA, Los Angeles, California; [3]Department of Surgery, Yale School of Medicine, New Haven, Connecticut; [4]Department of Medicine, Sarcoma Medical Oncology Service, Memorial Sloan Kettering Cancer Center, New York, New York; [5]Department of Pathology, UCLA, Los Angeles, California; and [6]Department of Nuclear Medicine, University of Duisburg–Essen and German Cancer Consortium–University Hospital Essen, Essen, Germany

The purpose of this study was to evaluate ^{18}F-FLT PET/CT as an early prognostic imaging biomarker of long-term overall survival and disease-specific survival (DSS) in soft-tissue sarcoma (STS) patients treated with neoadjuvant therapy (NAT) and surgical resection. **Methods:** This was a 10-y follow-up of a previous single-center, single-arm prospective clinical trial. Patients underwent ^{18}F-FLT PET/CT before treatment (PET1) and after NAT (PET2). Posttreatment pathology specimens were assessed for tumor necrosis or fibrosis and for Ki-67 and thymidine kinase 1 expression. Maximally selected cutoffs for PET and histopathologic factors were applied. Survival was calculated from the date of subject consent to the date of death or last follow-up. **Results:** The study population consisted of 26 patients who underwent PET1; 16 of the 26 with primary STS underwent PET2. Thirteen deaths occurred during a median follow-up of 104 mo. In the overall cohort, overall survival was longer in patients with a low than a high PET1 tumor SUV_{max} (dichotomized by an SUV_{max} of ≥8.5 vs. <8.5: not yet reached vs. 49.7 mo; $P = 0.0064$). DSS showed a trend toward significance ($P = 0.096$). In a subanalysis of primary STS, DSS was significantly longer in patients with a low PET1 tumor SUV_{max} (dichotomized by an SUV_{max} of ≥8 vs. <8; $P = 0.034$). There were no significant ^{18}F-FLT PET response thresholds corresponding to DSS or overall survival after NAT at PET2. **Conclusion:** ^{18}F-FLT PET may serve as a prognostic baseline imaging biomarker for DSS in patients with primary STS.

Key Words: ^{18}F-FLT PET; sarcoma; imaging biomarker

Soft-tissue sarcomas (STSs) comprise approximately 1% of adult cancers (*1*) but constitute a family of more than 50 histotypes (*2*) that present quite differently in biologic characteristics and clinical behavior.

Histologic tumor grading by the French Federation of Cancer Centers Sarcoma Group (FNCLCC) is regarded as the gold standard for prognostication and guides the clinical management of STS patients (*3*). The distinction between low, intermediate, and high grade is determined by 3 parameters: differentiation, mitotic activity, and the extent of tumor necrosis. However, the FNCLCC system has several limitations, including lack of applicability to all sarcoma histotypes, inherent difficulty in reproducibly assessing sarcoma differentiation, and undersampling from core-needle biopsy (*4,5*). In addition, the FNCLCC system was developed on untreated tumors. Grading on post–neoadjuvant therapy (NAT) resections in STS is not advised since tumor necrosis cannot be distinguished from NAT-induced necrosis.

Genomic tests might in the future replace or complement current histologic grading in STS (*6*). The complexity index in sarcomas is a prognostic gene expression signature that comprises 67 genes involved in pathways of mitosis control and chromosome segregation (*7*). The complexity index in sarcomas has been identified as a better prognostic factor of metastasis-free survival than the FNCLCC system, irrespective of the STS histotype (*7*).

Proliferative activity–dependent accumulation of 3′-deoxy-3′-fluorothymidine (^{18}F-FLT) has been demonstrated for a variety of solid and hematologic neoplasms; however, varying degrees of correlation between ^{18}F-FLT uptake and histologic markers of proliferation, such as Ki-67, have been reported (*8,9*).

In the current study, we correlated ^{18}F-FLT uptake at pre- and post-NAT PET, changes in ^{18}F-FLT uptake, and post-NAT histologic variables (percentage tumor necrosis, Ki-67, and thymidine kinase 1 [TK1] expression) with overall survival and disease-specific survival (DSS) in patients previously enrolled in a prospective single-center, single-arm exploratory study. The hypothesis was that ^{18}F-FLT PET might be used as a prognostic imaging biomarker of DSS in patients with STS.

MATERIALS AND METHODS

Study Design and Patients

Between October 2008 and September 2009, 26 patients with high-grade STS and 1 patient with osteosarcoma were enrolled in a prospective single-center, single-arm exploratory study that investigated the cell proliferation response to NAT as measured by ^{18}F-FLT PET/CT

TABLE 1
Clinical and Pathologic Characteristics ($n = 26$)

Characteristic	Data
Median age (y)	63 (range, 26–94)
Sex	
Male	13 (50%)
Female	13 (50%)
Site	
Extremity	12 (46%)
Chest/trunk	8 (31%)
Retroperitoneal/abdominal	6 (23%)
Presentation status	
Primary	17 (65%)
Primary + contemporary history of secondary malignancy	2 (8%)
Recurrent or residual	7 (27%)
Tumor size	
<5 cm	6 (23%)
5–10 cm	13 (50%)
>10 cm	7 (27%)
Histology	
NOS	7 (27%)
MPNST	3 (12%)
Gastrointestinal stromal tumor	3 (12%)
Angiosarcoma	2 (8%)
Leiomyosarcoma	5 (19%)
Fibromyxoid sarcoma	3 (12%)
Pleomorphic liposarcoma	1 (4%)
Dedifferentiated liposarcoma	1 (4%)
Synovial sarcoma	1 (4%)

NOS = sarcoma not otherwise specified; MPNST = malignant peripheral nerve sheath tumor.
Data are number followed by percentage in parentheses, except for age.

TABLE 2
Treatment Characteristics ($n = 26$)

Characteristic	Data
NAT	
CTx (including Gleevec)	11 (42%)
CRTx	10 (38%)
RTx	2 (8%)
No neoadjuvant	3 (12%)
Surgery	24 (92%)
Adjuvant therapy	
CTx	11 (42%)
CRTx	3 (12%)
RTx	2 (8%)
No adjuvant therapy	6 (23%)
Incomplete records	4 (15%)
Recurrent therapy	
CTx	3 (12%)
Surgery	3 (12%)
Surgery + CTx	2 (8%)
Surgery + RTx	1 (4%)
Surgery + CRTx	1 (4%)
Recurrence with incomplete records of retreatment	7 (27%)
Incomplete records of recurrence/retreatment	3 (12%)
No recurrence	6 (23%)
Pathologic	
Responder	3 (13%)
Nonresponder	21 (87%)

CTx = chemotherapy; CRTx = chemoradiation therapy; RTx = radiation therapy.
Data are number followed by percentage in parentheses, except for age.

The median interval between treatment initiation and PET1 and between PET1 and PET2 was 0.7 wk (interquartile range [IQR], 0.1–1.5 wk) and 11 wk (IQR, 10–16.7 wk), respectively. The patient demographics and clinical characteristics are summarized in Tables 1 and 2.

Follow-up of patients previously enrolled in IRB trial 07-03-110 was approved by the UCLA IRB, and the necessity for outcome-specific consent was waived by the IRB for the current trial (IRB study 20-001899).

^{18}F-FLT PET/CT Imaging and Analysis

Of the 46 ^{18}F-FLT PET/CT scans, 43 (93%) were performed on a Siemens Biograph 64 TruePoint PET/CT scanner and 3 (7%) on a Siemens Emotion Duo PET/CT scanner approximately 1 h after a median injected activity of 247.9 MBq (IQR, 229.4–255.3 MBq). Intravenous and oral contrast media were administered in 33 scans (72%) and 36 scans (78%), respectively.

Several SUV parameters were assessed on PET 1 and PET2: SUV_{max}, SUV_{peak}, SUV_{mean}, and SUV for total-lesion FLT with a 40%, 50%, 60%, and 80% cutoff of SUV_{max}. Because SUV_{max} proved to be equal or superior to the other PET parameters, we selected SUV_{max} for further analyses. ^{18}F-FLT PET/CT images were interpreted by 1 reader. The

(Institutional Review Board [IRB] trial 07-03-110) (8). This previous study enrolled adult patients (≥18 y) who were scheduled to undergo NAT before surgical resection of a biopsy-proven sarcoma. Exclusion criteria were unresectable disease, performance status preventing the initiation of NAT, systemic therapy within 6 mo of study participation, a synchronous second malignancy, and the inability to tolerate a PET/CT study. For the purpose of the current study, the patient with osteosarcoma was excluded; therefore, the current study population consisted of 26 patients; 19 of the 26 (73%) had primary disease, and 7 (27%) had recurrent or residual disease. Two of the 19 patients with primary disease had a contemporary history of a secondary malignancy (hepatocellular carcinoma and breast cancer).

All 26 patients underwent ^{18}F-FLT PET/CT before initiation of NAT, and 20 patients (77%), after completion of NAT. Six patients did not undergo ^{18}F-FLT PET/CT after NAT (PET2): two of these patients exhibited a low SUV_{max} at ^{18}F-FLT PET/CT before treatment (PET1) (SUV_{max}, 1.7 and 2.0), two had a further diagnostic workup after PET1 that revealed unresectable disease, one had a synchronous secondary malignancy at the time of PET 1 (hepatocellular carcinoma), and one declined to undergo PET2.

reader was aware of the sarcoma diagnosis but not of the treatment regimen or other clinical and outcome data.

Posttreatment pathology specimens were assessed by tumor necrosis or fibrosis and by Ki-67 and TK1 expression as described previously (8).

Treatment

Twenty-three of 26 patients (88%) underwent NAT followed by complete surgical resection. Ten patients (38%) underwent neoadjuvant ifosfamide-based treatments, 5 patients (19%) had gemcitabine-based therapy, 1 patient (4%) underwent treatment with doxorubicin (75 mg/m^2), 1 patient (4%) was treated with paclitaxel (175 mg/m^2) and bevacizumab, and 1 patient (4%) was treated with ridaforolimus as part of a phase II clinical trial. Standard chemotherapy administrations were previously reported (8). Gastrointestinal stromal tumors ($n = 3$; 12%) were treated with imatinib at a dose of 400 mg orally per day. Two patients (8%) received neoadjuvant external-beam radiation only. Ten patients (38%) underwent neoadjuvant chemoradiation therapy. Adjuvant and recurrent treatment regimens are listed in Table 2.

Histopathology

Pathology specimens were reviewed by a pathologist with expertise in sarcoma pathology, as reported previously (8).

Statistics

Quantitative variables are presented as median and IQR or as mean and SD when appropriate. Statistics were performed using R, version 4.0.2 (R Core Team 2020). SUV cutoffs were delineated using maximally selected rank statistics as implemented in the maxstat R package (http://cran.r-project.org/web/packages/maxstat/index.html). Maximally selected rank statistics evaluated the log-rank comparisons of survival along the continuous absolute SUV$_{max}$ spectrum. Selected cutoffs represent the defined highest threshold for statistical discrimination between values along the SUV$_{max}$ spectrum. Dichotomization via median SUV$_{max}$ was not included because the maximally selected SUV$_{max}$ of 8.5 was equivalent to the median SUV$_{max}$ of 8.7 with low ($n = 7$) and high ($n = 10$) groups for both. Changes in SUV$_{max}$ between PET1 and PET2 were dichotomized at a threshold of 60%. Post-NAT tumor necrosis, Ki-67, and TK1 expression were dichotomized at thresholds of at least 95%, 50%, and 18%, respectively. Survival was calculated from the date of subject consent to the date of death or last follow-up. Deaths included in the survival analysis were categorized as disease-specific death or all-cause mortality, which entailed non–disease-specific death and unknown causes of death. Survival was estimated using the method of Kaplan and Meier. A P value less than 0.05 was considered to indicate statistical significance.

RESULTS

Outcome Assessment

The cutoff for last follow-up was January 21, 2021. The median follow-up was 104 mo (maximum, 144.8 mo). The median overall survival was 106 mo (95% CI, 31.9–not yet reached [NYR]).

Eleven patients (42%) had no evidence of disease, 10 patients (38%) died of disease, 2 (8%) were alive with disease, and 3 (12%) died of another cause. The median follow-up in patients alive at the last follow-up date was 104 mo (IQR, 27.8–141.1 mo).

Imaging Characteristics

The tumor SUV$_{max}$ of all patients averaged 6.6 ± 3.7 (median, 7.1; range, 1.7–16.1) and 3.6 ± 2.1 (median, 3.4; range, 0.9–7.9) at PET1 and PET2, respectively (Fig. 1).

The tumor SUV$_{max}$ of primary STS averaged 8.1 ± 4.3 (median, 8.7; range, 1.7–17.5) and 2.8 ± 2.4 (median, 2.3; range, 0–6.9) at PET1 and PET2, respectively.
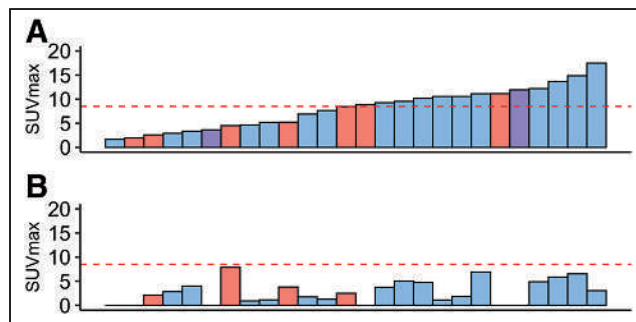
FIGURE 1. Waterfall diagram of SUV$_{max}$ at PET1 (A) and PET2 (B). Primary tumors are depicted in blue, recurrent or residual tumors in red, and patients with history of secondary malignancy in purple. Red line indicates maximally selected SUV$_{max}$ cutoff of 8.5 to dichotomize patients into low and high baseline ^{18}F-FLT uptake.

The tumor size of all patients averaged 8 ± 5 cm (median, 6.4 cm; range, 1.2–20.6 cm) at baseline and decreased to 6.9 ± 3.4 cm (median, 6.1 cm; range, 1.7–14.5 cm) at PET2.

Imaging Biomarkers

PET1. Overall survival was significantly longer in patients with a low than a high tumor SUV$_{max}$ (dichotomized by an SUV$_{max}$ of ≥ 8.5 vs. <8.5: NYR vs. 49.7 mo; $P = 0.0064$) (Fig. 2A). DSS showed a trend toward significance (NYR vs. 49.7 mo; $P = 0.096$) (Fig. 2B).

In a subanalysis of primary STS (17/26 patients), DSS was significantly longer in patients with a low than a high tumor SUV$_{max}$
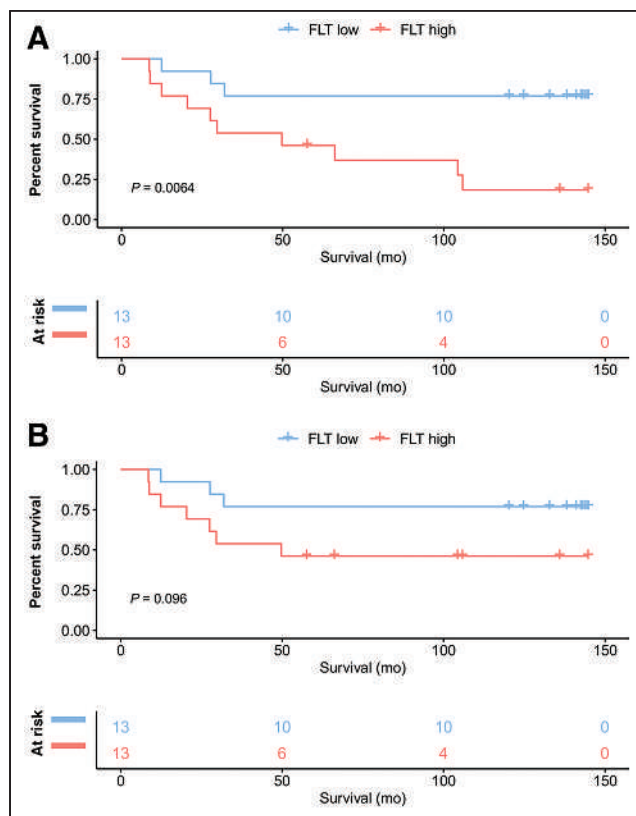
FIGURE 2. Kaplan–Meier curves for overall survival (A) and DSS (B) in all patients ($n = 26$) dichotomized by SUV$_{max}$ of ≥ 8.5 vs. <8.5 at PET1.
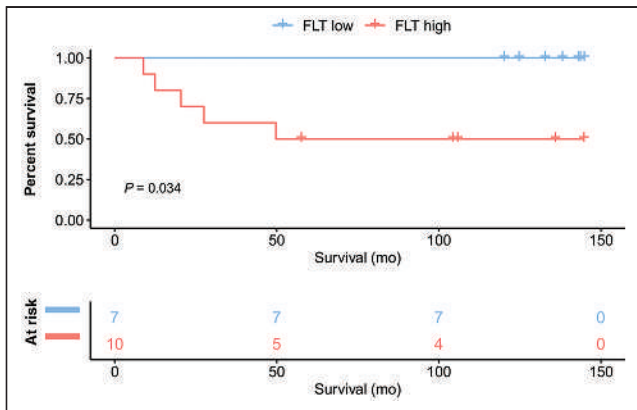
FIGURE 3. Kaplan–Meier curves for DSS in primary STS (17/26 patients) dichotomized by SUV_{max} of ≥ 8.5 vs. <8.5 at PET1.

(dichotomized by an SUV_{max} of ≥ 8 vs <8: NYR vs. NYR; $P = 0.034$) (Fig. 3).

PET2 and Changes Between PET1 and PET2. In primary-STS patients who underwent PET2 ($n = 16/17$), neither absolute PET2 tumor SUV_{max} (dichotomized by an SUV_{max} of ≥ 5 vs. <5: NYR vs. 20.4 mo; $P = 0.25$) nor decreases in SUV_{max} of at least 60% between PET1 and PET2 (NYR vs. NYR; $P = 0.56$) were significantly correlated with DSS survival.

Histopathologic Biomarkers

DSS in primary-STS patients (16/26 patients) with a histopathologic response in the resected specimens after NAT ($n = 3$) did not significantly differ from that in patients without a post-NAT histopathologic response ($n = 13$) (dichotomized by tumor necrosis and fibrosis of $\geq 95\%$ vs. $<95\%$: NYR vs. NYR; $P = 0.86$).

Ki-67 expression was available in 14 of 17 primary-STS patients. DSS showed a trend toward being prolonged in patients with a low ($n = 11$) versus a high post-NAT Ki-67 expression ($n = 3$) (dichotomized by an Ki-67 of $\geq 50\%$ vs. $<50\%$: 27.5 mo vs. NYR; $P = 0.057$) (Supplemental Fig. 1; supplemental materials are available at http://jnm.snmjournals.org).

TK1 expression was available in 14 of 17 primary-STS patients. DSS did not significantly differ between patients with a low post-NAT TK1 expression ($n = 4$) and those with a high post-NAT TK1 expression ($n = 10$) (dichotomized by an TK1 of $\geq 18\%$ vs. $<18\%$: NYR vs. NYR; $P = 0.25$).

DISCUSSION

In this post hoc analysis of patients with STS, low pretreatment ^{18}F-FLT uptake served as an early prognostic imaging biomarker of long-term survival. The prognostic value of ^{18}F-FLT uptake at initial diagnosis has been reported for several malignancies, such as lymphoma (10), non–small cell lung cancer (11), and pancreatic cancer (12). Here, we report the first—to our knowledge—long-term outcomes predicted by baseline ^{18}F-FLT uptake in STS patients who underwent NAT.

Because ^{18}F-FLT uptake in other tumors has frequently been associated with the proliferation rate of cancer cells, therapy-induced alterations in intratumoral ^{18}F-FLT uptake have been proposed as an early imaging biomarker for therapy response and outcome (6–8). However, in this study ^{18}F-FLT uptake after NAT and changes in ^{18}F-FLT uptake across treatment did not significantly correlate with improved survival.

Recent literature surrounding the application of ^{18}F-FLT illustrates that ^{18}F-FLT accumulation is not solely a correlate of tumor cell proliferation rate (13,14). ^{18}F-FLT is a substrate for TK1, a proximal mediator of the pyrimidine salvage pathway that functions in parallel with the de novo pathway to produce deoxythymidine triphosphate for DNA replication and repair (15). Thus, ^{18}F-FLT avidity is influenced by the relative activity of de novo and salvage pathways, which are in turn regulated by substrate abundance, gene expression, and oncogene or tumor suppressor activity (15,16). Uptake of ^{18}F-FLT is not solely isolated to tumor cells and is impacted by the active proliferation of T cells after removal of cytotoxic T-lymphocyte–associated antigen 4 checkpoint inhibition (17). More recently, ^{18}F-FLT uptake in tumors has been shown to be elevated alongside interferon signaling–driven thymidine phosphorylase expression in preclinical xenograft models (18,19). Given that innate and adaptive immune cells are a dominant source of interferon, ^{18}F-FLT uptake could also reflect intratumoral immune cell infiltration and elevated cytokine signaling.

An additional potential reason for discordant ^{18}F-FLT PET findings after NAT in the current study might be the late timing of PET2 12 wk after the start of NAT. The low ^{18}F-FLT uptake at PET2 might in part not represent a cytotoxic treatment effect but viable tumor with low ^{18}F-FLT uptake due to restricted tracer delivery, internalization, and trapping. All considered, future studies investigating ^{18}F-FLT should integrate clinical observations with a detailed molecular and cellular assessment of biopsy tissue, which could enable the identification of molecular mechanisms driving PET probe accumulation.

Several potential limitations of our study merit consideration. First, this was a small pilot study; therefore, it was not adequately powered to detect small differences. For example, patients with a low post-NAT Ki-67 ($\leq 50\%$) and a low post-NAT TK1 ($\leq 18\%$) showed a trend toward a prolonged DSS, but the significance of this finding needs further evaluation. Second, imaging cutoffs were not predefined but maximally selected. Third, patients with a variety of sarcoma subtypes were included in this study.

CONCLUSION

The current study demonstrates that low ^{18}F-FLT uptake at initial diagnosis correlates with long-term survival in primary STS and may be useful in determining treatment strategies. ^{18}F-FLT uptake at post-NAT PET does not improve outcome prediction.

DISCLOSURE

No potential conflict of interest relevant to this article was reported.

KEY POINTS

QUESTION: Can ^{18}F-FLT PET/CT be used as a prognostic imaging biomarker of DSS in patients with STS?

PERTINENT FINDINGS: We report the first long-term outcomes (median follow-up, 104 mo) predicted by ^{18}F-FLT PET/CT before initiation of NAT in patients with STS.

IMPLICATIONS FOR PATIENT CARE: Pretreatment tumor grading guides clinical decision making and prognostication of STS patients. However, given that standard histopathologic grading of STSs has its limitations, new biomarkers are needed to improve clinical management and prognostication and to serve as predictive factors for treatment response.

REFERENCES

1. Siegel RL, Miller KD, Jemal A. Cancer statistics, 2020. *CA Cancer J Clin.* 2020; 70:7–30.

2. Casali PG, Abecassis N, Aro HT, et al. Soft tissue and visceral sarcomas: ESMO-EURACAN Clinical Practice Guidelines for diagnosis, treatment and follow-up. *Ann Oncol.* 2018;29:iv51–iv67.

3. Trojani M, Contesso G, Coindre JM, et al. Soft-tissue sarcomas of adults; study of pathological prognostic variables and definition of a histopathological grading system. *Int J Cancer.* 1984;33:37–42.

4. Coindre JM, Trojani M, Contesso G, et al. Reproducibility of a histopathologic grading system for adult soft tissue sarcoma. *Cancer.* 1986;58:306–309.

5. Lin X, Davion S, Bertsch EC, Omar I, Nayar R, Laskin WB. Federation Nationale des Centers de Lutte Contre le Cancer grading of soft tissue sarcomas on needle core biopsies using surrogate markers. *Hum Pathol.* 2016;56:147–154.

6. Amin MB, Edge S, Greene F, et al., eds. *AJCC Cancer Staging Manual.* 8th ed. Springer International Publishing; 2017.

7. Chibon F, Lagarde P, Salas S, et al. Validated prediction of clinical outcome in sarcomas and multiple types of cancer on the basis of a gene expression signature related to genome complexity. *Nat Med.* 2010;16:781–787.

8. Benz MR, Czernin J, Allen-Auerbach MS, et al. 3′-deoxy-3′-[18F]fluorothymidine positron emission tomography for response assessment in soft tissue sarcoma: a pilot study to correlate imaging findings with tissue thymidine kinase 1 and Ki-67 activity and histopathologic response. *Cancer.* 2012;118:3135–3144.

9. Yap CS, Czernin J, Fishbein MC, et al. Evaluation of thoracic tumors with 18F-fluorothymidine and 18F-fluorodeoxyglucose-positron emission tomography. *Chest.* 2006;129:393–401.

10. Herrmann K, Buck AK, Schuster T, et al. Predictive value of initial 18F-FLT uptake in patients with aggressive non-Hodgkin lymphoma receiving R-CHOP treatment. *J Nucl Med.* 2011;52:690–696.

11. Scheffler M, Zander T, Nogova L, et al. Prognostic impact of [18F]fluorothymidine and [18F]fluoro-D-glucose baseline uptakes in patients with lung cancer treated first-line with erlotinib. *PLoS One.* 2013;8:e53081.

12. Wieder H, Beer AJ, Siveke J, et al. 18F-fluorothymidine PET for predicting survival in patients with resectable pancreatic cancer. *Oncotarget.* 2018;9: 10128–10134.

13. Shields AF. PET imaging of tumor growth: not as easy as it looks. *Clin Cancer Res.* 2012;18:1189–1191.

14. Zhang CC, Yan Z, Li W, et al. [18F]FLT-PET imaging does not always "light up" proliferating tumor cells. *Clin Cancer Res.* 2012;18:1303–1312.

15. Nathanson DA, Armijo AL, Tom M, et al. Co-targeting of convergent nucleotide biosynthetic pathways for leukemia eradication. *J Exp Med.* 2014;211: 473–486.

16. Villa E, Ali ES, Sahu U, Ben-Sahra I. Cancer cells tune the signaling pathways to empower de novo synthesis of nucleotides. *Cancers (Basel).* 2019;11:688.

17. Ribas A, Benz MR, Allen-Auerbach MS, et al. Imaging of CTLA4 blockade-induced cell replication with 18F-FLT PET in patients with advanced melanoma treated with tremelimumab. *J Nucl Med.* 2010;51:340–346.

18. Schelhaas S, Heinzmann K, Honess DJ, et al. 3′-deoxy-3′-[18F]fluorothymidine uptake is related to thymidine phosphorylase expression in various experimental tumor models. *Mol Imaging Biol.* 2018;20:194–199.

19. Eda H, Fujimoto K, Watanabe S, et al. Cytokines induce thymidine phosphorylase expression in tumor cells and make them more susceptible to 5′-deoxy-5-fluorouridine. *Cancer Chemother Pharmacol.* 1993;32:333–338.

Detection of Additional Primary Neoplasms on ^{18}F-Fluciclovine PET/CT in Patients with Primary Prostate Cancer

Ashwin Singh Parihar[1], Lisa R. Schmidt[1], Farrokh Dehdashti[1,2], and Richard L. Wahl[1,2]

[1]Mallinckrodt Institute of Radiology, Washington University School of Medicine, Saint Louis, Missouri; and [2]Siteman Cancer Center, Washington University School of Medicine, Saint Louis, Missouri

The aim of this study was to evaluate the detection rate of incidental second primary neoplasms in patients with prostate cancer on ^{18}F-fluciclovine PET/CT. **Methods:** Imaging reports and patient demographic data were retrospectively reviewed from 663 clinical ^{18}F-fluciclovine PET/CT studies, performed in 601 patients for the assessment of their prostate cancer (643 – recurrence evaluation, 20 – initial staging) from August 2016 to April 2021. Maximum SUV (SUV$_{max}$) of the suspected second neoplasms was determined. The results of ^{18}F-fluciclovine PET/CT were correlated with clinical and radiologic studies to determine the nature of the suspected second neoplasms. **Results:** Fifty-five patients (9.1%) had findings suggestive of a second neoplasm. Thirty-nine of 55 had a known second neoplasm diagnosed before the PET/CT. An incidental second primary neoplasm was first suspected on ^{18}F-fluciclovine PET/CT in 16 of 601 patients (2.7%). Three of the 16 patients had PET/CT suggestive of a meningioma that was corroborated on MRI. Of the remaining 13 patients, 11 had a tissue diagnosis confirming a malignancy. Second malignancies included renal cell carcinoma (RCC; 5/11; 45.5%), urothelial carcinoma ($n = 2$), multiple myeloma, chondrosarcoma, cutaneous squamous cell carcinoma, and squamous cell carcinoma of the esophagus and lung ($n = 1$, each; except for 1 patient with both esophageal and lung carcinomas). Among histopathologically confirmed malignancies, clear-cell RCC had the lowest uptake (SUV$_{max}$ 3.4), and cutaneous squamous cell carcinoma had the highest uptake (SUV$_{max}$ 13.6). Of the 2 patients with no histopathologic confirmation, 1 had ultrasound and MRI findings corroborating the diagnosis of RCC. The other patient had a solitary lung nodule suggestive of primary lung carcinoma and elected to undergo observation. **Conclusion:** Incidental findings consistent with a second primary neoplasm are not infrequently seen on ^{18}F-fluciclovine PET/CT performed for assessment of prostate cancer (9.1%). Of the incidentally detected primary cancers, RCC was the most common (45.5%). These findings indicate the need for a careful analysis of ^{18}F-fluciclovine PET/CT images, due to the broad tumor imaging capabilities of this radiotracer.

Key Words: ^{18}F-fluciclovine; Axumin; FACBC; second malignancy; additional neoplasms; prostate cancer

Anti-1-amino-3-^{18}F-fluorocyclobutane-1-carboxylic acid (^{18}F-fluciclovine) is a radiolabeled, synthetic amino-acid analog that was initially developed for the evaluation of cerebral gliomas, mainly because of its negligible uptake in the normal brain parenchyma (*1*). The uptake of ^{18}F-fluciclovine is mediated by the amino-acid transporters, primarily by the sodium-dependent alanine-serine-cysteine transporter-type 2, ASCT-2, along with the sodium-independent large neutral amino-acid transporter-type 1, LAT-1 (*2*). The uptake of ^{18}F-fluciclovine was incidentally noted in primary and metastatic sites of prostate cancer, leading to further studies and subsequent U.S. Food and Drug Administration approval of ^{18}F-fluciclovine for suspected recurrence of previously treated prostate cancer (*3*).

The amino-acid transporters are overexpressed in several malignancies because of the increased nutrient demands of the cancer cells (*4*). The overexpression of amino-acid transporters formed the basis of exploring the role of ^{18}F-fluciclovine PET/CT in nonprostate malignancies such as breast and lung cancers, renal cell carcinoma (RCC), and gliomas (*5–8*). The detection of additional primary neoplasms on ^{18}F-fluciclovine PET/CT has several implications. First, the understanding that most, if not all, radiotracers are nonspecific to a single cancer type, alerts the reader to the possibility of a second neoplasm when the pattern of disease involvement is discordant with the primary malignancy. Second, raising the suspicion of an additional neoplasm can prompt further investigations, including laboratory workup, imaging, and where appropriate, tissue analysis. Third and most importantly, identification of a second neoplasm can lead to significant changes in management, and prognosis—both in the case of a benign diagnosis, where the management of the primary malignancy can change to a less radical one (especially when the second lesion is the solitary suspected metastatic site) and in the case of a malignant diagnosis, where the treatment would need tailoring to fit in the second malignant diagnosis (and possibly an associated worsening of prognosis) (*9*).

Several single-case reports and short case series have documented the uptake of ^{18}F-fluciclovine PET/CT in multiple nonneoplastic, and nonprostate neoplastic (benign and malignant) entities (*10,11*). This nonspecificity to a single cancer type is not unique to ^{18}F-fluciclovine but is an attribute of most radiopharmaceuticals. Previous studies have described the detection of second primary neoplasms with ^{18}F-FDG, ^{18}F-choline, ^{68}Ga-prostate-specific membrane antigen (PSMA), and several other radiotracers (*12–16*). In the absence of a planned prior study in this space, we performed the present study to evaluate the detection rate of additional primary neoplasms in patients with prostate cancer on ^{18}F-fluciclovine PET/CT.

MATERIALS AND METHODS

Imaging reports and patient demographic data from 663 clinical ^{18}F-fluciclovine PET/CT studies, performed in 601 patients for the assessment of their prostate cancer (643, recurrence evaluation; 20, initial staging) from August 2016 to April 2021, were retrospectively reviewed for the diagnosis of a second neoplasm. The timeline of PET/CT and clinical/laboratory/other imaging studies was reviewed to ascertain the previously unknown neoplasms that were incidentally detected on ^{18}F-fluciclovine PET/CT. PET/CT images of these patients with incidentally detected second neoplasms were reviewed, and regions of interest were drawn to determine the maximum SUV (SUV_{max}) of the suspected lesions and average SUV (SUV_{mean}) of the blood pool (descending thoracic aorta) and bone marrow (L3 vertebra; L2 vertebra if L3 had disease involvement) for comparability. The results of ^{18}F-fluciclovine PET/CT were correlated with clinical and radiologic studies to determine the nature of the suspected second neoplasms. The study was approved by the institutional review board, and the need for written informed consent was waived.

RESULTS

Fifty-five of the 601 patients (9.1%) were diagnosed with a second neoplasm, at any time during their disease course, of which 39 had the diagnosis established before the ^{18}F-fluciclovine PET/CT (Supplemental Table 1; supplemental materials are available at http://jnm.snmjournals.org). An incidental second primary neoplasm was first suspected on ^{18}F-fluciclovine PET/CT in 16 of 601 patients (2.7%), with all 16 studies being performed for recurrence evaluation. Patient and imaging characteristics and management of the second neoplasms are shown in Table 1. Three of the 16 (18.7%) patients had ^{18}F-fluciclovine PET/CT results suggestive of a meningioma (Supplemental Fig. 1) that was corroborated on MRI. Of the remaining 13 patients, 11 had a tissue diagnosis confirming a malignancy. Second malignancies included RCC ($n = 5$; Fig. 1), urothelial carcinoma ($n = 2$; Fig. 2), multiple myeloma, chondrosarcoma, cutaneous squamous cell carcinoma, and squamous cell carcinoma of the esophagus and lung ($n = 1$, each; except for 1 patient with both

TABLE 1
Incidentally Detected Neoplasms on ^{18}F-Fluciclovine PET/CT: Patient and Imaging Characteristics

SN	Age*	PSA (ng/mL)*	Site of second neoplasm	Histopathology	SUV_{max} of lesion	SUV_{mean} of blood-pool	SUV_{mean} of marrow	Management of second neoplasm
1	73	0.81	Left lung - upper lobe	Not done	1.5	1.3	2.7	Observation
2	60	2.59	Right kidney	Not done	3.3	1	4.3	Observation
3	61	3.8	Left kidney	Clear-cell RCC	3.4	1.3	2.4	Partial nephrectomy
4	77	15.4	1. Right lung - lower lobe; 2. Esophagus	Squamous cell carcinoma†	3.4 (lung); 9.2 (esophagus)	1.5	3.6	Chemotherapy (carboplatin), radiation therapy
5	65	1.73	Left kidney	Clear cell RCC	3.7	1.1	3.2	Partial nephrectomy
6	76	0.5	Left kidney	Papillary RCC	3.7	1.3	2.3	Radical nephrectomy, IVC thrombectomy
7	67	6	Proximal right ureter	Urothelial carcinoma	4.1	1.6	4.1	Chemotherapy (carboplatin, gemcitabine)
8	72	1.9	Left kidney	Clear cell RCC	4.9	1.7	4.4	Partial nephrectomy
9	63	2.7	Left acetabulum	Chondrosarcoma	5.8	1.3	2	Chemotherapy (cisplatin, Adriamycin)
10	74	6.7	Left kidney	Clear-cell RCC	6.2	1.3	3.8	Partial nephrectomy
11	61	0.2	Sella	Not done (meningioma - MRI)	8.9	1.6	3.5	Observation
12	88	3.3	Extensive skeletal involvement	Multiple myeloma	9.2	1.4	5.1	Chemotherapy (bortezomib, lenalidomide)
13	48	1.2	Right frontal convexity	Not done (meningioma - MRI)	9.3	1.4	4.4	Observation
14	63	0.93	Urinary bladder	Urothelial carcinoma	9.8	1.5	3.7	Resection, BCG therapy
15	81	1.44	Right sphenoid	Not done (meningioma - MRI)	12.1	1.2	3.6	Observation
16	72	2.7	Cutaneous lesions	Squamous cell carcinoma	13.6	1.8	5.6	Excision

*Age and PSA reflect values at the time of imaging.
†Squamous cell carcinoma of the lung and esophagus were of separate origin.
BCG = *Bacillus* Calmette–Guérin; MRI = magnetic resonance imaging; PSA = prostate-specific antigen; RCC = renal cell carcinoma.
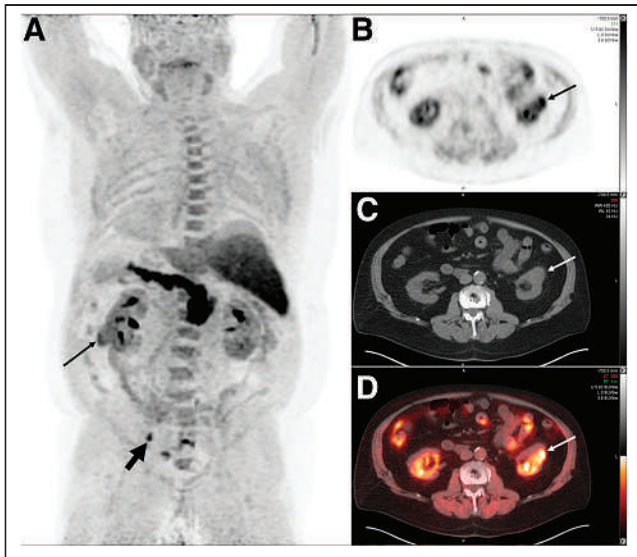
FIGURE 1. A 74-y-old man with adenocarcinoma of the prostate (Gleason score 4 + 3 = 7) after radical prostatectomy 19 y earlier presented with rising PSA (6.7 ng/mL). ^{18}F-fluciclovine PET/CT performed for restaging of biochemical recurrence showed intensely tracer avid left external iliac lymph node (thick arrow; maximum-intensity-projection image in posterior view [A]) likely suggesting metastatic prostate carcinoma. Additionally, a tracer-avid (SUV$_{max}$ 6.2) exophytic soft-tissue mass was noted in lower pole of left kidney (thin arrows; transaxial PET [B], CT [C], fused PET/CT [D]) that raised suspicion for primary renal malignancy. Patient underwent laparoscopic left partial nephrectomy, and histopathologic diagnosis was clear-cell RCC. PSA = prostate-specific antigen.

esophageal and lung carcinomas – Fig. 3). Among histopathologically confirmed malignancies, clear-cell RCC had the lowest uptake (SUV$_{max}$ 3.4; SUV$_{mean}$ blood-pool 1.3; SUV$_{mean}$ bone-marrow 2.4), and cutaneous squamous cell carcinoma had the highest uptake (SUV$_{max}$ 13.6; SUV$_{mean}$ blood-pool 1.8; SUV$_{mean}$ bone-marrow 5.6)
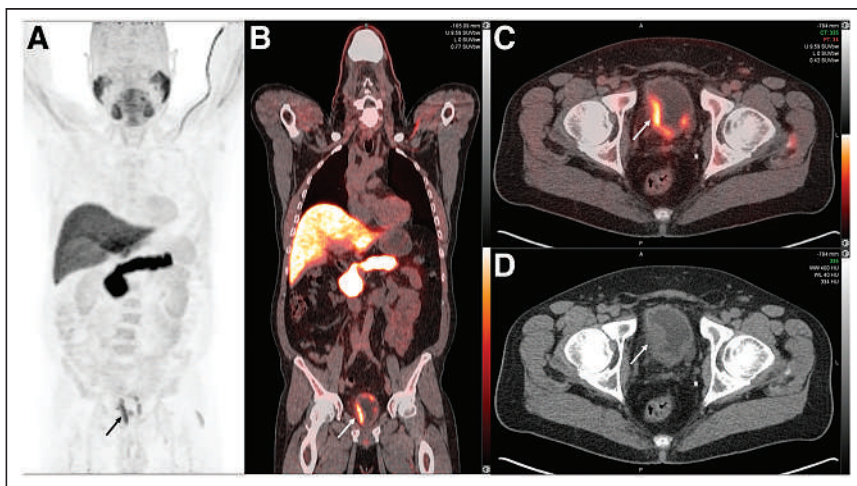
FIGURE 2. A 63-y-old man with adenocarcinoma of the prostate (Gleason score 4 + 3 = 7) after radical prostatectomy 7 y earlier presented with rising PSA levels (0.93 ng/mL). ^{18}F-fluciclovine PET/CT performed for restaging of biochemical recurrence showed multifocal tracer-avid (SUV$_{max}$ 9.8) soft-tissue nodules in wall of urinary bladder (arrow; maximum-intensity-projection image [A], coronal fused PET/CT [B], transaxial fused PET/CT [C], and CT [D]). Transurethral resection of nodules was performed, and histopathology showed high-grade papillary urothelial carcinoma. Patient was started on intravesical BCG (*Bacillus* Calmette–Guérin) therapy. PSA = prostate-specific antigen.

(Fig. 4). Of the 2 patients with no histopathologic confirmation (Table 1, patients 1 and 2), 1 had ultrasound and MRI findings corroborating the diagnosis of RCC. The other patient had a solitary lung nodule suggestive of primary lung carcinoma and elected to undergo observation.

All the 11 patients with a tissue diagnosis confirming a malignancy had a significant change in management with regards to standard treatment for prostate cancer (Table 1), with the majority (7/11; 63.6%) undergoing a primary surgical treatment with/without additional medical therapy.

DISCUSSION

Overall, 55 (9.1%) of 601 prostate cancer patients who underwent ^{18}F-fluciclovine PET/CT had a second neoplasm (48, malignant; 7, benign) detected at any time during the disease course, and 2.7% had a neoplasm that was first suspected on the PET/CT study. A Surveillance, Epidemiology, and End Results Medicare registry–based study of patients with prostate cancer treated with localized therapy showed that 9.9% patients had a second malignancy diagnosed after prostate cancer. The most common second malignancy was that of the lungs and bronchus (1.8%), followed by that of the urinary bladder (1.1%) (*17*). Among the 601 patients in the present study, a urinary bladder carcinoma (*n* = 12; ~2%) was the most common second malignancy diagnosed at any time during their disease course (11, before PET/CT; 1, on PET/CT), whereas RCC was the most common second malignancy first detected on PET/CT.

The detection of a second neoplasm on ^{18}F-fluciclovine PET/CT has several important implications. About 1 in 12 patients diagnosed with one of the common cancers develops a second malignancy, and mortality in approximately 55% patients is because of the second malignancy (*18*). The diagnosis of a second malignancy can often lead to a drastic change in the overall prognosis, morbidity, and mortality parameters and necessitates a change of the management (Table 1). It is important to consider the reader's experience in interpreting PET/CT studies with a specific radiotracer. Experienced readers categorizing incidental findings as requiring further workup have a high probability of detecting a second neoplastic entity. A study of 1,727 patients with ^{18}F-FDG PET/CT showed that actively investigated extrathyroidal lesions based on the readers' recommendations were subsequently confirmed as neoplastic in more than 60% patients (*19*). In this context, knowledge of the common second malignancies detected with ^{18}F-fluciclovine PET/CT can help the readers in being aware and facilitating additional investigations whenever appropriate. The uptake of ^{18}F-fluciclovine has been demonstrated in several physiologic and pathologic processes. Table 2 summarizes the previously described ^{18}F-fluciclovine–avid nonprostate pathologies on PET/CT, including benign, malignant, and nonneoplastic entities.

PET imaging is used to target specific components of the tumor microenvironment, such as metabolic handling of various substrates (e.g., glucose, amino acids,
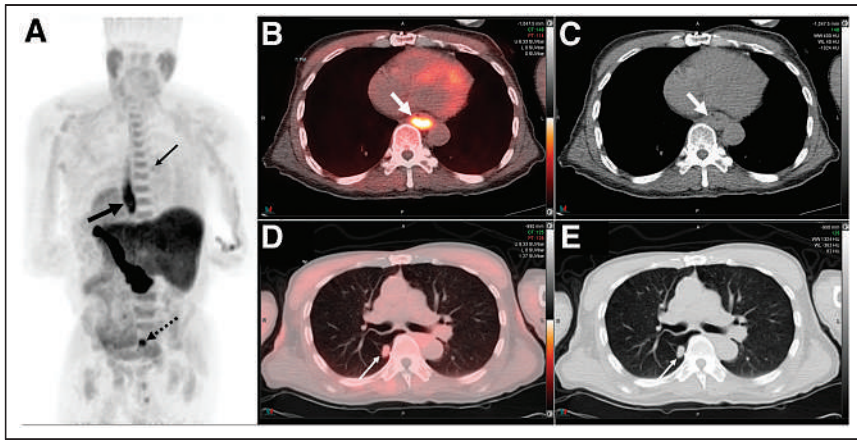
FIGURE 3. A 77-y-old man with adenocarcinoma of the prostate (Gleason score $4 + 3 = 7$) after radical prostatectomy 4 y earlier with subsequent biochemical failure (15.4 ng/mL). ^{18}F-fluciclovine PET/CT performed for restaging of biochemical recurrence showed tracer-avid presacral lymph node (dashed arrow; maximum-intensity-projection image in posterior view [A]) suggestive of metastatic prostate cancer. Additionally, linear increased tracer uptake (SUV$_{max}$ 9.2) was noted in asymmetric mural thickening involving mid and distal esophagus (solid thick arrows [A], transaxial fused PET/CT [B], and CT [C]) and a soft-tissue nodule (SUV$_{max}$ 3.4) in superior segment of right lung lower lobe (solid thin arrows [A], transaxial fused PET/CT [D], and CT [E]). Biopsy of esophageal lesion showed squamous cell carcinoma and biopsy of lung lesion showed distinct squamous cell carcinoma (not metastasis from esophageal primary). This patient was thus diagnosed with 3 distinct primary malignancies (prostate, esophagus, lung) with ongoing disease activity. Patient was started on carboplatin-based chemotherapy and external-beam radiation therapy.
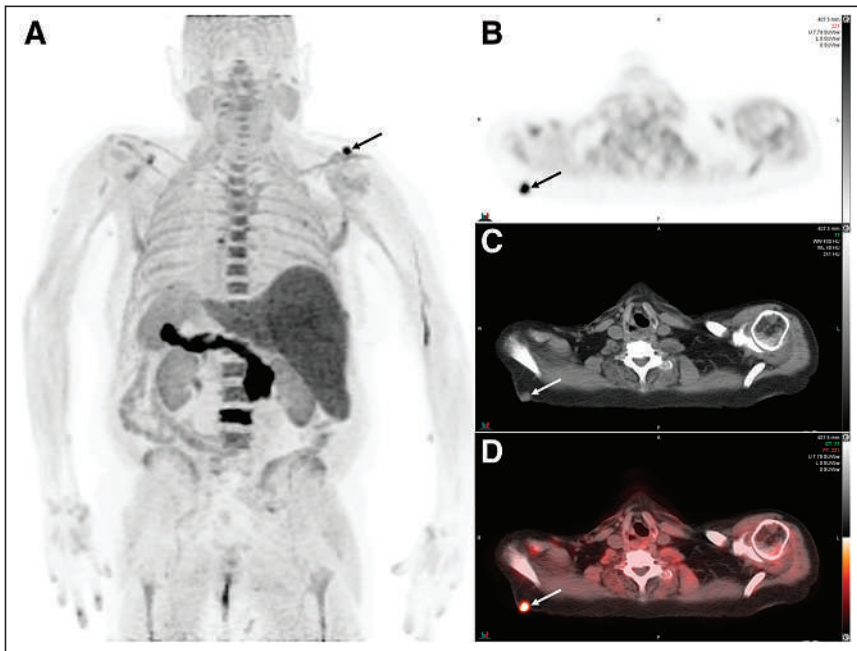
FIGURE 4. A 72-y-old man with adenocarcinoma of the prostate (Gleason score $5 + 5 = 10$) after intensity-modulated radiation therapy to pelvis and prostate 3 y earlier and currently on hormonal therapy presented with increasing PSA levels (2.7 ng/mL). ^{18}F-fluciclovine PET/CT performed for restaging of biochemical recurrence showed multiple osseous lesions suggestive of metastatic disease and markedly tracer-avid (SUV$_{max}$ 13.6) subcutaneous soft-tissue nodule in posterior right shoulder region (arrows; maximum-intensity-projection image in posterior view [A], transaxial PET [B], CT [C], fused PET/CT [D]), which is an atypical site for metastatic prostate cancer. Subsequent biopsy of soft-tissue lesion was performed, and histopathology showed poorly differentiated squamous cell carcinoma. Patient underwent complete excision of lesion. PSA = prostate-specific antigen.

fatty acids) by the tumor cells, hypoxia, perfusion, angiogenesis, expression of receptors on the cell membrane, proliferation, apoptosis, and nontumor immune cells among others (20–23). The premise of targeted PET/CT imaging is based on the typical microenvironment and preferential metabolic features of different tumor lineages. It is known that a wide variety of tumors overexpress ASCT2 and LAT1 transporters because of their high nutritional demands. Glutamine and leucine, transported by ASCT2 and LAT1, respectively, contribute to the anaplerotic pathways feeding the Krebs cycle. The expression of LAT1 is also upregulated by hypoxia inducible factor HIF2α and the oncogene c-Myc (4). Because ASCT2 and LAT1 are involved with both influx and efflux of amino acids, the intratumoral retention of ^{18}F-fluciclovine, and subsequent tumor detection, is dependent on the regional blood flow (for tracer delivery) and the relationship among the active amino acid transporters, yielding either a net influx or efflux of the radiotracer.

A lesion in an atypical location for the metastatic pattern of prostate cancer, different tracer avidity with respect to the primary cancer, disease bulk not correlating with the tumor markers (prostate-specific antigen), and morphologic findings on CT can often act as indicators suggestive of a second neoplastic site. Figure 3 shows a patient with 3 concurrent malignancies for which the avidity of the esophageal and lung lesions was markedly distinct, pointing toward a possible separate origin of these 2 lesions; this separate origin was subsequently confirmed on histopathology.

In this regard, ^{18}F-fluciclovine PET/CT, with the advantage of whole-body survey, can act as an indirect screening modality for second malignancies in these patients, especially in those who are already at a higher risk due to familial, genetic, or environmental predispositions (24). The confirmation of a second benign neoplasm is also helpful as these lesions might be suspected for metastatic prostate carcinoma. In these cases, a knowledge of the benign neoplasms that are known to demonstrate avidity on ^{18}F-fluciclovine PET/CT can be helpful (Table 2). Although the site and pattern of involvement can often point toward the possibility of a nonprostatic disease, the distinction between benign, malignant, and nonneoplastic entities might not always be straightforward. This is especially true of focal, tracer-avid lesions when the location and anatomic features are noncontributory in making a definitive diagnosis, and a tissue analysis is required.

TABLE 2
18F-Fluciclovine Uptake in Nonprostatic Disease Sites: Review of Published Literature

Site	Diagnosis	Nature	SUV$_{max}$	Additional treatment	Reference
Adrenal	Adenoma	Benign	N/A	N/A	(31)
Brain	Meningioma	Benign	N/A	N/A	(32)
	Pituitary adenoma	Benign	7.5	Resection	(33)
	Oligodendroglioma	Low-grade	6.5	N/A	(34)
	Gliomas	Low/High grade	–*	–*	(8)
Breast	IDC, ILC	Malignant	–*	–*	(5)
Gastrointestinal	Gastrointestinal stromal tumor	Malignant	23	Imatinib	(35)
	Rectal carcinoid (metastatic)	Malignant	1.9	N/A	(36)
	Colorectal carcinoma	Malignant	N/A	N/A	(37)
	Acute appendicitis	Nonneoplastic	5.4	Laparoscopic appendectomy	(38)
Genitourinary	Urothelial carcinoma	Malignant		N/A	(39)
	Penile SCC (metastatic)	Malignant	N/A	Excision	(40)
	Cervical SCC	Malignant	5.1	N/A	(41)
	RCC	Malignant	–*	–*	(7)
Head and neck	Oropharyngeal SCC	Malignant	10.8	Excision, adjuvant radiation therapy	(42)
	Warthin tumor	Benign	7.4	N/A	(43)
Hematolymphoid	Multiple myeloma	Malignant		N/A	(44)
	Lymphoma	Malignant	N/A	N/A	(31)
	Small lymphocytic leukemia	Malignant	11.1	N/A	(44)
Liver	Hepatocellular carcinoma	Malignant	N/A	90Y-radioembolization	(45)
Lung	NSCLC - sarcomatoid differentiation	Malignant	7.2	N/A	(44)
	NSCLC - adenocarcinoma	Malignant	5.9	Carboplatin + paclitaxel, radiation therapy	(46)
Miscellaneous	Neurofibroma	Benign	N/A	N/A	(31)
	Neuroendocrine neoplasm	Grade 1	N/A	Somatostatin analog therapy	(47)
	Neuroendocrine carcinoma (metastatic)	Malignant	7.3	Carboplatin/etoposide	(48)
	Desmoid tumor	Benign	3.3	N/A	(49)
Musculoskeletal	Melanoma (metastatic)	Malignant	4.3	Resection	(50)
	Liposarcoma	Malignant	N/A	Resection	(51)
	Paget disease	Nonneoplastic	4.6	N/A	(52)
	Osteoid Osteoma	Benign	N/A	N/A	(37)
Pancreatic	Pancreatic adenocarcinoma (metastatic)	Malignant	N/A	Gemcitabline + paclitaxel	(53)
Thymus	Thymoma	Benign	7.1	Excision	(54)

*Planned prospective studies with 18F-fluciclovine PET/CT in nonprostate malignancies.

IDC = infiltrative ductal carcinoma; ILC = infiltrative lobular carcinoma; N/A = details not available; NSCLC = non–small cell lung carcinoma; SCC = squamous cell carcinoma.

Conversely, diffuse tracer uptake in the lungs with obvious CT findings of pneumonia or diffuse tracer activity in an overactive muscle group can be easily interpreted.

Although the current literature does not have these data for 18F-fluciclovine PET/CT, a prior study on 18F-FDG PET/CT reported the detection rate of histopathologic proven second malignancy to be 1.2%, which is similar to 1.8% (11/601) in our study (12). Specifically in prostate cancer, 1.5% patients were reported to have a second malignancy on 11C-choline PET/CT, with primary lung carcinoma being the most commonly diagnosed (25). A study of 764 patients with prostate cancer reported the presence of a synchronous primary malignancy on 68Ga-PSMA-11 PET/CT in

5 (0.7%) patients (26). Of note, an additional 12 patients had suspicious lesions for which the final diagnosis was not reached. The relatively higher detection rate of second malignancies in our study could be attributed, at least in part, to the more ubiquitous expression of amino-acid transporters on tumor cells of different lineages, in comparison to PSMA. The most common incidentally detected second malignancy on ^{18}F-fluciclovine PET/CT in the present study was RCC. A pilot study on the use of ^{18}F-fluciclovine PET/CT in RCC found that most of the lesions had a low-grade tracer avidity, with the clear-cell variants showing tracer avidity equal to or less than the normal parenchyma whereas the avidity of 2 papillary RCC in a single patient was higher than the uptake in the background renal parenchyma (7). Four of the 5 histopathologically proven RCC in our study were clear-cell variants, with 2 of them showing avidity higher than the normal renal parenchyma (Fig. 2; SUV_{max} higher than the SUV_{mean} of blood pool and bone marrow), which could be easily appreciated on the maximum-intensity-projection images. The single papillary RCC lesion had a lower tracer avidity, which notably has been shown to be relatively hypovascular on contrast CT studies in comparison to clear-cell RCC (27). The discrepancy of degree of tracer uptake between the different histologies of RCC may be better reviewed in prospective studies with a larger cohort. However, a distinct renal mass with any degree of avidity on ^{18}F-fluciclovine PET/CT should raise suspicion and prompt further workup (7).

Meningioma was the only benign neoplasm first suspected on ^{18}F-fluciclovine PET/CT (and confirmed on subsequent MRI), forming 18.7% of all 16 neoplastic entities. Prior studies have reported that approximately 2% patients with prostate cancer have an incidentally detected meningioma on ^{18}F-fluciclovine PET/CT, forming one of the most common benign diagnoses (28). Meningiomas also show radiotracer uptake on somatostatin receptor imaging for neuroendocrine tumors, such as with ^{68}Ga-tetraazacyclododecanetetraacetic acid-[1-Nal3]octreotide PET/CT, and on prostate cancer imaging with ^{68}Ga-PSMA PET/CT (26,29). Meningiomas, especially when tracer-avid, can mimic metastases on a ^{18}F-fluciclovine PET/CT (with non–contrast-enhanced CT), although the brain is a rare site for prostate cancer metastases (30). MRI of the brain is helpful in uncertain diagnoses.

One of the limitations of the present study is its relatively lower sample size in comparison to other similar studies performed with ^{18}F-FDG PET/CT, although it is still the largest cohort reporting these findings on ^{18}F-fluciclovine PET/CT. Another limitation is the retrospective design of the study, which did not permit review of all the imaging studies to identify the separate contributions of the PET and CT components. One of the main strengths of this study is the availability of tissue diagnosis or an MRI correlate in most of the patients with suspected second neoplasms. Future studies can be prospectively planned in a larger patient cohort, assessing possible factors (such as genotype, environmental factors, toxins) that could predispose to synchronous malignancies and identifying robust imaging-based features that can distinguish metastatic prostate cancer from second neoplasms, either benign or malignant.

CONCLUSION

^{18}F-fluciclovine PET/CT identified a second neoplasm in 2.7% of the patients with prostate cancer, and 1.8% of all patients had a histopathologically confirmed second primary malignancy that was first detected on ^{18}F-fluciclovine PET/CT. The most common second malignancy detected on ^{18}F-fluciclovine PET/CT was RCC.

DISCLOSURE

No potential conflict of interest relevant to this article was reported.

KEY POINTS

QUESTION: What is the detection rate of second neoplasms in patients with prostate cancer on ^{18}F-fluciclovine PET/CT?

PERTINENT FINDINGS: In this retrospective study, we showed that ^{18}F-fluciclovine PET/CT detected a second neoplasm in 2.7% of patients with prostate cancer. Of these, the histopathology yielded the diagnosis of a second malignancy in 68.7% patients; the most common diagnosis was RCC.

IMPLICATIONS FOR PATIENT CARE: The study shows that second neoplasms are not uncommon in patients with prostate cancer, and ^{18}F-fluciclovine PET/CT can aid in their detection, which is vital for appropriate further management.

REFERENCES

1. Shoup TM, Olson J, Hoffman JM, et al. Synthesis and evaluation of [^{18}F]1-amino-3-fluorocyclobutane-1-carboxylic acid to image brain tumors. *J Nucl Med.* 1999; 40:331–338.
2. Okudaira H, Shikano N, Nishii R, et al. Putative transport mechanism and intracellular fate of trans-1-amino-3-^{18}F-Fluorocyclobutanecarboxylic acid in human prostate cancer. *J Nucl Med.* 2011;52:822–829.
3. Schuster DM, Votaw JR, Nieh PT, et al. Initial experience with the radiotracer anti-1-amino-3-^{18}F-fluorocyclobutane-1-carboxylic acid with PET/CT in prostate carcinoma. *J Nucl Med.* 2007;48:56–63.
4. Bhutia YD, Babu E, Ramachandran S, Ganapathy V. Amino acid transporters in cancer and their relevance to "glutamine addiction": novel targets for the design of a new class of anticancer drugs. *Cancer Res.* 2015;75:1782–1788.
5. Ulaner GA, Goldman DA, Gonen M, et al. Initial results of a prospective clinical trial of ^{18}F-fluciclovine PET/CT in newly diagnosed invasive ductal and invasive lobular breast cancers. *J Nucl Med.* 2016;57:1350–1356.
6. Amzat R, Taleghani P, Miller DL, et al. Pilot study of the utility of the synthetic pet amino-acid radiotracer anti-1-amino-3-[18f]fluorocyclobutane-1-carboxylic acid for the noninvasive imaging of pulmonary lesions. *Mol Imaging Biol.* 2013;15:633–643.
7. Schuster DM, Nye JA, Nieh PT, et al. Initial experience with the radiotracer anti-1-amino-3-[^{18}F] fluorocyclobutane-1-carboxylic acid (Anti-[^{18}F]FACBC) with PET in renal carcinoma. *Mol Imaging Biol.* 2009;11:434–438.
8. Karlberg A, Berntsen EM, Johansen H, et al. ^{18}F-FACBC PET/MRI in diagnostic assessment and neurosurgery of gliomas. *Clin Nucl Med.* 2019;44: 550–559.
9. Parihar AS, Ga A, Sood K, et al. Incidental detection of synchronous lung melanoma on ^{18}F-FDG PET/CT in a patient with parotid gland myoepithelial carcinoma. *Clin Nucl Med.* 2018;43:e127–e129.
10. Nguyen NC, Muthukrishnan A, Mountz JM. Differential ^{18}F-FDG and ^{18}F-fluciclovine uptake pattern in a patient with poorly differentiated adenocarcinoma of the lung and prostate cancer biochemical recurrence. *Clin Nucl Med.* 2020;45:e63–e64.
11. Romagnolo C, Cottignoli C, Palucci A, Biscontini G, Fringuelli FM, Burroni L. Pictorial essay: incidental findings on ^{18}F-fluciclovine PET/CT scan. *Clin Transl Imaging.* 2021;9:189–198.
12. Ishimori T, Patel PV, Wahl RL. Detection of unexpected additional primary malignancies with PET/CT. *J Nucl Med.* 2005;46:752–757.
13. Calabria F, Chiaravalloti A, Schillaci O. ^{18}F-choline PET/CT pitfalls in image interpretation: an update on 300 examined patients with prostate cancer. *Clin Nucl Med.* 2014;39:122–130.
14. Parihar AS, Vadi SK, Mittal BR, Kumar R, Bal A, Singh SK. ^{68}Ga-PSMA-HBED-CC-avid synchronous urinary bladder paraganglioma in a patient with metastatic prostate carcinoma. *Clin Nucl Med.* 2018;43:e329–e330.
15. Parihar AS, Sood A, Mittal BR, Kumar R, Singh H, Dhatt SS. ^{68}Ga-PSMA-HBED-CC PET/CT and ^{18}F-FDG PET/CT in Ewing sarcoma. *Clin Nucl Med.* 2020;45:e57–e58.

16. Parihar AS, Mittal BR, Sood A, Basher RK, Singh G. ^{68}Ga-prostate-specific membrane antigen PET/CT and ^{18}F-FDG PET/CT of primary signet ring cell breast adenocarcinoma. *Clin Nucl Med.* 2018;43:e414–e416.

17. Moon K, Stukenborg GJ, Keim J, Theodorescu D. Cancer incidence after localized therapy for prostate cancer. *Cancer.* 2006;107:991–998.

18. Donin N, Filson CP, Drakaki A, et al. Risk of second primary malignancies among cancer survivors in the United States, 1992-2008. *Cancer.* 2016;122:3075–3086.

19. Wang G, Lau EWF, Shakher R, et al. How do oncologists deal with incidental abnormalities on whole-body fluorine-18 fluorodeoxyglucose PET/CT? *Cancer.* 2007;109:117–124.

20. Lopci E, Nanni C, Castellucci P, et al. Imaging with non-FDG PET tracers: outlook for current clinical applications. *Insights Imaging.* 2010;1:373–385.

21. Parihar AS, Mittal BR, Kumar R, Shukla J, Bhattacharya A. ^{68}Ga-DOTA-RGD2 positron emission tomography/computed tomography in radioiodine refractory thyroid cancer: prospective comparison of diagnostic accuracy with ^{18}F-FDG positron emission tomography/computed tomography and evaluation toward potential theranostics. *Thyroid.* 2020;30:557–567.

22. Parihar AS, Sood A, Kumar R, Bhusari P, Shukla J, Mittal BR. Novel use of ^{177}Lu-DOTA-RGD2 in treatment of ^{68}Ga-DOTA-RGD2-avid lesions in papillary thyroid cancer with TENIS. *Eur J Nucl Med Mol Imaging.* 2018;45:1836–1837.

23. Wahl RL, Herman JM, Ford E. The promise and pitfalls of positron emission tomography and single-photon emission computed tomography molecular imaging–guided radiation therapy. *Semin Radiat Oncol.* 2011;21:88.

24. Wood ME, Vogel V, Ng A, Foxhall L, Goodwin P, Travis LB. Second malignant neoplasms: Assessment and strategies for risk reduction. *J Clin Oncol.* 2012;30:3734–3745.

25. García JR, Ponce A, Canales M, Ayuso J, Moragas M, Soler M. Detection of second tumors in ^{11}C-choline PET/CT studies performed due to biochemical recurrence of prostate cancer. *Rev Española Med Nucl e Imagen Mol (English Ed).* 2014;33:28–31.

26. Osman MM, Iravani A, Hicks RJ, Hofman MS. Detection of synchronous primary malignancies with ^{68}Ga-labeled prostate-specific membrane antigen PET/CT in patients with prostate cancer: frequency in 764 patients. *J Nucl Med.* 2017;58:1938–1942.

27. Ruppert-Kohlmayr AJ, Uggowitzer M, Meissnitzer T, Ruppert G. Differentiation of renal clear cell carcinoma and renal papillary carcinoma using quantitative CT enhancement parameters. *AJR.* 2004;183:1387–1391.

28. Baiomy A, Schellingerhout D, Chapin BF, et al. Rate of incidental central nervous system meningioma detected in patients undergoing ^{18}F-fluciclovine PET/CT imaging for evaluation of prostate cancer. *Nucl Med Commun.* 2021;Publish Ah:1-8.

29. Parihar AS, Basher RK, Rana N, Mittal BR. Incidental meningioma on ^{68}Ga-DOTANOC positron-emission tomography. *Indian J Nucl Med.* 2018;33:182.

30. Parihar AS, Chandekar K, Singh H, Sood A, Mittal BR. Orbital and brain metastases on ^{68}Ga-PSMA PET/CT in a patient with prostate carcinoma refractory to ^{177}Lu-PSMA and [225]Ac-PSMA therapy. *Asia Ocean J Nucl Med Biol.* 2021;9:67–70.

31. Robertson MS, Sakellis CG, Hyun H, Jacene HA. Extraprostatic uptake of ^{18}F-fluciclovine: Differentiation of nonprostatic neoplasms from metastatic prostate cancer. *AJR.* 2020;214:641–648.

32. Manganaro MS, Manganaro MS, Millet JD. Multifocal meningiomas mimicking dural-based intracranial metastases at ^{18}F-Fluciclovine PET/CT. *Clin Nucl Med.* 2019;44:594–595.

33. Wang J, Foley M, Kuker R. Pituitary adenoma on ^{18}F-fluciclovine PET/CT. *Clin Nucl Med.* 2020;45:e65–e66.

34. Pernthaler B, Nazerani Hooshmand T, Igrec J, Kvaternik H, Aigner RM. Oligodendroglioma in ^{68}Ga-PSMA-11 and ^{18}F-fluciclovine PET/CT. *Clin Nucl Med.* 2021;46:e231–e232.

35. Raghavan K, Flavell RR, Westphalen AC, Behr SC. Gastrointestinal stromal tumor incidentally detected on ^{18}F-fluciclovine PET/CT. *Clin Nucl Med.* 2021;46:345–347.

36. Bosserman AJ, Dai D, Lu Y. Distinct imaging characteristics of different metastases from primary prostate adenocarcinoma and rectal carcinoid tumor on ^{18}F-fluciclovine and ^{68}Ga-DOTATATE PET/CT. *Clin Nucl Med.* 2019;44:83–84.

37. Schuster DM, Nanni C, Fanti S, et al. Anti-1-amino-3-^{18}F-fluorocyclobutane-1-carboxylic acid: physiologic uptake patterns, incidental findings, and variants that may simulate disease. *J Nucl Med.* 2014;55:1986–1992.

38. Ahn GS, Barsky AR, Galperin-Aizenberg M, Vapiwala N, Pantel AR. ^{18}F-fluciclovine uptake in acute appendicitis. *Clin Nucl Med.* 2020;45:e453–e454.

39. Surasi DSS, Lu Y, Corn P, Pettaway C, Bathala T. Incidental detection of urothelial carcinoma on ^{18}F-fluciclovine PET/CT. *Clin Nucl Med.* 2021;46:e114–e115.

40. Bhanvadia RR, Woldu SL, Margulis V, Subramaniam RM, Bagrodia A. Incidental detection of metastatic penile squamous-cell carcinoma with anti-1-amino-3-F-18-fluorocyclobutane-1-carboxylic acid (18 F-Fluciclovine) PET/CT in a patient with recurrent prostate cancer. *Clin Genitourin Cancer.* 2019;17:e184–e186.

41. Nguyen NC, Moon CH, Beriwal S. ^{18}F-fluciclovine PET/MRI in a patient with squamous cell carcinoma of the uterine cervix correlated with ^{18}F-FDG PET/CT. *Clin Nucl Med.* 2020;45:802–804.

42. Jethanandani A, Chen MM, Gule-Monroe MK, Morrison WH, Lai SY, Johnson JM. Incidental detection of oropharyngeal cancer with fluciclovine PET. *Head Neck.* 2019;41:E141–E145.

43. Bitar R, Martiniova L, Bell D, Ravizzini G. Incidental ^{18}F-fluciclovine uptake in a warthin tumor of the parotid gland in a patient undergoing PET/CT imaging for biochemical recurrent prostate cancer. *Clin Nucl Med.* 2020;45:e208–e210.

44. Hoyle JM, Lenzie A, Galgano SJ, et al. Synchronous malignancies identified by ^{18}F-fluciclovine positron emission tomography for prostate cancer: case series and mini-review. *Clin Genitourin Cancer.* 2021;19:e37–e40.

45. Sannananja B, Shah HU, Behnia F. ^{18}F-fluciclovine uptake by an incidentally detected hepatocellular carcinoma in a case of biochemically recurrent prostate cancer. *Clin Nucl Med.* 2018;43:695–696.

46. Abiodun-Ojo OA, Akintayo AA, Sica GL, Alemozaffar M, Schuster DM. Incidental detection of lung adenocarcinoma presenting as an anterior mediastinal mass on ^{18}F-fluciclovine PET/CT in a patient with primary prostate cancer. *Clin Nucl Med.* 2020;45:e525–e527.

47. Balážová Z, Černý I, Vyškovský P. Incidental accumulation of fluciclovine in neuroendocrine tumour in a patient with oncological duplicity. *Case Rep Oncol.* 2020;13:431–435.

48. Abiodun-Ojo OA, Akintayo AA, Harik LR, Bilen M, Halkar RK. Poorly differentiated neuroendocrine tumor with ^{18}F-fluciclovine uptake in a patient with metastatic castrate-resistant prostate cancer. *Clin Nucl Med.* 2021;46:e282–e285.

49. Baiomy A, Jensen CT, Ward JF, Chasen BA, Ravizzini GC. Incidental ^{18}F-fluciclovine uptake in a desmoid tumor detected in a patient undergoing PET/CT imaging for prostate cancer. *Clin Nucl Med.* 2021;46:355–357.

50. Teoh EJ, Tsakok MT, Bradley KM, Hyde K, Subesinghe M, Gleeson FV. Recurrent malignant melanoma detected on ^{18}F-fluciclovine PET/CT imaging for prostate cancer. *Clin Nucl Med.* 2017;42:803–804.

51. Boatright C, Walker CM, Donald J, Cui W, Nagji AS. Incidental dedifferentiated mediastinal liposarcoma on F-18-fluciclovine PET/CT. *Clin Imaging.* 2020;59:21–24.

52. Akin-Akintayo OO, Bonta D, Barron B. Uptake of ^{18}F-fluciclovine in Paget disease. *Clin Nucl Med.* 2019;44:e614–e616.

53. Nguyen BD, Ocal TI. Recurrent pancreatic adenocarcinoma depicted by ^{18}F-fluciclovine PET/CT imaging. *Rev Española Med Nucl e Imagen Mol (English Ed.* 2019;38:258–259.

54. Tsikitas L, Karls S, Kranz AO, Friedman KP, Mahajan S. ^{18}F-fluciclovine uptake in thymoma demonstrated on PET/MRI. *Clin Nucl Med.* 2021;46:e168–e170.

CD8-Targeted PET Imaging of Tumor-Infiltrating T Cells in Patients with Cancer: A Phase I First-in-Humans Study of 89Zr-Df-IAB22M2C, a Radiolabeled Anti-CD8 Minibody

Michael D. Farwell[1,2], Raymond F. Gamache[1], Hasan Babazada[1], Matthew D. Hellmann[3–5], James J. Harding[4,5], Ron Korn[6], Alessandro Mascioni[7], William Le[7], Ian Wilson[7], Michael S. Gordon[8], Anna M. Wu[7,9], Gary A. Ulaner[10], Jedd D. Wolchok[3–5,11], Michael A. Postow*[4,5], and Neeta Pandit-Taskar*[3,12,13]

[1]Department of Radiology, Perelman School of Medicine, University of Pennsylvania, Philadelphia, Pennsylvania; [2]Abramson Cancer Center, Perelman School of Medicine, University of Pennsylvania, Philadelphia, Pennsylvania; [3]Parker Institute for Cancer Immunotherapy, Memorial Sloan Kettering Cancer Center, New York, New York; [4]Department of Medicine, Memorial Sloan Kettering Cancer Center, New York, New York; [5]Department of Medicine, Weill Cornell Medical College, New York, New York; [6]Imaging Endpoints, Scottsdale, Arizona; [7]ImaginAb, Inc., Inglewood, California; [8]HonorHealth Research Institute, Scottsdale, Arizona; [9]Department of Molecular Imaging and Therapy, Beckman Research Institute of the City of Hope, Duarte, California; [10]Molecular Imaging and Therapy, Hoag Family Cancer Institute, Newport Beach, California; [11]Human Oncology and Pathogenesis Program, Memorial Sloan Kettering Cancer Center, New York, New York; [12]Department of Radiology, Memorial Sloan Kettering Cancer Center, New York, New York; and [13]Department of Radiology, Weill Cornell Medical College, New York, New York

There is a need for in vivo diagnostic imaging probes that can noninvasively measure tumor-infiltrating CD8+ leukocytes. Such imaging probes could be used to predict early response to cancer immunotherapy, help select effective single or combination immunotherapies, and facilitate the development of new immunotherapies or immunotherapy combinations. This study was designed to optimize conditions for performing CD8 PET imaging with 89Zr-Df-IAB22M2C and determine whether CD8 PET imaging could provide a safe and effective noninvasive method of visualizing the whole-body biodistribution of CD8+ leukocytes. **Methods:** We conducted a phase 1 first-in-humans PET imaging study using an anti-CD8 radiolabeled minibody, 89Zr-Df-IAB22M2C, to detect whole-body and tumor CD8+ leukocyte distribution in patients with metastatic solid tumors. Patients received 111 MBq of 89Zr-Df-IAB22M2C followed by serial PET scanning over 5–7 d. A 2-stage design included a dose-escalation phase and a dose-expansion phase. Biodistribution, radiation dosimetry, and semiquantitative evaluation of 89Zr-Df-IAB22M2C uptake were performed in all patients. **Results:** Fifteen subjects with metastatic melanoma, non–small cell lung cancer, and hepatocellular carcinoma were enrolled. No drug-related adverse events or abnormal laboratory results were noted except for a transient increase in antidrug antibodies in 1 subject. 89Zr-Df-IAB22M2C accumulated in tumors and CD8-rich tissues (e.g., spleen, bone marrow, nodes), with maximum uptake at 24–48 h after injection and low background activity in CD8-poor tissues (e.g., muscle and lung). Radiotracer uptake in tumors was noted in 10 of 15 subjects, including 7 of 8 subjects on immunotherapy, 1 of 2 subjects on targeted therapy, and 2 of 5 treatment-naïve subjects. In 3 patients with advanced melanoma or hepatocellular carcinoma on immunotherapy, posttreatment CD8 PET/CT scans demonstrated increased 89Zr-Df-IAB22M2C uptake in tumor lesions, which correlated with response. **Conclusion:** CD8 PET imaging with 89Zr-Df-IAB22M2C is safe and has the potential to visualize the whole-body biodistribution of CD8+ leukocytes in tumors and reference tissues, and may predict early response to immunotherapy.

Key Words: 89Zr-Df-IAB22M2C; PET imaging; CD8+ T cell; minibody; immunotherapy

Immunotherapy has become standard of care for the treatment of many malignancies. Various strategies for enhancing the immune response to tumor antigens have been developed, most notably checkpoint inhibitors, as well as cancer vaccines, oncolytic viruses, and bispecific T-cell engager antibodies. In 2018, almost 44% of all cancer patients were eligible for treatment with checkpoint inhibitors based on U.S. Food and Drug Administration–approved regimens, but only a subset of patients respond (1–3).

T cells play a central role in the immune response to cancer, and tumor infiltration by CD8+ T cells, either on pretreatment biopsies or during the course of therapy, has been associated with response to immunotherapy (4–8). However, biopsies to assess T-cell infiltration are invasive and subject to sampling error, both within a lesion and across the entire burden of disease. Thus, a noninvasive method of visualizing CD8+ T-cell whole-body trafficking and tumor infiltration has the potential to play a pivotal role in guiding patient management by serving as an early measure of response, helping to select effective single or combination immunotherapies and facilitating the development of new immunotherapies by indicating pharmacodynamic activity. CD8 imaging may even play a role in identifying patients with tumors likely to be resistant to immunotherapy as well as in understanding immune-related adverse events resulting from immunotherapy.

IAB22M2C is a humanized 80-kDa minibody genetically engineered from the parent murine OKT8 antibody that targets human CD8 with high affinity. IAB22M2C is biologically inert, due to a

lack of Fc receptor interaction domains, and has more rapid clearance than a full-sized antibody, giving it favorable properties for in vivo imaging. In vitro and in vivo preclinical studies with [89]Zr-Df-IAB22M2C have shown that the probe does not impair CD8+ T-cell proliferation, activation, or cytotoxicity (9,10). In addition, preclinical PET imaging studies demonstrated the ability of [89]Zr-Df-IAB22M2C to detect infiltrating CD8+ T cells in a variety of mouse models (9–11).

On the basis of these preclinical data, we initiated a first-in-humans study to evaluate [89]Zr-Df-IAB22M2C in patients with solid tumors. An earlier report analyzed the data from the first 6 patients enrolled in the dose-escalation phase of the trial (12). Here, we report the results from the dose-expansion phase of the trial, which was designed to further explore minibody mass doses of the active pharmaceutical ingredient (API) for PET imaging and provide the final results of the safety, pharmacokinetics, biodistribution, and radiation dosimetry of [89]Zr-Df-IAB22M2C in all patients enrolled in the phase 1 trial.

MATERIALS AND METHODS

A prospective phase 1, open-label, nonrandomized, PET imaging study with [89]Zr-Df-IAB22M2C was performed under an investigational new drug application (IND 127861). The protocol was approved by the Institutional Review Board, and all patients provided written informed consent (ClinicalTrials.gov identifier NCT03107663).

Patients

Patients with histologically confirmed small cell or non–small cell lung cancer, squamous cell carcinoma of the head and neck, melanoma, Merkel cell carcinoma, renal cell carcinoma, bladder cancer, hepatocellular carcinoma, triple-negative breast cancer, gastroesophageal cancers, or Hodgkin lymphoma with at least 1 measurable lesion per RECIST 1.1 were eligible. Patients were either treatment-naïve or receiving standard-of-care therapy (without radiation therapy). All patients underwent baseline imaging, including CT or MRI performed as standard of care within 4 wk of [89]Zr-Df-IAB22M2C administration. The study was conducted in 2 stages. During stage 1 of the trial, the total IAB22M2C mass dose was escalated, starting with 0.2 mg of API and increasing to 0.5, 1.0, 1.5, 5, and 10 mg of API consecutively for the first 6 patients. In stage 2 (dose-expansion), an additional 9 patients were randomly assigned to receive either 0.5 mg ($n = 4$) or 1.5 mg ($n = 5$), given the results from the dose-escalation cohort suggesting that lower minibody masses provided better visualization of CD8-rich tissues and tumor lesions (12). All patients underwent serial PET imaging for biodistribution and dosimetry analysis.

[89]Zr-Df-IAB22M2C Minibody Formulation

IAB22M2C minibody, obtained from ImaginAb, Inc., was conjugated to Good Manufacturing Practice–grade deferoxamine from Macrocyclics at the Radiochemistry and Molecular Imaging Core Facility at Memorial Sloan Kettering Cancer Center. Sterile Df-IAB22M2C was stored at 4°C for up to 2 wk before radiolabeling. [89]Zr production and subsequent radiolabeling of Df-IAB22M2C were performed as previously described for other antibodies (13–15). Approximately 0.2–1 mg of Df-IAB22M2C was labeled with [89]Zr and purified by a PD-10 column. The final product was supplemented with cold IAB22M2C minibody and diluted with formulation buffer, as needed. Before release, the final radiolabeled product was tested for appearance, pH, radiochemical identity, and purity by size-exclusion high-performance liquid chromatography and instant thin-layer-chromatography; for radionuclidic purity by γ-spectroscopy; for endotoxin level by portable test system reader; and for immunoreactivity by the bead method. Sterility testing was performed after release. The radiolabeling efficiency was >80%, radiochemical purity was >95% (as determined by instant thin-layer-chromatography), and minibody binding was >90%.

[89]Zr-Df-IAB22M2C Administration

A dose of 111 MBq (3 mCi) ± 20% of [89]Zr-Df-IAB22M2C, in combination with cold IAB22M2C to make up the designated total mass balance, was administered intravenously over 5–10 min. No premedications were administered. Patients were monitored and vital signs measured for 1–2 h after injection, and also during additional imaging visits up to 48 h after injection. Electrocardiograms were recorded before and 10 min after injection. Side effects and reactions were graded per the Common Terminology Criteria for Adverse Events, version 4.0.

Blood samples were evaluated for antidrug antibodies (ADAs) at baseline, 3–4 wk after injection, and 8–12 wk after injection by BioAgilytix. Blood samples were evaluated for cytokines at baseline, and 4 and 24 h after injection by Charles River Laboratories.

[89]Zr-Df-IAB22M2C PET/CT Imaging and Analysis

Images were acquired at 3 centers using a Discovery 710 PET/CT scanner (GE Healthcare), a Discovery STE PET/CT scanner (GE Healthcare), or an Ingenuity PET/CT scanner (Phillips Medical Systems). Each patient underwent 4–5 whole-body PET/CT scans from the vertex of the skull to feet at 2–4, 24 ± 4, 48 ± 4, and 92–148 h after injection. If the patient agreed, an additional scan was acquired between the first and second scans at 6–8 h after injection. Emission scans were acquired in 3-dimensional mode at variable times per field of view (3 min on the day of injection, extending to 7 min at 92–148 h). PET/CT scans were acquired with low-dose CT for attenuation correction and lesion localization. A single low-dose CT scan at 24 h after injection was obtained with a 80 mA tube current (120 kVp; estimated radiation dose 9.0 mGy), whereas all other low-dose CT scans were obtained with a 10 mA current (120kVp; estimated radiation dose 1.1 mGy). Images were reconstructed with a 70-cm field of view into a 128 × 128 matrix using iterative ordered-subset expectation maximization (16 subsets; 2 iteration). All corrections recommended by the manufacturer were applied.

[89]Zr-Df-IAB22M2C PET/CT images were analyzed by Imaging Endpoints, LLC. Volumes of interest were drawn on PET/CT images over the lung, liver, spleen, kidney (left), muscle (paraspinal), aorta, bone marrow (L3 vertebrae), lymph nodes, and tumor lesions using dedicated software (mintLesion 3.2 software). All tumor lesions identified on baseline imaging studies were measured. For comparison of uptake trends, up to 3 target lesions per patient were analyzed; if more than 3 lesions were present, the largest lesions were selected. SUV was quantified using SUV_{MEAN} (normal tissues), SUV_{PEAK} (tumor lesions), or SUV_{MAX} (tumor lesions) normalized to lean body mass.

Serum and Whole-Body Clearance Measurements

Multiple blood samples were obtained for assessment, including a baseline sample before [89]Zr-Df-IAB22M2C infusion, followed by sampling at 5, 30, 60, 120, and 240 min after injection, and subsequently at the time of each PET scan, totaling 9–10 samples. Aliquots of serum were analyzed for radioactivity using a NaI (TI) γ-well-type detector (Wallace Wizard 1480 automatic γ-counter; Perkin Elmer); measured activity concentrations were decay-corrected and converted to percentage injected dose per liter. Aliquots of serum were also analyzed for [89]Zr-Df-IAB22M2C using a validated enzyme-linked immunosorbent assay method by Charles River Laboratories. Activity in the whole body was determined on the basis of whole-body PET scans.

A biexponential function was fitted to the serum data, and a monoexponential function was fitted to the whole-body data using GraphPad Prism (version 8.4.3; GraphPad Software Inc.). Biologic clearance rates and corresponding half-times were derived from the fitted curves.

Normal-Organ (Tissue) Dosimetry

Radiation dosimetry analysis on all 15 patients was conducted by CDE Dosimetry Services, Inc. Volumes of interest were drawn on PET images for all organs, showing uptake above general body uptake,

including heart, lung, liver, gallbladder, spleen, bone marrow, kidney, small intestine, large intestine, salivary gland, testis, and urinary bladder. Data modeling, estimation of normalized number of disintegrations, and production of dosimetry estimates were performed using the RADAR (RAdiation Dose Assessment Resource) method for internal dosimetry as implemented in the OLINDA/EXM (version 1.1) software (16). All of these methods, including the image quantification, were also in general concordance with the methodology and principles as presented in MIRD pamphlet no. 16 (17). The effective dose (ED) was determined using the methodology as described in International Commission of Radiological Protection (ICRP) publication 103 (18). Additional details for the dosimetry analysis are provided in the supplemental materials (supplemental materials are available at http://jnm.snmjournals.org).

Statistical Analysis

For patient demographics, medians and ranges were used to summarize continuous variables and percentages were used to summarize categoric variables. GraphPad Prism (version 8.4.3; GraphPad Software Inc.) was used for all statistical analyses. The results are indicated as mean $\pm$ SD, and P values less than 0.05 were considered significant; some results are shown as medians and interquartile ranges.

RESULTS

Fifteen patients were enrolled (Table 1); 6 patients were enrolled in the initial dose-escalation phase (12) followed by an additional 9 patients in the dose-expansion phase. In the dose-escalation phase, 1 patient was enrolled in each of the following API dose groups: 0.2, 0.5, 1, 1.5, 5, and 10 mg; in the dose-expansion phase, 4 patients were enrolled in the 0.5-mg API dose group and 5 patients enrolled in the 1.5-mg API dose group. At the time of imaging, 8 patients were on immunotherapy, 2 patients had discontinued prior treatment with last dose > 5 mo before imaging, 3 patients were treatment-naïve, and 2 patients were receiving targeted therapy. The mean injected activity was 106 MBq (2.87 mCi), with a range of 93–121 MBq (2.52–3.26 mCi). The minibody mass of the radiolabeled product was 0.12 mg for the 0.2-mg dose level; for other levels, the mean ($\pm$SD) mass was 0.34 ($\pm$0.02) mg.

Safety and Tolerability

Injections were well tolerated, with no infusion site reaction higher than grade 1 reported. No adverse events related to the study drug were observed. There were no clinically significant changes in vital signs, blood chemistry and hematology, blood cytokines, or electrocardiograms. ADA analysis demonstrated transient immunoreactivity to [89]Zr-Df-IAB22M2C in 1 of 15 patients at 3–4 wk after infusion, which became undetectable by 8–12 wk after infusion and was unaccompanied by symptoms or laboratory abnormalities.

Pharmacokinetics

Serum clearance was biexponential and dependent on the mass of minibody administered, with more rapid clearance at lower masses (Fig. 1A) likely due to a greater proportion of target-mediated clearance. For the dose-expansion cohort in which patients received 0.5 or 1.5 mg of minibody, the biologic half-times were 0.33 ± 0.10 h (range, 0.17–0.46 h) for the fast component (α phase, 61.5%) and 14 ± 7.0 h (range, 2.7–25 h) for the slow component (β phase, 38.5%), based on serum radioactivity, and 0.38 ± 0.29 h (range, 0.12–1.1 h) for the fast component (α phase, 75.5%) and 6.4 ± 3.4 h (range, 0.83–11 h) for the slow component (β phase, 24.5%), respectively, based on enzyme-linked immunosorbent assay measurements of [89]Zr-Df-IAB22M2C. At mass doses of 1.5 mg and lower, there was no detectable minibody in serum by

TABLE 1
Patient Characteristics

Characteristic	All patients (n = 15)
Median age (y)	64 (range, 30–81)
Sex (n)	
Male	9 (60)
Female	6 (40)
Tumor type (n)	
Melanoma	8 (53)
Non–small cell lung carcinoma	6 (40)
Hepatocellular carcinoma	1 (7)
Treatment profile at the time of imaging (n)	
On immunotherapy (<2 mo)	3 (20)
On immunotherapy (>2 mo)	5 (33)
On targeted therapy (1–6 mo)	2 (13)
Discontinued prior treatment (>5 mo)	2 (13)
Treatment naïve	3 (20)

Data in parentheses are percentages unless otherwise indicated.

48 h after injection (Fig. 1A). Whole-body clearance for the dose-expansion cohort conformed to monoexponential kinetics, with a mean whole-body biologic half-life of 233 h (range, 71–341 h).

Biodistribution and Normal-Tissue Uptake

In the dose-expansion cohort, [89]Zr-Df-IAB22M2C cleared rapidly from the blood, with very low activity by 24 h after injection. The highest uptake was seen in the spleen, followed by bone marrow and liver (Fig. 1B). Liver uptake remained fairly constant over the imaging interval, whereas bone marrow and spleen uptake gradually decreased over time. The gallbladder had minimal to no uptake in most patients; in a few patients, the gallbladder was visualized at 2–6 h after injection, and cleared on later images. Uptake in the gastrointestinal tract was variable but generally peaked at 6–24 h and decreased thereafter, consistent with hepatobiliary clearance. Renal uptake was primarily cortical and increased over time, with similar activity compared with liver from 6 h after injection onward. Low-level activity was seen in the bladder in most patients at early time points, with minimal activity on later images.

[89]Zr-Df-IAB22M2C accumulated in CD8-rich tissues (e.g., spleen, bone marrow, and lymph nodes), with maximum uptake at 24–48 h after injection (Fig. 2A) along with low background activity in CD8-poor tissues such as muscle and lung (Fig. 2B). Normal lymph nodes were [89]Zr-Df-IAB22M2C–avid in all patients, primarily in the cervical, axillary, and inguinal regions, but also in the mediastinum, hila, abdomen, and pelvis. Lymph nodes as small as 3 mm in short-axis diameter had an SUV_{MAX} of up to 6.9, and lymph nodes measuring 4 and 5 mm had an SUV_{MAX} of up to 11.8 and 17.4, respectively. Comparison of subjects in the dose-expansion cohort who were given 1.5 or 0.5 mg of API demonstrated reduced uptake in bone marrow and spleen at 1.5 mg of API but similar uptake in lymph nodes (Fig. 2A). In CD8-poor tissues (e.g., muscle and lung), no differences in uptake were noted between the 1.5- and 0.5-mg groups.
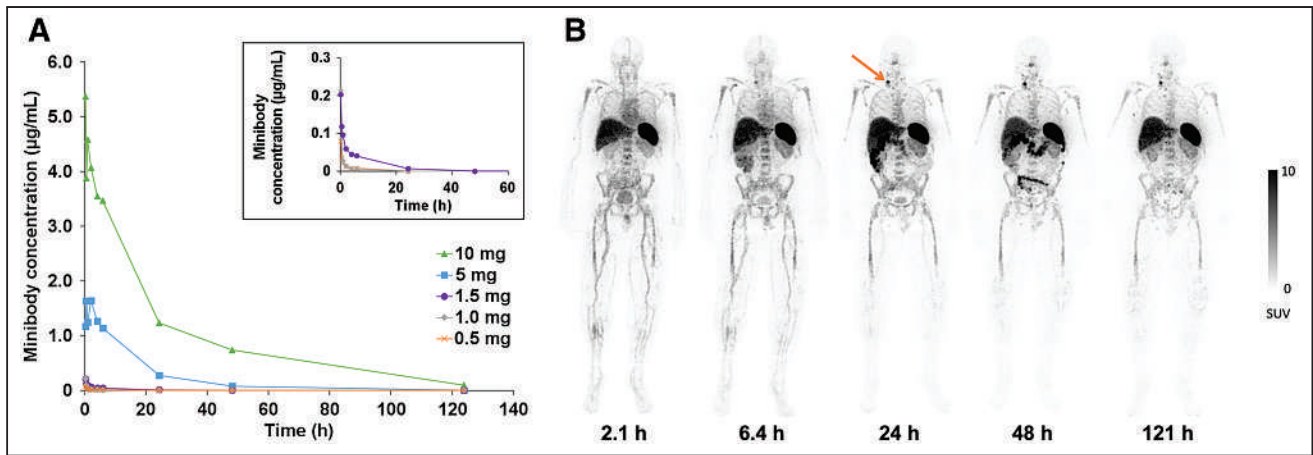
FIGURE 1. Serum clearance and biodistribution of ^{89}Zr-Df-IAB22M2C. (A) Serum clearance of ^{89}Zr-Df-IAB22M2C based on enzyme-linked immunosorbent assay measurements (limit of detection = 5 ng/mL). No minibody was detected in serum at the 0.2-mg dose. (B) Whole-body PET images of a patient at various times after injection of ^{89}Zr-Df-IAB22M2C (1.5-mg minibody dose) demonstrating the distribution of ^{89}Zr-Df-IAB22M2C in normal tissues and uptake in a nodal metastasis in the right neck (arrow), with good visualization of uptake in the nodal metastasis at 24–48 h after injection.

Normal-Tissue Dosimetry

The average absorbed dose estimates for normal tissues are provided in Supplemental Table 1. The organs receiving the largest dose were the spleen at 12 ± 4.9 mGy/MBq followed by the kidneys at 2.3 ± 0.62 mGy/MBq and liver at 1.9 ± 0.50 mGy/MBq. The mean ED (effective dose, ICRP 103 (18)) was 0.65 ± 0.080 mSv/MBq. Comparison of groups in the dose-expansion cohort revealed similar dosimetry in subjects who received 1.5 mg of minibody compared with 0.5 mg, with a trend toward lower absorbed doses in the spleen (11 vs. 15 mGy/MBq, respectively) and bone marrow (0.68 vs. 0.81 mGy/MBq, respectively) and a lower mean ED (0.64 vs. 0.67 mSv/MBq, respectively) at the higher mass dose.

Lesion Targeting and Uptake

Tumor lesion uptake data are listed in Supplemental Table 2. ^{89}Zr-Df-IAB22M2C accumulated in tumor lesions, with maximum values 24–48 h after injection (Fig. 2C), similar to CD8-rich tissues. Radiotracer uptake in tumors was variable and noted in 10 of 15 (67%) patients, favoring slightly higher tumor uptake on average in the 1.5-mg cohort compared with the 0.5-mg cohort although this was not statistically significant (Fig. 2D). Tumor uptake above background was observed in 7 of 8 (88%) patients receiving immunotherapy, 1 of 2 (50%) patients who had discontinued therapy, 1 of 3 (33%) patients who were treatment-naïve, and 1 of 2 (50%) patients on targeted therapy. When ^{89}Zr-Df-IAB22M2C uptake was analyzed by tumor type, the 2 largest cohorts (melanoma and non–small cell lung cancer) had similar ranges of tumor uptake with similar time–activity curves (results not shown). Several tumor lesions that were quite large had uptake at background (similar to blood pool), including metastatic lymph nodes measuring up to 5.4 cm and lung nodules measuring up to 4.7 cm (Supplemental Fig. 1). In addition, some tumor lesions that were small had significant uptake, such as a 0.7-cm metastatic lymph node with an SUV$_{MAX}$ of 5.4 (Fig. 3).

This trial was not designed to correlate tumor uptake with response to therapy; however, clinical follow-up was available for 3 patients. In 1 patient with regionally advanced melanoma, a CD8 PET/CT scan acquired 28 d after initiating immunotherapy (pembrolizumab) demonstrated marked ^{89}Zr-Df-IAB22M2C uptake in 2 nodal metastases in the left axilla (SUV$_{MAX}$ of 9.5 and 10.0) (Fig. 4), suggesting that the patient had a high degree of CD8+ leukocyte infiltration in the tumor; follow-up CT imaging in this patient demonstrated a complete response to therapy, which has lasted 2.3+ years. In another patient with metastatic melanoma, an ^{18}F-FDG PET/CT acquired at approximately 8 mo after immunotherapy (pembrolizumab) initiation demonstrated ^{18}F-FDG–avid metastases in the right neck with slightly increased size compared with prior studies that still qualified as stable disease. Subsequent CD8 PET/CT imaging, performed 1 mo after the ^{18}F-FDG PET/CT, demonstrated marked ^{89}Zr-Df-IAB22M2C activity in both metastases (SUV$_{MAX}$ of 5.4 and 14.6) (Fig. 3), suggesting that the tumor had a high degree of CD8+ leukocyte infiltration; follow-up imaging over the next 6 mo supported the possibility this reflected a productive antitumor immune response because the patient experienced stable disease in these lymph nodes. In a third patient with metastatic hepatocellular carcinoma who progressed on sorafenib, CD8 PET/CT imaging performed 14 d after starting nivolumab demonstrated markedly increased ^{89}Zr-Df-IAB22M2C activity in the primary tumor (SUV$_{MAX}$ = 19.3) (Supplemental Fig. 2), suggestive of tumor infiltration by CD8+ leukocytes; follow-up CT imaging demonstrated a partial response to therapy, which has lasted 3+ y. In addition, the patient had an associated drop in α-fetoprotein from 33.2 ng/mL (pretreatment) to 1.4 ng/mL (3 y after initiation of therapy).

DISCUSSION

A noninvasive method of visualizing CD8+ T-cell whole-body biodistribution and tumor infiltration, both before and during therapy, has the potential to play a pivotal role in guiding patient management. In this first-in-humans trial, CD8-targeted PET imaging with ^{89}Zr-Df-IAB22M2C, a humanized anti-CD8 minibody, was demonstrated in patients with a variety of malignancies. An earlier report analyzed the data from the first 6 patients enrolled in the dose-escalation phase of the trial (12). Here, we report the final results from the trial, including results from the dose-expansion phase, which was designed to identify the optimal minibody mass dose for PET imaging. In this study, ^{89}Zr-Df-IAB22M2C was found to be safe and well tolerated, with no infusion reactions higher than grade 1 and no drug-related adverse events. ADAs
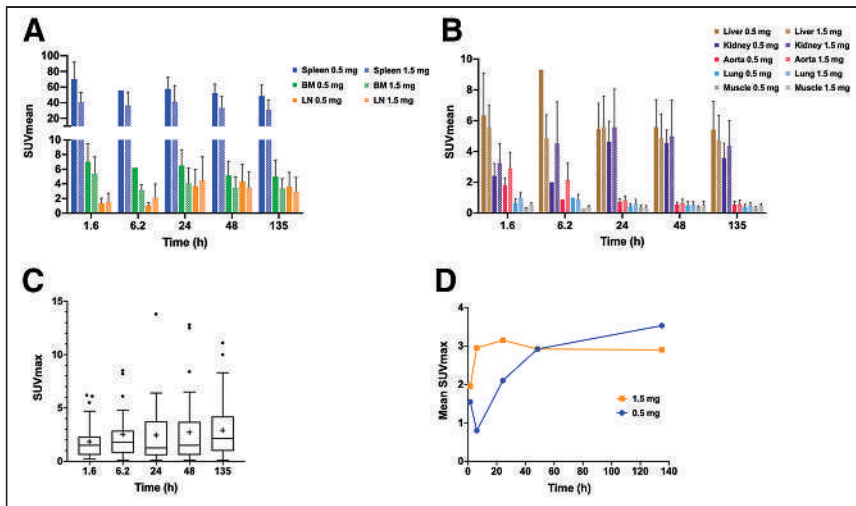
FIGURE 2. [89]Zr-Df-IAB22M2C uptake in normal tissues and tumor lesions versus time. (A) [89]Zr-Df-IAB22M2C uptake in CD8-rich reference tissues in patients administered 0.5 and 1.5 mg of minibody mass. (B) [89]Zr-Df-IAB22M2C uptake in CD8-poor reference tissues in patients administered 0.5 and 1.5 mg of minibody mass. (C) Box and whisker plots of [89]Zr-Df-IAB22M2C uptake in tumor lesions from all subjects ($n = 15$). Boxes outline first and third quartile values. Median SUV$_{MAX}$ values are indicated by horizontal line and mean SUV$_{MAX}$ values are indicated with $+$. Outlier values are indicated by dots. (D) [89]Zr-Df-IAB22M2C mean tumor uptake in patients who received 0.5 and 1.5 mg of minibody mass. BM = bone marrow; LN = lymph nodes.

were detected in 1 patient at 3–4 wk after infusion, which became undetectable by 8–12 wk after infusion.

The biodistribution of [89]Zr-Df-IAB22M2C was consistent with CD8+ leukocyte targeting: not all CD8+ leukocytes are T cells, with robust uptake of [89]Zr-Df-IAB22M2C in CD8-rich tissues (e.g., spleen, bone marrow, and lymph nodes) with maximum uptake at 24–48 h after injection, and relatively low uptake in CD8-poor tissues (e.g., muscle and lung). Radiotracer-avid normal lymph nodes were frequently seen in the neck, axilla, and inguinal regions, which is

expected, as these are common sites for reactive processes due to infectious or environmental stimuli. Even very small lymph nodes (measuring 3 mm in short-axis diameter) were radiotracer-avid, suggesting that the imaging probe has high sensitivity for CD8+ leukocytes. In addition, [89]Zr-Df-IAB22M2C uptake in CD8-rich tissues was saturable, with lower uptake in the spleen and bone marrow in the 1.5-mg cohort than in the 0.5-mg cohort. No differences in lymph node uptake were seen between the 1.5- and 0.5-mg cohorts, possibly due to greater blood flow to, and availability of, target sites in the spleen and bone marrow relative to lymph nodes. In CD8-poor tissues (e.g., muscle and lung), no differences in uptake were noted between the 1.5- and 0.5-mg groups. Although there were differences in uptake over time, and in the 1.5- versus 0.5-mg cohorts, these differences were fairly small, suggesting that [89]Zr-Df-IAB22M2C will provide a relatively stable signal despite variability in uptake time and minibody mass doses that can occur during clinical studies.

The radiation exposure for [89]Zr-Df-IAB22M2C, with an effective dose (ICRP 103 (18)) of 0.65 ± 0.080 mSv/MBq, was comparable to that for other [89]Zr-labeled imaging probes (19–23). The relative organ doses from [89]Zr-Df-IAB22M2C were also comparable to other [89]Zr-labeled imaging probes, although the spleen dose for [89]Zr-Df-IAB22M2C was higher. Comparison of groups in the dose-expansion cohort revealed similar dosimetry in subjects who received 1.5 mg of minibody compared with 0.5 mg, with a trend toward lower absorbed doses in the spleen (11 vs. 15 mGy/MBq, respectively) and bone marrow (0.68 vs. 0.81 mGy/MBq, respectively) and a lower effective dose (0.64 vs. 0.67 mSv/MBq, respectively) at the higher mass dose.

Analysis of [89]Zr-Df-IAB22M2C uptake in tumor lesions revealed maximum uptake at 24–48 h after injection, with slightly higher uptake in the 1.5-mg cohort than in the 0.5-mg cohort, similar to CD8-rich tissues. Although the number of patients was small, most (88%) tumor lesions were radiotracer-avid in patients on immunotherapy, which may reflect the modulation of the immune system and infiltration of tumor lesions by CD8+ leukocytes. A variety of different lesions (lung nodules, nodal metastases, liver metastases), including large lesions, had radiotracer activity at background, demonstrating that [89]Zr-Df-IAB22M2C has low nonspecific uptake and thus has the potential to quantify CD8+ leukocytes across a wide dynamic range, including those with few to no CD8+ cells, often termed "immune desert" on histologic appearance (24). Although this trial was not designed to correlate tumor
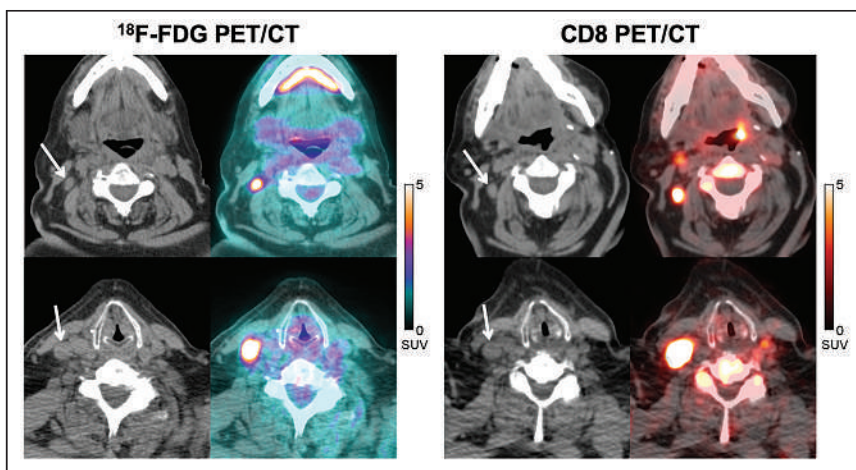
FIGURE 3. A 77-y-old man with metastatic melanoma treated with pembrolizumab. CT and fused ^{18}F-FDG PET/CT images (left) acquired at approximately 8 mo after initiation of immunotherapy demonstrate 2 ^{18}F-FDG–avid nodal metastases in right neck (SUV$_{MAX}$ = 8.0, top image; SUV$_{MAX}$ = 16.8, bottom image), which could represent viable metastases. Corresponding CT and fused CD8 PET/CT images (right) obtained at 1 mo after ^{18}F-FDG PET/CT demonstrate significant tracer activity in both metastases (SUV$_{MAX}$ = 5.4, top image; SUV$_{MAX}$ = 14.6, bottom image), which suggests that some of the ^{18}F-FDG activity could be due to tumor-infiltrating CD8+ T cells rather than tumor cells. Follow-up imaging over the next 6 mo demonstrated stable disease, supportive of this hypothesis.
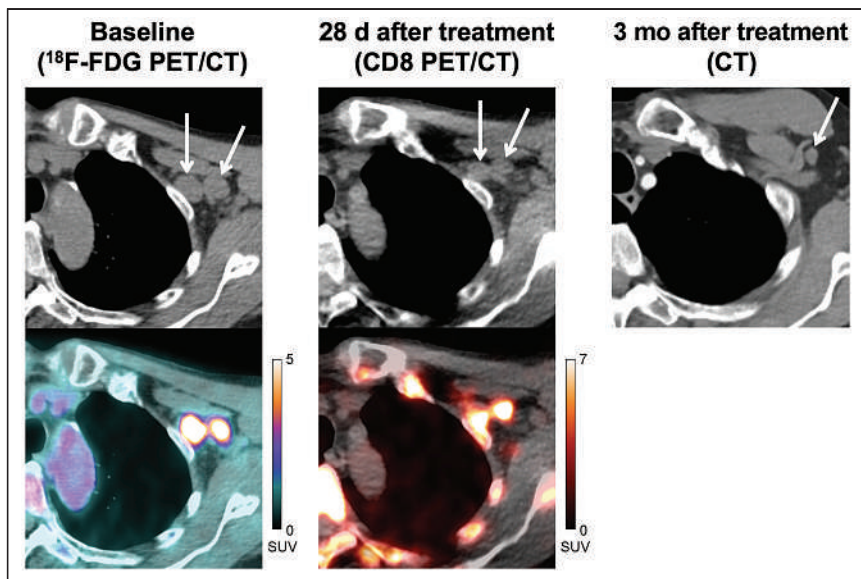
FIGURE 4. A 71-y-old man with locally advanced stage III melanoma treated with pembrolizumab. Baseline CT and fused ^{18}F-FDG PET/CT images (left) demonstrate 2 ^{18}F-FDG–avid metastases in left axilla (SUV$_{MAX}$ = 10.0, medial node; SUV$_{MAX}$ = 7.6, lateral node). CT and fused CD8 PET/CT images (middle) obtained at 28 d after start of immunotherapy demonstrate increased tracer activity in both metastases (SUV$_{MAX}$ = 9.5, medial node; SUV$_{MAX}$ = 10.0, lateral node), suggestive of tumor infiltration by CD8+ T cells. Follow-up imaging with contrast-enhanced CT (right) demonstrated complete response to therapy.

uptake with response to therapy, clinical follow-up was available for 3 patients with metastatic melanoma or hepatocellular carcinoma on immunotherapy (pembrolizumab or nivolumab). All 3 patients demonstrated increased ^{89}Zr-Df-IAB22M2C uptake in tumor lesions after initiation of immunotherapy, indicating the presence of CD8+ tumor–infiltrating leukocytes, and correlated with subsequent benefit from immunotherapy. Interestingly, all 3 patients had variable uptake at sites of metastases (Supplemental Table 2), with some lesions demonstrating marked uptake (SUV$_{MAX}$ ≥ 10) and other lesions near background activity, suggesting that the kinetics of response might vary between lesions and the presence of one or more PET-positive lesions might be enough to predict response. Although formal study in larger cohorts is needed, these cases illustrate the potential CD8 PET/CT imaging could ultimately have in clinical care to help assess response to immunotherapy.

^{18}F-FDG and ^{18}F-FLT PET/CT have also been used to assess response to immunotherapy (25–32). However, these probes do not specifically target the immune system, so changes in organ and tumor uptake can be difficult to interpret. Recently, the results from a PET imaging trial with ^{89}ZED88082A, a CD8-targeted probe, were presented (33). ^{89}ZED88082A demonstrated uptake in the spleen, lymph nodes, and bone marrow similar to that of ^{89}Zr-Df-IAB22M2C; however, comparison of tumor uptake is difficult given differences in patient populations.

One limitation of this study is the heterogeneous, small patient population, with different tumor types, tumor burden, and treatment history. However, despite these differences the scans were remarkably similar, with comparable normal-tissue biodistribution and stable uptake in both CD8-rich (SUV$_{MAX}$ range, 3.7–58) and CD8-poor (SUV$_{MAX}$ range, 0.35–0.60) tissues (based on known histology of these tissues rather than directly on biopsy material from study patients) from 24 h onward. An additional limitation of this study is a lack of correlative biopsy data, although the biodistribution of ^{89}Zr-Df-IAB22M2C aligned with the expected distribution of CD8+ leukocytes, with saturable signal in CD8-rich tissues at higher doses of cold minibody. An ongoing phase 2 trial (NCT03802123) will test both the diagnostic performance and the predictive performance of ^{89}Zr-Df-IAB22M2C, by correlating CD8 signal on PET/CT imaging to CD8+ T-cell infiltration from biopsy samples, and response to cancer immunotherapy, respectively.

CONCLUSION

This first-in-humans study demonstrated that PET imaging with ^{89}Zr-Df-IAB22M2C is safe and well tolerated, and has the potential to visualize the whole-body biodistribution of CD8+ leukocytes in tumors and reference tissues, which may predict response to immunotherapy. The results from this study, including the optimal scan timing (24 h after injection) and minibody mass dose (1.5 mg), are being used in the phase 2 study of ^{89}Zr-Df-IAB22M2C, which is currently under way.

KEY POINTS

QUESTION: Is it feasible to image CD8+ leukocytes in patients with cancer using ^{89}Zr-IAB22M2C PET/CT?

PERTINENT FINDINGS: ^{89}Zr-Df-IAB22M2C was found to be safe and well tolerated, with tumor uptake spanning a wide dynamic range. Additionally, the optimal scan timing (24 h after injection) and minibody mass dose (1.5 mg) were selected. In 3 cases with clinical follow-up, increased ^{89}Zr-Df-IAB22M2C uptake in tumor lesions correlated with response.

IMPLICATIONS FOR PATIENT CARE: CD8 PET/CT imaging with ^{89}Zr-Df-IAB22M2C is currently being studied as a predictor of or early measure of response to cancer immunotherapy.

REFERENCES

1. Haslam A, Prasad V. Estimation of the percentage of US patients with cancer who are eligible for and respond to checkpoint inhibitor immunotherapy drugs. *JAMA Netw Open.* 2019;2:e192535.

2. Brahmer JR, Tykodi SS, Chow LQ, et al. Safety and activity of anti-PD-L1 antibody in patients with advanced cancer. *N Engl J Med.* 2012;366:2455–2465.

3. Topalian SL, Hodi FS, Brahmer JR, et al. Safety, activity, and immune correlates of anti-PD-1 antibody in cancer. *N Engl J Med.* 2012;366:2443–2454.

4. Azimi F, Scolyer RA, Rumcheva P, et al. Tumor-infiltrating lymphocyte grade is an independent predictor of sentinel lymph node status and survival in patients with cutaneous melanoma. *J Clin Oncol.* 2012;30:2678–2683.

5. Gooden MJ, de Bock GH, Leffers N, Daemen T, Nijman HW. The prognostic influence of tumour-infiltrating lymphocytes in cancer: a systematic review with meta-analysis. *Br J Cancer.* 2011;105:93–103.

6. Huang AC, Orlowski RJ, Xu X, et al. A single dose of neoadjuvant PD-1 blockade predicts clinical outcomes in resectable melanoma. *Nat Med.* 2019;25:454–461.

7. Ribas A, Dummer R, Puzanov I, et al. Oncolytic virotherapy promotes intratumoral T cell infiltration and improves anti-PD-1 immunotherapy. *Cell.* 2018;174:1031–1032.

8. Tumeh PC, Harview CL, Yearley JH, et al. PD-1 blockade induces responses by inhibiting adaptive immune resistance. *Nature.* 2014;515:568–571.

9. Griessinger CM, Olafsen T, Mascioni A, et al. The PET-tracer (89)Zr-Df-IAB22M2C enables monitoring of intratumoral CD8 T-cell infiltrates in tumor-bearing humanized mice after T-cell bispecific antibody treatment. *Cancer Res.* 2020;80:2903–2913.

10. Olafsen T, Torgov M, Zhang GG, et al. PET imaging of cytotoxic human T cells using an ^{89}Zr-labeled anti-CD8 minibody. *J Immunother Cancer.* 2015;3(suppl 2):P388.

11. Olafsen T, Jiang ZK, Romero J, et al. Sensitivity of ^{89}Zr-labeled anti-CD8 minibody for PET imaging of infiltrating CD8+ T cells [abstract]. *Cancer Res.* 2016;76:LB-188.

12. Pandit-Taskar N, Postow MA, Hellmann MD, et al. First-in-humans imaging with ^{89}Zr-Df-IAB22M2C anti-CD8 minibody in patients with solid malignancies: preliminary pharmacokinetics, biodistribution, and lesion targeting. *J Nucl Med.* 2020;61:512–519.

13. Holland JP, Caldas-Lopes E, Divilov V, et al. Measuring the pharmacodynamic effects of a novel Hsp90 inhibitor on HER2/neu expression in mice using Zr-DFO-trastuzumab. *PLoS One.* 2010;5:e8859.

14. Holland JP, Divilov V, Bander NH, Smith-Jones PM, Larson SM, Lewis JS. ^{89}Zr-DFO-J591 for immunoPET of prostate-specific membrane antigen expression in vivo. *J Nucl Med.* 2010;51:1293–1300.

15. Holland JP, Sheh Y, Lewis JS. Standardized methods for the production of high specific-activity zirconium-89. *Nucl Med Biol.* 2009;36:729–739.

16. Stabin MG, Sparks RB, Crowe E. OLINDA/EXM: the second-generation personal computer software for internal dose assessment in nuclear medicine. *J Nucl Med.* 2005;46:1023–1027.

17. Siegel JA, Thomas SR, Stubbs JB, et al. MIRD pamphlet no. 16: techniques for quantitative radiopharmaceutical biodistribution data acquisition and analysis for use in human radiation dose estimates. *J Nucl Med.* 1999;40:37S–61S.

18. International Commission on Radiological Protection (ICRP). The 2007 Recommendations of the International Commission on Radiological Protection. ICRP publication 103. *Ann ICRP.* 2007;37:1–332.

19. Börjesson PK, Jauw YW, de Bree R, et al. Radiation dosimetry of ^{89}Zr-labeled chimeric monoclonal antibody U36 as used for immuno-PET in head and neck cancer patients. *J Nucl Med.* 2009;50:1828–1836.

20. Laforest R, Lapi SE, Oyama R, et al. [^{89}Zr]Trastuzumab: evaluation of radiation dosimetry, safety, and optimal imaging parameters in women with HER2-positive breast cancer. *Mol Imaging Biol.* 2016;18:952–959.

21. Lindenberg L, Adler S, Turkbey IB, et al. Dosimetry and first human experience with ^{89}Zr-panitumumab. *Am J Nucl Med Mol Imaging.* 2017;7:195–203.

22. Pandit-Taskar N, O'Donoghue JA, Ruan S, et al. First-in-human imaging with ^{89}Zr-Df-IAB2M anti-PSMA minibody in patients with metastatic prostate cancer: pharmacokinetics, biodistribution, dosimetry, and lesion uptake. *J Nucl Med.* 2016;57:1858–1864.

23. Ulaner GA, Lyashchenko SK, Riedl C, et al. First-in-human human epidermal growth factor receptor 2-targeted imaging using ^{89}Zr-pertuzumab PET/CT: dosimetry and clinical application in patients with breast cancer. *J Nucl Med.* 2018;59:900–906.

24. Chen DS, Mellman I. Elements of cancer immunity and the cancer-immune set point. *Nature.* 2017;541:321–330.

25. Cho SY, Lipson EJ, Im HJ, et al. Prediction of response to immune checkpoint inhibitor therapy using early-time-point ^{18}F-FDG PET/CT imaging in patients with advanced melanoma. *J Nucl Med.* 2017;58:1421–1428.

26. Iravani A, Osman MM, Weppler AM, et al. FDG PET/CT for tumoral and systemic immune response monitoring of advanced melanoma during first-line combination ipilimumab and nivolumab treatment. *Eur J Nucl Med Mol Imaging.* 2020;47:2776–2786.

27. Ito K, Teng R, Schoder H, et al. ^{18}F-FDG PET/CT for monitoring of ipilimumab therapy in patients with metastatic melanoma. *J Nucl Med.* 2019;60:335–341.

28. Nobashi T, Baratto L, Reddy SA, et al. Predicting response to immunotherapy by evaluating tumors, lymphoid cell-rich organs, and immune-related adverse events using FDG-PET/CT. *Clin Nucl Med.* 2019;44:e272–e279.

29. Scarpelli M, Zahm C, Perlman S, McNeel DG, Jeraj R, Liu G. FLT PET/CT imaging of metastatic prostate cancer patients treated with pTVG-HP DNA vaccine and pembrolizumab. *J Immunother Cancer.* 2019;7:23.

30. Seith F, Forschner A, Schmidt H, et al. ^{18}F-FDG-PET detects complete response to PD1-therapy in melanoma patients two weeks after therapy start. *Eur J Nucl Med Mol Imaging.* 2018;45:95–101.

31. Umeda Y, Morikawa M, Anzai M, et al. Predictive value of integrated ^{18}F-FDG PET/MRI in the early response to nivolumab in patients with previously treated non-small cell lung cancer. *J Immunother Cancer.* 2020;8: e000349.

32. Yeh R, Trager MH, Rizk EM, et al. FLT-PET at 6 weeks predicts response assessed by CT at 12 weeks in melanoma patients treated with pembrolizumab. *Clin Nucl Med.* 2020;45:267–275.

33. de Ruijter LK, van de Donk PP, Hooiveld-Noeken JS, et al. 89ZED88082A PET imaging to visualize CD8+ T cells in patients with cancer treated with immune checkpoint inhibitor [abstract]. *Cancer Res.* 2021;81:LB037.

Initial Clinical Experience with ^{90}Y-FAPI-46 Radioligand Therapy for Advanced-Stage Solid Tumors: A Case Series of 9 Patients

Justin Ferdinandus[1,2], Pedro Fragoso Costa[1,2], Lukas Kessler[1,2], Manuel Weber[1,2], Nader Hirmas[1,2], Karina Kostbade[2,3], Sebastian Bauer[2,3], Martin Schuler[2,3], Marit Ahrens[4], Hans-Ulrich Schildhaus[2,5], Christoph Rischpler[1,2], Hong Grafe[1,2], Jens T. Siveke[3,6,7], Ken Herrmann[1,2], Wolfgang P. Fendler*[1,2], and Rainer Hamacher*[2,3]

[1]Department of Nuclear Medicine, West German Cancer Center, University Hospital Essen, University of Duisburg-Essen, Essen, Germany, and Uital Essen, Essen, Germany; [2]German Cancer Consortium (DKTK), Partner Site University Hospital Essen, and German Cancer Research Center (DKFZ), Essen, Germany; [3]Department of Medical Oncology, West German Cancer Center, University Hospital Essen, University of Duisburg–Essen, Essen, Germany; [4]Medical Clinic II, University Hospital Frankfurt, Frankfurt am Main, Germany; [5]Department of Pathology, West German Cancer Center, University Hospital Essen, Essen, Germany; [6]Bridge Institute of Experimental Tumor Therapy, West German Cancer Center, University Medicine Essen, Essen, Germany; and [7]Division of Solid Tumor Translational Oncology, German Cancer Consortium (DKTK, Partner Site Essen) and German Cancer Research Center (DKFZ), Heidelberg, Germany

Fibroblast activation protein (FAP) is overexpressed in several solid tumors and therefore represents an attractive target for radiotheranostic applications. Recent investigations demonstrated rapid and high uptake of small-molecule inhibitors of FAP (^{68}Ga-FAPI-46) for PET imaging. Here, we report our initial experience of the feasibility and safety of ^{90}Y-FAPI-46 for radioligand therapy of extensively pretreated patients with solid tumors. **Methods:** Patients were considered for ^{90}Y-FAPI-46 therapy if they showed both an exhaustion of all approved therapies based on multidisciplinary tumor board decision, and high FAP expression, defined as SUV_{max} greater than or equal to 10 in more than 50% of all lesions. If tolerated, ^{90}Y-FAPI-46 bremsstrahlung scintigraphy was performed after therapy to confirm systemic distribution and focal tumor uptake, and ^{90}Y-FAPI-46 PET scans were performed at multiple time points to determine absorbed dose. Blood-based dosimetry was used to determine bone marrow absorbed dose. Adverse events were graded using Common Terminology Criteria for Adverse Events (version 5.0). **Results:** Nine patients either with metastatic soft-tissue or bone sarcoma ($n = 6$) or with pancreatic cancer ($n = 3$) were treated between June 2020 and March 2021. Patients received a median of 3.8 GBq (interquartile range [IQR], 3.25–5.40 GBq) for the first cycle, and 3 patients received subsequent cycles with a median of 7.4 GBq (IQR, 7.3–7.5 GBq). Posttreatment ^{90}Y-FAPI-46 bremsstrahlung scintigraphy demonstrated sufficient ^{90}Y-FAPI-46 uptake in tumor lesions in 7 of 9 patients (78%). Mean absorbed dose was 0.52 Gy/GBq (IQR, 0.41–0.65 Gy/GBq) in the kidney, 0.04 Gy/GBq (IQR, 0.03–0.06 Gy/GBq) in bone marrow, and less than 0.26 Gy/GBq in the lung and liver. Measured tumor lesions received up to 2.28 Gy/GBq (median, 1.28 Gy/GBq). New laboratory G3 or G4 toxicities were noted in 4 patients (44%, $n = 2$ patients with thrombocytopenia only, $n = 2$ patients with new onset of thrombocytopenia and anemia). Other G3 or G4 laboratory-based adverse events occurred in 2 patients or fewer. No acute toxicities attributed to ^{90}Y-FAPI-46 were noted. Radiographic disease control was noted in 4 patients (50%).

Conclusion: FAP-targeted radioligand therapy with ^{90}Y-FAPI-46 was well tolerated, with a low rate of attributable adverse events. Low radiation doses to at-risk organs suggest feasibility of repeat cycles of ^{90}Y-FAPI-46. We observed signs of tumor response, but further studies are warranted to determine efficacy and the toxicity profile in a larger cohort.

Key Words: FAPI; theranostics; fibroblast activation protein; solid tumors

T he fibroblast activation protein (FAP) is expressed by cancer-associated fibroblasts as well as cancer cells such as sarcoma and mesothelioma (*1–3*). Therefore, FAP is an attractive target for both imaging and radionuclide therapy of solid tumors. Previously, several groups have described high tumor uptake for ^{68}Ga- or ^{18}F-labeled PET compounds (*4–9*). For imaging, we used the FAP-targeted inhibitor FAPI-46 for diagnostic work-up of cancer types such as pancreatic cancer and sarcoma (*10,11*).

Recently, FAP-targeted radioligand therapy (RLT) has been described in several case reports (*12–14*); however, feasibility has not yet been systematically analyzed. In this case series, ^{90}Y-labeled FAPI-46 (^{90}Y-FAPI-46) RLT was offered to patients with advanced-stage solid tumors who have exhausted all established lines of treatment. ^{90}Y features high-branching-ratio β^- emission (99.99%) with an endpoint energy of 2.280 MeV, allowing high dose deposition within defined tumor lesions. Its relatively short half-life of 64.1 h makes it appropriate for therapeutic combinations in which the biochemical vector exhibits a short target retention time. Preclinical studies on FAPI-46 have demonstrated a decrease to 30% of tumor uptake from 1 to 24 h after injection (*14*). Posttreatment ^{90}Y-FAPI-46 scintigraphy is performed by measuring the β^- emission–associated bremsstrahlung radiation. ^{90}Y decays by internal conversion (0.0032%), emitting a positron with a total kinetic energy of 0.760 MeV. Positron emission enables PET quantitative data for dosimetry (*15*).

In this study, we report on the safety, dosimetry, and response for repeat ^{90}Y-FAPI-46 RLT in patients with advanced solid tumors.

MATERIALS AND METHODS

This was a monocentric, retrospective study of 9 patients with progressive, advanced-stage solid tumors receiving ^{90}Y-FAPI-46 under compassionate access for a clinical indication. Radionuclide treatment was recommended by a multidisciplinary tumor board. All patients either had previously progressed during established treatment options or were not eligible to receive other treatments. This study was approved by the institutional review board (reference 21-9842-BO). All patients provided written informed consent to undergo clinical RLT and for retrospective analysis of clinical data. All patients underwent PET imaging with ^{68}Ga-FAPI-46 before treatment to confirm the FAP positivity of tumor lesions, defined as an SUV_{max} greater than or equal to 10 in more than 50% of all lesions (Fig. 1). Imaging procedures were described previously (10); in brief, patients received a median of 103 MBq of ^{68}Ga-FAPI-46 (interquartile range [IQR], 87–133.5 MBq) intravenously and were scanned at a median of 37 min (IQR, 24.5–60 min) after injection. To be eligible for treatment, patients needed adequate bone marrow function (i.e., leukocytes > 2.5/nL, hemoglobin > 7.0 mg/dL, and thrombocytes > 75/nL), with exceptions for patients receiving regular transfusions. Before treatment, renal scintigraphy with ^{99m}Tc-MAG3 was performed to rule out urinary tract obstruction.

^{90}Y-FAPI-46 Synthesis

^{90}Y-FAPI-46 was synthesized using the Easyone synthesis module (Trasis) connected to shielded ^{90}Y-YCl$_3$ solution (Yttriga; Eckert and Ziegler). Before the automated synthesis started, the cassette was preloaded with FAPI-46 precursor (ABX, 8 μg/GBq), ascorbic acid, and sodium acetate buffer saline vials. The synthesis was fully automated using a good-manufacturing-practice–grade reagent and controlled by a preprogrammed sequence. The ^{90}Y-YCl$_3$ solution was transferred into the reactor, followed by the precursor and buffer mixture. For radiolabeling, the reaction mixture was heated to 90°C for 20 min. Afterward, the product was transferred into the bulk vial through a sterile filter and formulated with pentetic acid (1 mL, Ditripentat-Heyl; Heyl), ascorbic acid (~40 mg/GBq, vitamin C; Rotexmedica), and saline. The quality control procedures included reverse-phase–high-performance liquid chromatography, instant thin-layer chromatography, pH, endotoxin, and sterility testing. The average yield was 88% ± 7%, reverse-phase–high-performance liquid chromatography radiochemical purity was 98% ± 1%, concentration was 883 ± 70 MBq/mL, and shelf life was 24 h.

^{90}Y-FAPI-46 Administration

Patients underwent inpatient treatment to ensure radiation safety. Vital signs were monitored before and after administration of ^{90}Y-FAPI-46. Patients 1 and 2 received a planned activity of 7.4 GBq of ^{90}Y-FAPI-46 for the first cycle. All other patients received a planned first activity (scout dose) of 3.8 GBq of ^{90}Y-FAPI-46 with dosimetry. Focal ^{90}Y-FAPI-46 uptake was noted in more than 50% of tumor lesions on posttreatment ^{90}Y-FAPI-46 bremsstrahlung scintigraphy (Fig. 1), and if clinically indicated, patients were eligible to receive further cycles with 2 doses of 3.8 GBq of ^{90}Y-FAPI-46 (high dose), given on the same therapy day but 4 h apart. We chose fractionated applications to optimize prolonged radiation delivery on the basis of the observed short biologic half-life during scout cycles, which appeared to be less than 24 h. A therapeutic solution was administered intravenously with 500 mL of saline. Bremsstrahlung scintigraphy was performed approximately 24 h or, if possible, 0.5 h after therapy to confirm systemic distribution and focal tumor uptake. Whole-body planar imaging was performed at a scan speed of 10 cm/min, with an energy window of 90 − 125 keV and using a medium-energy collimator. All patients were discharged 48 h after administration, in accordance with radiation protection regulations.

Dosimetry

If tolerated, patients underwent dosimetry after therapy. ^{90}Y-FAPI-46 PET scans were not performed in cases of severe pain, a long acquisition (n = 3 during cycle 1 and n = 1 during cycle 2), or inability to tolerate or allow repeated blood sampling (n = 4). Bone marrow dosimetry was measured using repeated blood samples (0.5, 1, 2, 4, 24, 36, and 48 h after injection) and estimated according to OLINDA/MIRD recommendations. Dose absorbed by tumor lesions and kidneys was estimated using PET acquisitions. PET images were acquired at multiple time points (0.5, 3, and 18–24 h after injection) after ^{90}Y-FAPI-46 application. Data from at least 2 time points were necessary to determine lesion dose. Tumor and organ dosimetry was assessed by analyzing the respective regions of interest in the PET
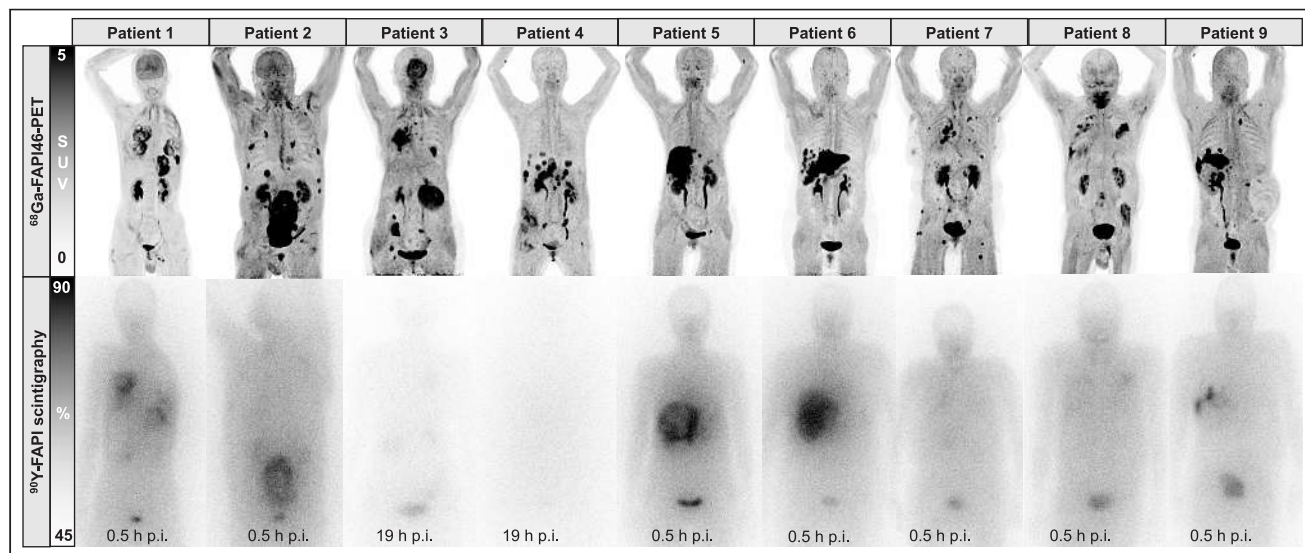
FIGURE 1. Pretreatment ^{68}Ga-FAPI-46 PET images and posttreatment ^{90}Y-FAPI-46 bremsstrahlung scintigraphs after first cycle of ^{90}Y-FAPI-46 RLT. p.i. = after injection.

images, from which the pharmacokinetic behavior was fitted to mono-exponential functions. Images were acquired in a Siemens mCT or Biograph Vision scanner, following an optimized protocol for quantification (16). PET quantification accuracy was validated in a National Electrical Manufacturers Association phantom, being considered most favorable when scanned in a silicon photomultiplier PET/CT scanner. Maximum liver and lung doses were assessed individually on the basis of minimum measurable ^{90}Y-FAPI-46 uptake in prior PET phantom studies. We considered the number of disintegrations that would take place in the organ, assuming the minimum detectable activity concentration of 100 kBq/mL and the pharmacokinetics observed in blood dosimetry at the standard organ volumetry stated in the OLINDA.

Outcomes and Statistical Analysis

Toxicity was recorded as per the Common Terminology Criteria for Adverse Events (version 5.0). Clinical, laboratory, and imaging follow-up was performed as per clinical routine, with laboratory and clinical visits every 2–4 wk and imaging within 1–2 mo. Imaging response was defined as per RECIST (version 1.1) for CT and PERCIST for ^{18}F-FDG PET/CT (17,18). Disease control was defined as complete (metabolic) response, partial (metabolic) response, or stable (metabolic) disease. All patients received baseline imaging with ^{18}F-FDG PET/CT to rule out sites of discordant disease. ^{18}F-FDG PET/CT was performed 2 wk after the first cycle in 7 patients (78%) (Supplemental Figs. 1–9; supplemental materials are available at http://jnm.snmjournals.org). For overall response rate, response was defined as complete (metabolic) response or partial (metabolic) response. Descriptive statistics were used to present data; median and IQR were used for continuous measures, and absolute number and percentage were used for categoric data. No statistical tests were used for this study. All statistical analysis was performed using R statistics (version 3.4.1, www.r-project.org).

RESULTS

Patient Characteristics

Nine patients either with metastatic soft-tissue or bone sarcoma ($n = 6$) or with pancreatic cancer ($n = 3$) were treated between June 2020 and March 2021 (Table 1). The median age was 57 y (IQR, 55–62 y). At baseline, most patients had a median of 6 (IQR, 2–6.5) previous systemic treatment lines (Table 1) and were progressive during their last regimen. The Eastern Cooperative Oncology Group score for most patients was greater than or equal to 2 ($n = 6$; 67%), and only 3 patients had an Eastern Cooperative Oncology Group score of 1 at baseline (Table 1).

Treatment and Dosimetry

Patients received a median dose of 3.8 GBq (IQR, 3.25–5.40 GBq) for the first cycle and 7.4 GBq (IQR, 7.3–7.5 GBq) for any subsequent cycle. Patient 3 received 3 cycles of ^{90}Y-FAPI-46 with a cumulative activity of 18.3 GBq. Patients 8 and 9 each have received 2 cycles of ^{90}Y-FAPI-46 for a total of 11.2 and 10.0 GBq, respectively. All other patients ($n = 6$) stopped treatment after the first cycle because of lack of focal ^{90}Y-FAPI-46 uptake based on posttreatment ^{90}Y-FAPI-46 scintigraphy in the tumor after the first cycle ($n = 2$) or rapid deterioration or death before the second cycle ($n = 4$).

Median renal absorbed dose was 0.52 Gy/GBq (IQR, 0.41–0.65 Gy/GBq; $n = 4$) per cycle. A median bone marrow absorbed dose of 0.04 Gy/GBq (IQR, 0.03–0.06 Gy/GBq; $n = 5$) was observed over all cycles. Liver and lung dosimetry was considered only for those patients on whom bone marrow dosimetry was performed. The maximum observed dose in liver and lung was less than or equal to 0.26 Gy/GBq, based on the assumptions presented in the methodology section.

TABLE 1
Patient Characteristics

Patient no.	Age (y)	Sex	Histology	Tumor sites (primary and metastatic)	Eastern Cooperative Oncology group	No. of previous systemic therapies	Concomitant therapy	Subsequent therapy	^{68}Ga-FAPI-46 (SUV$_{max}$ baseline)	Status	Follow-up (d)
1	22	Male	Osteosarcoma	Lung, heart, lymph nodes	2	7	–	–	12.1	Dead	24
2	66	Male	Chordoma	Bone, soft tissue, liver, lung, lymph nodes	3	2	–	Nivolumab	22.3	Dead	67
3	54	Female	Fibrosarcoma	Lung, lymph nodes, pancreas, bone	1	6	–	–	18.3	Follow-up	100
4	57	Female	PDAC	Liver, lung, lymph nodes, bone	3	2	–	Cisplatin	14.9	Dead	57
5	61	Female	PDAC	Pancreas, liver, lung, lymph nodes, bone	2	9	Trametinib	–	19.4	Dead	41
6	56	Female	PDAC	Pancreas, liver, lung, lymph nodes, kidney	2	6		–	16.5	Dead	105
7	63	Female	GNET	Lung, liver, lymph nodes, bone, soft tissue	1	3	–	Nivolumab	16.1	Follow-up	44
8	61	Male	Conventional chondrosarcoma	Lung, lymph nodes, pancreas, bone	2	1	–	–	16.7	Follow-up	36
9	56	Male	Spindle cell sarcoma	Kidney, liver, lung pleura	1	6	–	–	28	Follow-up	36

PDAC = pancreatic ductal adenocarcinoma; GNET = gastrointestinal neuroectodermal tumor.
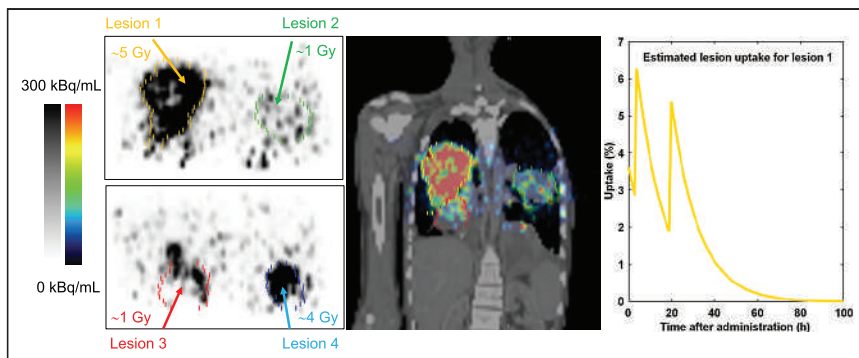
FIGURE 2. Posttreatment ^{90}Y-FAPI-46 PET images 4 h after injection with corresponding absorbed dose estimates for 4 lesions in patient 2.

Lesion dosimetry was available for 9 lesions in 6 patients, exemplarily shown for patient 2 (Fig. 2). Median tumor effective half-life was 8.7 h (range, 5.5−18 h). Median dose absorbed by tumor lesions after the first cycle was 1.28 Gy/GBq (IQR, 0.83–1.71 Gy/GBq) per cycle for target lesions and 0.95 Gy/GBq (IQR, 0.74–1.32 Gy/GBq) for secondary lesions. The highest doses were observed in patients 6 (1.37 Gy/GBq), 3 (1.23 Gy/GBq), and 9 (2.28 Gy/GBq). For subsequent cycles in patients 3 and 9, a median lesion dose of 1.28 and 2.04 Gy/GBq per cycle was measured, respectively. Table 2 outlines the dosimetry results.

Adverse Events and Follow-up

The median follow-up time was 44 d (IQR, 36–83.5 d). Three patients are still receiving RLT and had received 2 or 3 cycles at that point. Five patients died during follow-up. All 5 deaths were considered to be due to tumor progression and not related to ^{90}Y-FAPI-46

(Tables 1 and 3). In patients with progression, the median time until progression or death was 18.5 d (IQR, 14.8–38.5 d). There were no acute or allergic reactions observed immediately after infusion of ^{90}Y-FAPI-46. One patient, with advanced pulmonary metastasis and progressive intratumoral arteriovenous shunts, died because of acute respiratory failure attributed to tumor progression shortly after receiving his second cycle. Another patient developed a fever shortly after her first cycle, which was likely due to acute urinary tract infection and noncompliance with antibiotic medication. At baseline, 5 patients had one or more ongoing toxicities greater than or equal to grade 3. These were anemia ($n = 2$), increase of alkaline phosphatase ($n = 1$), or increase of γ-glutamyltransferase ($n = 3$) (Table 3). During follow-up, 4 patients showed new grade 3 or grade 4 laboratory toxicities (Table 3; Fig. 3). These 4 new adverse events were grade 3 thrombocytopenia ($n = 4$) possibly related to ^{90}Y-FAPI-46 and were also in temporal relation to either tumor progression or initiation of other concomitant systemic therapy (Fig. 3). One patient showed new grade 3 anemia, and 2 patients showed new increases of hepatic or pancreatobiliary serum markers greater than or equal to grade 3 (Table 3). All 3 of these new adverse events were rated as disease progression, given that all 3 of these patients had pancreatic cancer (Fig. 3). A detailed course of the relevant laboratory parameters is shown in Supplemental Figure 10.

Response Evaluation

Radiologic response as per RECIST (version 1.1) was available for 8 patients. The median time between imaging and the first

TABLE 2
^{90}Y-FAPI-46 Administered Activity and Absorbed Doses Per Cycle

Patient no.	Cycle no.	Activity (GBq)	Radiation dose (Gy/GBq)				
			Tumor lesion 1	Tumor lesion 2	Kidney	Liver and lung*	Bone marrow
1	1	7.1	0.74	0.63	—	—	—
2	1	7.0	—	—	—	—	—
3	1	3.5	1.23	1.23	0.75	<0.18	0.06
	2	7.3	1.28	0.95	0.41	<0.19	0.04
	3	7.5	1.47	1.35	0.61	<0.15	0.04
4	1	3.8	—	—	—	—	—
5	1	3.8	—	—	—	<0.16	0.06
6	1	3.0	1.37	—	—	—	—
7	1	3.5	0.91	0.84	0.52	<0.16	0.03
8	1	3.8	0.49	—	0.11	<0.26	0.08
	2	7.4	—	—	—	—	0.08
9	1	2.6	2.28	—	0.65	<0.21	0.04
	2	7.4	1.79	—	0.45	<0.25	0.02
Median			1.28	0.95	0.52	<0.19	0.04
IQR			0.83–1.71	0.74–1.32	0.41–0.65	<0.16–0.24	0.04–0.07

*Estimation based on maximum detectable activity concentration and blood tracer kinetic.

TABLE 3
Adverse Events After Onset of Treatment, Related or Unrelated

Patient no.	General	Hematology								Kidney		Liver						Pancreatobiliary						New G3/G4 AE (laboratory)
		WBCs		ANC		Hb		PLTs		sCr		T Bil		AST		ALT		GGT		ALP		Amylase		
		B	F	B	F	B	F	B	F	B	F	B	F	B	F	B	F	B	F	B	F	B	F	
1	Acute respiratory distress, tumor-related (G5)	–	–	–	–	G3	G2	–	G3	–	–	–	–	–	–	–	–	G2	G1	G1	–	–	–	Yes
2	Tumor pain (G2)	–	–	–	–	–	G1	–	G1	–	–	–	–	–	–	–	–	G1	G1	G1	G1	–	–	No
3	None	–	–	–	G1	–	–	–	G1	–	–	–	–	–	–	–	–	G1	G1	G1	G1	–	–	No
4	Tumor progression, (G5)	G1	G2	–	G1	G3	G3	G1	G3	–	G2	–	G3	–	G1	–	–	G1	G3	G2	G2	–	–	Yes
5	Tumor progression (G5)	–	–	–	–	G1	G2	G1	G3	–	G1	–	G2	G2	G4	G1	G4	G3	G4	G3	G3	–	–	Yes
6	Pneumonia*, tumor progression (G5)	–	–	–	–	G1	G3	G1	G3	–	G2	–	G2	–	G2	–	–	G3	–	G1	G2	–	–	Yes
7	Fever, urinary tract infection*	–	–	–	–	G1	G2	–	–	–	–	–	–	–	–	–	–	–	–	–	–	–	–	No
8	None	–	–	–	–	G1	–	–	–	–	–	–	–	–	–	–	–	–	G1	G1	G1	–	–	No
9	None	–	–	–	–	G1	G1	–	–	–	–	–	–	–	–	–	–	G3	G3	G2	G2	–	–	No
	Any new AE (%)	1 (11%)		1 (11%)		3 (33%)		6 (67%)		3 (33%)		3 (33%)		3 (33%)		1 (11%)		3 (33%)		1 (11%)		–		
	Any new G3/ G4 AE (%)	–		–		1 (11%)		4 (44%)		–		1 (11%)		1 (11%)		1 (11%)		2 (22%)		–		–		

*Relation to ^{90}Y-FAPI-46 was ruled out.

AE = adverse event; WBCs = white blood cells; ANC = absolute neutrophil count; Hb = hemoglobin; PLTs = platelets (thrombocytes); sCr = serum creatinine; T Bil = total bilirubin; AST = aspartate transaminase; ALT = alanine transaminase; GGT = γ-glutamyltransferase; ALP = alkaline phosphatase; B = baseline; F = follow-up.

G grade is defined as per CTCAE, version 5.0.

FIGURE 3. Swimmer plot of patients who received ^{90}Y-FAPI-46. Arrows indicate patients continuing ^{90}Y-FAPI-46 RLT at time of analysis. *Any new onset of toxicity greater than or equal to grade 3 according to Common Terminology Criteria for Adverse Events (version 5.0).

cycle of ^{90}Y-FAPI-46 was 16 d (IQR, 15–41 d). Disease control (stable disease) was noted in 4 of 8 patients (50%). No responses had been observed by the time of analysis. However, patient 3 had marked regression of a target lesion (-28%; Supplemental Fig. 3) after the first cycle with 3.5 GBq. Metabolic response as per PER-CIST (version 1.0) was available for 7 patients. Disease control was noted in 2 of 7 patients (29%), consisting of stable metabolic disease in one patient (14%; Supplemental Fig. 3) and partial metabolic response in the other (14%; Supplemental Fig. 9). Radiologic responses are outlined in Table 4.

DISCUSSION

We here report the first case series of patients with advanced-stage solid tumors treated with ^{90}Y-FAPI-46 RLT. Repeated ^{90}Y-FAPI-46 applications with individual dosimetry were used to ensure the safety of each patient and a maximum likelihood of treatment effect. For treatment initiation, patients had to have high uptake on ^{68}Ga-FAPI-46 PET in most tumor lesions, and for treatment continuation, patient

had to have focal uptake on the first posttreatment ^{90}Y-FAPI-46 bremsstrahlung scintigraphy (Fig. 1; Supplemental Figs. 1–9). Patients had exhausted all available on-label or evidence-based treatment options, and the most prevalent Eastern Cooperative Oncology Group score was 2 or higher. Treatment with ^{90}Y-FAPI-46 was offered under compassionate use with the intent of achieving antitumor effect with manageable toxicity. On the basis of the biodistribution observed on ^{68}Ga-FAPI-46, PET RLT using ^{90}Y-FAPI-46 was expected to deliver therapeutic radiation doses to the tumor while sparing organs at risk (4,11). Acute toxicities or immediate (e.g., allergic) reactions to RLT were not observed. During follow-up, adverse events began in almost all patients. However, only a small proportion was attributed to ^{90}Y-FAPI-46, given that most adverse events occurred after tumor progression or the switch of systemic therapy (Fig. 3). Additionally, we noted that toxicity in 1 patient who had received multiple RLT cycles with a cumulative activity of 18.3 GBq was limited to G1 thrombocytopenia. Ultimately, randomized trials on patients with symptomatic disease are needed for more detailed assessment of toxicity. Data from previous randomized trials evaluating ^{177}Lu-PSMA-617 or ^{177}Lu-DOTATATE identified hematotoxicity, especially thrombocytopenia, as a relevant (i.e., frequently occurring as grade 3/4) side effect (19,20). On the basis of our data, we expect a similar toxicity profile for ^{90}Y-FAPI-46. Therefore, repeated cycles of ^{90}Y-FAPI-46 RLT seem feasible, because the doses absorbed by the kidneys, bone marrow, liver, and lungs were low and comparable to those of other small-ligand ^{90}Y therapies (21). In our cohort, 3 patients received multiple cycles with a maximum cumulative activity of up to 18.3 GBq.

When all other available therapeutic options fail, achieving disease control is the primary goal for a novel therapy. Previously, Kratochwil et al. reported on a patient with spindle cell soft-tissue sarcoma who had

TABLE 4
Radiologic and Metabolic Best Overall Response

Patient no.	CT target response	CT nontarget response	RECIST response	PET target response	PET nontarget response	PERCIST response	SUV$_{max}$ ^{18}F-FDG baseline	SUV$_{max}$ ^{18}F-FDG follow-up
1	SD	SD	SD	PMR	SMD	PMD	14.8	21.8 ($+47\%$)
2	PD	SD	PD	PMD	PMD	PMD	28.6	22.3 (-22%)
3	SD	SD	SD	SMD	SMD	SMD	6.5	4.9 (-25%)
4	PD	PD	PD	SMD	PMD	PMD	5.1	3.8 (-26%)
5	PD	PD	PD	SMD	PMD	PMD	18.9	17.2 (-9%)
6	SD	SD	SD	—	—	—	6.1	—
7	—	—	—	—	—	—	14.3	—
8	SD	PD	PD	PMD	SMD	PMD	12.5	13.3 ($+6.4\%$)
9	SD	SD	SD	PMR	SMD	PMR	18	10.1 (-44%)
DCR (%)			4/8 (50%)			2/7 (29%)		
ORR (%)			0/8 (0%)			1/7 (14%)		

SD = stable disease; PMR = partial metabolic response; SMD = stable metabolic disease; PMD = progressive metabolic disease; PD = progressive disease; DCR = disease control rate; ORR = overall response rate.

a long period of stable disease under FAPI-46 RLT (12). Although the follow-up time is still short, we observed radiographic disease control in about half the patients, along with signs of tumor response. Patient 3 experienced meaningful benefit in the form of stable disease for over 4 mo, with regression of a large pancreatic tumor mass. Patient 9 showed a partial metabolic response and achieved the highest lesion dose with 13.2 Gy during cycle 2. Patients 3, 8, and 9 had additional cycles pending at the time of analysis. Interestingly, 3 of the 4 patients with disease control were patients with soft-tissue ($n = 2$) or bone ($n = 1$) sarcoma. The fourth patient had pancreatic cancer and received concomitant treatment with the tyrosine kinase inhibitor afatinib, which was well tolerated, therefore indicating the potential feasibility of combination therapy. In the quest to provide the most efficacious therapy with acceptable toxicity, especially in nonresponders, 2 future strategies should be considered: first, a more intense treatment regimen (i.e., short intercycle intervals or higher activities) and, second, RLT drug combination therapy. FAP and cancer-associated fibroblasts are drivers of immune escape (22,23); therefore, immunotherapy might be a rationale companion for FAP-targeted RLT. Preclinical studies in several cancer types suggest a synergistic effect of FAP targeting and immunotherapy (24–27). Recently, a case report showed good tolerance of ^{177}Lu-PSMA RLT in combination with pembrolizumab or sequentially after olaparib (28), which is currently being investigated in ongoing prospective phase 1/2 trials (NCT03874884, NCT03805594).

^{90}Y-FAPI-46 has a shorter half-life and higher energy per decay than ^{177}Lu-PSMA. Because of the short retention time in the tumor as described by Lindner et al. (14), ^{90}Y-FAPI-46 seemed more suitable for achieving therapeutic radiation doses in a tumor. ^{90}Y-FAPI-46 PET-based dosimetry has been successfully used for hepatic radioembolization dosimetry, after administration of ^{90}Y-labeled spheres (29). Phantom studies suggest that recent developments in sensitivity and timing resolution for PET scanners could be advantageous for accurate ^{90}Y quantification, (16) which could play a decisive role in the validation of ^{90}Y-labeled therapeutic drugs.

This study comes with limitations. The low number of patients and absence of a predefined imaging follow-up protocol does not allow for definitive conclusions regarding therapeutic efficacy and toxicity of ^{90}Y-FAPI-46. Further research to determine radiation dosimetry for ^{90}Y-FAPI-46 is warranted, because quantification and subsequent dosimetry are limited by the decay characteristics of ^{90}Y-FAPI-46 and the relatively low activity concentration in tissues. A low activity concentration combined with detector limits impairs accurate acquisition of the true lung and liver doses. However, the aim of this study was to report the initial clinical experience and to demonstrate the feasibility of ^{90}Y-FAPI-46 RLT.

CONCLUSION

FAP-targeted RLT with ^{90}Y-FAPI-46 was well tolerated, with a low rate of attributable adverse events, including thrombocytopenia. We found low radiation doses to the kidney and bone marrow, suggesting the feasibility of repeated cycles of ^{90}Y-FAPI-46. Although we observed the first signs of therapeutic efficacy, larger trials are needed to determine efficacy and the toxicity profile.

DISCLOSURE

ACKNOWLEDGMENTS

KEY POINTS

QUESTION: Is radionuclide therapy with ^{90}Y-FAPI-46 feasible for patients with advanced-stage solid tumors, and what are the side effects and absorbed doses?

PERTINENT FINDINGS: ^{90}Y-FAPI-46 leads to therapeutic irradiation of tumor lesions, and the radiation exposure of critical organs is low. Further, we observed, after a short follow-up, a low rate of toxicities, including thrombocytopenia, attributed to ^{90}Y-FAPI-46 in patients with advanced and symptomatic disease.

IMPLICATIONS FOR PATIENT CARE: Radionuclide therapy with ^{90}Y-FAPI-46 seems to be well tolerated, and repeated cycles are possible.

REFERENCES

1. Henry LR, Lee HO, Lee JS, et al. Clinical implications of fibroblast activation protein in patients with colon cancer. *Clin Cancer Res.* 2007;13:1736–1741.
2. Cohen SJ, Alpaugh RK, Palazzo I, et al. Fibroblast activation protein and its relationship to clinical outcome in pancreatic adenocarcinoma. *Pancreas.* 2008;37:154–158.
3. Dohi O, Ohtani H, Hatori M, et al. Histogenesis-specific expression of fibroblast activation protein and dipeptidylpeptidase-IV in human bone and soft tissue tumours. *Histopathology.* 2009;55:432–440.

4. Meyer C, Dahlbom M, Lindner T, et al. Radiation dosimetry and biodistribution of ^{68}Ga-FAPI-46 PET imaging in cancer patients. *J Nucl Med.* 2020;61:1171–1177.

5. Chen H, Pang Y, Wu J, et al. Comparison of [68Ga]Ga-DOTA-FAPI-04 and [18F] FDG PET/CT for the diagnosis of primary and metastatic lesions in patients with various types of cancer. *Eur J Nucl Med Mol Imaging.* 2020;47:1820–1832.

6. Giesel FL, Kratochwil C, Lindner T, et al. ^{68}Ga-FAPI PET/CT: biodistribution and preliminary dosimetry estimate of 2 DOTA-containing FAP-targeting agents in patients with various cancers. *J Nucl Med.* 2019;60:386–392.

7. Koerber SA, Staudinger F, Kratochwil C, et al. The role of ^{68}Ga-FAPI PET/CT for patients with malignancies of the lower gastrointestinal tract: first clinical experience. *J Nucl Med.* 2020;61:1331–1336.

8. Syed M, Flechsig P, Liermann J, et al. Fibroblast activation protein inhibitor (FAPI) PET for diagnostics and advanced targeted radiotherapy in head and neck cancers. *Eur J Nucl Med Mol Imaging.* 2020;47:2836–2845.

9. Kratochwil C, Flechsig P, Lindner T, et al. ^{68}Ga-FAPI PET/CT: tracer uptake in 28 different kinds of cancer. *J Nucl Med.* 2019;60:801–805.

10. Kessler L, Ferdinandus J, Hirmas N, et al. Ga-68-FAPI as diagnostic tool in sarcoma: data from the FAPI-PET prospective observational trial. *J Nucl Med.* April 30, 2021 [Epub ahead of print].

11. Ferdinandus J, Kessler L, Hirmas N, et al. Equivalent tumor detection for early and late FAPI-46 PET acquisition. *Eur J Nucl Med Mol Imaging.* 2021;48:3221–3227.

12. Kratochwil C, Giesel FL, Rathke H, et al. [153Sm]Samarium-labeled FAPI-46 radioligand therapy in a patient with lung metastases of a sarcoma. *Eur J Nucl Med Mol Imaging.* 2021;48:3011–3013.

13. Ballal S, Yadav MP, Kramer V, et al. A theranostic approach of [68Ga]Ga-DOTA. SA.FAPi PET/CT-guided [177Lu]Lu-DOTA.SA.FAPi radionuclide therapy in an end-stage breast cancer patient: new frontier in targeted radionuclide therapy. *Eur J Nucl Med Mol Imaging.* 2021;48:942–944.

14. Lindner T, Loktev A, Altmann A, et al. Development of quinoline-based theranostic ligands for the targeting of fibroblast activation protein. *J Nucl Med.* 2018;59: 1415–1422.

15. Wright CL, Zhang J, Tweedle MF, Knopp MV, Hall NC. Theranostic imaging of yttrium-90. *Biomed Res Int.* 2015;2015:481279.

16. Kunnen B, Beijst C, Lam M, Viergever MA, de Jong H. Comparison of the Biograph Vision and Biograph mCT for quantitative ^{90}Y PET/CT imaging for radioembolisation. *EJNMMI Phys.* 2020;7:14.

17. Eisenhauer EA, Therasse P, Bogaerts J, et al. New response evaluation criteria in solid tumours: revised RECIST guideline (version 1.1). *Eur J Cancer.* 2009;45: 228–247.

18. Wahl RL, Jacene H, Kasamon Y, Lodge MA. From RECIST to PERCIST: evolving considerations for PET response criteria in solid tumors. *J Nucl Med.* 2009;50 (suppl 1):122S–150S.

19. Strosberg J, El-Haddad G, Wolin E, et al. Phase 3 trial of ^{177}Lu-Dotatate for midgut neuroendocrine tumors. *N Engl J Med.* 2017;376:125–135.

20. Hofman MS, Emmett L, Sandhu S, et al. [177Lu]Lu-PSMA-617 versus cabazitaxel in patients with metastatic castration-resistant prostate cancer (TheraP): a randomised, open-label, phase 2 trial. *Lancet.* 2021;397:797–804.

21. Imhof A, Brunner P, Marincek N, et al. Response, survival, and long-term toxicity after therapy with the radiolabeled somatostatin analogue ^{90}Y-DOTA]-TOC in metastasized neuroendocrine cancers. *J Clin Oncol.* 2011;29:2416–2423.

22. Ziani L, Chouaib S, Thiery J. Alteration of the antitumor immune response by cancer-associated fibroblasts. *Front Immunol.* 2018;9:414.

23. Fearon DT. The carcinoma-associated fibroblast expressing fibroblast activation protein and escape from immune surveillance. *Cancer Immunol Res.* 2014;2:187–193.

24. Feig C, Jones JO, Kraman M, et al. Targeting CXCL12 from FAP-expressing carcinoma-associated fibroblasts synergizes with anti-PD-L1 immunotherapy in pancreatic cancer. *Proc Natl Acad Sci USA.* 2013;110:20212–20217.

25. Kraman M, Bambrough PJ, Arnold JN, et al. Suppression of antitumor immunity by stromal cells expressing fibroblast activation protein-alpha. *Science.* 2010;330: 827–830.

26. Wen X, He X, Jiao F, et al. Fibroblast activation protein-alpha-positive fibroblasts promote gastric cancer progression and resistance to immune checkpoint blockade. *Oncol Res.* 2017;25:629–640.

27. Chen L, Qiu X, Wang X, He J. FAP positive fibroblasts induce immune checkpoint blockade resistance in colorectal cancer via promoting immunosuppression. *Biochem Biophys Res Commun.* 2017;487:8–14.

28. Prasad V, Zengerling F, Steinacker JP, et al. First experiences with ^{177}Lu-PSMA therapy in combination with pembrolizumab or after pretreatment with olaparib in single patients. *J Nucl Med.* 2021;62:975–978.

29. Lhommel R, van Elmbt L, Goffette P, et al. Feasibility of ^{90}Y TOF PET-based dosimetry in liver metastasis therapy using SIR-Spheres. *Eur J Nucl Med Mol Imaging.* 2010;37:1654–1662.

A Comparison of ^{18}F-DCFPyL, ^{18}F-NaF, and ^{18}F-FDG PET/CT in a Prospective Cohort of Men with Metastatic Prostate Cancer

Aloÿse Fourquet[1], Adrian Rosenberg[1], Esther Mena[1], Joanna J. Shih[2], Baris Turkbey[1], Maxime Blain[3], Ethan Bergvall[1], Frank Lin[1], Stephen Adler[4], Ilhan Lim[5], Ravi A. Madan[6], Fatima Karzai[6], James L. Gulley[6], William L. Dahut[6], Bradford J. Wood[3], Richard Chang[3], Elliot Levy[3], Peter L. Choyke[1], and Liza Lindenberg[1,7]

[1]Molecular Imaging Branch, National Cancer Institute, National Institutes of Health, Bethesda, Maryland; [2]Division of Cancer treatment and Diagnosis: Biometric Research Program, National Cancer Institute, National Institutes of Health, Bethesda, Maryland; [3]Center for Interventional Oncology, Radiology and Imaging Sciences, Clinical Center, National Cancer Institute, National Institutes of Health, Bethesda, Maryland; [4]Clinical Research Directorate, Frederick National Laboratory for Cancer Research, National Cancer Institute, National Institutes of Health, Bethesda, Maryland; [5]Department of Nuclear Medicine, Korea Cancer Center Hospital, Korea Institute of Radiological and Medical Sciences, Seoul, Korea; [6]Genitourinary Malignancies Branch, National Cancer Institute, National Institutes of Health, Bethesda, Maryland; and [7]F. Edward Hebert School of Medicine, Uniformed Services University of the Health Sciences, Bethesda, Maryland

^{18}F-DCFPyL, ^{18}F-sodium fluoride (^{18}F-NaF), and ^{18}F-FDG PET/CT were compared in a prospective cohort of men with metastatic prostate cancer (PCa). **Methods:** Sixty-seven men (group 1) with documented metastatic PCa underwent ^{18}F-DCFPyL and ^{18}F-NaF PET/CT and a subgroup of 30 men (group 2) underwent additional imaging with ^{18}F-FDG PET/CT. The tracers were compared for their detection rates, imaging concordance, associations with prostate-specific antigen (PSA), treatment at the time of imaging, and castration status. **Results:** Overall, 61 men had metastatic disease detected on one or more scans, and 6 men had no disease uptake on any of the PET/CT scans (and were subsequently excluded from the analysis). In group 1, ^{18}F-NaF detected significantly more metastatic lesions than ^{18}F-DCFPyL (median of 3 lesions vs. 2, P = 0.001) even after eliminating benign causes of ^{18}F-NaF uptake. This difference was particularly clear for men receiving treatment (P = 0.005) or who were castration-resistant (P = 0.014). The median percentage of bone lesions that were concordant on ^{18}F-DCFPyL and ^{18}F-NaF was 50%. In group 2, ^{18}F-DCFPyL detected more lesions than ^{18}F-FDG (median of 5 lesions vs. 2, P = 0.0003), regardless of PSA level, castration status, or treatment. The median percentage of lesions that were concordant on ^{18}F-DCFPyL and ^{18}F-FDG was 22.2%. This percentage was slightly higher for castration-resistant than castration-sensitive men (P = 0.048). **Conclusion:** ^{18}F-DCFPyL PET/CT is the most versatile of the 3 PET agents for metastatic PCa; however, ^{18}F-NaF detects more bone metastases. Imaging reveals substantial tumor heterogeneity with only 50% concordance between ^{18}F-DCFPyL and ^{18}F-NaF and 22% concordance for ^{18}F-DCFPyL and ^{18}F-FDG. These findings indicate considerable phenotypic differences among metastatic lesions.

Key Words: prostate cancer; metastatic; PSMA; NaF; FDG

Prostate cancer (PCa) is the second leading cause of cancer death among men in the United States, with a 5-y survival rate of only 31% in men with metastatic disease (1). In recent years, precision medicine has offered the hope of improving outcome with treatments tailored to the molecular and clinical characteristics of an individual patient's malignancy (2,3).

In this context, several targeted radiotracers have emerged to assess PCa by PET/CT. ^{18}F-sodium fluoride (^{18}F-NaF) demonstrates uptake at sites of bone remodeling and osteoblastic activity, with higher sensitivity and specificity for detecting bone metastases than conventional bone scintigraphy (4,5). ^{18}F-DCFPyL targets prostate-specific membrane antigen (PSMA), a membrane glycoprotein highly expressed on PCa cells, especially in metastatic disease (6–8). The most widely used PET agent, ^{18}F-FDG, reflects glucose metabolism commonly upregulated in malignant cells. Although most localized PCa tumors are not ^{18}F-FDG–avid (9), its uptake increases with aggressive and widely metastatic disease (10). Direct comparisons of these agents could cast light on their relative value in men with metastatic PCa.

Therefore, we prospectively compare the performance of ^{18}F-DCFPyL with ^{18}F-NaF and ^{18}F-DCFPyL with ^{18}F-FDG in men with metastatic PCa to understand patterns of overlap and discordance and their potential significance.

MATERIALS AND METHODS

Patient Selection and Study Design

This single-institution open-label prospective, Health Insurance Portability and Accountability Act–compliant study was approved by the institutional review board (NCT03173924) and radiation safety branch. All patients were enrolled after written informed consent was obtained. Eligibility criteria included men with histopathologically confirmed PCa and identifiable metastatic disease on standard-of-care imaging (CT or conventional bone scan). Exclusion criteria included subjects for whom participating would significantly delay standard therapy. There were no exclusion criteria regarding prior or ongoing therapies. Diagnostic and prior treatment history, castration status, and current treatments were recorded after clinical review of medical records.

PET Imaging Protocol

Group 1 subjects underwent ^{18}F-DCFPyL and ^{18}F-NaF PET/CT on separate occasions but within 35 d of each other. ^{18}F-DCFPyL was intravenously injected (mean injected dose, 291.3 MBq [range, 221.4–399.7 MBq]), followed by a head-to-toe PET/CT scan at a mean time of 121.7 ± 7.9 min after injection. ^{18}F-NaF was administered intravenously (mean injected dose, 125.2 MBq [range, 97.9–201.7 MBq]), followed by a head-to-toe PET/CT at a mean time of 63.7 ± 6.0 min after injection.

A subcohort of 30 patients imaged with ^{18}F-DCFPyL also underwent ^{18}F-FDG PET/CT imaging on a separate occasion (group 2) within 33 d of each other. ^{18}F-FDG was administered intravenously (mean injected dose, 377.0 MBq [range, 327.3–433.7 MBq]), with whole-body scanning at a mean time of 61.4 ± 4.6 min after injection.

Imaging was performed on a 3D time-of-flight–mode Discovery MI DR camera (GE Healthcare) with low-dose (120 kV, 60 mAs) CT-based attenuation correction along with random, normalization, dead time and scatter correction.

When technically feasible and after patient consent, a biopsy of at least 1 suggestive lesion identified on imaging was performed within 4–6 mo of scanning.

Imaging Analysis

PET/CT review and analysis was performed using a MIM workstation (version 6.9.2; MIM Software Inc.) by 3 experienced nuclear medicine physicians. Only lesions that were highly suggestive of metastatic or recurrent disease by consensus were included. Indeterminate lesions were excluded from the analysis. In particular, benign causes of increased uptake on ^{18}F-NaF scans were eliminated from the dataset.

SUV, tumor volume (TV), and total lesion uptake (TLU) were reported for every lesion after a semiautomatic segmentation analysis tool for contouring (PET-Edge) was applied. TLU was calculated as the multiplication of SUV_{mean} and TV for each lesion. All values obtained per person were summed to calculate the TLU at the patient level. The total tumor burden (TB) was calculated as the sum of TV from all reported lesions per person.

When the scan showed extensive disease, with lesions too numerous to delineate manually, a semiautomatic software algorithm based on an SUV threshold was used. The pathologic threshold SUV was set at 3 for both ^{18}F-DCFPyL and ^{18}F-FDG and 10 for ^{18}F-NaF. Physiologic uptake and benign and indeterminate lesions were then removed by the readers so that only highly suggestive foci were included in the analysis. In these men, exact lesion number was impossible to count, thus only the TB and the TLU were recorded.

Lesion detection rates and imaging concordance were determined at the patient level and lesion level for the 3 agents. Positive lesions in the same location on different scans were considered concordant regardless of variation in volume or extent. Lesion detection rate and imaging concordance were correlated with PSA, castration status, and treatment at the time of imaging. Men were considered castration-resistant (CRPC) if they had a history of androgen deprivation therapy (ADT) with castrate serum testosterone (<50 ng/dL) plus biochemical or radiologic progression, and were considered castration-sensitive (CSPC) if they never had ADT or if they had a history of ADT but did not fit criteria of CRPC.

Statistical Analysis

^{18}F-DCFPyL, ^{18}F-NaF, and ^{18}F-FDG PET characteristics (number of lesions, TB, and TLU) were correlated to PSA values using Spearman rank correlation. Differences in imaging PET parameters across individual characteristics, such as castration status and treatment at the time of imaging, were evaluated using the Wilcoxon rank-sum test. Comparisons of number of lesions and TB between ^{18}F-NaF and ^{18}F-DCFPyL (for bone lesions only) and between ^{18}F-FDG and ^{18}F-DCFPyL were performed with the paired Wilcoxon test. Lesions were categorized as concordant or discordant across tracers. Concordance between tracers at the patient level was evaluated using Wilcoxon rank-sum and Spearman rank correlation. All tests were 2-sided, and P values < 0.05 were considered significant.

RESULTS

Population

Overall, a total of 67 patients (median age, 67.8 y; age range, 51–84 y) with documented metastatic PCa met criteria for the protocol between June 2017 and February 2020. Six patients were excluded from the analysis because there was no disease uptake on any of the PET/CT scans; therefore only 61 evaluable patients were analyzed. Seven patients (11.5%) had newly diagnosed metastatic PCa and had not received any treatment at the time of imaging. Further specific patient demographics are listed in Table 1. The mean time between ^{18}F-DCFPyL and ^{18}F-NaF and between ^{18}F-DCFPyL and ^{18}F-FDG scans was 7 d (range, 1–35 d) and 8 d (range, 1–33 d),

TABLE 1
Patient Demographics ($n = 61$)

Characteristic	Data
Median age (y)	67.8 (range, 51–84)
ISUP grade	
1	5 (8.2%)
2	6 (9.8%)
3	9 (14.8%)
4	15 (24.6%)
5	25 (41.0%)
Not available	1 (1.6%)
Initial treatment	
None	7 (11.5%)
Surgery (prostatectomy +/− lymph node dissection)	28 (45.9%)
Definitive radiation therapy +/− ADT	12 (19.6%)
ADT	7 (11.5%)
ADT + chemotherapy	5 (8.2%)
Cryotherapy	2 (3.3%)
Castration status	
Castration-sensitive	41 (67.3%)
Castration-resistant	20 (32.7%)
Median PSA (ng/mL)	9.97 (range 0.02–7270.8)
Median PSA doubling time (months)	5.1 (range 0.7–81.7)
Median PSA velocity (ng/mL/y)	15.4 (range 0.1–5967.4)
Therapy at time of imaging	
No treatment	34 (55.7%)
ADT	18 (29.5%)
ADT + other	3 (4.9%)
Other (chemotherapy, immunotherapy, estradiol patch)	6 (9.8%)

ISUP = International Society of Urological Pathologists.
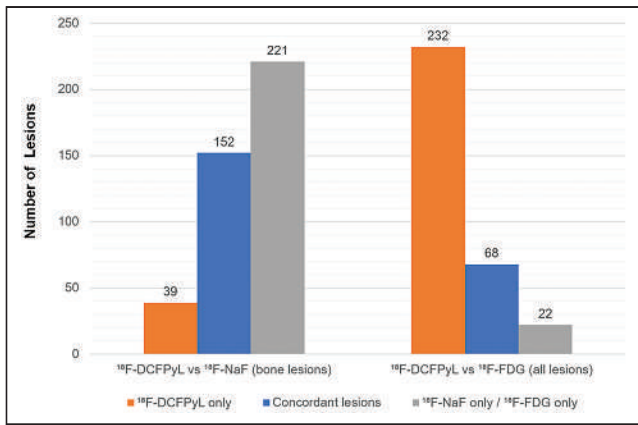
FIGURE 1. Lesion number comparisons.

respectively. Patients did not experience adverse events or clinically detected pharmacologic effects after PET scans.

Comparison Between ^{18}F-DCFPyL and ^{18}F-NaF (Group 1)

Patient-Based Detection Rate and Concordance Between Radiotracers. All 61 patients had at least 1 pathologic focus consistent with metastatic bone disease on ^{18}F-DCFPyL. The ^{18}F-NaF detection rate was 77.0% for metastatic bone disease.

The median percentage of bone lesions that were concordant between ^{18}F-DCFPyL and ^{18}F-NaF was 50%. The imaging concordance between ^{18}F-NaF and ^{18}F-DCFPyL was independent of castration status, PSA values, treatment at the time of imaging, and time from diagnosis to imaging.

Lesion-Based Detection Rate. A total of 412 bone lesions were detected by ^{18}F-DCFPyL or ^{18}F-NaF. Lesions from 6 patients with extensive disease ("superscans") were excluded from this analysis because an accurate lesion count was not feasible. ^{18}F-NaF detected 373 of 412 (90.5%) bone lesions and ^{18}F-DCFPyL detected 191 (46.4%). A total of 152 of these bone lesions were concordant between ^{18}F-NaF and ^{18}F-DCFPyL, 39 were detected by ^{18}F-DCFPyL only, and 221 were detected by ^{18}F-NaF only (Fig. 1). The median number of bone lesions detected by ^{18}F-NaF was higher than that by ^{18}F-DCFPyL ($P = 0.001$) (Fig. 2). Lesion tumor volume detected only by ^{18}F-NaF was significantly lower than that of lesions detected by both ^{18}F-NaF and ^{18}F-DCFPyL ($P < 0.05$). In this population, ^{18}F-DCFPyL identified 450 soft-tissue lesions (186 pelvic lymph nodes, 112 retroperitoneal lymph nodes, 92 distant lymph nodes, and 11 visceral lesions) in addition to the bone lesions.

Correlation with PSA. The number of lesions, TLU, and total TV derived from ^{18}F-DCFPyL and ^{18}F-NaF correlated with PSA and PSA velocity (Table 2). The strongest correlation was seen between PSA and TLU ($\rho = 0.6$, $P < 0.001$) and total TV ($\rho = 0.55$, $P < 0.001$) detected by ^{18}F-DCFPyL. These PET metrics showed a weak correlation with PSA doubling time.

The median number of bone lesions detected by ^{18}F-NaF was slightly higher than that by ^{18}F-DCFPyL at low PSA levels and rose with increasing PSA (Fig. 3A). The same trend was noted for TV, with a greater TV detected by ^{18}F-NaF than by ^{18}F-DCFPyL, but the difference was not significant.

Correlation with Treatment at the Time of Imaging. Men were subdivided into 2 groups according to their treatment at the time of imaging: 1 group consisted of 27 men receiving treatment (mainly ADT and chemotherapy) and the other group consisted of 34 men with no treatment at the time of imaging. Number of lesions, TB, and TLU were higher in the group receiving treatment than in men without treatment (P values ranging from 0.016 to 0.057) (Table 3).

For men without treatment, there was no significant difference in median number of bone lesions detected by ^{18}F-NaF versus ^{18}F-DCFPyL, but more bone lesions were detected by ^{18}F-NaF than by ^{18}F-DCFPyL among men receiving treatment (Fig. 3B). Although the difference was not significant, the same pattern was noted for TV with higher bone tumor volume detected by ^{18}F-NaF in comparison to ^{18}F-DCFPyL.

Correlation with Castration Status. Number of lesions, TB, and TLU showed a positive correlation with CRPC status (P values between 0.005 and 0.042) (Table 3).

In CSPC patients, there was no significant difference in median number of bone lesions detected by ^{18}F-NaF versus ^{18}F-DCFPyL, but more bone lesions were detected by ^{18}F-NaF among CRPC patients (9 vs. 5 lesions; $P = 0.014$) (Fig. 4A). The TB detected by ^{18}F-NaF was higher than that by ^{18}F-DCFPyL for CRPC patients ($P = 0.017$) and CSPC patients ($P = 0.051$).

Histopathology. A biopsy was performed in 32 patients (52.5%). Five patients had biopsies from 2 different locations. Among the 37 samples, 5 were prostate gland, 6 lymph nodes, 22 bone lesions, and 4 visceral lesions. Most of the samples (94.6%) demonstrated metastases of PCa. Of 22 bone lesions, ^{18}F-NaF demonstrated 2
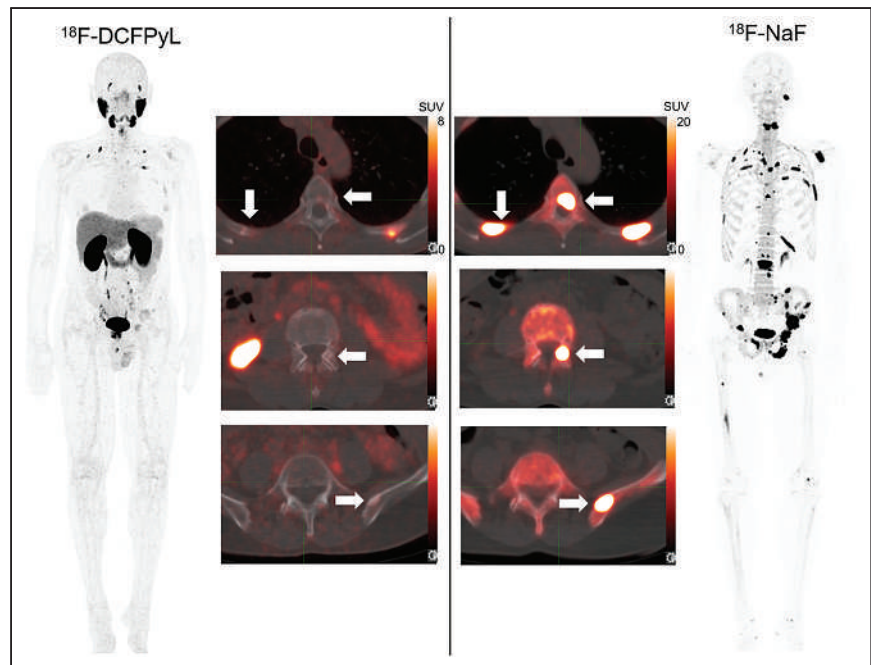
FIGURE 2. ^{18}F-DCFPyL (left) and ^{18}F-NaF (right) discordance. A 61-y-old man with metastatic PCa involving lymph nodes and bones. PSA at imaging was 49.69 ng/mL. More bone lesions were seen with ^{18}F-NaF than with ^{18}F-DCFPyL (arrows).

TABLE 2
Correlation of PSA Characteristics with PET Metrics Derived from ^{18}F-DCFPyL, ^{18}F-NaF, and ^{18}F-FDG, Using Spearman Correlation Coefficient

Parameter	^{18}F-DCFPyL		^{18}F-NaF		^{18}F-FDG	
	PSA	PSA velocity	PSA	PSA velocity	PSA	PSA velocity
No. of lesions	0.47 (<0.001)	0.38 (0.003)	0.41 (0.001)	0.25 (0.06)	0.21 (0.268)	0.39 (0.038)
Total lesion uptake	0.6 (<0.001)	0.53 (<0.001)	0.31 (0.014)	0.33 (0.015)	0.44 (0.014)	0.32 (0.087)
Total tumor burden	0.55 (<0.001)	0.5 (<0.001)	0.34 (0.007)	0.29 (0.028)	0.44 (0.016)	0.34 (0.074)

Expressed as correlation coefficient (ρ) with P values in parentheses.

false-positives (rib, sacrum) and 20 true-positives. ^{18}F-DCFPyL revealed 2 false-positives (rib, sacrum), 1 false-negative (sternum), and 34 true-positives (19 in bone).

Comparison Between ^{18}F-DCFPyL and ^{18}F-FDG (Group 2)

Patient-Based Detection Rate and Concordance Between Radiotracers. A cohort of 30 patients underwent both ^{18}F-DCFPyL and ^{18}F-FDG PET/CT imaging. The ^{18}F-FDG detection rate was 93.3% on a per-patient basis. The median percentage of lesions that were concordant between ^{18}F-DCFPyL and ^{18}F-FDG was 22% (Fig. 5). Imaging concordance between ^{18}F-DCFPyL and ^{18}F-FDG

was higher in men with CRPC (66.5%) than CSPC (20%) ($P = 0.019$) and was independent of other factors.

Lesion-Based Detection Rate. Among the 322 lesions detected by ^{18}F-FDG or ^{18}F-DCFPyL (244 soft-tissue lesions and 78 bone lesions), 68 were concordant, 232 were detected by ^{18}F-DCFPyL only, and 22 were detected by ^{18}F-FDG only. The median number of lesions detected by ^{18}F-DCFPyL was 5 (interquartile range, 3–15.5), which was significantly higher than ^{18}F-FDG (median of 2 lesions [interquartile range, 1–3.5], $P = 0.0003$).

Correlation with PSA, Treatment at the Time of Imaging, and Castration Status. Most metrics derived from ^{18}F-FDG correlated with PSA and PSA velocity, castration status, and treatment at the time of imaging (Table 2; Fig. 3C).

^{18}F-DCFPyL demonstrated more lesions than ^{18}F-FDG regardless of PSA, treatment, and castration status (Fig. 4B).

The total TV detected by ^{18}F-DCFPyL was greater than that by ^{18}F-FDG in the group with a PSA > 10 ng/mL ($P = 0.033$), when patients were not on treatment ($P = 0.044$) and in the CSPC group ($P = 0.017$).

Histopathology. A biopsy was performed in 17 men who underwent ^{18}F-FDG, revealing 3 false-negatives (iliac, ischium, and prostate) and 15 true-positives for the PET tracer.

DISCUSSION

Accurate assessment of disease burden is essential for the management of patients with metastatic PCa. However, it is unlikely that a single targeted imaging agent will detect all lesions given the heterogeneous nature of metastatic disease (*11*). With very different mechanisms of radiotracer uptake, the low percentage of concordant lesions among the 3 PET agents studied (^{18}F-DCFPyL, ^{18}F-NaF, and ^{18}F-FDG) supports the concept that many phenotypes of metastases exist, even within the same person.

In this study, ^{18}F-NaF showed the highest sensitivity for bone metastases. These results support the results in the study from Harmon et al. in which bone lesion detection rates for ^{18}F-NaF and a first-generation
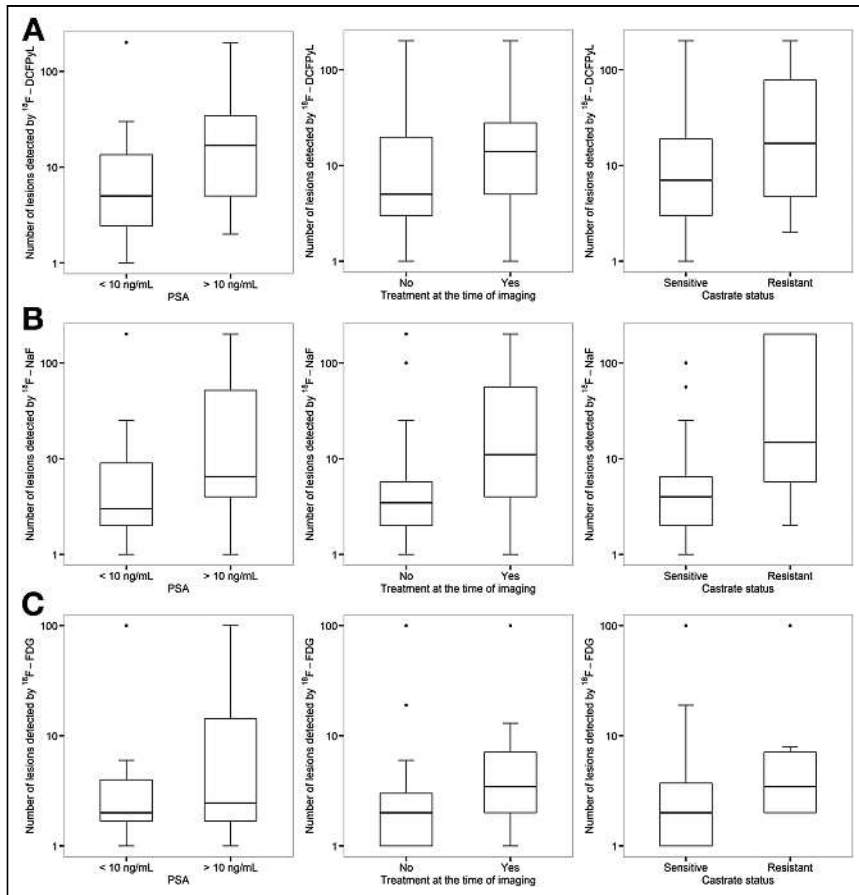
FIGURE 3. Number of lesions detected by ^{18}F-DCFPyL (A), ^{18}F-NaF (B), and ^{18}F-FDG (C) according to median PSA (left), treatment at the time of imaging (middle), and castration status (right).

TABLE 3
TABLE 3
^{18}F-DCFPyL, ^{18}F-NaF, and ^{18}F-FDG Median Number of Lesions, Total Tumor Volume, and Total Lesion Uptake According to Median PSA, Treatment at the Time of Imaging, and Castration Status

Feature	No. of lesions			Total tumor burden			Total lesion uptake		
	Median	IQR	P	Median	IQR	P	Median	IQR	P
PSA (ng/mL)									
PyL			0.005			<0.001			<0.001
<10	5	2.5–13.5		12.7	4.3–34.2		99.9	26–232.2	
>10	17	5–34		62.8	14.8–200		680.9	154.1–3,211	
NaF			0.006			0.079			0.115
<10	2	0–4		6	0–41.1		49.6	0–1,373.4	
>10	5.5	2–34		13.4	3.4–252		130.8	41.4–3,736.4	
FDG			0.5			0.052			0.05
<10	2	1–4		6.2	2.4–23.9		28	7.8–58.5	
>10	2	1–13		48.8	3.8–191		211	18–941	
Treatment ongoing									
PyL			0.057			0.016			0.021
No	5	3–20		16.6	4.2–51.9		117	20.1–507.6	
Yes	14	5–28		36.4	13.4–174		305.3	138.4–1,487	
NaF			0.05			0.024			0.048
No	3	1–5		5.8	0.4–18.9		56.8	4.3–404.6	
Yes	6	1.5–30.5		54.6	1.2–190		1062	19.5–2,466.3	
FDG			0.04			0.036			0.032
No	1.5	1–3		5	0.7–25.1		18	5–59	
Yes	3.5	2–7		38.7	10–87.3		112.5	33.2–237.2	
Castration status									
PyL			0.042			0.013			0.018
CS	7	3–19		21.3	4.4–60.2		122.3	37.9–575.9	
CR	17	5–93		77	13.6–192		302.4	157.9–2,123	
NaF			0.012			0.005			0.012
CS	3	1–5		5.82	0.4–20.5		49.6	3–475.5	
CR	9	3–95		93.1	11.1–655		1,256.2	70.4–4,475.6	
FDG			0.057			0.153			0.108
CS	2	1–3		6.21	1.8–45.8		21	7–139	
CR	3.5	2–7		25.6	10–86.1		71.5	33.3–518.5	

Expressed as median, with interquartile ranges in parentheses and *P* values in italic.

IQR = interquartile range; PyL = ^{18}F-DCFPyL; NaF = ^{18}F-NaF; FDG = ^{18}F-FDG; CS = castration-sensitive; CR = castration-resistant

PSMA-targeting agent were 98.4% and 45.4%, respectively, which are similar to our detection rates (93% for ^{18}F-NaF vs. 46% for ^{18}F-DCFPyL) (*12*). Our findings also agree with the study by Uprimny et al. in which ^{18}F-NaF PET detected a higher number of metastatic bone lesions than ^{68}Ga-PSMA-11 PET (*13*). These results differ from 2 other studies that found no difference in diagnostic sensitivity for bone metastases between these 2 radiotracers (*14,15*).

It has been argued that ^{18}F-NaF scans are susceptible to false-positives due to benign disease mimicking metastases (*16*). However, in this series, in which histologic confirmation was available in several cases, there were only 2 false-positives among 22 osseous lesions detected with ^{18}F-NaF after trained nuclear medicine physicians eliminated obvious benign lesions from consideration. Because PCa cells induce bone formation in adjacent osteocytes, it is likely that only a few cancer cells can affect many regional osteocytes, leading to an amplification of signal on ^{18}F-NaF scans, heightening sensitivity compared with ^{18}F-DCFPyl. We believe that ^{18}F-NaF reflects active disease but may recognize disease below the detection threshold of ^{18}F-DCFPyL (*17,18*). The relatively high rates of recurrent disease after ^{177}Lu-PSMA therapy in sites not previously identified suggest there is a reservoir of PSMA-negative metastases in the bone that may be detectable by ^{18}F-NaF but not by PSMA radiotracers (*19*).

One explanation for the lesion mismatch between ^{18}F-NaF and ^{18}F-DCFPyl is that castration resistance could disproportionately
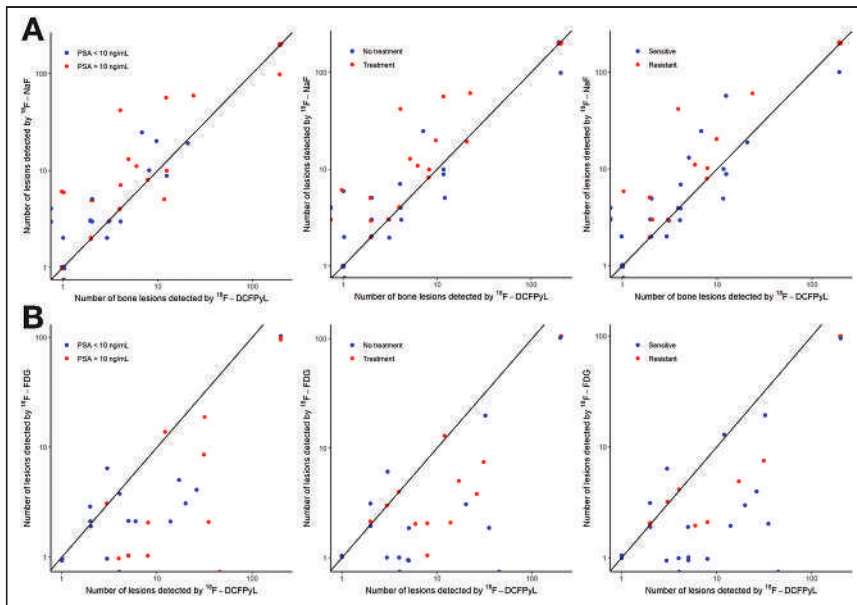
FIGURE 4. Comparison of median number of lesions detected by ^{18}F-NaF and ^{18}F-DCFPyL (bone lesions only) (A) and by ^{18}F-FDG and ^{18}F-DCFPyL (B) according to median PSA (left), treatment at the time of imaging (middle), and castration status.

influence the performance of ^{18}F-NaF relative to ^{18}F-DCFPyL (20). In CSPC patients, there was no difference in the median number of bone lesions detected by ^{18}F-NaF versus ^{18}F-DCFPyL, but more bone lesions were detected by ^{18}F-NaF among more heavily pretreated CRPC patients ($P = 0.014$). In immunohistochemistry studies, only 44% of bone metastases expressed PSMA, and osseous lesions with low PSMA detection were associated with CRPC, which could readily explain our findings of discordance with ^{18}F-NaF (7).

^{18}F-FDG– and PSMA-targeting agents showed low concordance in our study. PSMA-negative, FDG-positive lesions are thought to be more aggressive and are linked with poor outcomes as they are encountered more frequently in amphicrine and neuroendocrine phenotypes of CRPC (21). In our research, ^{18}F-DCFPyL detected significantly more lesions than ^{18}F-FDG ($P < 0.0001$) on both a per-patient and per-lesion basis regardless of castration or treatment status. In about 10% of men, some lesions were positive on ^{18}F-FDG and negative on ^{18}F-DCFPyL despite an overall higher lesion number seen by ^{18}F-DCFPyL, implying that a limited number of metastases may exhibit aggressive metabolic features with low PSMA (FDG+, PSMA–) earlier in the course of disease (22). Indeed, similar to the study by Wang et al. (23), we noted discordance between the 2 scans with 22 of 322 lesions (6.8%) detected by ^{18}F-FDG alone in 8 of 30 patients (27%), of which 3 were CRPC and 5 were CSPC. These lesions may be clinically relevant, as decreased survival and therapeutic response have been noted in men with abnormal ^{18}F-FDG PET findings (21, 22,24,25). ^{18}F-FDG uptake has been suggested as a biomarker for CRPC and when accompanied by negative ^{18}F-DCFPyL findings, may suggest evolution to neuroendocrine prostate cancer (26). Interestingly, as the disease progressed from CSPC to CRPC, concordance between ^{18}F-FDG and ^{18}F-DCFPyL scans increased ($P = 0.048$). The discordance among ^{18}F-DCFPyL, ^{18}F-FDG, and ^{18}F-NaF scans in individual lesions confirms phenotypic heterogeneity of PCa metastases, explaining, in part, the difficulty in eradicating such lesions.

The main limitation of this study was the lack of histologic proof for many of the suspected metastases. However, where biopsies were obtained, they overwhelmingly confirmed the presence of cancer in positive scans. Furthermore, readers had access to PET/CT images obtained with the other radiotracers, which may have biased the interpretation of faint uptake when scans were evaluated. However, these unmasked readings reflect daily practice. Finally, the metastatic population was broadly diverse and further investigation stratified by prior therapy may help clarify the respective roles of these radiotracers in the various states of PCa.

CONCLUSION

Imaging men with metastatic PCa using ^{18}F-NaF, ^{18}F-DCFPyL, and ^{18}F-FDG PET demonstrated that ^{18}F-DCFPyL had the best overall performance, but concordance with other agents was low, reflecting phenotypic tumor differences. ^{18}F-NaF identified a significantly higher number of metastatic bone lesions than ^{18}F-DCFPyL. Our study suggests that ^{18}F-NaF might provide additional staging information compared with ^{18}F-DCFPyL, especially in castration-resistant patients and patients receiving treatment at the time of imaging. ^{18}F-DCFPyL functioned better than ^{18}F-FDG in overall lesion detection and was more concordant in CRPC. Further research is warranted to elucidate the utility of ^{18}F-FDG PET and ^{18}F-NaF as prognostic tools and complementary agents to ^{18}F-DCFPyL in understanding tumor heterogeneity patterns in PCa metastases.
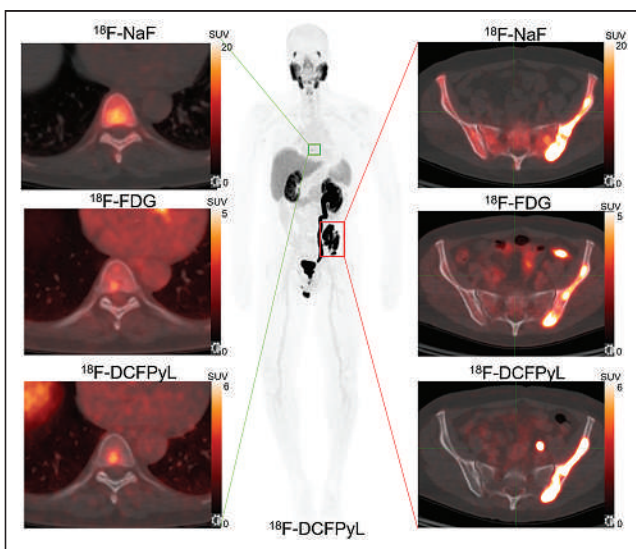
FIGURE 5. Concordant PET metastases. A 64-y-old man with metastatic CRPC. PSA at imaging was 464 ng/mL. Concordant pathologic foci were noted on all scans at T8 vertebral body and left iliac bone, consistent with metastasis.

KEY POINTS

QUESTION: How does ^{18}F-DCFPyL uptake compare with that of ^{18}F-NaF and ^{18}F-FDG PET/CT in men with metastatic PCa?

PERTINENT FINDINGS: In a prospective study of 67 men with metastatic PCa, ^{18}F-DCFPyL was the most versatile PET agent but ^{18}F-NaF detected more bone metastasis. Substantial tumor heterogeneity was revealed, with only 50% concordance between ^{18}F-DCFPyL and ^{18}F-NaF and 22% concordance between ^{18}F-DCFPyL and ^{18}F-FDG.

IMPLICATIONS FOR PATIENT CARE: ^{118}F-FDG and ^{18}F-NaF could be complementary agents to ^{18}F-DCFPyL in staging and illustrating heterogeneous disease characteristics that could optimize treatment strategies for men with metastatic PCa.

REFERENCES

1. American Cancer Society. *Cancer Facts & Figures 2020.* American Cancer Society; 2020.
2. Jackson SE, Chester JD. Personalised cancer medicine. *Int J Cancer.* 2015;137: 262–266.
3. Mateo J, Carreira S, Sandhu S, et al. DNA-repair defects and Olaparib in metastatic prostate cancer. *N Engl J Med.* 2015;373:1697–1708.
4. Langsteger W, Rezaee A, Pirich C, Beheshti M. ^{18}F-NaF-PET/CT and ^{99m}Tc-MDP bone scintigraphy in the detection of bone metastases in prostate cancer. *Semin Nucl Med.* 2016;46:491–501.
5. Löfgren J, Mortensen J, Rasmussen SH, et al. A prospective study comparing ^{99m}Tc-hydroxyethylene-diphosphonate planar bone scintigraphy and whole-body SPECT/CT with ^{18}F-fluoride PET/CT and ^{18}F-fluoride PET/MRI for diagnosing bone metastases. *J Nucl Med.* 2017;58:1778–1785.
6. Ghosh A, Heston WDW. Tumor target prostate specific membrane antigen (PSMA) and its regulation in prostate cancer. *J Cell Biochem.* 2004;91:528–539.
7. Silver DA, Pellicer I, Fair WR, Heston WD, Cordon-Cardo C. Prostate-specific membrane antigen expression in normal and malignant human tissues. *Clin Cancer Res.* 1997;3:81–85.
8. Wright GL, Haley C, Beckett ML, Schellhammer PF. Expression of prostate-specific membrane antigen in normal, benign, and malignant prostate tissues. *Urol Oncol.* 1995;1:18–28.
9. Reinicke K, Sotomayor P, Cisterna P, Delgado C, Nualart F, Godoy A. Cellular distribution of Glut-1 and Glut-5 in benign and malignant human prostate tissue. *J Cell Biochem.* 2012;113:553–562.
10. Jadvar H, Desai B, Ji L, et al. Baseline ^{18}F-FDG PET/CT parameters as imaging biomarkers of overall survival in castrate-resistant metastatic prostate cancer. *J Nucl Med.* 2013;54:1195–1201.
11. Tolkach Y, Kristiansen G. The heterogeneity of prostate cancer: a practical approach. *Pathobiology.* 2018;85:108–116.
12. Harmon SA, Bergvall E, Mena E, et al. A prospective comparison of ^{18}F-sodium fluoride PET/CT and PSMA-targeted ^{18}F-DCFBC PET/CT in metastatic prostate cancer. *J Nucl Med.* 2018;59:1665–1671.
13. Uprimny C, Svirydenka A, Fritz J, et al. Comparison of [^{68}Ga]Ga-PSMA-11 PET/CT with [^{18}F]NaF PET/CT in the evaluation of bone metastases in metastatic prostate cancer patients prior to radionuclide therapy. *Eur J Nucl Med Mol Imaging.* 2018;45:1873–1883.
14. Rowe SP, Li X, Trock BJ, et al. Prospective comparison of PET imaging with PSMA-targeted ^{18}F-DCFPyL versus Na18F for bone lesion detection in patients with metastatic prostate cancer. *J Nucl Med.* 2020;61:183–188.
15. Zhou J, Gou Z, Wu R, Yuan Y, Yu G, Zhao Y. Comparison of PSMA-PET/CT, choline-PET/CT, NaF-PET/CT, MRI, and bone scintigraphy in the diagnosis of bone metastases in patients with prostate cancer: a systematic review and meta-analysis. *Skeletal Radiol.* 2019;48:1915–1924.
16. Usmani S, Ahmed N, Muzaffar S, et al. Spectrum of false positive ^{18}F-sodium fluoride (NaF) bone PET/CT findings in oncology imaging: a narrative pictorial review of cases from a single institution. *Hell J Nucl Med.* 2020;23:67–75.
17. Rodrigues G, Bae K, Roach M, et al. Impact of ultrahigh baseline PSA levels on biochemical and clinical outcomes in two radiation therapy oncology group prostate clinical trials. *Int J Radiat Oncol Biol Phys.* 2011;80:445–452.
18. Koo KC, Park SU, Kim KH, et al. Predictors of survival in prostate cancer patients with bone metastasis and extremely high prostate-specific antigen levels. *Prostate Int.* 2015;3:10–15.
19. Violet J, Sandhu S, Iravani A, et al. Long-term follow-up and outcomes of retreatment in an expanded 50-patient single-center phase II prospective trial of ^{177}Lu-PSMA-617 theranostics in metastatic castration-resistant prostate cancer. *J Nucl Med.* 2020;61:857–865.
20. Afshar-Oromieh A, Debus N, Uhrig M, et al. Impact of long-term androgen deprivation therapy on PSMA ligand PET/CT in patients with castration-sensitive prostate cancer. *Eur J Nucl Med Mol Imaging.* 2018;45:2045–2054.
21. Hofman MS, Violet J, Hicks RJ, et al. [^{177}Lu]-PSMA-617 radionuclide treatment in patients with metastatic castration-resistant prostate cancer (LuPSMA trial): a single-centre, single-arm, phase 2 study. *Lancet Oncol.* 2018;19:825–833.
22. Jadvar H. Is there utility for FDG PET in prostate cancer? *Semin Nucl Med.* 2016; 46:502–506.
23. Wang B, Liu C, Wei Y, et al. A prospective trial of 68 Ga-PSMA and 18 F-FDG PET/CT in nonmetastatic prostate cancer patients with an early PSA progression during castration. *Clin Cancer Res.* 2020;26:4551–4558.
24. Meirelles GSP, Schoder H, Ravizzini GC, et al. Prognostic value of baseline [^{18}F] fluorodeoxyglucose positron emission tomography and ^{99m}Tc-MDP bone scan in progressing metastatic prostate cancer. *Clin Cancer Res.* 2010;16:6093–6099.
25. Zukotynski KA, Kim CK, Gerbaudo VH, et al. ^{18}F-FDG-PET/CT and ^{18}F-NaF-PET/CT in men with castrate-resistant prostate cancer. *Am J Nucl Med Mol Imaging.* 2014;5:72–82.
26. Jadvar H, Velez EM, Desai B, Ji L, Colletti PM, Quinn DI. Prediction of time to hormonal treatment failure in metastatic castration-sensitive prostate cancer with ^{18}F-FDG PET/CT. *J Nucl Med.* 2019;60:1524–1530.

The Influence of Specific Activity on the Biodistribution of 18F-rhPSMA-7.3: A Retrospective Analysis of Clinical PET Data

Thomas Langbein[1], Alexander Wurzer[2], Andrei Gafita[1,3], Andrew Robertson[1], Hui Wang[1], Ayça Arçay[1,4], Michael Herz[1], Hans-Juergen Wester[2], Wolfgang A. Weber[1], and Matthias Eiber[1]

[1]Department of Nuclear Medicine, Klinikum rechts der Isar, School of Medicine, Technical University of Munich, Munich, Germany; [2]Chair of Pharmaceutical Radiochemistry, Technical University of Munich, Garching, Germany; [3]Ahmanson Translational Theranostics Division, Department of Molecular and Medical Pharmacology, UCLA, Los Angeles, California; and [4]Department of Nuclear Medicine, Akdeniz University, Antalya, Turkey

We investigated whether the time between synthesis and injection and the resulting decrease in specific activity affects the normal-organ and tumor uptake of the PSMA ligand 18F-rhPSMA-7.3 in patients with prostate cancer. **Methods:** The biodistribution of 18F-rhPSMA-7.3 on PET/CT scans obtained with a high specific activity (median, 178.9 MBq/μg; $n = 42$) and a low specific activity (median, 19.3 MBq/μg; $n = 42$) was compared. **Results:** Tracer uptake by the parotid gland, submandibular gland, and spleen was moderately but significantly lower in the low-specific-activity group than in the high-specific-activity group (median SUV_{mean}, 16.7 vs. 19.2; 18.1 vs. 22.3; and 7.8 vs. 9.6, respectively). No other statistically significant differences were found for normal organs or tumor lesions. **Conclusion:** A 10-fold decrease in specific activity has only minor effects on the biodistribution of 18F-rhPSMA-7.3. These findings suggest that 18F-labeled PSMA ligands can be centrally produced and shipped to PET clinics in a similar way to 18F-FDG.

Key Words: PSMA; PET/CT; biodistribution; molar activity; 18F

Several 18F-labeled prostate-specific membrane antigen (PSMA) ligands are currently in clinical development for imaging of patients with prostate cancer (1–3). In the future, it is envisioned that these ligands will be produced by central radiopharmacies in batch sizes similar to 18F-FDG and shipped to PET clinics. In such a setting, radioactive decay will lead to a continuous decrease in the specific activity of the PSMA ligands. This decrease in specific activity could, in principle, lead to lower tumor uptake, since the 18F-labeled PSMA ligands compete with the nonlabeled PSMA ligands for binding to the limited number of PSMA molecules. Such a saturation of tracer uptake by a nonradioactive precursor does not occur for 18F-FDG because 18F-FDG follows the flow of glucose, which is present at concentrations that are orders of magnitude higher.

18F-rhPSMA-7.3 represents the lead compound in a class of radiohybrid PSMA (rhPSMA) ligands that can be labeled with 18F for imaging but also with radiometals for therapeutic use (4). 18F-rhPSMA-7.3 is a single diastereoisomer form of 18F-rhPSMA-7, for which promising preliminary imaging data have been reported (5,6). Two multicenter, phase III trials are in progress to investigate the diagnostic accuracy of 18F-rhPSMA-7.3 in primary staging (NCT04186819) and recurrence (NCT04186845) of prostate cancer.

Preclinical investigations have shown that the biodistribution of 18F-labeled PSMA ligands in mice is significantly affected by the specific activity, with decreased uptake in tumor lesions and salivary glands at lower specific activities (7). The present study explored whether such effects also occur in humans over the range of specific activities typically injected for PSMA PET/CT studies.

MATERIALS AND METHODS

Study Design

We retrospectively reviewed data from patients who underwent 18F-rhPSMA-7.3 PET/CT at our institution between August 2018 and October 2019 (Supplemental Fig. 1; supplemental materials are available at http://jnm.snmjournals.org). All reported investigations were conducted in accordance with the Helsinki Declaration and with national regulations. The retrospective analysis was approved by the Ethics Committee of the Technical University Munich (permit 290/18S), and the requirement to obtain informed consent was waived. 18F-rhPSMA-7.3 administration complied with the German Medicinal Products Act, Arzneimittelgesetz §13 2b, and the responsible regulatory body (Government of Oberbayern).

18F-rhPSMA-7.3 Synthesis, Administration, and Image Acquisition

18F-rhPSMA-7.3 was synthesized as recently reported (4) and administered as an intravenous bolus (median, 321 MBq; interquartile range [IQR], 290–360 MBq) at a median of 71 min (IQR, 66–79 min) before the PET/CT scan began. Patients underwent 18F-rhPSMA-7.3 PET/CT on a Biograph mCT flow scanner (Siemens Medical Solutions) as recently described (5,6).

Patient Selection

The patients had received the injection of 18F-rhPSMA-7.3 at various time points after production and, consequently, had been administered

different specific activities of ^{18}F-rhPSMA-7.3. The specific activity at the time of tracer injection was calculated for every patient using the exact time of injection, the injected activity, and the radiolabeling quality control data for the particular batch, while accounting for the known radioactive decay of ^{18}F. Two patient groups were created (high or low specific activity), aiming for a 10-fold difference between groups. In addition, groups were matched for uptake time and body weight, and only patients with a low tumor load were included to avoid tumor sink effects. A low tumor load was defined as no more than 1% of total injected dose accumulated in tumor lesions determined by isocontour volume-of-interest measurements at 50% of the SUV$_{max}$.

Biodistribution Assessment

SUV$_{mean}$ was determined within standardized isocontour volumes of interest with 50% of the SUV$_{max}$ and a diameter of 30 mm (salivary glands, liver, spleen, kidneys, bone, muscle, blood pool, and tumor lesions). For

FIGURE 1. ^{18}F-rhPSMA-7.3 SUV$_{mean}$ stratified by injected specific activity. n.s. = not statistically significant.

evaluation of the tumor uptake, volumes of interest were placed over a maximum of 3 lesions per patient in decreasing order of the SUV$_{max}$, and SUV$_{mean}$ was averaged. The image-derived whole-organ radioactivity concentration (kBq/mL) based on full-organ segmentation (salivary glands, liver, spleen, and kidneys) was determined using semiautomatic analysis with the software qPSMA as previously described (8). Volume-of-interest placement and image analyses were performed by 2 experienced nuclear medicine physicians.

Statistical Analysis

The Mann–Whitney U test was used to test for differences between uptake parameters between the high- and the low-specific-activity groups. Additionally, a 1-way multivariate AVOVA was performed to analyze the effect of specific activities on biodistribution. Normal distribution of variables was evaluated by Q–Q plots and the Shapiro–Wilk W test. Data are presented as median and IQR; a P value of less than 0.05 was considered statistically significant. Statistical analysis was performed with SPSS Statistics, version 24 (IBM Corp.), and MedCalc, version 14.8.1 (MedCalc Software Ltd.).

RESULTS

Patient Population

From a total of 1,975 patients, 84 were selected and stratified into 2 groups of equal size. The median interval between tracer synthesis and injection was 72 min (IQR, 54–89 min) versus 367 min (IQR, 342–397 min) for the high and low groups ($P < 0.001$), resulting in a median specific activity of 178.9 MBq/μg (IQR, 158.6–199.1 MBq/μg) and 19.3 MBq/μg (IQR, 17.7–22.5 MBq/μg), respectively, for ^{18}F-rhPSMA-7.3 ($P < 0.001$). Median injected activity per kilogram of body weight (4.0 MBq/kg [IQR, 3.9–4.0 MBq/kg] vs. 4.0 MBq/kg [IQR, 3.9–4.0 MBq/kg])

and median ^{18}F-rhPSMA-7.3 uptake time (70 min [IQR, 65–76 min] vs. 75 min [IQR, 68–87 min]) were similar in the high and low groups ($P = 0.62$ and 0.06, respectively). No substantial differences between the groups were present for any clinical parameter (Supplemental Table 1). Supplemental Table 2 provides data for specific activities at calibration and injection.

Normal-Organ Biodistribution and Tumor Lesions Evaluated by SUV$_{mean}$

Median SUV$_{mean}$ in the low-specific-activity group was significantly lower for parotid glands ($P = 0.014$), submandibular glands ($P = 0.002$), and spleen ($P = 0.012$) (Fig. 1; Supplemental Table 3). No significant differences in SUV$_{mean}$ were found for the other investigated organs. Median SUV$_{mean}$ was 9.0 (IQR, 4.4–14.8) and
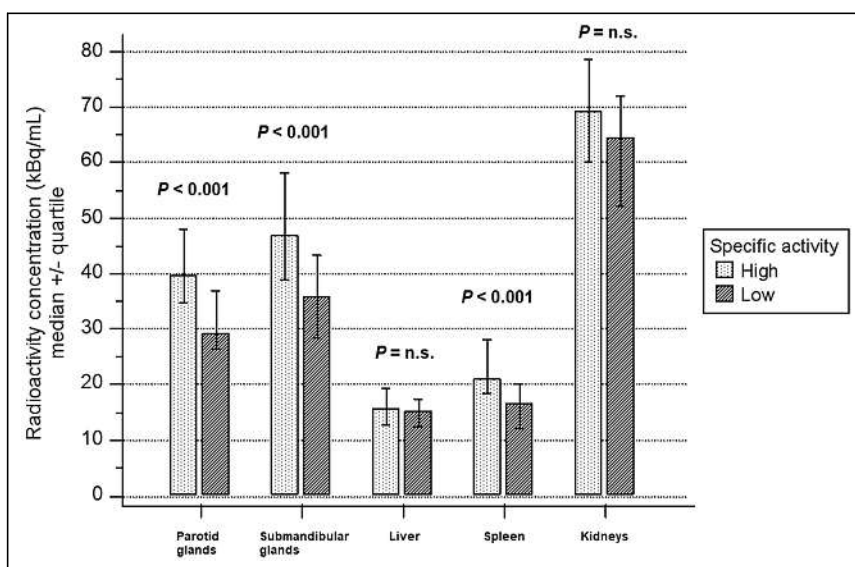
FIGURE 2. ^{18}F-rhPSMA-7.3 whole-organ radioactivity concentration stratified by injected specific activity. n.s. = not statistically significant.

9.5 (IQR, 6.5–19.0) for tumor lesions in the high- versus low-specific-activity groups, respectively, and not significantly different ($P = 0.273$). No statistical difference in tumor lesion distribution was observed between the 2 groups (Supplemental Fig. 2).

Whole-Organ Radioactivity Concentrations

Whole-organ radioactivity concentrations (kBq/mL) for the high-versus low-specific-activity groups were 39.6 (IQR, 34.8–48.0) versus 29.4 (IQR, 26.5–37.0), 46.9 (IQR, 38.9–58.1) versus 35.8 (IQR, 28.6–43.2), 15.7 (IQR, 12.6–19.4) versus 15.1 (IQR, 12.4–17.5), 21.1 (IQR, 18.4–28.1) versus 16.5 (IQR, 12.2–20.0), and 69.3 (IQR, 60.0–78.6) versus 64.6 (IQR, 52.1–72.1) for the parotid glands, submandibular glands, liver, spleen, and kidneys, respectively. Results for the low-specific-activity group were significantly lower for salivary glands and spleen (each $P < 0.001$), whereas liver and kidneys did not show significant differences (Fig. 2).

A 1-way multivariate ANOVA confirmed the statistically significant difference between the high- and low-specific-activity groups for tracer distribution determined by SUV_{mean} and full-organ segmentation (combined dependent variables, $F_{14,60} = 3.928$, $P < 0.001$, partial $\eta^2 = 0.478$, Wilks $\Lambda = 0.522$.)

DISCUSSION

In this retrospective analysis, we explored the impact of ^{18}F-rhPSMA-7.3 specific activity on biodistribution in normal organs and tumors. Our data show that uptake patterns in organs relevant to clinical imaging interpretation are not substantially affected by different specific activities, with only the salivary glands and spleen demonstrating a moderate, albeit significant, decrease in the low- compared with high-specific-activity groups. Tumor uptake appeared stable over the 10-fold difference investigated. Our results indicate that clinical PET interpretation is not affected using a single large-batch production over several hours during the workday and the resultant wide range of injected specific activities.

Similar effects have already been demonstrated by Soeda et al. in a preclinical setting (7). In a mouse xenograft model derived from human lymph node metastases, a substantial decline in the SUV_{mean} of tumor lesions and salivary glands was observed on ^{18}F-PSMA-1007 PET/CT when the molar activity was reduced over a 100-fold range (7). Despite decreased tumor uptake, the tumor–to–salivary gland ratio increased as salivary gland uptake was even further reduced compared with tumors. The authors concluded that the increased tumor–to–salivary gland ratio might play a role in reducing off-target uptake of PSMA-targeting radioligand therapies. Comparable findings have been demonstrated with ^{68}Ga-labeled PSMA inhibitors using triazacyclononane-triphosphinate chelators (9). By the addition of unlabeled compounds, the accumulation was altered significantly in the kidneys and salivary glands but less so in the tumor, with a more beneficial kidney-to-tumor ratio in lower molar activities of 8 versus 1,200 MBq/nmol (9).

To translate these animal data into a clinical context, 2 different methodologies for detection of imaging-derived biodistribution of ^{18}F-rhPSMA-7.3 were applied. Recently, the biodistribution of ^{18}F-rhPSMA-7.3 was investigated in 6 healthy subjects, with ^{18}F-rhPSMA-7.3 showing high physiologic uptake in the kidneys and salivary glands (10). Our study demonstrated that uptake by most organs is not influenced by administration of lower specific

activities, as might occur in a busy PET clinic. This consistency of uptake appears essential for a clinical PET/CT reading. Additionally, tumor uptake did not vary significantly, even with a 10-fold difference in the injected specific activity.

This difference in specific activity represents the realistic spectrum of what is observed in a real-world scenario for PET imaging. Although some of the mentioned preclinical findings could also be observed in our investigation with significant effect, they appeared to be without clinical relevance in the case of salivary gland and spleen uptake. Notably, because therapeutic applications usually require higher molar masses ($\sim$50–200 µg), our data cannot be extrapolated to the potential therapeutic use of rhPSMA-7.3.

The results of our study indicate that salivary gland uptake is saturable, suggesting binding to a target protein within the salivary glands. Similar findings were shown in preclinical studies of ^{177}Lu-PSMA-617, for which uptake in the salivary glands and kidneys of PC3-PIP tumor–bearing mice significantly declined without an impact on tumor uptake when cold PSMA-11 was added (11).

Some limitations of our study should be considered, for example, the retrospective design. However, we believe that our observations are true reflections of the variance in specific activity in daily clinical practice. Second, our cohort comprised a relatively heterogeneous patient group at different stages of prostate cancer. Nevertheless, we tried to control for any potential influence on biodistribution, selecting patients on the basis of a low tumor load. The heterogeneous population and the known high variance of in vivo PSMA expression might explain the wide range of reported SUV_{mean} in tumor lesions.

In summary, our data suggest that a single production of ^{18}F-rhPSMA-7.3 can be used in a clinical setting throughout the whole working day without a clinically relevant effect on biodistribution, especially tumor lesion uptake, despite a significantly decreasing specific activity. This observation underlines the potential logistical and economic advantages of ^{18}F-labeled PSMA ligands resulting from a single large-batch production in a cyclotron facility over generator-produced ^{68}Ga-based ligands with a short half-life and the need for multiple batches throughout the day (12).

CONCLUSION

Differences in the injected specific activity of ^{18}F-rhPSMA-7.3 observed throughout a usual working day have no clinically relevant effect on biodistribution and, especially, uptake by tumor lesions. These results support central production of ^{18}F-labeled PSMA ligands with shipment to PET clinics, similarly to ^{18}F-FDG.

KEY POINTS

QUESTION: Does the specific activity of the radiopharmaceutical administered to a patient affect the way it is distributed among organs?

PERTINENT FINDINGS: This retrospective data review showed that although the salivary glands and spleen appear to be saturable with decreasing specific activities, there was no clinically meaningful difference in organ uptake in patients with prostate cancer.

IMPLICATIONS FOR PATIENT CARE: A single batch of ^{18}F-rhPSMA-7.3 can be used throughout the day to scan multiple patients, with no effect on image quality being observed between the first and last patients of the day.

REFERENCES

1. Dietlein M, Kobe C, Kuhnert G, et al. Comparison of [^{18}F]DCFPyL and [^{68}Ga]Ga-PSMA-HBED-CC for PSMA-PET imaging in patients with relapsed prostate cancer. *Mol Imaging Biol.* 2015;17:575–584.

2. Giesel FL, Hadaschik B, Cardinale J, et al. F-18 labelled PSMA-1007: biodistribution, radiation dosimetry and histopathological validation of tumor lesions in prostate cancer patients. *Eur J Nucl Med Mol Imaging.* 2017;44:678–688.

3. Werner RA, Derlin T, Lapa C, et al. ^{18}F-labeled, PSMA-targeted radiotracers: leveraging the advantages of radiofluorination for prostate cancer molecular imaging. *Theranostics.* 2020;10:1–16.

4. Wurzer A, DiCarlo D, Schmidt A, et al. Radiohybrid ligands: a novel tracer concept exemplified by [18]F- or ^{68}Ga-labeled rhPSMA-inhibitors. *J Nucl Med.* 2020;61:735–742.

5. Eiber M, Kronke M, Wurzer A, et al. ^{18}F-rhPSMA-7 positron emission tomography for the detection of biochemical recurrence of prostate cancer following radical prostatectomy. *J Nucl Med.* 2020;61:696–701.

6. Kroenke M, Wurzer A, Schwamborn K, et al. Histologically-confirmed diagnostic efficacy of ^{18}F-rhPSMA-7 positron emission tomography for N-staging of patients with primary high risk prostate cancer. *J Nucl Med.* 2020;61:710–715.

7. Soeda F, Watabe T, Naka S, et al. Impact of ^{18}F-PSMA-1007 uptake in prostate cancer using different peptide concentrations: preclinical PET/CT study on mice. *J Nucl Med.* 2019;60:1594–1599.

8. Gafita A, Bieth M, Kronke M, et al. qPSMA: Semiautomatic software for whole-body tumor burden assessment in prostate cancer using ^{68}Ga-PSMA11 PET/CT. *J Nucl Med.* 2019;60:1277–1283.

9. Wurzer A, Pollmann J, Schmidt A, Reich D, Wester HJ, Notni J. Molar activity of Ga-68 labeled PSMA inhibitor conjugates determines PET imaging results. *Mol Pharm.* 2018;15:4296–4302.

10. Tolvanen T, Kalliokoski KK, Malaspina S, et al. Safety, biodistribution and radiation dosimetry of ^{18}F-rhPSMA-7.3 in healthy adult volunteers. *J Nucl Med.* 2021;62:679–684.

11. Kalidindi TM, Lee SG, Jou K, et al. A simple strategy to reduce the salivary gland and kidney uptake of PSMA-targeting small molecule radiopharmaceuticals. *Eur J Nucl Med Mol Imaging.* 2021;48:2642–2651.

12. Kesch C, Kratochwil C, Mier W, Kopka K, Giesel FL. [68]Ga or ^{18}F for prostate cancer imaging? *J Nucl Med.* 2017;58:687–688.

Repeatability of ^{68}Ga-PSMA-HBED-CC PET/CT–Derived Total Molecular Tumor Volume

Robert Seifert[1–3], Patrick Sandach[1,2], David Kersting[1,2], Wolfgang P. Fendler[1,2], Boris Hadaschik[2,4], Ken Herrmann[1,2], John J. Sunderland[5], and Janet H. Pollard[5,6]

[1]Department of Nuclear Medicine, University of Duisburg–Essen and German Cancer Consortium–University Hospital, Essen, Germany; [2]West German Cancer Center, Essen, Germany; [3]Department of Nuclear Medicine, University Hospital Münster, University of Münster, Münster, Germany; [4]Department of Urology, University Hospital Essen, and German Cancer Consortium–University Hospital, Essen, Germany; [5]Department of Radiology, University of Iowa Carver College of Medicine, Iowa City, Iowa; and [6]Department of Radiology, Iowa City Veterans Healthcare Center, Iowa City, Iowa

Molecular tumor volume (MTV) is a parameter of interest in prostate cancer for assessing total disease burden on prostate-specific membrane antigen (PSMA) PET. Although software segmentation tools can delineate whole-body MTV, a necessary step toward meaningful monitoring of total tumor burden and treatment response through PET is establishing the repeatability of these metrics. The present study assessed the repeatability of total MTV and related metrics for ^{68}Ga-PSMA-HBED-CC in prostate cancer. **Methods:** Eighteen patients from a prior repeatability study who underwent 2 test–retest PSMA PET/CT scans within a mean interval of 5 d were reanalyzed. Within-subject coefficient of variation and repeatability coefficients (RCs) were analyzed on a per-lesion and per-patient basis. For the per-lesion analysis, individual lesions were segmented for analysis by a single reader. For the per-patient analysis, subgroups of up to 10 lesions (single reader) and the total tumor volume per patient were segmented (independently by 2 readers). Image parameters were MTV, SUV_{max}, SUV_{peak}, SUV_{mean}, total lesion PSMA, and the related metric PSMA quotient (which integrates lesion volume and PSMA avidity). **Results:** In total, 192 segmentations were analyzed for the per-lesion analysis and 1,662 segmentations for the per-patient analysis (combining the 2 readers and 2 scans). The RC of the MTV of single lesions was 77% (95% CI, 63%–96%). The RC improved to 33% after aggregation of up to 10 manually selected lesions into subgroups assessed per patient (95% CI, 25%–46%). The RC of the semiautomatic MTV_{total} (the sum of all voxels in the whole-body total tumor segmentation per patient) was 35% (95% CI, 25%–50%), the Bland-Altman bias was −6.70 (95% CI, −14.32–0.93). Alternating readers between scans led to a comparable RC of 37% (95% CI, 28%–49%) for MTV_{total}, meaning that the metric is robust between scanning sessions and between readers. **Conclusion:** ^{68}Ga-PSMA-HBED-CC PET–derived semiautomatic MTV_{total} is repeatable and reader-independent, with a change of ±35% representing a true change in tumor volume. Volumetry of single manually selected lesions has considerably lower repeatability, and volumetry based on subgroups of these lesions, although showing acceptable repeatability, is less systematic. The semiautomatic analysis of MTV_{total} used in this study offers an efficient and robust means of assessing response to therapy.

Key Words: PSMA PET; tumor volume; repeatability

Prostate cancer is a leading cause of death in men (1). Especially in advanced prostate cancer, therapy monitoring is challenging. The blood tumor marker prostate-specific antigen is routinely used to monitor disease progression (2). However, prostate-specific antigen levels may be influenced by tumor dedifferentiation and androgen deprivation therapy, which raises the need for image-based methods for global tumor assessment (3,4). For now, bone scanning and CT are the established methods for assessing treatment response in advanced disease (2). More recently, prostate-specific membrane antigen (PSMA) imaging with PET has been shown to be superior to conventional imaging for both initial and recurrent cancer staging (5,6). Therefore, PSMA PET seems to be a promising methodology to quantify the prostate cancer tumor volume over time.

The recently proposed PSMA PET progression criteria, as well as a recently published consensus meeting, recommended consideration of PSMA PET–derived volumetric measurements to detect progressive disease (7,8). Indeed, several studies have shown that the quantification of the total tumor volume using PSMA PET is feasible and that it is a statistically significant negative predictor for overall survival in patients with advanced prostate cancer (9–12). Total tumor uptake values analogous to total lesion glycolysis for ^{18}F-FDG can also be assessed with PSMA PET.

To date, the repeatability of PSMA PET–derived volumetric and total tumor uptake measurements has not been sufficiently investigated. Previously, Pollard et al. reported ^{68}Ga-PSMA-HBED-CC PET repeatability for SUV_{max} in bone and nodal metastases from prostate cancer (13). A variety of factors beyond true change in tumor can lead to variability in quantitative PET imaging, including the segmentation methods used. To reliably assess quantitative change between PSMA PET scans, it is necessary to understand the normal variability within the patient, radiotracer, and imaging system. The present study evaluates the repeatability of volumetric and uptake measurements for individual tumors and total tumor volume on test–retest ^{68}Ga-PSMA-HBED-CC PET/CT.

MATERIALS AND METHODS

Patients and Image Acquisition

Eighteen patients were included in the analysis. The institutional review board approved the study protocol (NCT02952469), and all subjects gave written informed consent. Dataset details were previously reported by Pollard et al. in their study of test–retest repeatability (13). Here, the identical

dataset was used. Briefly, all patients underwent 2 PSMA PET/CT acquisitions within a mean interval of 5 d (range, 2–14 d). Patient characteristics are shown in Table 1. ^{68}Ga-gallium-PSMA-HBED-CC (also known as PSMA-11 and referred to simply as PSMA in the remainder of this paper) was synthesized as previously published (13). Either a Biograph mCT (with FlowMotion) or a Biograph TruePoint PET/CT system was used for image acquisition (Siemens Healthineers). The follow-up scan was performed on the same scanner as the initial scan. PET data were acquired using a previously published protocol (PET scan starting 60 min after tracer injection with scan coverage from vertex to mid thigh, 3- to 4-min scan time per bed position) (13). A 3-dimensional ordered-subset expectation maximization algorithm was used for image reconstruction (with time-of-flight information in case of the mCT).

Tumor Analysis per Lesion

For the repeatability analysis of individual lesions, up to 10 metastases (skeletal or nodal) or primary tumor lesions were segmented in both the first and second scans by a single reader using a manual segmentation with a 50% isocontour. A single-reader model was chosen for the single-lesion and the subgroup analysis portions of the study. Because the same small number of lesions needed to be selected on each PET scan, the single-reader approach minimized variability introduced by interrater differences in lesion selection and segmentation. Lesions were identified as nonphysiologic sites of uptake with an SUV exceeding the regional background activity. Lesions were selected at random from the regions segmented by the whole-body molecular tumor volume (MTV) analysis, described in detail in the section on total tumor analysis. For each lesion, SUV_{max}, SUV_{peak}, SUV_{mean}, lesion MTV (MTV_{lesion}), total lesion

PSMA ($PSMA\text{-}TL_{lesion}$), and total lesion quotient ($PSMA\text{-}TLQ_{lesion}$) were measured. MTV_{lesion} was determined by the sum of the voxels (Eq. 1) within a threshold 50% isocontour of the local SUV_{max}. $PSMA\text{-}TL_{lesion}$ and $PSMA\text{-}TLQ_{lesion}$ were calculated as in Equations 2 and 3.

$$MTV_{lesion} = \sum_{i=0}^{total}(voxel_i) \qquad \text{Eq. 1}$$

$$PSMA-TL_{lesion} = MTV_{lesion} \times lesion\ SUV_{mean} \qquad \text{Eq. 2}$$

$$PSMA-TLQ_{lesion} = \frac{MTV_{lesion}}{lesion\ SUV_{mean}} \qquad \text{Eq. 3}$$

Tumor Subgroup Analysis per Patient

One reader manually selected at random a group of up to 10 lesions per patient from the regions segmented by the whole-body MTV analysis technique (described in the next section). In patients with a large number of metastatic lesions, lesions were selected randomly to reflect a broad distribution of anatomic regions. The lesions in this subgroup were individually manually segmented and were assessed as an aggregate. The mean of SUV_{max} and SUV_{mean} (subgroup mean SUV_{max} and subgroup mean SUV_{mean}, respectively) were calculated. The sum and mean of MTV_{lesion}, the sum of $PSMA\text{-}TL_{lesion}$, and the sum of $PSMA\text{-}TLQ_{lesion}$ ($MTV_{subgroup}$, subgroup MTV_{mean}, $PSMA\text{-}TL_{subgroup}$, and $PSMA\text{-}TLQ_{subgroup}$, respectively) were calculated as in Equations 4–7, where n is the number of lesions within the subgroup and i is the ordinal number of the lesion. $PSMA\text{-}TL_{lesion}$ is analogous to total lesion glycolysis for ^{18}F-FDG and, when calculated for aggregate tumors, the individual $PSMA\text{-}TL_{lesion}$ values are summed.

$$MTV_{subgroup} = \sum_{i=1}^{n}(MTV_{lesion\ i}) \qquad \text{Eq. 4}$$

TABLE 1
Patient Characteristics and MTV_{total} Reported for Each Scan and Reader

Patient no.	PSA within ≤90 d (ng/mL)	Gleason score at diagnosis	MTV_{total} (mL)			
			R1, scan 1	R2, scan 1	R1, scan 2	R2, scan 2
1	0.15	7 (4 + 5)	0	0	0	0
2	4.35	6 (3 + 3)	4.81	5.88	4.81	5.88
3	104.5	9 (4 + 5)	395.7	404.02	399.18	402.22
4	0.14	9 (4 + 5)	59.91	62.59	82.42	66.9
5	0.66	9 (5 + 4)	6.42	6.77	5.18	7.56
6	0.22	9 (5 + 4)	3.78	4.67	3.78	4.67
7	56.3	Presumptive diagnosis	38.89	35.59	41.36	22.49
8	95.5	7 (4 + 3)	206.38	247.85	236.35	221.08
9	276.3	9 (4 + 5)	643.19	741.4	643.19	642.43
10	0.04	Presumptive diagnosis	0	0	0	0
11	0.64	9 (4 + 5)	7.78	8.33	7.78	8.33
12	2.8	Lymph node biopsy	31.49	44.68	30.53	46.24
13	40.1	10 (5 + 5)	464.53	587.13	552.7	515.05
14	19.7	7 (3 + 4)	18.87	22.83	18.87	22.83
15	2.5	Bone biopsy	2.26	1.96	2.26	1.96
16	54.1	9 (5 + 4)	85.89	102.6	92.3	86.56
17	2.5	9 (5 + 4)	21.78	21.81	22.29	21.81
18	2.5	9 (5 + 4)	6.52	6.31	5.53	7.34

PSA = prostate-specific antigen; R1 = reader 1; R2 = reader 2.

$$\text{Subgroup MTV}_{\text{mean}} = \frac{\sum_{i=1}^{n}(\text{MTV}_{\text{lesion }i})}{n} \qquad \text{Eq. 5}$$

$$\text{PSMA}-\text{TL}_{\text{subgroup}} = \sum_{i=1}^{n}(\text{PSMA}-\text{TL}_{\text{lesion }i}) \qquad \text{Eq. 6}$$

$$\text{PSMA}-\text{TLQ}_{\text{subgroup}} = \sum_{i=1}^{n}(\text{PSMA}-\text{TLQ}_{\text{lesion }i}) \qquad \text{Eq. 7}$$

Total Tumor Analysis per Patient

For the total tumor analysis, all lesions were segmented using a semiautomatic approach as previously published (9). The investigational MICIIS research software prototype was used for the single lesion and total tumor analyses (previously named MI Whole-Body Analysis Suite; Siemens Healthineers). Briefly, all voxels with an SUV_{peak} exceeding the following liver-specific threshold were selected as candidate foci:

$$\text{SUV}_{\text{peak}}\text{threshold} \geq \frac{4.3}{\text{liver SUV}_{\text{mean}}} \times (\text{liver SUV}_{\text{mean}}+\text{liver SUV}_{\text{SD}}),$$

$$\text{Eq. 8}$$

where the liver-specific threshold was calculated as previously described and SUV_{SD} is the SD of the SUV distribution in the liver volume of interest (9,10). The threshold described in Equation 8 adjusts for the tumor sink effect, which has a tendency to lower liver uptake; the first part of the formula is a corrective coefficient for the SUV reduction due to the sink effect, and the second part is the calculation for the uncorrected liver threshold. Individual-lesion segmentation was based on a threshold 50% isocontour of the local SUV_{max}. In analogy to the European Association of Nuclear Medicine recommendations for ^{18}F-FDG PET imaging, a threshold 50% isocontour-based approach was chosen for this study (14). Segmentation errors such as inclusion of sites of normal physiologic uptake or exclusion of tumor lesions were adjusted manually. There were no adjustments of segmented tumor contours in addition to inclusion or exclusion of lesions. Example whole-body tumor segmentations and segmentation errors are shown in Figures 1 and 2. Two readers with PET experience independently delineated all tumor lesions, and their delineated PET data were analyzed separately.

The sum of all voxels in the whole-body total tumor segmentation per patient was designated $\text{MTV}_{\text{total}}$. The mean of the volume of the individual segmented volumes comprising the $\text{MTV}_{\text{total}}$ was calculated as in Equation 5 and was designated total MTV_{mean}. Likewise, the mean of SUV_{max} and SUV_{mean} of these component volumes was designated total mean SUV_{max} and total mean SUV_{mean}, respectively. The $\text{PSMA-TL}_{\text{lesion}}$ and $\text{PSMA-TLQ}_{\text{lesion}}$ values for the component volumes were summed as in Equations 6 and 7 and were designated $\text{PSMA-TL}_{\text{total}}$ and $\text{PSMA-TLQ}_{\text{total}}$, respectively.

Statistical Analysis

Statistical methods for the sample size of the original dataset used in this analysis were reported by Pollard et al. (13). The Pearson correlation coefficient was used for descriptive statistics. Bland–Altman plots were created for absolute (rather than relative percent) differences in $\text{MTV}_{\text{total}}$ and mean SUV_{max} (15). Correlation in $\text{MTV}_{\text{total}}$ between readers for the same scan and between scans for the same reader was evaluated with intraclass correlation coefficients. The repeatability assessment using a relative comparison approach was done as described by Obuchowski (16). The within-subject coefficient of variation (wCV) is given by

$$\text{wCV} = \sqrt{\frac{\sum_{i=1}^{n} \frac{(\text{scan A}_i - \text{scan B}_i)^2}{2 \times \left(\frac{1}{2}(\text{scan A}_i + \text{scan B}_i)\right)^2}}{n}} \qquad \text{Eq. 9}$$

where n is the number of subjects and scans A and B are the quantitative PET measurements from the first and second PET scans,
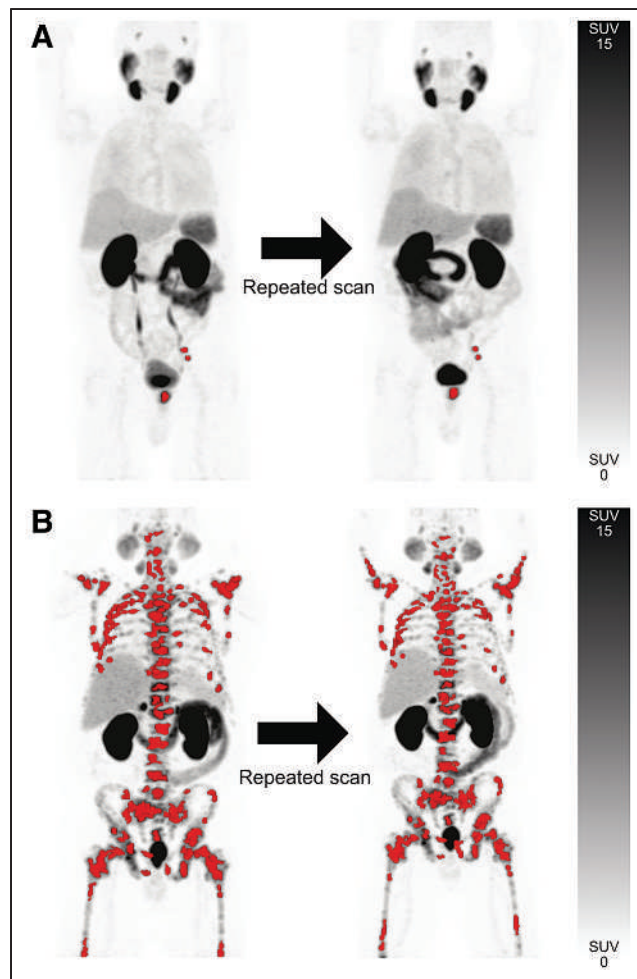
FIGURE 1. Semiautomatic total tumor segmentations with red overlay designating sites of segmented lesions in scans 1 and 2 for patient with disease limited to prostate and left pelvic lymph nodes (A) and patient with extensive skeletal metastases (B). Interval between scans was 2 d for both patients.

respectively. The repeatability coefficient (RC) is given by

$$\text{RC} = 1.96 \times \text{wCV} \times \sqrt{2} \qquad \text{Eq. 10}$$

The CIs for wCV and RC were determined by bootstrapping with 1,000 replicates. RC variability in relation to lesion SUV_{max} was evaluated by an exploratory approach for subsets of lesions in multiple steps. For each step, all lesions that had an SUV_{max} below an arbitrarily defined SUV_{max} threshold were included. A distinct threshold was used for each step; the lowest SUV_{max} threshold was 1, and the increment was 5. Statistical analyses were performed using R, version 3.5.2 (The R Foundation, https://www.r-project.org/) and Microsoft Excel 2016, version 16.0.5110.1000. Statistical analysis was done by David Kersting and Robert Seifert.

RESULTS

Test–Retest Scan Parameters

As previously published for the same cohort, the median interval between scans 1 and 2 was 5 d (range, 2–14 d). No statistically significant difference between scans 1 and 2 was observed regarding injected dose (mean, 133.1 vs. 133.1 MBq; $P = 1.0$) or image
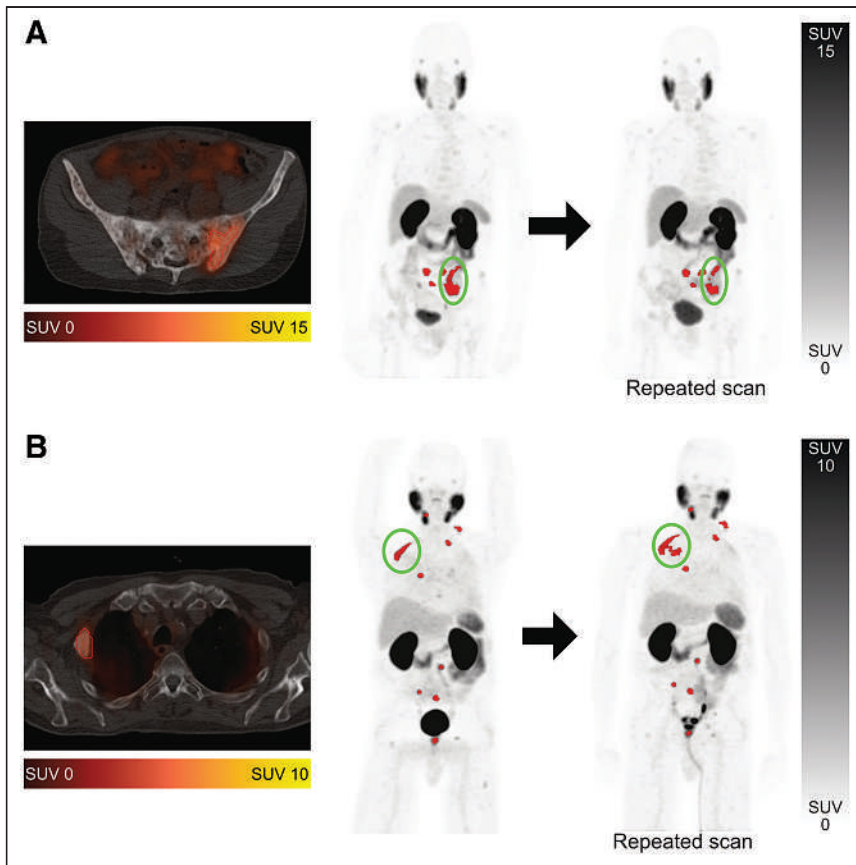
FIGURE 2. Examples of segmentation challenges on ^{68}Ga-PSMA-HBED-CC PET/CT. Segmented tumor metastases are shown in red. (A) Metastasis in os ilium was segmented as single lesion on first scan but as 3 separate lesions in second scan (encircled). (B) Metastasis in rib was segmented accurately on first scan but inaccurately on second scan, with isocontour including portion of lung (encircled). Error was resolved manually.

delay (mean, 60. 6 vs. 60.7 min; $P = 0.9$). Patient characteristics are shown in Table 1.

Repeatability of Manually Segmented Individual Lesions

For the per-lesion analysis, 96 metastases from 18 patients were manually delineated by a single reader, resulting in a total number of 192 segmentations from the 2 scans. Segmented lesions were regarded as independent observations. The RCs of MTV$_{lesion}$ and related metrics are shown in Table 2. Linear regression and Bland–Altman scatterplots for MTV$_{lesion}$ on scans 1 and 2 showed a relatively strong correlation ($P < 0.001$, $R^2 = 0.85$) and no significant bias based on visual analysis (Figs. 3A and 3B). However, MTV$_{lesion}$ demonstrated poor repeatability, with an RC of 76.9% (95% CI, 62.9%–95.9%), and similarly poor repeatability when accounting for differences in lesion volume, with an RC of 64.7% (range, 49.3%–91.6%), for lesions 5 cm^3 or larger and 83.9% (range, 65.5%–110.7%) for lesions smaller than 5 cm^3. The Bland–Altman bias of MTV$_{lesion}$ was −0.39 (95% CI, −1.00 to 0.22) for all lesions. The deviation in MTV$_{lesion}$ between scans 1 and 2 correlated to a statistically significantly extent with the deviation in SUV$_{max}$ between scans 1 and 2 ($P < 0.001$, $R^2 = 0.17$) (Fig. 3C).

Repeatability of Manually Segmented Subgroup of Lesions per Patient

Given the poor repeatability of MTV$_{lesion}$, a larger subgroup of manually selected and segmented lesions was evaluated for repeatability per

patient. Inclusion of multiple lesions for assessment as a subgroup allows for mitigation of individual lesion variability by averaging positive and negative variation across a larger number of lesions. The repeatability of MTV$_{subgroup}$ and related metrics is presented in Table 3. MTV$_{subgroup}$ demonstrated improved repeatability, with an RC of 33.1% (95% CI, 24.2%–46.2%), compared with MTV$_{lesion}$ and showed a repeatability comparable to that of the semiautomatic whole-body approach of MTV$_{total}$. The Bland–Altman bias of MTV$_{subgroup}$ was −2.32 (95% CI, −5.81 to 1.17). Supplemental Table 1 shows the association of RC, with SUV$_{max}$ RC decreasing with increasing minimum SUV$_{max}$ of segmented lesions (supplemental materials are available at http://jnm.snmjournals.org). This finding indicates that the repeatability was better when lesions with a low SUV$_{max}$ were discarded from the manually segmented subgroup of lesions.

Repeatability of Semiautomatic Segmentation of Total Tumor Volume per Patient

In total, 1,662 segmentations were performed for the per-patient analysis, including segmentations for the 2 readers and 2 scans. The MTV$_{total}$ for each reader for scans 1 and 2 is presented in Table 1. The RCs of the whole-body MTV$_{total}$ and related metrics are shown separately for both readers in Table 4. The RC of MTV$_{total}$ was 35.0% (95% CI, 24.9%–49.7%) in mean; the RCs for each reader were 37% and 33%. Linear regression and Bland–Altman scatterplots for MTV$_{total}$ and mean SUV$_{max}$ for scans 1 and 2 showed a strong correlation ($P < 0.001$, $R^2 = 0.99$) and no significant bias based on visual analysis (Fig. 4). The corresponding Bland–Altman bias of MTV$_{total}$ was −6.70 (95% CI, −14.32 to 0.93). The RC of MTV$_{total}$ and related metrics remained robust even when readers were hypothetically exchanged between scan timepoints with an RC of MTV$_{total}$ of 37.3% (95% CI, 27.9%–49.3%) (Table 5). A high correlation of MTV$_{total}$ between scans for the same reader (intraclass correlation coefficient, 0.998; $P < 0.001$) and between readers for the same scan (intraclass correlation coefficient, 0.993; $P < 0.001$) was noted (Fig. 5). MTV$_{total}$ showed a

TABLE 2
Repeatability of Manually Segmented Individual Lesions (MTV$_{lesion}$)

Metric	wCV (%)	RC (%)	95% CI of RC (%)
MTV$_{lesion}$	27.7	76.9	62.9–95.9
PSMA-TL$_{lesion}$	23.3	64.7	53.4–80.67
PSMA-TLQ$_{lesion}$	34.5	95.7	81.5–114.5
Lesion SUV$_{max}$	12.4	34.4	29.6–41.2
Lesion SUV$_{peak}$	9.9	27.3	23.3–32.8
Lesion SUV$_{mean}$	11.8	32.7	27.5–40.2
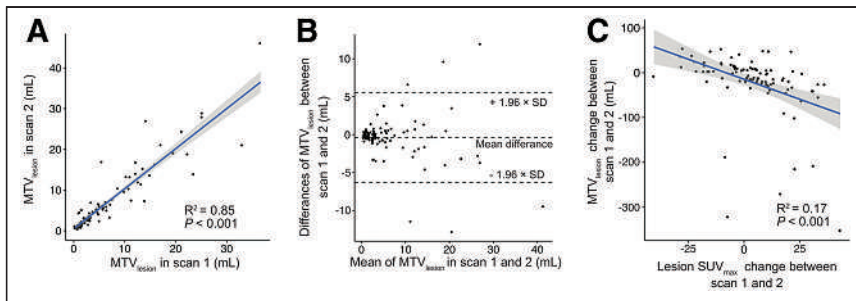
FIGURE 3. Analysis of individual manually segmented ^{68}Ga-PSMA-HBED-CC–avid lesions. Linear regression and Bland–Altman plots (A and B) of MTV$_{lesion}$ show correlation between scans. (C) Association is noted between MTV$_{lesion}$ and SUV$_{max}$ changes between scans 1 and 2.

moderate correlation with prostate-specific antigen values ($P < 0.002$, $R^2 = 0.53$) (Fig. 6). Other metrics using the semiautomatic technique, such as total mean SUV$_{max}$, total mean SUV$_{mean}$, and PSMA-TL$_{total}$, also showed improved repeatability as compared with individual lesion segmentation, with RC ranging from 23.6% to 28.4%.

DISCUSSION

PSMA PET is now widely used to monitor patients with prostate cancer (5,6,17,18). Especially for recurrent prostate cancer, PSMA PET has demonstrated high sensitivity and specificity for localizing prostate cancer cells in the body (5,6). Growing

TABLE 3
Repeatability of Manually Selected Lesion Subgroup per Patient (MTV$_{subgroup}$)

Metric	wCV (%)	RC (%)	95% CI of RC
MTV$_{subgroup}$	12.0	33.1	24.2–46.2
Subgroup MTV$_{mean}$	12.0	33.1	24.8–47.7
PSMA-TL$_{subgroup}$	7.4	20.6	16.0–26.9
PSMA-TLQ$_{subgroup}$	18.4	51.0	36.5–78.0
Subgroup mean SUV$_{max}$	12.3	34.0	20.0–59.4
Subgroup mean SUV$_{peak}$	6.6	18.3	13.3–24.5
Subgroup mean SUV$_{mean}$	9.1	25.2	17.5–35.7

evidence suggests that PSMA PET is also a useful clinical tool in patients with more advanced prostate cancer (19–21).

Measures of total tumor volume and total uptake on PSMA PET have been described, but its use in prostate cancer monitoring remains under debate (9,10). Analogous to the TNM system, a molecular imaging TNM (miTNM) system has been proposed, which scores extent of disease with regard to local tumor, regional lymph node metastases, bone metastases, and other distant metastases. (22). Given the distinct biologic aggressiveness and survival implications of various metastatic sites, the TNM-based system will likely remain an important prognostic tool in prostate cancer (23). However, because progressive disease is not always accompanied only by the occurrence of new metastases but also can include enlargement of existing metastases, the best assessment tools would therefore encompass assessment of both anatomic and total tumor volume, enabling consideration of both global disease status and aggressiveness of the involved sites. Studies have shown the prognostic value of PET volumetry and measures of total uptake. PSMA MTV$_{total}$ of high volume disease is a statistically significant poor prognostic factor for overall survival, and PSMA uptake of all metastases (SUV$_{mean}$ per patient) improves prognostication of overall survival in patients treated with ^{177}Lu-lutetium-PSMA-617 therapy (12,24–27).

The recently proposed PSMA PET progression criteria recommend assuming progressive prostate cancer in the setting of a 30% tumor volume increase (8). However, this threshold was chosen arbitrarily in the absence of volume-based PSMA repeatability data. Also, there are currently no consensus recommendations for PSMA PET segmentation algorithms among the various approaches that have been proposed for quantifying the PSMA tumor volume (9,10). A necessary step toward use of PSMA PET for reliable monitoring of disease is development of reliable and efficient methods for measuring total disease burden and determination of their repeatability.

Our analysis of repeatability evaluated PET volumetric and uptake measures using 3 different approaches to segmentation: manual segmentation of individual tumors, manual selection of a subgroup of tumors per patient, and semiautomatic segmentation of total tumor burden per patient. The repeatability of individual tumor volumes (MTV$_{lesion}$) was poor (RC, 77%). An explanation may be that the

TABLE 4
Repeatability of Semiautomatic MTV$_{total}$ per Patient

Metric	R1 wCV (%)	R2 wCV (%)	Mean wCV (%)	R1 RC (%)	R2 RC (%)	Mean RC (%)	95% CI of mean RC
MTV$_{total}$	13.4	11.9	12.7	37.0	33.0	35.0	24.9–49.7
Total MTV$_{mean}$	13.4	11.9	12.7	37.1	33.0	35.0	25.0–48.8
PSMA-TL$_{total}$	8.4	12.1	10.3	23.3	33.5	28.4	20.7–41.9
PSMA-TLQ$_{total}$	19.4	17.3	18.4	53.9	48.0	50.9	32.7–84.7
Total mean SUV$_{max}$	8.4	8.6	8.5	23.3	23.9	23.6	17.0–32.4
Total mean SUV$_{mean}$	8.1	8.0	8.1	22.6	22.2	22.4	16.4–30.7

R1 = reader 1; R2 = reader 2.
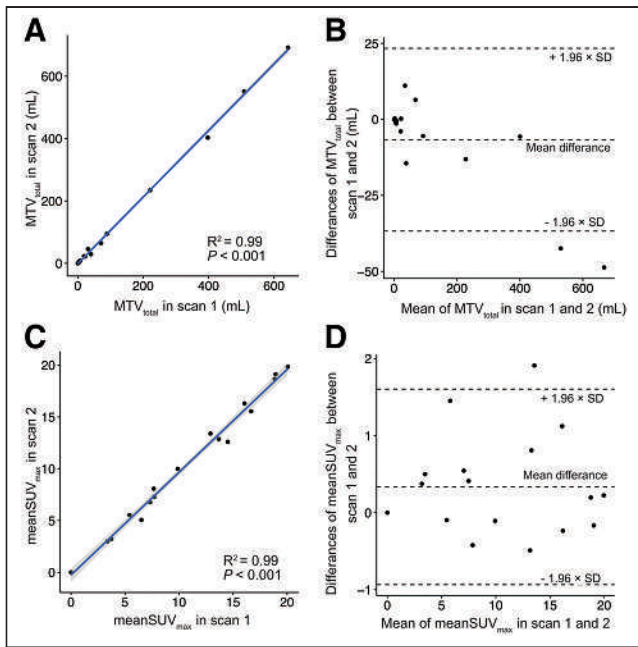
FIGURE 4. Analysis of semiautomatic whole-body segmentation of ^{68}Ga-PSMA-HBED-CC–avid lesions. Linear regression (A and C) and Bland–Altman plots (B and D) of MTV_{total} and mean SUV_{max} show excellent correlation between scans and suggest no association between total tumor volume or lesion intensity and test–retest differences. Results for readers 1 and 2 were averaged for purposes of these graphs. (A and C) MTV_{total} and mean SUV_{max} for scan 1 are plotted separately against same metric for scan 2. (B and D) Mean of MTV_{total} or mean SUV_{max} between scans 1 and 2 was plotted against absolute difference in metric between 2 scans.

reported wCV for SUV_{max} (12%–14%, Pollard et al. (*13*)), combined with a volumetric measurement in which a small change in radius from the 50% SUV_{max} threshold results in a large change in volume, predictably results in large variability. Therefore, monitoring disease on the basis of individual manually segmented tumors does not appear to be a reliable marker for treatment response. The RC for subgroup MTV_{mean} and total MTV_{mean} was 33% and 35%, respectively, which is similar to that reported in the literature for ^{18}F-FDG for other

TABLE 5
Repeatability of MTV_{total} with Different Readers Between Scans

Metric	R1, R2 RC (%)	R2, R1 RC (%)	Mean RC (%)	95% CI of mean RC
MTV_{total}	29.9	44.7	37.3	27.9–49.3
Total MTV_{mean}	29.9	44.7	37.3	29.9–44.7
PSMA-TL_{total}	24.9	37.2	31.0	24.5–39.5
PSMA-TLQ_{total}	52.5	58.4	55.5	38.1–83.6
Total mean SUV_{max}	28.3	20.7	24.5	17.5–33.5
Total mean SUV_{mean}	27.4	18.7	23.1	17.2–31.1

R1, R2 = first scan read by reader 1, second scan read by reader 2; R2, R1 = first scan read by reader 2, second scan read by reader 1.
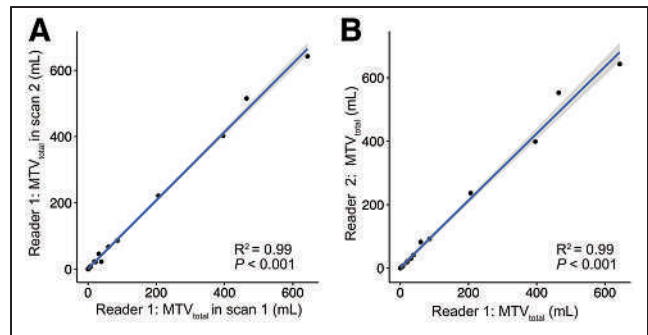
FIGURE 5. Graphical analysis of intra- and interreader agreement in reporting MTV_{total}, showing high correlation in measures between scans 1 and 2 for same reader (reader 1) (A) and showing high correlation in measures between 2 independent readers for same scan (scan 1) (B).

cancers (*28,29*). An MTV based on a larger sample of tumors or total tumor volume rather than individual tumors appears to be more reliable, likely because the noise-sensitive SUV_{max}-based thresholds and resulting volume differences have both plus and minus biases across all lesions, resulting in a tendency to cancel out. Although robust, the method based on selection of a subgroup of tumors would be time-consuming in clinical practice and prone to bias in lesion selection. Because of the limited data available, no clear recommendation for a minimum number of lesions for the subgroup of lesions can be made; moreover, the repeatability of quantified volume is likely influenced by the characteristics of the chosen lesions (e.g., lesion size and tissue type). MTV_{total} remains robust even when alternating readers between baseline and follow-up scans, suggesting that this method would hold up in clinical practice when scans are not always read by the same person. Therefore, the standardized semiautomatic segmentation method for MTV_{total} proposed by Seifert et al., which worked well in this study, may be a solution (*9*). Future investigation should focus on
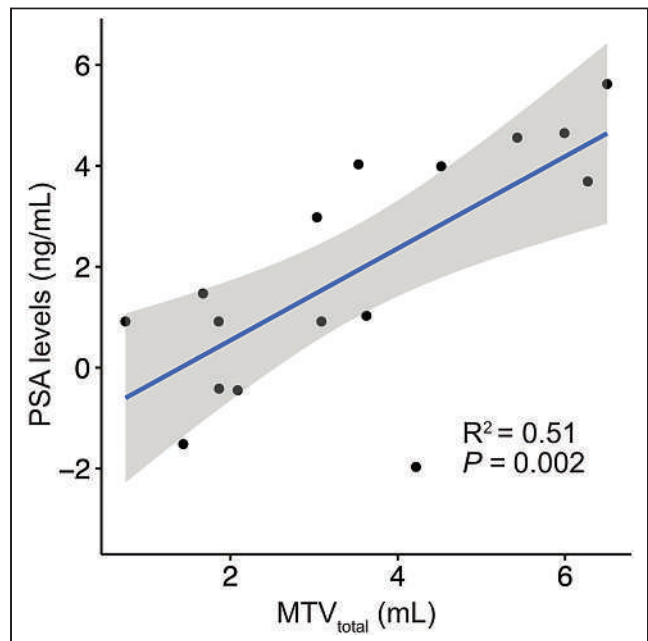
FIGURE 6. Graphical analysis of prostate-specific antigen vs. MTV_{total}, with log–log plot showing moderate correlation.

the fully automatic analysis of PSMA PET scans in analogy to ^{18}F-FDG PET approaches (30). MTV_{total} showed a moderate correlation with prostate-specific antigen, suggesting that further assessment of this metric for use as a surrogate biomarker for disease status is warranted.

Besides volumetry, we evaluated SUV measures, which showed repeatability similar to that reported by Pollard et al. (13). We also evaluated PSMA-TL and PSMA-TLQ, metrics that integrate tumor volume and uptake analogous to total lesion glycolysis for ^{18}F-FDG. These metrics showed poor repeatability in individual lesions, but improved repeatability for the subgroup of tumors and total tumor burden, and thus warrant further investigation (12). Interestingly, PMA-TLQ had greater variability than PSMA-TL. This might be partly explained by the fact that the tumor volume is normalized with the relatively stable (i.e., high-repeatability) SUV_{mean}. Thereby, changes in the tumor volume have a larger influence on the resulting composite metric.

The present study had some limitations. The fact that patient number was relatively small might influence the translatability to a larger patient population. The results might not be directly translatable to other PSMA ligands, especially to those that are conjugates with nongallium radioisotopes. The segmentation technique may cause difficulties when single lesions are segmented separately in follow-up scans or when confluent lesions occur (Fig. 2). However, manual user-dependent adjustments can eliminate those artifacts. Finally, the test–retest dataset was performed under carefully controlled conditions (e.g., ensuring the same scanner for scans 1 and 2, minimizing variation in uptake time and dose), which do not reflect the potential variations encountered in the real-world clinic setting.

CONCLUSION

^{68}Ga-PSMA-HBED-CC PET–derived MTV_{total} with semiautomatic whole-body segmentation is highly repeatable and suitable for monitoring disease in advanced prostate cancer. Other methods evaluated in this study, such as single-lesion volumes and subgroup of lesions per patient, are limited by inferior repeatability (MTV_{lesion}) or labor intensiveness ($MTV_{subgroup}$). MTV_{total} therefore presents an efficient and robust means of monitoring disease longitudinally. A change of greater than 35% in the magnitude of MTV_{total} can be viewed as a real change in tumor status progression or response to therapy.

DISCLOSURE

KEY POINTS

QUESTION: What is the estimated test–retest repeatability of whole-body MTV_{total} for ^{68}Ga-PSMA-HBED-CC PET/CT in patients with metastatic prostate cancer?

PERTINENT FINDINGS: This study evaluated the test–retest repeatability of semiautomatic segmentation of whole-body MTV_{total}, showing a wCV of 12.7% and an RC of ±35%. The repeatability of manually segmented individual tumors (MTV_{lesion}) was poor, whereas the repeatability of a manually selected subgroup of tumors per patient ($MTV_{subgroup}$) was robust but limited by labor intensiveness.

IMPLICATIONS FOR PATIENT CARE: Understanding test–retest repeatability for metrics of metastatic disease burden is important for the development of ^{68}Ga PSMA HBED-CC PET/CT as a quantitative imaging biomarker. This study suggests that semiautomatically segmented whole-body MTV_{total} is efficient and robust for monitoring disease status.

REFERENCES

1. Siegel RL, Miller KD, Jemal A. Cancer statistics, 2020. *CA Cancer J Clin.* 2020; 70:7–30.
2. Scher HI, Morris MJ, Stadler WM, et al. Trial design and objectives for castration-resistant prostate cancer: updated recommendations from the prostate cancer clinical trials working group 3. *J Clin Oncol.* 2016;34:1402–1418.
3. Denmeade SR, Sokoll LJ, Dalrymple S, et al. Dissociation between androgen responsiveness for malignant growth vs. expression of prostate specific differentiation markers PSA, hK2, and PSMA in human prostate cancer models. *Prostate.* 2003;54:249–257.
4. Yuan TC, Veeramani S, Lin MF. Neuroendocrine-like prostate cancer cells: neuroendocrine transdifferentiation of prostate adenocarcinoma cells. *Endocr Relat Cancer.* 2007;14:531–547.
5. Fendler WP, Calais J, Eiber M, et al. Assessment of ^{68}Ga-PSMA-11 PET accuracy in localizing recurrent prostate cancer: a prospective single-arm clinical trial. *JAMA Oncol.* 2019;5:856–863.
6. Hofman MS, Lawrentschuk N, Francis RJ, et al. Prostate-specific membrane antigen PET-CT in patients with high-risk prostate cancer before curative-intent surgery or radiotherapy (proPSMA): a prospective, randomised, multicentre study. *Lancet.* 2020;395:1208–1216.
7. Fanti S, Goffin K, Hadaschik BA, et al. Consensus statements on PSMA PET/CT response assessment criteria in prostate cancer. *Eur J Nucl Med Mol Imaging.* 2021;48:469–476.
8. Fanti S, Hadaschik B, Herrmann K. Proposal for systemic-therapy response-assessment criteria at the time of PSMA PET/CT imaging: the PSMA PET progression criteria. *J Nucl Med.* 2020;61:678–682.
9. Seifert R, Herrmann K, Kleesiek J, et al. Semiautomatically quantified tumor volume using ^{68}Ga-PSMA-11 PET as a biomarker for survival in patients with advanced prostate cancer. *J Nucl Med.* 2020;61:1786–1792.
10. Gafita A, Bieth M, Krönke M, et al. qPSMA: semiautomatic software for whole-body tumor burden assessment in prostate cancer using ^{68}Ga-PSMA11 PET/CT. *J Nucl Med.* 2019;60:1277–1283.
11. Grubmüller B, Senn D, Kramer G, et al. Response assessment using ^{68}Ga-PSMA ligand PET in patients undergoing ^{177}Lu-PSMA radioligand therapy for metastatic castration-resistant prostate cancer. *Eur J Nucl Med Mol Imaging.* 2019;46:1063–1072.
12. Seifert R, Kessel K, Schlack K, et al. PSMA PET total tumor volume predicts outcome of patients with advanced prostate cancer receiving [^{177}Lu]Lu-PSMA-617 radioligand therapy in a bicentric analysis. *Eur J Nucl Med Mol Imaging.* 2021;48:1200–1210.
13. Pollard JH, Raman C, Zakharia Y, et al. Quantitative test-retest measurement of ^{68}Ga-PSMA-HBED-CC in tumor and normal tissue. *J Nucl Med.* 2020;61: 1145–1152.
14. Boellaard R, Delgado-Bolton R, Oyen WJG, et al. FDG PET/CT: EANM procedure guidelines for tumour imaging—version 2.0. *Eur J Nucl Med Mol Imaging.* 2015;42:328–354.
15. Bland JM, Altman DG. Statistical methods for assessing agreement between two methods of clinical measurement. *Lancet.* 1986;1:307–310.

16. Obuchowski NA. Interpreting change in quantitative imaging biomarkers. *Acad Radiol.* 2018;25:372–379.

17. Rahbar K, Afshar-Oromieh A, Jadvar H, Ahmadzadehfar H. PSMA theranostics: current status and future directions. *Mol Imaging.* 2018;17:1536012118776068.

18. Rahbar K, Weckesser M, Ahmadzadehfar H, Schafers M, Stegger L, Bogemann M. Advantage of ^{18}F-PSMA-1007 over ^{68}Ga-PSMA-11 PET imaging for differentiation of local recurrence vs. urinary tracer excretion. *Eur J Nucl Med Mol Imaging.* 2018;45:1076–1077.

19. Fendler WP, Weber M, Iravani A, et al. Prostate-specific membrane antigen ligand positron emission tomography in men with nonmetastatic castration-resistant prostate cancer. *Clin Cancer Res.* 2019;25:7448–7454.

20. Farolfi A, Hirmas N, Gafita A, et al. Identification of PCWG3 target populations is more accurate and reproducible with PSMA PET than with conventional imaging: a multicenter retrospective study. *J Nucl Med.* 2021;62:675–678.

21. Weber M, Kurek C, Barbato F, et al. PSMA-ligand PET for early castration-resistant prostate cancer: a retrospective single-center study. *J Nucl Med.* 2021;62:88–91.

22. Eiber M, Herrmann K, Calais J, et al. Prostate cancer molecular imaging standardized evaluation (PROMISE): proposed miTNM classification for the interpretation of PSMA-ligand PET/CT. *J Nucl Med.* 2018;59:469–478.

23. Halabi S, Kelly WK, Ma H, et al. Meta-analysis evaluating the impact of site of metastasis on overall survival in men with castration-resistant prostate cancer. *J Clin Oncol.* 2016;34:1652–1659.

24. Kyriakopoulos CE, Chen Y-H, Carducci MA, et al. Chemohormonal therapy in metastatic hormone-sensitive prostate cancer: long-term survival analysis of the randomized phase III E3805 CHAARTED trial. *J Clin Oncol.* 2018;36:1080–1087.

25. Chi KN, Agarwal N, Bjartell A, et al. Apalutamide for metastatic, castration-sensitive prostate cancer. *N Engl J Med.* 2019;381:13–24.

26. Sweeney CJ, Chen Y-H, Carducci M, et al. Chemohormonal therapy in metastatic hormone-sensitive prostate cancer. *N Engl J Med.* 2015;373:737–746.

27. Seifert R, Seitzer K, Herrmann K, et al. Analysis of PSMA expression and outcome in patients with advanced prostate cancer receiving ^{177}Lu-PSMA-617 radioligand therapy. *Theranostics.* 2020;10:7812–7820.

28. Kramer GM, Frings V, Hoetjes N, et al. Repeatability of quantitative whole-body ^{18}F-FDG PET/CT uptake measures as function of uptake interval and lesion selection in non-small cell lung cancer patients. *J Nucl Med.* 2016;57:1343–1349.

29. Kruse V, Mees G, Maes A, et al. Reproducibility of FDG PET based metabolic tumor volume measurements and of their FDG distribution within. *Q J Nucl Med Mol Imaging.* 2015;59:462–468.

30. Sibille L, Seifert R, Avramovic N, et al. ^{18}F-FDG PET/CT uptake classification in lymphoma and lung cancer by using deep convolutional neural networks. *Radiology.* 2020;294:445–452.

Biokinetics and Dosimetry of ^{177}Lu-Pentixather

Heribert Hänscheid[1], Andreas Schirbel[1], Philipp Hartrampf[1], Sabrina Kraus[2], Rudolf A. Werner[1], Hermann Einsele[2], Hans-Jürgen Wester[3], Michael Lassmann[1], Martin Kortüm[2], and Andreas K. Buck[1]

[1]Department of Nuclear Medicine, University Hospital Würzburg, Würzburg, Germany; [2]Department of Internal Medicine II, University Hospital Würzburg, Würzburg, Germany; and [3]Department of Pharmaceutical Radiochemistry, TU Munich, Munich, Germany

The chemokine receptor 4 (CXCR4), which is overexpressed in many solid and hematologic malignancies, can be targeted for radiopeptide therapy via the antagonist pentixather. The biokinetics and dosimetry of ^{177}Lu-pentixather and ^{90}Y-pentixather were analyzed in this study. **Methods:** This retrospective study was a standardized reevaluation of data collected for treatment planning. Nineteen patients with complete sets of planar whole-body scans over at least 4 d and a single SPECT/CT scan after administration of 200 MBq of ^{177}Lu-pentixather were included. Kinetics were measured in the whole body, in tissues with activity retention, and in 10 individuals in the blood. Time-integrated activity coefficients and tissue-absorbed doses were derived. **Results:** Increased uptake of pentixather was observed in the kidneys, liver, spleen, and bone marrow, inducing respective median absorbed doses of 0.91 Gy (range, 0.38–3.47 Gy), 0.71 Gy (range, 0.39–1.17 Gy), 0.58 Gy (range, 0.34–2.26 Gy), and 0.47 Gy (range, 0.14–2.33 Gy) per GBq of ^{177}Lu-pentixather and 3.75 Gy (range, 1.48–12.2 Gy), 1.61 Gy (range, 1.14–2.97 Gy), 1.66 Gy (range, 0.97–6.69 Gy), and 1.06 Gy (range, 0.27–4.45 Gy) per GBq of ^{90}Y-pentixather. In most tissues, activity increased during the first day after the administration of ^{177}Lu-pentixather and afterward decayed with mean effective half-lives of 41 $\pm$ 10 h (range, 24–64 h) in the kidneys and median half-lives of 109, 86, and 92 h in the liver, spleen, and bone marrow, respectively. Maximum uptake per kidney was 2.2% $\pm$ 1.0% (range, 0.6%–5.1%). In organs showing no specific uptake, absorbed doses exceeding 0.3 Gy/GBq of ^{90}Y-pentixather were estimated for the urinary bladder and for tissues adjacent to accumulating organs such as the adrenal glands, bone surface, and gallbladder. Dose estimates for tumors and extramedullary lesions ranged from 1.5 to 18.2 Gy/GBq of ^{90}Y-pentixather. **Conclusion:** In patients with hematologic neoplasms, absorbed doses calculated for bone marrow and extramedullary lesions are sufficient to be effective as an adjunct to high-dose chemotherapies before stem cell transplantation.

Key Words: pentixather; biokinetics; dosimetry; CXCR4; endoradiotherapy

The chemokine receptor 4 (CXCR4) influences the development of malignant diseases by activating various signaling pathways that influence cell proliferation, angiogenesis, metastasis, and therapeutic resistance (*1*). On the other hand, being overexpressed in many solid and hematologic neoplasms, CXCR4 is a promising target structure for radioligand therapy (*2*). A CXCR4 antagonist that has already been used in the therapy of various malignant diseases is the peptide pentixather labeled with ^{177}Lu or ^{90}Y (*3–8*). Pentixather and its ^{177}Lu- and ^{90}Y-complexes exhibit high selectivity and specificity and good binding affinities to human CXCR4 (*4*). In blood, ^{177}Lu-pentixather shows high binding to serum albumin, CXCR4-mediated binding to leukocytes and platelets, and excellent metabolic stability with virtually no tracer degradation (*4*).

The present report provides the results of a uniformly performed dosimetric reevaluation of measurements after pretherapeutic administration of ^{177}Lu-pentixather to 19 patients. This compound was originally intended to be used for both dosimetry and therapy. The nuclide ^{177}Lu has continued to be used for dosimetry and ^{90}Y for therapy because ^{90}Y-pentixather proved to be preferable for therapy, pretherapeutic dosimetry with low ^{90}Y activities is not possible, and pentixather labeled with a diagnostic nuclide such as ^{111}In has not yet been produced and tested.

MATERIALS AND METHODS

Patients

All patients with dosimetric studies with ^{177}Lu-pentixather and measurements up to at least 4 d after the administration from June 2014 to December 2019 were considered for this retrospective analysis. A boy aged 8 y was excluded, although no obvious differences in activity kinetics were apparent as compared with adults. After excluding 1 study that had to be repeated, 19 studies were eligible for inclusion. The patients (11 women, 8 men; age range, 40–75 y; mean $\pm$ SD, 60 $\pm$ 9 y) had multiple myeloma ($n = 9$), acute myeloid leukemia ($n = 3$), diffuse large B-cell lymphoma ($n = 2$), pre-B acute lymphoblastic leukemia ($n = 1$), T-cell leukemia ($n = 1$), adrenocortical carcinoma ($n = 2$), or thymoma ($n = 1$) and had been treated before by multiple lines of chemotherapy ($n = 19$), stem-cell transplantation (autologous, $n = 10$; allogeneic, $n = 5$), or external-beam radiation therapy ($n = 9$). One patient (patient 7) had only 1 kidney. Details on the included individuals are shown in Table 1.

At the time of study inclusion, all patients had refractory disease and had exhausted the standard treatment options. On the basis of the German Drug Law, §13(2b), and after evaluation by an interdisciplinary panel of specialists, the potential benefit of CXCR4-targeted endoradiotherapy in combination with high-dose chemotherapy and stem-cell transplantation was investigated. All patients gave written informed consent, and the local ethics committee expressed no objections to the retrospective evaluation and publication of the data in accordance with data protection regulations (reference number 20200915 01).

Radiochemistry

For pretherapeutic dosimetry, ^{177}Lu-pentixather is synthesized by adding a solution of 75 μg of pentixather (PentixaPharm) and 3.5 μg of gentisic acid in 525 μL of sodium acetate buffer solution (0.4 M, pH 5.2) to a vial containing about 300 MBq of no-carrier-added ^{177}LuCl$_3$ (ITG; isomeric purity, $<10^{-7}$ ^{177m}Lu) in 200 μL of 0.04 M

TABLE 1
Patient Characteristics at Time of Dosimetric Assessment with ^{177}Lu-Pentixather

Patient no.	Sex	Age (y)	Weight (kg)	Height (cm)	eGFR	Disease	Since (mo)	Previous treatment			
								C	R	Auto	Allo
1	M	61	60	158	99	MM	18	x		1	
2	F	66	64	163	100	MM	54	x		3	
3	F	53	74	165	54	MM	123	x		3	
4	M	65	93	192	46	MM	101	x		2	
5	M	74	60	173	54	MM	22	x	x	2	
6	M	71	80	175	79	MM	77	x	x	2	
7	F	66	60	166	40	MM	138	x	x	1	
8	F	57	104	157	96	MM	49	x	x	1	
9	M	59	77	172	50	MM	23	x	x	2	
10	M	46	70	183	92	AML	7	x			1
11	M	60	78	182	82	AML	19	x			1
12	F	54	62	168	67	AML	27	x			1
13	F	64	80	163	85	DLBCL	42	x			1
14	F	59	68	172	20	DLBCL	32	x	x	1	
15	F	75	75	168	59	pre-B ALL	15	x			
16	F	50	78	172	54	TCL	21	x			1
17	F	55	64	160	96	ACC	46	x	x		
18	M	55	90	175	92	ACC	14	x	x		
19	F	40	52	163	n/a	Thymoma	37	x	x		

eGFR = Chronic Kidney Disease Epidemiology Collaboration glomerular filtrate rate estimate in mL/min per 1.73 m^2; C = chemo; R = irradiation; auto = autologous stem cells; allo = allogeneic stem cells; MM = multiple myeloma; AML = acute myeloid leukemia; DLBCL = diffuse large B-cell lymphoma; pre-B ALL = pre-B acute lymphoblastic leukemia; TCL = T-cell leukemia; ACC = adrenocortical carcinoma; n/a = not available.

HCl and heating the vial for 35 min at 100°C. After cooling, the solution is diluted with saline, passed through a 0.22-mm sterile filter, and tested for radiochemical purity by gradient high-performance liquid chromatography and thin-layer chromatography. Bubble point and pH value are determined before releasing the product.

The radiosynthesis of ^{90}Y-pentixather for therapy follows the same protocol but using higher amounts of pentixather (200 μg), gentisic acid (7 μg), and radioactivity (2–10 GBq of ^{90}YCl$_3$).

Measurements and Data Evaluation

Each patient received about 200 MBq of ^{177}Lu-pentixather (Supplemental Table 1; supplemental materials are available at http://jnm. snmjournals.org) for pretherapeutic dosimetry to confirm eligibility for treatment and to determine the maximum therapeutic activity. The radiopharmaceutical was administered without concomitant medication to protect the kidneys. Activity kinetics were analyzed in the whole body, kidney, liver, spleen, red marrow, and tumorous lesions from repeated whole-body scans and a SPECT/CT scan for normalization to absolute activity concentrations.

Whole-body scanning was performed with the same dual-head γ-camera and identical camera settings at 0.1 h, 4 h, 1 d, 2 d, and 4 d or later after the activity administration. Additional scans after 1 h or 3 d were included if available. For accumulating tissues, net counts were extracted from appropriate regions of interest and fitted by a decay function using ordinary least-squares regression ("Whole-Body Scans" section in supplemental materials; Supplemental Figs. 1 and 2).

Total-body net counts were normalized to the net counts observed in the first scan at 0.1 h. For other tissues, estimates of time-integrated activity coefficients and the specific absorbed doses, that is, the absolute absorbed doses per unit administered activity, were deduced by normalizing the kinetics to activity concentrations measured 1 d (2 d in patient 9) after the administration by SPECT/CT ("Tomographic Imaging" section in supplemental materials; Supplemental Fig. 3).

When possible, activity in entire organs was quantified in SPECT/CT. In large organs, livers, and enlarged spleens, activity was quantified in a partial volume and activity was scaled to the complete mass measured by CT. For the red bone marrow, the activity–time function was determined in the planar images with a large region of interest over the pelvis and spine and normalized to the activity measured on SPECT/CT in the L2–L4 spine, which was assumed to contain 6.7% of the total red marrow activity (9).

In a subgroup of 10 patients, blood samples were collected concomitantly with the whole-body scans. The whole-blood activity concentrations were measured, and the time-integrated activity coefficients per liter of blood were calculated by integration of a triexponential fit function over time.

From the kinetics measured with ^{177}Lu-pentixather, those expected for ^{90}Y-pentixather were calculated by converting the decay constants to the shorter physical half-life of ^{90}Y (64.0 h instead of 159.5 h for ^{177}Lu).

The free internal dosimetry software IDAC-DOSE (version 2.1 (10)) was used to determine specific absorbed doses in evaluated

tissues from the measured time-integrated activity coefficients per unit mass scaled to the sex-specific reference masses and multiplied by the organ- and sex-specific S values in IDAC-DOSE. The software was also used to estimate absorbed doses in unevaluated tissues from the medians of the measured time-integrated activity coefficients and the kidney–bladder model as previously described (11) with a 3.5-h voiding interval. The percentage of total-body activity not located in the evaluated accumulating tissues was attributed to the remainder of the body.

The free software JASP (version 0.14.1; https://jasp-stats.org/) was used for statistical analyses. The distributions determined in this study were tested for normality using the Shapiro–Wilk test, with rejection of the null hypothesis for P values of less than 0.05. Parameters of normally distributed data are reported as mean ± SD and range or as median and quartiles (minimum, first quartile, third quartile, and maximum).

RESULTS

The biokinetics of ^{177}Lu-pentixather were heterogeneous in the group of included patients. Figure 1 shows the whole-body scans 2 d after the administration of the diagnostic activity in 3 of the patients: patient 7, with only 1 kidney, showed the highest specific absorbed doses in the kidney and liver; patient 15, with pre-B acute lymphoblastic leukemia, showed the highest specific absorbed dose in the red marrow and spleen, as well as the highest whole-body time-integrated activity coefficient; and patient 2, with multiple myeloma, showed the highest specific absorbed dose in an extramedullar lesion and the highest time-integrated activity coefficient per liter of blood.

Tables 2 and 3 list the time-integrated activity coefficients and specific absorbed doses for the evaluated tissues for ^{177}Lu-pentixather and ^{90}Y-pentixather, respectively. Figure 2 shows typical time functions of activity retention in organs and tissues, exemplified by patient 3.

The red bone marrow was the dose-limiting organ when the absorbed dose was limited to 2 Gy to preserve function. The mean effective half-life in the bone marrow was 97 ± 31 h (range, 39 h to physical half-life) after ^{177}Lu (kinetics decay-corrected to ^{90}Y: 50 ± 9 h; range, 29 to physical half-life). In 14 patients, the red marrow activity concentration initially increased and reached a maximum at 23 ± 11 h after the administration before decreasing.

If stem cell support is available and myeloablation is tolerated or intended, the therapeutic activity is limited not by the red marrow but by the absorbed dose to the kidneys (23 Gy). This would have increased the tolerable activity by a median factor of 4.9 (range, 1.6–70.9) after ^{177}Lu and a factor of 2.8 (range, 1–34.7) after ^{90}Y even without kidney-protective medication. Uptake per kidney generally increased at 4 h and later up to a mean maximum of 2.2% ± 1.0% (range, 0.6%–5.1%) of the administered activity at 18 ± 7 h after the administration and a subsequent decrease with a mean effective half-life of 41 ± 10 h (range, 24–64 h). The fitted half-life of the increasing component was 27 h in patient 7 and a median of 7.8 h (quartiles: 2.4, 4.9, 12.2, and 15.4 h) in patients with 2 kidneys. Decay-corrected to ^{90}Y, the mean maximum uptake would have been 1.9% ± 0.9% (range, 0.5%–4.0%) after 14 ± 6 h, and the mean effective half-life would have been 29 ± 5 h (range, 20–40 h).

Compared with the kidney, the kinetics in the liver were retarded, with a later maximum of retention (6.1% ± 1.8%; range, 2.2%–10.0%) after 35 ± 11 h and a longer median effective half-life of 109 h (quartiles: 77 h, 92 h, 146 h, and physical half-life) after ^{177}Lu. Respective data for ^{90}Y-pentixather would have been 4.9% ± 1.6% (range, 1.8%–8.6%) retention after 23 ± 7 h and a
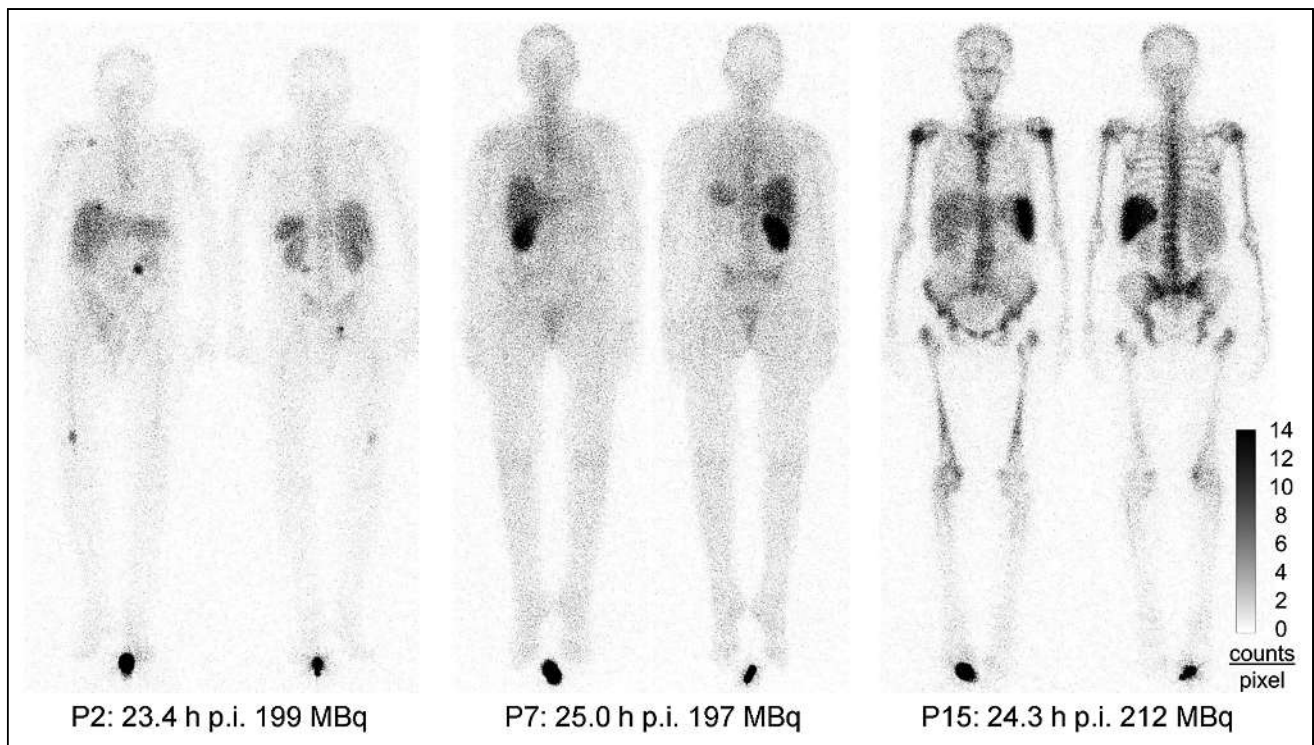
FIGURE 1. Examples of different activity distributions after ^{177}Lu-pentixather in patients 2 and 7 (P2 and P7, respectively), with multiple myeloma, and patient 15 (P15), with pre-B acute lymphoblastic leukemia. Although uptake in single kidney of patient 7 was 5%, sum of uptakes in both kidneys of patient 15 was only 1.1%. In contrast, retention was 3-fold higher in bone marrow and 11-fold higher in spleen of patient 15. p.i. = after injection.

TABLE 2
[177]Lu-Pentixather Time-Integrated Activity Coefficients in Whole Body, Organs, Tumorous Lesions, Red Marrow, and Blood, as Well as Tissue-Absorbed Doses per Administered Activity in Organs and Lesions

Patient no.	WB ã (h)	Kidneys ã (h)	Kidneys D/A (Gy/GBq)	Liver ã (h)	Liver D/A (Gy/GBq)	Spleen ã (h)	Spleen D/A (Gy/GBq)	Red marrow ã (h)	Red marrow D/A (Gy/GBq)	Lesion D/A (Gy/GBq)	Blood ã (h/L)
1	51.6	4.39	1.01	3.8	0.39	2.06	0.58	4.0	0.14	2.2	0.21
2	56.1	2.42	0.71	14.4	0.82	2.49	1.55	8.1	0.37	6.9	0.58
3	55.3	4.85	2.10	15.2	0.93	1.27	0.72	14.3	0.66		0.48
4	97.6	4.61	1.48	16.2	0.80	2.03	0.70	13.7	0.48		0.28
5	87.7	1.92	0.87	12.2	0.91	3.71	1.59	16.8	0.59	1.7	
6	62.1	1.74	0.50	11.7	0.62	0.63	0.34	11.8	0.41	3.1	
7	111.0	6.25	3.47	15.0	1.17	1.34	1.12	10.6	0.48		
8	61.6	5.28	1.21	10.0	0.39	0.90	0.38	9.4	0.43		
9	111.6	4.76	1.12	13.2	0.67	1.18	0.47	13.6	0.47		
10	50.5	4.51	0.90	9.0	0.43	2.47	0.40	9.9	0.35		0.32
11	55.9	4.34	1.14	8.0	0.42	1.43	0.48	9.1	0.32		0.34
12	77.8	2.03	0.79	13.9	0.71	3.46	0.75	21.3	0.97	1.1	
13	114.9	7.87	0.91	21.9	0.67	2.65	0.35	22.8	1.04	2.1	
14	83.6	1.63	0.59	16.7	0.88	11.5	1.20	16.4	0.75		
15	140.9	1.04	0.38	15.5	0.71	14.0	2.26	51.0	2.33		
16	108.8	3.22	1.07	14.1	0.50	6.51	1.03	12.2	0.56	1.6	0.28
17	73.6	1.93	0.52	20.1	0.92	2.38	0.56	5.5	0.25	2.3	0.28
18	51.6	3.47	0.67	12.0	0.41	3.30	0.42	4.0	0.14	1.1	0.32
19	48.0	5.23	1.96	9.4	0.81	0.44	0.48	8.5	0.39	0.7	0.44
P	0.03	0.31	<0.01	0.95	0.21	<0.01	< 0.01	<0.01	<0.01	< 0.01	0.23
Minimum	48.0	1.04	0.38	3.7	0.39	0.44	0.34	4.0	0.14	0.7	0.21
First quartile	55.6	1.98	0.70	10.9	0.47	1.30	0.45	8.8	0.36	1.2	0.28
Median	73.6	4.34	0.91	13.9	0.71	2.38	0.58	11.8	0.47	1.9	0.32
Third quartile	103.2	4.80	1.18	15.4	0.85	3.38	1.08	15.4	0.62	2.3	0.42
Maximum	140.9	7.87	3.47	21.9	1.17	14.0	2.26	51.0	2.33	6.9	0.58
Mean	79.0	3.77	1.13	13.3	0.69	3.36	0.81	13.8	0.59	2.3	0.35
SD	27.9	1.82	0.73	4.2	0.22	3.61	0.52	10.4	0.49	1.8	0.11

WB = whole body; ã = time-integrated activity coefficient; D/A = tissue-absorbed doses per administered activity.
P values are from Shapiro–Wilk test of normality.

median effective half-life of 54 h (quartiles: 45 h, 49 h, 54 h, and physical half-life).

High values for the time-integrated activity coefficient for the spleen (Tables 2 and 3) were associated with splenomegaly due to malignant infiltration. In affected patients, a high absorbed dose to the spleen is considered a desirable therapeutic effect. Measured spleen masses in patients 14, 15 (Fig. 1), and 16 were 824, 530, and 539 g, respectively. Fifteen patients showed a delayed retention maximum. The mean effective half-life in the spleen was 99 ± 36 h (range, 51 h to physical half-life) after [177]Lu ([90]Y: 50 ± 9 h; range, 35 h to physical half-life).

In malignant extramedullary lesions, activity initially almost always increased, reaching a maximum after a median of 11 h and then decreasing with effective half-lives of 122 ± 32 h (range, 78 h to physical half-life) after [177]Lu ([90]Y: 56 ± 7 h; range, 45 h to

physical half-life). The calculated values for the tissue-absorbed doses per unit administered activity ranged from 0.7 to 6.9 Gy/GBq of ^{177}Lu and from 1.5 to 18.2 Gy/GBq of [90]Y.

Estimates of absorbed doses in organs apparently without specific activity accumulation are shown in Supplemental Table 2. Absorbed doses of about 0.05 Gy/GBq of ^{177}Lu-pentixather and 0.2 Gy/GBq of ^{90}Y-pentixather are expected in most organs. Somewhat higher values are estimated for the urinary bladder and for tissues adjacent to accumulating organs such as the adrenals, bone surface, and gallbladder.

DISCUSSION

High and long-lasting retention of pentixather in the bone marrow leads to high specific absorbed doses to the hematopoietic

TABLE 3
^{90}Y-Pentixather Time-Integrated Activity Coefficients in Whole Body, Organs, Tumorous Lesions, Red Marrow, and Blood, as Well as Tissue-Absorbed Doses per Administered Activity in Organs and Lesions (Recalculated from Kinetics Measured with ^{177}Lu-Pentixather)

Patient no.	WB ã (h)	Kidneys ã (h)	Kidneys D/A (Gy/GBq)	Liver ã (h)	Liver D/A (Gy/GBq)	Spleen ã (h)	Spleen D/A (Gy/GBq)	Red marrow ã (h)	Red marrow D/A (Gy/GBq)	Lesion D/A (Gy/GBq)	Blood ã (h/L)
1	31.5	3.03	3.91	1.9	1.18	1.05	1.66	2.3	0.34	6.1	0.19
2	33.6	1.90	3.16	5.8	1.91	0.95	3.30	4.0	0.77	18.2	0.48
3	35.1	2.95	7.32	6.0	2.12	0.53	1.70	7.4	1.42		0.42
4	51.6	2.97	5.36	6.3	1.80	0.82	1.58	6.0	0.88		0.28
5	50.8	1.22	3.10	6.1	2.65	1.26	3.04	8.4	1.23	4.1	
6	40.1	1.31	2.12	5.2	1.61	0.40	1.20	7.4	1.09	9.2	
7	54.2	3.87	12.2	6.6	2.97	0.69	3.22	6.5	1.25		
8	34.5	3.74	4.85	5.4	1.22	0.45	1.07	5.1	0.98		
9	58.5	3.22	4.29	6.1	1.77	0.67	1.51	7.2	1.06		
10	32.8	3.32	3.75	4.6	1.29	1.07	0.97	4.9	0.72		0.28
11	35.7	2.83	4.21	3.8	1.16	0.76	1.42	4.7	0.69		0.30
12	47.2	1.41	3.16	5.4	1.61	2.06	2.51	10.1	1.94	3.4	
13	59.3	4.89	3.21	8.5	1.51	1.42	1.05	8.9	1.72	4.7	
14	49.6	1.04	2.15	7.6	2.32	6.63	3.85	9.6	1.85		
15	67.7	0.71	1.48	6.0	1.57	7.40	6.69	23.2	4.45		
16	63.8	2.38	4.50	7.8	1.59	3.04	2.70	7.1	1.36	4.2	0.26
17	41.1	1.39	2.15	8.7	2.31	1.41	1.88	3.1	0.59	5.4	0.44
18	34.5	2.47	2.67	5.7	1.14	1.58	1.13	1.8	0.27	3.6	0.28
19	29.9	3.53	7.52	3.6	1.80	0.25	1.53	3.5	0.68	1.5	0.40
P	0.08	0.53	<0.01	0.55	0.13	<0.01	<0.01	<0.01	<0.01	<0.01	0.31
Minimum	29.9	0.71	1.48	2.0	1.14	0.25	0.97	1.83	0.27	1.5	0.19
First quartile	34.5	1.40	2.88	5.3	1.40	0.68	1.31	4.35	0.71	3.7	0.28
Median	41.1	2.83	3.75	6.0	1.61	1.05	1.66	6.50	1.06	4.5	0.29
Third quartile	52.9	3.27	4.67	6.4	2.02	1.50	2.87	7.88	1.39	5.9	0.41
Maximum	67.7	4.89	12.2	8.7	2.97	7.40	6.69	23.2	4.45	18.2	0.48
Mean	44.8	2.54	4.27	5.9	1.77	1.71	2.21	6.90	1.22	6.0	0.33
SD	12.0	1.14	2.52	1.7	0.51	1.99	1.39	4.61	0.91	4.7	0.10

WB = whole body; ã = time-integrated activity coefficient; D/A = tissue-absorbed doses per administered activity.
P values are from Shapiro–Wilk test of normality.

system. The estimates for the bone marrow–absorbed dose indicate that the safety limit of 2 Gy is usually reached after about 4 GBq of ^{177}Lu or 2 GBq of ^{90}Y. The absorbed doses achievable in malignant tissues with these activities are considered insufficient to achieve an adequate therapeutic effect on malignant tissue, especially in solid tumors with moderate CXCR4 expression. In hematologic neoplasms, on the other hand, therapy with pentixather can be a reasonable complement to high-dose chemotherapy regimens followed by subsequent hematopoietic stem cell transplantation, with the potential to effectively fight radiation-sensitive lesions.

With the exception of patients 11, 14, and 15, who experienced unexpected obstacles regarding stem cell availability, and patient 5, whose health deteriorated, all patients with hematologic diseases received therapy. Patients 17, 18, and 19, with adrenocortical carcinoma or thymoma, remained untreated. Patients 1–4 received ^{177}Lu-pentixather for treatment ("Posttherapeutic Measurements" section in the supplemental materials; Supplemental Figs. 4 and 5), and all others received ^{90}Y-pentixather. ^{177}Lu-pentixather for therapy has the advantage that its γ-radiation can be used scintigraphically for verification of the activity distribution and for dosimetry, but ^{177}Lu-pentixather has an unfavorably long half-life in the bone marrow. With therapeutic doses of 10 Gy or more to the red bone marrow, the activity in the marrow must decay for at least 4–5 half-lives before stem cell transplantation to safely avoid compromising engraftment. Although this level of decay is ensured 2 wk after
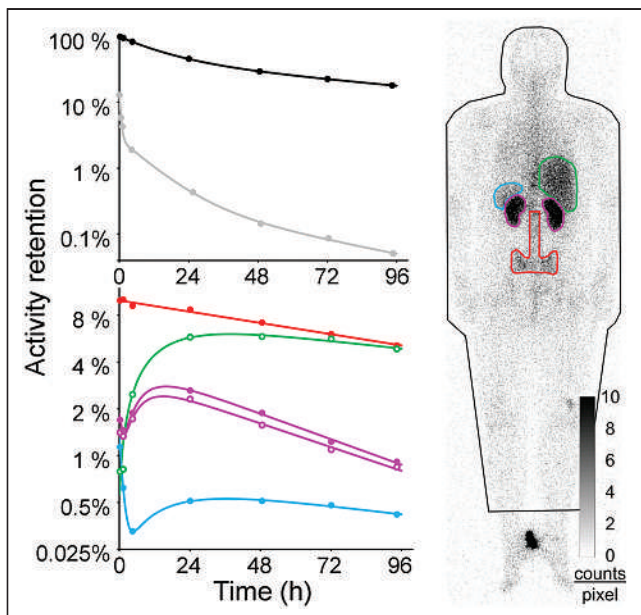
FIGURE 2. Regions of interest used to derive time functions of activity retention in whole body (black), red bone marrow (red), liver (green), right kidney (purple solid circles), left kidney (purple open circles), and spleen (blue) in patient 3 with respective fit functions. Scintigram shows posterior whole-body image 24 h after 197 MBq of ^{177}Lu-pentixather. Gray symbols with fit function represent activity retention per liter of whole blood.

[90]Y-pentixather, an interval of up to 4 wk may be necessary for ^{177}Lu-pentixather. The longer time between ^{177}Lu-pentixather treatment and transplantation is disadvantageous because the prolonged phase of aplasia poses an increased risk of infectious complications.

Since pentixather, like other radiolabeled peptides, is filtered through the kidneys, activity retention in the renal tubules must be considered. It is not yet known whether ^{90}Y, like somatostatin receptor agonists, has higher renal toxicity because of its higher β-energy and dose rate, nor is it known which renal dose limits are appropriate for pentixather labeled with ^{177}Lu or [90]Y. The limit of 23 Gy for the tolerable absorbed dose, which is often used for the kidneys (12), is reached after 20–30 GBq of ^{177}Lu-pentixather or 5–8 GBq of ^{90}Y-pentixather in most patients. Although 10 GBq of ^{90}Y-pentixather could have been safely administered in 20% of patients, the specific absorbed dose determined for the patient with only 1 kidney (patient 7) was 12.2 Gy/GBq, limiting the safely administrable activity to 1.9 GBq. In patients with 2 kidneys, who were not included in this study because dosimetric measurements were performed over 3 d only, the highest calculated dose was 12.7 Gy/GBq of ^{90}Y-pentixather.

Concomitant medication with amino acids, such as that recommended for somatostatin receptor therapy with radiolabeled peptides (12), also reduces retention of pentixather in the kidneys (Supplemental Table 3). The reduction factor of 64% ± 13% (range, 50%–80%) reported previously (8) was derived from only 6 treatments with ^{177}Lu-pentixather and remains to be validated.

The above figures indicate that, in an approach that uses myeloablative therapy with fixed activities, hardly more than 2.5 GBq of ^{90}Y-pentixather can be administered without exceeding a kidney dose of 23 Gy in individual patients. The estimated specific absorbed doses to bone marrow and lesions indicate that this limitation is likely to leave many patients inadequately dosed, which strongly supports the theranostic approach with pretherapeutic dosimetry.

The data in the present study were not collected prospectively in an optimized study design. The dosimetric measurements were performed with the lowest activity that seemed necessary, limiting the accuracy of the scintigraphic imaging and its evaluation ("Uncertainties" section in supplemental materials). Some estimate of the dosimetric accuracy is provided by the intraindividual comparison of the absorbed doses determined for the right and left kidneys after ^{177}Lu-pentixather, which incorporates the uncertainties of both volume segmentation and measurement and fit of activity kinetics. The dose derived for the right kidney was 108% ± 14% (range, 78%–128%) that derived for the left kidney.

In tissues with a delayed retention maximum and a long half-life for the retained activity, namely the liver, spleen, and red bone marrow, measurements over 4 d are often not sufficient to determine the half-life with good accuracy. Later measurements, however, were not necessary to estimate the absorbed doses to the kidneys and would have required an additional patient visit and the use of higher activities, which were avoided to minimize the risk that the kinetics would be affected by the dose administered pretherapeutically. For therapy with ^{90}Y-pentixather, scans over 3 d are sufficient to measure the kinetics in the kidneys ("Uncertainties" section in supplemental materials).

[90]Y-pentixather kinetics data shown here were not measured but calculated by converting the ^{177}Lu-pentixather results, assuming comparable kinetics for [nat]Lu and [nat]Y. Comparison of kinetics during therapy with prediction has not been technically possible in our patients treated with ^{90}Y-pentixather but is intended in the future by quantification of the positrons of the ^{90}Y decay with a PET/CT scan of higher sensitivity. Since the metal that is used affects the CXCR4 affinity and thus potentially the biokinetics, deviations of actual absorbed doses from estimates are possible. The binding affinity of [nat]Y-pentixather to CXCR4 is slightly lower than that of [nat]Lu-pentixather (4), which is most likely to affect binding in target tissues. Also, an influence on excretion and kinetics in healthy organs cannot generally be excluded.

An interesting alternative for the treatment of hematologic malignancies could be the labeling of pentixather with an α-emitter to effectively target smaller cell clusters. [nat]Bi-pentixather has a higher binding affinity to CXCR4 than does [nat]Lu-pentixather (4), but even for the most suitable isotope, [213]Bi, the half-life of only 46 min is likely to be too short.

Bone marrow dosimetry is uncertain even in healthy individuals. In patients with malignant transformation of the hematologic system, the bone marrow may be severely modified in an individualized manner. The activity pattern in the medullary spaces is often very inhomogeneous, and the assumption of 6.7% bone marrow content in the evaluated vertebrae is even more uncertain than in healthy subjects. The doses mentioned should therefore be regarded as calculated values for estimating the approximate magnitude.

CONCLUSION

The absorbed radiation doses achievable with labeled pentixather are often insufficient for radiologic destruction of solid tumors. In hematologic neoplasms, however, ^{90}Y-pentixather can be effective against radiosensitive lesions and as a useful adjunct to the

conditioning regimen before stem cell transplantation. Although the kidneys are the dose-limiting organ in myeloablative therapy, high exposures also occur in the liver and spleen. Of the remaining organs, absorbed doses exceeding 0.3 Gy/GBq are estimated for the urinary bladder and for tissues adjacent to accumulating organs such as the adrenal glands, bone surface, and gallbladder.

DISCLOSURE

KEY POINTS

QUESTION: How do the biokinetics of the CXCR4 antagonist pentixather affect endoradiotherapy?

PERTINENT FINDINGS: Dosimetric studies with 200 MBq of ^{177}Lu-pentixather in 19 patients demonstrated very heterogeneous absorbed doses per administered activity in organs and tissues and identified the red bone marrow and kidneys as dose-limiting organs.

IMPLICATIONS FOR PATIENT CARE: Therapy with ^{90}Y-pentixather may be considered if the malignant tissue is radiosensitive, myeloablation is accepted, and excessive renal absorbed dose is avoided by pretherapeutic dosimetry.

REFERENCES

1. Chatterjee S, Behnam Azad B, Nimmagadda S. The intricate role of CXCR4 in cancer. *Adv Cancer Res.* 2014;124:31–82.
2. Walenkamp AME, Lapa C, Herrmann K, Wester HJ. CXCR4 ligands: the next big hit? *J Nucl Med.* 2017;58(suppl):77S–82S.
3. Herrmann K, Schottelius M, Lapa C, et al. First-in-human experience of CXCR4-directed endoradiotherapy with Lu-177- and Y-90-labeled pentixather in advanced-stage multiple myeloma with extensive intra- and extramedullary disease. *J Nucl Med.* 2016;57:248–251.
4. Schottelius M, Osl T, Poschenrieder A, et al. [Lu-177]pentixather: comprehensive preclinical characterization of a first CXCR4-directed endoradiotherapeutic agent. *Theranostics.* 2017;7:2350–2362.
5. Habringer S, Lapa C, Herhaus P, et al. Dual targeting of acute leukemia and supporting niche by CXCR4-directed theranostics. *Theranostics.* 2018;8:369–383.
6. Lapa C, Hanscheid H, Kircher M, et al. Feasibility of CXCR4-directed radioligand therapy in advanced diffuse large B-cell lymphoma. *J Nucl Med.* 2019;60:60–64.
7. Maurer S, Herhaus P, Lippenmeyer R, et al. Side effects of CXC-chemokine receptor 4-directed endoradiotherapy with pentixather before hematopoietic stem cell transplantation. *J Nucl Med.* 2019;60:1399–1405.
8. Lapa C, Herrmann K, Schirbel A, et al. CXCR4-directed endoradiotherapy induces high response rates in extramedullary relapsed multiple myeloma. *Theranostics.* 2017;7:1589–1597.
9. Shen S, Meredith RF, Duan J, et al. Improved prediction of myelotoxicity using a patient-specific imaging dose estimate for non-marrow-targeting Y-90-antibody therapy. *J Nucl Med.* 2002;43:1245–1253.
10. Andersson M, Johansson L, Eckerman K, Mattsson S. IDAC-Dose 2.1, an internal dosimetry program for diagnostic nuclear medicine based on the ICRP adult reference voxel phantoms. *EJNMMI Res.* 2017;7:88.
11. ICRP publication 106: radiation dose to patients from radiopharmaceuticals—a third amendment to ICRP publication 53. *Ann ICRP.* 2008;38:1–197.
12. Bodei L, Mueller-Brand J, Baum RP, et al. The joint IAEA, EANM, and SNMMI practical guidance on peptide receptor radionuclide therapy (PRRNT) in neuroendocrine tumours. *Eur J Nucl Med Mol Imaging.* 2013;40:800–816.

Modeling Early Radiation DNA Damage Occurring During ^{177}Lu-DOTATATE Radionuclide Therapy

Giulia Tamborino[1,2], Yann Perrot[3], Marijke De Saint-Hubert[1], Lara Struelens[1], Julie Nonnekens[2,4], Marion De Jong[2], Mark W. Konijnenberg[2], and Carmen Villagrasa[4]

[1]Research in Dosimetric Applications, Belgian Nuclear Research Centre, Mol, Belgium; [2]Department of Radiology and Nuclear Medicine, Erasmus MC Cancer Institute, Erasmus University Medical Center, Rotterdam, The Netherlands; [3]IRSN, Institut de Radioprotection et de Sûreté Nucléaire, Fontenay aux Roses, France; and [4]Department of Molecular Genetics, Oncode Institute, Erasmus MC Cancer Institute, Erasmus University Medical Center, Rotterdam, The Netherlands

The aim of this study was to build a simulation framework to evaluate the number of DNA double-strand breaks (DSBs) induced by in vitro targeted radionuclide therapy (TRT). This work represents the first step toward exploring underlying biologic mechanisms and the influence of physical and chemical parameters to enable a better response prediction in patients. We used this tool to characterize early DSB induction by ^{177}Lu-DOTATATE, a commonly used TRT for neuroendocrine tumors. **Methods:** A multiscale approach was implemented to simulate the number of DSBs produced over 4 h by the cumulated decays of ^{177}Lu distributed according to the somatostatin receptor binding. The approach involves 2 sequential simulations performed with Geant4/Geant4-DNA. The radioactive source is sampled according to uptake experiments on the distribution of activities within the medium and the planar cellular cluster, assuming instant and permanent internalization. A phase space is scored around the nucleus of the central cell. Then, the phase space is used to generate particles entering the nucleus containing a multiscale description of the DNA in order to score the number of DSBs per particle source. The final DSB computations are compared with experimental data, measured by immunofluorescent detection of p53-binding protein 1 foci. **Results:** The probability of electrons reaching the nucleus was significantly influenced by the shape of the cell compartment, causing a large variance in the induction pattern of DSBs. A significant difference was found in the DSBs induced by activity distributions in cell and medium, as is explained by the specific energy ($\bar{z}$) distributions. The average number of simulated DSBs was 14 DSBs per cell (range, 7–24 DSBs per cell), compared with 13 DSBs per cell (range, 2–30 DSBs per cell) experimentally determined. We found a linear correlation between the mean absorbed dose to the nucleus and the number of DSBs per cell: 0.014 DSBs per cell mGy^{-1} for internalization in the Golgi apparatus and 0.017 DSBs per cell mGy^{-1} for internalization in the cytoplasm. **Conclusion:** This simulation tool can lead to a more reliable absorbed-dose–to–DNA correlation and help in prediction of biologic response.

The most common way of exposing cancer patients to radiation is through external-beam radiotherapy (EBRT). The success and effectiveness of EBRT can, at least partially, be attributed to knowledge of its radiobiologic principles and their integration into dose–response modeling (1).

An alternative form of anticancer therapy is targeted radionuclide therapy (TRT). TRT is based on injection of a radiolabeled molecule that has the advantage of targeting specific cancer cells, enabling delivery of a cytotoxic absorbed dose to eradicate both a primary tumor site and metastases (2).

In striking contrast to EBRT, TRT is marked by a scarcity of radiobiologic investigations and dose–response modeling. The physical characteristics of TRT—that is, heterogeneous radiation caused by variable uptake at cellular and subcellular levels, protracted exposure causing overlapped biologic mechanisms such as DNA damage formation and repair, and low dose-rate—differ significantly from those of EBRT. Hence, TRT-specific radiobiologic knowledge and biophysical modeling need to be developed (3).

The initial step into understanding the cell's radiobiologic response is represented by calculation of the energy deposition on a subcellular scale and, in particular, in the cell nucleus, where radioinduced DNA damage can be considered a key biologic output for predicting cellular fate (4). Ultimately, a mechanistically informed model, including the cell's response dependence on phenotype, cell cycle, microenvironment, type of radiation, and delivery method, would elucidate the underlying biologic mechanisms and hence allow prediction of the radiosensitivity of individual tissues under a particular irradiation condition (5).

DNA is recognized as a key target, and currently, simulations of in vitro DNA damage in the context of TRT have been focused primarily on low-energy electrons, namely Auger electrons (e.g., ^{125}I-iodo-2′-deoxyuridine,^{111}In-DTPA-D-Phe[1]-octreotide, and ^{64}CuCl$_2$), because of their significant decrease in energy density as a function of distance in nanometers (6).

Various models of DNA target, ranging from DNA linear fragments represented by structured cylinders (7) to either simplified (8) or complex atomic representations (9,10), have been applied

for this purpose using various Monte Carlo codes. On the other hand, a combination of precalculated cluster DNA damage yields by Monte Carlo damage simulation code (11) and local dose distributions within a local effect model has been used as alternative fast approach (12).

For Auger emitters internalized in the nucleus, the choice of DNA model and the placement of the radionuclide with respect to the DNA structure are the main parameters influencing the resulting double-strand break (DSB) computation (10) because of their nanometer range. As a consequence, cell morphology and cell population are not modeled in this scenario. On the contrary, longer-range radionuclides, such as ^{177}Lu, require a detailed cell morphology and population modeling to account for both self- and cross-irradiation in a planar cell colony (13). Furthermore, once the irradiation field has been characterized, an event-by-event description of the radiation track structure at the nanometer level within the nucleus, combined with a simulation including a description of the target at the relevant scale (e.g., atom, molecule), needs to be adopted in order to yield conclusions on the biophysical mechanisms involved. In this respect, faster Monte Carlo approaches for DSB simulation, intrinsically relying on uniform external irradiation parameters, would not provide a deeper understanding of the mechanisms involved and, as such, would not help to contribute to the final goal of developing methods to select the best approach to individualized treatment optimization. In a similar way, nanodosimetric simulations calculating the ionization cluster size distributions in water cylinders corresponding to DNA segments (14) rely on adjustable parameters—inferred from EBRT exposure—to account for the missing geometric DNA details and, hence, would not completely serve this purpose.

A successful example of TRT, leading to markedly prolonged survival and an increased quality of life in comparison to nonradioactive targeted therapy (15,16), is ^{177}Lu-DOTATATE. ^{177}Lu-DOTATATE treatment targets tumor cells overexpressing the somatostatin receptor type 2 (SSTR$_2$) and is authorized in Europe and the United States as Lutathera (Advanced Accelerator Applications) for therapy of metastasized neuroendocrine tumors (17).

This work proposed a simulation framework evaluating the number of DNA DSBs occurring during in vitro ^{177}Lu-DOTATATE experiments with planar colonies, thereby accounting for detailed cellular morphologies and source localizations. We analyzed the impact of different modeling assumptions and compared them with experimental data. This study represents a first step toward a better understanding of the underlying biologic mechanisms of ^{177}Lu-DOTATATE exposure by providing a detailed description of early DSB distribution.

MATERIALS AND METHODS

A 2-step simulation process was adopted aiming to model, first, the internal irradiation setup, characterizing particles entering the nucleus belonging to a planar colony, and, second, the DNA damage induced in that specific nuclear shape. The uptake assay, immunofluorescent staining, and imaging of the cellular morphologies were previously established (13,18), and details are described in the supplemental materials (available at http://jnm.snmjournals.org).

Modeling the Internal Irradiation Setup

Cellular polygonal mesh models from representative 4Pi confocal microscopic images of human osteosarcoma cells (U2OS-SSTR$_2$) were used to model 3 cellular morphologies in Geometry Description Markup Language format. Each cellular shape consists of the cellular membrane (CM), cytoplasm (Cy), Golgi apparatus (G), and nucleus.

The nucleus was simplified by either an ellipsoid or an elliptic cylinder, preserving its original volume and proximity to the other cellular compartments (Fig. 1A). The geometric characteristics of the 3 cells are summarized in Table 1.

Simulations were performed on Geant4.10.06 (19–21). A parameterization process replicating each cellular shape, and its subcompartments, within an array was used to create 3 planar populations of 50 adjacent cells of the same shape (Fig. 1B). The number of cells was chosen to allow a cell layer dimension greater than the average range of ^{177}Lu β particles (continuous slowing down approximation range at average energy and maximum energy = 270 μm and 1.76 mm, respectively). Indeed, the ^{177}Lu cross dose (i.e., the absorbed dose delivered by surrounding cells to a target cell) decreases exponentially with distance, and hence, increasing the planar cellular cluster size with additional cell layers after a given value (on average, 3–4 cell layers) would not significantly contribute to the total absorbed dose received by the nucleus of the central cell (13). The computational memory consumption was drastically reduced by the Geant4 parameterization process, since the tessellated geometries (i.e., polygonal mesh) used to model each cellular morphology were stored only once in the memory. The cells were attached to the bottom of a water cylinder.

The decay spectrum of ^{177}Lu is reported in Supplemental Table 1 for reference. In this study, the full continuous radar (β) and discrete internal conversion (IC) electron (ICRP107) spectra were simulated, whereas photon and Auger electron emissions were neglected. Photon emissions are considered negligible for cellular dosimetric purposes (22), and Auger electrons are unlikely to reach the nucleus from Cy or G and CM. Each of these source components was sampled separately in order to distinguish the contribution of β and IC electrons coming from the same nuclear transition.

The radioactive source (^{177}Lu-DOTATATE) was assumed to be instantly and permanently incorporated within the cell (internalized), whereas a smaller portion remained membrane-bound on the basis of the uptake measurements. The probability of emission within the cell (73%) or the membrane (27%) was sampled according to previous
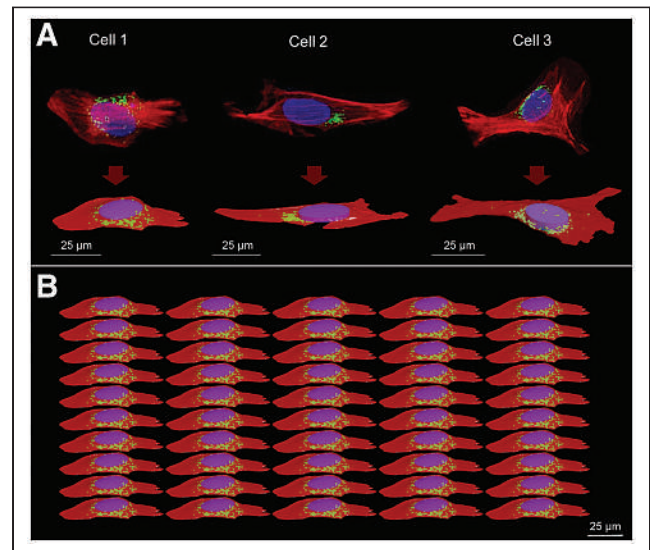
FIGURE 1. Cellular morphologies. (A) 4Pi confocal microscope images with corresponding polygonal mesh structures. (B) Example of cell population representing modeled planar cellular cluster in Geant 4 (perspective view) where all cells are identical. Nucleus, G, and Cy are represented in blue/purple, green, and red, respectively. Cell population models reproduce confluence level of 50% ± 5%, estimated from radiobiologic observations. Geometric characteristics of the 3 cells are reported in Table 1.

TABLE 1
Geometric Characteristics of the 3 Cell Morphologies

Parameter	Volume (μm^3)		
	Cell 1	Cell 2	Cell 3
Cy	3,465.64	1,876.58	4,228.08
G	68.46	24.34	63.18
Nucleus	811.79	714.71	1,105.84
Size* (μm)			
Cy	Bounding box: $x = 72.24$, $y = 31.78$, $z = 5.99$	Bounding box: $x = 99.21$, $y = 30.86$, $z = 3.52$	Bounding box: $x = 88.70$, $y = 64.28$, $z = 6.29$
Nucleus	Ellipsoid: $a = 12$, $b = 8.5$, $c = 1.9$	Elliptic cylinder: $a = 13$, $b = 7$, $c = 1.25$	Elliptic cylinder: $a = 8$, $b = 11$, $c = 2$

*Reported in half-dimensions for nucleus.
CM thickness $= 0.0075$ μm (42,43).

uptake experiments with 2.5 MBq/mL (13), and hence, following the average cell population behavior. Two internalization hypotheses (i.e., G or Cy) were investigated (Fig. 2), and because of the impossibility of distinguishing an intraorganelle variation in the activity distribution, the activity was sampled uniformly in each cell compartment (G, Cy, and CM). The radioactive source was sampled in all cells simultaneously.

The unspecific contribution of the medium to DSB induction was investigated in a separate simulation for 1 nuclear geometry (cell 1), given that the absorbed dose from medium to nucleus is not significantly influenced by the nuclear volume. Here, the source was uniformly distributed in a cylinder with a size corresponding to the maximum range of ^{177}Lu-β particles (diameter and height, 1.76 mm).

The Livermore low-energy physics models were adopted in Geant4 to track electrons down to an energy of 100 eV, and the default production threshold of secondary electrons was set to 0.2 μm (adapted to cell nuclear volumes), which corresponds to 1.75 keV in liquid water. Atomic deexcitation processes, such as Auger cascades and fluorescence, were included in the simulations. The chemical composition of CM, Cy, G, and the nucleus was the same as water ($\rho = 1$ g/cm^3) (National Institute of Standards and Technology database). The position, direction, energy, compartment of emission, and event identifier, which identifies particles derived from the same primary, were recorded for each particle entering the nucleus of the central cell, assumed as representative for the cell population. The number of particles run per simulation ensured a phase space file larger than 1 million particles.

FIGURE 2. Immunofluorescent staining of U2OS-SSTR$_2$ cells and corresponding simulation hypotheses. (A) From left to right, images report nucleus, G, and SSTR$_2$ stainings for untreated cells (top) and cells incubated with DOTATATE (bottom). Merged image at end highlights colocalization of SSTR$_2$ with G after 1 h of incubation with DOTATATE. Scale bar $= 5$ μm. (B) Example of internalized source simulation for cell morphology 2. Nucleus, G, and Cy are reported in green, light blue, and light gray, respectively. Electron tracks are drawn in red, with yellow energy deposition points, which become blue when traversing nucleus.

DNA Damage Simulation

DSB yield calculations were performed with a computational chain (23) using the Geant4-DNA (24–27) extension of the Geant4 toolkit (version 10.1). In this case, all electron interactions are simulated in a discrete manner (i.e., step-by step) down to the electron thermalization, making possible the track structure simulation required at the nanometer scale; as such, they simulate explicitly all interactions and do not use any production cut. The simulation chain includes not only these physical interactions but also the physicochemical and chemical stages within a representative cell nucleus with DNA structure (Supplemental Fig. 1). Therefore, simulations were performed to compute DNA strand breaks (i.e., direct damage of the DNA backbone and indirect damage of the DNA backbone-sugar leading to strand breaks). DSBs were scored from the simulated strand breaks as defined previously (13), that is, at least 2 strand breaks located
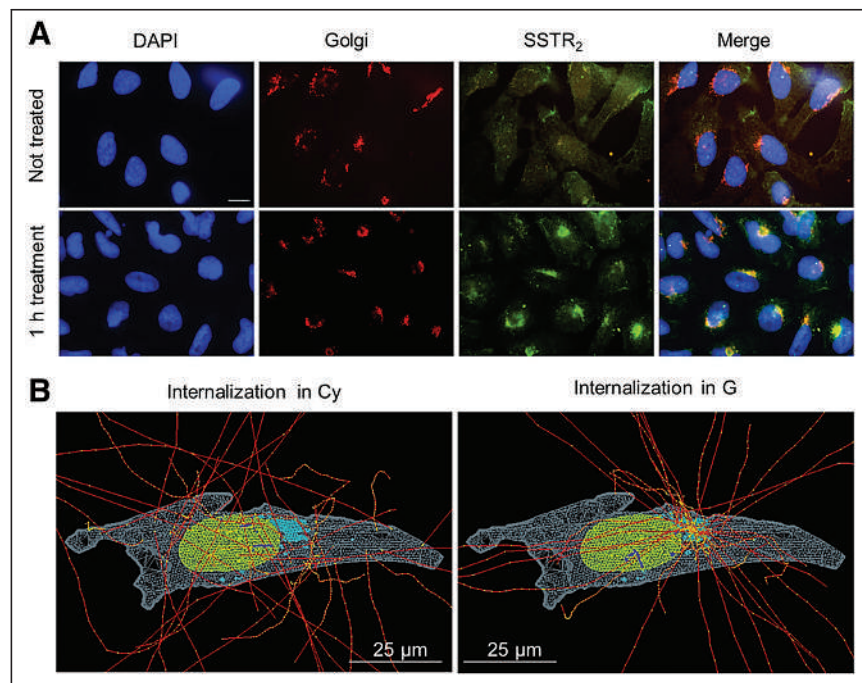
in opposite strands and separated by less than 10 base pairs. The genomic content of cell nuclei composed of chromatin fibers in the G0/G1 phase of the cell cycle was generated with the DNAFabric software (*28,29*). The simulation chain coupled to these geometries allowed calculation of DSBs per source particle (SP) reaching the nucleus, as recorded in the phase space file. Source particles characterized by the same event identifier, whose tracks are related to the same primary, were simulated together until a relative SD of 5% on the average DSBs per SP was reached. The DSB yields are reported in terms of DSBs per SP and per gigabase pair (Gbp) ($N_{DSBs/(SP\ Gbp)}$), and for the calculations of total number of DSBs, all nuclei are assumed to have 6 Gbp ($N_{DSBs/SP}$) (where N [within the DSB formulas] or n [when neither uppercase nor lowercase letter is subscripted] is *number* and where N [when subscripted and following the arrow] indicates *nucleus*).

DSB Calculations and Measurement

The output of the DSB simulations ($N_{DSBs/SP}$) is converted to the number of DSBs corresponding to an added activity of 2.5 MBq/mL, as follows:

$$N_{DSBs} = \left((n_M\ p_{M\rightarrow N} + n_C\ p_{C\rightarrow N}) \times N_{DSBs/SP} \right)_{\beta}$$

$$+ 0.15 \left((n_M\ p_{M\rightarrow N} + n_C\ p_{C\rightarrow N}) \times N_{DSBs/SP} \right)_{IC\text{-electrons}},$$

where n_M and n_C are the number of decays cumulated in a time interval within the medium and the cells (membrane-bound and internalized), respectively; and $p_{M\rightarrow N}$ and $p_{C\rightarrow N}$ are the probabilities that emissions from medium or cells will reach the nucleus of the central cell. The factors related to the cell contribution ($n_C\ p_{C\rightarrow N}$) comprise either G or Cy irradiation. The total N_{DSBs} are then calculated accounting for the contribution of β and IC electrons, weighting on the corresponding probabilities of emission from [177]Lu (i.e., 1 and 0.15 per decay, respectively).

The simulated results are compared with the experimental number of DSBs per cell measured by p53-binding protein 1 (53BP1) foci formation as previously reported (*18*). Briefly, Z-stack imaging was performed using a TCS SP5 confocal microscope (Leica), and foci were counted from at least 50 cells of 2 independent experiments using Image J software (*30*) (settings: median blur, 1.0; maximum projection and find maxima; noise tolerance, 75 for cells and 100 for slices). The untreated average DSB level was subtracted from the measured data.

Detailed Dosimetric Characterization of the Nucleus Irradiation

Source particles entering the nucleus of the central cell for each phase space file were compared in terms of energy and position/direction of entrance in the nucleus.

Furthermore, separate simulations scoring the specific energy within the nucleus were performed for each phase space file in order to justify the possible difference in DSB yields. Indeed, the determination of the energy distribution (and hence the macroscopic linear energy transfer) of electrons entering the nucleus alone is not sufficient to characterize the relationship of the electron tracks to biologic effectiveness. For this purpose, Geant4-DNA models and processes (physics list option 2) were used to enable track-structure (i.e., step-by-step) simulations of electrons in liquid water down to the millielectronvolt energy range. The energy deposited event by event within the nucleus was used to score the specific energy distribution.

Statistical Analysis

The unpaired t test (2 group samples) and 1-way ANOVA (more than 3 group samples) were used to assess the significant difference ($P < 0.05$) between sets of data (DSB yields, probabilities to reach the nucleus, number of SPs traversing the nucleus) within the shape modeling and source localization comparison. A 2-way ANOVA was performed as well, to learn how cellular shapes and source localizations, in combination, affect these sets of data.

RESULTS

Cellular Shape and Internalization Compartment Influence Level of Nucleus Irradiation

The probability of reaching the nucleus from the cell ($p_{C\rightarrow N}$) is 3–4 times higher than from the medium ($p_{M\rightarrow N}$) because of geometric factors. Moreover, $p_{C\rightarrow N}$ significantly depends on the proximity and distribution of the cell compartment with respect to the nucleus, as shown in Figure 3. The more the radioactive cell compartment closely surrounds the nucleus, the more $p_{C\rightarrow N}$ increases, as for G in cell 3.

To include the contribution of the medium in the previous comparison, Figure 3B reports the number of ^{177}Lu disintegrations reaching the nucleus per particle type and cell corresponding to 2.5 MBq/mL of added activity. Once again, cell morphology and source location have a strong combined effect on the number of tracks reaching, and hence potentially damaging, the nucleus and its genetic content.

DSB Induction Is Significantly Different When [177]Lu Is Located Inside Cell or in Medium

The DSB yields normalized to the amount of genetic material (Gbp) and SPs reaching the nucleus ($N_{DSBs/(SP\ Gbp)}$) differed significantly depending on the irradiation geometry (i.e., source and target shape and size in relation to particle track). The DSBs induced by the β particles in the medium are significantly lower than the ones induced by the 3 cell sources. Furthermore, even though the difference among the 3 cell morphologies is not significant, the localization (i.e., G or Cy) and the specific shape of the radioactive cell compartment cause a spread in the biologic damage, as shown in Figure 4A.

The variation in DSB yields among the analyzed cells is caused by the position and direction of particles entering the nucleus, which significantly depend on the cellular morphology. These characteristics affect the hit probability, which is the probability of having an energy deposition event potentially damage the DNA structure. Specifically, the broader angular distribution of the
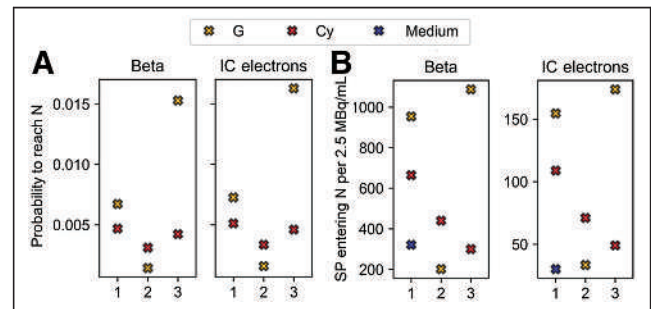
FIGURE 3. Comparison between probabilities (A) and number (B) of SPs entering nucleus for 3 cell models, as indicated by *x*-axis, and the 3 source localizations (Cy, G [including contribution of CM], and medium when comparable to cell sources), including planar cross-irradiation. Number of particles entering nucleus refers to 2.5 MBq/mL of added activity to which experimental data correspond. Medium contribution is assumed to be same for the 3 morphologies on basis of simulations for cell 1. Each graph is subdivided into 2 windows corresponding to the 2 emission types (β and IC), as indicated by titles. N = nucleus.
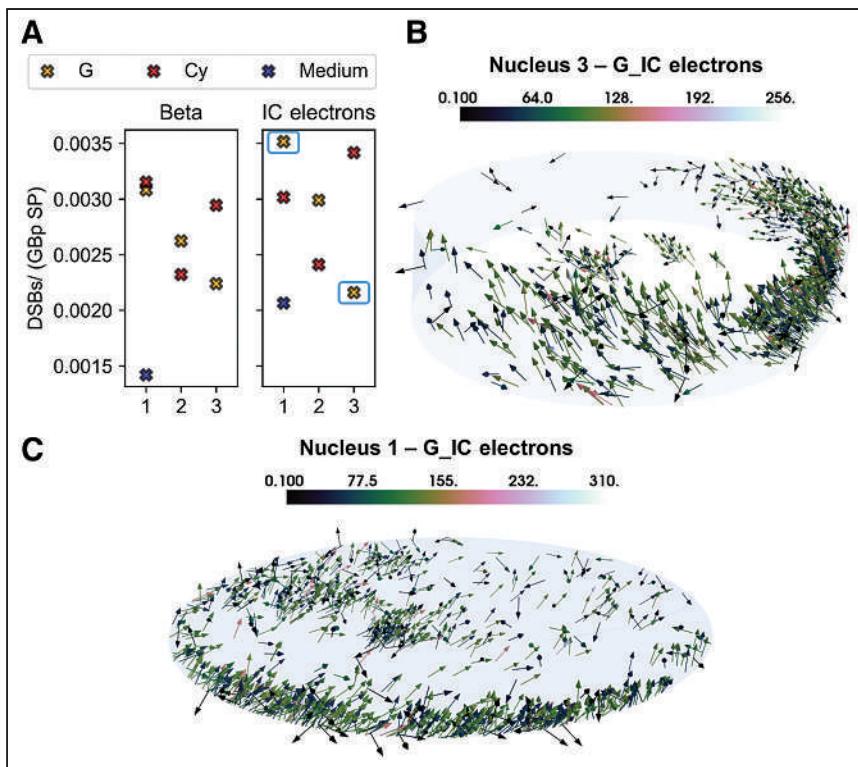
FIGURE 4. Simulation results and graphical explanation. (A) DSB-yield (DSBs/Gbp SP) comparison for the 3 cell morphologies (as indicated by x-axis), the 3 source localizations (Cy, G [including contribution of CM], and medium), and the 2 emission types. Medium contribution is assumed to be same for the 3 morphologies on basis of simulations for cell 1. (B) Total nucleus irradiation (i.e., self- and cross-irradiation) characterizing nucleus 3 when IC electrons are emitted from G. (C) Total nucleus irradiation (i.e., self- and cross-irradiation) characterizing nucleus 1 when IC electrons are emitted from G. Color bars indicate energy (keV) at entrance of nucleus.

Specific Energy in Nucleus Explains DSB Yield Difference Between Cell and Medium Source

The source localization does not significantly affect the energy distributions of particles entering the nucleus (Figs. 5A and 5B), explaining why the DSB range/Gy Gbp is similar for all cell morphologies. Indeed, the energy distributions of electrons coming from medium or cells, and hence their slowing down, are similar as well, between the β electrons and the IC electrons. However, the nucleus geometry affects the electron pathlength, causing significant differences in the energy deposition patterns within the nucleus itself (Fig. 6).

Specifically, the microdosimetric energy spectrum of particles coming from the medium is significantly shifted to lower energies with respect to all the sources (Fig. 6; Table 2), reflecting the DSB yield comparison. The difference among cell morphologies is also the result of these spectral differences, as the difference is evident when comparing the corresponding specific energy in Table 2 with the DSB yields in Figure 4.

Simulated DSBs Match Experimental Data

The total number of simulated DSBs per cell for a 2.5 MBq/mL dose of ^{177}Lu-DOTATATE ranges between 7 and 24 (Figs. 7A and 7B), compared with a range of 2–30 experimentally determined (Fig. 7C) (18). The mean DSBs per cell correspond to 14 and 13 for simulations and experiments, respectively.

As expected, the DSBs are induced mostly by β particles, whereas the IC-electron component results are significant only for specific cellular morphologies (Fig. 7A). The medium contribution is not assumed to vary depending on the nuclear geometry; hence, its relative impact depends strictly on the cell source contribution to each morphology (Fig. 7B).

Linear correlations ($R^2 = 1$) with slopes of 0.014 and 0.017 DSBs per cell mGy^{-1} are found between the average specific energy and the simulated number of DSBs, when assuming the internalized source in G or Cy, respectively (Fig. 7D). Absorbed dose values corresponding to 2.5 MBq/mL are reported in Supplemental Table 2, and the absence of correlation when using average absorbed dose calculations is highlighted in Supplemental Figure 2.

DISCUSSION

Modeling of DNA damage after TRT exposure can lead, through comparison with experimental data, to a better understanding of the underlying mechanisms of this treatment modality. Ultimately, it will allow evaluation of treatment efficacy, granting the flexibility of a simulation environment and, as such, new opportunities for the evaluation of novel radiopharmaceuticals. The first step toward this aim was made here, in which we accounted for detailed cellular

scattered β particles entering the nucleus from the medium increases the electrons that traverse it with a lower efficiency (greater polar angle). The same applies to the comparison between cell morphologies and cell compartments (Figs. 4B and 4C); in this case, the difference is predominantly less noticeable, given the overall similar source-to-nucleus proximity. Indeed, the proportion of events damaging the internalized source ranges from 0.91 to 0.93 for nucleus 1, from 0.45 to 0.62 for nucleus 2, and from 0.46 to 0.67 for nucleus 3, depending on internalization hypothesis and emission type. If the source is in the medium, the same range is reduced to 0.39–0.49. To understand these differences, we analyzed the distribution of energy deposition events in the nucleus by means of microdosimetric simulations.

When the DSB yields are divided by the mean absorbed dose delivered per particle source in each nucleus, the number of DSBs/(Gy Gbp SP) ranges between 2.3 and 3.0, depending on internalization hypothesis and particle type.

In terms of DSB complexity, that is, the number of close strand breaks that can be attributed to the same DSB, there is no significant difference among cell morphologies and type of particle emitted (β vs. IC electrons). The proportion of simple DSBs (i.e., DSBs made of 2 single-strand breaks) ranges between 79.7% and 92.2% with respect to the complex DSBs (i.e., DSBs made of 3 or more single-strand breaks, with at least 1 of them located in a strand opposite from the others), as expected for radiation with low linear-energy transfer.
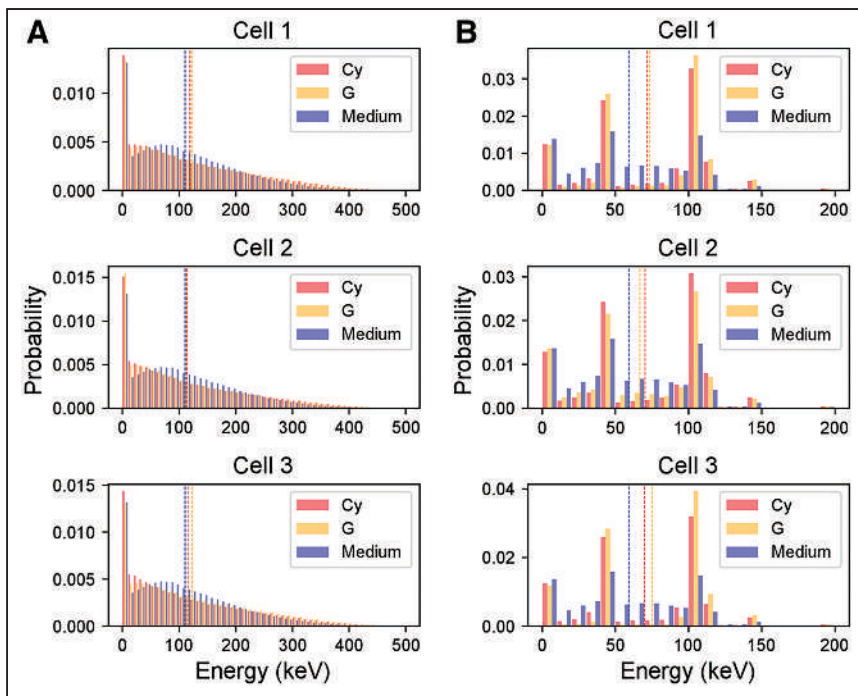
FIGURE 5. Energy spectra of electrons entering nucleus of the 3 cell morphologies. (A) Distributions corresponding to β particles. (B) Distributions corresponding to IC electrons. Each color corresponds to the 3 source localizations (Cy, G [including contribution of CM], and medium). Dotted lines indicate mean value of energy spectra. Spectrum of medium is assumed to be same as cell 1 for the 3 morphologies and is replicated in each graph for comparison with cell sources. Energy bin is 10 keV.

morphologies and activity distributions to replicate a typical (^{177}Lu-DOTATATE) planar in vitro TRT environment and tested the feasibility of performing DSB simulations through a simulation chain created for external radiation exposure.

The importance of an improved cellular morphology modeling has already been highlighted for macrodosimetric calculations (i.e., S values) involving a planar colony of cells exposed to

FIGURE 6. Probability density functions of energy deposited per particle in nucleus of the 3 cell morphologies. Each distribution corresponds to the 3 source localizations (Cy, G [including contribution of CM], and medium) and the 2 emission types (β and IC). Dotted lines indicate mean value of microscopic energy distributions, from which mean specific energy ($\bar{z}$) is evaluated (Table 2). Spectrum of medium is assumed to be same as cell 1 for the 3 morphologies and is replicated in each graph for comparison with cell sources.

^{177}Lu-DOTATATE (13); however, its impact on DSB yields had never, to our knowledge, been assessed before. Noticeably, detailed cellular morphology modeling and activity localization sampling were indispensable in correctly estimating the number of induced DSBs, since they significantly influence the probability that electrons will reach the nucleus and the distribution of track lengths within the nucleus itself. The volumetric and shape characterization of the nucleus is fundamental to correctly evaluate the energy deposition pattern as well.

Interestingly, the energy distributions of electrons entering the nucleus from the medium are not shifted to lower energies with respect to the cell source. For this reason, the difference in DSB yields induced by unbound (i.e., medium) and bound (i.e., cell) activity is not caused by different energy spectra of particles entering the nucleus. Indeed, in our simulations, the portion of electrons with energy below 10 keV, that is, the electrons with the highest relative biological effectiveness for DSB induction, were found to be very similar (within 1%) in all phase space files, indicating a possible similarity in the relative biological effectiveness for DSB induction (31). Instead, the energy deposition pattern within the nucleus reflected the difference in DSB yields, underlying the importance of both microdosimetric analysis and activity characterization on a cellular scale to predict biologic effects for radiation of low linear-energy transfer as well. Microdosimetry, in fact, accounts for the characteristics of the electron tracks (i.e., finite range and change of linear-energy transfer along the track, energy-loss straggling, δ-ray escape, and angular scattering) in order to correctly evaluate the concentration of energy transferred to the nucleus and hence the biologic effectiveness of the SPs.

Altogether, the need for detailed cellular morphology modeling, accurate sampling, and a microdosimetric framework able to explain biologic effects, as highlighted in this work, is in striking contrast to the current dosimetric approach of implementing simplifying cell models (i.e., concentric spheres) and a semianalytic radiation transport model adopting the continuous-slowing-down approximation (32). Indeed, not accounting for the typical complexity and heterogeneity at the cellular or multicellular levels and relying on averaged large-scale dosimetry might be the reason for missing dose–response correlations that could be translated on a clinical scale.

To our knowledge, this was the first study simulating DSB formation after ^{177}Lu-DOTATATE exposure while including all stages of damage induction; hence, we
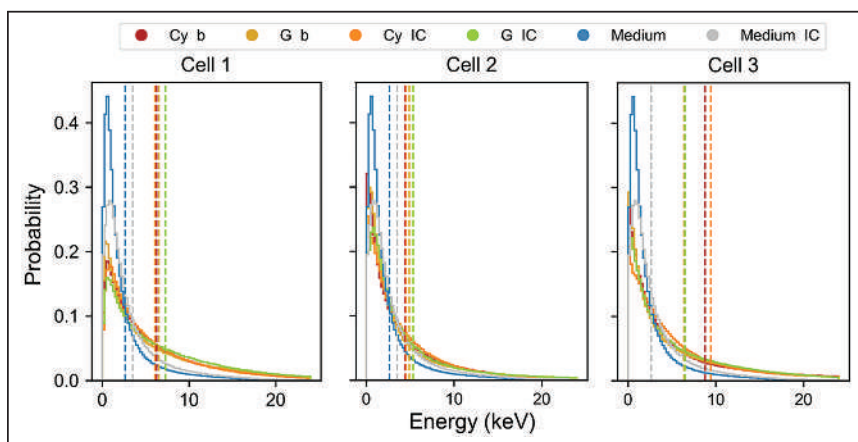
TABLE 2
Mean Specific Energy per Particle Entering Nucleus of the 3 Cell Morphologies

Parameter	$\bar{z}$ (Gy)		
	Cell 1	Cell 2	Cell 3
Cy β	1.24	0.99	1.27
G β	1.29	1.10	0.92
Cy IC	1.20	1.02	1.36
G IC	1.44	1.20	0.94
Medium β	0.52		
Medium IC	0.69		

Medium values (β and IC electrons) are calculated for nucleus 1 and assumed same for the 3 morphologies.

compared our results with photons (producing similar secondary electron spectra) and electron beam irradiation data available in the literature. The number of DSB yields in this work ($2.3–3.0$ DSBs/Gbp^{-1} Gy^{-1} SP^{-1}) was comparable to that in a study by Tang et al. (33), in which the simulated results ranged between 3.5 and 2.8 DSBs/(Gbp Gy) for 220-kVp and 4-MV x-ray irradiations, respectively. Similarly, Nikjoo et al. (34) estimated a DSB yield of 3.32 DSBs/(Gy Gbp) for 100-keV electrons, assuming 6 Gbp of genetic material and $3.9 \ 10^{-12}$ Da/cell. In both cases, the portion of complex DSBs was similar to this study. In this work, the DSB complexity was independent from the source localization. Hence, repair mechanisms acting on DSBs caused by medium or cell source will most likely be the same.

The parameters implemented in the simulations to score DNA damage induction can strongly influence the final DSB yields. The good agreement reached with the aforementioned studies could be explained by the similar parameters set to score direct or indirect strand breaks. Indeed, increasing the chemical simulation end-time from 2.5 ns (as set in this work) to 10 ns would increase the number of DSBs by a factor of approximately 1.3 (33), and either decreasing the threshold for direct single-strand break induction from 17.5 eV to lower values or introducing a linear probability of between 5 and 37.5 eV would significantly affect the total number of DSBs (34,35). We did not study how these parameter variations would affect our calculations, given that our results were already comparable to the experimental data (18) and that the computational time required for these simulations is considerably long.

Nevertheless, our simulated results represent a lower bound on the average number of DSBs and their complexity. Our modeling approach, in fact, neglects the contribution of photons and Auger electrons emitted by ^{177}Lu, the resonant formation of strand breaks by very low energetic electrons (<20 eV) (36–38), the induction of non-DSB oxidative clustered DNA lesions, and the consequence of sugar and base residue repair, which can increase the final strand break yield. In addition, cells exposed to ^{177}Lu-DOTATATE are not synchronized in a specific cell-phase, as we assumed for the purpose of simplification, but are characterized by a distribution of radiosensitivity, associated with their cell phase, that should be accounted for when simulating different nuclei. Lastly, we did not include the possibility of DSB repair, given that repair mechanisms involved in TRT are not yet fully understood. Specifically, during TRT, since DNA damage induction persists over time, induction and repair occur simultaneously and hence repair mechanisms might differ significantly from EBRT. However, our approach might be justified by the very low DSB reduction pace (0.96% in 4 h) or, better, the substantial equilibrium between induction and DSB repair, indicated by the average (among the cell population) experimental decrease in the number of 53BP1 foci over 3 d (18). However, sublethal damage repair differs among the cell population
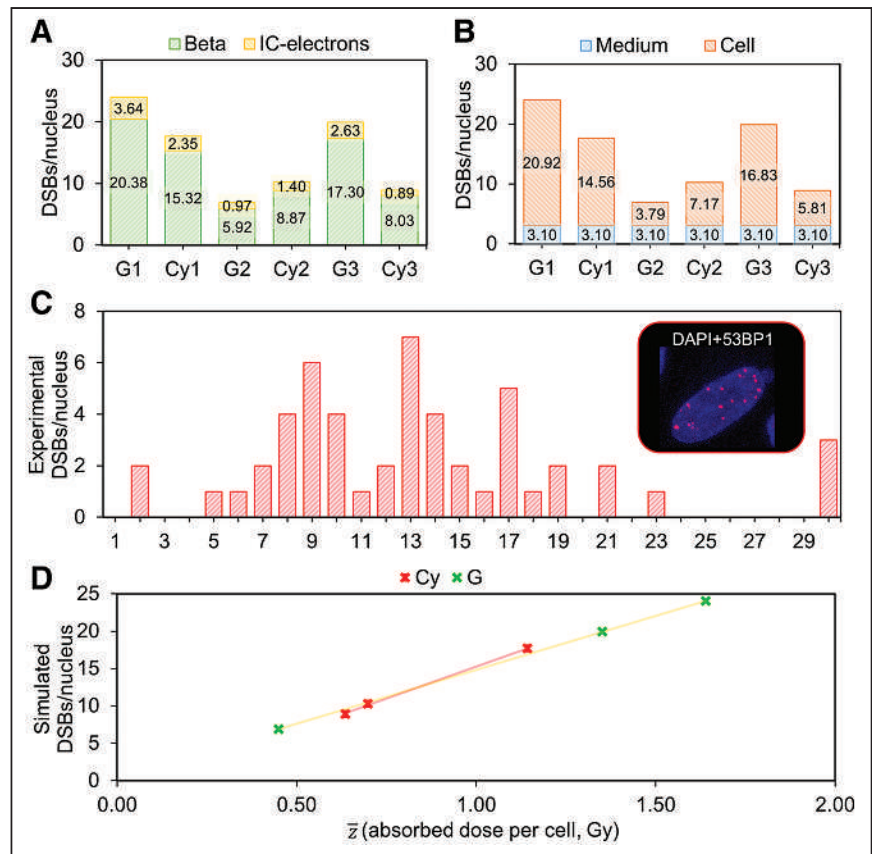
FIGURE 7. DSB simulations, comparison with experimental data, and correlation with absorbed dose to nucleus. (A) Simulated number of DSBs per nucleus corresponding to the 3 cell morphologies and internalization hypotheses (Cy vs. G, including CM), indicating contribution of each particle type (β and IC electrons). (B) Simulated DSBs per nucleus corresponding to the 3 cell morphologies and internalization hypotheses (Cy vs. G, including CM), indicating contribution of medium or cell source (internalized and membrane-bound). (C) Frequency histogram of experimental number of DSBs per nucleus induced by 4 h of administration of 2.5 MBq/mL activity of ^{177}Lu-DOTATATE, measured by 53BP1. (D) Linear correlations between absorbed dose to nuclei and simulated number of DSBs when internalized source is located in Cy and in G. DAPI = 4′,6-diamidino-2-phenylindole.

depending on cell phase and dose rate variation too. Moreover, the DSBs are measured by means of 53BP1 foci—that is, repair foci—and hence might be slightly underestimated as well. Indeed, only breaks in which repair is induced are accounted for with this measurement, and the fluorescently labeled compound might not successfully bind to the 53BP1.

At present, only Eberlein et al. proved the existence of a correlation (with slope 0.0127 DSBs mGy^{-1} $cell^{-1}$) between the absorbed dose to blood of patients undergoing ^{177}Lu-DOTATATE treatment and the induction of DBSs, measured by the colocalized biomarkers γH2AX and 53BP1 (39). Remarkably, we found a similar number of DSBs per cell and per milligray (0.014 vs. 0.017 DSBs mGy^{-1} $cell^{-1}$), which serves as further validation of our computational approach.

Further improvements in the computational chain pertain to the inclusion of base damage affecting the DSB complexity (40), different oxygen levels in the nuclear medium, different cellular shapes in a single-exposure scenario, intraorganelle variation in the internalized activity fraction, realistic cellular media, and a more representative distribution of the genetic material, according to the cell cycle and including realistic proportions of euchromatin and heterochromatin. Some of these improvements are currently being developed by the Geant4-DNA community and will be included in future simulations. More studies investigating the temporal variation in dose rates over time against biologic phenomena such as DNA repair capacity and cell cycle progression over the cell population would help to further improve biophysical modeling as well.

To develop a comprehensive model, not limited to a planar in vitro application but representative of an in vivo tumor scenario, a 3-dimensional aggregation of cells characterized by a variable $SSTR_2$ expression should be modeled. For this purpose, the variability of $SSTR_2$ expression among cellular population samples should be analyzed by means of fluorescence-activated cell sorting analysis or flow cytometry, so that the intensity of the receptor staining can be normalized and used to sample a heterogeneous receptor expression among the cell population. As such, various probability distributions of the $SSTR_2$ expression can be generated to test the influence on the absorbed dose estimation. Moreover, the effect of ^{177}Lu-DOTATATE on peritumoral vessels will influence tumor hemodynamics and, to a lesser extent, its cross-dose irradiation, which could be explicitly simulated by changing the proportion of activity bound to the vessels, according to tumor differentiation and aggressiveness. Somatostatin is known to cause vasoconstriction resulting in regional hypoxia or necrosis (41). The oxygen effect should be considered by modifying the chemistry processes (e.g., by adding the specific chemical processes that lead to the creation and the chemical reactions of radicals involving oxygen) or by simply correcting with the oxygen enhancement ratio for DSB induction. Finally, even though direct radiation effects will form the major contribution to cellular responses, bystander effects and abscopal effects should be studied in tissues with low-receptor expression. Indeed, bystander signaling may be present in receptor-negative cells within a matrix of receptor-positive cells but will be obscured by many other factors influencing cell survival. To model such effects, initial studies should be performed focused on selecting relevant radiation-perturbed molecular pathways or intracellular targets, which, when hit by radiation, initiate the emission of bystander signals (e.g., mitochondria, nuclear membrane, and ribosomes), in order to inform a more systemic description of the biologic response to radiation after TRT exposure.

CONCLUSION

In this work, we developed a simulation framework to evaluate the number of DNA DSBs occurring during in vitro TRT, which, through further modifications and comparison with experimental data, can lead to a better understanding of the underlying biologic mechanisms of this therapy. Adopting this methodology, we found good agreement with experimental data and a clear correlation between the absorbed dose and the average number of DSBs per cell after ^{177}Lu-DOTATATE exposure was established. Furthermore, this work highlights the importance of overcoming classic macrodosimetric approaches to be able to investigate and find correlations with the biologic response after TRT exposure, as is instrumental for personalized dosimetry.

DISCLOSURE

No potential conflict of interest relevant to this article was reported.

KEY POINTS

QUESTION: Can a simulation framework be established to evaluate the number of DNA DSBs induced by in vitro TRT?

PERTINENT FINDINGS: We found a linear correlation between the mean specific energy to the nucleus and the number of DSBs per cell: 0.014 DSBs per cell mGy^{-1} for internalization in G and 0.017 DSBs per cell mGy^{-1} for internalization in Cy. Furthermore, we found a spread in the induction of DSBs caused by the specific shape of the radioactive cell compartment and a significant difference in the DSB yields induced by bound and unbound activity fractions.

IMPLICATIONS FOR PATIENT CARE: Ultimately, this simulation tool will elucidate the underlying biological mechanisms of TRT and interpret DNA-damage biomarkers. Knowledge of the physical, chemical, and biologic actions by TRT will lead the way to its optimization and a better response prediction in patients.

REFERENCES

1. De Ruysscher D, Niedermann G, Burnet NG, Siva S, Lee AWM, Hegi-Johnson F. Radiotherapy toxicity. *Nat Rev Dis Primers.* 2019;5:13.

2. de Jong M, Breeman WAP, Bernard BF, et al. [^{177}Lu-DOTA^0,Tyr^3]octreotate for somatostatin receptor-targeted radionuclide therapy. *Int J Cancer.* 2001;92:628–633.

3. Pouget JP, Lozza C, Deshayes E, Boudousq V, Navarro-Teulon I. Introduction to radiobiology of targeted radionuclide therapy. *Front Med (Lausanne).* 2015;2:12.

4. Graf F, Fahrer J, Maus S, et al. DNA double strand breaks as predictor of efficacy of the alpha-particle emitter Ac-225 and the electron emitter Lu-177 for somatostatin receptor targeted radiotherapy. *PLoS One.* 2014;9:e88239.

5. McMahon SJ. The linear quadratic model: usage, interpretation and challenges. *Phys Med Biol.* 2018;64:01TR01.

6. Thierens HM, Monsieurs MA, Brans B, Van Driessche T, Christiaens I, Dierckx RA. Dosimetry from organ to cellular dimensions. *Comput Med Imaging Graph.* 2001;25:187–193.

7. Charlton DE, Humm JL. A method of calculating initial DNA strand breakage following the decay of incorporated ^{125}I. *Int J Radiat Biol Relat Stud Phys Chem Med.* 1988;53:353–365.

8. Pomplun E. A new DNA target model for track structure calculations and its first application to I-125 auger electrons. *Int J Radiat Biol.* 1991;59:625–642.

9. Terrissol M, Peudon A, Kümmerle E, Pomplun E. On the biological efficiency of I-123 and I-125 decay on the molecular level. *Int J Radiat Biol.* 2008;84:1063–1068.

10. Piroozfar B, Raisali G, Alirezapour B, Mirzaii M. The effect of ^{111}In radionuclide distance and auger electron energy on direct induction of DNA double-

strand breaks: a Monte Carlo study using Geant4 toolkit. *Int J Radiat Biol.* 2018;94:385–393.

11. Semenenko VA, Stewart RD. A fast Monte Carlo algorithm to simulate the spectrum of DNA damages formed by ionizing radiation. *Radiat Res.* 2004;161: 451–457.

12. Hsiao YY, Hung TH, Tu SJ, Tung CJ. Fast Monte Carlo simulation of DNA damage induction by Auger-electron emission. *Int J Radiat Biol.* 2014;90:392–400.

13. Tamborino G, De Saint-Hubert M, Struelens L, et al. Cellular dosimetry of [^{177}Lu]Lu-DOTA-[Tyr^3]octreotate radionuclide therapy: the impact of modeling assumptions on the correlation with in vitro cytotoxicity. *EJNMMI Phys.* 2020;7:8.

14. Carrasco-Hernández J, Ramos-Méndez J, Faddegon B, et al. Monte Carlo track-structure for the radionuclide copper-64: characterization of S-values, nanodosimetry and quantification of direct damage to DNA. *Phys Med Biol.* 2020;65:155005.

15. Strosberg J, Wolin E, Chasen B, et al. Health-related quality of life in patients with progressive midgut neuroendocrine tumors treated with ^{177}Lu-DOTATATE in the phase III NETTER-1 trial. *J Clin Oncol.* 2018;36:2578–2584.

16. Strosberg J, El-Haddad G, Wolin E, et al. Phase 3 trial of ^{177}Lu-DOTATATE for midgut neuroendocrine tumors. *N Engl J Med.* 2017;376:125–135.

17. Hennrich U, Kopka K. Lutathera®: the first FDA- and EMA-approved radiopharmaceutical for peptide receptor radionuclide therapy. *Pharmaceuticals (Basel).* 2019;12:114.

18. Nonnekens J, van Kranenburg M, Beerens CEMT, et al. Potentiation of peptide receptor radionuclide therapy by the PARP inhibitor olaparib. *Theranostics.* 2016; 6:1821–1832.

19. Agostinelli S, Allison J, Amako K, et al. GEANT4: a simulation toolkit. *Nucl Instruments Methods Phys Res Sect A Accel Spectrometers Detect Assoc Equip.* 2003;506:250–303.

20. Allison J, Amako K, Apostolakis J, et al. Recent developments in GEANT4. *Nucl Instruments Methods Phys Res Sect A Accel Spectrometers Detect Assoc Equip.* 2016;835:186–225.

21. Allison J, Amako K, Apostolakis J, et al. Geant4 developments and applications. *IEEE Trans Nucl Sci.* 2006;53:270–278.

22. Goddu SM, Howell RW, Bouchet LG, Bolch WE, Rao DSMC. MIRD Cellular S Values. *Society of Nuclear Medicine and Molecular Imaging*; 1997.

23. Meylan S, Incerti S, Karamitros M, et al. Simulation of early DNA damage after the irradiation of a fibroblast cell nucleus using Geant4-DNA. *Sci Rep.* 2017;7: 11923.

24. Incerti S, Baldacchino G, Bernal M, et al. The Geant4-DNA project. *Int J Model Simulation Sci Comput.* 2010;1:157–178.

25. Incerti S, Ivanchenko A, Karamitros M, et al. Comparison of GEANT4 very low energy cross section models with experimental data in water. *Med Phys.* 2010;37: 4692–4708.

26. Bernal MA, Bordage MC, Brown JMC, et al. Track structure modeling in liquid water: a review of the Geant4-DNA very low energy extension of the Geant4 Monte Carlo simulation toolkit. *Phys Med.* 2015;31:861–874.

27. Incerti S, Kyriakou I, Bernal MA, et al. Geant4-DNA example applications for track structure simulations in liquid water: a report from the Geant4-DNA project. *Med Phys.* 2018;45:e722–e739.

28. Meylan S, Vimont U, Incerti S, Clairand I, Villagrasa C. Geant4-DNA simulations using complex DNA geometries generated by the DnaFabric tool. *Comput Phys Commun.* 2016;204:159–169.

29. Tang N, Bueno M, Meylan S, et al. Influence of chromatin compaction on simulated early radiation-induced DNA damage using Geant4-DNA. *Med Phys.* 2019; 46:1501–1511.

30. Schindelin J, Arganda-Carreras I, Frise E, et al. Fiji: an open-source platform for biological-image analysis. *Nat Methods.* 2012;9:676–682.

31. Nikjoo H, Lindborg L. RBE of low energy electrons and photons. *Phys Med Biol.* 2010;55:R65–R109.

32. Vaziri B, Wu H, Dhawan AP, Du P, Howell RW. MIRD pamphlet no. 25: MIRD-cell V2.0 software tool for dosimetric analysis of biologic response of multicellular populations. *J Nucl Med.* 2014;55:1557–1564.

33. Tang N, Bueno M, Meylan S, et al. Assessment of radio-induced damage in endothelial cells irradiated with 40 kVp, 220 kVp, and 4 MV x-rays by means of micro and nanodosimetric calculations. *Int J Mol Sci.* 2019;20:6204.

34. Nikjoo H, O'Neill P, Wilson WE, Goodhead DT. Computational approach for determining the spectrum of DNA damage induced by ionizing radiation. *Radiat Res.* 2001;156:577–583.

35. Villagrasa C, Meylan S, Gonon G, et al. Geant4-DNA simulation of DNA damage caused by direct and indirect radiation effects and comparison with biological data. *EPJ Web Conf.* 2017;153:04019.

36. Boudaïffa B, Cloutier P, Hunting D, Huels MA, Sanche L. Resonant formation of DNA strand breaks by low-energy (3 to 20 eV) electrons. *Science.* 2000;287: 1658–1660.

37. Simons J. How do low-energy (0.1-2 eV) electrons cause DNA-strand breaks? *Acc Chem Res.* 2006;39:772–779.

38. Martin F, Burrow PD, Cai Z, Cloutier P, Hunting D, Sanche L. DNA strand breaks induced by 0-4 eV electrons: the role of shape resonances. *Phys Rev Lett.* 2004;93: 068101.

39. Eberlein U, Peper M, Fernández M, Lassmann M, Scherthan H. Calibration of the γ-H2AX DNA double strand break focus assay for internal radiation exposure of blood lymphocytes. *PLoS One.* 2015;10:e0123174.

40. Nikjoo H, O'Neill P, Terrisol M, Goodhead DT. Quantitative modelling of DNA damage using Monte Carlo track structure method. *Radiat Environ Biophys.* 1999; 38:31–38.

41. Reubi JC, Schaer J, Laissue JA, Waser B. Somatostatin receptors and their subtypes in human tumors and in peritumoral vessels. *Metabolism.* 1996;45(suppl 1):39-41.

42. Reed R, Houston TW, Todd PM. Structure and function of the sarcolemma of skeletal muscle. *Nature.* 1966;211:534–536.

43. Mitra K, Ubarretxena-Belandia I, Taguchi T, Warren G, Engelman DM. Modulation of the bilayer thickness of exocytic pathway membranes by membrane proteins rather than cholesterol. *Proc Natl Acad Sci USA.* 2004;101:4083–4088.

Comparison of Exogenous Ketone Administration Versus Dietary Carbohydrate Restriction on Myocardial Glucose Suppression: A Crossover Clinical Trial

Senthil Selvaraj[1], Kenneth B. Margulies[1], Supritha Dugyala[2], Erin Schubert[2], Ann Tierney[3], Zoltan Arany[1], Daniel A. Pryma[2], Svati H. Shah[4], J. Eduardo Rame, Daniel P. Kelly[5], and Paco E. Bravo[1,2]

[1]Division of Cardiology, Department of Medicine, Perelman School of Medicine of the University of Pennsylvania, Philadelphia, Pennsylvania; [2]Division of Nuclear Medicine, Department of Radiology, Perelman School of Medicine of the University of Pennsylvania, Philadelphia, Pennsylvania; [3]Department of Biostatistics, Perelman School of Medicine of the University of Pennsylvania, Philadelphia, Pennsylvania; [4]Division of Cardiology, Department of Medicine, Duke Molecular Physiology Institute, Duke University School of Medicine, Durham, North Carolina; and [5]Department of Cardiology, Thomas Jefferson University, Abington, Pennsylvania

The ketogenic diet (KD) is the standard of care to achieve myocardial glucose suppression (MGS) for assessing inflammation using ^{18}F-FDG PET. However, failure to suppress physiologic glucose uptake remains a significant diagnostic barrier. Although extending the duration of KD may be effective, exogenously delivered ketones may provide a convenient, reliable, and same-day alternative. The aims of our study were to determine whether exogenous ketone administration is noninferior to the KD to achieve MGS and whether serum β-hydroxybutyrate (BHB) levels can predict MGS. **Methods:** KEETO-CROSS (Ketogenic Endogenous versus Exogenous Therapies for myoCaRdial glucOse Suppres-Sion) is a crossover, noninferiority trial of the KD (endogenous ketosis) versus ketone ester ([KE] exogenous ketosis) drink. Twenty healthy participants were enrolled into 3 arms: weight-based KE drink, 24-h KD, and 72-h KD ($n = 18$ completed all arms). The primary outcome was achievement of complete MGS on PET (noninferiority margin 5%). The area under receiver-operating-characteristics (AUROC) of endogenous BHB levels (analyzed in a laboratory and by point-of-care device) for predicting MGS was analyzed in 37 scans completed on the KD. **Results:** The mean age was 30 ± 7 y, 50% were women, and 45% were nonwhite. The median achieved BHB levels (mmol/L) were 3.82 (25th–75th percentile, 2.55–4.97) (KE drink), 0.77 (25th–75th percentile, 0.58–1.02) (25th–75th percentile, 24-h KD), and 1.30 (25th–75th percentile, 0.80–2.24) (72-h KD). The primary outcome was achieved in 44% (KE drink), 78% (24-h KD), and 83% (72-h KD) of participants (noninferiority $P = 0.97$ and 0.98 for KE vs. 24-h and 72-h KD). Endogenous BHB levels robustly predicted MGS (AUROC, 0.88; 95% CI 0.71, 1.00). A BHB of 0.58 or more correctly classified 92% of scans. A point-of-care device provided comparable predictive value. **Conclusion:** In healthy volunteers, KE was inferior to KD for achieving MGS. Serum BHB is a highly predictive biomarker for MGS and can be clinically implemented upstream of ^{18}F-FDG PET, with rapid facilitation by point-of-care testing, to reduce false-positive scans.

Key Words: ketogenic diet; ketone ester; FDG; PET; myocardial glucose uptake

Detecting inflammation is clinically relevant for diagnosing several cardiovascular diseases, though it remains challenging to achieve by current techniques. Noninvasive diagnosis of a growing number of inflammatory pathologies, as well as malignant cardiac masses, relies on visualizing glucose uptake by abnormal cells using ^{18}F FDG PET. However, because normal myocardium can also use glucose (1), distinguishing physiologic from pathologic uptake can be particularly problematic and remains the Achilles heel of using ^{18}F-FDG PET for such diagnostic testing (2).

Short-term dietary modification through a low-carbohydrate, high-fat ketogenic diet (KD) to suppress physiologic glucose uptake is the standard of care for evaluating myocardial inflammation using radiolabeled markers of glucose utilization. The KD accomplishes this metabolic switch by reducing insulin-dependent myocardial glucose uptake, while inflammatory cells continue to consume glucose through non–insulin-dependent glucose transporters. However, myocardial ^{18}F-FDG suppression rates remain suboptimal, and retrospective data suggest myocardial glucose suppression (MGS) is achieved in 81%–84% of subjects even after strict, highly supervised dietary restrictions (3,4). Nondiagnostic and false-positive scans lead to misdiagnosis, inappropriate immunotherapy, repeated scans with excess radiation exposure, and unnecessary costs to the patient and health-care system.

One strategy to improve appropriate MGS is to increase the length of dietary modification (5). However, adherence to the KD may not always be feasible, is often challenging, and requires advanced patient preparation. The negative correlation between carbohydrate and ketone use by the heart has been known for years (6), and exogenous ketones significantly reduce myocardial glucose uptake through substrate competition and inhibition of intracellular glucose phosphorylation (7). A ketone ester (KE) compound can rapidly and safely achieve high levels of ketosis and may efficiently and effectively prepare patients for same-day evaluation of myocardial inflammation by ^{18}F-FDG PET (8). However, no studies have directly compared a KE with a KD strategy for achieving MGS. Additionally, given the inverse relationship between ketosis and MGS, ketone biomarkers may logically predict MGS. Despite promising data, neither hypothesis has been evaluated.

Ketogenic Endogenous versus Exogenous Therapies for myo-CaRdial glucOse SuppresSion (KEETO-CROSS) is a crossover, noninferiority trial of an MGS strategy comparing KE with the gold-standard 24-h KD, as well as 72-h KD, in participants free of cardiovascular disease. We sought to determine whether a nutritional

ketosis strategy would provide noninferior diagnostic value compared with short-term KD to achieve MGS on ^{18}F-FDG PET. We secondarily assessed the value of serum ketone levels (β-hydroxybutyrate [BHB]) as an upstream biomarker of MGS on ^{18}F-FDG PET to reduce false-positive and nondiagnostic scans.

MATERIALS AND METHODS

KEETO-CROSS Study Design

We conducted a crossover, open-label, noninferiority trial comparing exogenous ketosis (KE) with endogenous ketosis (KD) (NCT04275453). Participants were randomly assigned to the KE arm (1 visit) or KD arm (including 2 visits occurring at 24 and 72 h) with at least a 1-wk washout period in between arms. Participants aged 18–60 y were enrolled at the University of Pennsylvania between January 2020 and January 2021. To ensure that any myocardial glucose uptake would be physiologic rather than indicative of underlying pathology, we excluded individuals with any reported history of cardiovascular disease (including hypertension, hyperlipidemia, and diabetes mellitus). We also excluded pregnant and breast-feeding women. Recruitment was continued until a total of 18 participants attended all 3 visits (KE, 24-h KD, and 72-h KD) to adequately power the trial. The CONSORT diagram for KEETO-CROSS is depicted in Supplemental Figure 1 (supplemental materials are available at http://jnm.snmjournals.org). The study was approved by an institutional review board and informed consent was obtained.

Patient Preparation Methods

KE Arm. Participants in the KE arm were permitted to eat a regular diet during the day before their study visit and started fasting at least by midnight before ^{18}F-FDG PET (Fig. 1). During the visit, participants received weight-based dosing (714 mg/kg) of (*R*)-3-hydroxybutyl (*R*)-3-hydroxybutyrate (H.V.M.N.), which has been extensively studied for the purposes of achieving ketosis (*8–10*). Briefly, this KE undergoes rapid enzymatic hydrolysis ultimately to form BHB (and other ketone bodies), achieving high BHB levels in less than 1 h with a short compound half-life (0.8–3.1 h). This high dose was selected to engender robust ketosis and substrate competition. Participants were injected with ^{18}F-FDG at 1 h after KE ingestion because the peak ketotic effect of the KE occurs around this time.

KD Arm. During the KD arm, participants presented for 2 visits: one after 24 h of KD and then again after 72 h of KD (Fig. 1). The day before the 24-h KD visit, participants began a low-carbohydrate, high-fat diet intended to achieve less than 20 g of carbohydrate intake per day (supplemental materials) and fasted from at least midnight until ^{18}F-FDG PET scanning the next day. Thereafter, they continued the KD for 2 additional days, fasting again from at least midnight before the 72-h KD visit. A detailed dietary log was maintained by study participants during the dietary arm and reviewed by a nuclear cardiologist before ^{18}F-FDG injection. All participants were deemed to have adequate dietary adherence by dietary log review.

Laboratory Testing and Echocardiography

Details of laboratory testing (for BHB, insulin, glucagon, nonesterified fatty acid [NEFA], and glucose levels) and echocardiography are available in the supplemental materials.

^{18}F-FDG PET Protocol and Study Outcomes

Participants underwent ^{18}F-FDG PET using a PET/CT scanner (Ingenuity TF; Philips). At study visits, ^{18}F-FDG (~185 MBq [~5.0 mCi]) was injected, and PET images of the chest were acquired 1 h later. Low-dose CT images were also acquired for attenuation-correction purposes and to aid in distinguishing ^{18}F-FDG activity in the myocardium and blood pool on fused PET/CT images. Images were analyzed using MIM software by a board-certified nuclear cardiologist masked to participant characteristics. The primary outcome of the trial was
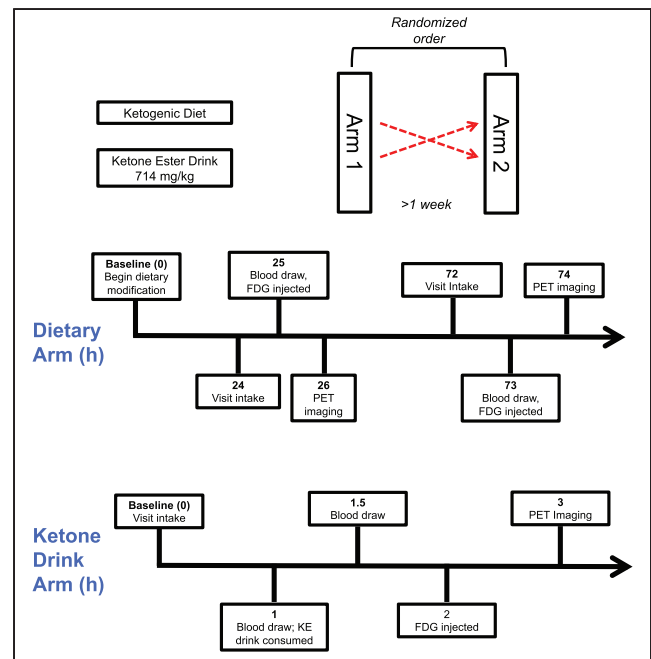
FIGURE 1. KEETO-CROSS study design. Participants were assigned in random order to KE and 24/72-h KD arms, and after at least a 1-wk washout period, participants returned for remaining arm. Visit time points in hours depicted. KD = ketogenic diet; KE = ketone ester.

complete MGS, defined by ^{18}F-FDG activity in all segments of the myocardium lower than the blood pool (*2*). The secondary trial outcome was the ratio of the average myocardial to blood pool SUV in the septal and lateral walls.

Statistical Analysis

Baseline characteristics were described using mean ± SD and medians and 25th–75th percentiles or percentages as appropriate for the levels of measurement and distributions of the variables. Biomarker levels were compared using nonparametric testing because they were right-skewed, and the false-discovery rate method was used for multiple testing correction.

We prespecified a modified-intention-to-treat analysis among participants who completed all 3 visits. A sample size of 18 participants provided 80% power to detect a 10% difference between the KE and 24-h KD group with a 5% noninferiority bound at an α-level of 5% and SD of paired differences of 0.36, assuming a correlation of 0.62 between studies. The primary (dichotomous) outcome of the trial was assessed using the exact noninferiority test of the difference between paired binomial proportions. Because noninferiority was only specified for the primary outcome, the secondary (continuous) outcome was analyzed using Wilcoxon signed-rank test because data were right-skewed. To limit multiple testing, the primary analysis compared KE and the 24-h KD (gold standard), whereas other comparisons are considered exploratory. To understand reasons for MGS failure with the KE drink, we used logistic regression to assess the relationship between log-transformed, post-KE drink biomarker levels with MGS, displaying the odds ratio per SD increase for ease of comparison between biomarkers.

In a prespecified analysis, we assessed ROCs of biomarkers using c-statistics to predict achievement of MGS, accounting for clustering at the participant level when applicable. For ease of comparison between biomarkers, c-statistics for insulin and glucose levels were displayed modeling the risk for MGS failure because these biomarkers are theoretically inversely related to MGS, whereas other biomarkers

are directly related. We used continuous splines with 4 knots after confirming nonlinearity to model endogenous BHB levels and the myocardium to blood-pool SUV ratio. Logistic splines were also used to model the relationship between MGS and endogenous ketone levels. We further assessed the diagnostic value of point-of-care BHB values after the protocol modification. Bland–Altman plot and Spearman ρ were used to compare ketone levels by laboratory and point-of-care analysis. Analyses were performed separately for endogenous and exogenous ketone levels because each mode of ketosis reflects differing cardiovascular physiology and mechanisms of action (*1*).

Analyses were performed using STATA version 14 (STATA Corp.) and StatXact-12 (Cytel). For the primary outcome assessing noninferiority, a 1-sided P value of <0.05 was considered significant, whereas other analyses used a 2-sided P value of <0.05.

RESULTS

The baseline characteristics of the 20 KEETO-CROSS heathy participants who completed 57 ^{18}F-FDG PET scans are shown in Supplemental Table 1. The mean age was 30 ± 7 y, 50% were women, and 45% were nonwhite. The average duration of fasting (hours) before ^{18}F-FDG injection was 15.9 ± 1.3 (KE drink arm), 16.7 ± 1.6 (24-h KD arm), and 15.2 ± 2.0 (72-h KD arm).

From a hemodynamic perspective, systolic blood pressure (119 ± 12 to 124 ± 11 mm Hg; $P = 0.023$) and heart rate (62 ± 12 to 71 ± 13 beats per minute; $P < 0.001$) increased significantly at approximately 30 min after consumption of the KE drink. Heart rate also showed a trend for increment (68 ± 13 and 76 ± 12 bpm; $P = 0.14$), whereas systolic blood pressure (117 ± 15 and 117 ± 11 mm Hg; $P = 0.90$) did not change with diet-induced ketosis at 24 and 72 h, respectively.

Metabolite and Hormones Levels by Study Arm

BHB, NEFA, insulin, and glucagon levels by study visit are displayed in Figure 2 for the 18 participants in the modified intention-to-treat analysis. BHB levels (presented as median and 25th–75th percentile) increased rapidly and significantly from immediately prior (median, 0.12; 25th–75th percentile, 0.10–0.26 mmol/L) to 30 min after KE drink ingestion (median, 3.82; 25th–75th percentile, 2.55–4.97 mmol/L, $P < 0.001$). Post-KE drink levels were significantly higher than that achieved by 24-h KD (median, 0.77; 25th–75th percentile, 0.58–1.02 mmol/L, $P < 0.001$) and 72-h KD (median, 1.30; 25th–75th percentile, 0.80–2.24 mmol/L, $P = 0.029$). A similar pattern was observed when comparing the post-KE drink insulin levels with other times points. Glucagon and NEFA levels were lower after the KE drink than for the 24- and 72-h KD arms ($P < 0.05$ for all comparisons), though they were not different from pre-KE drink levels ($P > 0.20$ for both comparisons). As expected, glucose levels were lower after the 24-KD and 72-KD groups compared with overnight fasting, reflected by the pre-KE drink levels (Supplemental Table 2).

KEETO-CROSS Primary and Secondary Outcomes

Using the modified intention-to-treat protocol, we assessed the primary outcome (complete MGS) in the 18 participants who completed all 3 study visits (Fig. 3). Complete MGS was achieved in 8 of 18 (44%), 14 of 18 (78%), and 15 of 18 (83%) participants in the KE, 24-h KD, and 72-h KD arms, respectively. KE failed to meet the noninferiority bound compared with the KD arms (noninferiority $P = 0.97$ and 0.98 for KE vs. 24-h and 72-h KD, respectively).

Among the 18 participants completing all 3 visits, the secondary outcome (average SUV myocardium/blood pool, presented as median) was 1.01 (25th–75th percentile, 0.72–1.70), 0.67
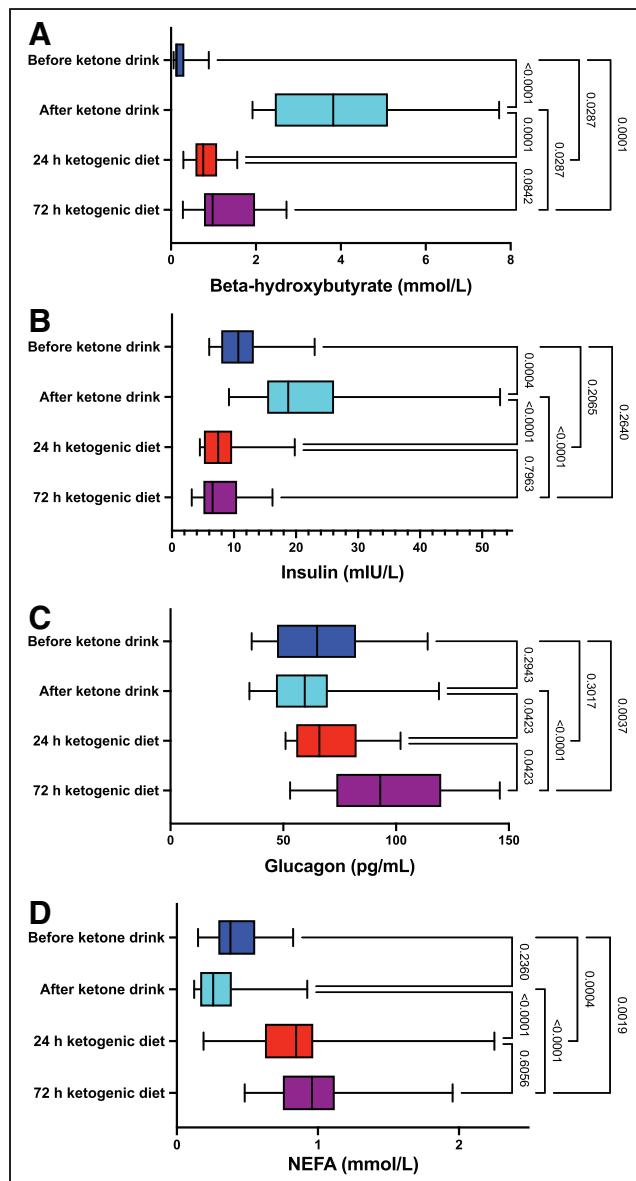
FIGURE 2. Biomarker levels by study arm. Box-and-whisker plots for ketone (A), insulin (B), glucagon (C), and NEFA (D) levels are displayed by study visit for the 18 participants included in the modified intention-to-treat analysis. Whiskers depict minimum and maximum values. *P* values corrected for multiple testing.

(25th–75th percentile, 0.61–0.79), and 0.63 (25th–75th percentile, 0.56–0.66) in the KE, 24-h KD, and 72-h KD arms, respectively ($P = 0.008$ for KE vs. 24-h KD, and $P = 0.004$ for KE vs. 72-h KD) (Fig. 3).

Individual-level responses to MGS strategies are shown in Supplemental Figure 2. Two participants failed at least 1 dietary strategy and suppressed with the KE (Supplemental Fig. 3).

Utility of Biomarkers to Predict Myocardial Glucose Suppression

Figure 4 shows area under the receiver-operating-characteristics curve (AUROC) for endogenous serum BHB levels to predict MGS in the KD arms ($n = 37$ scans). Serum BHB levels robustly predicted MGS (c-statistic 0.88, 95% CI 0.71–1.00). A threshold serum BHB level < 0.34 mmol/L correctly classified failure to
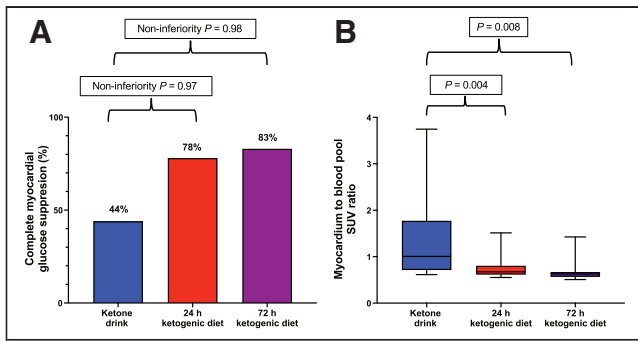
FIGURE 3. Primary and secondary endpoints of KEETO-CROSS study shown for the 18 participants who completed all study visits. (A) Percentages of primary endpoint achievement (complete myocardial glucose suppression). (B) Box-and-whisker plots of secondary outcome (average SUV of myocardium to blood pool).

achieve MGS, whereas BHB levels $\geq$ 1.09 mmol/L correctly classified MGS success, in these ^{18}F-FDG PET scans. As a single threshold, using a BHB level $\geq$ 0.58 mmol/L for predicting MGS resulted in the highest correct classification of any value (92%), including 6 of 7 (86%) scans that were correctly classified as likely failure and 28 of 30 (93%) studies that were correctly classified as likely MGS based on BHB results. Glucose (c-statistic 0.78, 95% CI 0.61–0.95), glucagon (0.75, 95% CI 0.56–0.94), insulin (0.69, 95% CI 0.44–0.92), and NEFA (0.66, 95% CI 0.42–0.90) were less predictive of MGS, in comparison with BHB.

Representative images further illustrating the correlation between common myocardial ^{18}F-FDG uptake patterns and their respective BHB levels are shown in Figure 5. The relationships between BHB levels and glucose uptake using spline analyses are shown in Figures 6 and 7.

We also assessed the relationships between pre-KE drink BHB levels, post-KE drink BHB levels, and the difference between these levels with MGS. All 3 measurements were lower among those who failed MGS than those who appropriately suppressed
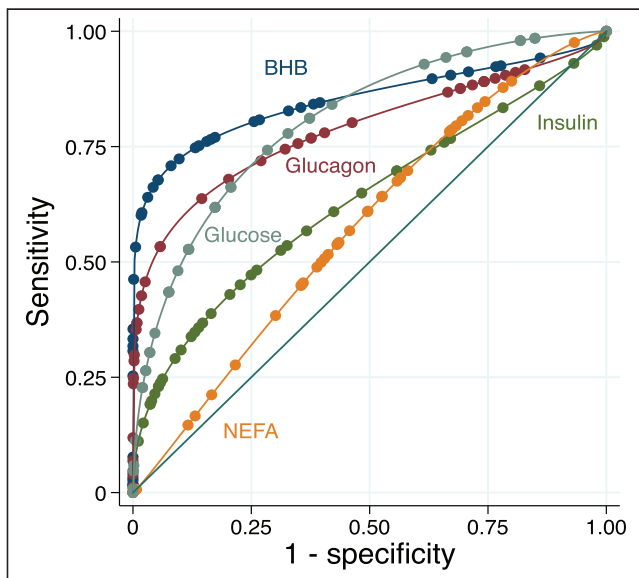
($P < 0.05$ for all comparisons) (Supplemental Table 3). All 3 measurements also significantly predicted MGS (AUROC 0.85, 95% CI 0.62–1.00; AUROC 0.85, 95% CI 0.67–1.00; AUROC 0.82, 95% CI 0.60–1.00, respectively).

Log BHB levels after the KE drink were significantly associated with MGS (standardized odds ratio 4.92, 95% CI 1.25–18.43, $P = 0.022$). Alternatively, log-transformed NEFA levels (standardized odds ratio 2.07, $P = 0.16$), insulin levels (standardized odds ratio 1.02, $P = 0.97$), and glucagon levels (standardized odds ratio 1.37, $P = 0.51$) were not predictive of MGS after the KE drink.

Utility of Point-of-Care (POC) Ketone Testing to Predict MGS

To enhance clinical utility and provide a rapid assessment of ketosis before ^{18}F-FDG PET, we also investigated POC ketone testing (paired testing available in 59 samples). Bland–Altman and scatter plots are shown in Supplemental Figures 4 and 5 comparing laboratory-derived BHB values and POC BHB values. The mean difference of laboratory- and POC-derived BHB levels was 0.04 (95% CI −0.88, 0.97 mmol/L), and correlation was strong (Spearman ρ 0.96, $P < 0.001$).

Since agreement was worst at the highest BHB levels, which were obtained after KE administration, we also assessed BHB levels obtained during the KD visits separately (as these lower values are encountered clinically with the KD preparation, $n = 28$ samples). The mean difference of laboratory- and POC-derived BHB levels was −0.02 (95% CI −0.29, 0.25 mmol/L), and correlation was strong (Spearman ρ 0.98, $P < 0.001$) (Supplemental Figs. 6 and 7).

POC BHB levels during the KD significantly predicted MGS (c-statistic 0.87, 95% CI 0.66–1.00) (Supplemental Figs. 8 and 9). Using POC BHB levels $\geq$ 0.6 mmol/L for predicting MGS correctly classified 89% of scans.

FIGURE 4. Receiver-operating-characteristic curve analysis for BHB, insulin, glucagon, NEFA, and glucose to predict myocardial glucose suppression in all participants during ketogenic diet.

FIGURE 5. Myocardial ^{18}F-FDG uptake patterns in healthy volunteers. Representative images (displayed using same window width 0–5) of most common myocardial ^{18}F-FDG uptake patterns encountered in our healthy cohort, with their corresponding BHB levels. Patterns C–E can be potentially mistaken as myocardial inflammation; however, accompanying BHB levels should raise concern for incomplete suppression. LV = left ventricular.
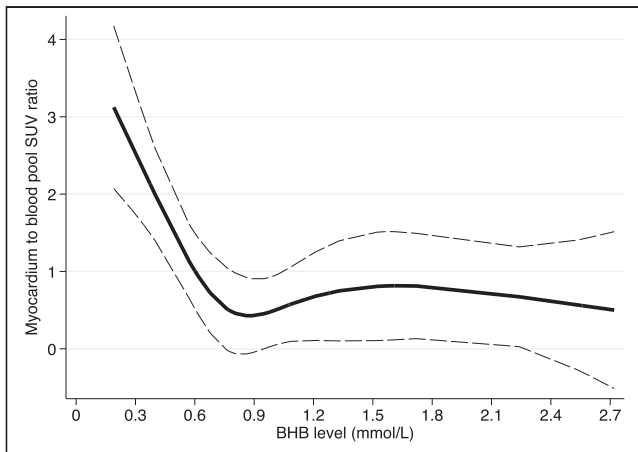
FIGURE 6. Relationship between endogenous ketone levels and myocardial glucose uptake. Continuous spline analysis with 4 knots depicts relationship between endogenous ketone levels (BHB) and secondary outcome (SUV ratio of myocardium to blood pool).

Adverse Events

Mild (grade 1) adverse events occurred in 9 participants in the KE drink arm (these adverse events were mostly gastrointestinal [nausea or heartburn, $n = 7$] including 1 participant who experienced emesis, and 2 participants who reported a headache). In the KD arm, 1 participant reported presyncope (grade 1), and another participant reported back pain (grade 2), which led to study discontinuation.

DISCUSSION

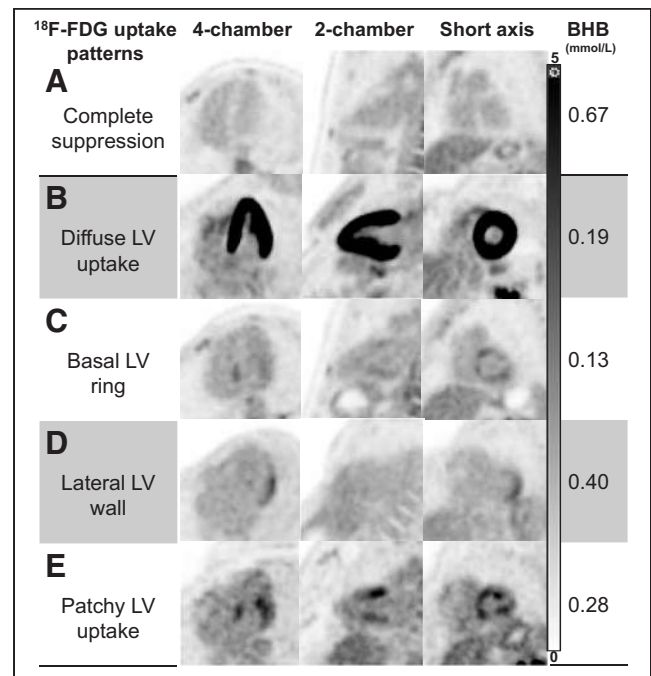^{18}F-FDG PET plays a critical role in assessing cardiovascular inflammation, infection, and tumors, yet adequate myocardial preparation to suppress physiologic glucose uptake remains a substantial diagnostic barrier, particularly as certain patterns of incomplete suppression (Fig. 5) can be indistinguishable from pathology. Such challenges may ultimately lead to misdiagnosis, inappropriate therapy, along with potentially harmful side effects, extra radiation exposure for repeated testing, and unnecessary costs to the patient and health-care system.

In KEETO-CROSS, an open-label, crossover trial of healthy participants, we found that a generalized strategy of KE was inferior to 24- and 72-h KD to achieve MGS. However, a few individuals who failed the KD were able to suppress with the KE drink. Importantly, however, we found that serum BHB levels during the KD robustly predicted MGS and identified potential thresholds that can be used upstream of ^{18}F-FDG PET to predict MGS, thereby reducing false-positive or indeterminate scans. To facilitate clinical implementation, we tested the utility of a POC ketone meter that showed an ability to predict MGS similar to laboratory-based analysis. Thus, our findings support the continued use of the dietary modification through the KD rather than KE to achieve MGS, provide strong evidence for assessing BHB levels before ^{18}F-FDG PET to ensure adequate dietary preparation, and demonstrate how a POC ketone device can be implemented to aid in rapid-decision making.

Despite several strategies to facilitate the myocardial "metabolic switch" to suppress physiologic glucose uptake, current MGS rates vary substantially, though much of these data are derived retrospectively and from convenience cohorts referred for clinical indications (2). The current trial was designed to address these challenges by investigating the use of an oral KE, which could facilitate same-day
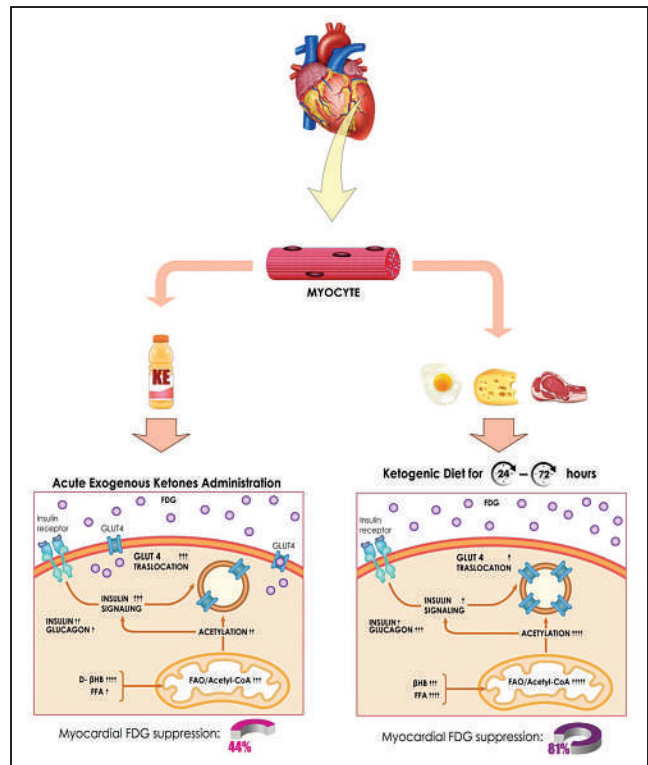
FIGURE 7. Proposed molecular mechanisms associated with myocardial ^{18}F-FDG suppression between acute exogenous ketone administration (lower left) and endogenous ketosis induced by dietary modification (lower right). Posttranslational protein acetylation and attenuation of insulin signaling are both required mechanisms for successful inhibition of glucose transporter member 4 (GLUT4) translocation. Acute administration of KE drink leads to a severalfold increment in β-hydroxybutyrate (βHB) levels but also appears to decrease free fatty acid (FFA) levels, which may ultimately affect modulation of insulin signaling and process of acetylation. In contrast, although KD yields lower βHB levels after 24–72 h, it increases FFA and glucagon and lowers insulin levels on a sustained fashion, eventually augmenting fatty acid oxidation (FAO) over glucose oxidation ("Randle effect"), increasing protein acetylation, and limiting insulin signaling. These molecular differences in substrate handling may explain why myocardial ^{18}F-FDG suppression rates were 44% for KE and 81% for KD. Adapted from "Insulin Mechanism," by BioRender.com (2021 (17)).

scans without patient preparation, in healthy volunteers. Endogenous and exogenous ketosis suppress myocardial glucose uptake in different ways (Fig. 7). Although endogenous ketosis has been standard-of-care for MGS, exogenous ketones also reduce myocardial glucose uptake, as shown in preclinical and clinical work (11,12). However, our results demonstrate that despite significant acute ketosis achieved, rates of suppression were inferior to the KD. We hypothesize several mechanisms for failure of the KE to uniformly suppress myocardial glucose uptake in these healthy volunteers. Posttranslational protein acetylation and attenuation of insulin signaling are necessary for the efficient inhibition of the glucose transporter member 4 (GLUT4) translocation (13) and thus ^{18}F-FDG accumulation in myocytes. In this sense, acute exogenous ketone delivery may not engender effective substrate competition and a "Randle Effect" in the healthy heart given normal mitochondrial function (7,14). For example, post-KE drink NEFA levels were significantly lower than that achieved by KD. In this way, the KD may be more effective because it feeds both ketones and fatty acids for substrate competition, leading to increased fatty acid oxidation and protein acetylation.

Second, failure of exogenous ketones could relate to increased insulin levels and, thus, signaling, an effect that can be counterproductive to achieving MGS. Although, we did not find a relationship between post-KE insulin levels and MGS. Third, the hemodynamic effect of exogenous ketones could theoretically contribute to increased myocardial glucose uptake, consistent with the vital sign changes in our study (11). Finally, the metabolic effect of exogenous ketone administration may be more dependent on the duration, rather than the peak levels, of ketosis before the "metabolic switch" occurs. In this sense, it remains to be proven whether extending the delay between KE and ^{18}F-FDG administration would have led to improved suppression rates.

Notably, we found that ketone levels strongly predicted MGS. Broadly speaking, ketogenesis is a complex process that is influenced by hormonal signaling (including insulin and glucagon levels), transcriptional regulation, and posttranscriptional modification (1). As the end result of several biologic processes that reflect the milieu of glucose regulation, it is not surprising that ketone levels significantly relate to MGS. In our study, endogenous BHB levels had an AUROC of 0.88 for predicting MGS, and a cutoff of 0.58 mmol/L accurately classified MGS 92% of the time. This predictive ability of BHB was stronger than those with insulin, glucagon, glucose, and NEFA, consistent with other studies that have found modest predictive ability for these biomarkers (15), and clarifies that ketosis is a more potent driver, or predictive biomarker, of MGS than these other metabolic processes. Such potent prediction has clinical implications, as BHB levels can be routinely assessed before ^{18}F-FDG PET to ensure adequate patient preparation. For instance, we found that 86% of subjects with BHB levels < 0.58 mmol/L failed to make the metabolic switch, and oftentimes, the patterns of incomplete suppression were indistinguishable from inflammation (Fig. 5). Consequently, if BHB levels are below this threshold, a longer duration of the KD (e.g., 72 h) can be undertaken with the visit rescheduled. Such an approach could considerably minimize false-positive or nondiagnostic scans, decreasing diagnostic uncertainty in clinical reading, inappropriate diagnoses, unnecessary costs, and radiation exposure from repeated scans. Alternatively, KE could be theoretically combined with the KD in participants below the threshold, since higher levels of ketosis after KE significantly predicted MGS. Moreover, POC ketone testing allows for rapid triage of patients and has already been implemented in other clinical settings (16). Such testing showed high agreement with laboratory-based analyses at levels encountered during KD and similarly predicted MGS. Given the reasonable costs of ketone meters, it may be possible for patients to monitor ketone levels remotely before ^{18}F-FDG PET, potentially avoiding unnecessary travel and improving clinical throughput if levels predict inadequate preparation. Importantly, however, further studies in cohorts of patients with heart failure will be needed given relative myocardial glucose avidity in the failing heart (1).

There are some limitations. Although we chose to study KE against an active comparator (KD, which is standard-of-care), a placebo (fasting-only) arm would have provided firm conclusions on whether KE (and not just prolonged fasting) did suppress myocardial glucose uptake in some participants. However, an additional arm would have engendered greater radiation exposure against a weak comparator, and historical data on MGS are available for fasting-only patient preparations (2). In addition, our sample size is modest. Finally, our study design is open-label, which was limited by practicality of the dietary intervention, though endpoint adjudication is blinded. Strengths include a strict definition of complete MGS, crossover design, inclusion of extended-duration KD in addition to the gold-standard 24-h KD preparation, analysis of several relevant hormones and metabolites, and assessment of a POC device.

CONCLUSION

A general strategy of exogenously administered KE was inferior to KD to achieve MGS. BHB levels strongly predicted MGS in healthy participants and can be clinically implemented before ^{18}F-FDG PET to minimize false-positive or nondiagnostic scans, potentially decreasing inappropriate diagnoses, radiation exposure, and health-care system costs. POC ketone testing can provide rapid and accurate triage for adequate patient preparation for ^{18}F-FDG PET. Further study to validate the diagnostic value of BHB levels in other patient cohorts, including older individuals, diabetics, and subjects with cardiomyopathies, is warranted.

DISCLOSURE

ACKNOWLEDGMENTS

KEY POINTS

QUESTION: Is exogenous ketone administration noninferior to the standard ketogenic diet to achieve myocardial glucose suppression, and can a serum biomarker predict myocardial glucose uptake status?

PERTINENT FINDINGS: Exogenous ketone administration was inferior to the ketogenic diet to achieve myocardial glucose suppression. BHB levels strongly predicted the metabolic switch of glucose uptake in the heart of healthy volunteers.

IMPLICATIONS FOR PATIENT CARE: BHB testing can provide rapid and accurate triage for adequate patient preparation for cardiovascular inflammation imaging with ^{18}F-FDG PET.

REFERENCES

1. Selvaraj S, Kelly DP, Margulies KB. Implications of altered ketone metabolism and therapeutic ketosis in heart failure. *Circulation.* 2020;141:1800–1812.

2. Osborne MT, Hulten EA, Murthy VL, et al. Patient preparation for cardiac fluorine-18 fluorodeoxyglucose positron emission tomography imaging of inflammation. *J Nucl Cardiol.* 2017;24:86–99.

3. Cheng VY, Slomka PJ, Ahlen M, Thomson LE, Waxman AD, Berman DS. Impact of carbohydrate restriction with and without fatty acid loading on myocardial ^{18}F-FDG uptake during PET: A randomized controlled trial. *J Nucl Cardiol.* 2010;17:286–291.

4. Harisankar CN, Mittal BR, Agrawal KL, Abrar ML, Bhattacharya A. Utility of high fat and low carbohydrate diet in suppressing myocardial FDG uptake. *J Nucl Cardiol.* 2011;18:926–936.

5. Lu Y, Grant C, Xie K, Sweiss NJ. Suppression of myocardial ^{18}F-FDG uptake through prolonged high-fat, high-protein, and very-low-carbohydrate diet before FDG-PET/CT for evaluation of patients with suspected cardiac Sarcoidosis. *Clin Nucl Med.* 2017;42:88–94.

6. Bing RJ, Siegel A, Ungar I, Gilbert M. Metabolism of the human heart. II. Studies on fat, ketone and amino acid metabolism. *Am J Med.* 1954;16:504–515.

7. Randle PJ, Newsholme EA, Garland PB. Regulation of glucose uptake by muscle. 8. Effects of fatty acids, ketone bodies and pyruvate, and of alloxan-diabetes and starvation, on the uptake and metabolic fate of glucose in rat heart and diaphragm muscles. *Biochem J.* 1964;93:652–665.

8. Clarke K, Tchabanenko K, Pawlosky R, et al. Kinetics, safety and tolerability of (R)-3-hydroxybutyl (R)-3-hydroxybutyrate in healthy adult subjects. *Regul Toxicol Pharmacol.* 2012;63:401–408.

9. Shivva V, Cox PJ, Clarke K, Veech RL, Tucker IG, Duffull SB. The population pharmacokinetics of D-beta-hydroxybutyrate following administration of (R)-3-hydroxybutyl (R)-3-hydroxybutyrate. *AAPS J.* 2016;18:678–688.

10. Stubbs BJ, Cox PJ, Evans RD, et al. On the metabolism of exogenous ketones in humans. *Front Physiol.* 2017;8:848.

11. Gormsen LC, Svart M, Thomsen HH, et al. Ketone body infusion with 3-hydroxybutyrate reduces myocardial glucose uptake and increases blood flow in humans: a positron emission tomography study. *J Am Heart Assoc.* 2017;6.

12. Russell RR, 3rd, Cline GW, Guthrie PH, Goodwin GW, Shulman GI, Taegtmeyer H. Regulation of exogenous and endogenous glucose metabolism by insulin and acetoacetate in the isolated working rat heart. A: a three tracer study of glycolysis, glycogen metabolism, and glucose oxidation. *J Clin Invest.* 1997;100:2892–2899.

13. Renguet E, Bultot L, Beauloye C, Horman S, Bertrand L. The regulation of insulin-stimulated cardiac glucose transport via protein acetylation. *Front Cardiovasc Med.* 2018;5:70.

14. Selvaraj S, Margulies KB. Exogenous ketones in the healthy heart: the plot thickens. *Cardiovasc Res.* 2021;117:995–996.

15. Larson SR, Pieper JA, Hulten EA, et al. Characterization of a highly effective preparation for suppression of myocardial glucose utilization. *J Nucl Cardiol.* 2020;27:849–861.

16. Dhatariya K. The use of point-of-care blood ketone monitors in the management of diabetic ketoacidosis in adults. *Ann Clin Biochem.* 2014;51:525–527.

17. Insulin mechanism. BioRender website. https://app.biorender.com/biorender-templates/figures/5c65c7b6bce1963300935374/t-5edea9a02e012f00aea78da4-insulin-mechanism. Accessed March 29, 2022.

Brain Stem Glucose Hypermetabolism in Amyotrophic Lateral Sclerosis/Frontotemporal Dementia and Shortened Survival: An ^{18}F-FDG PET/MRI Study

Matteo Zanovello[1], Gianni Sorarù[1,2], Cristina Campi[3], Mariagiulia Anglani[4], Alessandro Spimpolo[5], Sara Berti[5], Cinzia Bussè[1], Stefano Mozzetta[1], Annachiara Cagnin[1,2], and Diego Cecchin[2,5]

[1]Neurology Unit, Department of Neurosciences, University of Padova, Padova, Italy; [2]Padova Neuroscience Center, University of Padova, Padova, Italy; [3]Department of Mathematics, University of Genova, Genova, Italy; [4]Neuroradiology Unit, Department of Neurology, University Hospital of Padova, Padova, Italy; and [5]Nuclear Medicine Unit, Department of Medicine, University Hospital of Padova, Padova, Italy

A few ^{18}F-FDG PET/CT studies have revealed the presence of brain hypermetabolism in the brain stem and cervical spinal cord of patients within the amyotrophic lateral sclerosis/frontotemporal dementia (ALS/FTD) continuum. We aimed to investigate this finding through a hybrid PET/MRI system, allowing a more precise depiction of the spatial pattern of metabolic changes in the brain stem and cervical spinal cord. **Methods:** Twenty-eight patients with a diagnosis of ALS or a diagnosis of the behavioral variant of FTD plus motoneuron disease, as well as 13 control subjects, underwent ^{18}F-FDG PET/MRI. Mean normalized ^{18}F-FDG uptake in the midbrain/pons, medulla oblongata, and cervical spinal cord as defined on the individual's MRI scans were compared between groups. Furthermore, the associations between regional ^{18}F-FDG uptake and clinical and demographic characteristics—including gene mutation, type of onset (bulbar, spinal, dementia), and clinical characteristics—were investigated. **Results:** A significant ($P < 0.005$) increment in glucose metabolism in the midbrain/pons and medulla oblongata was found in ALS/FTD patients (spinal-ALS and FTD–motor neuron disease subgroups) in comparison to controls. No relevant associations between clinical and metabolic features were reported, although medulla oblongata hypermetabolism was associated with shortened survival ($P < 0.001$). **Conclusion:** Increased glucose metabolism in the brain stem might be due to neuroinflammation, one of the key steps in the pathogenic cascade that leads to neurodegeneration in ALS/FTD. ^{18}F-FDG PET/MRI could be a valuable tool to assess glial changes in the ALS/FTD spectrum and could serve as a prognostic biomarker. Large prospective initiatives would likely shed more light on the promising application of PET/MRI in this setting.

Key Words: amyotrophic lateral sclerosis; FTD; PET; survival; brain stem

The clinical overlap between amyotrophic lateral sclerosis (ALS) and frontotemporal dementia (FTD) has been widely recognized, with behavioral/cognitive symptoms occurring in a certain number of patients with ALS, and signs of motoneuron

disease in several patients with FTD (1). This, along with the discovery of shared genetics and pathophysiologic mechanisms, has informed the recharacterization of the 2 diseases as the extremes of a common neurodegenerative spectrum (ALS/FTD).

From a pathophysiologic perspective, these diseases present proteinaceous cytoplasmic aggregates that eventually lead to neuronal degeneration and loss. Glial cells are also actively involved in the ALS/FTD pathology. Among these are astrocytes, which cause excitotoxicity when their role in synaptic glutamate reuptake is impaired, and microglia, which the phenotype evolves from neuroprotective to neurotoxic through the course of the disease (2). Neuropathologic studies in ALS patients have found depletion of motor neurons and diffuse glial infiltration in the gray and white matter of the spinal cord and the motor cortex (3). As predicted, both activated microglia and astrocyte markers have been observed in imaging studies of ALS (4,5) and FTD patients (6,7).

Several neuroimaging techniques have been applied to ALS and FTD cohorts to explore their use as potential disease biomarkers. Cortical MRI hallmarks of ALS are bilateral atrophy of the primary motor cortex (precentral gyrus) and degeneration of the corticospinal tract and corpus callosum (8). An MRI study including diffusion tensor imaging (9) showed reduced fractional anisotropy in corticospinal tracts, frontal and temporal lobes, and the regions that connect the motor and premotor cortex. Moreover, at a functional level, changes in the connectivity of neural networks within motor and extramotor domains have been demonstrated through electroencephalography (10) and functional MRI (11) studies. These insights, in line with findings that show how patients with different degrees of cognitive impairment have significantly different patterns of frontal lobe metabolic impairment when assessed using ^{18}F-FDG PET (12), could partially explain the heterogeneous clinical manifestations and spreading of the disease.

In line with this possibility, several PET/CT studies on ALS/FTD patients, including proven *C9orf72* carriers, focused on cortical structures, showing frontal and temporal hypometabolism (13,14). Conversely, the few that explored other central nervous system regions found increased ^{18}F-FDG uptake in the cerebellum, brain stem (15,16), and spinal cord (17–19) of patients with ALS when compared with controls. The reason for the increase in regional glucose uptake is still a matter of debate.

In light of these findings, we chose to assess glucose metabolic patterns, analyzing separately the midbrain/pons, medulla oblongata, and cervical spinal cord of ALS/FTD patients, as compared with

control subjects, by means of coacquired PET and MR images. As PET/CT images can lead to difficulties in delineating volumes of interest (VOIs), this was the first study (to our knowledge) in this setting to exploit the potential of the hybrid PET/MRI technique, which, relating ^{18}F-FDG values to precise anatomic substrates, can improve result accuracy. Furthermore, we aimed to estimate the association between the degree of ^{18}F-FDG uptake and clinical characteristics such as type of clinical presentation, including site of onset, presence of the *C9orf72* mutation, disease progression, and survival.

MATERIALS AND METHODS

Participants

In total, 28 patients diagnosed with ALS ($n = 16$) or FTD who developed motor neuron disease (MND) in the course of the disease ($n = 12$) and underwent ^{18}F-FDG PET/MRI (Biograph mMR; Siemens) at the Nuclear Medicine Unit of the University of Padova were retrospectively recruited between July and December 2019. Probable or definite ALS was diagnosed according to the El Escorial revised criteria (20), and the diagnosis was confirmed in all patients during their clinical follow-up. Patients with FTD were diagnosed with a behavioral variant of FTD according to the Rascovsky criteria (21) and developed signs of MND. The median time between diagnosis and ^{18}F-FDG PET/MRI was 1 mo.

Thirteen participants who were referred to the nuclear medicine unit with a diagnosis other than neurologic disease, and were not showing any signs of brain disease under the same scanning procedure, served as control subjects.

The 28 patients were further classified according to the clinical presentation at the time of diagnosis as having bulbar ALS ($n = 5$), spinal ALS ($n = 11$), or FTD-MND ($n = 12$). Six patients (2 with spinal ALS and 4 with FTD-MND) carried a GGGGCC hexanucleotide repeat expansion in the first intron of the *C9orf72* gene, and one (spinal ALS) carried a mutation of the *VCP* gene (9p13.3) coding for the valosin-containing protein.

The exclusion criteria included having a history of other neurologic disorders, cerebrovascular disease, diabetes mellitus, or systemic inflammatory disease. Moreover, other exclusion criteria were diagnostic uncertainty according to the El Escorial revised criteria and PET/MRI scans nonevaluable because of significant movement artifacts. The local ethical committee approved the retrospective study (protocol AOP1673-4831/AO/20). All patients and controls gave written informed consent before undergoing ^{18}F-FDG PET/MRI, in accordance with the principles outlined in the Declaration of Helsinki.

Clinical Data

Demographic variables, as well as the time from onset or diagnosis to the ^{18}F-FDG PET/MRI scan, were obtained for each patient. Moreover, the ALS-Functional Rating Scale, revised (ALS-FRS-r), was calculated (for ALS patients only, being a retrospective study) both at the time of diagnosis and at the latest available neurologic visit. Furthermore, a progression rate, also known as Δ-ALS-FRS-r (22), was calculated as $(48 - $ ALS-FRS-r at time of diagnosis)/duration from onset to diagnosis (mo) for 15/18 ALS patients (for 3 patients, ALS-FRS-r was not available at the time of diagnosis). Muscle strength was assessed through the Medical Research Council scale.

Image Acquisition and Analysis

PET/MRI was performed between July 2015 and November 2019. Following the European Association of Nuclear Medicine guidelines (23), patients had to fast for 6 h before the injection of the radiopharmaceutical, and blood glucose had to be less than 200 mg/dL. A single 3 MBq/kg intravenous bolus of ^{18}F-FDG was injected under resting conditions (in a

dimly light room with the patient's eyes closed) before the scan. PET and MRI scans were simultaneously acquired using a Siemens Healthcare Biograph mMR, which included several sequences (T1-weighted, T2-weighted, susceptibility-weighted, and diffusion-weighted) and a PET brain scan (acquisition time, 1,500 s; reconstructed using a 344×344 mm matrix and a 3-dimensional iterative reconstruction algorithm).

Postprocessing was performed using the Image Fusion tool within PMOD software (PMOD Technologies LLC): briefly, each ^{18}F-FDG PET scan was finely realigned to the pertinent 3-dimensional, isotropic (1 mm) T1-weighted MRI scan on the basis of a rigid transformation (smoothing: gaussian filter width of 6.0 mm; dissimilarity function: normalized mutual information; interpolation method: trilinear; sample rate: 5.2/4.0 mm start/final; minimization method: Powell; function tolerance: 1.0–4).

PMOD was then used to create VOIs (Fig. 1) both for patients and for control subjects. Creation of VOIs started with manual positioning—on 3-dimensional T1-weighted images—of visually adjusted cubical VOIs on the midbrain/pons, medulla oblongata, and cervical spinal cord (the region between the skull base and the plane adjacent to the caudal face of the C4 vertebral body). Isocontouring took place next (inside the defined cubical VOIs), with a threshold higher than 40% of the overall maximum uptake; several 3-dimensional VOIs were outlined (midbrain/pons, medulla oblongata, and cervical spinal cord). Finally, visually adjusted spheric VOIs were manually positioned in the parietooccipital white matter (as background VOIs) on the T1-weighted MR images.
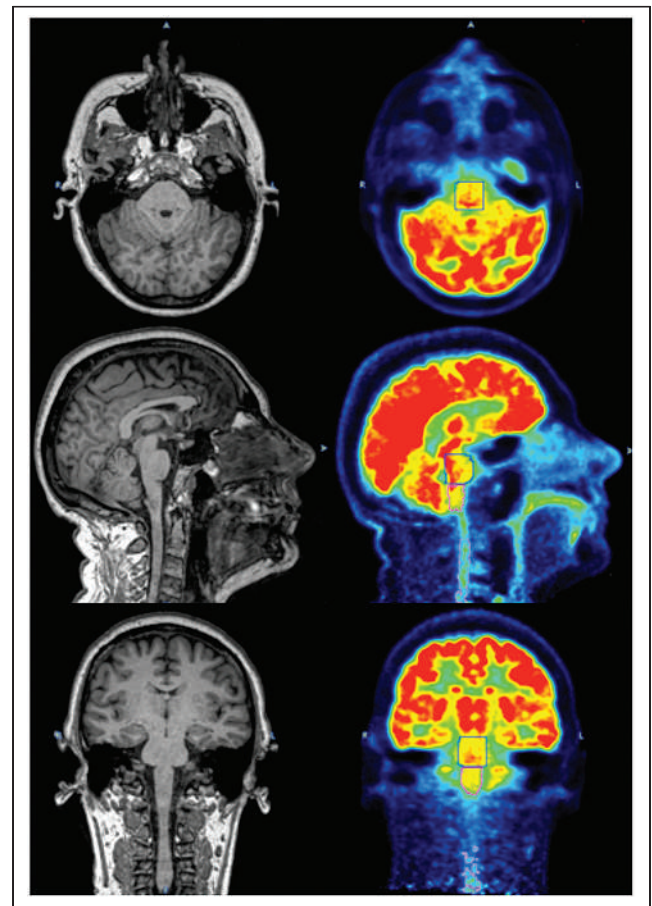
FIGURE 1. ^{18}F-FDG PET images (right) showing VOIs created using corresponding T1-weighted MR images (left). Axial (top), sagittal (middle), and coronal (bottom) views are shown.

TABLE 1
Clinical and Demographic Characteristics of Study Subjects

Characteristic	ALS/FTD patients	Controls	P
Sex (n)	15/13	10/3	0.279
M	15	10	
F	13	3	
Weight (kg)	69.4 ± 12.1	76 ± 11.8	0.115
Height (m)	1.68 ± 0.10	1.73 ± 0.07	0.123
Age at PET (y)	62.6 ± 8.2	52.8 ± 13.6	0.0035
C9orf72 mutation (n)	6/28	0/13	—
Site of onset (n)			
Bulbar	5/28		
Spinal	11/28		
Cortical	12/28		

For each subject, the mean uptake within each VOI was normalized using the mean uptake of the occipital white matter background VOIs (24), because this area has been reported to experience fewer ^{18}F-FDG metabolic alterations (14).

Statistical Analysis

All data are reported as mean ± SD. After evaluating the gaussian distribution of data, unpaired t tests were performed to relate uptake value to categoric variables, whereas continuous variables were analyzed through correlation and linear regression testing. Since the age distribution significantly differed between patients and controls, a residual analysis for regression was applied when comparing the 2 groups (25). Log-rank testing was applied for survival analysis. A P value of less than 0.05 was considered significant. Univariate and multivariate survival analyses (considering genetics, site of onset, age at PET, and time from onset to PET) were performed.

RESULTS

The main clinical findings in ALS/FTD patients and control subjects are shown in Tables 1 and 2. No significant differences

TABLE 2
Clinical Characteristics at Single-Subject Level

Clinical phenotype	Sex	Dead	Age at PET (y)	Genetics	First ALS-FRS-r (points)	Last ALS-FRS-r (points)	Progression rate (ratio)	Time from symptom onset to PET (mo)
Spinal	M	No	55	Negative	45	37	0.43	7
Spinal	F	No	60	Negative	46	44	0.08	25
Spinal	M	No	55	Negative	43	36	0.71	8
Spinal	M	No	63	Negative	37	37	0.23	47
Spinal	F	No	54	C9orf72	42	18	0.18	53
Spinal	F	No	67	C9orf72	41	24	0.20	69
Spinal	F	No	76	Unknown	32	30	0.67	23
Spinal	F	Yes	58	Negative	37	4	0.65	17
Spinal	M	Yes	62	VCP	40	20	0.07	163
Spinal	F	Yes	61	Negative	39	33	0.49	21
Spinal	M	Yes	51	Negative	40	27	1.33	28
Bulbar	F	No	73	Negative	45	24	0.13	24
Bulbar	M	No	68	Negative	/	/	/	12
Bulbar	M	No	75	Negative	42	36	0.26	30
Bulbar	F	Yes	76	Negative	32	23	0.89	18
Bulbar	M	Yes	74	Negative	44	44	0.33	13
FTD-MND	F	No	72	Unknown				41
FTD-MND	M	No	52	C9orf72				20
FTD-MND	M	No	56	Negative				4
FTD-MND	F	No	55	C9orf72				22
FTD-MND	F	No	64	C9orf72				28
FTD-MND	M	No	60	Negative				23
FTD-MND	F	No	63	Negative				22
FTD-MND	M	No	68	Negative				17
FTD-MND	M	Yes	68	Unknown				96
FTD-MND	F	Yes	73	C9orf72				48
FTD-MND	M	Yes	52	Negative				33
FTD-MND	M	Yes	61	Negative				18

/ = missing clinical scores for this patient.

FIGURE 2. (Top) Paired plots showing strong correlation between uptake in 3 regions of each subgroup. (Bottom) Density plots displaying frequency of patients with low (e.g., controls) or high (e.g., ALS/FTD continuum) uptake of ^{18}F-FDG for each subgroup. SC = spinal cord.

were found between the sex, weight, and height of the 2 groups, whereas the age distribution between patients (62.6 $\pm$ 8.2 y) and controls (52.8 $\pm$ 13.6 y) differed significantly.

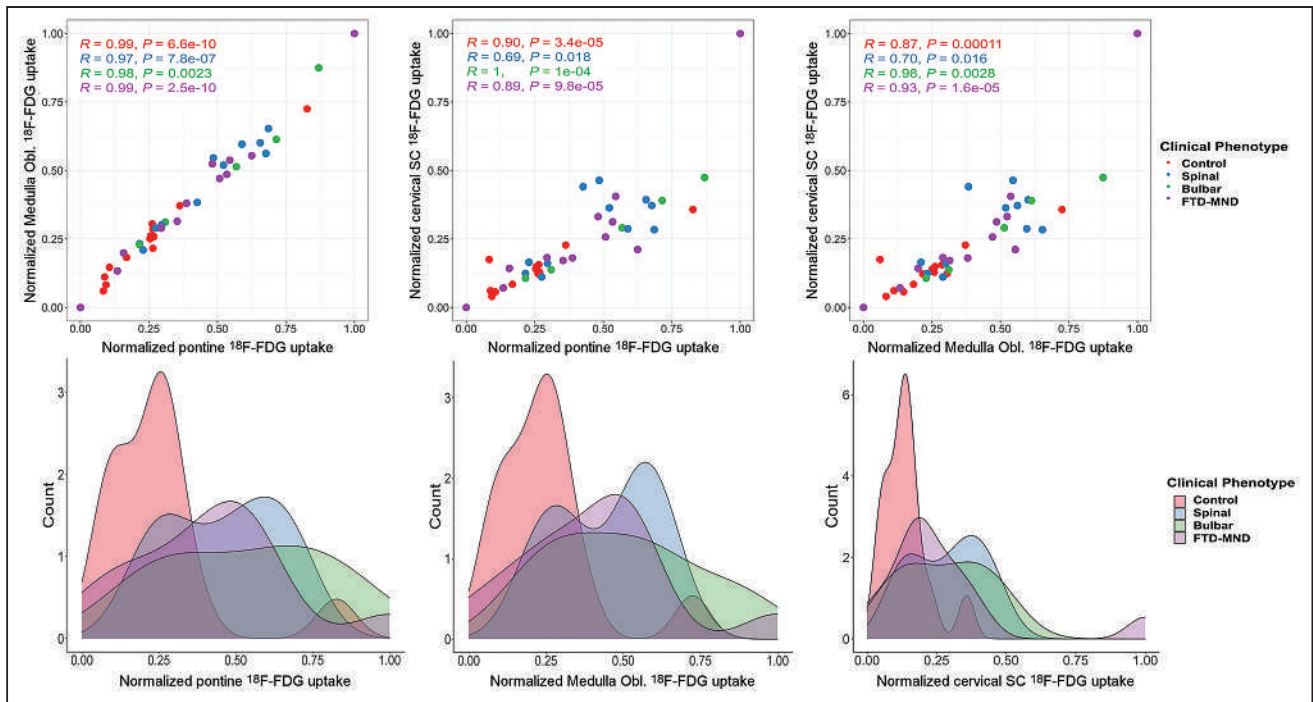Examining MRI T2-weighted fluid-attenuated inversion recovery sequences, we found mild to moderate corticospinal tract hyperintensities in 8% of FTD-MND patients and 40% of ALS subjects. Susceptibility-weighted imaging (available for only ALS patients) revealed a variable degree of the motor band sign (cortical ferromagnetic deposition in primary motor cortex) in 64% of subjects.

We examined the relationship between metabolic patterns within the VOIs under examination with other clinical measures and the genetic background (*C9orf72* mutation), although none of them showed a significant association.

After the PET/MRI study, follow-up lasted between 2 and 55 mo (median, 33 mo), during which patients showed a steep drop in their average ALS-FRS-r score (from 37.2 $\pm$ 6.5 to 29.4 $\pm$ 10.6). The calculated progression rate (Table 2) mildly correlated with medulla oblongata hypermetabolism (correlation coefficient, 0.45) but not with pontine (correlation coefficient, -0.02) or cervical spinal cord (correlation coefficient, 0.3) hypermetabolism. The variation in ALS-FRS-r score (last ALS-FRS-r as compared with the first one) did not, however, demonstrate a significant correlation with ^{18}F-FDG hypermetabolism considering pontine (correlation coefficient, -0.13), medulla oblongata (correlation coefficient, 0.31), or cervical spinal cord (correlation coefficient, 0.31) regions.

During the study follow-up, 10 patients died (7 ALS and 3 FTD-MND); however, univariate Cox regression analysis did not prove significant for *C9orf72* mutation, sex, clinical phenotype, or cognitive impairment (FTD-MND patients).

An analysis of the metabolic patterns of the midbrain/pons, medulla oblongata, and cervical spinal cord revealed a strong correlation between metabolic patterns of the 3 VOIs (Fig. 2A). Moreover, as visible from the density plots (Fig. 2B), the distribution of the uptake values was unbalanced between controls and patients, with the former showing decreased ^{18}F-FDG uptake in all regions under examination compared with the latter.

After normalization for the background VOIs and adjustment for age (*25*), an increase in glucose metabolism in ALS/FTD patients, when compared with controls, was detected in all 3 regions under examination. ^{18}F-FDG uptake reached significantly higher values for patients than for controls in the midbrain/pons and medulla oblongata (Fig. 3) but not in the cervical spinal cord.

Analysis of spinal, bulbar, and FTD-MND subgroups showed a statistically significant relative hypermetabolism in the midbrain/pons and medulla oblongata when normalized to the white matter in patients with spinal and behavioral onset with respect to controls (Fig. 4). Uptake in patients with bulbar onset was not significantly different from controls, most likely because of their small number (*n* = 5). On the other hand, analysis among the 3 subgroups (bulbar, spinal, and FTD-MND) did not show any significant difference in ^{18}F-FDG uptake in any of the explored regions, apart from the cervical spinal cord between spinal and bulbar-onset patients.

The Kaplan–Meier analysis and univariate Cox regression analysis (Table 3) at 50 mo after PET/MRI showed that the patients with normalized medulla oblongata uptake above the fifth decile (9/16 ALS and 5/12 FTD-MND presented normalized medulla oblongata uptake > 50%) had a significantly higher mortality rate than those below the fifth decile (log-rank test, $P < 0.001$) (Fig. 5), whereas the analysis results were not significant for the other regions under examination. A multivariate Cox regression analysis confirmed that a higher medulla oblongata uptake and a longer time from symptom onset to PET are independently associated with a shorter survival (Table 3). Clinical bulbar signs (such as dysarthria and dysphagia) at the time of PET examination (in 9/16 ALS and 2/12 FTD-MND subjects) did not statistically correlate (correlation coefficient, 0.18) with normalized hypermetabolism in the medulla oblongata.
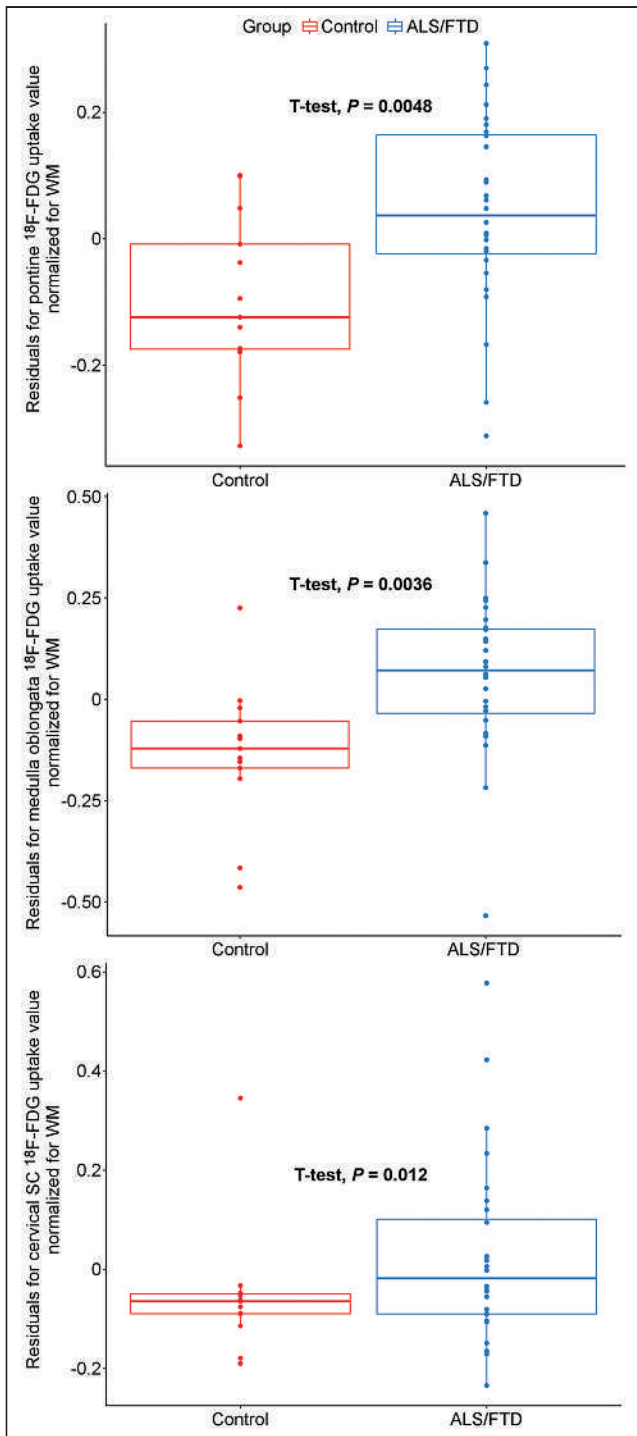
FIGURE 3. Results of residual analysis for regression between control and patient (ALS/FTD) normalized uptake values in midbrain/pons (top), medulla oblongata (middle), and cervical spinal cord (bottom). SC = spinal cord.

FIGURE 4. Subgroup analysis for ^{18}F-FDG uptake. SC = spinal cord.

DISCUSSION

This study, to our current knowledge, was the first to exploit integrated ^{18}F-FDG PET/MRI to study the metabolic patterns of patients with ALS and FTD. In our population, MRI could be useful when differentiating ALS subjects from FTD-MND because corticospinal tract hyperintensities seem to be more frequent in the former group (40% vs. 8%). Furthermore, we have noticed the motor band sign (susceptibility-weighted sequence) in the majority (64%) of ALS subjects. This qualitative finding could complement, at a single-subject level, the diagnostic accuracy of PET regional glucose hyper- and hypometabolism.

We detected midbrain/pons and medulla oblongata increased uptake in patients as compared with controls, confirming previous PET/CT findings (15,16). Furthermore, we determined how medulla oblongata metabolism relates to patient survival, suggesting a possible prognostic value for PET/MRI.

The results of our study indicated that the uptake of all 3 brain regions investigated (midbrain/pons, medulla oblongata, and cervical spinal cord) correlates significantly, as shown by the paired correlation (Fig. 2A). An explanation for the correlation of metabolic patterns in the 3 regions is the involvement of the corticospinal and

TABLE 3
Univariate and Multivariate Survival Analysis

	Univariate survival analysis		Multivariate survival analysis	
Factor	Hazard ratio	P	Hazard ratio	P
Medulla oblongata uptake	10.2 (2.14 to 48.56)	0.00352*	1.016e+07 (15.95 to 6.47e+12)	0.0180*
Age at PET	1.02 (0.93 to 1.11)	0.642	0.6667 (0.42 to 1.05)	0.0845
Site of onset				
Bulbar	1 (reference)	—	1 (reference)	—
Spinal	0.8532 (0.15 to 4.67)	0.855	5.459e−06 (5.23e−11 to 0.57)	0.0398*
FTD	0.8532 (0.15 to 4.67)	0.855	3.716e−06 (2.6e−11 to 0.53)	0.0390*
Genetics				
Negative	1 (reference)	—	1 (reference)	—
VCP	2.4632 (0.29 to 20.67)	0.406	0.1239 (8.01e−07 to 1.923e+4)	0.7320
C9orf72	0.3441 (0.04 to 2.8)	0.319	1.161e+03 (0.148 to 9.07e+06)	0.1228
Unknown	1.0770 (0.13 to 8.78)	0.945	5.778e+04 (0.12 to 2.8e+10)	0.1008
Time from onset to PET	1.008 (0.99 to 1.02)	0.233	1.152 (1.02 to 1.29)	0.0175*

*Statistically significant.

Data in parentheses are 95% CIs. Higher medulla oblongata uptake and longer time from symptoms onset to PET are associated with shorter survival.
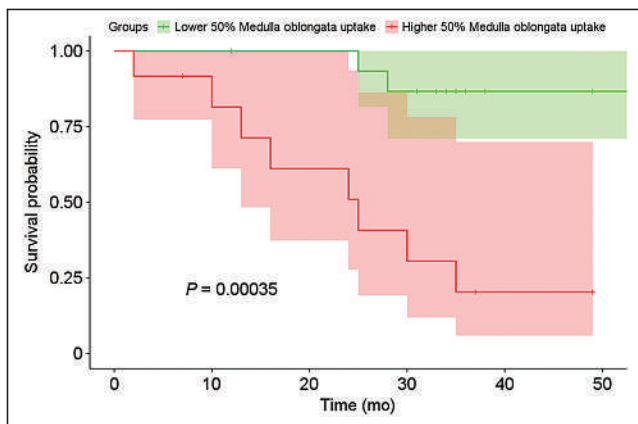
FIGURE 5. Kaplan–Meier curve. After normalization of uptake for occipital white matter, patients were split into 2 subgroups: the 14 individuals with medulla oblongata uptake over 50th percentile showed significantly shorter survival than patients with medulla oblongata uptake below 50th percentile. Survival is expressed in months after PET/MRI scan. P value was calculated through log-rank test.

corticobulbar tracts containing the projections of upper motor neurons from the motor cortex. A bimodal distribution could be seen in the density plot distribution of controls as compared with the ALS/FTD continuum in Figure 2B. The second lower peak of the bimodal distribution was, however, due to a single, slightly outlier, control subject.

Theoretically, the expected effect of a neurodegenerative disease is a reduction in tissue metabolic rate caused by neuronal loss; indeed, frontal hypometabolism is one of the cortical signatures of the diseases along the ALS/FTD spectrum (12–14). Nevertheless,

strong evidence has been brought in favor of neuro-inflammation as one of the key steps in the pathogenic cascade that leads to ALS/FTD. Initially described in pathology studies, glial infiltration has later been confirmed in vivo both in models and in humans (4,5).

A possible explanation, which links neuroinflammation with neurodegeneration, involves these 2 types of glial cells, namely activated microglia and astrocytes. Activated microglia, which have been found in the motor cortex, pons, and thalamus of patients with ALS, contribute to the pathogenesis propagating and sustaining the tissue damage through the release of free radicals and other neurotoxic substances such as glutamate. Moreover, a shift from a neuroprotective to a disrupting phenotype is apparent starting in the early stages of the disease (2). Astrocytes physiologically account for a consistent share of central nervous system glucose consumption. Thereafter, they start glycolysis to provide lactate to neurons; in hindsight, astrocytes play a key role in coupling glucose metabolism with synaptic activity. In the case of neurodegeneration, glutamate excess leads to an increased glucose accumulation in astrocytes, even though neurons degenerate (26). Moreover, during the course of the disease, astrocytes replace dead neurons and axons following the corticospinal and corticobulbar tracts, further increasing the metabolic uptake of the degenerating brain region. Neuroimaging evidence for the involvement of these glial cells in the pathogenesis of ALS/FTD has been brought by studies that exploited neuroinflammation-specific ligands such as ^{11}C-L-deprenyl-D_2 (4), mapping of astrocyte activation, the activated microglia marker [11]C(R)-PK11195 (5,6), and translocator protein ligand ^{18}F-DPA-714 (27), showing increased tracer uptake along the corticospinal tract.

From a metabolic perspective, these phenomena result in an increased relative ^{18}F-FDG uptake in regions of neuronal

degeneration in affected individuals compared with controls. However, when evaluating the relative weight of the 2 cell types, one must consider that the microglia seem to relate more to hypometabolic areas, as shown in frontotemporal areas of FTD patients (5,6), whereas astrocytosis drives glucose consumption and is, therefore, more likely associated with the hypermetabolic burden (26), in line with previous findings (4). We acknowledge that this evidence cannot prove the exclusive role of 1 of these 2 glial cells—a role that is based on a continuous interplay involving other cell types also—and that longitudinal studies will be needed to better characterize the interplay between neurodegeneration and hypermetabolism and differences in their behavior between upper and lower motor neurons.

An alternative reason for the finding of glucose hypermetabolism in ALS/FTD patients can be a methodologic issue involving the normalization process of ^{18}F-FDG data. We normalized the uptake values of the regions of interest for the values of the occipital white matter to exclude interindividual differences. Normalizing for other regions would require an a priori assumption, namely that none of the background VOIs will be affected by hypo- or hypermetabolism. In the present study, occipital white matter was chosen as the reference because it seems spared from the ALS/FTD neurodegenerative process (14,24), and none of the PET/CT studies on subjects affected with the disease showed significant metabolic variations in that region.

Another issue we faced was the difference in age distribution between the 2 groups. To ignore this effect on the uptake values, we adjusted for age through a linear regression model (25) and we then used the residual values for the group analysis (Fig. 3). However, we usually expect a higher metabolism in younger patients with respect to controls. On the contrary, in this setting, although the controls were younger than the patients, they had a lower metabolism; this fact reassures us about the choice of groups selected and about the obtained results.

Although considering a small cohort, the subgroup analysis included patients with differences in ALS onset, namely spinal ($n = 11$), bulbar ($n = 5$), and behavioral/cognitive ($n = 12$). Although the groups with spinal or behavioral onset showed higher ^{18}F-FDG uptake than did controls, bulbar onset did not prove significant because of the small number of individuals in that group. Interestingly, the density plot of normalized ^{18}F-FDG uptake in FTD-MND was similar to that of patients with ALS (Figs. 2 and 4). Therefore, we can state that hypermetabolism in the corticospinal tract could be a common feature for all the ALS subgroups, thereby suggesting, once again, common metabolic and pathophysiologic patterns within the disease spectrum. Prospective studies involving a larger number of individuals with different sites of onset, including FTD patients without clinical MND, as well as comparisons between cortical and subcortical regions with lower motor neurons (to elucidate the possible metabolic relations between upper and lower motor neurons), are expected to strengthen the current results.

Bulbar-onset ALS is a prognostic factor associated with short survival (28). Here, we instead showed that the metabolic uptake of the medulla oblongata was significantly associated with short survival (Fig. 5). This finding supports the hypothesis that neuroinflammation of midbrain structures is one of the main mechanisms involved in ALS progression, highlighting a potential role for neurometabolic studies as prognostic and outcome predictors. Moreover, a previous study (17) reported a significant relationship between the whole-spinal-cord–normalized uptake value and patient survival; thus, it will be necessary to compare the metabolic patterns of these 2 regions to draw consistent evidence.

CONCLUSION

This study analyzed the brain metabolism of ALS/FTD patients through PET/MRI and demonstrated that bulbar uptake could be a strong survival predictor. Notwithstanding the limited sample size and the retrospective design, we confirmed the presence of increased glucose metabolism in the midbrain/pons and medulla oblongata, supporting the importance of neuroinflammation in the pathogenesis of the disease spectrum. Considering the present need for reliable diagnostic and prognostic biomarkers in ALS and FTD, our results support PET neuroimaging as one of the most promising candidates for this role, although the cost and expertise required pose a barrier to the translation of this technology to clinical practice. A further step will be to design longitudinal studies involving large cohorts of age-matched patients—individuals with ALS-mimics and healthy controls—to assess the early predictive value of PET imaging, understand the neuroradiologic course of the disease, and evaluate the effect of therapies. These studies will need to thoroughly indagate central nervous system metabolism and to relate metabolic patterns within different brain regions to disease genotype and phenotype, with particular regard to the differences between upper- and lower-motor-neuron involvement.

DISCLOSURE

No potential conflict of interest relevant to this article was reported.

KEY POINTS

QUESTION: Is there a significant increment in glucose metabolism in the midbrain/pons and medulla oblongata of ALS/FTD patients as compared with controls, and is it related to mortality rates?

PERTINENT FINDINGS: An increase in glucose metabolism in ALS/FTD patients, as compared with controls, was noted in all 3 regions under examination (midbrain/pons, medulla oblongata, and cervical spinal cord). The Kaplan–Meier analysis at 50 mo after PET/MRI showed that the patients with normalized medulla oblongata uptake above the fifth decile had a significantly higher mortality rate than those below the fifth decile (log-rank test, $P < 0.001$).

IMPLICATIONS FOR PATIENT CARE: Considering the present need for reliable diagnostic and prognostic biomarkers in ALS and FTD, our results support PET neuroimaging of the medulla oblongata as one of the most promising candidates for this role.

REFERENCES

1. Robberecht W, Philips T. The changing scene of amyotrophic lateral sclerosis. *Nat Rev Neurosci.* 2013;14:248–264.
2. McCauley ME, Baloh RH. Inflammation in ALS/FTD pathogenesis. *Acta Neuropathol (Berl).* 2019;137:715–730.
3. Ince PG, Highley JR, Kirby J, et al. Molecular pathology and genetic advances in amyotrophic lateral sclerosis: an emerging molecular pathway and the significance of glial pathology. *Acta Neuropathol (Berl).* 2011;122:657–671.
4. Johansson A, Engler H, Blomquist G, et al. Evidence for astrocytosis in ALS demonstrated by [^{11}C](L)-deprenyl-D2 PET. *J Neurol Sci.* 2007;255:17–22.

5. Turner MR, Cagnin A, Turkheimer FE, et al. Evidence of widespread cerebral microglial activation in amyotrophic lateral sclerosis: an [^{11}C](R)-PK11195 positron emission tomography study. *Neurobiol Dis.* 2004;15:601–609.

6. Bevan-Jones WR, Cope TE, Jones PS, et al. Neuroinflammation and protein aggregation co-localize across the frontotemporal dementia spectrum. *Brain.* 2020;143:1010–1026.

7. Cagnin A, Rossor M, Sampson EL, Mackinnon T, Banati RB. In vivo detection of microglial activation in frontotemporal dementia. *Ann Neurol.* 2004;56:894–897.

8. Agosta F, Valsasina P, Riva N, et al. The cortical signature of amyotrophic lateral sclerosis. *PLoS One.* 2012;7:e42816.

9. Crespi C, Dodich A, Cappa SF, et al. Multimodal MRI quantification of the common neurostructural bases within the FTD-ALS continuum. *Neurobiol Aging.* 2018;62:95–104.

10. Iyer PM, Egan C, Pinto-Grau M, et al. Functional connectivity changes in resting-state EEG as potential biomarker for amyotrophic lateral sclerosis. *PLoS One.* 2015;10:e0128682.

11. Trojsi F, Esposito F, de Stefano M, et al. Functional overlap and divergence between ALS and bvFTD. *Neurobiol Aging.* 2015;36:413–423.

12. Canosa A, Pagani M, Cistaro A, et al. ^{18}F-FDG-PET correlates of cognitive impairment in ALS. *Neurology.* 2016;86:44–49.

13. Cistaro A, Pagani M, Montuschi A, et al. The metabolic signature of C9ORF72-related ALS: FDG PET comparison with nonmutated patients. *Eur J Nucl Med Mol Imaging.* 2014;41:844–852.

14. Chiò A, Pagani M, Agosta F, Calvo A, Cistaro A, Filippi M. Neuroimaging in amyotrophic lateral sclerosis: insights into structural and functional changes. *Lancet Neurol.* 2014;13:1228–1240.

15. Van Laere K, Vanhee A, Verschueren J, et al. Value of ^{18}fluorodeoxyglucose-positron-emission tomography in amyotrophic lateral sclerosis: a prospective study. *JAMA Neurol.* 2014;71:553–561.

16. Pagani M, Chiò A, Valentini MC, et al. Functional pattern of brain FDG-PET in amyotrophic lateral sclerosis. *Neurology.* 2014;83:1067–1074.

17. Marini C, Cistaro A, Campi C, et al. A PET/CT approach to spinal cord metabolism in amyotrophic lateral sclerosis. *Eur J Nucl Med Mol Imaging.* 2016;43:2061–2071.

18. Yamashita T, Hatakeyama T, Sato K, et al. Flow-metabolism uncoupling in the cervical spinal cord of ALS patients. *Neurol Sci.* 2017;38:659–665.

19. Marini C, Morbelli S, Cistaro A, et al. Interplay between spinal cord and cerebral cortex metabolism in amyotrophic lateral sclerosis. *Brain.* 2018;141:2272–2279.

20. Brooks BR, Miller RG, Swash M, Munsat TL; World Federation of Neurology Research Group on Motor Neuron Diseases. El Escorial revisited: revised criteria for the diagnosis of amyotrophic lateral sclerosis. *Amyotroph Lateral Scler Other Motor Neuron Disord.* 2000;1:293–299.

21. Rascovsky K, Hodges JR, Knopman D, et al. Sensitivity of revised diagnostic criteria for the behavioural variant of frontotemporal dementia. *Brain.* 2011;134:2456–2477.

22. Kimura F, Fujimura C, Ishida S, et al. Progression rate of ALSFRS-R at time of diagnosis predicts survival time in ALS. *Neurology.* 2006;66:265–267.

23. Varrone A, Asenbaum S, Vander Borght T, et al. EANM procedure guidelines for PET brain imaging using ^{18}F-FDG, version 2. *Eur J Nucl Med Mol Imaging.* 2009;36:2103–2110.

24. Borghammer P, Jonsdottir KY, Cumming P, et al. Normalization in PET group comparison studies: the importance of a valid reference region. *Neuroimage.* 2008;40:529–540.

25. Dobson AJBA. *An Introduction to Generalized Linear Models.* 3rd ed. CRC Press; 2008.

26. Zimmer ER, Parent MJ, Souza DG, et al. ^{18}F-FDG PET signal is driven by astroglial glutamate transport. *Nat Neurosci.* 2017;20:393–395.

27. Corcia P, Tauber C, Vercoullie J, et al. Molecular imaging of microglial activation in amyotrophic lateral sclerosis. *PLoS One.* 2012;7:e52941.

28. Dupuis L, Pradat P-F, Ludolph AC, Loeffler J-P. Energy metabolism in amyotrophic lateral sclerosis. *Lancet Neurol.* 2011;10:75–82.

^{18}F-Fluorocholine PET/CT Is More Sensitive Than ^{11}C-Methionine PET/CT for the Localization of Hyperfunctioning Parathyroid Tissue in Primary Hyperparathyroidism

Céline Mathey[1], Caroline Keyzer[2], Didier Blocklet[1], Gaetan Van Simaeys[1], Nicola Trotta[1], Simon Lacroix[1], Bernard Corvilain[3], Serge Goldman[1], and Rodrigo Moreno-Reyes[1]

[1]Department of Nuclear Medicine and PET/Biomedical Cyclotron Unit, Hôpital Érasme, Université Libre de Bruxelles, Brussels, Belgium; [2]Department of Medical Imaging, Hôpital Erasme, Université Libre de Bruxelles, Brussels, Belgium; and [3]Department of Endocrinology, Hôpital Érasme, Université Libre de Bruxelles, Brussels, Belgium

Preoperative molecular imaging is paramount to direct surgery in primary hyperparathyroidism (pHPT). We investigated the diagnostic performance of ^{18}F-fluorocholine (^{18}F-FCH) PET/CT compared with ^{11}C-methionine (^{11}C-MET) PET/CT for localization of hyperfunctioning parathyroid tissue in patients with pHPT and negative or inconclusive ^{99m}Tc-sestaMIBI (^{99m}Tc-MIBI) SPECT findings. **Methods:** Fifty-eight patients with biochemical evidence of pHPT and negative or inconclusive ^{99m}Tc-MIBI SPECT findings were referred for presurgical detection and localization of hyperfunctioning parathyroid tissue by ^{11}C-MET and ^{18}F-FCH PET/CT. The PET/CT results were classified into 3 categories (positive, inconclusive, or negative) based on the nodular aspect of tracer uptake and the visualization of corresponding nodules on CT. The PET/CT results were correlated with the surgical and histopathologic findings, which were used as the gold standard. **Results:** Fifty-three patients were included for analysis. ^{18}F-FCH PET/CT was positive in 39 patients (74%), inconclusive in 5 (9%), and negative in 9 (17%), compared with 25 (47%), 12 (23%), and 16 (30%), respectively, for ^{11}C-MET PET/CT. ^{18}F-FCH localized 11 additional foci (6 positive and 5 inconclusive), compared with ^{11}C-MET. Twenty-six patients (sex ratio, 10/16 M/F) underwent surgery, with resection of 31 lesions (22 adenomas, 6 hyperplastic glands, and 3 carcinomas) and 1 normal gland. At follow-up, 21 patients (81%) were considered cured after surgery, whereas 3 patients (12%) had persistence of hypercalcemia. With inconclusive cases being considered negative, ^{18}F-FCH PET/CT correctly localized 26 lesions in 24 of 26 patients (92%), compared with 16 lesions in 15 of 26 patients (58%) localized by ^{11}C-MET PET/CT. Per-patient–based sensitivity and positive predictive value were 96% and 96%, respectively, for ^{18}F-FCH and 60% and 94%, respectively, for ^{11}C-MET ($P <$ 0.0001). Per-lesion–based sensitivity and positive predictive value were 84% and 90%, respectively, for ^{18}F-FCH and 52% and 94%, respectively, for ^{11}C-MET ($P <$ 0.0001). **Conclusion:** In the presence of biochemical evidence of pHPT with negative or inconclusive ^{99m}Tc-MIBI SPECT findings, ^{18}F-FCH PET/CT performs better than ^{11}C-MET PET/CT for the detection of pathologic parathyroid tissue, allowing localization of parathyroid adenoma or hyperplasia in 96% of patients.

Key Words: primary hyperparathyroidism; parathyroid adenoma; ^{18}F-fluorocholine; ^{11}C-methionine; PET/CT

P rimary hyperparathyroidism (pHPT) is one of the most frequent endocrine disorders, with a prevalence of about 2% in women older than 50 y. Long-term consequences of pHPT affect mainly the skeleton (osteoporosis, fractures) and the kidney (nephrolithiasis, impaired renal function). Diagnosis is based on increased serum calcium, low phosphorus levels, and inappropriate parathyroid hormone (PTH) levels (*1*). pHPT is associated with a solitary parathyroid adenoma (PA) in 80%–90% of patients or, more rarely, multiglandular disease or diffuse parathyroid hyperplasia (*1*).

Optimal management of pHPT consists of preoperative localization of the abnormal parathyroid gland, allowing for minimally invasive parathyroidectomy (*2,3*). Conventional first-line presurgical imaging is based on ^{99m}Tc-sestaMIBI (^{99m}Tc-MIBI) parathyroid scintigraphy with subtraction images, usually complemented by ultrasonography. It ideally includes a SPECT/CT acquisition, with a detection rate of 84%–88% (*4,5*).

Currently, in cases of negative or equivocal scintigraphy results, results discrepant with ultrasonography, or persistence or recurrence of HPT after surgery, an alternative investigation is recommended involving hybrid PET/CT technique, usually with an amino acid tracer such as ^{11}C-methionine (^{11}C-MET) (*6,7*). Use of PET/CT for that purpose offers a shorter acquisition time and higher spatial resolution and sensitivity (*8*). Metaanalyses reported ^{11}C-MET to have sensitivity of 77%–81% in a per-patient–based analysis in patients with pHPT and negative or inconclusive ^{99m}Tc-MIBI SPECT findings (*6,9*). However, the short half-life of ^{11}C-MET imposes on-site production and strict acquisition conditions (*6*).

More recently,^{18}F-fluorocholine (^{18}F-FCH) PET/CT used for imaging prostatic neoplasia assessment (*10*) has been shown capable of localizing an abnormal parathyroid gland in patients with negative or inconclusive ^{99m}Tc-MIBI SPECT results (*3,8,11,12*). It has the advantages over ^{11}C-MET of a longer half-time and a more favorable positron energy. Choline is a precursor of phospholipids, which are essential constituents of cellular lipidic structures. ^{18}F-FCH is therefore a tracer of lipid metabolism whose uptake increases after increased intracellular metabolism requiring synthesis of phospholipids.

The aim of this study was to investigate whether, in patients with pHPT and negative or inconclusive ^{99m}Tc-MIBI SPECT results, the diagnostic performance of ^{18}F-FCH PET/CT is similar to that of ^{11}C-MET PET/CT from a preoperative perspective. The secondary objective was to compare the performance of the 2 methods in the detection of individual hyperfunctioning parathyroid lesions.

MATERIALS AND METHODS

Patients

Between November 2015 and December 2018, we prospectively included 58 patients with biologically proven pHPT (hypercalcemia and elevated or inappropriately normal PTH levels) and negative or inconclusive results on ^{99m}Tc-MIBI imaging performed at various institutions, including ours, and involving SPECT with or without combined CT.

On inclusion, and when there was no recent blood test (<3 mo) confirming hyperparathyroidism, a blood sample was taken to measure serum values of calcium, phosphorus, PTH, albumin, and vitamin D. The serum calcium level was measured the day after surgery to check for normalization.

Institutional ethics committee approval was obtained before the start of this prospective study, and all subjects signed an informed-consent form (P2015/307).

PET/CT Procedure

All PET/CT was performed on a Gemini GXL ($n = 15$) or a TF64 ($n = 38$) PET/CT camera (Philips), with essentially identical protocols on both systems. All patients sequentially underwent ^{11}C-MET and ^{18}F-FCH PET/CT (Supplemental Fig. 1; supplemental materials are available at http://jnm.snmjournals.org).

^{11}C-MET PET/CT. All patients were injected with an average bolus of 555 MBq of ^{11}C-MET while in a fasting state. Fifteen minutes after injection, unenhanced CT (40 mAs; 120 kV; slice thickness, 2.0 mm; interval, 1.5 mm) was performed, followed by a PET acquisition of the neck and upper mediastinum (3 bed positions, 7 min per bed position). Images were reconstructed with 2 different algorithms depending on the PET camera (blob-basis function ordered-subsets time of flight or line-of-response–based row-action maximum likelihood).

^{18}F-FCH PET/CT. Approximately 3 h after ^{11}C-MET injection, unenhanced CT (40 mAs; 120 kV; slice thickness, 2.0 mm; interval, 1.5 mm) was acquired. Then, with the patient lying in the PET/CT tomograph, a 4-MBq dose of ^{18}F-FCH per kilogram of body mass was administered intravenously. ^{18}F-FCH was prepared in 2 steps using a fully automated radiochemistry synthesizer (Trasis All-in-One) (13). A 15-min dynamic PET acquisition covering the neck was started at the time of tracer injection, followed by a static acquisition (early ^{18}F-FCH [^{18}F-FCH$_E$]) on the neck and the upper mediastinum (3 bed positions, 7 min per bed position). PET/CT imaging of the neck and upper mediastinum was repeated 60 min after injection (late ^{18}F-FCH [^{18}F-FCH$_L$]) and used for image analysis in the present work. Images were reconstructed with 2 different algorithms depending on the PET camera (blob-basis function ordered-subsets time of flight or line-of-response–based row-action-maximum likelihood).

Image Interpretation. All PET/CT images were analyzed independently by a nuclear medicine physician (11 y of experience) and a radiologist (18 y of experience), who were aware of previous imaging and laboratory findings for the patients, and by a nuclear medicine physician (27 y of experience) masked to any clinical and imaging information. Discordant image interpretation occurred in 11 patients. In all these cases, a consensus reading led to a final common interpretation. There was no pause between ^{18}F-FCH and ^{11}C-MET readings.

The images (maximum-intensity projection and 3-dimensional volume) were evaluated visually to determine the number and exact location of uptake areas suggestive of hyperfunctioning parathyroid glands.

The results were classified into 3 categories based on the aspect of the tracer uptake area and the visualization of corresponding nodules on CT: positive, in cases of a clear circumscribed uptake area on PET images or a faint circumscribed uptake area corresponding to a nodular lesion on CT; inconclusive, in cases of a faint uptake area with no corresponding nodule on CT; or negative, in cases of no discernable tracer uptake area. Lesion localization was assigned to 6 anatomic regions: right and left upper, right and left lower, intrathyroidal, and ectopic. In cases of a discrepancy between readers' assessments, the appropriate category and anatomic localization were assigned by consensus.

The semiquantitative analysis was performed with Philips IntelliSpace Portal software (version 9). The SUV_{max} and SUV_{mean} of the PA were measured. We estimated the contrast between the lesion and the thyroid using the ratio of PA SUV_{max} to thyroid SUV_{mean} (PA/thyroid). By this ratio, we evaluated the capacity to identify the parathyroid activity close to the organ it usually lies behind. The SUV_{max} and SUV_{mean} of the thyroid were measured by placing a spheric volume of interest 1 cm^3 in diameter on the contralateral thyroid lobe unless morphologically pathologic or the right lobe in the absence of a lesion.

Surgery and Histology

Surgeons were aware of ^{11}C-MET and ^{18}F-FCH PET/CT data for all patients. They used this information to direct the surgical procedure, which was an open, minimally invasive parathyroidectomy in cases of a single area of uptake on ^{11}C-MET or ^{18}F-FCH PET/CT. If multiple lesions or an ectopic location were suspected, the surgical approach was adapted. In cases of a coexisting multinodular goiter or suggestive thyroid nodules, an additional hemithyroidectomy or total thyroidectomy was performed. All operated cases had at least 1 lesion categorized as positive on either the ^{11}C-MET or the ^{18}F-FCH PET/CT, except for 1 patient with negative results on PET/CT, for whom full surgical exploration was decided for recurrent pHPT.

The results of ^{11}C-MET and ^{18}F-FCH PET/CT were compared with the surgical exploration and histopathologic findings. Surgical success was established according to normalization of postoperative serum calcium level.

Statistical Analysis

Quantitative variables are expressed as mean ± SD for normally distributed continuous variables and as median with 25th and 75th percentiles for nonnormal continuous variables.

For the sake of comparison, negative, inconclusive, and positive lesions were scored 0, 1, and 2, respectively. Tracer comparison of visual scoring performance was evaluated with a Wilcoxon matched-pairs signed-rank test. For visual decision performance on matched pairs of ^{11}C-MET and ^{18}F-FCH PET/CT images, inconclusive results were considered negative, and the McNemar test with the continuity correction was used.

The sensitivity and positive predictive value of PET/CT imaging were evaluated on a per-lesion and per-patient basis and calculated using histology analysis as the gold standard. Since no histologic data were available in most patients with negative results on PET/CT, specificity and negative predictive values were not evaluated.

The D'Agostino and Pearson test and the Shapiro–Wilk test were used to assess the normality of the sample values. Repeated measures of each relevant quantitative parameter (SUV_{max} PA and PA/thyroid) were analyzed with the Friedman test. Dunn tests were subsequently applied for multiple comparisons between tracers (^{11}C-MET, ^{18}F-FCH$_E$, and ^{18}F-FCH$_L$). Nonparametric Spearman correlation r was calculated between ^{18}F-FCH$_E$ and ^{18}F-FCH$_L$ PET/CT with respect to ^{11}C-MET images for PA/thyroid. After exclusion of negative cases, simple linear regression was further calculated to evaluate how this quantitative parameter varies in ^{18}F-FCH$_E$ and ^{18}F-FCH$_L$ PET/CT with respect to the corresponding

parameter on ^{11}C-MET images. Runs tests were performed to assess lack of fit. Goodness of fit was assessed with R^2. Statistical analyses were performed using Prism, version 9.0 (GraphPad Software), and its online McNemar test calculator. For all tests, a P value of less than 0.05 was considered statistically significant.

RESULTS

Among 58 patients who prospectively underwent ^{11}C-MET and ^{18}F-FCH PET/CT, 53 patients were included in the analysis (Fig. 1). Five patients were excluded because of unconfirmed pHPT ($n = 4$) or technical problems ($n = 1$). The characteristics of the 53 patients are summarized in Table 1. Among them, 7 had a previous history of parathyroidectomy and persistent or recurrent pHPT. Four patients with familial pHPT were included, 3 of whom had previous surgery. Participants underwent ^{11}C-MET and ^{18}F-FCH PET/CT on the same day, except for 7 patients who underwent their 2 PET/CT scan within 5 mo. Twenty-six patients (16 women and 10 men) had parathyroidectomy, with histopathologic confirmation of the presence of adenoma or hyperplasia in 24 patients. Fourteen patients had negative (9/53) or inconclusive (5/53) PET/CT results. Goiter was present in 10 patients (19%), and 29 patients had nodular thyroid disease (55%).

^{18}F-FCH PET/CT Outperforms ^{11}C-MET PET/CT for Lesion Localization at Both Early and Late Time Points in the Prospect of Surgery Guidance

^{18}F-FCH PET/CT was positive in 39 patients (74%) and inconclusive in 5 patients (9%), compared with 25 patients (47%) and 12 patients (23%), respectively, for ^{11}C-MET PET/CT (Table 2). The visual scoring performance of ^{18}F-FCH PET/CT was greatly superior to that of ^{11}C-MET PET/CT on a per-patient basis (Wilcoxon $P < 0.0001$). Also, the McNemar test of matched-pairs discordant results also demonstrated the superiority of ^{18}F-FCH over ^{11}C-MET PET/CT in visual decision performance on a per-patient basis ($P = 0.0005$; $\chi^2 = 12.071$ with $1°$ of freedom), with 14 patients positive only with ^{18}F-FCH PET/CT and no patient positive only with ^{11}C-MET PET/CT, whereas 25 patients were positive and 14 were negative with both tracers. Of 26 patients with negative or inconclusive ^{99m}Tc-MIBI results and positive PET/CT results (either ^{11}C-MET or ^{18}F-FCH) who had surgery, 17 were switched from a cervical exploration to a minimally invasive parathyroidectomy approach.

In 24 of 26 (92%) patients who had surgery, hyperfunctioning parathyroid tissue (adenoma/hyperplasia/cancer) was correctly localized with ^{18}F-FCH (26 lesions), compared with 15 patients with ^{11}C-MET (16 lesions). On a per-patient basis, the positive predictive value was 96% for ^{18}F-FCH and 94% for ^{11}C-MET. One patient was negative on both PET/CT scans and underwent a surgical exploration allowing the resection of a PA followed by calcemia normalization. No hyperfunctioning parathyroid tissue was found in a patient with persistent pHPT after surgery. The per-patient sensitivity of ^{18}F-FCH PET/CT was 96%, compared with 60% for ^{11}C-MET PET/CT ($P < 0.0001$). In addition, 5 patients had multiglandular disease detected on ^{18}F-FCH PET/CT (19%). Postoperative calcemia used to define therapeutic success was obtained at 11.5 ± 6.9 mo after surgery. Twenty-one (81%) patients who underwent parathyroidectomy were considered cured, 3 (12%) patients had recurrent or persistent hypercalcemia, and 2 patients were lost to follow-up.

The comparison of lesion visual scoring performance between the 2 tracers is reported in Supplemental Table 1. ^{18}F-FCH PET/CT detected a single uptake area in 37 of 53 patients and multiple uptake areas in 7 of 53 patients. On per-lesion basis (Table 2), ^{18}F-FCH PET/CT showed 47 positive and 9 inconclusive uptake areas. ^{18}F-FCH PET/CT allowed detection of 11 additional uptake areas (6 positive and 5 inconclusive) compared with ^{11}C-MET PET/CT. Thirteen inconclusive uptake areas on ^{11}C-MET were positive on ^{18}F-FCH. Three ectopic parathyroid glands in the superior mediastinum and 2 intrathyroidal localizations were identified with both PET tracers. Comparison of tracers for visual scoring performance on a per-lesion basis revealed the superiority of ^{18}F-FCH over ^{11}C-MET PET/CT (Wilcoxon $P < 0.0001$). Again, the McNemar test revealed, as well, the superiority of ^{18}F-FCH over ^{11}C-MET PET/CT for visual decision performance on a per-lesion basis ($P < 0.0001$; $\chi^2 = 17.053$ with $1°$ of freedom), with 19 lesions positive only with ^{18}F-FCH PET/CT and no lesion positive only with ^{11}C-MET PET/CT, whereas 28 lesions were positive and 18 were negative with both tracers. Except for 2 lesions with rapid washout visualized only on ^{18}F-FCH$_E$, and 1 uncertain lesion found only on ^{18}F-FCH$_L$, all lesions were visualized on early and late acquisitions,
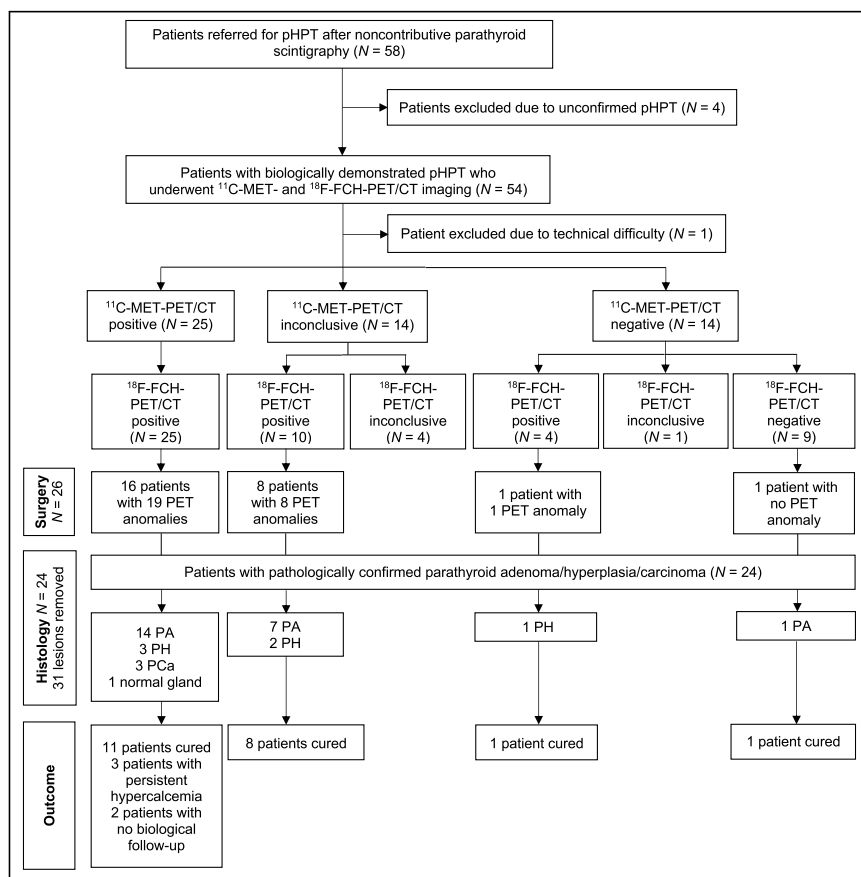

FIGURE 1. Flowchart. PCa = parathyroid carcinoma; PH = parathyroid hyperplasia.

TABLE 1
Patient Characteristics (n = 53)

Characteristic	Value	Normal value
Sex (M/F)	16/37	
Age (y)	58 ± 16	
Body mass index (kg/m^2)	28.2 ± 5.5	
Prior parathyroidectomy	7 (13)	
Prior		
^{99m}Tc-MIBI SPECT/CT		
Negative	38 (72)	
Inconclusive	15 (28)	
Ultrasonography	35 (66)	
Other	9 (17)	
Baseline laboratory values		
PTH (ng/L)	72.0 (54–101)	4–49
Calcium (mmol/L)	2.67 (2.62–2.69)	2.12–2.62
Phosphorus (mmol/L)	0.75 ± 0.17	0.81–1.45
25-hydroxycholecalciferol (ng/mL)	24.74 ± 8.97	30–80
^{11}C-MET results		
Positive	25 (47)	
Negative*	28 (53)	
^{18}F-FCH results		
Positive	39 (74)	
Negative*	14 (26)	
Surgical results (n = 26)		
Pathologic parathyroid tissue found	24 (92)	
Biologic normalization during follow-up	21 (81)[†]	

*Negative imaging includes negative or inconclusive results.

[†]2 patients were lost to follow-up.

Qualitative data are number and percentage; continuous data are mean ± SD; nonnormal continuous data are median and 25th–75th percentiles (D'Agostino–Pearson omnibus test).

without a significant difference in visual scoring assessment of contrast. Two cases are illustrated in Supplemental Figure 2.

In total, 31 glands were surgically removed, and histology revealed 22 PAs, 6 hyperplastic glands, and 3 parathyroid carcinomas

TABLE 2
Contingency Tables

Parameter	Positive ^{18}F-FCH	Negative ^{18}F-FCH	Total
Per patient			
Positive ^{11}C-MET	25	0	25
Negative ^{11}C-MET	14	14	28
Total	39	14	53
Per lesion			
Positive ^{11}C-MET	28	0	38
Negative ^{11}C-MET	19	18	37
Total	47	18	75

(Supplemental Table 2). The locations of removed glands are listed in Supplemental Table 1.

All localizations described on PET/CT were concordant with surgery, except for 1 patient with a multiple endocrine neoplasia in which the uptake area was found in the lower left retropolar region on PET/CT whereas the PA was identified in the lower right retropolar region; 2 normal glands were also surgically removed on the left in this patient. In another patient with multiple foci observed on ^{18}F-FCH and ^{11}C-MET, pathologic tissue had probably been left in place because he was not cured after removal of 1 correctly localized lesion (parathyroid hyperplasia) and 2 thyroid nodules. One uptake area found on both PET/CT scans was not explored during surgery, and in 4 cases, parathyroid hyperplasia was found in false-negative ^{18}F-FCH PET/CT locations. On a per-lesion basis (Supplemental Table 2), sensitivity and positive predictive value were 84% and 90%, respectively, for ^{18}F-FCH PET/CT and 52% and 94%, respectively, for ^{11}C-MET PET/CT ($P < 0.0001$).

Contrast-to-Thyroid and PA Uptake Are Significantly Higher with ^{18}F-FCH PET/CT Than with ^{11}C-MET PET/CT

The visual comparison of the contrast-to-background in the detected anomalies for ^{18}F-FCH and ^{11}C-MET revealed a

superiority of ^{18}F-FCH over ^{11}C-MET, both at early and at late imaging times (Supplemental Fig. 3). Higher uptake was observed in 71%–82% (39–45/55) of anomalies for ^{18}F-FCH than for ^{11}C-MET, and a similar uptake of the 2 tracers was observed in 25% (14/55) and 16% (9/55) of cases for ^{18}F-FCH$_E$ and ^{18}F-FCH$_L$, respectively. When we consider only the cases that underwent parathyroidectomy, we found similar proportions. Only 1 case operated on had a lesion better visualized on ^{11}C-MET than on ^{18}F-FCH PET/CT.

Supplemental Figure 4 shows the distribution of SUV$_{max}$ PA and PA/thyroid for each tracer. SUV$_{max}$ PA on ^{18}F-FCH$_E$ and ^{18}F-FCH$_L$, given as median, was 3.26 (25th–75th percentiles, 2.45–4.74) and 3.52 (25th–75th percentiles, 2.58–4.91), respectively, whereas the median SUV$_{max}$ PA on ^{11}C-MET was 1.51 (25th–75th percentiles, 0.96–2.73). So, the SUV$_{max}$ PA on ^{18}F-FCH$_E$ and ^{18}F-FCH$_L$ was approximatively twice higher than ^{11}C-MET SUV$_{max}$ ($P < 0.0001$). There was no statistically significant difference between SUV$_{max}$ PA and PA/thyroid on ^{18}F-FCH$_E$ and ^{18}F-FCH$_L$ ($P = 0.3569$). PA/thyroid on ^{18}F-FCH$_E$ and ^{18}F-FCH$_L$ was 1.39 (25th–75th percentiles, 1.29–1.54) and 1.39 (25th–75th percentiles, 1.29–1.68), respectively ($P = 0.1005$). The quantitative analysis resulted in nonsignificant differences for both SUV$_{max}$ and PA/thyroid between adenoma and hyperplasia on both ^{18}F-FCH and ^{11}C-MET PET/CT.

We observed a positive correlation between PA/thyroid on ^{11}C-MET and ^{18}F-FCH PET/CT, despite the difference in the incorporation mechanisms (Fig. 2). Linear fit revealed that PA/thyroid was 11% higher in ^{18}F-FCH$_E$ and 31% higher in ^{18}F-FCH$_L$ than in ^{11}C-MET: for ^{18}F-FCH$_E$, $r = 0.6843$, with a slope of 1.11 and an intercept of 0.0175, and $r^2 = 0.79$; for ^{18}F-FCH$_L$, $r = 0.5665$, with a slope of 1.315 and an intercept of 0.046, and $r^2 = 0.75$.

DISCUSSION

To the best of our knowledge, this was the first study comparing ^{11}C-MET and ^{18}F-FCH tracers for the preoperative detection and localization of hyperfunctioning parathyroid tissue. Our results demonstrate the diagnostic superiority of ^{18}F-FCH over ^{11}C-MET PET/CT for PA and hyperplasia detection in patients with negative or inconclusive results on ^{99m}Tc-MIBI exploration.

Precise preoperative localization of a hyperfunctioning parathyroid gland is a prerequisite for efficient minimally invasive surgery. For this purpose, PET/CT recently emerged as a complementary second-line imaging technique with the advantage of a higher

resolution associated with PET than with SPECT, as well as a shorter acquisition time (14).

Several publications concluded that the diagnostic performance of ^{18}F-FCH and ^{11}C-MET PET/CT for the localization of parathyroid lesions is better than that of conventional imaging methods (3,7,8,11,15–17). The present study confirmed the added value of this new tracer in the detection and precise localization of hyperfunctioning parathyroid tissue in the subgroup of patients with pHPT and negative or inconclusive results for ^{99m}Tc-MIBI with SPECT. The sensitivity of ^{18}F-FCH PET/CT was 96% on a per-patient basis and 84% on a per-lesion basis. As in the APACH1 study (8), we considered the histopathologic results as the gold standard for per-lesion analyses (8). Our findings are comparable to those reported in previous studies. A recent metaanalysis (18) concluded on pooled sensitivity of 93.7% and 91.3% on patient-based and lesion-based analyses, respectively. The detection rates of lesions were 77%–94% (on a patient basis) and 80%–96% (on a lesion basis) (15).

Our cohort included patients for whom the choice of surgical management was challenging (familial hyperparathyroidism, relapsing or persistent HPT, multiglandular forms) compared with most previous studies. Five of the 6 patients with persistent or relapsed postsurgical pHPT had areas of abnormal uptake revealed by ^{18}F-FCH, and we detected 19% of histologically confirmed multiglandular diseases. Still, most of our patients presented with a confirmed solitary lesion (81%), which was consistent with the rate reported in the literature (74% in Beheshti et al. (5)). There was no SUV$_{max}$ cutoff in ^{18}F-FCH that could be set to distinguish PA from parathyroid hyperplasia.

The optimal time point for ^{18}F-FCH image acquisition remains controversial (3,17,19,20). This controversy results from a 3-phase temporal pattern of ^{18}F-FCH PA uptake, with an early washout followed by an intermediate phase of stability and a late phase of increase (21). We therefore opted for a dual-time-point mode of acquisition in this study. On the basis of the visual evaluation of the images and the analysis of PA/thyroid, that is, a target-to-background ratio, we did not better discern lesions on the late images than on the early ones. Rep et al. (17) described in late-acquisition images a greater accumulation of ^{18}F-FCH in PA than in the thyroid, with a slightly slower decrease in signal, translating into a better lesion contrast. In agreement with our results, Broos et al. (19) reported a decrease in absolute uptake in PA over time, with an increase in contrast relative to the thyroid because of a weaker retention in the thyroid. Conversely, Michaud et al. (16) concluded that late images did not yield additional findings over early ones. Noticeably, in all previous studies, early images were acquired at 5 min after injection, whereas we decided for a slightly later acquisition. We found 2 patients with lesions showing a rapid ^{18}F-FCH washout in our population. Nevertheless, since most parathyroid lesions were observed on both acquisitions, we recommend performing the acquisition at 15 min, reserving additional late imaging for patients whose early acquisition has negative or inconclusive results, as also suggested by Uslu-Besli (22).

Before ^{18}F-FCH, ^{11}C-MET has been widely used as a reliable second-line agent in pHPT. Overall, in our study, ^{18}F-FCH showed a significantly higher sensitivity, with more cases diagnosed and higher accuracy than for ^{11}C-MET. The advantage of ^{18}F-FCH imaging
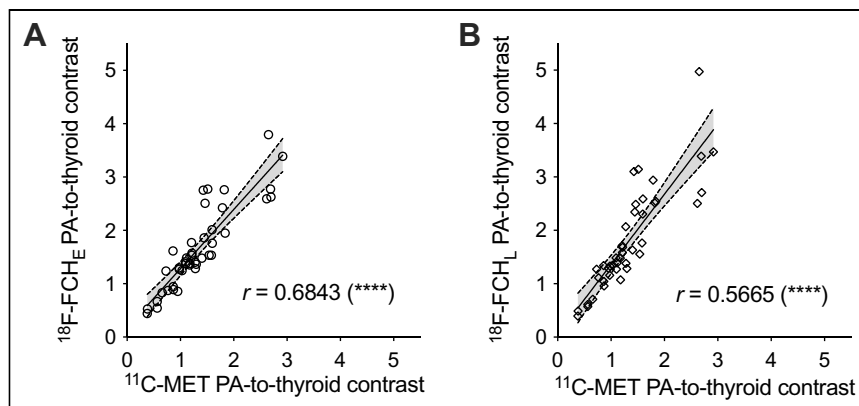

FIGURE 2. Correlation between ^{18}F-FCH (early [A] and late [B]) and ^{11}C-MET uptake. ****$P < 0.0001$.
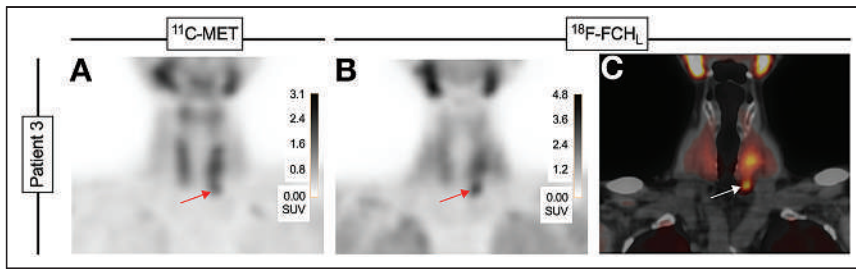
FIGURE 3. Patient 3. Coronal PET/CT images of 67-y-old woman with pHPT and inconclusive ^{99m}Tc-MIBI SPECT/CT (doubtful right inferior focus). (A) ^{11}C-MET images show asymmetric thyroid lobes with lower extension on left (arrow). (B) ^{18}F-FCH_L images shows nodular uptake under base of left thyroid lobe (arrow). (C) PET/CT images detail nodular aspect of ^{18}F-FCH uptake (arrow) in PA confirmed at histopathologic analysis.

over ^{11}C-MET imaging seems to be strongly related to the fact that it produces more conclusive data. Indeed, 13 anomalies judged inconclusive on ^{11}C-MET PET/CT were considered positive on ^{18}F-FCH PET/CT. The superior imaging qualities of ^{18}F-labeled radiotracers over ^{11}C-labeled ones probably contribute to this better performance of ^{18}F-FCH. Apart from an effect of the positron energy, differences in the molecular properties and uptake mechanisms involved probably explain the differences in diagnostic performance between ^{18}F-FCH and ^{11}C-MET. Indeed, the 2 tracers explore very different biochemical pathways. ^{11}C-MET uptake most probably depends on expression and activity of amino acid transporters such as L-type amino acid transporter 1 and secondarily on its incorporation in the protein prepro-PTH. So, ^{11}C-MET uptake may be closely dependent on the level of synthesis and release of PTH. In contrast, ^{18}F-FCH uptake enters chief cells—those responsible for PTH production—and oxyphilic cells of parathyroid tissue through a specific membrane transporter. After reaching the cytoplasm, ^{18}F-FCH accumulates in the mitochondria in relation to its positive charge, as is the case for ^{99m}Tc-MIBI. In the chief cells, ^{18}F-FCH is also phosphorylated by a choline-kinase, which is overexpressed in patients with pHPT, leading to a phosphorylated form—that is, phosphatidylcholine—incorporated into the cytoplasmic membrane. The fact that 2 different mechanisms favor ^{18}F-FCH incorporation into the PTH-producing cells may represent an advantage over the other tracers such as ^{11}C-MET and ^{99m}Tc-MIBI (23).

For the evaluation of patients with pHPT and negative or inconclusive ^{99m}Tc-MIBI SPECT results, a pooled sensitivity of 86% had been reported in a per patient-based analysis of ^{11}C-MET PET/CT (24). Two other metaanalyses reported sensitivity ranging from 69% to 81% and a detection rate per patient of 70% (6,9). In our population, we reached a slightly lower sensitivity (60%), probably related to a high prevalence of clinical statuses that negatively influence the outcome of presurgical localization imaging, that is, postsurgical recurrence and familiar forms of pHPT (12,15). The visual analysis more frequently resulted in inconclusive uptake on ^{11}C-MET than on ^{18}F-FCH PET/CT. Noticeably, as in other analyses (11), we assimilated inconclusive results to negative ones because we considered that such results would preclude valuable image-guided planning of a minimally invasive parathyroidectomy. Such a position is not adopted by all authors (8).

Our study had some limitations. First, it did not directly compare ^{18}F-FCH PET/CT with ^{99m}Tc-MIBI SPECT/CT. Such analyses have already been made, showing the far superiority of ^{18}F-FCH imaging (3,8,11,15–17). This comparison was not among the objectives of our study since we selected only patients with pHPT and negative or

inconclusive ^{99m}Tc-MIBI exploration. Consequently, our results cannot be extrapolated to patients with tertiary hyperparathyroidism and cannot determine to what extent ^{18}F-FCH should replace ^{99m}Tc-MIBI as first-line molecular imaging in pHPT. Also, not all patients underwent surgery after presurgical PET/CT. So, our findings on the diagnostic impact of ^{18}F-FCH PET/CT relate only to the 26 of 53 patients for whom histopathologic data were available.

Finally, although ^{18}F-FCH PET/CT shows good performance for hyperfunctioning parathyroid tissue localization, potential drawbacks must be considered before adopting this modality as the single presurgical imaging procedure in pHPT. As in previous studies (12), we observed false-positive and false-negative findings. The 3 false-positive results related to 1 case of localization discordance between PET/CT and surgery, 1 case of uptake in a normal parathyroid gland, and 1 case of uptake in a thyroid nodule. Even if all 3 cases are classified as false-positive because of the lack of histologic evidence of PA or parathyroid hyperplasia, 2 patients were not cured after surgery, leaving open the possibility that resection did not involve the lesions pointed out by ^{18}F-FCH PET/CT. Five false-negative results concerned 4 cases of parathyroid hyperplasia and 1 patient with recurrent pHPT who ultimately had a PA resection during an extensive bilateral neck exploration. As in previous studies (11,14,16), discordant PET/CT interpretation between readers occurred in 2 situations in which nodular uptake was found within the thyroid gland. The differential diagnosis between a hypermetabolic thyroid nodule and an intrathyroidal PA appeared difficult because of the lack of comparison with a specific thyroid tracer (14). Still, as illustrated in Figure 3 and Supplemental Figure 2, mild to moderate physiologic ^{18}F-FCH uptake by the thyroid did not affect image interpretation in most of our cases, contrary to what has been reported (5). Another source of potential misinterpretation (Supplemental Table 3) is the presence of reactive lymph nodes in classic locations for PAs. Globally, despite the high prevalence of nodular thyroid in our patients and the frequent occurrence of hypermetabolic lymph nodes, both ^{18}F-FCH and ^{11}C-MET PET/CT correctly localized the parathyroid lesions in most surgically treated patients.

To determine which PET tracer should be privileged for a particular indication, various factors must be considered, including availability, diagnostic performance, and duration of examination (25). ^{18}F-FCH outperforms ^{11}C-MET for these 3 criteria.

CONCLUSION

Our study demonstrated that in the presence of biochemical evidence of pHPT with negative or inconclusive ^{99m}Tc-MIBI results, ^{18}F-FCH PET/CT performs better than ^{11}C-MET PET/CT for the detection of pathologic parathyroid tissue, allowing localization of PA or hyperplasia in 96% of patients. Since ^{18}F-FCH has been proved to be superior to ^{99m}Tc-MIBI in previous studies, our results position ^{18}F-FCH PET/CT as the modality of choice for lesion localization in pHPT.

DISCLOSURE

No potential conflict of interest relevant to this article was reported.

<div style="background:#eee;">

KEY POINTS

QUESTION: Is ^{18}F-FCH superior to ^{11}C-MET PET/CT for the localization of hyperfunctioning parathyroid tissue in patients with pHPT and negative or inconclusive ^{99m}Tc-MIBI SPECT findings?

PERTINENT FINDINGS: In this prospective clinical study, ^{18}F-FCH correctly localized lesions in 92% of patients, compared with 58% by ^{11}C-MET.

IMPLICATIONS FOR PATIENT CARE: ^{18}F-FCH is more sensitive than ^{11}C-MET for the localization of hyperfunctioning parathyroid tissue in patients with pHPT and negative or inconclusive ^{99m}Tc-MIBI SPECT results.

</div>

REFERENCES

1. Hindié E, Zanotti-Fregonara P, Tabarin A, et al. The role of radionuclide imaging in the surgical management of primary hyperparathyroidism. *J Nucl Med.* 2015;56: 737–744.

2. Bilezikian JP, Brandi ML, Eastell R, et al. Guidelines for the management of asymptomatic primary hyperparathyroidism: summary statement from the fourth international workshop. *J Clin Endocrinol Metab.* 2014;99:3561–3569.

3. Lezaic L, Rep S, Sever MJ, Kocjan T, Hocevar M, Fettich J. ^{18}F-fluorocholine PET/CT for localization of hyperfunctioning parathyroid tissue in primary hyperparathyroidism: a pilot study. *Eur J Nucl Med Mol Imaging.* 2014;41:2083–2089.

4. Treglia G, Sadeghi R, Schalin-Jäntti C, et al. Detection rate of ^{99m}Tc-MIBI single photon emission computed tomography (SPECT)/CT in preoperative planning for patients with primary hyperparathyroidism: a meta-analysis. *Head Neck.* 2016;38(suppl 1):E2159–E2172.

5. Beheshti M, Hehenwarter L, Paymani Z, et al. ^{18}F-fluorocholine PET/CT in the assessment of primary hyperparathyroidism compared with ^{99m}Tc-MIBI or ^{99m}Tc-tetrofosmin SPECT/CT: a prospective dual-centre study in 100 patients. *Eur J Nucl Med Mol Imaging.* 2018;45:1762–1771.

6. Kluijfhout WP, Pasternak JD, Drake FT, et al. Use of PET tracers for parathyroid localization: a systematic review and meta-analysis. *Langenbecks Arch Surg.* 2016; 401:925–935.

7. Tang B-N-T, Moreno-Reyes R, Blocklet D, et al. Accurate pre-operative localization of pathological parathyroid glands using ^{11}C-methionine PET/CT. *Contrast Media Mol Imaging.* 2008;3:157–163.

8. Quak E, Blanchard D, Houdu B, et al. F18-choline PET/CT guided surgery in primary hyperparathyroidism when ultrasound and MIBI SPECT/CT are negative or inconclusive: the APACH1 study. *Eur J Nucl Med Mol Imaging.* 2018; 45:658–666.

9. Caldarella C, Treglia G, Isgrò MA, Giordano A. Diagnostic performance of positron emission tomography using ^{11}C-methionine in patients with suspected parathyroid adenoma: a meta-analysis. *Endocrine.* 2013;43:78–83.

10. Quak E, Lheureux S, Reznik Y, Bardet S, Aide N. F18-choline, a novel PET tracer for parathyroid adenoma? *J Clin Endocrinol Metab.* 2013;98:3111–3112.

11. Michaud L, Burgess A, Huchet V, et al. Is ^{18}F-fluorocholine-positron emission tomography/computerized tomography a new imaging tool for detecting hyperfunctioning parathyroid glands in primary or secondary hyperparathyroidism? *J Clin Endocrinol Metab.* 2014;99:4531–4536.

12. Grimaldi S, Young J, Kamenicky P, et al. Challenging pre-surgical localization of hyperfunctioning parathyroid glands in primary hyperparathyroidism: the added value of ^{18}F-fluorocholine PET/CT. *Eur J Nucl Med Mol Imaging.* 2018;45:1772–1780.

13. Otabashi M, Desfours C, Vergote T, Brichard L, Morelle J-L, Philippart G. Automated production of high purity [^{18}F]fluorocholine at high activity on the AllInOne Synthesizer [abstract]. *J Nucl Med.* 2016;57(suppl 2):2732.

14. Imperiale A, Taïeb D, Hindié E. ^{18}F-fluorocholine PET/CT as a second line nuclear imaging technique before surgery for primary hyperparathyroidism. *Eur J Nucl Med Mol Imaging.* 2018;45:654–657.

15. Kluijfhout WP, Vorselaars WMCM, van den Berk SAM, et al. Fluorine-18 fluorocholine PET-CT localizes hyperparathyroidism in patients with inconclusive conventional imaging: a multicenter study from The Netherlands. *Nucl Med Commun.* 2016;37:1246–1252.

16. Michaud L, Balogova S, Burgess A, et al. A pilot comparison of ^{18}F-fluorocholine PET/CT, ultrasonography and ^{123}I/^{99m}Tc-sestaMIBI dual-phase dual-isotope scintigraphy in the preoperative localization of hyperfunctioning parathyroid glands in primary or secondary hyperparathyroidism: influence of thyroid anomalies. *Medicine (Baltimore).* 2015;94:e1701.

17. Rep S, Lezaic L, Kocjan T, et al. Optimal scan time for evaluation of parathyroid adenoma with [^{18}F]-fluorocholine PET/CT. *Radiol Oncol.* 2015;49:327–333.

18. Evangelista L, Ravelli I, Magnani F, et al. ^{18}F-choline PET/CT and PET/MRI in primary and recurrent hyperparathyroidism: a systematic review of the literature. *Ann Nucl Med.* 2020;34:601–619.

19. Broos WA, Wondergem M, van der Zant F, Knol R. Dual-time-point ^{18}F-fluorocholine PET/CT in parathyroid imaging. *J Nucl Med.* 2019;60:1605–1610.

20. Jun G, Pampaloni MH, Villanueva-Meyer J, Ravanfar V, Suh I, Hope T. 18-F-fluorocholine PETMR: optimizing injection delay for parathyroid adenoma localization [abstract]. *J Nucl Med.* 2018;59(suppl 1):236.

21. Morland D, Richard C, Godard F, Deguelte S, Delemer B. Temporal uptake patterns of ^{18}F-fluorocholine among hyperfunctioning parathyroid glands. *Clin Nucl Med.* 2018;43:504–505.

22. Uslu-Beşli L, Sonmezoglu K, Teksoz S, et al. Performance of F-18 fluorocholine PET/CT for detection of hyperfunctioning parathyroid tissue in patients with elevated parathyroid hormone levels and negative or discrepant results in conventional imaging. *Korean J Radiol.* 2020;21:236–247.

23. Ferrari C, Santo G, Mammucci P, Pisani AR, Sardaro A, Rubini G. Diagnostic value of choline PET in the preoperative localization of hyperfunctioning parathyroid gland(s): a comprehensive overview. *Biomedicines.* 2021;9:231.

24. Yuan L, Liu J, Kan Y, Yang J, Wang X. The diagnostic value of ^{11}C-methionine PET in hyperparathyroidism with negative ^{99m}Tc-MIBI SPECT: a meta-analysis. *Acta Radiol.* 2017;58:558–564.

25. Giovanella L, Bacigalupo L, Treglia G, Piccardo A. Will ^{18}F-fluorocholine PET/CT replace other methods of preoperative parathyroid imaging? *Endocrine.* 2021; 71:285–297.

Glucagonlike Peptide-1 Receptor Imaging in Individuals with Type 2 Diabetes

Hsiaoju Lee[1] and Lisa J. States[2]

[1]University of Pennsylvania, Philadelphia, Pennsylvania; and [2]Children's Hospital of Philadelphia, Philadelphia, Pennsylvania

Radiolabeled exendin 4, the glucagonlike peptide-1 (GLP-1) receptor agonist, has great prospects for imaging and perhaps quantification of pancreatic β-cells. The GLP-1 receptor is found in high density in the pancreas and liver and plays a key role in postprandial blood glucose homeostasis, including stimulation of insulin synthesis and promotion of β-cell proliferation. β-cells constitute only a small volume of the pancreatic mass, comprising up to 2% of the pancreatic mass and 65%–80% of endocrine cells in the islets of Langerhans. A synthetic peptide agonist of the GLP-1 receptor, exendin-4, also known as exenatide, is used for the treatment of diabetes mellitus, making it an ideal peptide for radiotracer development (1,2). The desire to quantify β-cell mass has been a focus of radiotracer research since the initial first-in-humans studies by Boss et al., which have led to a variety of SPECT and PET radiotracers focused on different targets of glucose metabolism. Initially, Boss described a high-specificity and nanomolar-affinity radioiodinated tracer for the GLP-1 receptor (3). It is assumed from studies by Eng et al. that the GLP-1 receptor density reflects β-cell mass (4). Improvements in the spatial resolution and sensitivity of PET scanners have fueled the recent focus on PET radiotracers for this application.

In this issue of *The Journal of Nuclear Medicine,* the article by Eriksson et al. (5) demonstrates a stepwise approach necessary for GLP-1-receptor–targeting radiotracer development from the lab to the clinic. The authors investigated the utility of ^{68}Ga-labeled 1,4,7-tris(carboxymethylaza)cyclododecane-10-azaacetyl (DO3A)-exendin-4 (^{68}Ga-exendin4) in adults with type 2 diabetes (T2D) and its association with β-cell mass in overweight-to-obese T2D individuals, building on prior studies (6,7). Furthermore, the authors provided a simplified imaging protocol, a step toward higher throughput needed for large clinical trials.

The strengths of this article include the description of preclinical data collected in vitro and in vivo using nonhuman primates. The in vitro studies define binding specificity and internalization characteristics and were followed by nonhuman primate studies evaluating dose escalation and self-blocking effect. The evaluation of biodistribution and physiology in nonhuman primates provided safety information and guidance for the application in human adults.

In addition to the preclinical data, the authors also provided the initial evaluation in overweight-to-obese individuals. This study of 13 human subjects, 12 men and 1 woman, gives information on biodistribution and kinetics in the mostly male subjects. The results of this study show high pancreatic uptake compared with background activity. An unsuspected finding was variability in pancreatic radiotracer uptake across patients. This prompted further investigation, which revealed no association of uptake with pancreatic volume or patient age, as β-cell mass is thought to be uniformly distributed and to decrease with age.

The self-blocking evaluation described in this paper is an important analysis used in the evaluation of a novel radiotracer to show strong binding in the presence of cold peptide, representing endogenous proteins or administered medication. This competitive binding is of great importance because the treatment dose of exenatide is in the microgram range. The authors studied the effect of higher mass by coinjecting the study participants with up to 0.2 μg/kg. The study team did not observe a difference in the volume of distribution at the lower dose; however, a decrease in binding was seen at 0.45 μg/kg. We found this information encouraging for the development of an ^{18}F-labeled exendin-4 analog, which suffered the drawback of requiring a higher amount of labeling precursor and difficulties of purification. Compared with ^{68}Ga, ^{18}F-labeled tracers offer several distinct advantages, including longer half-life (118 vs. 60 min), higher amount of starting activity (cyclotron bombardment vs. limit on the ^{68}Ge generator synthesis), and ideal imaging qualities. All warrant the need to develop an ^{18}F-labeled exendin-4 analog. A successful ^{18}F-labeled exendin-4 analog can also enable the distribution of large-scale, multicenter trials needed for tackling the complex question of β-cell mass quantification and monitoring and provides less focus on sophisticated equipment and expertise (cyclotron and radiochemist) while still allowing joint efforts in research.

The proposed goal of this study was achieved by providing a recommendation for a protocol to be used in human subjects for subsequent phase II and III trials in adults. This phase I study also evaluated the safety and utility of a safe dose range, resulting in a proposed dose. Technical efficacy was achieved by providing image generation and procedural feasibility, which is addressed in the discussion. A limitation of this study is related to sample size. Although a phase I study does not require a control population or randomization, a larger cohort pool enables the establishment of a better baseline. The small sample size makes it impractical to consider a variety of subject characteristics. Further investigations should evaluate female subjects and subjects of racial backgrounds known to have a high incidence of diabetes.

As stated in the abstract, the overall goal of this project is to enable longitudinal studies of the GLP-1 receptor in the human pancreas. The next step in this research would be a test–retest study to evaluate the within-subject variability of tracer uptake. The changes caused by the pathologic progression of T2D or type 1 diabetes (T1D) are likely to be small and will have to be followed over time to assess disease stability or progression. A tracer with small test–retest variability would be crucial to detect the difference throughout the course of disease. This would allow for monitoring changes in density, occupancy, or functionality (8). The intrasubject variability is an important step needed to assess feasibility for repeat studies to evaluate the efficacy of medications. One of the questions to be answered is the reason for subject variability in tracer uptake. Is this caused by the status of the GLP-1 receptor, the volume of the pancreas, or other reasons? Additional studies to elucidate the relationship will provide additional insight to show clinical utility in the monitoring of treatment. A radiotracer to evaluate the density of the β-cell mass would have a great impact on the management of disease, on understanding of the pathologic processes, and on evaluation of the ability of medical treatment to stabilize or potentially reverse disease.

The overall impact of this work extends beyond this subgroup of T2D. Diabetes is not only an adult disease. T1D is a pediatric disease with onset typically in the second decade of life and is characterized by a progressive destruction of up to 70% of β-cell mass. T1D is increasing in prevalence and accounts for up to 10% of cases of diabetes worldwide (9). Diabetes progression is evaluated clinically on the basis of insulin needs; however, insulin needs do not necessarily predict β-cell mass, as there is a significant loss of β-cell mass before detection. This promising PET radiotracer can potentially have a pivotal role in the assessment of the stage of disease and response to therapy for both T1D and T2D. If successful, the translation to pediatric care will have the potential to alter the progression of disease in adolescents and young adults, thus improving the quality of life for children and adults with diabetes. This article is an important contribution to the literature and successfully shows technical efficacy, reproducible image generation of the pancreas, and procedural feasibility with a proposed protocol.

DISCLOSURE

No potential conflict of interest relevant to this article was reported.

REFERENCES

1. Htike ZZ, Zaccardi F, Papamargaritis D, Webb DR, Khunti K, Davies MJ. Efficacy and safety of glucagon-like peptide-1 receptor agonists in type 2 diabetes: a systematic review and mixed-treatment comparison analysis. *Diabetes Obes Metab.* 2017; 19:524–536.
2. Yap MKK, Misuan N. Exendin-4 from *Heloderma suspectum* venom: from discovery to its latest application as type II diabetes combatant. *Basic Clin Pharmacol Toxicol.* 2019;124:513–527.
3. Boss M, Buitinga M, Jansen TJP, Brom M, Visser EP, Gotthardt M. PET-based human dosimetry of ^{68}Ga-NODAGA-exendin-4, a tracer for β-cell imaging. *J Nucl Med.* 2020;61:112–116.
4. Eng J, Kleinman WA, Singh L, Singh G, Raufman JP. Isolation and characterization of exendin-4, an exendin-3 analogue, from *Heloderma suspectum* venom: further evidence for an exendin receptor on dispersed acini from guinea pig pancreas. *J Biol Chem.* 1992;267:7402–7405.
5. Eriksson O, Velikyan I, Haack T, et al. Glucagonlike peptide-1 receptor imaging in individuals with type 2 diabetes. *J Nucl Med.* 2021;63:794–800.
6. Tillner J, Posch MG, Wagner F, et al. A novel dual glucagon-like peptide and glucagon receptor agonist SAR425899: results of randomized, placebo-controlled first-in-human and first-in-patient trials. *Diabetes Obes Metab.* 2019;21:120–128.
7. Eriksson O, Haack T, Hijazi Y, et al. Receptor occupancy of dual glucagon-like peptide 1/glucagon receptor agonist SAR425899 in individuals with type 2 diabetes. *Sci Rep.* 2020;10:16758.
8. Van de Bittner GC, Ricq EL, Hooker JM. A philosophy for CNS radiotracer design. *Acc Chem Res.* 2014;47:3127–3134.
9. Lipman TH, Levitt Katz LE, Ratcliffe SJ, et al. Increasing incidence of type 1 diabetes in youth: twenty years of the Philadelphia Pediatric Diabetes Registry. *Diabetes Care.* 2013;36:1597–1603.

Glucagonlike Peptide-1 Receptor Imaging in Individuals with Type 2 Diabetes

Olof Eriksson[1,2], Irina Velikyan[3,4], Torsten Haack[5], Martin Bossart[5], Iina Laitinen[6], Philip J. Larsen[7], Jan Erik Berglund[8], Gunnar Antoni[3,4], Lars Johansson[1], Stefan Pierrou[1], Joachim Tillner[9], and Michael Wagner[5]

[1]Antaros Medical AB, Uppsala, Sweden; [2]Science for Life Laboratory, Department of Medicinal Chemistry, Uppsala University, Uppsala, Sweden; [3]Department of Medicinal Chemistry, Uppsala University, Uppsala, Sweden; [4]Akademiska Sjukhuset, Uppsala, Sweden; [5]R&D Research Platform, Integrated Drug Discovery, Sanofi, Frankfurt, Germany; [6]Global Imaging, Sanofi, Frankfurt, Germany; [7]Diabetes Research, Sanofi, Frankfurt, Germany; [8]Clinical Trial Consultants AB, Uppsala, Sweden; and [9]Translational Medicine, Sanofi, Frankfurt, Germany

The glucagonlike peptide-1 receptor (GLP1R) is a gut hormone receptor, intricately linked to regulation of blood glucose homeostasis via several mechanisms. It is an established and emergent drug target in metabolic disease. The PET radioligand ^{68}Ga-DO3A-VS-exendin4 (^{68}Ga-exendin4) has the potential to enable longitudinal studies of GLP1R in the human pancreas. **Methods:** ^{68}Ga-exendin4 PET/CT examinations were performed on overweight-to-obese individuals with type 2 diabetes ($n = 13$) as part of a larger target engagement study (NCT03350191). A scanning protocol was developed to optimize reproducibility (target amount of 0.5 MBq/kg [corresponding to peptide amount of <0.2 μg/kg], blood sampling, and tracer stability assessment). The pancreas and abdominal organs were segmented, and binding was correlated with clinical parameters. **Results:** Uptake of ^{68}Ga-exendin4 in the pancreas, but not in other abdominal tissues, was high but variable between individuals. There was no evidence of self-blocking of GLP1R by the tracer in this protocol, despite the high potency of exendin4. The results showed that a full dynamic scan can be simplified to a short static scan, potentially increasing throughput and reducing patient discomfort. The ^{68}Ga-exendin4 concentration in the pancreas (i.e., GLP1R density) correlated inversely with the age of the individual and tended to correlate positively with body mass index. However, the total GLP1R content in the pancreas did not. **Conclusion:** In summary, we present an optimized and simplified ^{68}Ga-exendin4 scanning protocol to enable reproducible imaging of GLP1R in the pancreas. ^{68}Ga-exendin4 PET may enable quantification of longitudinal changes in pancreatic GLP1R during the development of type 2 diabetes, as well as target engagement studies of novel glucagonlike peptide-1 agonists.

Key Words: GLP1R; PET; exendin; type 2 diabetes; β-cell mass

The glucagonlike peptide-1 (GLP1) receptor (GLP1R) is a gut hormone receptor intricately linked to regulation of blood glucose homeostasis via several mechanisms such as insulin secretion, gastric emptying, and control of food intake (1). Endogenous GLP1 peptide is released from the intestinal L cells in response to nutrient intake. Synthetic GLP1 agonists are already approved for treatment of such conditions as type 2 diabetes (T2D), and further insight into their mechanism of action is still of the utmost interest. Several recent studies have demonstrated beneficial effects of GLP1 agonists on hemoglobin A1c, cardiac function, and survival (2,3).

Exendin4 is a synthetic peptide that binds to GLP1R with nanomolar affinity and high specificity (4). The development of ^{68}Ga-radiolabeled analogs of exendin4 (5,6) has recently enabled noninvasive PET imaging in humans, primarily for the diagnosis and localization of insulinomas (7,8), as well as expression of GLP1R in the pancreas.

The possibility of longitudinal imaging to quantify GLP1R density in the pancreas is of interest both in the assessment of drug mechanisms of action (e.g., in the context of unimolecular dual and trigonal agonists) (9,10) and because of the potential association between GLP1R expression and the remaining β-cell mass (11). Here, we used ^{68}Ga-DO3A-VS-exendin4 (^{68}Ga-exendin4) for PET imaging of GLP1R in the human pancreas. The current study was performed as part of a clinical trial investigating the target engagement of a novel GLP1/glucagon receptor dual agonist, SAR425899, in individuals with T2D (clinicaltrials.gov identifier NCT03350191) (12).

Here, we demonstrate for the first time—to our knowledge—the noninvasive quantification of GLP1R density in the pancreas of individuals with T2D by PET imaging. We furthermore outline a protocol for reproducible, longitudinal, and accurate ^{68}Ga-exendin4 PET/CT scanning and explore the origin of the variability of pancreatic GLP1R density this patient population.

MATERIALS AND METHODS

Nonhuman Primate (NHP) PET Study

A ^{68}Ga-exendin4 PET/CT imaging study on healthy cynomolgus NHPs was in part reported and described in detail previously (5). Briefly, NHPs were scanned by ^{68}Ga-exendin4 PET using a dose escalation study design in which several examinations were performed, several hours apart, over the course of one or several experimental days. Each subsequent scan entailed a higher peptide mass and radioactive dose to minimize influence from the preceding scan (Table 1). The resulting dataset enabled analysis of the self-blocking effect of the increasing amounts of coinjected unlabeled exendin4 precursor peptide.

TABLE 1
Overview of Dose Escalation of ^{68}Ga-Exendin4 and Coinjected DO3A-VS-Exendin4 in NHPs

Scan	Unit of measurement	NHP				
		1	2	3	4	5
	kg (body weight)	5.6	5.5	7.4	9.0	6.0
1	μg/kg	2	0.05	0.15	0.05	0.0025
	MBq	11.1	2.0	4.6	2.3	0.2
2	μg/kg	—	1	20	1	0.5
	MBq	—	6.5	11.1	6.7	6.9
3	μg/kg	—	10	—	3	15
	MBq	—	5.2	—	4.9	18.7

NHPs 2 and 5 were same individual scanned twice, 6 mo apart.

Previously, only the simplified SUV analysis of 3 of the NHPs (8 scans) was reported (5). In preparation for the design of the clinical study, to better understand the peptide doses at which self-blocking starts to occur, we reanalyzed the dynamic NHP data from all 12 scans by graphical analysis using an image-derived blood plasma input.

Pancreas and other tissues of interest (such as spleen as a negative reference tissue) were delineated using PMOD, version 4.0 (PMOD Technologies). The PET signal for each tissue and time frame was corrected for the injected amount, and the image-derived input function was extracted by segmenting voxels fully within the lumen of the descending aorta as identified on early PET frames and coregistered CT projections. The aorta signal was further corrected for the plasma partition.

The volume of distribution (V_t) of ^{68}Ga-exendin4 in the pancreas was estimated by graphical analysis according to Logan by applying the image-derived input function using the PMOD PKIN module (13). Patlak graphical analysis was also attempted (14), assuming irreversible uptake of ^{68}Ga-exendin4 in tissue due to receptor agonism and internalization, but this model failed in some individuals and is not reported.

The pancreatic V_t for each scan was plotted against the amount of coinjected unlabeled precursor peptide to explore the self-blocking at different doses.

Furthermore, the pancreatic V_t was plotted against the static uptake values at different time points, to determine whether static SUVs could replace full dynamic PET scans with invasive plasma sampling.

Clinical Study Design
These ^{68}Ga-exendin4 PET/CT examinations were acquired as part of a phase Ib single-center, open-label study assessing the glucagon receptor and GLP1R occupancy of dual-agonist SAR425899 in overweight-to-obese T2D patients (clinicaltrials.gov identifier NCT03 350191). Individuals with T2D ($n = 13$) were recruited and underwent PET/CT scanning for GLP1R availability in the pancreas (^{68}Ga-exendin4) and glucagon receptor availability in the liver (^{68}Ga-DO3A-VS-Tuna-2) at baseline. Participants were then treated with up to 0.12 or 0.2 mg of SAR425899 daily from 3 wk, followed by on-drug scanning with ^{68}Ga-exendin4 and ^{68}Ga-DO3A-VS-Tuna-2. Six participants completed the full NTC03350191 occupancy study, and the results from those individuals, especially the occupancy of SAR425899 as evaluated by PET, were previously reported (12). This study reports the results of all 13 baseline ^{68}Ga-exendin4 PET scans and the details of the procedures. The baseline examination of the 13 ^{68}Ga-DO3A-VS-Tuna-2 examinations was similarly reported independently (15).

Patient Population
Overweight-to-obese individuals diagnosed with T2D ($n = 13$) were recruited to the study. The participants had a median age of 69 y (range, 50–76 y) and a mean body mass index (BMI) of $31.2 \pm 3.0 \, \text{kg/m}^2$. Of the 13 participants, 12 were men and 1 was a woman. Patients were not allowed to be on any antidiabetic medication during the study except for stable metformin or sulfonylurea treatment.

No control group with nondiabetic individuals was included, since the full study was aimed at assessing drug efficacy and occupancy and thus included 3 wk of drug treatment with SAR425899.

All study participants provided written informed consent. Study protocols were approved by national health authorities and an independent ethics committee, and the trial was performed in accordance with the guidelines established by the Declaration of Helsinki and the International Conference on Harmonization–Good Clinical Practice.

PET/CT Examinations
Good-manufacturing-practice DO3A-exendin4 was provided by Sanofi. Good-manufacturing-practice–quality ^{68}Ga-exendin4 was produced on an automated synthesizer (Modular Lab Pharm Tracer; Eckert and Ziegler) as developed and reported previously (12,16). The radiochemical purity was over 90%, with no unknown single impurity of over 5%.

The PET assessments were performed 3 h after a standardized meal followed by fasting, to minimize the variability in GLP1 levels at the time of scanning. The individuals were examined over the abdomen with a Discovery MI PET/CT scanner (20-cm field of view; GE Healthcare). Low-dose CT was performed for attenuation correction and anatomic coregistration of PET images. The dose of the CT scan was limited by dosimetry considerations, given that each individual underwent up to 4 PET/CT examinations over the entire clinical study.

A 0.5 MBq/kg target dose of ^{68}Ga-exendin4 (0.46 ± 0.03 MBq/kg, corresponding to 0.14 ± 0.04 μg of peptide per kilogram) was administered intravenously as a bolus. The amount of administered ^{68}Ga-exendin4 was based primarily on limiting the associated dose of DO3A-VS-exendin4 precursor peptide to below 0.2 μg/kg. This limit was imposed to minimize any self-blocking, and the cutoff was determined from the NHP dose escalation studies.

Dynamic PET was initiated at administration and continued for 60 min. Blood sampling for glucose was performed before and during the scan as a safety precaution, as exendin4 can stimulate insulin secretion at pharmacologic doses. For 3 individuals, arterial sampling was performed at 5, 30, and 60 min after ^{68}Ga-exendin4 administration to measure the radioactivity in whole blood and plasma and to determine the metabolic stability of the tracer (the methods are shown in the supplemental materials, available at http://jnm.snmjournals.org) (17).

PET images were reconstructed using an iterative VUE Point FX-S algorithm (GE Healthcare) (3 iterations, 3 subsets, 256 × 256 matrix, 3-mm z-axis postprocessing filter) with all relevant corrections performed (30 frames in total: 12 × 10 s, 6 × 30 s, 5 × 120 s, 5 × 300 s, 2 × 600 s).

PET Image Analysis
Abdominal tissues of interest, including pancreas (target tissue), aorta (input signal), kidney (excretion), and spleen and erector spinae muscle (negative reference tissues) were manually segmented on coregistered PET/CT images using Carimas software, version 2.9 (Turku PET Center). The aorta was delineated by segmenting single voxels fully within the lumen of the descending aorta. The arterial plasma image-derived input function was generated by correcting the aorta signal for plasma–to–whole-blood partitioning and for the percentage of intact ^{68}Ga-exendin4 during the scan (based on a population estimate).

The kinetic data were fitted to different compartmental models and graphical analyses, including 1- and 2-tissue-compartment models and Patlak and Logan analysis. On the basis of the fitting, performance, and complexity of the models (Supplemental Tables 1–5), Patlak graphical analysis was selected as the optimal analysis method for the dynamic PET data. Furthermore, ^{68}Ga-exendin4 triggers internalization in GLP1R-positive tissues, leading to intracellular ^{68}Ga trapping (Supplemental Figs. 1A–1B), theoretically fulfilling the irreversible binding criteria during the time of the scanning as assumed in Patlak analysis. The ^{68}Ga-exendin4 net uptake rate (K_i) was estimated using Patlak graphical analysis in Microsoft Excel (*14*).

K_i (mL/[mL·h]) was considered a measurement of the concentration of ^{68}Ga-exendin4 binding in the pancreas (likely proportional to the GLP1R density in the pancreas). The total GLP1R content was thus estimated by multiplying K_i (mL/[mL·h]) by the pancreatic volume (mL) as segmented from the PET/CT images.

Statistics

Data on a group level are reported as mean ± SD. Differences between groups were assessed by 1-way ANOVA. Correlations were assessed by linear regression and the Pearson correlation coefficient (GraphPad Prism for Mac [Apple], version 8.0).

Data and Resource Availability Statements

The data that support the findings of this study are available from Sanofi, but restrictions apply to the availability of these data, which were used under license for the current study and therefore are not publicly available. Data are, however, available from the authors on reasonable request and with the permission of Sanofi.

RESULTS

NHP PET Dose Escalation Study

^{68}Ga-exendin4 exhibited visually strong binding and a high V_t in the pancreas on all scans coinjecting up to a 0.2 μg/kg dose of unlabeled DO3A-VS-exendin4 precursor peptide (Fig. 1A). There was already a sharp decrease in binding at a peptide mass dose of 1 μg/kg, whereas doses in excess of 10 μg/kg reduced the pancreas binding to the background level. The dose inducing a 50% decrease in binding (the in vivo half-maximal inhibitory concentration) was estimated to be approximately 0.45 μg/kg, indicating very high potency.

Binding was also estimated with a simple semiquantitative SUV measurement of pancreatic binding during the static time frame from 50 to 60 min after injection ($SUV_{55\,min}$). $SUV_{55\,min}$ correlated strongly with V_t ($P < 0.0001$, $r = 0.96$) (Fig. 1B).

Binding and Biodistribution in Individuals with T2D

^{68}Ga-exendin4 was rapidly distributed in the abdominal tissues after intravenous administration (Figs. 2A and 2B). Initially, the aorta and the left ventricle (i.e., blood signal) were clearly seen, followed by uptake in the pancreas, kidney, and liver in the first 5 min. For the remainder of the scan (60 min), increasing uptake in the pancreas and kidney continued, whereas the remaining tissues demonstrated clearance.

After 60 min, the uptake of ^{68}Ga-exendin4 (assessed as $SUV_{55\,min}$) was clearly higher in the pancreas than in, for example, the spleen, which has high perfusion comparable to that of the pancreas but is devoid of GLP1R (Fig. 2C). There was marked variability, almost 4-fold, in the magnitude of the pancreas uptake in different individuals (Figs. 2C and 2D). Importantly, this variability was not reflected in other abdominal tissues or the blood signal, indicating it is not due to general differences in biodistribution or metabolism.

^{68}Ga-exendin4 uptake was obvious in all 3 pancreatic segments—caput (head), corpus (body), and cauda (tail)—but tended to be higher in the cauda. However, separate delineation of the cauda was difficult because of potential spillover from the kidney in some individuals.

Metabolic Stability, Self-Blocking, and Protocol Simplification

After administration, ^{68}Ga-exendin4 demonstrated high stability in the blood, with more than 90% of the intact tracer being present in plasma at 60 min (Table 2). ^{68}Ga-exendin4 also exhibited high plasma partitioning (≈ 1.8) throughout the scan; that is, most tracer was free in the plasma and available for distribution into tissue (Table 2). The net K_i of ^{68}Ga-exendin4 in the pancreas was calculated by Patlak graphical analysis, using the metabolite-corrected arterial plasma curve as input (Table 3).

As per the study design, all individuals were administered less than a 0.2 μg/kg dose of DO3A-VS-exendin4 peptide to avoid self-blocking due to the high potency of the compound for GLP1R. As predicted, there was no negative correlation between the peptide mass dose and the net K_i, indicating that the self-blocking at these levels was also negligible in humans (Fig. 3A).

$SUV_{55\,min}$ correlated well with the net K_i ($P < 0.0001$, $r = 0.92$), indicating that the lengthy dynamic scanning and invasive blood sampling may be replaced by shorter static scanning from 50 to 60 min after tracer administration with only a minor loss in accuracy (Fig. 3B).

Correlation of Binding with Age and BMI

There was a distinct variability in the ^{68}Ga-exendin4 net K_i in the pancreas. We therefore explored the potential correlation between ^{68}Ga-exendin4 binding and the characteristics and biometrics of patients. The variability in ^{68}Ga-exendin4 binding as assessed by K_i (i.e., GLP1R density) correlated negatively with the age of the participant ($P < 0.05$, $r = -0.61$) (Fig. 4A). The same correlation with age, but using $SUV_{55\,min}$, was -0.50 ($P = 0.082$). Furthermore, there was a tendency toward a positive correlation between ^{68}Ga-exendin4
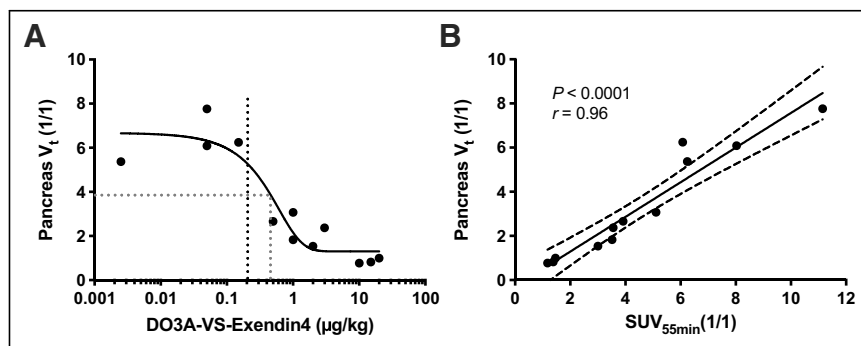

FIGURE 1. In vivo binding of ^{68}Ga-exendin4 in NHP pancreas. (A) Dose escalation studies demonstrated strong binding in pancreas at mass doses below 0.2 μg/kg (black dotted line), which was progressively blocked by coinjection of increasing amounts of unlabeled DO3A-VS-exendin4 precursor peptide. A 50% blocking dose is indicated by gray dotted line. (B) There was strong correlation between V_t (obtained from dynamic 90-min scan and requiring blood plasma input signal) and $SUV_{55\,min}$, indicating that just static scan from 50 to 60 min can replace dynamic scan.

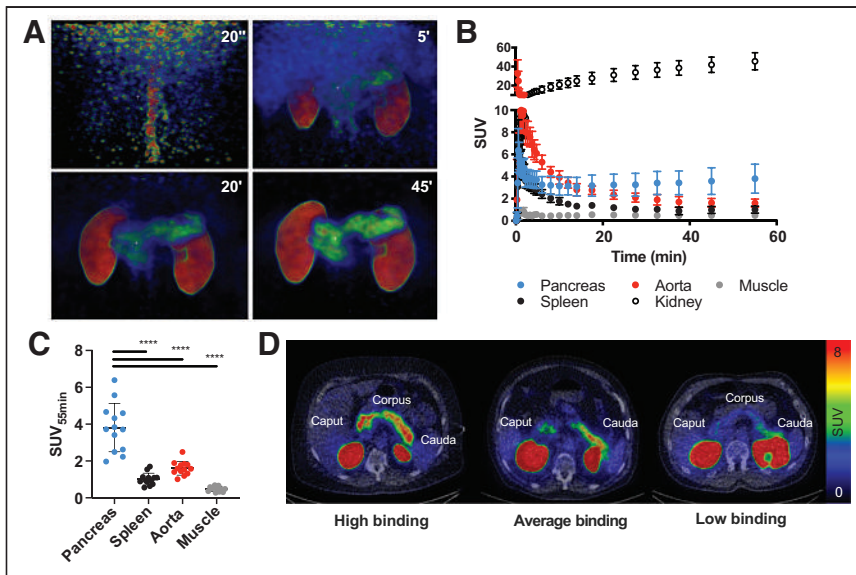**FIGURE 2.** Abdominal biodistribution of ^{68}Ga-exendin4 in humans with T2D. (A and B) ^{68}Ga-exendin4 was rapidly distributed, followed by washout from most tissues except pancreas and kidneys (average of 13 individuals). Representative maximum-intensity-projection PET images are shown. (C) There was strong variability in pancreas binding, which was not reflected in other tissues. (D) Representative transaxial PET/CT images demonstrate high, average, or low pancreas binding of ^{68}Ga-exendin4. ****indicates $P < 0.0001$.

binding in the pancreas and the BMI of the participants ($P = 0.064$, $r = 0.53$) (Fig. 4B). Similarly, the correlation between BMI and $SUV_{55\ min}$ was 0.43 ($P = 0.145$). However, when we estimated the total ^{68}Ga-exendin4 binding (i.e., total GLP1R content) by multiplying by the pancreatic volume, no correlations remained (Figs. 4C and 4D). The pancreatic volume of the participants ranged between 48 and 135 mL and did not correlate with, for example, age or BMI in this cohort (Figs. 4E and 4F).

DISCUSSION

In this study, we demonstrated the binding and biodistribution of ^{68}Ga-exendin4 in the pancreas of humans with T2D. Furthermore, we developed an optimized and simplified ^{68}Ga-exendin4 scanning protocol based on these initial experiences.

Native exendin4 is a highly potent GLP1R agonist, with subnanomolar potency (18). Radiolabeled ^{68}Ga-exendin4 has excellent specificity for GLP1R (Supplemental Fig. 1A) and affinity in the nanomolar range (19). In the absence of suitable antagonists, agonists such as exendin4 can be used as PET tracers, but care must be taken to avoid unwanted pharmacologic effects. We have previously demonstrated that ^{68}Ga-exendin4 also exhibits self-blocking at low administered precursor peptide mass doses in NHPs. Doses

of around 0.5 µg/kg elicit up to 50% blocking of the signal. This result is not entirely unexpected, given the high potency of ^{68}Ga-exendin4 for GLP1R. In fact, peptide mass effects of similar magnitude were seen for 2 other gut hormone peptide PET tracers, ^{68}Ga-DO3A-VS-Tuna-2 (a glucagon receptor agonist) and ^{68}Ga-S02-GIP-T4 (a glucose-dependent insulinotropic polypeptide receptor agonist), both with a potency in the picomolar range (20,21).

Here, we further demonstrated from NHP data that a peptide mass effect can be avoided at less than 0.2 µg/kg doses of coinjected DO3A-VS-exendin4. This finding influenced the design of the clinical study, which subsequently showed minimal mass effects. Thus, any future clinical studies with ^{68}Ga-exendin4 should aim to administer no more than a 0.2 µg/kg dose of precursor peptide. This limitation will likely entail an optimized automated radiochemistry setup (16), since a molar activity of at least 20–30 MBq/nmol will be required. Furthermore, even at an optimal molar activity, 0.2 µg/kg will probably correspond to no more than 50–100 MBq to be administered; this, in turn, necessitates highly sensitive PET instrumentation for sufficient image quality.

Quantitative PET assessment usually entails quite complex correction of imaging data, including dynamic imaging acquisition of a long duration, arterial sampling, and metabolic stability measurement. Such complicated scanning protocols present logistical challenges and are uncomfortable for the patient. Additionally, the

TABLE 2
Metabolic Stability and Blood Plasma Ratio of ^{68}Ga-Exendin4 in Individuals with T2D ($n = 3$)

Time (min)	Intact peptide (%)	Plasma-to-blood ratio (1/1)
5	98.1 ± 0.9	1.76 ± 0.06
30	95.2 ± 0.4	1.80 ± 0.05
60	90.1 ± 1.4	1.79 ± 0.05

TABLE 3
Patlak Graphical Analysis K_i Net Uptake Rate and Goodness of Fit for All Individuals Examined with ^{68}Ga-Exendin4

Individual	Volume (mL)	$SUV_{55\ min}$ (1/1)	K_i (mL/[mL·h])	R^2
1	78	3.4	0.60	0.99
2	69	6.4	0.93	1.0
3	48	2.0	0.38	0.97
4	66	3.8	0.62	0.98
5	63	3.7	0.63	0.98
6	78	4.3	0.83	0.99
7	59	2.2	0.45	0.99
8	73	3.7	0.59	1.0
9	57	2.5	0.38	0.99
10	49	2.6	0.43	0.97
11	75	4.6	0.83	0.99
12	135	4.7	0.58	0.99
13	117	5.6	0.97	1.0

$SUV_{55\ min}$ and pancreas volumes in same individuals are included for comparison.
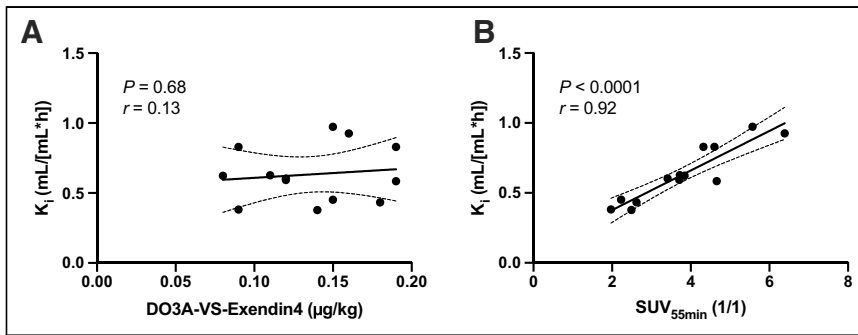
FIGURE 3. In vivo binding of ^{68}Ga-exendin4 in human T2D pancreas. (A) There was no obvious self-blocking mass effect at peptide doses below 0.2 μg/kg (i.e., no negative correlation). (B) In human pancreas, there was strong correlation between model parameter obtained from dynamic scan including blood (Patlak K_i) and $SUV_{55\,min}$, indicating that static scan is sufficient for accurate quantification.

analysis is time-consuming and requires specialized software and expertise. Semiquantitative measurements derived from static scanning protocols, such as SUVs, on the other hand, are simpler from the point of view of both the patient and the hospital, in addition to allowing for rapid analysis.

In both the NHP and the clinical studies, we could show that the static SUV (SUV_{55min}) exhibited a very strong correlation with the modeled parameter (which was derived from the full dynamic scanning protocol including blood sampling and metabolic stability correction of the input signal). Thus, it can be assumed that a shortened static scan at 50–60 min after injection provides reasonable accuracy in the assessment of GLP1R density in the pancreas, with only a minor loss in reproducibility compared with a full dynamic scan. In many cases, this trade-off may be acceptable to substantially increase patient comfort and simplify scanning procedures and logistics. However, ^{68}Ga-exendin4 uptake as assessed by $SUV_{55\,min}$ did not correlate as well with, for example, age as did Patlak net K_i, indicating that the simplification of the analysis and scanning protocol may reduce the power of the assessment.

A limitation of this study is the lack of a test–retest assessment, that is, repeated scanning of the same subject without any intervention in between. Such data would provide important information on the reproducibility of the assessment—either analyses by SUV_{55min} or analyses by Patlak net K_i. Unfortunately, test–retest scanning was not possible because of the design of the full occupancy study (clinicaltrials.gov identifier NCT03350191) (*12*).

In short, future PET studies using ^{68}Ga-exendin4 for assessment of GLP1R in the pancreas should aim to coinject less than a 0.2 μg/kg dose of peptide. Moreover, patient comfort and scanning throughput could be increased by limiting the scanning protocol to a static scan approximately 60 min after injection.

Despite the rigorous standardization of our scanning protocol, ^{68}Ga-exendin4 exhibited a marked variability in pancreatic binding. We further explored potential reasons for this variability. There was a negative correlation with age in this study, indicating a lower GLP1R density in the pancreas of older individuals. A progressive decrease in GLP1R in the mouse brain has previously been reported (*22*). One of the major sources of ^{68}Ga-exendin4 binding in the human pancreas is the β cells, which exhibit strong GLP1R expression (*23*). The known decline of β-cell number and function with age (*24*) thus presents a possible mechanism for this reduction in ^{68}Ga-exendin4 with increasing age. However, when we calculated the total GLP1R content (by multiplying ^{68}Ga-exendin4 binding by the pancreas volume), the negative correlation did not prevail.

We also visually observed a general trend toward higher ^{68}Ga-exendin4 uptake
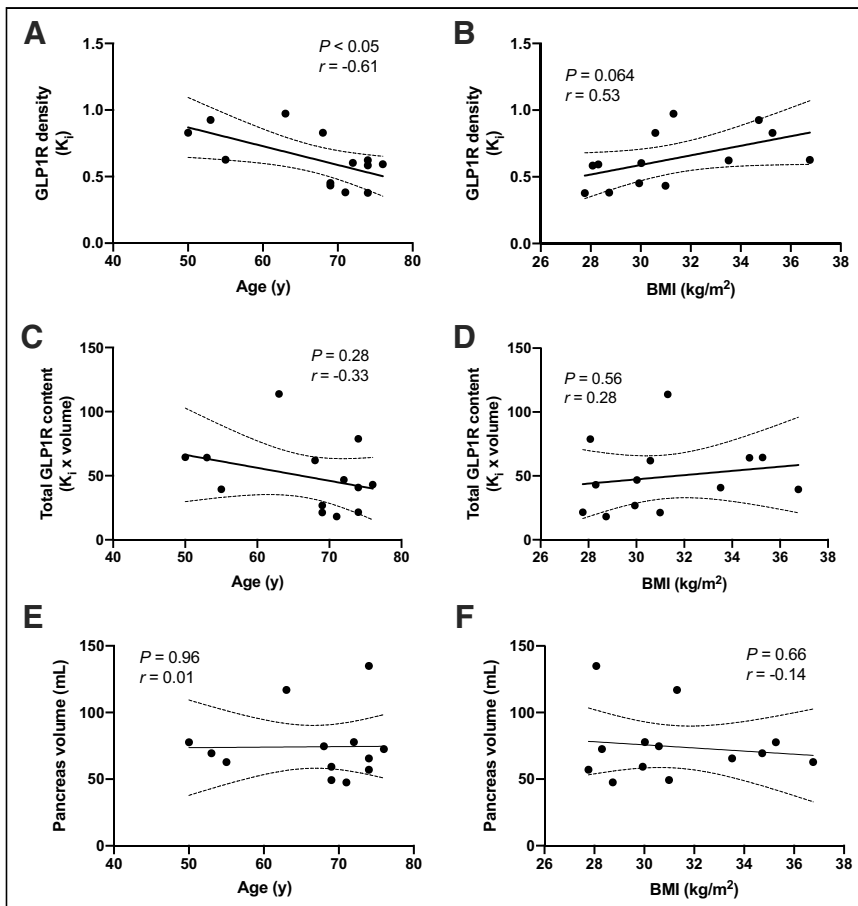

FIGURE 4. Correlation of ^{68}Ga-exendin4 pancreas binding with biometric parameters. (A and B) Pancreatic GLP1R density (concentration of ^{68}Ga-exendin4 binding) correlated negatively with age of examined individuals (A) and exhibited tendency to correlate with BMI (*P* = 0.064) (B). (C and D) However, total pancreas GLP1R content (i.e., ^{68}Ga-exendin4 concentration multiplied by volume) did not correlate with age (C) or BMI (D) of participants. (E and F) Similarly, size of pancreas did not correlate with either age (E) or BMI (F) in this study.

in the cauda of the pancreas in many individuals. This is again interesting in the context of β cells, since the cauda has been shown to exhibit approximately 2-fold the islet density of the caput and the corpus (25). Thus, we observed several features of the ^{68}Ga-exendin4 binding that were consistent with known β-cell distribution and function. Additionally, the large variability in ^{68}Ga-exendin4 observed here (almost 4-fold) is in line with the large variability in β-cell mass seen in individuals with T2D as assessed by biopsy morphometric studies (26). More studies dedicated to this question are required to further establish the association between ^{68}Ga-exendin4 binding and the β-cell mass in the human pancreas in T2D.

We observed a trend toward a positive correlation between ^{68}Ga-exendin4 binding and BMI in this cohort; that is, an increasing pancreatic GLP1R density correlated with a higher BMI. It is difficult to assess whether this is a reasonable observation, as there are limited data on GLP1R density in the pancreas of obese subjects—likely because of the challenge of obtaining diverse biopsy material of high quality, lack of reliable monoclonal antibodies for GLP1R, and the time-consuming effort required for sectioning, staining, and analyzing a sufficiently large dataset to draw firm conclusions. Again, the correlation with BMI did not remain when the total GLP1R content in the pancreas was estimated by multiplying by volume.

A limitation of the study and the correlations discussed above is the imbalanced sex distribution of the study population. Of the 13 included individuals, 12 were male and only 1 was female. Pancreatic binding in the female individual in this study was around the population average. However, the correlations seen here may reflect mainly the male population.

[68]Ga-exendin4 could conceivably serve as a biomarker for response to therapy. GLP1 efficacy studies sometimes delineate subgroups of nonresponding individuals—both in studies targeting populations with diabetes (27) and in studies targeting populations with neurologic disease (28). In this small cohort, some of the participants ($n = 7$) completed 3 wk of up-titration with the dual GLP1/glucagon agonist SAR425899, and all responded to treatment with blood glucose lowering and weight reduction, regardless of exhibiting a wide range of GLP1R density in the pancreas (12). Therefore, excessively up- or down-regulated GLP1R in the pancreas does not seem to predict GLP1 agonist responders or nonresponders in this admittedly small cohort.

CONCLUSION

We present an optimized and simplified ^{68}Ga-exendin4 scanning protocol to enable reproducible imaging of GLP1R in the human pancreas. ^{68}Ga-exendin4 PET may enable longitudinal quantification of changes in pancreatic GLP1R during the development of T2D, as well as target engagement studies of novel GLP1 agonists.

DISCLOSURE

ACKNOWLEDGMENTS

KEY POINTS

QUESTION: Can GLP1R density in the pancreas of individuals with T2D be evaluated by ^{68}Ga-exendin4 PET?

PERTINENT FINDINGS: ^{68}Ga-exendin4 binding in the T2D pancreas was high, consistent with the known expression patterns of GIP1R in the abdominal area. GLP1R density correlated inversely with the age of the individual and tended to correlate positively with BMI.

IMPLICATIONS FOR PATIENT CARE: ^{68}Ga-exendin4 PET may enable quantification of longitudinal changes in pancreatic GLP1R during the development of T2D, as well as target occupancy in drug development studies.

REFERENCES

1. Andersen A, Lund A, Knop FK, Vilsbøll T. Glucagon-like peptide 1 in health and disease. *Nat Rev Endocrinol.* 2018;14:390–403.
2. Marso SP, Daniels GH, Brown-Frandsen K, et al; LEADER Steering Committee; LEADER Trial Investigators. Liraglutide and cardiovascular outcomes in type 2 diabetes. *N Engl J Med.* 2016;375:311–322.
3. Marso SP, Bain SC, Consoli A, et al.; SUSTAIN-6 Investigators. Semaglutide and cardiovascular outcomes in patients with type 2 diabetes. *N Engl J Med.* 2016;375: 1834–1844.
4. Eng J, Kleinman WA, Singh L, Singh G, Raufman JP. Isolation and characterization of exendin-4, an exendin-3 analogue, from *Heloderma suspectum* venom: further evidence for an exendin receptor on dispersed acini from guinea pig pancreas. *J Biol Chem.* 1992;267:7402–7405.
5. Selvaraju RK, Velikyan I, Johansson L, et al. In vivo imaging of the glucagon like peptide-1 receptor in pancreas by [^{68}Ga]DO3A-exendin4. *J Nucl Med.* 2013;54: 1458–1463.
6. Boss M, Buitinga M, Jansen TJP, Brom M, Visser EP, Gotthardt M. PET-based human dosimetry of ^{68}Ga-NODAGA-exendin-4, a tracer for β-cell imaging. *J Nucl Med.* 2020;61:112–116.
7. Christ E, Wild D, Ederer S, et al. Glucagon-like peptide-1 receptor imaging for the localisation of insulinomas: a prospective multicentre imaging study. *Lancet Diabetes Endocrinol.* 2013;1:115–122.
8. Eriksson O, Velikyan I, Selvaraju RK, et al. Detection of metastatic insulinoma by positron emission tomography with [^{68}Ga]exendin-4: a case report. *J Clin Endocrinol Metab.* 2014;99:1519–1524.
9. Tillner J, Posch MG, Wagner F, et al. A novel dual glucagon-like peptide and glucagon receptor agonist SAR425899: results of randomized, placebo-controlled first-in-human and first-in-patient trials. *Diabetes Obes Metab.* 2019;21:120–128.
10. Frias JP, Nauck MA, Van J, et al. Efficacy and safety of LY3298176, a novel dual GIP and GLP-1 receptor agonist, in patients with type 2 diabetes: a randomised, placebo-controlled and active comparator-controlled phase 2 trial. *Lancet.* 2018; 392:2180–2193.
11. Brom M, Joosten L, Frielink C, et al. Validation of ^{111}In-exendin SPECT for the determination of the β-cell mass in BioBreeding diabetes-prone rats. *Diabetes.* 2018;67:2012–2018.
12. Eriksson O, Haack T, Hijazzi Y, et al. Receptor occupancy of dual glucagon-like peptide 1/glucagon receptor agonist SAR425899 in individuals with type 2 diabetes mellitus. *Sci Rep.* 2020;10:16758.

13. Logan J, Fowler JS, Volkow ND, et al. Graphical analysis of reversible radioligand binding from time–activity measurements applied to [N-^{11}C-methyl]-(−)-cocaine PET studies in human subjects. *J Cereb Blood Flow Metab.* 1990;10:740–747.

14. Patlak CS, Blasberg RG. Graphical evaluation of blood-to-brain transfer constants from multiple-time uptake data. Generalizations. *J Cereb Blood Flow Metab.* 1985;5:584–590.

15. Eriksson O, Velikyan I, Haack T, et al. Hepatic binding, biodistribution and dosimetry of glucagon receptor PET tracer [^{68}Ga]Ga-DO3A-VS-Tuna-2 in human subjects with type 2 diabetes. *J Nucl Med.* 2021;62:833–838.

16. Velikyan I, Rosenstrom U, Eriksson O. Fully automated GMP production of [^{68}Ga]Ga-DO3A-VS-Cys[40]-exendin-4 for clinical use. *Am J Nucl Med Mol Imaging.* 2017;7:111–125.

17. Selvaraju RK, Velikyan I, Asplund V, et al. Pre-clinical evaluation of [^{68}Ga]Ga-DO3A-VS-Cys[40]-exendin-4 for imaging of insulinoma. *Nucl Med Biol.* 2014;41:471–476.

18. Göke R, Fehmann HC, Linn T, et al. Exendin-4 is a high potency agonist and truncated exendin-(9-39)-amide an antagonist at the glucagon-like peptide 1-(7-36)-amide receptor of insulin-secreting beta-cells. *J Biol Chem.* 1993;268:19650–19655.

19. Eriksson O, Rosenström U, Eriksson B, Velikyan I. Species differences in pancreatic binding of DO3A-VS-Cys[40]-exendin4. *Acta Diabetol.* 2017;54:1039–1045.

20. Velikyan I, Bossart M, Haack T, et al. First-in-class positron emission tomography tracer for the glucagon receptor. *EJNMMI Res.* 2019;9:17.

21. Eriksson O, Velikyan I, Haack T, et al. Drug occupancy assessment at the gastric inhibitory polypeptide (GIP) receptor by positron emission tomography. *Diabetes.* 2021;70:842–853.

22. Wang L, Liu Y, Xu Y, et al. Age-related change of GLP-1R expression in rats can be detected by [^{18}F]AlF-NOTA-MAL-Cys[39]-exendin-4. *Brain Res.* 2018;1698:213–219.

23. Kirk RK, Pyke C, von Herrath MG, et al. Immunohistochemical assessment of glucagon-like peptide 1 receptor (GLP-1R) expression in the pancreas of patients with type 2 diabetes. *Diabetes Obes Metab.* 2017;19:705–712.

24. Kushner JA. The role of aging upon β cell turnover. *J Clin Invest.* 2013;123:990–995.

25. Wang X, Misawa R, Zielinski MC, et al. Regional differences in islet distribution in the human pancreas: preferential beta-cell loss in the head region in patients with type 2 diabetes. *PLoS One.* 2013;8:e67454.

26. Rahier J, Guiot Y, Goebbels RM, Sempoux C, Henquin JC. Pancreatic beta-cell mass in European subjects with type 2 diabetes. *Diabetes Obes Metab.* 2008;10(suppl 4):32–42.

27. Khan M, Ouyang J, Perkins K, Nair S, Joseph F. Determining predictors of early response to exenatide in patients with type 2 diabetes mellitus. *J Diabetes Res.* 2015;2015:162718.

28. Athauda D, Maclagan K, Skene SS, et al. Exenatide once weekly versus placebo in Parkinson's disease: a randomised, double-blind, placebo-controlled trial. *Lancet.* 2017;390:1664–1675.

^{18}F-FDOPA PET for the Noninvasive Prediction of Glioma Molecular Parameters: A Radiomics Study

TO THE EDITOR: We have read with interest the paper by Zaragori et al. about the role of PET using 6-^{18}F-fluoro-L-DOPA (^{18}F-FDOPA) in the prediction of molecular parameters by radiomics (*1*). We agree that radiomics is a promising approach to improve the accuracy of amino acid PET (*2*). This has been demonstrated, for example, for the differentiation of recurrent tumor from treatment-related changes (*3,4*).

Zaragori et al. report that radiomics features of static and dynamic ^{18}F-FDOPA data in patients with a neuropathologic diagnosis of grade II, III, or IV glioma were able to predict IDH mutations and the 1p/19q codeletion with an area under the curve of 0.831 and 0.724, respectively. The authors conclude that ^{18}F-FDOPA PET using a full set of radiomics features is an effective tool for the noninvasive prediction of IDH mutations and for prediction of the 1p/19q codeletion in routine practice.

Although we have no doubt about the quality of the study, we would like to point out a problem with the preselection of patients. For this study, 74 patients with grade II–IV gliomas were retrospectively selected from a larger collective. The authors assume that the results of the study are valid for the noninvasive prediction of molecular parameters in patients with suspected glioma, that is, in the setting of preoperative diagnostics in which, apart from clinical and radiologic parameters, no information is available about the histology of the tumors.

Previous studies investigating the final diagnosis of patients referred for amino acid PET with suspected brain tumor, however, reported that 20%–40% had benign lesions or nonglial tumors (e.g., inflammation, ischemia, or lymphoma) (*5–7*). The radiomic features of these lesions were not considered in the present analysis and could significantly affect the results of the study. Therefore, the validity of the study for noninvasive prediction of molecular parameters in the setting of preoperative diagnostics is at least doubtful.

A similar issue could also be observed in another recently published study (*8*), which investigated the prediction of TERTp mutation status in IDH wild-type (IDHwt) high-grade gliomas using pretreatment dynamic *O*-(2-^{18}F-fluoroethyl)-L-tyrosine (^{18}F-FET) PET radiomics. In that study, patients with IDHwt tumors were selected from a mixed population of patients, and the authors reported that radiomics based on time-to-peak images extracted from dynamic ^{18}F-FET PET scans could predict the TERTp mutation status of IDHwt diffuse astrocytic high-grade gliomas with high accuracy preoperatively. Since the IDH mutation status in the preoperative population is not known, the analysis is considerably affected by the IDH-negative gliomas and benign lesions, and the validity of this study also—in the setting of preoperative diagnostics—has to be viewed with great caution.

Summarizing, we would like to point out that image analysis methods aiming at noninvasive prediction of molecular parameters have to be based on a representative preoperative population. Preselection of such populations based on postoperative histologic data leads to an erroneous and not clinically useful conclusion.

We conclude that the results of such studies can be considered only as hypotheses and have no relevance for clinical practice.

REFERENCES

1. Zaragori T, Oster J, Roch V, et al. ^{18}F-FDOPA PET for the noninvasive prediction of glioma molecular parameters: a radiomics study. *J Nucl Med.* 2022;63:147–157.
2. Lohmann P, Galldiks N, Kocher M, et al. Radiomics in neuro-oncology: basics, workflow, and applications. *Methods.* 2021;188:112–121.
3. Ahrari S, Zaragori T, Rozenblum L, et al. Relevance of dynamic ^{18}F-DOPA PET radiomics for differentiation of high-grade glioma progression from treatment-related changes. *Biomedicines.* 2021;9:1924.
4. Lohmann P, Elahmadawy MA, Gutsche R, et al. FET PET radiomics for differentiating pseudoprogression from early tumor progression in glioma patients post-chemoradiation. *Cancers (Basel).* 2020;12:3835.
5. Pichler R, Dunzinger A, Wurm G, et al. Is there a place for FET PET in the initial evaluation of brain lesions with unknown significance? *Eur J Nucl Med Mol Imaging.* 2010;37:1521–1528.
6. Rapp M, Heinzel A, Galldiks N, et al. Diagnostic performance of ^{18}F-FET PET in newly diagnosed cerebral lesions suggestive of glioma. *J Nucl Med.* 2013;54:229–235.
7. Hutterer M, Nowosielski M, Putzer D, et al. [F-18]-fluoro-ethyl-L-tyrosine PET: a valuable diagnostic tool in neuro-oncology, but not all that glitters is glioma. *Neuro Oncol.* 2013;15:341–351.
8. Li Z, Kaiser L, Holzgreve A, et al. Prediction of TERTp-mutation status in IDH-wild-type high-grade gliomas using pre-treatment dynamic [^{18}F]FET PET radiomics. *Eur J Nucl Med Mol Imaging.* 2021;48:4415–4425.

Karl-Josef Langen*
Felix M. Mottaghy
**Forschungszentrum Jülich*
Jülich, Germany
E-mail: k.j.langen@fz-juelich.de

Reply: ^{18}F-FDOPA PET for the Noninvasive Prediction of Glioma Molecular Parameters: A Radiomics Study

REPLY: We read with interest the letter to the editor by Langen and colleagues in response to our recent study published in *The Journal of Nuclear Medicine* (1). We agree with them that radiomics analysis is a promising approach for PET imaging in neurooncology, although its application in clinical practice needs to be defined more precisely on the basis of the clinical question at hand. The added value of 6-^{18}F-fluoro-L-DOPA (^{18}F-FDOPA) PET radiomics over conventional static analysis, derived from SUV parameters, appears to hold more promise for the initial diagnosis (1) than for detecting recurrent disease (2). Extensive effort is also needed to study these radiomics tools prospectively, including in a real clinical setting of nonglioma lesion, as well as to make these tools available and amenable to accurate interpretation by nuclear physicians in clinical routine practice. We would like to respond to this letter by raising 3 points.

First, and from a methodologic point of view, radiomics analysis needs to be compared with a robust benchmark (*3,4*). Immunohistologic analysis of tumor samples is still considered the gold standard for defining brain tumors at the initial diagnosis. Although these
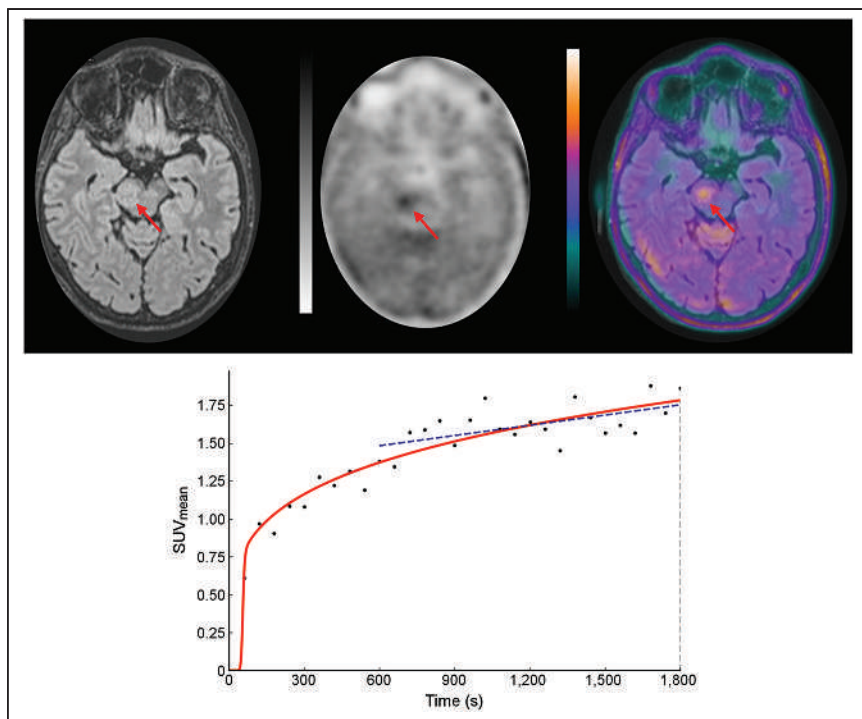
FIGURE 1. Axial slices of inflammatory lesion of midbrain (arrows) in hypersignal fluid-attenuated inversion recovery MRI (top left panel), showing moderate ^{18}F-FDOPA uptake in PET image (top middle panel) and PET/MR image (top right panel) in 68-y-old woman. Interestingly, dynamic acquisitions (bottom panel) showed constantly increasing SUV curve suggestive of nonaggressive lesion.

analyses are considered as the reference in oncology, we know that they suffer from several limitations. Information extracted from immunohistologic analysis is representative of only the region from which the sample was taken and of only the time of collection, which means that this type of analysis is both spatially (5–7) and temporally limited (8). In this vein and for lack of a better alternative, the recently published retrospective amino acid PET radiomics studies exploring the prognostic benefits of molecular parameters of brain tumors at initial diagnosis were, similarly to ours, all based on immunohistologic analyses (9–11). In differential diagnoses, brain tumors, brain inflammatory lesions, ischemia, or primary central nervous system lymphomas are typically "do not touch" lesions (12), with correspondingly very low rates of available histologic analyses, which restricts their inclusion in these types of retrospective studies. In their study, Renard et al. (13) underline that less than one third of their pseudotumor patients had available histology.

Second, PET imaging in neurooncology needs be interpreted in the era of multimodal and multiparametric approaches as advocated by the current European guidelines, which recommend amino acid PET at the initial tumor diagnosis as an adjunct to MRI (14). High-grade gliomas may be accurately distinguished from primary central nervous system lymphomas using morphologic MRI (15), with recent MRI technical advances expected to further increase performance in differentiating from inflammatory brain lesions (16). These improvements in MRI-based brain lesion characterizations will allow more specific identification of the best candidate brain lesions to refer for amino acid PET imaging. Moreover, conventional static analysis of ^{18}F-FDOPA PET imaging is also useful in discriminating between pseudotumoral and tumoral lesions (13).

Finally, the 2 amino acid PET studies mentioned by Langen and colleagues (1,11) reported the prognostic significance of dynamic

parameters, obtained from VOI-based or voxel-based extractions combined with radiomics analysis, for respectively predicting IDH and TERTp mutations. As already extensively discussed elsewhere (17), aggressive brain gliomas are associated with high tracer uptake within the first few minutes after injection followed by a decrease in the uptake curve, whereas less aggressive gliomas typically show a slow increase in amino acid uptake, with the highest values observed at later time frames. Amino acid PET imaging of brain inflammation is also associated with a consistently increasing SUV curve (14). Figure 1 provides representative ^{18}F-FDOPA PET images of a brain inflammation case. Other dynamic amino acid PET studies also suggest that lymphomas (18) and benign lesions (19) show dynamic patterns similar to the ones observed in less aggressive gliomas. Dynamic PET imaging of brain lesions at the initial diagnosis, in addition to conventional static analysis (13), should therefore help identify nonglioma brain lesions. This possibility will, of course, need to be further confirmed by well-designed prospective studies.

To summarize, radiomics analysis of amino acid PET imaging has the potential to emerge as a truly effective tool for the noninvasive characterization of gliomas, provided that multimodal and multiparametric imaging is used. Currently, the primary aim of radiomics analyses in neurooncology is to generate hypotheses with promising results, to consider in a next step toward prospective evaluation in the real clinical setting.

REFERENCES

1. Zaragori T, Oster J, Roch V, et al. ^{18}F-FDOPA PET for the noninvasive prediction of glioma molecular parameters: a radiomics study. *J Nucl Med.* 2022;63:147–157.
2. Ahrari S, Zaragori T, Rozenblum L, et al. Relevance of dynamic ^{18}F-DOPA PET radiomics for differentiation of high-grade glioma progression from treatment-related changes. *Biomedicines.* 2021;9:1924.
3. Lohmann P, Galldiks N, Kocher M, et al. Radiomics in neuro-oncology: basics, workflow, and applications. *Methods.* 2021;188:112–121.
4. Orlhac F, Nioche C, Klyuzhin I, Rahmim A, Buvat I. Radiomics in PET imaging. *PET Clin.* 2021;16:597–612.
5. Gerlinger M, Rowan AJ, Horswell S, et al. Intratumor heterogeneity and branched evolution revealed by multiregion sequencing. *N Engl J Med.* 2012;366:883–892.
6. Bettoni F, Masotti C, Habr-Gama A, et al. Intratumoral genetic heterogeneity in rectal cancer: are single biopsies representative of the entirety of the tumor? *Ann Surg.* 2017; 265:e4–e6.
7. Zhang XC, Xu C, Mitchell RM, et al. Tumor evolution and intratumor heterogeneity of an oropharyngeal squamous cell carcinoma revealed by whole-genome sequencing. *Neoplasia.* 2013;15:1371–1378.
8. Sequist LV, Waltman BA, Dias-Santagata D, et al. Genotypic and histological evolution of lung cancers acquiring resistance to EGFR inhibitors. *Sci Transl Med.* 2011;3:75ra26.
9. Lohmann P, Lerche C, Bauer EK, et al. Predicting IDH genotype in gliomas using FET PET radiomics. *Sci Rep.* 2018;8:13328.

10. Haubold J, Demircioglu A, Gratz M, et al. Non-invasive tumor decoding and pheno-typing of cerebral gliomas utilizing multiparametric ^{18}F-FET PET-MRI and MR Fingerprinting. *Eur J Nucl Med Mol Imaging.* 2020;47:1435–1445.

11. Zhicong Li, Kaiser L, Holzgreve A, et al. Prediction of TERTp-mutation status in IDH-wildtype high-grade gliomas using pre-treatment dynamic ^{18}F-FET PET radiomics. *Eur J Nucl Med.* 2021;48:4415–4425.

12. Huisman TAGM. Tumor-like lesions of the brain. *Cancer Imaging.* 2009;9 Spec No A:S10–S13.

13. Renard D, Collombier L, Laurent-Chabalier S, et al. ^{18}F-FDOPA-PET in pseudotumoral brain lesions. *J Neurol.* 2021;268:1266–1275.

14. Law I, Albert NL, Arbizu J, et al. Joint EANM/EANO/RANO practice guidelines/SNMMI procedure standards for imaging of gliomas using PET with radiolabelled amino acids and [18F]FDG: version 1.0. *Eur J Nucl Med Mol Imaging.* 2019;46:540–557.

15. Malikova H, Koubska E, Weichet J, et al. Can morphological MRI differentiate between primary central nervous system lymphoma and glioblastoma? *Cancer Imaging.* 2016;16:40.

16. Han Y, Yang Y, Shi Z, et al. Distinguishing brain inflammation from grade II glioma in population without contrast enhancement: a radiomics analysis based on conventional MRI. *Eur J Radiol.* 2021;134:109467.

17. Verger A, Imbert L, Zaragori T. Dynamic amino-acid PET in neuro-oncology: a prognostic tool becomes essential. *Eur J Nucl Med Mol Imaging.* 2021;48:4129–4132.

18. Aki T, Nakayama N, Yonezawa S, et al. Evaluation of brain tumors using dynamic ^{11}C-methionine-PET. *J Neurooncol.* 2012;109:115–122.

19. Chan DL, Hsiao E, Schembri G, et al. FET PET in the evaluation of indeterminate brain lesions on MRI: Differentiating glioma from other non-neoplastic causes – A pilot study. *J Clin Neurosci.* 2018;58:130–135.

Timothée Zaragori
Antoine Verger*
Université de Lorraine
Nancy, France
E-mail: a.verger@chru-nancy.fr

Single–Time-Point Tumor Dosimetry Assuming Normal Distribution of Tumor Kinetics

TO THE EDITOR: An excellent recent review by Sgouros et al. on the multifaceted complexities of tumor dose–response was highly informative (*1*). However, it did not address a practical aspect—how to routinely implement tumor dosimetry in the context of today's stifling economic mantra of "cheaper, better, faster." The fine balancing act between clinical needs and health-care economics is an everyday challenge in any busy clinic. But there is hope, in the form of single–time-point dosimetry as a compromise for resource-intensive multiple–time-point imaging.

Previous work by Hänscheid et al. on single–time-point dosimetry works well for normal organs, but its application to metastases is questionable because of widely heterogeneous tumor biology (*2*). Tumors are, by definition, inherently abnormal. Therefore, the effective half-life (T_{eff}) of any tumor type will have a wide spread of values. This means that a single average T_{eff} defined for a tumor type might not be sufficiently personalized to an individual patient.

An alternative framework for single–time-point tumor dosimetry is proposed here to complement that by Hänscheid et al. (*2*). It assumes a normal distribution of tumor T_{eff} around its mean and uses ± 1 SD to rationalize tumor T_{eff} values for faint (poor), mild (weak), moderate (good), and intense (excellent) tumor avidity. Whichever method of single–time-point tumor dosimetry the user

eventually chooses will depend on whether each method's assumptions are reasonably valid for the patient at hand.

To illustrate this alternative method, let us consider ^{131}I-avid bone metastases from differentiated thyroid cancer. For this exercise, it is necessary to quote preliminary data. From a very small dataset of 8 bone metastases by 2 studies (6 lesions) and 2 lesions from our own data, the mean tumor T_{eff} in ^{131}I-avid bone metastasis prepared by thyroid hormone withdrawal was approximately 4.07 ± 2.52 d (*3,4*). Its wide SD reflects the highly heterogeneous biology of metastases.

Next, we invoke the central-limit theorem to assume a normal distribution of tumor T_{eff} around its mean. This assumption is obviously false in the current example of only 8 lesions but will eventually trend closer to the truth with future additional data. Within this normal distribution framework, bone metastases that are visually assessed to have faint ^{131}I avidity will be to the left of -1 SD (T_{eff}, <1.55 d), mild avidity will be at -1 SD (T_{eff}, 1.55 d), moderate avidity will be at the mean (T_{eff}, 4.07 d), and intense avidity will be at $+1$ SD (T_{eff}, 6.59 d). The visual classification of ^{131}I avidity may be referenced to the liver, analogous to the Krenning score (*5*).

Lesion mass is measured by sectional volumetry. Lesion activity at time t (d) after administration of ^{131}I is measured by calibrated scintigraphy. Finally, the tumor-absorbed dose (Gy) may be calculated by the method described by Jentzen et al., which assumes a linear initial time–activity concentration rate and a time to peak tumor uptake of 8 h, followed by monoexponential clearance in accordance with tumor T_{eff} (*6*). This alternative method of single–time-point dosimetry could also be applied to ^{131}I-avid soft-tissue metastases, with preliminary data suggesting that the mean tumor T_{eff} prepared by thyroid hormone withdrawal could be approximately 2.55 ± 0.35 d (*7,8*).

REFERENCES

1. Sgouros G, Dewaraja YK, Escorcia F, et al. Tumor response to radiopharmaceutical therapies: the knowns and the unknowns. *J Nucl Med.* 2021;62(suppl 3):12S–22S.

2. Hänscheid H, Lapa C, Buck AK, Lassmann M, Werner RA. Dose mapping after endoradiotherapy with ^{177}Lu-DOTATATE/DOTATOC by a single measurement after 4 days. *J Nucl Med.* 2018;59:75–81.

3. Eschmann SM, Reischl G, Bilger K, et al. Evaluation of dosimetry of radioiodine therapy in benign and malignant thyroid disorders by means of iodine-124 and PET. *Eur J Nucl Med Mol Imaging.* 2002;29:760–767.

4. Pötzi C, Moameni A, Karanikas G, et al. Comparison of iodine uptake in tumour and nontumour tissue under thyroid hormone deprivation and with recombinant human thyrotropin in thyroid cancer patients. *Clin Endocrinol (Oxf).* 2006;65:519–523.

5. Hofman MS, Lau WF, Hicks RJ. Somatostatin receptor imaging with ^{68}Ga DOTA-TATE PET/CT: clinical utility, normal patterns, pearls, and pitfalls in interpretation. *Radiographics.* 2015;35:500–516.

6. Jentzen W, Freudenberg L, Eising EG, Sonnenschein W, Knust J, Bockisch A. Optimized [124]I PET dosimetry protocol for radioiodine therapy of differentiated thyroid cancer. *J Nucl Med.* 2008;49:1017–1023.

7. Maxon HR, Thomas SR, Hertzberg VS, et al. Relation between effective radiation dose and outcome of radioiodine therapy for thyroid cancer. *N Engl J Med.* 1983;309:937–941.

8. Kumar P, Bal C, Damle NA, Ballal S, Dwivedi SN, Agarwala S. Lesion-wise comparison of pre-therapy and post-therapy effective half-life of iodine-131 in pediatric and young adult patients with differentiated thyroid cancer undergoing radioiodine therapy. *Nucl Med Mol Imaging.* 2019;53:199–207.

Yung Hsiang Kao
The Royal Melbourne Hospital
Melbourne, Australia
E-mail: yung.kao@mh.org.au

Reply: Single–Time-Point Tumor Dosimetry Assuming Normal Distribution of Tumor Kinetics

REPLY: We thank Dr. Kao for carefully reading our article (*1*) and for illustrating the value of single–time-point imaging in the practical implementation of patient-specific dosimetry for radiopharmaceutical therapy. We chose to focus on fundamental knowns and unknowns, particularly tumor dose–response relationships, rather than addressing the admittedly challenging logistics of patient-specific dosimetry. As noted in Dr. Kao's letter, single–time-point formulations exist that may be applied to normal-organ and tumor-absorbed doses, although due to the potentially larger variability in tumor kinetics there may be larger error associated with application to tumor. However, the error in the tumor activity quantification step, depending on tumor size, likely dominates the uncertainty in the dose calculations. Overall, the uncertainty associated with single–time-point methods is unlikely to be clinically impactful. Clinical experience suggests that a severalfold difference in tumor-absorbed dose is needed to overcome the impact of differences in tumor radiosensitivity, dose distribution within the tumor, dose-rate differences, and other biologic effects that impact tumor response to therapy in patients.

Recognizing the imperative of achieving the right balance, we would promote an approach that enables the treating physician—in establishing treatment doses—to consider the multifaceted trade-offs among absorbed dose accuracy, health economics, the challenges of a busy clinic, and the clinical aspects of the disease. By defining a level of certainty or uncertainty in all calculated absorbed dose values, including those obtained by reduced–time-point or single–time-point methods, the treating physician is provided the information needed to make what is ultimately a clinical decision for a specific patient. If, on the basis of the disease extent and endpoints to be achieved, the physician seeks greater precision in the normal-organ and tumor-absorbed dose estimates, an extended multiple–time-point imaging protocol may be devised in conjunction with the medical physicist.

It is encouraging that in addition to the work described in the letter, the loss of accuracy associated with using a single imaging time point compared with using multiple time points has been recently investigated. Among the ever-growing list of papers in this area, we note the early work on peptide receptor radionuclide therapy by Madsen et al. (*2*) and Hänscheid et al. (*3*) and the more recent extension of this approach to other RPTs by Hou et al. (*4*) and Jackson et al. (*5*).

We thank Dr. Kao and *The Journal of Nuclear Medicine* editor-in-chief for giving us the opportunity to address this important topic.
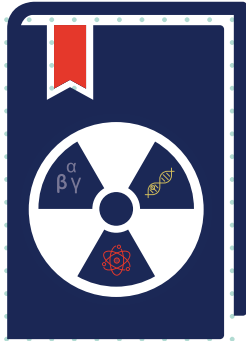
REFERENCES

1. Sgouros G, Dewaraja YK, Escorcia F, et al. Tumor response to radiopharmaceutical therapies: the knowns and the unknowns. *J Nucl Med.* 2021;62(suppl 3):12S–22S.
2. Madsen MT, Menda Y, O'Dorisio TM, O'Dorisio MS. Technical note: single time point dose estimate for exponential clearance. *Med Phys.* 2018;45:2318–2324.
3. Hänscheid H, Lapa C, Buck AK, Lassmann M, Werner RA. Dose mapping after endoradiotherapy with ^{177}Lu-DOTATATE/DOTATOC by a single measurement after 4 days. *J Nucl Med.* 2018;59:75–81.
4. Hou X, Brosch J, Uribe C, et al. Feasibility of single-time-point dosimetry for radiopharmaceutical therapies. *J Nucl Med.* 2021;62:1006–1011.
5. Jackson PA, Hofman MS, Hicks RJ, Scalzo M, Violet J. Radiation dosimetry in ^{177}Lu-PSMA-617 therapy using a single posttreatment SPECT/CT scan: a novel methodology to generate time- and tissue-specific dose factors. *J Nucl Med.* 2020;61:1030–1036.

George Sgouros*
Yuni K. Dewaraja
Freddy Escorcia
Stephen A. Graves
Thomas A. Hope
Amir Iravani
Neeta Pandit-Taskar
Babak Saboury
Sara St. James
Pat B. Zanzonico
*Johns Hopkins University
Baltimore, Maryland
E-mail: gsgouros@jhmi.edu

A STREAMLINED CLINICAL CARE PATH ENABLED BY DIGITAL 360° SPECT/CT IMAGING

VERITON-CT®
DIGITAL SPECT/CT

Optimization of every step

For optimal patient outcomes, clinicians require access to imaging that ensures the most accurate diagnosis and appropriate treatment management decisions.

Spectrum Dynamics has integrated its ground-breaking Broadview Technology design into the VERITON-CT system, providing a digital platform that handles routine 3D workflow in one place. The result is optimization of every step, from image acquisition to interpretation.
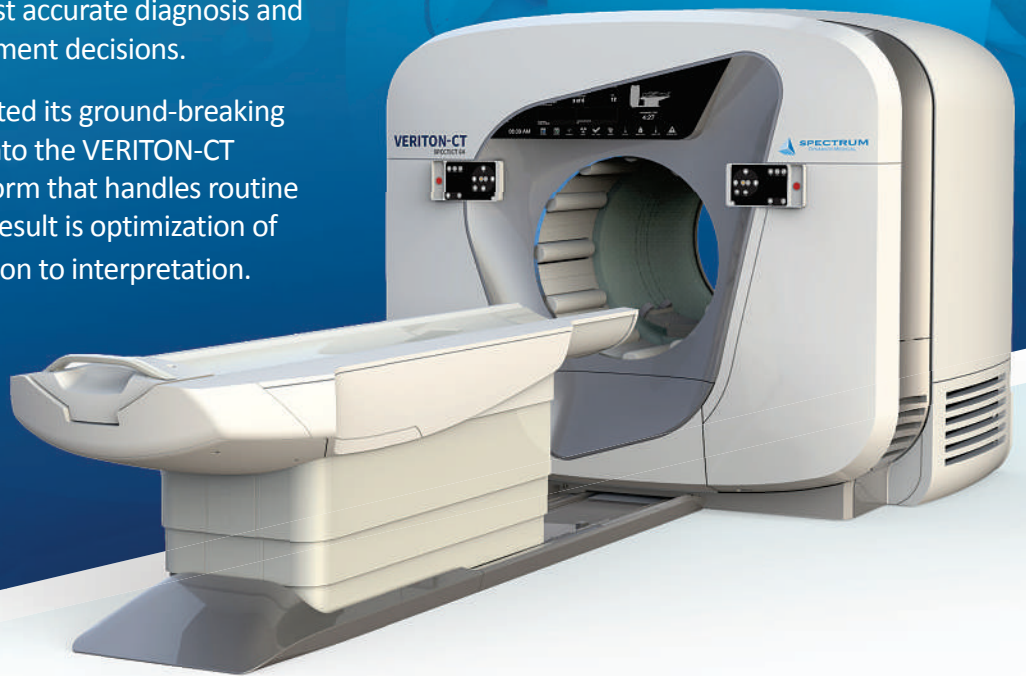
VERITON-CT digital SPECT/CT combines the best-in-class CZT detectors, novel system design, high resolution CT, and advanced software technology to elevate the performance of CZT digital SPECT.

Digital Technology
360° design for high sensitivity and coverage
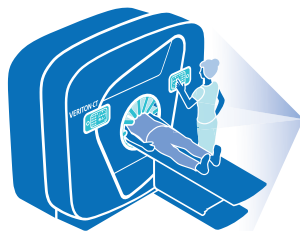
Workflow is reproducible and optimized for patient needs

Image quality tools in TruView Console for advanced reconstruction and artifact reduction for both NM and CT data

Quantitative analysis accessible in TruView Console integration with MIM-SD platform

Comprehensive results from transformative technology that provides a greater volume of high quality data for informed decision-making

SPECTRUM DYNAMICS MEDICAL

spectrum-dynamics.com